Title
Reconstruction of microbial and environmental conditions in an Australian hypersaline ecosystem from the mid-Pleistocene through the present

Author
Jones, Claudia Meredith

Publication Date
2011

Peer reviewed|Thesis/dissertation

Reconstruction of microbial and environmental conditions in an Australian hypersaline ecosystem from the mid-Pleistocene through the present

by

Claudia Meredith Jones

A dissertation submitted in partial satisfaction of the

requirements for the degree of

Doctor of Philosophy

in

Earth and Planetary Sciences

in the

Graduate Division

of the

University of California, Berkeley

Committee in charge:

Professor Jillian F. Banfield, Chair
Professor James Bishop
Professor Jochen Brocks
Professor Robert C. Rhew

Fall 2011

Reconstruction of microbial and environmental conditions in an Australian hypersaline ecosystem from the mid-Pleistocene through the present

by Claudia Meredith Jones

Abstract

Reconstruction of microbial and environmental conditions in an Australian hypersaline ecosystem from the mid-Pleistocene through the present

by

Claudia Meredith Jones

Doctor of Philosophy in Earth and Planetary Sciences

University of California, Berkeley

Professor Jillian F. Banfield, Chair

Global-scale climate change is an extensively studied topic: researchers monitor climatic indicators from sea surface temperature to atmospheric CO_2 concentrations. However, historical records do not exist on timescales sufficiently extensive to permit projection of future events. To remedy this situation, researchers utilize data collected from sediments and rock formations deposited in pre-historical times in order to refine the predictive capabilities of current climate models. One can see from the relatively small number of datasets comprising samples from both the northern and southern hemispheres that climate change through time has not been uniform across the globe.

Complicating the interpretation of this variability is the dearth of data sets from the southern hemisphere. Many of the data sets generated from samples collected in the southern hemisphere are derived from strata deposited in marine environments. Therefore, while we can, with reasonable certainty, reconstruct temperature at the sea surface and conditions in the atmosphere, scenarios that quantify the magnitude and geographic extent of climatic change occurring on southern continents are less clear. This problem is due in part to sampling bias and to the smaller land mass in the southern hemisphere.

This research provides empiric (as opposed to model-based) constraints on regional climate shifts in southeastern Australia through multiple glacial-interglacial cycles over the past ~400 ka. Because lake sediment records have the potential to provide a contiguous history of temperature and aridity in a terrestrial environment, we collected cores from the lakebed and through the lunette of Lake Tyrrell in northern Victoria, Australia. Lake Tyrrell is hypersaline and ephemeral; consequently, deflation of sediments has created gaps in the sediment sequence, and many sedimentary elements traditionally used for palaeoenvironmental reconstruction are poorly-preserved or absent. Since all of the lakes in the region share these limitations, it was necessary to develop methods to extract useful information from the available sampling sites.

As a new approach, we combined the analyses of the identities, quantities and isotopic signatures of preserved lipid biomarkers with traditional proxies such as pollen, charcoal, mineral content and sedimentary textures. Together, these data describe changes in the chemistry

of the lake, in the community composition of microbes within the lake, and in the higher plant ecosystem around the lake and within the catchment.

Evidence of at least three glacial-interglacial cycles is preserved in Tyrrell lakebed and lunette sediments, though the temporal sequence is uncertain due to the lack of dateable materials within the Tyrrell sediments. During what we interpret as the two most recent glacial maxima (~20 ka and 140 ka), the lake dried completely and higher plants colonized the surface following leaching of salt from the surface sediment. At one of the two preceding glacial maxima (either 260 ka or 340 ka), the lake dried to <1m depth, became groundwater-fed, and supported the growth of microbial mats. These mats colonized the interface between the halite crust and the sediment surface. Halophilic archaea and algae lived within the water column. Both the chemistry and microbiology of the lake were comparable to the modern system. During interglacial periods, increased precipitation and runoff increased lake depth to several meters. Lower salinity promoted the growth of dinoflagellates and eustigmatophyte algae in the water column, and of anaerobic bacteria within sediments.

In contrast to the shifts in lake water levels and chemistry, the plant community within the catchment stayed relatively constant through the end of the Pleistocene. It was composed of a dryland casuarina wood with a grassy understory. During the Holocene, increased precipitation following the last glacial maxima (LGM) caused the casuarina woodland to be replaced by *Callitris* thickets and grasses. Two shifts in the isotopic signature of plant waxes indicate changes in the relative abundance of C_3 vs C_4 grasses over this period. Increased dominance of C_4 grasses following the last glacial maximum points to a strengthening in the Australian summer monsoon. Although direct dating was not possible, periods of increased precipitation between 7.5 – 9.5 ka and 11.5 – 13.5 ka are recorded at proximitous sites. Lake Tyrrell is currently the southernmost terrestrial site from which this precipitation increase has been reported. Over the past 200 years, land use practices following European settlement have caused C_3 grasses to become increasingly dominant.

The data presented here demonstrate that it is possible to obtain information about the timing and extent of climate change in Australia through the Pleistocene and Holocene from ephemeral salt lake sediments. Lipid biomarkers are a particularly useful proxy, as they are preserved even in oxidized, saline sediments. Moreover, they provide taxa-specific information on organisms living within and around lakes, and can be used to reconstruct palaeo-temperatures and lake levels. Isotopic analyses of individual biomarkers, when interpreted in conjunction with charcoal and pollen, generate a picture of the changes in the terrestrial plant ecosystem of the catchment. By employing lipid biomarker analysis alongside traditional proxies, researchers can more accurately quantify changes in palaeo-climate at the regional scale, in order to refine predictive models of continental and global scale climate change.

Table of Contents

Appendices

Dedication

This work is dedicated to my mother and father, Wendy and Timothy Jones. Their guidance and support have been invaluable to me throughout my life.

Acknowledgments

I would like to thank my advisor and committee chair, Dr. Jillian F. Banfield, for her guidance and support during my graduate studies. Her ideas, encouragement and critiques made me a better researcher and contributed to my growth as a human being.

I would also like to thank Dr. Jochen J. Brocks of the Australian National University (ANU), who acted as my research host, advisor, scientific advocate and sounding board during my tenure as a guest researcher at the ANU. Our academic discussions greatly enhanced my ability to think critically and dispassionately about my work.

I thank Drs. James Bishop and Robert Rhew for their critical reading of and comments on my dissertation chapters. The clarity and force of the arguments presented therein were much improved by their input.

The following individuals are thanked for academic discussions, guidance and support during the course of my graduate studies: Drs. Gomaa Omar and Robert Giegengack of the University of Pennsylvania; Dr. Andrew Pike of the NOAA; Dr. Karla Heidelberg of the University of Southern California; Dr. Eric Allen of UC San Diego; Dr. John Volkman of CSIRO Hobart; Drs. John Moreau and Jim Bowler of the University of Melbourne; Dr. Jon Luly of James Cook University; Drs. John Magee, Mat Prebble, Patrick DeDeckker, Ulrike Troitzsch, and Richard Armstrong of the Australian National University; Dr. Emmanuelle Grosjean of Geoscience Australia; Dr. Warren Sharpe of the Berkeley Geochronology Center; and all members of the Brocks (2007-2011) and Banfield (2005-2011) research groups.

For assistance with instrumentation and analysis, the following individuals are thanked: Tim Teague and Kent Ross of UC Berkeley, Janet Hope and Drs. Ulrike Troitzsch and Linda McMorrow of the Australian National University, Bernd Kopke and Dr. Jürgen Rüllkotter of the Institute of Chemistry and Biology of the Marine Environment at the University of Oldeburg, Dr. Emma Pearson at Newcastle University, Ursula Pietrzak of the Centre for Palynology and Palaeoecology at Monash University, and Geotechnical Services, Inc.

For administrative and technical support, I thank Margie Winn, Micaelee Ellswythe, Gretchen von Duering, Marilyn Saarni and Charley Paffenbarger of the Department of Earth & Planetary Science at UC Berkeley, and Robyn Petch, Nigel Craddy and Damien Kelleher of the Research School of Earth Sciences at the Australian National University.

For providing access and permission to collect at the sampling sites, I thank Cheetham Salt Works, the Department of Planning and Community Development of Victoria and the Aboriginal Affairs Victoria Heritage Services.

Finally, I would like to thank my friends and family for their unwavering support throughout my academic career.

List of Figures

List of Tables

List of Equations

Chapter 1.

Introduction

Palaeoenvironmental science is the study of past environments, and of changes in an environment through time. The data gathered describe the geology, chemistry and organismal community of a defined area at a specific point in time, which researchers use to reconstruct landscapes of the past. Multiple reconstructions for a single geographic location can be created by sampling many time points at that location. Subsequently, such reconstructions are contextualized by studies of modern ecosystems, in order to identify the physical factors that control the process of ecosystem evolution. In this way, studies of palaeoenvironments provide information about the changes in regional climate that occurred during the time window sampled. Finally, reconstructions from different geographic locations across the globe can be concatenated to describe global-scale climate shifts.

Lake basins are particularly useful in palaeoenvironmental studies, because they are sites where sediments are deposited relatively continuously. Australia is a fairly arid continent, with few large, permanent lakes, so most palaeo-climate studies of the region are based on marine sediment cores. At the same time, it is known that modern conditions on the Australian continent are particularly sensitive to climatic shifts, which are not expressed consistently across the continent. This means that terrestrially-based, regional records of the effects of climate change on Australia are of value. In this work, I reconstruct regional climatic conditions in southeastern Australia from the late Pleistocene (~400 ka) through the present using data from sediment cores collected at a hypersaline lake.

1.1 Lake Tyrrell – geography, hydrology, geochemistry

Lake Tyrrell lies approximately in the center of the Murray Basin Plains, in a region known as the Mallee. This region is characterized by its distinctive vegetation, which is dominated by Mallee gums (a growth type of eucalypt in which many small stems rise from a central bole), grasses and salt tolerant shrubs (Hills 1940). Rainfall averages between 300-400 mm per year (Luly 1990). However, evaporation rates are much higher – over 1300 mm per year (Bowler and Teller 1986). Thus, Lake Tyrrell is located in the semi-arid or sub-arid region of northwestern Victoria, which, as defined by Hills (1940), is an area with “a climate that is essentially arid during the dry season, and sub-arid or even pluvial during the wet season”. In such regions during the arid summers, drought conditions ensue and streams cease to flow, as is the case at Lake Tyrrell.

The hydrology of the lake has been extensively reviewed by Macumber (1991) and others; only a brief summary will be presented here. Lake Tyrrell is the largest salt lake in Victoria (Bowler and Magee 1978), occupying its own basin 35 km in diameter created by a downwarping of Tertiary sediments to the east of the Tyrrell fault (Macumber 1991). This fault also acts as a groundwater divide, such that groundwater entering the lake originates from the sinking of brines in Lakes Timboram and Wahpool, located to the east of Lake Tyrrell (Figure 1.1) (Dickson and Giblin 2009). Additional water enters the lake through the intermittent flow of Tyrrell Creek (Figure 1.1); however, the main source of water to the lake is groundwater, by way of reflux brines through the lake floor (Macumber 1991) and along the margins in the ‘spring zone’ (Dickson and Giblin 2009). Tyrrell is essentially a groundwater discharge point whose

location is determined by the intersection of the floor of the basin and the potentiometric surface of the water table (Macumber 1979).

The geochemistry of the lake water, the shoreline springs, and the reflux brines have been reviewed in some detail (Dickson and Herczeg 1992; Jones *et al.* 1994; Long *et al.* 1992; Lyons *et al.* 1992; Macumber 1991). To summarize, Tyrrell brine is approximately thalassohaline (relative proportions of salts similar to those of seawater), with a slight enrichment of Mg^{2+} and SO_4^{2-} as the secondary cation and anion, respectively (Long *et al.* 2009). Salinity of the surface water typically ranges from 250-330 g/L (Dickson and Giblin 2009), while reflux brines contained in the sub-oxic Parilla Sand aquifer beneath the lake floor have a total dissolved solid (TDS) content of ~250 g/L (Long *et al.* 2009). Both are near neutral pH. Regional groundwater, which enters the lake in the spring zone along the northwestern shore, is oxic with a pH <4, and is of approximately seawater salinity (~36 g/L) (Long *et al.* 2009). Reflux brines from Lakes Timboram and Wahpool enter Lake Tyrrell through springs along the eastern shore; these brines are typically sub-oxic to anoxic, of near neutral pH, and are less saline than Tyrrell brines – about 120 g/L TDS (Long *et al.* 2009). Tyrrell Creek, although it contributes only slightly to the lake's water budget, is the most acidic of all waters – its pH is usually 2.3-2.75, and it is also highly saline, ~330 g/L (Macumber 1991).

A distinguishing feature of the Tyrrell waters is the relatively high iron content. Tyrrell creek water contains ~200 mg/L of soluble iron, and the springs on the western shore up to 40 mg/L (Macumber 1991). Tyrrell brines contain 6-7 mg/L Fe, which is 1000 times higher than in seawater (Dickson and Giblin 2009). It is primarily this feature, along with the acidity of some of the brines, that renders Lake Tyrrell partially analogous to ancient Martian acid-saline systems (Benison and Laclair 2003).

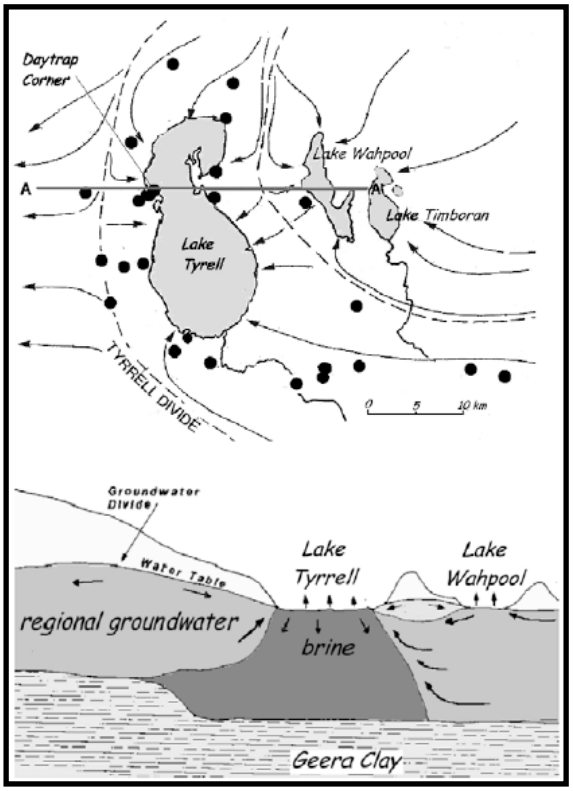

Figure 1.1 Map of Lakes Tyrrell, Timboram and Wahpool

Inset shows groundwater flow paths and the groundwater divide created by the Tyrrell fault (indicated as "Tyrrell Divide"). The Geera Clay (~160 m thick, deposited during a marine transgression in the late Miocene and the Pliocene) is the aquitard underlying the Renmark Group aquifer, which contains regional groundwater (Macumber 1992). This group includes three stratigraphic units, here given from base to surface: the Parilla Sand (60-70 m thick, deposited during the Tertiary marine regression), the Blanchetown Clay (up to 20 m thick, deposited during the early- to mid-Pleistocene by a freshwater megalake), and the Tyrrell Beds (~4 m thick, deposited by Lake Tyrrell during the late Pleistocene) (Bowler *et al.* 2006). Adapted from Dickson and Giblin (2009).

1.2 Importance of Lake Tyrrell for palaeoenvironmental studies

Lake Tyrrell is of particular interest to palaeoclimatologists, due to the time period represented in its sediment sequence and its geographic location, midway between the arid interior of the continent and the coastal highlands. The Tyrrell beds, whose age extends through the Holocene (~11.5 ka – present) and into the late-Pleistocene (1.8 Ma – 11.5 ka) (Bowler *et al.* 2006), are underlain by a sequence of fresh water clays whose thickness varies with geographic location. Termed the Blanchetown Clay, the sequence was deposited by the Plio-Pleistocene megalake, Lake Bungunnia (An *et al.* 1986; Stephenson 1986).

Together, the Tyrrell Beds and Blanchetown Clay preserve records of multiple glacial-interglacial cycles comprising a period of significant environmental change on the Australian continent (Bowler *et al.* 2006). In particular, Bowler and Teller (1986) interpret facies variations within the Tyrrell Beds as preserving evidence of four separate hydrologic cycles over the past ~36 ka: the first cycle is drying at ~36 ka, when a soil formed within the lake bed. The second cycle was a return to wetter conditions when the lake re-filled, ~30-25 ka. This was followed by a cycle of drying and extensive deflation (removal of sediments by wind) commencing at ~22 ka. It was during this time that the lunette – the dunes or ridges surrounding the lake – was built (Bowler 1976), largely as a result of deflation of the lake bed. The fourth and final cycle began at ~10 ka, when the lake became groundwater fed and conditions approximated those within the modern lake.

Each depositional cycle is characterized by a distinct sedimentary assemblage (Bowler and Teller 1986). Stage 1 sediments are deeper water facies, reflecting conditions prior to the initial drying event. They comprise un-laminated, non-calcareous clays, indicating a fresh to brackish lake (TDS <30 g/L) of ~10-12 m in depth. When precipitation decreased and/or evaporation increased, Stage 2 laminated, calcareous and oriented clays, typical of a saline water body (TDS 60-120 g/L) of 4-9 m depth, were deposited. As the lake became increasingly dependent on groundwater for recharge, water levels fell farther and salinity increased to >120 g/L. This led to Stage 3 deposition, typified by gypsum and oriented clay laminae. Stage 4 sediments are those deposited by a hypersaline water body (>350 g/L TDS) of <1 m depth, and contain higher quantities of halite. Stage 5 and Stage 6 sediments are those deposited when the lake is dry, and are composed of clay pellets and proto-soils, respectively.

The Tyrrell Basin lies midway between a tropical/sub-tropical region of summer rains, and an arid coastal region of winter rains (Figure 1.2). An equator ward compression of the dominant westerly winds, believed to have occurred during Pleistocene glaciations (Bowler 1970), would have altered the precipitation regime in the catchment, and so the water balance in the lake. The resulting fluctuations in salinity would be recorded in the sedimentary sequence, and would provide information on the changes in the dominant wind pattern.

Despite its fortuitous geographic location, Lake Tyrrell presents some special challenges in the matter of sampling and analysis. Sediments deposited in sub-arid regions are often highly oxidized, due to the deeper penetration of vadose waters containing oxygen and carbon dioxide in solution as a result of generally lower and fluctuating water tables (Hills 1940). In addition, deflation during dry-lake periods was very common, destroying what might have been promising repositories of data. Bowler and Teller estimate that ~4-5 m of sediment – or about half the total sediment deposited – have been removed from the floor of Lake Tyrrell in successive

deflationary episodes (Bowler and Teller 1986). However, this need not be an insurmountable obstacle, as will be demonstrated below.

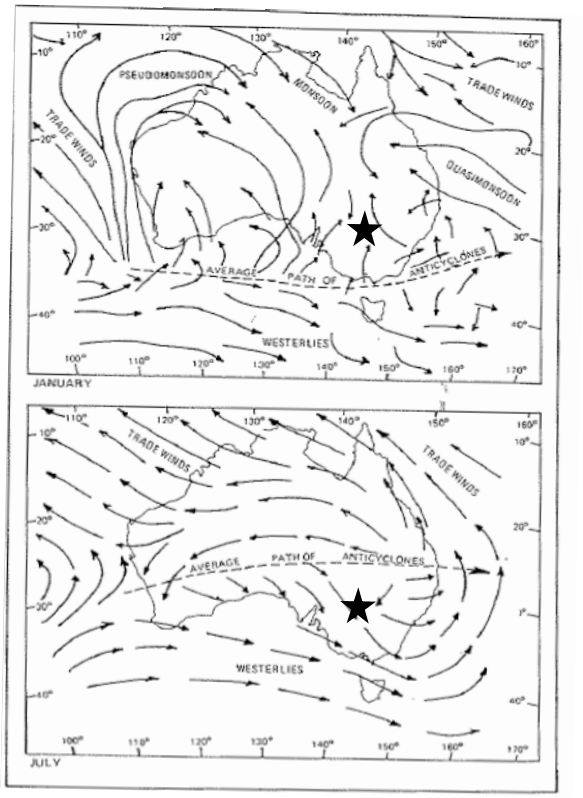

Figure 1.2 Summer and winter wind regimes over Australia.
Generalized tracks are represented by arrows. Note that summer is in January and winter in July. Approximate location of Lake Tyrrell denoted by a star. Adapted from Luly (1990)

1.3 An introduction to the palaeoenvironmental proxies used in this work

One of the major themes of this work was to use multiple, independent indicators of past environmental conditions in order to construct a picture of the local climate at Lake Tyrrell over the past ~400 ka. To that end, I have employed analyses of lipid biomarkers, stable isotopes of carbon and sulfur, mineralogy, pollen and charcoal, and sedimentary textures in the palaeo-environmental reconstruction of the lake from a core of its bed. The rationale for each proxy, as well as a brief introduction to its principles, appears here in order to facilitate interpretation of results presented in later chapters.

1.3.1 Evidence for biotic/metabolic processes

1.3.1.1 Lipid biomarkers

Lipid biomarkers are molecular fossils derived from compounds produced by living organisms. As an organism degrades after death, lipids are released. Biotic and abiotic processes lead to the recycling of some lipids, and the breakdown of others. Functional groups are altered, or in some cases, disappear. Ultimately, burial in sediments leads to the preservation of these compounds over geologic time (Peters *et al.* 2005a).

Researchers identify and quantify biomarkers extracted from sediments to gain information about environmental conditions that prevailed during and after deposition.

Biomarkers are indicative of the organism that produced them, although their taxonomic specificity varies by individual compound and across compound classes (Peters *et al.* 2005b, a; Seckbach 2006; Volkman 1986). In addition, biomarkers can provide information on diagenetic conditions experienced during the deposition and burial of organic matter, the degree of degradation of the organic material, and in some cases, the age of source sediments (Peters *et al.* 2005a). Most importantly for this work, it has been previously demonstrated that particular environments produce characteristic suites of lipid biomarkers (Peters *et al.* 2005a). Thus, when certain biomarker assemblages are present in a sample, if it can be shown that they are not the result of contamination, these assemblages can be taken as indicative of the existence of particular palaeoenvironments.

The analysis of lipids extracted from sediment samples or from living cultures presents some special problems, because the extract is composed of a complex mixture of compounds. In order to separate and quantify these compounds, two pieces of equipment, interfaced together, are commonly employed: the gas chromatograph and the mass spectrometer. While there are many different instrumental set-ups, in a general way the sequence of events in the treatment of a single sample is standard. First, the lipids are extracted from the sample using organic solvents – this can be done by hand or with the aid of various devices designed to increase either the heat or the pressure (or both) at which the extraction occurs. Next, the extract is processed, either to simplify the complex mixture or simply to remove water and non-lipid material prior to injection into the gas chromatograph. Third, the purified extract is derivatized in some fashion, in order to render the compounds in the mixture amenable to analysis via the GC-MS (gas chromatograph interfaced with mass spectrometer). Fourth, the derivatized extract, usually including a known amount of an additional standard compound added by the analyst to aid in quantification of the component compounds, is injected into the GC. Here the compounds are separated by polarity and molecular mass.

As compounds elute off the column, they enter the ion source of the mass spectrometer. Here, a metallic filament to which voltage is applied emits electrons, which ionize the compounds. Ionization produces gas phase ions that are fragments of the original compound; these fragments are then separated in the flight tube of the mass spectrometer by their mass-to-charge ratio, and subsequently detected. The final product of such an analysis is a chromatogram, or series of ‘peaks’, on a graph, where the x-axis is elution time and the y-axis represents the voltage of the detector (which is proportional to abundance *within a compound class*). Each of these peaks has an associated mass spectrum, derived from the fragments detected by the mass spectrometer. The fragments are plotted on a graph where the x-axis is the mass-to-charge ratio (*m/z*) and the y-axis is intensity. By comparing the elution time of a peak and its mass spectrum to those of known compounds in a database or in the literature, it is possible to identify the compounds in a sample. The quantity of each can then be established, in a relative way, by comparison of the integrated peak area with the peak area of the standard.

For this work, the lipids were extracted from sediments using a Dionex ASE (Accelerated Solvent Extractor, Figure 1.3) at elevated temperature and pressure, in order to increase extraction efficiency. Extraction of lipids from salt, water and living biomass was done by hand (Figure 1.4), using a modified Bligh-Dyer method (see Chapter 2 for complete protocol and references). Sulfur was removed from extracts with activated copper, and a trimethyl-silylating agent was used to derivatize compounds prior to injection on the GC. Synthetic FAMEs (fatty acid methyl esters) and halogenated or methylated alcohols and alkanes with known elution positions were employed as standards.

Figure 1.3 Dionex ASE 200 including multiple-solvent bottle apparatus.
Set-up is identical to that employed in the Brocks Biogeochemistry Laboratory at the Research School of Earth Sciences, the Australian National University. Note the numerous metal "bombs" in the upper carousel with corresponding glass vials in the lower carousel, which allows for the sequential extraction of up to 24 samples in a single run. Image courtesy of J. Brocks.

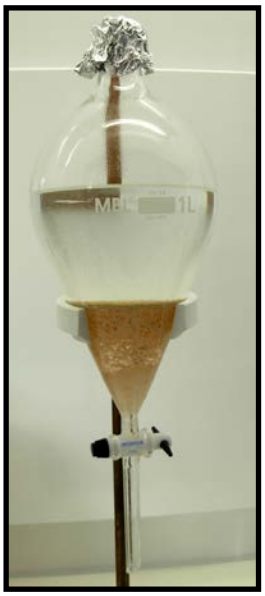

Figure 1.4 Example of equipment set-up for modified Bligh-Dyer extraction
Sample is added to the separatory funnel along with organic solvents of different polarities. After shaking, the contents are allowed to settle, producing the characteristic separation of solvents into an upper, more polar layer and an underlying, less polar layer. The separatory funnel is equipped with a Teflon stopcock at the base, which allows the bottom layer of solvent containing the compounds of interest to be drawn off without contamination induced by passage through the overlying aqueous layer. Image taken by author.

Figure 1.5 GC-MS laboratory of the Brocks' Biogeochemistry Group at ANU
The GC is equipped with an automatic sample changer and injector (carousel and tower on left), to allow for multiple samples to be run in sequence in the absence of a technician. Ionization chamber can be seen in the center; the analyzer, containing the electric and magnetic fields, the housing for the magnet and the detector are on the right. Image taken by author.

Samples were run on a silica gel capillary column, after which they were ionized by electron impact (EI) and analyzed with a magnetic sector mass spectrometer equipped with an electron multiplier for fragment detection (Figure 1.5). The advantage of this experimental set-up is that it permits the worker to analyze sub-nanogram quantities of a compound in a reproducible way. Capillary columns behave more consistently than packed columns, and EI, as it is a purely physical process, results in more reproducible spectra than other, chemically based ionization processes (Lambert *et al.* 1998). The use of a magnetic sector mass spectrometer permits high resolution measurements (on the order of 10^4) that are mass independent over a large dynamic range in compound concentration (on the order of 10^7) (Lambert *et al.* 1998). In addition, magnetic sector machines are known for producing precise peak shapes due to rapid scanning, and mass spectra containing reproducible ion abundances.

1.3.1.2 Stable carbon isotopes

There are two naturally occurring stable isotopes of carbon, ^{12}C and ^{13}C, the natural abundance of which is ~99:1 (Benyon *et al.* 1968). The organic compounds that are the product of autotrophs fixing carbon from CO_2 are typically "lighter" than the pool of CO_2 from which they are derived, meaning that they are enriched in ^{12}C and depleted in ^{13}C. Depletion of the heavier isotope is expressed as a delta value:

Equation 1.1 $$\delta^{13}C = [\{(^{13}C/^{12}C)_{sample}/(^{13}C/^{12}C)_{standard}\} - 1] * 1000$$

Delta values are expressed as per mil (‰), so that small differences in isotopic ratio can be expressed as integers. The extent of this enrichment is dependent on both the number of steps in the process of biotic fractionation and the isotopic selectivity at each step (Hayes 2001). Higher plants typically fix carbon via the C_3 or C_4 pathway, named for the number of carbons in the major intermediary product of each pathway (CAM plants are not relevant to this work, and so are not discussed here). Briefly, the C_3 pathway is comprised of the following enzymes, in order: Rubisco, phosphoenolpyruvate (PEP) carboxylase and PEP carboxykinase. The final product of this pathway is oxaloactetate, a 4-carbon compound. By contrast, the C_4 pathway employs physical separation to increase the efficiency of the overall pathway, first fixing CO_2 in mesophyll cells using PEP carboxylase. The resulting oxaloacetate is converted to malate, diffuses into bundle-sheath cells, and is decarboxylated to yield CO_2, which is then fixed by Rubisco (Hayes 2001).

As a result of the differing pathways utilized, the ^{12}C enrichment of the fixed carbon products differs between C_3 and C_4 plants. The characteristic value of the isotopic enrichment is termed a fractionation (ε), which is mathematically equivalent to:

Equation 1.2 $$\varepsilon_{R\text{-}P} = 1000 * (\alpha_{(R\text{-}P)} - 1)$$
where $\alpha_{(R\text{-}P)} = [(^{13}C/^{12}C)_R]/[(^{13}C/^{12}C)_P]$, and R = reactant, P = product

For terrestrial plants, this fractionation factor depends not only on the pathway employed for photosynthesis, but also on the $\delta^{13}C$ of atmospheric CO_2 and on the plants' stomatal conductance, which can vary with aridity (Eglinton and Eglinton 2008). For this work, the $\delta^{13}C$ values of cuticular waxes (*n*-alkanes of C_{25} through C_{33}) preserved in sediments were traced through time. These compounds can be distinguished from *n*-alkanes produced by organisms within the lake, as hypersaline systems are typically carbon-limited, rendering the carbon fixed

therein isotopically heavy ($\delta^{13}C$ value heavier than -20‰), relative to that of surrounding terrestrial vegetation (Schouten *et al.* 2001). In general, *n*-alkanes produced by plants utilizing the C_4 pathway have an average $\delta^{13}C$ value of -22‰, while those produced by plants employing the C_3 pathway have an average value of -34‰ (Eglinton and Eglinton 2008). Due to this difference, we can use the measured value of $\delta^{13}C$ of *n*-alkanes within a sample to determine the relative contributions of C_3 and C_4 plants, which in turn can be interpreted in terms of community shifts in higher plant populations through time.

In order to measure the $\delta^{13}C$ value of individual *n*-alkanes, a GC-IRMS (gas chromatograph-isotope ration mass spectrometer) was employed, such that compounds could be separated within a mixture and measured individually. A ThermoFinnigan MAT 252 was tuned such that the delta value of as little as 10 ng of an individual compound could be determined with accuracy and precision within < 1‰ (pers. commun., Bernd Kopke). The principles governing the mass spectrometer are the same as those outlined above, with the caveat that the mass range measured is much smaller: *m/z* 44, 45, and 46. These masses are those of $^{12}CO_2$, $^{13}CO_2$, and $^{14}CO_2$; the CO_2 is produced from combustion of the lipid as it elutes from the GC.

1.3.1.3 Stable sulfur isotopes

Stable isotopes of sulfur include the following:

Table 1.1[a] Natural abundance of stable isotopes of sulfur

Isotope	Natural abundance (%)[b]
^{32}S	95.02
^{33}S	0.75
^{34}S	4.21
^{36}S	0.02

[a]adapted from (Canfield 2001)
[b]for Vienna Cañon Diablo Troilite

Stable sulfur isotopic analyses can be used to determine whether microbes have been involved in the precipitation of sulfide minerals within a sulfate-dominated system. Sulfate-reducers discriminate against the heavier isotopes in favor of the lightest, ^{32}S. While ^{36}S is not present in great enough natural abundance for reliable measurements of its relative abundance to be made in most systems, ^{34}S is. Relative abundance is calculated with respect to a standard of known isotopic composition, and written in the delta notation, thus:

Equation 1.3 $$\delta^{34}S = [\{(^{34}S/^{32}S)_{sample}/(^{34}S/^{32}S)_{standard}\} - 1] * 1000$$

As with carbon, delta values are expressed as per mil (‰), so that small differences in isotopic ratio can be expressed as integers.

In this study, the products of dissimilatory sulfate reduction (DSR) were examined. DSR is a process by which prokaryotes "gain energy for their growth by catalyzing exergonic chemical reactions in which organic carbon or H_2 (gas) is oxidized, while sulfate is reduced" (Canfield 2001). The reactions proceed as follows:

Equation 1.4 $$SO_4^{2-} + 2CH_2O \rightarrow H_2S + 2HCO_3^-$$

Equation 1.5 $2H^+ + SO_4^{2-} + 4H_2 \rightarrow H_2S + 4H_2O$

These may be treated as non-reversible reactions, with the result that the same reaction with a heavier isotope will have lower rate constant than that with the lighter isotope. The resulting product will then be enriched in the lighter isotope (DePaolo 2011). This enrichment of the product in the light isotope is altered in a biotic system by rates of reduction, type of electron donor, and sulfate concentrations (Canfield 2001). In addition, different species of sulfate-reducers have characteristic associated fractionations, which differ from each other. These differences are partially a result of rate-limitation of either sulfate uptake or enzymatic operation within the cell, and do not seem to correlate well with known phylogeny (Detmers *et al.* 2001). However, it is known that complete oxidizers (organisms that completely oxidize their electron donors) generally exhibit stronger fractionation (>15‰) than less complete oxidizers (<18.7‰) (Canfield 2001; Detmers *et al.* 2001).

Biotically-mediated sulfide production in sediment usually results in the formation of framboids. Framboids are cubic, icosahedral or pentagonal crystallites of iron sulfides, usually pyrite (FeS_2) (Astafieva *et al.* 2005). They form as a result of the reaction between the H_2S produced by bacterial sulfate reduction and iron oxyhydroxides present in the sediment, as Fe^{2+} is an efficient scavenger of sulfide, especially in hypersaline sediments (Javor 1989). In the Lake Tyrrell system, an excess of sulfate is available in the form of the evaporite gypsum ($CaSO_4 \bullet nH_2O$), which, like all modern evaporitic gypsum, is isotopically heavy, with an average delta value of +20‰ (Holser and Kaplan 1966). As the fractionations associated with the abiotic processes of gypsum dissolution and pyrite precipitation are on the order of 1‰ (Holser and Kaplan 1966), and those associated with the protonation of HS^- and the volatilization of H_2S are ~2‰) (Javor 1989), then larger fractionations evident in sedimentary pyrite can be attributed to the activity of sulfate reducers, with the magnitude of the fractionation providing a clue to the species.

In order to measure *in situ* the $\delta^{34}S$ of pyrite appearing as framboids and as intergrowths with gypsum (see Figure 1.6) within the Lake Tyrrell core, we utilized the stable isotope Sensitive High Resolution Ion MicroProbe (SHRIMP) at the Research School of Earth Sciences at the Australian National University.

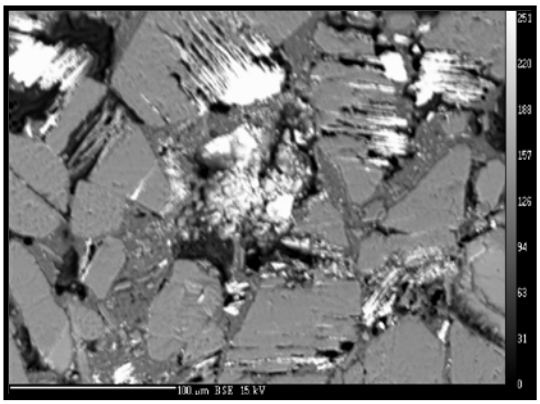

Figure 1.6 Back-scattered image of pyrite intergrowths in gypsum from a thin section of the Lake Tyrrell core

The bright areas are pyrite, and the gray crystals are gypsum. Note that some of the pyrite has grown into the cleavage planes of the gypsum crystals, replacing it, while some is present as framboids in the interstitial space. Image taken by author on Cameca SX100 electron microprobe operating in backscattered mode.

The SHRIMP works to measure sulfur isotopes by sputtering a polished sample with a beam of positive ions from a cesium gun. The positive Cs ions contact the sample surface at 45°, sputtering negative secondary ions (S^-) extracted at 90° to the sample surface. The spot size of the beam is ~5μm, and the ablation pit created thereby is less than 1μm deep (Eldridge *et al.* 1987), so that multiple measurements can be made on a single sample. The secondary ions are transferred to the electrostatic analyzer (see Figure 1.7), which compensates for the velocity spread of the ion beam by separating ions with different energy onto different pathways (http://shrimp.anu.edu.au/shrimp/operation_mass_spectr.htm). The ions then pass through the magnetic sector mass spectrometer, where they are separated according to their mass-to-charge ratio, as previously explained, and finally into the detector. The strength of the SHRIMP system is its precision (~0.1‰) and accuracy (~0.3‰), in conjunction with excellent spatial resolution.

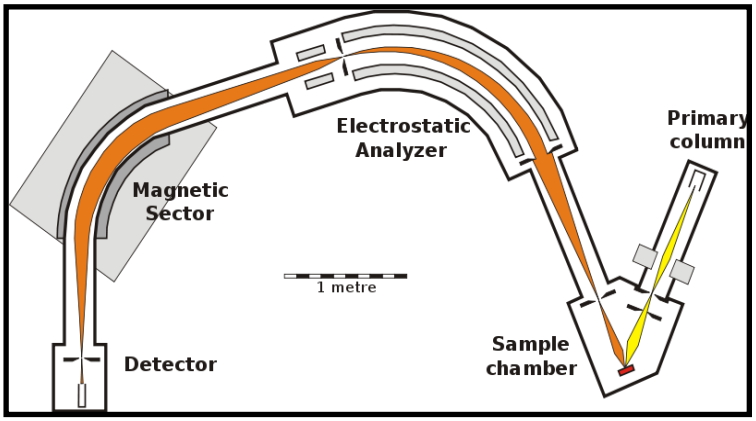

Figure 1.7 Schematic of a typical SHRIMP
Note multiple focusing lenses, including a quadrupole lens between the magnet and the electrostatic analyzer, which allows for high transmission rates with minimal aberrations (http://shrimp.anu.edu.au/shrimp/operation_mass_spectr.htm)
Image adapted from Williams (1998)

1.3.2 Evidence for abiotic processes

1.3.2.1 Analyses of mineral content in sediments and sedimentary textures

Mineral content of sediments provides information on both the provenance and post-depositional environment of the sample. The Tyrrell beds are dominated by clays, evaporites and clastic quartz grains (Bowler and Teller 1986; Teller *et al.* 1982), deposited as products of aeolian activity, runoff, and changing salinity within the lake. The significance of mineral content lies in the relative proportions of these three general groups: a predominance of primary evaporites denotes a depositional regime consisting of the precipitation of salts, which is in turn indicative of a groundwater dominated system (Magee 1988). When clays predominate, heavy input of aeolian material or wash-in from the lunette is indicated. If the deposition was aeolian, then a drier climate is indicated, in which groundwater levels did not intersect the lake floor such that salts were not deposited (Bowler and Teller 1986; Magee 1997). If the clays were sourced from runoff, then a flood event occurred (Magee 1988). Distinguishing between these two possibilities is easily accomplished by analysis of sedimentary textures, to be discussed below. Finally, if quartz sand is the dominant mineral, then a beach like environment is indicated, pointing to higher water levels in the lake (Bowler and Teller 1986) and a wetter climate overall. It is important to note here that mineral content cannot be interpreted in the absence of textural analysis, as changes in pore water chemistry subsequent to the deposition of sediments may alter the mineral content by dissolution of primary minerals or deposition of secondary minerals (Torgersen *et al.* 1986).

In order to distinguish primary from secondary minerals, a textural analysis of thin sections of sediments must be performed. Sedimentary textures provide information on the mode of mineral deposition (for example, aeolian, lacustrine, biotically-mediated) as well as on the nature and extent of any post-depositional alteration (Magee 1988; Magee 1997). As such, textural analysis of sediments is an indispensable component of palaeoenvironmental reconstruction, as it can be used to rank samples in order of extent of preservation. In this way, mineral, biomarker and pollen content of samples that have been minimally altered may be treated as the most robust data points in the final analysis, and samples that have experienced greater post-depositional alteration will not skew the results. At Lake Tyrrell, changing groundwater levels and fluctuation in precipitation levels through time have caused the complete dissolution of halite and extensive secondary gypsum formation within clays deposited under fresher regimes. In the absence of textural analysis, estimates of palaeo-salinity would be impossible.

Analysis of mineral content typically begins with light microscopy; sediment samples are prepared into thin sections for this purpose. Preparing thin sections from sediment is much the same as preparing thin sections of rock (Nesse 1991); however, there are a few extra guidelines that must be adhered to so that texture is preserved. First, sections of sediment of the desired length and thickness must be carefully cut from the core or larger sediment section; these must be supported to retain coherence as they are dried in the dark at room temperature for up to six weeks. Faster drying leads to efflorescence of salts and destruction of primary textures. After drying, sections must be gradually impregnated with epoxy under low vacuum for a period of 3-5 days, again to preclude efflorescence of salts. Finally, during cutting, hexane must be used in place of water as the lubricant, since water will dissolve salts within the block. As salts such as gypsum and carbonate are much softer than quartz (Nesse 1991), sections which contain a mixture of these minerals may not be able to be polished to the recommended thickness of 30 μm, as this would remove all traces of the softer minerals. Therefore, sedimentary thin sections may be thicker than those made from metamorphic or igneous rocks, and this must be taken into account during later analysis.

A preliminary categorization of mineral content may be performed concurrently with textural analysis under the petrographic microscope. However, quantitative analysis of mineral content is typically done via x-ray diffraction of a powdered sample (Wenk and Bulakh 2004). X-ray diffraction is based on the precept that minerals have a regular, lattice-based structure whose inter-atomic distances are too small (1-5 angstroms, where 1 angstrom = 0.1 nm) to be probed with visible light. The wavelength of visible light is 400-700 nm, whereas x-rays have wavelengths of 0.1-5 angstroms. In the x-ray tube of a diffractometer, x-rays are generated by bombarding an anode metal (copper, in this study) with electrons produced by heating a tungsten filament. The x-rays are then filtered with a graphite monochromator, such that only those of a single wavelength (the Kα wavelength of Cu, 1.54 angstroms) strike the sample. The powder of the sample contains all the minerals present in the sample, with crystallites in random orientation. As x-rays strike the sample at an incident angle θ, scattering occurs. While some scattering is destructive, some is constructive, creating new wave fronts that reinforce each other. This is known as diffraction, which occurs when scattering from atoms in multiple layers of the crystal lattice is in phase (Figure 1.8). Diffraction is a consequence of the path difference of x-rays striking different layers being a whole multiple of the incoming wavelength, such that

Equation 1.6 path difference = BC + CD (Figure 1.8)

and BC = CD
and sin θ = BC/AC
so that path difference = 2 * AC * sin θ = n*λ

The lattice inter-planar spacing of crystallite causing the scattering, shown as AC above but conventionally referred to as "d", can easily be deduced using the Bragg equation:

Equation 1.7 $2d * \sin\theta = n*\lambda$

where d = lattice inter-planar spacing of the crystal
θ = incidence angle of x-rays
n = an integer representing the order of diffraction; may be incorporated into the d-spacing if the lattice plane (*hkl*) is indicated
λ = wavelength of x-rays

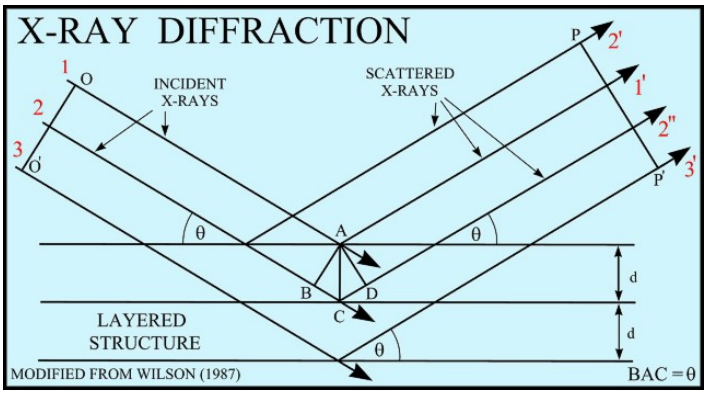

Figure 1.8 Schematic of x-rays being diffracted by multiple layers of crystal lattice
Geometry of diffraction is indicated by paths through letters A-D and angle θ.
d = inter-planar spacing of crystal lattice.
BAC = θ.
Note that one incident ray (2) can diffract to create multiple scattered rays (2' and 2").
Image courtesy http://pubs.usgs.gov

As a sample is scanned, the detector rotates through 2*θ degrees, and the sample through θ degrees, maintaining the reflection conditions for the sample surface – i.e., only lattice planes parallel to the sample surface are diffracting (Wenk and Bulakh 2004). The detector records the intensity of diffraction at each angle. Thus, for any intensity peak in the scan, θ and λ are known, so all that remains is to solve for d. Every mineral has a characteristic set of d-spacings associated with different orders of diffraction for each of its inter-planar lattice spacings; these are tabulated and can be referred to in order to identify a particular diffraction pattern. In the case of a powder sample containing many minerals, computer programs are used to fit known diffraction patterns to the overall pattern, such that all minerals present in the sample at > 3% abundance by weight can be identified.

Quantitative analysis involves making a Rietveld refinement of the total diffraction pattern. Named for its originator, Hugo Rietveld, a Rietveld refinement is a least-squares method designed to minimize a function defined as the difference between an observed diffraction pattern and a calculated pattern based on a combination of the diffraction patterns of all the minerals in the sample. Refinement parameters include those that vary between instruments, such as background and zero value, and those that vary between minerals or between samples, such as unit cell values, extent of preferred orientation, peak asymmetry, and particle size and absorption (Sietronics 2006). While a refinement for a single mineral phase can be performed by hand, for mixed powder samples there are a variety of computer programs available. These programs work

through multiple iterations, or refinements, as the user sets limits on the parameters based on his or her knowledge of the diffraction behavior of the sample and the minerals therein. Once overall error is minimized, the program produces quantities of each mineral in weight percent along with associated error. For this work, we used Siroquant (Sietronics 2006), developed by the CSIRO in Australia.

1.3.2.2 Pollen and charcoal analyses

Classification of pollen grains and charcoal particles in a sample is used to assess the composition of plant communities present in the catchment (Faegri *et al.* 2000; Luly 1990), to examine the impact of fire and human habitation on those communities (Prebble *et al.* 2005), and most importantly, to infer larger scale climatic shifts based on changes in plant community composition through time (Boyd 1990; Luly 1993; Traverse 2007). As discussed previously, Lake Tyrrell lies near the summer-winter rain boundary, so that small northerly or southerly shifts in this band translate to large changes in the precipitation regime at the lake (Singh and Luly 1991), and consequently in the surrounding flora. This sensitivity makes Lake Tyrrell a particularly valuable target for palynological analysis. However, it was long thought that salt lakes in arid or semi-arid environments would be poor candidates for such studies due to the highly arid and oxidized nature of the sediments (Boyd 1990) and their correspondingly low organic content (Singh 1981). Singh and others demonstrated that pollen was well preserved in salt lake sediments (Boyd 1990; Singh 1981; Singh and Luly 1991), so that these could act as valuable repositories of information about palaeo-flora.

Using both mineralogical and palynological analyses, Luly was able to reconstruct palaeoenvironments at Lake Tyrrell through the Holocene (Luly 1990, 1993); however, sequences deposited during the Pleistocene were not examined. In this work, pollen and charcoal were used to both support and augment palaeoenvironmental reconstructions based on mineral content, sedimentary textures, and biomarker analysis. The pollen provided an extra dimension to these reconstructions, as pollen is sourced from a much larger area of the catchment (Luly 1990), and so reflects conditions throughout the catchment, as opposed to local conditions at the lake itself. Typical palynological studies involve taking samples at centimeter intervals of a core of a few meters length and tracking shifts in taxa composition and relative proportions of pollen from each taxon present (Traverse 2007). As that was neither practical nor economically feasible for the length of core used in this study (13 m), subsamples were taken at intervals as dictated by changes in mineralogy. Differences in the relative proportions of keystone taxa between samples were treated as evidence of gradual changes in the community, whereas the appearance of taxa characteristic of disturbed or fire-prone plant communities, or a spike in charcoal abundance, were interpreted as evidence of more sudden changes.

Pollen grains and charcoal particles are identified and counted using a light microscope and specially-prepared thin sections. Samples of a known volume of sediment are lyophilized, and a tablet containing a known number of *Lycopodium* spores is added as a standard. The Lycopodiaceae are relatives of the ferns not found in Australia, and their spores are not amenable to preservation in sediment sequences, so that they make an excellent standard. Addition of a standard permits calculation of pollen concentration values (i.e. relative abundance) and provides an indicator for accidental pollen destruction during sample processing (Faegri *et al.* 2000). The sample is then digested and separated using a series of acids, bases and heavy liquids, so that all minerals are dissolved or discarded, and only organic material remains behind (Faegri et al. 2000; Traverse 2007). This material is then preserved in glycerol, and may be spread on a slide

and fixed under a cover slip. Finally, a certain number of grains or certain area of the slide is counted, and the identities and proportions of the pollen and the amount of charcoal in the total sample calculated.

1.3.2.3 Imaging - electron microscopy

Electron microscopy is useful for sample imaging and analysis primarily due to the heightened resolution and magnification that can be achieved as compared with conventional light microscopy. The wavelength of an accelerated electron is governed by the de Broglie equation, and can be approximated as:

Equation 1.8 $\lambda = h/\sqrt{(2m\text{Ve})} \approx \sqrt{(1.5/\text{V})}$

where λ = wavelength (nm), h = Planck's constant, m = mass of the electron, V = electric potential (volts), and e = charge of the electron (Wenk and Bulakh 2004).

This means that as V is increased, wavelength decreases. Voltages applied to electrons during electron microscopy typically yield wavelengths ~100,000 times smaller than that of visible light (Wenk 1975). This is important as the resolution that can be obtained is governed by the Rayleigh formula:

Equation 1.9 $R = (0.61^* \lambda)/\alpha$

where R = size of resolved object, λ = wavelength, and α = effective aperture of the objective lens (Wenk 1975).

Thus, R is directly proportional to wavelength, so that sub-nanometer scale resolution is possible with the electron microscope, whereas with conventional light microscopy, the limits of resolution are ~1000 nm (Wenk and Bulakh 2004). In addition to heightened resolution, electron microscopy has the advantages of higher magnification (up to 3 orders of magnitude better than in light microscopy), and greater depth of field and focus (Wenk 1975).

Although there are a number of different types of electron microscopes, the principles governing each are the same. Briefly, electrons are produced in a conventional electron gun by heating a v-shaped filament of tungsten or lanthanum hexaboride. The electrons are then accelerated down the column toward a positive anode. The electrons then pass through a series of condenser and objective lenses before hitting the sample. These lenses are electrostatic and electromagnetic, and work in a way analogous to optical lenses (Wenk and Bulakh 2004). When the electrons come into contact with the sample, both elastic and inelastic scattering occur. Elastic scattering, where the trajectory of the electrons changes but the kinetic energy and velocity remain constant, produces the diffraction patterns used in transmission electron microscopy (Wenk 1975). As that technique was not employed for this work, it will not be discussed further. In inelastic scattering, the incident electrons interact with electrons of atoms in the sample, displacing some from their orbitals. This causes instability in the atom, such that energy must now be dispersed, either through emission of secondary electrons, x-rays, heat or luminescence (Giannakopoulos *et al.* 2008). In addition, some of the incident electrons may be 'back-scattered' after interaction with the sample surface (Wenk and Bulakh 2004). Different detectors are used to measure each of these various types of emissions. Depending on the type of electron or energy detected, images of a sample surface and information about its elemental content can be generated.

Secondary electrons are used for imaging a sample's surface. As they are low in energy (< 5 eV), they can escape only from the top ~10 nm of a sample. Secondary electron yield depends primarily on sample topography (Wenk and Bulakh 2004), and increases as the angle of incidence increases (Giannakopoulos *et al.* 2008), so that contrast in an image is directly related to the three-dimensional structure of the sample. By contrast, yield of back-scattered electrons is tightly correlated with atomic number, with elements of higher atomic number appearing brighter than those of lower atomic number due to increased scattering (Giannakopoulos *et al.* 2008). As such, back-scattered electrons are used to produce images illustrating compositional changes in a sample. Finally, x-rays are emitted when incident electrons interact with inner-shell electrons of elements in the sample. Each element emits x-rays of a characteristic wavelength for the shell from which the transition originated. These x-rays are typically collected and quantified using either energy-dispersive (EDS) or wavelength dispersive spectroscopy (WDS). EDS detectors are solid-state semiconductors that can 'count' all wavelengths simultaneously, while WDS detectors use Bragg diffraction from a crystal with known d-spacing to 'filter' wavelengths, in order to quantify select wavelengths specified by the user (Wenk and Bulakh 2004). EDS yields more information in a shorter time, while WDS is more quantitative. For this work, EDS detectors were used in conjunction with both an electron microprobe and a scanning electron microscope for classification of sulfides.

Application of the electron microprobe was restricted to analyses of sulfides in thin section. Thin sections were prepared as described in section 1.3.2.1; however, cover slips were not used. The sample was then coated in graphite, to facilitate conduction, thereby preventing charge build-up. Back-scattered images were collected in order to locate areas of interest, and x-ray emissions of iron-sulfides were detected via EDS in order to determine elemental content. These were compared with standards to ensure accurate elemental quantification, so that iron-sulfides with different stoichiometries could be distinguished.

Secondary electron microscopy was performed on un-polished fragments of epoxy-impregnated sediments in an effort to discern the morphology of the iron-sulfides and whether remnant sulfate-reducing bacteria were present in association with same. Samples were coated with graphite to aid in conduction, and secondary electron images, back-scattered images, and x-ray spectra were collected. Secondary electron imaging, as the resolution is generally superior to that found in back-scattered images (primarily a result of yield), was employed in the search for microbial remains. Back-scattered images were used in conjunction with EDS detection of x-rays to map compositional domains. EDS results were used both to classify sulfides and for identification of accessory evaporites and other unknowns present in the sample.

1.4 The study of arid palaeoenvironments as it relates to modern land use policy

Nearly 40% of the world's food is grown on irrigated land (Beresford *et al.* 2001), and it is unfortunately this land that is most at risk of salinization. Irrigation adds dissolved salts to soils: shallow-rooted crops, planted at the expense of deeper rooted native vegetation, allow the water table to rise, bringing salts to the surface. Inadequate drainage water-logs soils, so that salts can no longer be leached out of the soil profile by rain (Essington 2004). As a result, 5% of the world's arable lands and 23% of cultivated lands are saline (Essington 2004), with an additional 4 million acres of farmland lost to salinization each year (Beresford *et al.* 2001).

Australia is particularly vulnerable, as increasing aridity resulting from intensified atmospheric circulation during the last glacial maximum (LGM) (Bowler 1976) has been

magnified by more recent decreases in precipitation (Bowler 1970; Singh and Luly 1991). These changes have rendered much of the arable land in the country arid to semi-arid. Irresponsible land management has compounded the problem, to the point that the water supplies of major cities like Adelaide, as well as the agricultural industries and ecology of the Murray-Darling Basin, are severely compromised (Beresford *et al.* 2001).

In order to allocate regional water supplies such that the needs of urban and rural residents are balanced against the preservation of riparian and wetland habitats for plants and animals, policy makers must have access to data on the water budget of a catchment. However, water supply is not a constant: it changes with time as a result of fluctuations in regional weather patterns, which in turn are altered by changes in global climate. While statistical and dynamical modeling can be used to forecast global-scale climate shifts, predictions for specific regions or time windows are typically less well-constrained (Barnston *et al.* 1999). Evidence of the effect of past climate shifts upon a region provides a useful baseline from which to assess the accuracy and precision of model output. Therefore, palaeoclimatology is central to the creation of better climate models and of sustainable policies of land and water usage.

1.5 References

An Z, Bowler JM, Opdyke ND, Macumber PG, Firman JB (1986) Palaeomagnetic stratigraphy of Lake Bungunnia: Plio-Pleistocene precursor of aridity in the Murray Basin, southeastern Australia *Palaeogeography, Palaeoclimatology, Palaeoecology* 54: 219-239

Astafieva MM, Rozanov AY, Hoover R (2005) Framboids: their structure and origin *Paleontological Journal* 39: 457-464

Barnston AG, Glantz MH, He Y (1999) Predictive skill of statistical and dynamical climate models in SST forecasts during the 1997–98 El Niño episode and the 1998 La Niña onset *Bulletin of the American Meteorological Society* 80: 217-243

Benison KC, Laclair DA (2003) Modern and ancient extremely acid saline deposits: terrestrial analogs for martian environments? *Astrobiology* 3: 609-618

Benyon JH, Saunders RA, Williams AE, *The Mass Spectra of Organic Molecules*. (Elsevier Publishing Company, 1968)

Beresford Q, Bekle H, Phillips H, Mulcock J, *The Salinity Crisis: landscapes, communities and politics*. (University of Western Australia Press, Crawley, 2001)

Bowler JM (1970) "Late Quaternary environments: a study of lakes and associated sediments in south-eastern Australia", doctoral dissertation, The Australian National University

Bowler JM (1976) Aridity in Australia: age, origins and expression in aeolian landforms and sediments *Earth Science Reviews* 12: 279-310

Bowler JM, Magee JW (1978) Geomorphology of the Mallee Region in semi-arid Northern Victoria and Western New South Wales *Proceedings of the Royal Society of Victoria* 90: 5-26

Bowler JM, Teller JT (1986) Quaternary evaporites and hydrological changes, Lake Tyrrell, north-west Victoria *Australian Journal of Earth Sciences* 33: 43-63

Bowler JM, Kotsonis A, Lawrence CR (2006) Environmental evolution of the Mallee Region, Western Murray Basin *Proceedings of the Royal Society of Victoria*: 161-210

Boyd WE (1990) Quaternary pollen analysis in the arid zone of Australia: Dalhousie Springs, central Australia *Review of Palaeobotany and Palynology* 64: 331-340

Canfield DE, in *Stable Isotope Geochemistry,* Valley JW, Cole D, Eds. (2001), vol. 43 pp. 607-636

DePaolo DJ (2011) Surface kinetic model for isotopic and trace element fractionation during precipitation of calcite from aqueous solutions *Geochimica et Cosmochimica Acta* 75: 1039-1056

Detmers J, Bruchert V, Habicht KS, Kuever J (2001) Diversity of sulfur isotope fractionations by sulfate-reducing prokaryotes *Applied and Environmental Microbiology* 67: 888-894

Dickson BL, Herczeg AL (1992) Naturally-Occurring Radionuclides in Acid Saline Groundwaters around Lake Tyrrell, Victoria, Australia *Chemical Geology* 96: 95-114

Dickson BL, Giblin AM (2009) Features of acid-saline systems of Southern Australia *Applied Geochemistry* 24: 297-302

Eglinton TI, Eglinton G (2008) Molecular proxies for paleoclimatology *Earth and Planetary Science Letters* 275: 1-16

Eldridge CS, Compston W, Williams IS, Walshe JL, Both RA (1987) *In situ* microanalysis for 34S/32S ratios using the ion microprobe SHRIMP *International Journal of Mass Spectrometry and Ion Processes* 76: 65-83

Essington ME, in *Soil and water chemistry: an integrated approach*. (CRC Press, Boca Raton, 2004)
Faegri K, Iversen J, Kaland PE, Krzywinski K, *Textbook of Pollen Analysis*. (The Blackburn Press, ed. 4th, 2000)
Giannakopoulos K, Voutou B, Stefanaki EC, "Electron Microscopy: the basics" (National Center for Scientific Research Demokritos, Greece, 2008)
Hayes JM, in *Stable Isotope Geochemistry*, Valley JW, Cole D, Eds. (2001), vol. 43 pp. 225-277
Hills ES, *The Physiography of Victoria: an Introduction to Geomorphology*. (Whitcombe & Tombs Pty. Ltd., Melbourne and Sydney, 1940)
Holser WT, Kaplan IR (1966) Isotope geochemistry of sedimentary sulfates *Chemical Geology* 1: 93-135
Javor B, *Hypersaline Environments: Microbiology and Biogeochemistry*. Brock/Springer Series in Contemporary Bioscience (Springer-Verlag, Berlin, 1989)
Jones BF, Hanor JS, Evans WR (1994) Sources of Dissolved Salts in the Central Murray Basin, Australia *Chemical Geology* 111: 135-154
Lambert JB, Shurvell HF, Lightner D, Cooks RG, *Organic Structural Spectroscopy*. (Prentice Hall, 1998)
Long DT, Lyons WB, Hines ME (2009) Influence of hydrogeology, microbiology and landscape history on the geochemistry of acid hypersaline waters, N.W. Victoria *Applied Geochemistry* 24: 285-296
Long DT, Fegan NE, Lyons WB, Hines ME, Macumber PG, Giblin AM (1992) Geochemistry of Acid Brines - Lake Tyrrell, Victoria, Australia *Chemical Geology* 96: 33-52
Luly JG (1990) "A pollen analytical investigation of Holocene palaeoenvironments at Lake Tyrrell, semi-arid northwestern Victoria, Australia", doctoral dissertation, Department of Biogeography & Geomorphology, The Australian National University, Research School Pacific Studies
Luly JG (1993) Holocene Palaeoenvironments Near Lake Tyrrell, Semi-Arid Northwestern Victoria, Australia *Journal of Biogeography* 20: 587-598
Lyons WB, Welch S, Long DT, Hines ME, Giblin AM, Carey AE, Macumber PG, Lent RM, Herczeg AL (1992) The Trace-Metal Geochemistry of the Lake Tyrrell System Brines (Victoria, Australia) *Chemical Geology* 96: 115-132
Macumber PG, in *Aeolian Landscapes in the Semi-Arid Zone of SE Australia* Storrier RR, Stannard ME, Eds. (Australian Soc of Soil Science, Riverina Branch, Mildura, VIC, 1979), vol. 1980, pp. 67-84
Macumber PG (1991) "Interaction between groundwater and surface systems in Northern Victoria", doctoral dissertation, Geology Department, School of Earth Sciences, Melbourne University
Macumber PG (1992) Hydrological processes in the Tyrrell Basin, southeastern Australia *Chemical Geology* 96: 1-18
Magee JW (1988) "Chemical and Clastic Sediments and Late Quaternary History, Prungle Lakes, New South Wales", master's thesis, Department of Biogeography & Geomorphology, Research School of Pacific Studies, The Australian National University
Magee JW (1997) "Late Quaternary environments and palaeohydrology of Lake Eyre, arid central Australia", doctoral dissertation, Division of Archaeology and Natural History, Research School of Pacific and Asian Studies, The Australian National University

Nesse WD, *Introduction to Optical Mineralogy*. (Oxford University Press, Oxford, ed. 2nd, 1991)
Peters KE, Walters CC, Moldowan JM, *The Biomarker Guide: Biomarkers and Isotopes in the Environment and Human History*. The Biomarker Guide (Cambridge University Press, Cambridge, 2005a) vol. 1
Peters KE, Walters CC, Moldowan JM, *The Biomarker Guide: Biomarkers and Isotopes in Petroleum Exploration and Earth History* The Biomarker Guide (Cambridge University Press, Cambridge, 2005b) vol. 2
Prebble M, Sim R, Finn J, Fink D (2005) A Holocene pollen and diatom record from lowland tropical Australia *Quaternary Research* 64: 357-371
Schouten S, Hartgers WA, Lopez JF, Grimalt JO, Damste JSS (2001) A molecular isotopic study of 13C-enriched organic matter in evaporitic deposits: recognition of CO2-limited ecosystems *Organic Geochemistry* 32: 277-286
Seckbach J, *Life As we Know It*. Seckbach J, Ed., Cellular Origins, Life in Extreme Habitats and Astrobiology (Springer, 2006) vol. 10
Sietronics. (Sietronics Pty Limited, Belconnen, ACT, Australia, 2006)
Singh G, in *Salt Lakes*, Williams WD, Ed. (Dr W. Junk, Adelaide, Australia, 1981), vol. 5 pp. 419-430
Singh G, Luly JG (1991) Changes in vegetation and seasonal climate since the last full glacial at Lake Frome, South Australia *Palaeogeography, Palaeoclimatology, Palaeoecology* 84: 75-86
Stephenson AE (1986) Lake Bungunnia - A Plio-Pleistocene megalake in southern Australia *Palaeogeography, Palaeoclimatology, Palaeoecology* 57: 137-156
Teller JT, Bowler JM, Macumber PG (1982) Modern sedimentation in Lake Tyrrell, Victoria, Australia *Journal of the Geological Society of Australia* 29: 159-175
Torgersen T, Deckker PD, Chivas AR, Bowler JM (1986) Salt Lakes: a discussion of processes influencing palaeoenvironmental interpretation and recommendations for future study *Palaeogeography, Palaeoclimatology, Palaeoecology* 54: 7-19
Traverse A, *Paleopalynology*. Topics in Geobiology (Springer, ed. 2nd, 2007)
Volkman JK (1986) A review of sterol markers for marine and terrigenous organic matter *Organic Geochemistry* 9: 83-99
Wenk H-R, Bulakh A, *Minerals: Their Constitution and Origin*. (Cambridge University Press, Cambridge, 2004)
Wenk HR, Ed., *Electron Microscopy in Mineralogy*, (Springer-Verlag, Berlin, 1975)

Chapter 2.

The utility of lipid biomarkers preserved in sediments of ephemeral saline lakes as palaeoenvironmental indicators

2.1 Abstract

An understanding of the progress and extent of aridity across the Australian continent during the climatic fluctuations of the Pleistocene is essential to the creation of accurate palaeo-climate reconstructions. However, continentally-based records are few, due to a lack of both sampling sites and palaeoenvironmental proxies preserved therein.

Here we evaluated the utility of lipid biomarker analyses of ephemeral hypersaline lake sediments for the reconstruction of regional climate fluctuations through analysis of lipid profiles and with reference to conventional mineralogical and palynological indices. We found that solvent extractable lipids are present at depth in oxidizing, hypersaline conditions, in sediment sequences where pollen and microfossils were absent (and possibly destroyed).

We were able to eliminate lab-based and cross-sample contamination, and show that these lipids are indigenous to the sediments in which they are found. Our data demonstrate that lipid biomarker suites can be correlated with mineral assemblages to provide information about the community structure within the lake, and the organisms growing around the lake. This information in turn can provide constraints on evaporitic and precipitation regimes in and around the lake through time.

2.2 Introduction

Much of the interior of the Australian continent is hot and dry, but it was not always that way. Faunal and sedimentary evidence indicate that during the Tertiary (65.5 – 1.8 Ma), Australia's climate was humid-subtropical (Bowler 1976). Australia began to dry out in the Late Tertiary (~2.5 Ma) when increased sea surface temperatures in the Indian and Southern Oceans raised the temperature and lowered the humidity of air masses penetrating the continent (Bowler 1976). These changes did not affect all parts of the continent equally; moreover, drying was accelerated by the onset of glaciation during the Pleistocene (1.8 Ma – 11.5 ka) (Bowler 1976).

Multiple lines of evidence from diverse locations are needed in order to reconstruct the nature, extent and onset of aridity across the Australian continent. Because erosion is the dominant process shaping the modern Australian landscape, well-preserved continental sedimentary successions covering the last 200,000 years are sparse. Playa lakes and boinkas are areas where saline groundwater intersects with the land surface. These are dispersed throughout the subtropical zone of the continent where sediment can accumulate and groundwater levels contact the surface. Due to their saline nature, however, preservation of microfossils can be poor (DeDeckker 1988b; Ryves *et al.* 2006), and salt efflorescence during times of dryness leads to periodic deflation and discontinuities within sediment sequences. Therefore, reconstruction of palaeoenvironments based on Australian salt lake sediment sequences has been particularly challenging.

As a new approach, we decided to combine an analysis of lipid biomarkers with other, more traditional proxies to reconstruct environmental conditions within and around a lake through the Pleistocene and Holocene. Lipid biomarkers are chemical fossils that are diagnostic of the organisms that produced them and that are stable in rocks and sediments over geologic timescales (Peters and Moldowan 1993). As such, they are indicative of the

presence and, to an extent, the relative abundance of organisms within a palaeo-community (Jahnke *et al.* 2008). By extrapolation, environmental parameters required for these organisms' survival in the present day can be used to reconstruct the conditions at the time when the biomarkers were deposited (Brocks *et al.* 2005). In addition, once the source of a biomarker has been established, the compound can be utilized for radiocarbon dating, thereby eliminating issues of "old" or "young" carbon contamination inherent in bulk radiocarbon dating. Thus, biomarker data can be integrated with palynological, sedimentological and isotopic studies to refine the timescales and magnitudes of climatic changes at a regional level, and also to provide information about the types of organisms that inhabited the region through time.

Lipid biomarkers from perennial saline lake sediments on other continents (Barbe *et al*. 1990; Jiang *et al.* 2007; Pearson *et al.* 2008; Toste 1976; Volkman *et al.* 1988) have been successfully employed as sources of palaeoenvironmental data; however, their utility in the study of ephemeral lake sequences remains largely unexplored. As with macrofossils and microfossils, the preservation of indigenous biomarkers is dependent on the conditions encountered during deposition and diagenesis. Dry, oxic conditions are not conducive to biomarker preservation. Unfortunately, playa lakes are intermittently dry, and desiccation cracks in the lakebed may promote oxidation of sediments to depth. Thus, although biomarker analysis of salt lake sediments was recognized as a potentially valuable tool for palaeo-climate studies in Australia (Torgersen *et al.* 1986), the idea was not pursued due to the widespread assumptions that conditions experienced by ephemeral lake beds would be unsuitable for biomarker preservation (DeDeckker 1988a). Moreover, it was anticipated that cracks in the lakebed and lateral movement of groundwater and subsurface bacterial activity would overprint biomarker sequences with modern lipids (DeDeckker 2008).

Also at issue were problems with accurate dating of the sediment sequences themselves (Bowler and Teller 1986; Luly *et al.* 1986). Accurate dating is needed to place the remaining sequences in temporal context, but bulk carbon dating of more recent sediments in Australian playa lakes is difficult and often unreliable due to the low organic matter content of the lake sediments (Gillespie et al. 1991; Luly *et al.* 1986) and input of allochthonous carbon from the surrounding catchment area (Bowler and Teller 1986). For older sediments, optically-stimulated luminescence dating or electron spin resonance dating of the quartz fraction of sediments may be of use; however, the clay content of salt lake sediments can artificially shorten the time window over which this technique is useful (Fitzsimmons 2009). Uranium-series dating of secondary minerals in alluvial sediments, including ferricretes, gypcretes and calcretes, has been successfully applied to constrain the timing of wet-dry phases over the last 300,000 years (Nanson *et al.* 1992; Nanson *et al.* 1991). However, when applied in lakes, post-depositional exchange of both uranium and thorium with the environment and high levels of initial ^{232}Th can make it difficult to reliably calculate ages by this method (Herczeg and Chapman 1991).

The mid- to late-Pleistocene includes arguably "the greatest environmental transformation of the last 20 million years" (Bowler *et al.* 2006), rendering it integral to the study of past climate change in southeastern Australia. Before investigating the feasibility of various dating techniques, it was necessary to ascertain whether ephemeral, hypersaline environments would contain extractable quantities of indigenous biomarkers in deeply buried sediments. In the current study, we tested whether organic molecules could be extracted from a ~13 m core through the lakebed at the northern end of Lake Tyrrell, a hypersaline playa lake of 160 km^2 in northwestern Victoria, Australia. We evaluated the syngeneity of these molecules to establish their utility as biomarkers on the basis of mineralogical, palynological, sedimentological, and organic geochemical data.

2.3 Samples and methods

2.3.1 Study sites and sample collection

A core of 12.98 m in length was taken at Folly Point (35°17.112' S, 142°49.270' E) in July 2008 (Figure 2.1). The coring location was selected to capture the full range of Tyrrell stratigraphy – lunette, Tyrrell Beds, Blanchetown Clay – and to facilitate comparison of sediments collected with those of a previously described core (Bowler and Teller 1986). The core was collected using an Edson 360 Versadrill top drive truck mounted rig. The rig employs a hollow auger system, and the cores obtained were 62.5 mm in diameter. Core sections were extruded from metal coring tubes immediately upon retrieval from the drill hole. Sections were logged for depth and color, enclosed in polyethylene plastic and placed within PVC tubes that had been split lengthwise. Upon returning to the lab, core sections were split lengthwise, and archived halves photographed and stored at -20°C. Working halves were logged, sub-sampled and stored at 4°C for further sampling and analysis.

Samples were collected throughout the core at approximately even spacing of ~500 cm, with some variation to capture the range of lithologies present (See Appendix 1 and Table 3.1). These included samples of the lunette material overlying the Tyrrell Beds and from the Blanchetown Clay beneath them. A subset, chosen to represent the full range of depth, lithologies, and biomarker facies extant, were subjected to further detailed analysis. In addition, mats and salt were recovered from the northern end of the lake (Site 12 in Figure 2.1) during August 2006 using metal spatulas cleaned in methanol. Samples were stored in baked glass jars with baked foil tops at 4°C until processing.

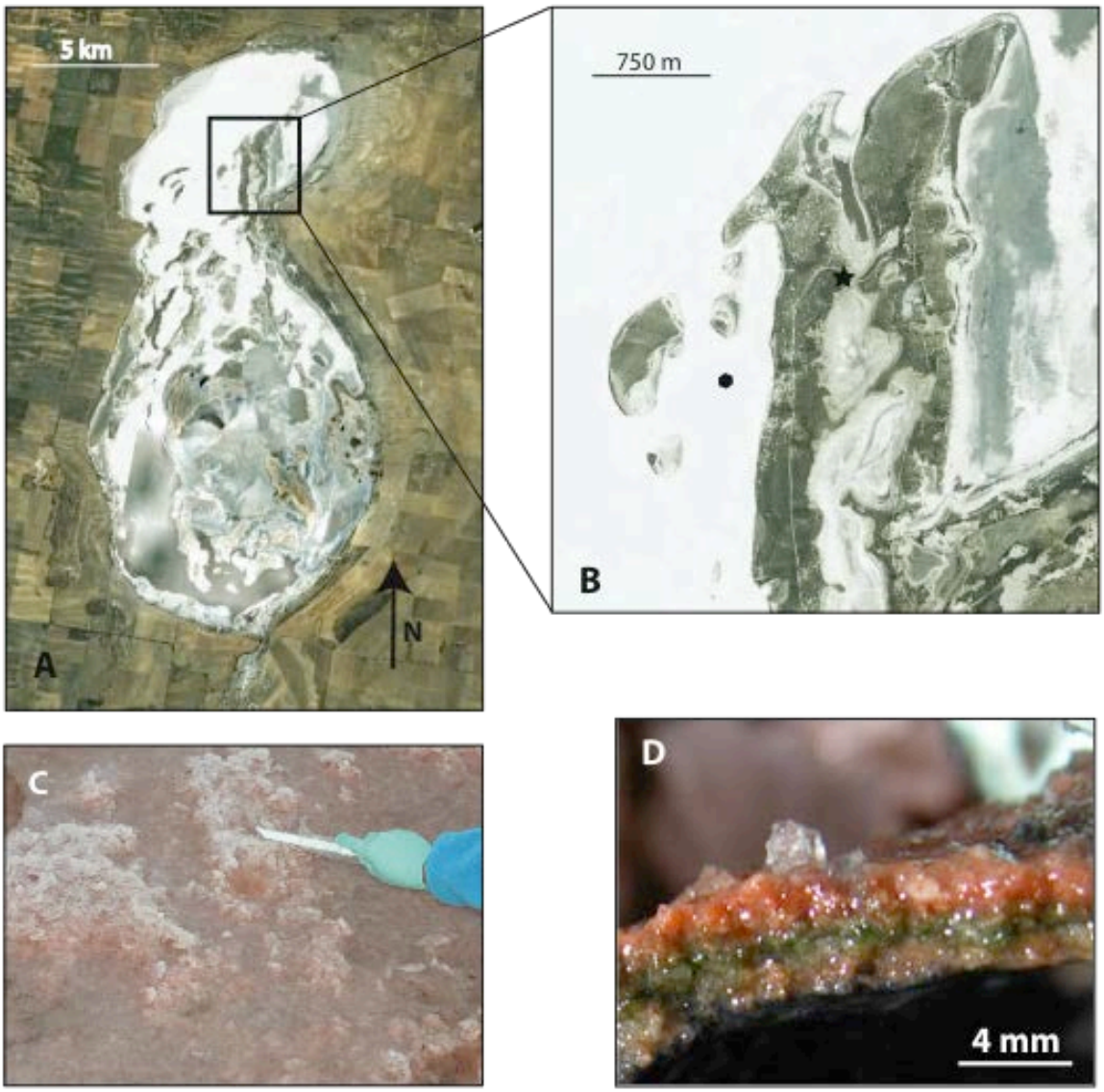

Figure 2.1 Lake Tyrrell sampling locations

A. Satellite view of Lake Tyrrell, sampling location is boxed. Image source is Google Earth.
B. Close-up of Folly Point. Core location indicated by ★, algal mat and salt sampling location (Site 12) indicated by ⬣. Image source is Google Earth.
C. Surficial salt at Site 12, spatula for scale. Note pink color imparted by planktonic halophiles. Image courtesy of J. Banfield.
D. Multi-layered algal mats collected from below salt at Site 12. Image courtesy of J. Brocks.

2.3.2 Mineralogical analysis

Sub-samples for the identification and quantification of mineral phases were taken in parallel with lipid samples. Powder x-ray diffraction was performed with a SIEMENS D501 Bragg-Brentano diffractometer equipped with a graphite monochromator and scintillation detector, using CuKα radiation.

Samples for the analysis of bulk mineral phases were lyophilized, and crushed and homogenized with a mortar and pestle. These were then milled for 10 minutes in isopropanol with a McCrone Micronizing Mill and dried at 40°C. For the quantification of amorphous material, 20 wt % corundum (1.0 μM Al_2O_3, Baikowski) was added to each sample and thoroughly mixed in. Samples were suspended on a side-packed sample holder and analyzed from 2° to 70° 2-theta, at a step width of 0.02° and a scan speed of 1.0°/minute.

Clay separation was performed on sub-samples that had not been lyophilized, according to the Millipore Filter Transfer Method (Moore and Reynolds 1997). Clay samples were analyzed after Mg-saturation (scan range 2-42° 2-theta, step width 0.02°, scan speed 1°/minute), saturation with ethylene glycol (scan range 2-32° 2-theta, step width 0.02°, scan speed 1°/minute), and heating to 350°C (scan range 2-28° 2-theta, step width 0.02°, scan speed 1°/minute) and to 550°C (scan range 2-28° 2-theta, step width 0.02°, scan speed 1°/minute).

Spectra were interpreted using the Bruker AXS software package Diffrac*plus* Eva 10 (2003) for identification, and Siroquant V3 for quantification (using the bulk scan).

2.3.3 Thin section analysis

Cores were inspected for sedimentary textures using a binocular microscope. Sample depths at which sedimentary textures changed or at which lipid samples had been taken were sub-sampled for sedimentological analysis. Samples for thin section analysis (75 mm x 25 mm) were cut from the core at these depths, wrapped in baked aluminum foil and dried at room temperature (to reduce salt efflorescence and cracking) in the laboratory for four weeks. They were subsequently impregnated with polyester resin (Valspar rapid-cure water/white-clear casting resin, Valspar Australia Corp. Pty. Ltd.; polyester catalyst, ACT Fiberglass Supplies; 99.25% resin/0.75% catalyst) and allowed to cure at room temperature for 6 weeks, after which thin sections were prepared by the conventional method using non-aqueous lubricants during all steps.

2.3.4 Total organic carbon (TOC) analysis of sediments

Samples for TOC analysis were taken in parallel with lipid sub-samples. These were subsequently lyophilized in a freeze-drier, then crushed and homogenized in a mortar and pestle cleaned with 5% nitric acid. Carbonates were removed by sulfurous acid treatment and TOC analysis was performed on a Leco CS-444 (accuracy of +/- 0.01% in comparison to standards, detection limit of 0.05%, replicates run periodically to check for precision).

2.3.5 Palynological analysis of sediments

Subsamples for pollen (~5 cm^3 each) were taken from the core at depths corresponding with lipid samples and prepared as follows. A *Lycopodium* tablet (batch 483216, with 18583 +/- 9% spores per tablet) was added to provide an exotic marker taxon. Samples for pollen analysis were dispersed in 10% $Na_4P_2O_7$ followed by 15 minutes in hot 10% KOH. Residues were put through 210 μm and 7 μm sieves prior to a wash in 10% HCl and acetolysis for 10 minutes. Inorganic residues were removed by density separation using sodium polytungstate and an overnight bath in HF, followed by a 10% HCl wash. Samples were dehydrated in absolute ethanol and suspended in glycerol for microscopic examination.

Pollen were counted on a Leitz Dialux microscope at 400 magnifications. The pollen sum was 400 grains of native taxa or ¼ of a slide counted, whichever occurred first.

2.3.6 Lipid extraction and fractionation

Sediment and algal mats were lyophilized in a freeze-drier, then crushed and homogenized in a mortar and pestle cleaned with methanol. Homogenized samples were extracted using a Dionex ASE (DCM:MeOH 9:1 v/v, 100°C, 1000 p.s.i., 5 cycles), which forces pressurized, heated solvent through the samples to extract organic matter. This technique has been demonstrated to increase both the yield and efficiency of extraction for cells and sediments (Calvo *et al.* 2003; Macnaughton *et al.* 1997). Salt was extracted using a modified Bligh-Dyer technique (Bligh and Dyer 1959; Volkman *et al.* 1997), as it would have corroded the ASE.

After passing extracts through pipette columns of activated copper to remove sulfur, extracts were evaporated to dryness under a stream of pure N_2 gas, re-dissolved in a known volume of DCM, and a known aliquot of 25% or 50%, depending upon extract yield, was preserved as total lipid extract (TLE) for GC-MS analysis. To this aliquot an internal standard, 18-methyleicosanoic acid methyl ester (18-MEAME), was added and then the sample was derivatized with BSTFA (bis(trimethylsilyl)trifluoroacetamide) containing 1% TMCS (trimethylchlorosilane).

Parallel to samples, four laboratory blanks were performed using combusted sand (baked at 450°C for 9 hours). These were carried through all steps, from lyophilization to GC-MS analysis.

To simplify the TLE of mat and salt extracts, 50% of the underivatized TLE was saponified using the method of Volkman *et al.* (1998). Saponifiable fractions were archived at -20°C. We aliquoted 25% of the non-saponifiable lipid fraction and added standards for quantification (18-MEAME) and derivatization efficacy (12-Br-dodecan-1-ol). After derivatization with BSTFA, samples were analyzed by GC-MS.

To test whether the bulk of lipids originally deposited and preserved had been bound into proto-kerogen, or were present as ‘free’ solvent-extractable compounds, we performed sequential alkaline saponification/acid hydrolysis (Mayberry and Lane 1993) on five samples (S12 mats, LT 4, LT 7, LT 10, LT 20) that had previously been extracted using the Dionex ASE. We modified the technique of Mayberry and Lane (1993), designed to release ester and amide linked compounds, with the addition of vortexing and a reduction in the time of heating during acidification. These modifications were made in order to enhance the transfer of esters to the aqueous phase (Bannon *et al.* 1982) and avoid the destruction of sensitive compounds (Ichihara *et al.* 1996). 3-5 g dry weight of each sample were placed into capped Teflon© tubes that had been pre-cleaned with MeOH and DCM. Saponification in 4 mL of 0.5M KOH/MeOH at 60°C for 1 hour was followed by acidification with 2 mL of 10M HCl to yield a final concentration of 2.2M H^+. Subsequently, 1.5 mL of *n*-heptane was added to each sample, and the samples were vortexed for 15s. Samples were heated to 100°C on a heating block, and retained at this temperature for 2 hours, over which period they were vortexed briefly at ~30 minute intervals. Finally, samples were allowed to cool to 40°C and extracted three times with 5 mL DCM. This organic phase was washed three times with 5 mL of hexane-cleaned Milli-Q water, and passed through pipette columns of activated copper to remove sulfur. Extracts were evaporated to dryness under a stream of pure N_2 gas and re-dissolved in a known volume of DCM. A known aliquot of 50% was preserved as total lipid extract (TLE) for GC-MS analysis. To this aliquot an internal standard, 18-methyleicosanoic acid methyl ester (18-MEAME), was added and then the sample was derivatized with BSTFA (bis(trimethylsilyl)trifluoroacetamide) containing 1% TMCS (trimethylchlorosilane).

2.3.7 Instrumental analysis and compound quantification

Lipid samples were analyzed using gas chromatography-mass spectrometry (GC-MS). An Agilent 6890 series gas chromatograph was coupled to a Micromass Waters Autospec Premier magnetic sector mass spectrometer. The electron source was run with the following parameters: 70 eV, 250 μA trap current, 260°C source temperature, 290°C interface temperature, and an accelerating voltage of 8000 V. Splitless injection at 300°C onto a DB-5 MS column (57.5 m x 0.25 mm i.d.; 0.25 μM film thickness) introduced extracts of LT4, 7, 10 and 20 to an oven temperature programmed from 40°C (hold time 2 minutes) to 315°C at 4°C/minute, then held for 50 minutes. Samples from the lunette, mats and salt were injected at 40°C on a PTV injector for 0.1 minutes, heated to 300°C at 260°C per minute, and held at 300°C for 5 minutes. In addition to the oven temperature program described above, a second oven temperature ramping program of 8°C/minute was employed to ensure adequate separation of lighter compounds and elution of heavy isoprenoids on a new DB5-MS column. Helium was used as the carrier gas with a flow rate of 1 mL per minute for all samples.

The mass spectrometer was run in EI+ mode, and data acquisition was performed in full scan mode (*m/z* 55-600, 0.7 s cycle time, interscan delay of 0.2 s). Compounds were identified by comparison with mass spectra and chromatographic data in the literature, and using the NIST 2.0 (2005) MS library. Compound concentrations were estimated using uncorrected GC-MS peak areas relative to 18-MEAME. It was not possible to determine gravimetric yields because all extracts contained residual salt. Instead, extract yields were estimated by the integration of the total GC-MS signal area relative to 18-MEAME, after subtraction of blanks (Table 2.3).

2.4 Results

We drilled into the sediments of Lake Tyrrell through the lunette at Folly Point, intersecting the Tyrrell Beds formation at ~200 cm depth. At ~600 cm depth there was a sharp transition between laminated clay-gypsum couplets of the Tyrrell Beds and brown clays characteristic of the Blanchetown clay formation (Teller *et al.* 1982). An overview of the recovered core with sampling positions indicated appears in Appendix 1.

2.4.1 Results of thin section analysis

Thin sections of samples collected, along with detailed views of diagnostic features, are shown in Appendix 2. Thin section analyses of material collected from the base of the lunette (~200 cm depth, Appendix 2, Figure A2.1) reveals mineralogical and textural uniformity. The dominant components are pelletal clay with scattered quartz grains surrounded by clay argillans (Appendix 2, Figures A2.1 C-D). Thin section analysis of LT 4 (234 – 241 cm depth and within the Tyrrell beds, Appendix 2, Figure A2.2) indicates extensive post-depositional alteration: quartz crystals with grain cutans, oriented clay halos along cracks and iron-oxide staining (Appendix 2, Figures A2.2 A-G). These textural features are consistent with an initial phase of soil development.

LT 7 (412 – 419 cm depth, Appendix 2, Figure A2.6) contains multiple mm-scale layers, including un-zoned clay matrix interspersed with displacive gypsum crystals (Appendix 2, Figures A2.6 G-H), followed by primary gypsum and oriented clay micro-laminae containing what appear to be fecal pellets (Appendix 2, Figures A2.6 E-F). Above these micro-laminae is a clay matrix containing displacive gypsum crystals (80 μM - 2 mm length) in parallel to sub-parallel orientation, and a quartz lens containing a poorly-sorted mixture of rounded, sub-rounded and angular grains (diameter 40-360 μM) (Appendix 2, Figures A2.6 C-D). There is some iron-oxide staining throughout the section. Some micro-

laminae are distorted. This may be due to post-depositional crystal growth; however, this also may have occurred during preparation of the thin section.

LT 10 (519 – 526 cm depth, Appendix 2, Figure A2.9) is composed of alternating mm-scale layers of gypsum and oriented and non-oriented clays. Interspersed within one of the gypsum layers are what appear to be fecal pellets or accretions of fecal pellets of ~50 μM in diameter (Appendix 2, Figure A2.9 B).

LT 20 (1014 – 1021 cm depth and within the Blanchetown Clay, Appendix 2, Figure A2.13) is composed of clays with lenses of quartz sand, as well as alternating laminae of fine clay and medium silt near the top of the section (Appendix 2, Figures A2.13 E-F). Limited regions of iron-oxide staining are present within the sample (Appendix 2, Figure A2.13 C); however, laminae are undisturbed, indicating minimal post-depositional alteration.

2.4.2 Results of mineralogical analysis

Analysis of the mineral content of samples by x-ray diffraction was used to estimate clays and evaporite mineral content and to test for evidence of alteration by oxidation and dolomitization. Results are presented in Table 2.1.

All samples except LT 10 contained high amounts of amorphous material, an issue that did not seem to vary with mineral content (another subsample, not described here, had an identical mineral composition to LT 10, but a calculated amorphous content of ~30%, whereas LT 10 contained 0%). Amorphous material was not observed on examination of associated thin sections. In order to ensure that sample preparation technique was not contributing amorphous material, various processing methods were attempted, including hand-milling in hexane and dry milling, and samples of pure gypsum and quartz (source: mineralogical collection, Research School of Earth Sciences, Australian National University) were processed. It is possible that it is an artifact of the program (Siroquant) when attempting to quantify phases in complex samples. For results presented, mineral content was normalized to 100%, disregarding the amorphous content, as it did not correlate with any mineral type.

Briefly, LT 1 (taken from the lunette) is dominated by clays, which, taken together make up ~75% of the sample. LT 4 is comprised of ~25% dolomite in addition to clays and quartz. LT 7 contains more than twice as much clay as gypsum and ~1% dolomite whereas sample LT 10 is > 90% gypsum, and contains no dolomite, no oxides and hardly any clays. LT 20 (taken from the Blanchetown Clay) contains > 60% quartz, with the remainder composed primarily of clays and feldspars.

Table 2.1 Mineral content of samples (normalized)[a]

Sample name	LT 1	LT 4	LT 7	LT 10	LT 20
Depth (cm)	20	223	411	519	1013
TOC[b]	0.22	0.10	0.14	0.16	0.18
Evaporites					
Total evaporites	**4.8±0.01**	**29.3±0.12**	**31.6±0.13**	**91.1±0.51**	**5.2±0.02**
Halite	2.2±0.01	3.4±0.02	7.0±0.04	0.4±0.00	5.2±0.02
Gypsum	1.2±0.01	nd	23.4±0.12	90.7±0.51	nd
Celestite	nd	nd	nd	nd	nd
Calcite	1.5±0.01	nd	nd	nd	nd
Dolomite	nd	25.9±0.12	1.2±0.01	nd	nd
Magnesite	nd	nd	nd	nd	nd
Other minerals (detrital, oxides)					
Total other minerals	**19.6±0.09**	**16.8±0.08**	**8.1±0.04**	**2.4±0.01**	**71.5±0.25**
Quartz	19.6±0.09	16.8±0.08	8.1±0.04	2.4±0.01	64.0±0.25
Hematite	nd	nd	nd	nd	nd
Plagioclase feldspar	nd	nd	nd	nd	6.2±0.02
Alkali feldspar	nd	nd	nd	nd	1.3±0.01
Muscovite	nd	nd	nd	nd	nd
Clays					
Total clays	**75.6±0.21**	**53.9±0.16**	**60.3±0.23**	**6.5±0.04**	**23.3±0.07**
Unidentified clay component	16.9±0.07	7.5±0.03	nd	nd	2.5±0.01
Illite	38.3±0.17	33.7±0.15	36.6±0.19	5.6±0.03	16.2±0.06
Kaolinite	20.4±0.09	11.9±0.05	23.6±0.13	0.9±0.01	4.6±0.02
Vermiculite	nd	0.8±0.00	nd	nd	nd

[a]All mineral amounts and errors in weight %, errors are 1 sigma (estimated standard deviation); normalized to eliminate amorphous content - see explanation in text.
[b]TOC reported as wt% of sediment, measurement error 0.01%
nd = not detected

None of the samples contain measurable quantities of iron oxides using XRD, and all contain a small amount of halite. Some mineral phases were identified with Diffrac*plus* Eva 10 in both bulk and clay scans, but could not be quantified with Siroquant as the quantities were too small. These include muscovite, albite, montmorillonite, microcline, vermiculite and smectite in LT 20, and vermiculite and montmorillonite in LT 4. As these minerals were present in only trace quantities, they will not be discussed further.

2.4.3 Results of palynological analysis

Pollen were found in three of the four samples selected for analysis. Relative abundances of major taxa present are listed in Table 2.2. LT 4 did not contain pollen or other macerals, possible due to overall poor preservation conditions as indicated by thin section analysis.

Table 2.2 Pollen data for Lake Tyrrell S12 drill core subsamples[a]

		LT 7 (412 – 413.5 cm)			LT 10 (519 – 520.5 cm)			LT 20 (1014 – 1015.5 cm)[b]		
	Major taxa present	# grains	% total sample	grains per cc sample	# grains	% total sample	grains per cc sample	# grains	% total sample	grains per cc sample
Dryland taxa	Poaceae	112	30.8	3822	129	29.8	3376	74	19.0	6708
	Casuarinaceae	71	19.5	2423	110	25.4	2879	44	11.3	3989
	Asteraceae (Tubuliflorae)	98	26.9	3345	118	27.3	3088	109	28.0	9881
	Chenopodi-aceae	28	7.7	956	16	3.7	419	73	18.8	6617
	Brassicaceae	3	0.8	102	3	0.7	79	nd[c]	-	-
	Callitris	3	0.8	102	1	0.2	26	2	0.5	181
	Eucalyptus	1	0.3	34	3	0.7	79	nd	-	-
	Dodonaea	5	1.4	171	15	3.5	393	7	1.8	635
Aquatic taxa	Cyperaceae	2	0.5	68	3	0.7	79	nd	-	-
	Cf *Triglochin*	4	1.1	137	4	0.9	105	nd	-	-
	Myriophyllum	6	1.6	205	7	1.6	183	6	1.5	544
	Typha	1	0.3	34	nd	-	-	4	1.0	363
Tertiary pollen[d]	Restionaceae (*Milfordia hypolaenoides and M. homeo-punctata)*	1	0.3	34	4	0.9	105	2	0.5	181
	Cyathea	1	0.3	34	nd	-	-	12	3.1	1088
	Gleichenia	nd	-	-	1	0.2	26	nd	-	-
	Araucariaceae	nd	-	-	nd	-	-	5	1.3	453
	Podocarpus	nd	-	-	nd	-	-	2	0.5	181

[a]No pollen was detected in slides prepared from LT 4 (225 – 226.5 cm)

[b]Large numbers of *Botryococcus* and *Pediastrum* spores were present in LT 20

[c]nd = not detected

[d]Indicates pollen deriving from plants common during the Tertiary (65.5 – 1.8 Ma), but typically absent in Quaternary assemblages

LT 7 and 10, from the Tyrrell Beds (< 400 ka (Bowler and Teller 1986)), have higher Poaceae and a lower representation of Tertiary aged palynomorphs than LT 20, but are otherwise similar. A *Cyathea* spore and a couple of pollen grains of *Milfordia homeopunctata* were identified, but none of the other Tertiary age taxa are present. Neither sample contains *Pediastrum* or *Botryococcus*. Pollen of the aquatic taxa *Typha* and *Myriophyllum* are rare enough to suggest that they may have been transported from regions distant from the lake.

LT 20 from the Blanchetown Clay (> 700 ka (An *et al.* 1986; McLaren *et al.* 2009)) contains pollen from taxa such as Araucariaceae, *Podocarpus*, Gleicheniaceae and *Milfordia homeopunctata*, which have affinities with Tertiary age palynofloras in the Murray Basin and elsewhere (Hill 1994). Aquatic taxa in the sample include *Typha* and *Myriophyllum*, though the abundance of each is small. Also present are the micro alga *Pediastrum* and abundant *Botryococcus* spores.

All samples contain small amounts (<5% abundance) of *Dodonaea*, the presence of which is usually ascribed to disturbance in a vegetation assemblage, possibly due to fire (Bekele 2000).

2.4.4 Results of lipid biomarker analysis

Comprehensive laboratory blanks did not contain any lipid biomarkers discussed in this study, with the exception of cholesterol (**1**). This compound was present in 12-20x lower abundance in the blanks than in sample extracts.

All samples contained extractable lipids, however lipids were present in much lower quantities than was TOC (Table 2.3). To test whether processes operating post-deposition had destroyed indigenous lipid biomarkers or had only bound them into proto-kerogen, we performed sequential saponification (alkaline), hydrolysis (acidic) and solvent extraction on sediment that had already been ASE extracted for each subsample. With the exception of LT 7, the yield from this extraction technique was lower than that from initial ASE solvent extraction (Table 2.3). It is possible that the high proportion of clays in LT 7 (Table 2.1) decreased solvent penetration and increased sorption of lipids to sediment particles, such that ASE extraction was less efficient. Based on these data, we conclude that post-depositional processes, such as soil formation, did not include the incorporation of indigenous lipids into the bound fraction.

Table 2.3 Total organic carbon and lipid extract yields[a] for Lake Tyrrell S12 mat, salt and sediment core samples

Sample name	Sample depth (cm)	TOC (wt %)[b]	TLE (ug/g sample extracted) ASE extraction	TLE (wt %)[c] ASE extraction	TLE (ug/g sample extracted) sequential hydrolysis-saponification[d]	TLE (wt %)[c] sequential hydrolysis-saponification
S12 salt	0	nm	1.21	0.000121	nm	nm
S12 mats	1	1.27	57.1	0.00571	159.2	0.01592
LT 1	20	0.22	5.69	0.000569	nm	nm
LT 4	223	0.10	1.43	0.000143	1.11	0.000111
LT 7	411	0.14	2.81	0.000281	8.24	0.000824
LT 10	519	0.16	8.92	0.000892	1.66	0.000166
LT 20	1013	0.18	4.93	0.000493	1.21	0.000121

[a]Extract yields calculated as described in section 2.3.7

[b]TOC reported as wt% of sediment, measurement error 0.01%

[c]TLE wt% calculated from extract yield by mass of sample

[d]Sequential hydrolysis-saponification described in section 2.3.6

nm = not measured

Biomarkers relevant for Chapters 2 and 3 are presented in Table 2.4. Environmental sources of biomarkers are referenced in Appendix 4, where the diagnostic mass spectra for each biomarker in Table 2.4 may be found. Within the text, compound numbers from Table 2.4 are given in parentheses in bold typeface after compound name.

Table 2.4 Lipid biomarkers detected in S12 salt, mats and drill core

Compound identifier[a]	Compound name (trivial; IUPAC name)	M+ (*m/z*)[b]	Integration ion (*m/z*)[c]	Environmental source[d]
■	*n*-alkanes	C_nH_{2n+2}	85	Ubiquitous
●	*n*-alkanols	$C_nH_{2n+2}O$	103	Ubiquitous
○	*n*-alkanoic acids (straight chain)	$C_nH_{2n}O_2$	117	Ubiquitous
STEROLS*				
1	Cholesterol (cholest-5-en-3β-ol)	458	129	Eukaryotes
2	Lophenol (4α-methyl-5α-cholest-7-en-3β-ol)	472	472	Dinoflagellates; also an intermediate in sterol biosynthesis
3	Brassicasterol (24β-methylcholest-5,22-dien-3β-ol)	470	129	Haptophytes, cryptophytes and diatoms; some dinoflagellates
4	Ergost-7en-3β-ol (24-methylcholest-7-en-3β-ol)	472	472	Algae; *Dunaliella salina*
5	Ergosterol (Ergost-5,7,22-trien-3β-ol)	468	363	Main sterol of *Dunaliella salina*
6	Campesterol (24α-methyl-cholest-5-en-3β-ol)	472	129	Higher plants
7	Stigmasterol (24α-ethyl-cholest-5,22-dien-3-ol)	484	129	Higher plants
8	β-sitosterol (24α-ethylcholest-5-en-3β-ol)	486	129	Higher plants, *Dunaliella salina*
9	Stigmast-7-en-3β-ol (24-ethylcholest-7en-3β-ol)	486	255	Green algae; *Dunaliella salina*
10	Dinosterol (4α,23,24-trimethyl-5α (H) cholest-22E-en-3β-ol)	500	69	Dinoflagellates, some diatoms
11	4α-methyl-24-ethyl-5α-cholest-22E-en-3β-ol	500	500	Gymnodinoid dinoflagellates
12	5-dehydrodinosterol (4α,23,24-trimethylcholest-5,22-dien-3β-ol)	498	139	Dinoflagellates (*Scripsiella*, *Gymnodinium* species)
13	Dihydrolanosterol (4,4,14 trimethylcholest-8-en-3β-ol)	500	395	precursor molecule in cholesterol biosynthesis after hydrogenation of lanosterol
STANOLS				
14	5β-coprostanol (5β-cholestan-3β-ol)	460	215	Cholesterol breakdown in animal guts
15	Epi-cholestanol (5α-cholestan-3α-ol)	460	215	Cholesterol breakdown in sediments
16	Epi-coprostanol (5β-cholestan-3α-ol)	460	215	Isomerization of 5β-coprostanol in sediments
17	5α-cholestanol (5α-cholestan-3β-ol)	460	215	Biohydrogenation of cholesterol in reducing sediments; also produced *in vivo* by dinoflagellates

18	5β-ergostanol (5β-ergostan-3α-ol)	474	215	Biohydrogenation of ergosterol and ergostanol
19	Ergostanol (5α-ergostan-3β-ol)	474	215	Biohydrogenation of ergosterol and ergostanol
20	24-methylenecholestanol (24-methyl-5β-cholestan-24(28)-en-3β-ol)	472	388	Biohydrogenation of sterol produced by dinoflagellates or diatoms
21	4,24-dimethylcholestanol (4α, 24S-dimethyl-5α-cholestan-3β-ol)	488	359	Dinoflagellates
22	5β-stigmastanol (24-ethyl-5β-cholestan-3β-ol)	488	215	Hydrogenation of stigmasterol or isomerization of 5α-stigmastanol
23	5α,3α-stigmastanol (24-ethyl-5α-cholestan-3α-ol)	488	215	Hydrogenation of stigmasterol
24	Stigmastanol (24-ethyl-5α-cholestan-3β-ol)	488	215	Hydrogenation of stigmasterol or isomerization of 5α stigmastanol
25	4α-methyl, 24-ethylcholestan-3β-ol	502	373	Dinoflagellates
26	Dinostanol (4α,23,24-trimethyl-5α (H) cholestan-3β-ol)	502	261	Dinoflagellates
STEROID KETONES				
27	5α-cholestan-3-one	386	231	Oxidation, hydrogenation of cholesterol in sediments
28	4α,24-dimethylcholestan-3-one	414	245	Oxidation of 4,24-dimethylcholestanol in sediments
29	4α-methyl, 24-ethylcholestan-3-one	428	245	Oxidation of 4α-methyl, 24-ethylcholestanol in sediments
30	Cycloartan-3-one	426	313	Oxidation of cycloartanol in sediments
31	Stigmastenone (Stigmast-4-en-3-one)	412	124	Oxidation of stigmasterol in sediments
STERENES				
32	5α-cholest-2-ene	370	215	Dehydration of C_{27} sterol (cholesterol)
33	5α-ergost-2-ene	384	215	Dehydration of C_{28} sterols
34	5α-stigmast-2-ene	398	215	Dehydration of C_{29} sterols
ISOPRENOIDS				
35	$C_{20,20}$ archaeol (bis-O-phytanyl glycerol)	724	TIC[e]	Archaea
36	$C_{20,25}$ archaeol (O-phytanyl-O-sesterpanylglycerol)	794	TIC[e]	Archaea
37	Phytol	368	143	side-chain of chlorophyll A; also ether-linked C_{20} alcohol sidechain in archaeol
38	Phytanol (dihydrophytol, or 3,7,11,15-tetramethylhexadecan-1-ol)	370	355	Reduction of phytol

39	Phytone (6,10,14-trimethylpentadecan-2-one)	268	85	Biotic or abiotic oxidation of phytol
40	Phytanic acid (3,7,11,15-tetramethylhexadecanoic acid)	384	117	Oxidation of phytanol
41	Squalene	410	69	Sterol precursor
42	Dihydrosqualene	412	69	Sterol precursor
HOPANOIDS				
43	C_{31} hopanol ((22R)-17(H), 21(H)-homohopan-31-ol); stereochemistry is either 17β, 21α or 17α, 21β	514	191	Stereoisomer generated by hydrogenation of C_{31} β,β hopanol in sediments
44	C_{31} hopanol ((22R)-17β (H), 21β (H)-homohopan-31-ol)	514	191	Bacteria
45	C_{32} hopanol ((22R)-17β (H), 21β (H)-bishomohopan-32-ol)	528	191	Bacteria
46	C_{32} hopanoic acid ((22R)-17β (H), 21β (H)-bishomohopan-32-oic acid)	542	191	Bacteria
47	C_{33} hopanol ((22R)-17α(H), 21β(H)-trishomohopan-33-ol)	542	191	Bacteria
48	C_{33} hopanol ((22R)-17β (H), 21α (H)-trishomohopan-33-ol)	542	191	Bacteria
49	30-nor-hopane (α,β)	398	191	Biotic or abiotic degradation of functionalized hopanoids
50	30-nor-moretane (β,α)	398	191	Biotic or abiotic degradation of functionalized hopanoids
51	30-nor-hopane (β,β)	398	191	Biotic or abiotic degradation of functionalized hopanoids
52	C_{30} hopane (α,β)	412	191	Biotic or abiotic degradation of functionalized hopanoids
53	C_{30} hopane (β,α)	412	191	Biotic or abiotic degradation of functionalized hopanoids
54	C_{30} hopane (β,β)	412	191	Biotic or abiotic degradation of functionalized hopanoids
55	C_{31} hopane (α,β)	426	191	Biotic or abiotic degradation of functionalized hopanoids
56	C_{31} hopane (β,α)	426	191	Biotic or abiotic degradation of functionalized hopanoids
57	C_{31} hopane (β,β)	426	191	Biotic or abiotic degradation of functionalized hopanoids
58	Diploptene	410	191	Bacteria

59	22,29,30-trinorhopan-21-one	384	191	Forms due to abiotic oxidation of hop-17(21)-ene
TRITERPENOIDS				
60	Tetrahymanol (Gammaceran-3β-ol)	500	191	Ciliated protists or soil bacteria
61	Gammacerone (Gammacer-3-one)	426	191	Oxidation of tetrahymanol in sediments
62	Taraxerol (Taraxer-14-en-3β-ol)	498	204	Dandelions/weeds, mangroves
63	Germanicol (Olean-18-en-3β-ol)	498	204	Higher plants
64	Lupeol (Lup-20(29)-en-3β-ol)	498	189	Higher plants
65	Friedelan-3-one	426	191	Oxidation of higher plant triterpenoids
DIOLS, KETO-OLS, ENOLS				
66	C_{20} αω diol (1,20 diol)	458	149	unknown
67	C_{22} αω diol (1,22 diol)	486	149	unknown
68	C_{24} αω diol (1,24 diol)	514	149	unknown
69	C_{28} αω diol (1,28 diol)	570	149	Precursor molecule for long chain diol and keto-ol synthesis in Eustigmatophyte algae
70	C_{30} diol(s) – mixture of 1,15; 1,14; 1,13 positional isomers of dihydroxytriacontane	598	149	Eustigmatophyte algae or diatoms
71	C_{32} 1,15 diol (1,15-dihydroxydotriacontane)	626	149	Eustigmatophyte algae
72	C_{30} 1,13 keto-ol (1-hydroxy-13-keto-triacontane)	524	130	Eustigmatophyte algae
73	C_{32} 1,15 keto-ol (1-hydroxy-15-keto-dotriacontane)	552	130	Eustigmatophyte algae
74	C_{32} alkenol (position of double bond unknown)	536	96	Precursor molecule for long chain diol and keto-ol synthesis in Eustigmatophyte algae
ALKENONES (LCAs)				
75	$C_{37:3}$ methyl long chain alkenone	528	81	Haptophyte microalgae
76	$C_{37:2}$ methyl long chain alkenone	530	81	Haptophyte microalgae
77	$C_{38:2}$ ethyl long chain alkenone	544	81	Haptophyte microalgae
78	$C_{39:2}$ long chain alkenone	558	81	Haptophyte microalgae
MISCELLANEOUS AND UNIDENTIFIED LIPIDS				
79	Alpha-tocopherol	502	502	chloroplasts of all photosynthetic organisms, including higher plants and cyanobacteria
80	U1: C_{29} sterol, possibly 4,24-dimethylcholestenol	486	486	Possibly dinoflagellates[f]
81	U2: C_{29} Δ5,22 sterol	484	484	Algal sterol[f]
82	U3: C_{30} sterol, 5 DBEs	500	485	Microalgal sterol[f]
83	U4: Lupenone-like triterpenoid (C_{30}, 6 DBEs)	424	177	Higher plants[f]
84	U5: unknown	500	395	unknown
85	U6: unknown	574	409	unknown

86	U7: C_{29} sterol, possibly 24-ethylcholestenol (not Δ5 or Δ7, but some other double bond position)	486	486	Algal sterol[f]
87	U8: 24-methylenecholestanol (stereochemistry unknown, likely 5α,3α based on elution position; but could be 5β,3α or 5α,3β)	472	388	Biohydrogenation of sterol produced by dinoflagellates or diatoms; or isomerization of 24-methyl-5β-cholestan-24(28)-en-3β-ol in sediments
88	U9: C_{28} sterol, Me-group probably in sidechain, double bond position unknown	472	472	Microalgal sterol[f]
89	U10: C_{27} sterol with 8 DBEs (i.e. 4 double bonds); seems to have positional isomers or stereoisomers (see Appendix 4)	452	452	Unknown – possibly due to dehydration of cholesterol (biotic or abiotic)
90	U11: C_{28} stanol, possibly methylated at C4 position	474	474	Microalgae[f] – dinoflagellates and haptophytes are known to produce 4-methyl sterols
91	U12: C_{29} dimethyl stanol, 24Me Δ22; other methyl position unknown (stereo- or positional isomers only slightly separated on column, integrated together)	486	257	Possibly dinoflagellates[f]

[a]Compound numbers correspond to those in Figures 2.2 and 2.3, Figures 3.5, 3.7, 3.15, 3.16, 3.20, 3.21, 3.22, 3.24 and Appendix 4. Compounds are sorted by class.

[b]M+ is the molecular ion; it is given including a derivatizing –TMSiOH group for polar compounds.

[c]Integration ions are those used for quantification (see section 2.3.7).

[d]Environmental sources are referenced in Appendix 4.

[e]TIC is total ion chromatogram.

[f]Source assignments for unknown compounds are based on source assignments for structurally similar compounds. For steroids, carbon number can be used to assign sources, as C_{27} steroids are produced by euakryotes, C_{28} steroids are most commonly produced by phytoplankton (including diatoms), C_{29} steroids are produced by green algae and higher plants, and C_{30} steroids are produced by dinoflagellates.

*Compound numbers of sterols by # carbons: C_{27}: **1**; C_{28}: **2-6**; C_{29}: **7-9**; C_{30}: **10-13**

All drill core samples contain *n*-alkanes of 10 – 35 carbons in concentrations ranging from 0.03 – 0.14 μg/g sediment extracted; *n*-alkanols of 12 – 34 carbons in concentrations ranging from 0.004 – 0.02 μg/g sediment extracted; and *n*-alkanoic acids of 5 – 30 carbons, 32 and 34 carbons in concentrations ranging from 0.00006 – 0.20 μg/g sediment extracted. Although these compounds are present throughout the drill core and so do not contribute greatly to our discussion of syngeneity, distribution patterns are important in a palaeoenvironmental context. Therefore these compounds are discussed in Chapter 3, which comprises a palaeoenvironmental reconstruction of Lake Tyrrell based on Tyrrell Bed biomarkers, mineral content and sedimentary features. Compounds central to the assessment of syngeneity appear in Table 2.4 and Figures 2.2 and 2.3.

Samples analyzed for modern lipids include samples of the salt (S12 salt, Figure 2.2A), underlying mats (S12 mats, Figure 2.2B) and surficial lunette sediments (LT 1, Figure 2.2C). Both the salt and mat samples contained a variety of high molecular weight lipids, so that saponification of the sample was necessary in order to facilitate identification of overlapping peaks (see section 2.3.6). This process hydrolyzed wax esters present in the

original unsaponified samples; these compounds were not observed in any other unsaponified samples. In addition to wax esters, the salt and mat extracts contained prominent peaks for even-carbon-number terminal diols from C_{20} – C_{24} (**66-68**), C_{27} – C_{30} sterols (**1-13**) and stanols (**14-26**), the isoprenoids phytol (**37**) and phytanol (**38**) and the $C_{20,20}$ (**35**) and $C_{20,25}$ (**36**) archaeols (Figures 2.2A and 2.2B). The salt sample also contained large amounts of squalene (**41**) and dihydrosqualene (**42**) (Figure 2.2A). Smaller amounts of plant-derived triterpenoids (**62-65**) and bacterial hopanoids (**43-59**) are also present. Surficial lunette sediments contained only a small number of C_{28} – C_{29} sterols (**2-9**) and stanols (**18-24**) in addition to the typical suite of *n*-alkanes, *n*-alkanols and *n*-alkanoic acids present in all samples (Figure 2.2C).

LT 4 is generally poor in lipids (Table 2.3), and contains very few sterols. Instead, high molecular weight compounds consist primarily of *n*-alkanes and *n*-alkanols (Figure 2.3A). Also present is tetrahymanol (**60**).

The pattern of high molecular weight neutral lipids (a/k/a complex lipids; this designation refers to all numbered compounds in Table 2.4) in LT 7 is dominated by a variety of 4-methyl sterols, stanols, and stanones of C_{27} – C_{30} (**2, 11-13; 21, 25-26; 28-29**) in high abundance. Also present are the $C_{20,20}$ (**35**) and $C_{20,25}$ (**36**) archaeols, some hopanoids (**52-54**) and some triterpenoids (**60-62**). LT 10 contains many of the same compounds, but the pattern is dominated by the archaeols (both $C_{20,20}$ (**35**) and $C_{20,25}$ (**36**)), with smaller amounts of dinosterol (**10**), dinostanol (**26**), tetrahymanol (**60**), gammacerone (**61**), plant sterols (**6-8**) and hopanoids (**54, 56**). Also present are a number of stanols (**14-24, 26**), reduced forms of the sterols found in this sample. By contrast, LT 20 is dominated by alcohols, diols (**69-71**) and keto-ols (**72, 73**), and contains small amounts of nearly all of the stereoisomers of the C_{29} – C_{31} hopanes (**52-57**).

As the $C_{20,20}$ (**35**) and $C_{20,25}$ (**36**) archaeols are present in all samples except LT 1 and LT 4, their abundance in each sample was quantified in order to determine whether the abundance of the compounds was related to mineralogy, or was instead an indicator of modern contamination at depth. Results are presented in Figures 2.4 and 2.5.

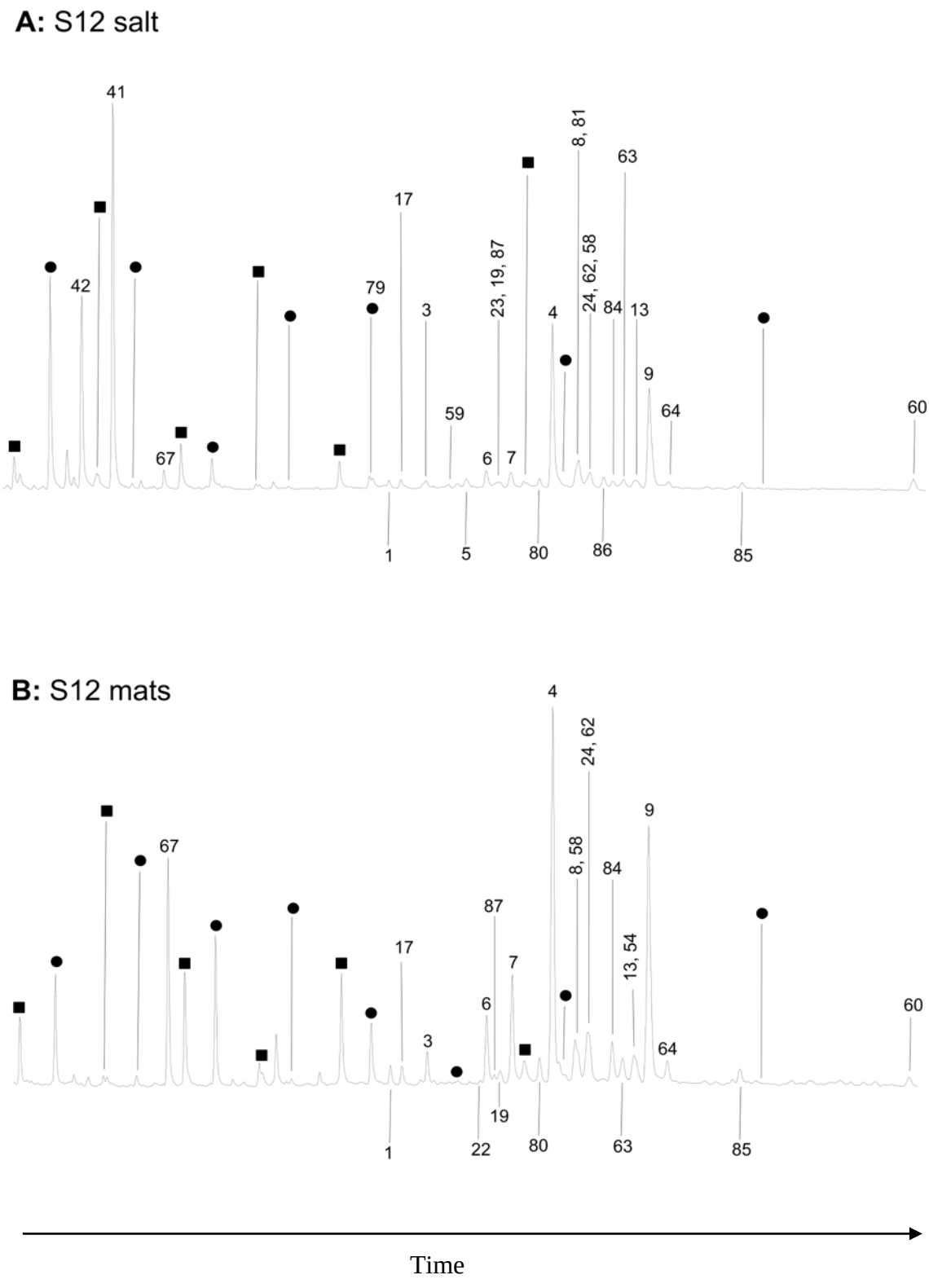
A: S12 salt
41
42
67
79
17
3
59
1
5
23, 19, 87
6
7
4
8, 81
24, 62, 58
80
63
84
13
9
64
86
60
85
B: S12 mats
4
24, 62
67
9
8, 58
84
87
17
7
13, 54
6
3
64
60
19
1
22
80
63
85
Time

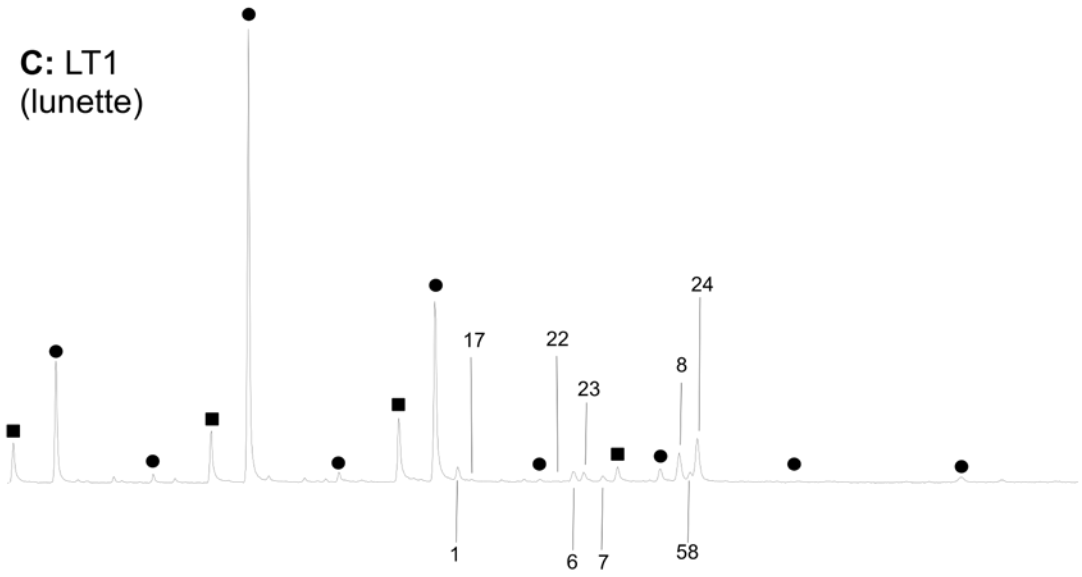

Figure 2.2 Selected ion chromatograms of modern salt (A) and mat (B) samples and lunette (C).

Selected ion chromatograms are composed of the summed traces of integration ions for all compounds present, with each compound displayed using the integration ion. Compound numbers and symbols correspond to those given in Table 2.4. Archaeols and hopanols/hopanoic acids not shown. First compound displayed is nC$_{27}$ alkane, last is tetrahymanol (**60**) for all chromatograms.

n-alkanes displayed: salt and mats, C27-C31, C33; LT 1, C27-C33 ODD. *n*-alkanols displayed: salt, C24-C28, C30, C32; mats, C24-C30, C32; LT 1, C24-C32. *n*-alkanoic acids displayed: none.

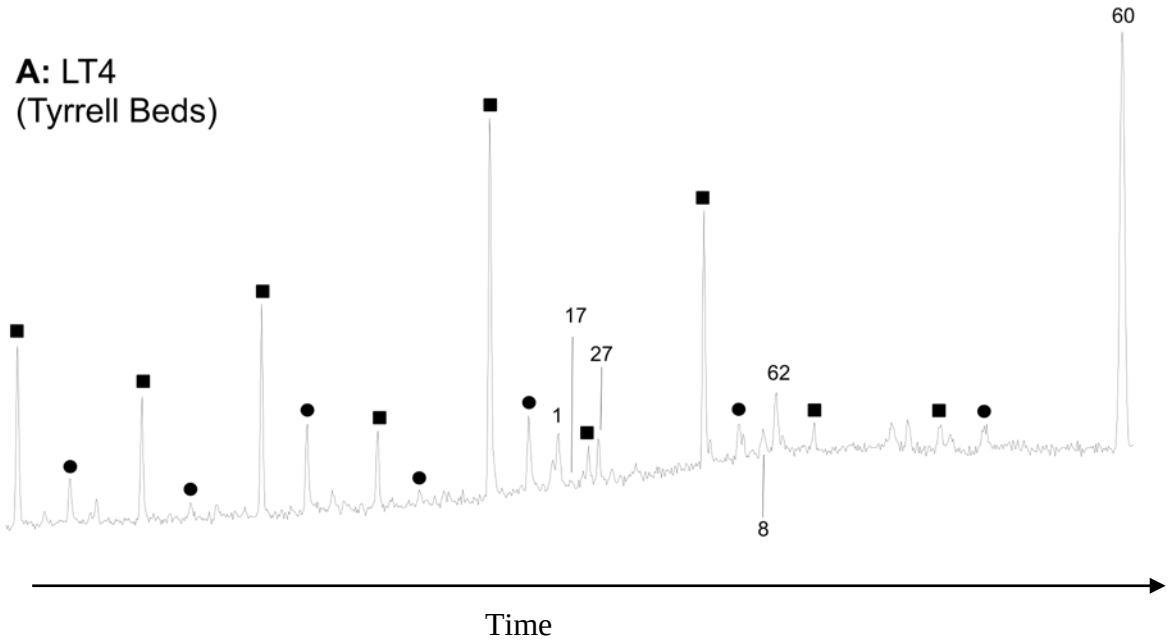

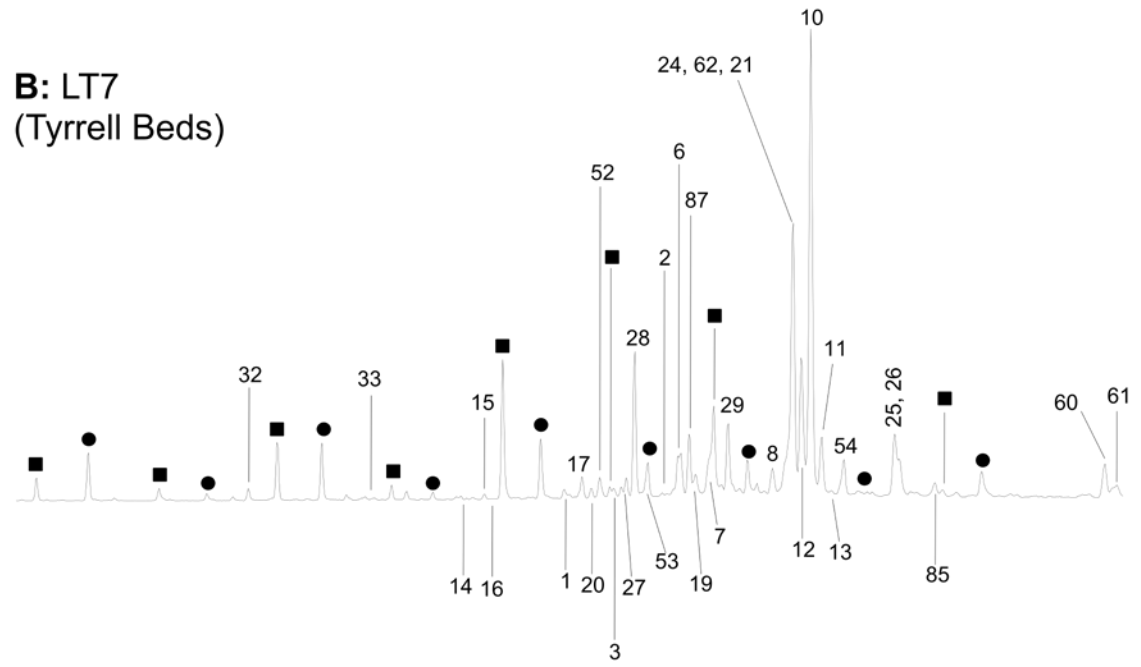
B: LT7
(Tyrrell Beds)
10
24, 62, 21
6
52
87
2
28
11
32
33
15
29
25, 26
60
61
17
8
54
14 16
1 20 27
53
19
7
12 13
85
3

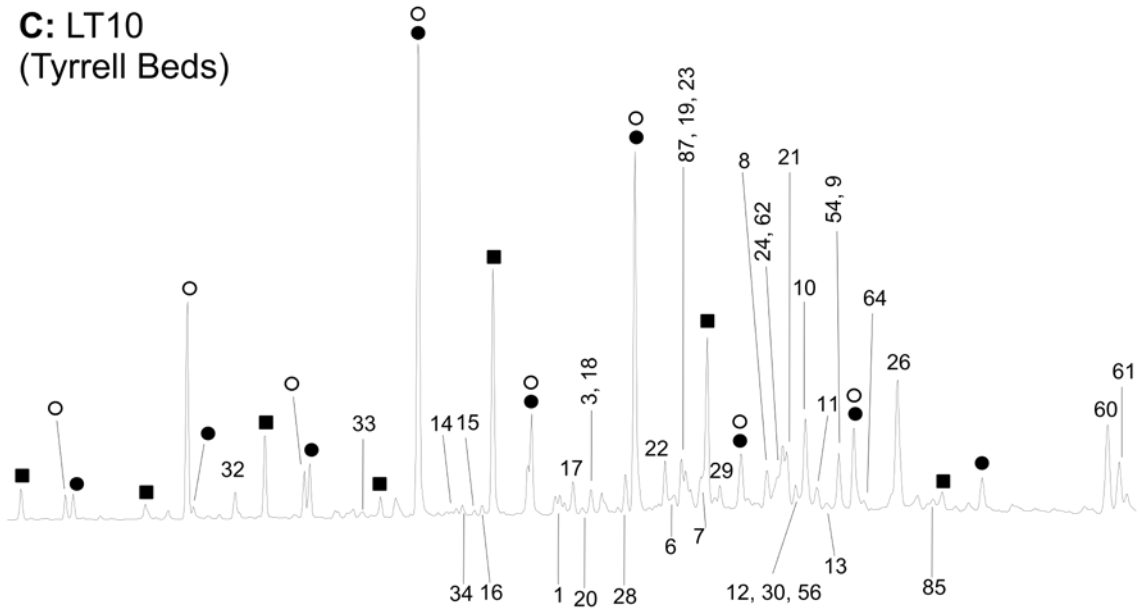
C: LT10
(Tyrrell Beds)
87, 19, 23
8
21
54, 9
24, 62
10
64
26
61
3, 18
11
60
33
14 15
22
32
17
29
6
7
13
34 16
1 20 28
12, 30, 56
85

Time

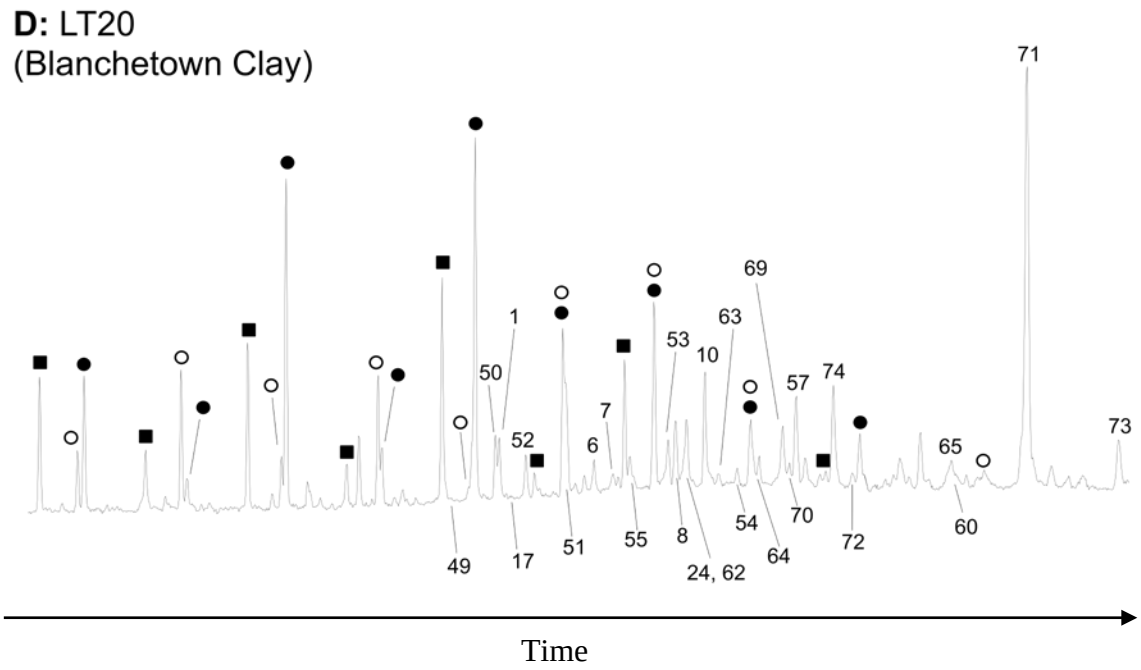

Figure 2.3 Selected ion chromatograms of Tyrrell core subsamples.
Selected ion chromatograms are composed of the summed traces of integration ions for all compounds present, with each compound displayed using the integration ion. Compound numbers and symbols correspond to those in Table 2.4. Archaeols and hopanols/hopanoic acids not shown. First compound displayed is nC$_{27}$ alkane, last is tetrahymanol (**60**) unless otherwise indicated.
n-alkanes displayed: LT 4, C27-C35; LT 7 and 20, C27-C33, C35; LT 10, C27-C31, C33, C35.
n-alkanols displayed: LT 4, C24-C28, C30, C32; LT 7, 10, and 20, C24-C32
n-alkanoic acids displayed: LT 4 and 7, none; LT 10, C23-C30; LT 20, C23-C30, C32
For LT 7 and 10, last compound displayed is gammacer-3-one (**61**); this compound is not present in any of the other samples shown here. For 20, last compound displayed is C32 1,15 keto-ol (**73**); diols and keto-ols not present in other samples.

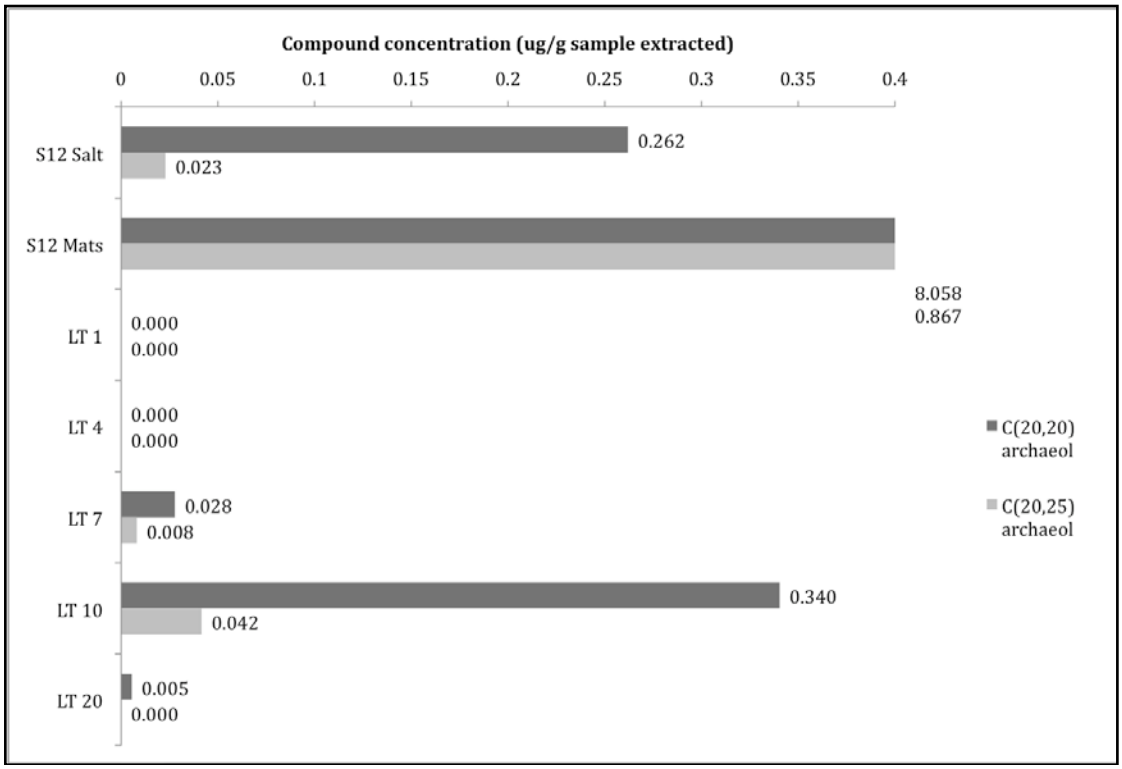

Figure 2.4 Abundance of $C_{20,20}$ and $C_{20,25}$ archaeols in modern mat, salt and lunette samples compared to S12 drill core samples

Note that the abundance of archaeols present in the S12 mat sample exceeded the scale of the graph; concentrations are noted to the right of the bars.

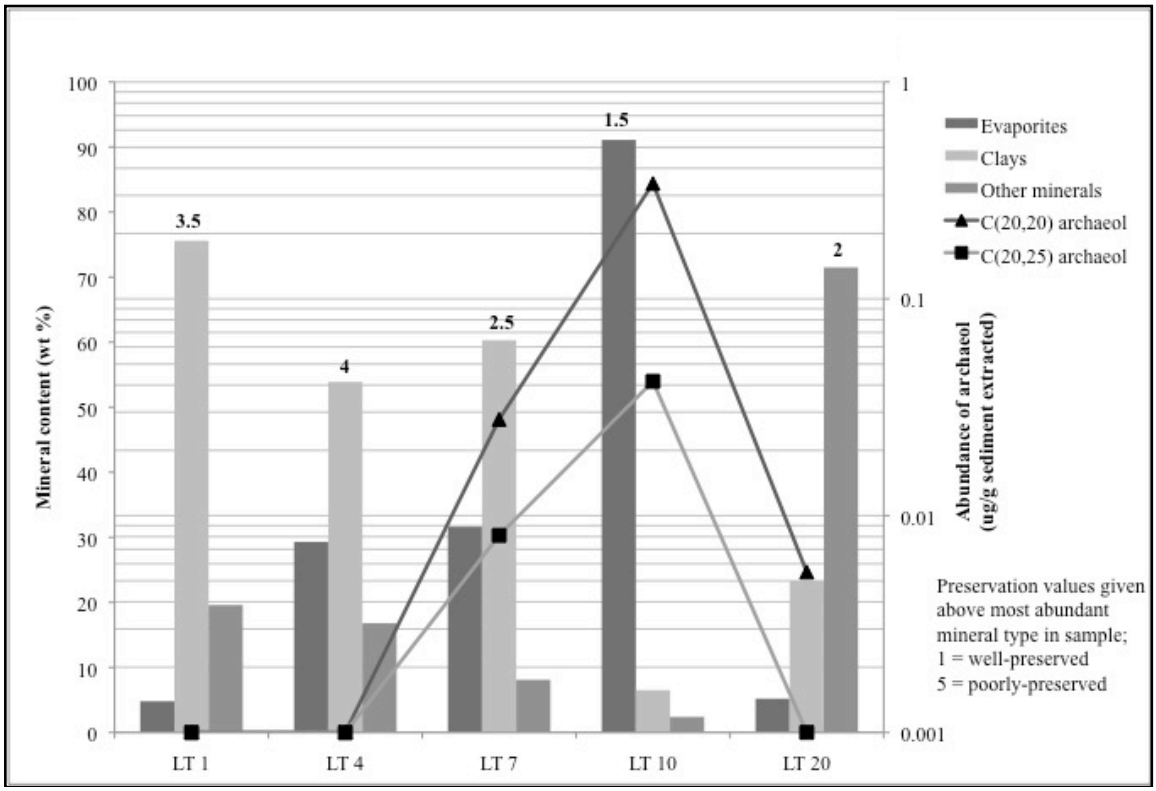

Figure 2.5 Variation in concentration of archaeols with mineral content of lunette and S12 drill core samples

Note that concentration axis is $\log_{10}$ scale. LT 1 and LT 4 contain no archaeols, LT 20 contains no $C_{20,25}$ archaeol. The 0.001 ug/g abundance given for these data points is an artifact of plotting zero values on a $\log_{10}$ scale axis

2.5 Discussion

The primary objective of this study was to determine if lipids preserved at depth are indigenous to, and were deposited concurrently with, the sediments from which they are extracted. We interpret lipids at a specific depth as syngenetic (i.e. not contamination) if they are not in the system blank, are not introduced from younger or older sediments or modern biotic material, and are indicative of a palaeo-community whose existence is consistent with palaeoenvironmental information derived from analyses of mineralogy, sedimentary texture and pollen.

2.5.1 Sources of lab and modern contamination

As system blanks did not contain any of the compounds of interest in this investigation, lab contamination can be eliminated from consideration. To determine whether cross-sample contamination could have destroyed the indigenous lipid signature, we compared compound presence/absence and abundance across samples. Simple lipid compounds (*n*-alkanoic acids, *n*-alkanols and *n*-alkanes) are common to most or all samples. However, these compounds are ubiquitous in the natural environment (Peters and Moldowan 1993), so that they are of limited utility as indicators of syngeneity. Consequently, these lipid classes were excluded from further analyses designed to assess cross-contamination. Instead, we compared patterns of high-molecular weight neutral lipids (a/k/a complex lipids), such as steroids, triterpenoids, hopanoids, mid-chain and terminal diols, hydroxy-ketones and isoprenoidal alcohols across samples from within the core and from modern mat and salt. These compounds have well-defined source organisms, so that differences in biomarker

abundance and composition between samples are indicative of changes in the community of source organisms.

Biomarkers extracted from modern algal mats, overlying salts and lunette material were compared to those extracted from samples from the core to test whether contamination by modern or re-worked material could account for lipids present at depth. As noted in section 2.4.4, wax esters were present in the unsaponified TLE of the S12 mat sample. These compounds are known to be resistant to diagenetic alteration or degradation in lacustrine sediments because of their low solubility and low susceptibility to microbial re-working (Meyers and Ishiwatari 1993). Therefore, if modern mat material had fallen into cracks in the lake bed, for example, and contaminated deeper sediments, we would expect to see wax esters in unsaponified extracts of drill core sediments. In fact, wax esters are absent at depth.

The modern salt sample also contained squalene (**41**) and dihydrosqualene (**42**), neither of which were found in any of the core samples. These C_{30} isoprenoids are precursors for sterol biosynthesis (Peters and Moldowan 1993), but also compose ~36% of neutral lipids in the halophilic archaeal taxa *Halobacterium, Haloferax* and *Haloarcula* (Kamekura and Kates 1988). It has been shown that the proportion of squalene to dihydrosqualene is 1:0.4 in *Halobacterium cutirubrum* under aerobic conditions (Kamekura and Kates 1988). In the S12 salt extract the proportion is 1.0:0.49, so it is possible that *H. cutirubrum* (or a closely related organism) is the source of the C_{30} isoprenoids. As the abundance of the C_{30} isoprenoids is quite high in the salt (1-3% of complex lipids, see Figure 3.7 compounds 41 and 42), if contamination from modern salt had affected deeper samples, we would expect to see squalene or its hydrated product, squalane, within the core. Since we do not see these compounds, we can conclude that it is unlikely that significant concentration of compounds from modern salt have penetrated to depth in lake sediments.

Also present in very high abundance in both modern salt and mat samples were the $C_{20,20}$ (**35**) and $C_{20,25}$ (**36**) archaeols (Figure 2.4), which are produced by halophilic archaea (Mullakhanbhai and Francis 1972). $C_{20,25}$ archaeol has been identified in haloalkaliphilic archaea such as *Natronobacteria* or *Natronococcus* (Kamekura and Kates 1988), methanogens (Javor 1989), all strains of *Halococcus morrhuae*, *Halobacterium halobium* (Morita *et al.* 1998) various members of *Halobacteriaceae* (Dyall-Smith 1995) and in an unidentified nonalkaliphilic extreme halophile isolated from sea sands in Japan (Kamekura 1993). It is unlikely that the $C_{20,25}$ isoprenoid in the modern mats and salt derives from haloalkaliphiles, as the mineral assemblage does not indicate an alkaline environment (Macumber 1991). *Halococcus* and *Halobacterium* species are found in the modern lake (Banfield *et al.* 2009). Therefore it is reasonable to suppose that the $C_{20,25}$ isoprenoid derives from one of these, or another, unidentified nonalkaliphilic extreme halophile.

The isoprenoids phytol (**37**) and phytanol (**38**) are usually interpreted as biomarkers for higher plant input, as they derive from the breakdown of the chlorophyll side-chain in sediments (Meyers and Ishiwatari 1993; Rhead 1971; Volkman 1986; Volkman *et al.* 1981). In hypersaline systems, however, these compounds have been shown to derive predominantly from cleavage of the phosphatidyl glycerophosphate ethers of halophilic archaea (Nissenbaum *et al.* 1972; Oldenburg *et al.* 2000). In modern salt and mat samples of Lake Tyrrell, higher plant sterols (campesterol (**6**) and stigmasterol (**7**)), tripterpenoids (germanicol (**63**) and lupeol (**64**)) and *n*-alkanes are present in much lower abundance than archaeal isoprenoids (Table 3.3 and Figure 3.7). From these data, we conclude that halophilic archaea are major contributors to the lipid biomarker pool under hypersaline conditions. The presence of phytol and phytanol at depth, if found in conjunction with an evaporitic mineral matrix, could be used to confirm syngeneity of lipids and to estimate palaeo-salinity at halite saturation, even if halite had been dissolved away.

Many of the $C_{27} - C_{30}$ sterols and stanols in the mat and salt samples are also present at depth, including cholesterol (**1**), brassicasterol (**3**), campesterol (**6**), stigmasterol (**7**), β-sitosterol (**8**) and dihydrolanosterol (**13**) (Figures 2.2A and B). The presence of these sterols is usually ascribed to input from animals (in this system, brine shrimp may contribute cholesterol (Payne and Kuwahara 1972)) and higher plants (Pancost and Boot 2004), so that it is not surprising that they should appear throughout the core. In the modern samples, there may be a different source: all of these sterols have been found in uni-cellular algae (Volkman 1986), and the two sterols in highest abundance in the modern mats and salt are ergost-7-en-3β-ol (**4**) and stigmast-7-en-3β-ol (**9**), which are the primary sterols found in the halophilic green alga *Dunaliella* sp. (Oldenburg *et al.* 2000). Also present in the mats and salt is ergosterol (**5**), one of two sterols found in *Dunaliella salina* (Peeler *et al.* 1989). *Dunaliella salina* is known to be present in the lake water (Banfield *et al.* 2009), so the abundance of its primary sterols in conjunction with the other $C_{27} - C_{30}$ sterols, and considering the small amounts of plant terpenoids such as lupeol (**64**) and germanicol (**63**), points to an algal origin for most of the sterols in these samples. Ergosterol (**5**) is not present in any samples at depth, but ergostanol (**19**), produced by biohydrogenation of ergosterol in sediments, is (Figures 2.3B and C). This again indicates that modern contaminants are not present at depth, but that modern environments may be analogous to palaeoenvironments.

Terminal diols in the range $C_{20} - C_{24}$ (**66**-**68**), the origins of which are unknown, are present in both the mats and the salt, but not in any of the core samples. Longer chain terminal diols ($C_{28} - C_{32}$) have been found in marine Eustigmatophyte algae such as *Nannochloropis* species (Mejanelle *et al.* 2003; Volkman *et al.* 1992), so it is possible that these shorter chain diols have a similar origin. Given the salinity of the lake (halite saturation) however, it is unlikely that a marine species would survive therein. The microalga *Dunaliella* may be the source, or some other, as-yet-unidentified alga. Again, the absence of these compounds at depth indicates that modern organisms are not the source of the lipids in older samples.

Interestingly, the modern salt and mat extracts contained no hopanols or hopanoid acids, and only trace amounts of C_{30} β,β hopane (**54**, Figure 2.2B), diploptene (**58**, Figures 2.2A and B) and 22,29,30-trinorhopan-21-one (Figure 2.2A). Hopanoids form through the cleavage of the polyol-bearing side chain of bacteriohopanpolyols (BHPs), compounds that have been identified as essential components of the lipid membranes of many prokaryotes, such as cyanobacteria (Rohmer *et al.* 1980). They are thought to perform a similar biochemical function (promoting membrane stability and regulating membrane fluidity) as sterol in eukaryotes (Ourisson *et al.* 1987). Hopanoid compounds are ubiquitous in modern sediments (Ourisson *et al.* 1979), and are interpreted as evidence of the presence of bacteria.

The contrast between the hopanoid profiles of the modern mat and salt samples and the sediment samples from depth is instructive. Diploptene (**58**) and 22,29,30-trinorhopan-21-one (**59**) are present in the modern samples, but absent at depth. Diploptene is a precursor to the common bacterial hopanoid diplopterol (ten Haven *et al.* 1989), and 22,29,30-trinorhopan-21-one forms through the abiotic oxidation of hop-17(21)-ene, itself a diagenetic product of diploptene (Kashirtsev *et al.* 2008). If contamination from modern mats and salt were affecting samples at depth, these compounds would be present at all or most depths, and would be relatively abundant in samples poor in indigenous lipids. Also present in the modern mat is C_{30} β,β hopane (**54**). The β,β isomer of the hopanoids represents the natural 'biotic' configuration; conversion to β,α and α,β isomers occurs only over time (Mackenzie and Maxwell 1981; Quirk *et al.* 1984). The absence of these other isomers in the modern mat, and their presence in LT 7, 10 and 20 indicates that older samples containing hopanoids cannot have sourced these hopanoids from modern overlying mats and salt.

Having eliminated modern salt and mats as sources of lipids at depth, we turn to the lipids present in the lunette. The lipids of the lunette samples derive mainly from higher plants, and from hydrogenation of those lipids in sediments. The attribution of campesterol (**6**), stigmasterol (**7**) and β-sitosterol (**8**) to higher plant input is supported by the overwhelming predominance of odd- over even-numbered carbon chain length *n*-alkanes (Figure 3.18) in the range of $C_{19} - C_{31}$, and the predominance of even- over odd-numbered carbon chain length *n*-alkanols (Figure 3.17) in the range of $C_{22} - C_{30}$ (Meyers 2003). There are also a number of C_{27} and C_{29} stanols in the sample. While some organisms, such as diatoms and dinoflagellates, do produce stanols instead of sterols (Nishimura and Koyama 1976; Withers 1987), the 5α-cholestanol (**17**) and suite of stigmastanol stereoisomers (**22-24**) in this samples are more likely the result of hydrogenation of their associated sterols. This diagenetic change is common in soils and sediments (Gaskell and Eglinton 1976; Nishimura 1977; Nishimura and Koyama 1977). The 5α isomers predominate over the 5β isomers, as would be expected in an oxygenated sedimentary environment (Reed 1977) such as the dry, sandy-clay lunette (Table 2.1).

The presence of higher plant lipids would be expected throughout the core, as terrigenous input into lakes is generally high (Meyers 2003; Meyers and Ishiwatari 1993). In addition, plant lipids are preferentially preserved in lacustrine sediments relative to autochthonous lipids, as it is largely the unreactive or recalcitrant compounds that survive microbial and abiotic re-working on land in order to enter the lake (Meyers and Ishiwatari 1993). However, the lunette sample also contains diploptene (**58**, Figure 2.2C), which, as previously discussed, is a marker for bacterial activity. This compound is not found in LT 4, 7, 10 or 20, indicating that the lunette is not the source of lipids at depth.

I have shown that lipids extracted from samples in the core are not laboratory contamination, nor are they sourced from modern salt, mat, or lunette material. Therefore, it is unlikely that cracks in the lakebed are allowing penetration of significant quantities of modern material to depth. The only other way for modern lipids to enter sediments at depth would be as soluble compounds in groundwater. Two pieces of data argue against this possibility: first, lipids, even those with polar moieties, are fairly insoluble in water. For example, a 14-carbon alkanoic acid has a solubility in water of just 0.02 g per liter of water, and solubility of alkanoic acids decreases exponentially with increasing chain length (http://www.cyberlipid.org/fa/acid0001.htm). This effect is exacerbated when the water is traveling through clays: lipids (especially polar lipids and high molecular weight lipids) will preferentially sorb to clays in systems containing water and clays (Brothers *et al.* 1991; Carlson and Chamberlain 1986; Krooss and Leythaeuser 1988). Second, groundwater in Lake Tyrrell is sourced from reflux brines within the lake itself or from brines of Lakes Timboram and Wahpool (Macumber 1991), both of which are saline. Therefore, any compounds brought in by groundwater would be sourced from halophilic organisms, and would be present throughout the core, such that the lipid profile of a sample deposited under a fresher regime would be inconsistent with that sample's mineralogy. Below, we describe the lipid profile, mineral content, sedimentary textures, and pollen of four subsamples from the Lake Tyrrell S12 core, from both the Tyrrell Beds and the Blanchetown Clay, to determine whether lipids therein are consistent with the depositional environment of the sample as reconstructed through mineralogy, pedology and palynology.

2.5.2 Tyrrell Beds samples

The three core subsamples from the Tyrrell Beds differ in their mineral content, their pollen content, and their level of preservation of primary components of the sediment. In order to interpret these data, each component must be examined with reference to the others. This is because post-depositional processes, such as secondary mineralization, can alter

sediment textures and mineral content, and destroy pollen. For this reason, it is essential to account for differential sample preservation and post-depositional processes when contextualizing observations across samples.

For example, one sedimentary component shared between all the samples, including those from the lunette and the Blanchetown Clay, is halite. Estimates of palaeo-salinity are central to reconstructions of lake level and hence, regional precipitation, and halite is known to precipitate from brines at salinity levels in excess of 350 g/L TDS (total dissolved solids) (Bowler and Teller 1986). However, the accessory halite present in all samples likely formed post-depositionally – i.e., it precipitated from interstitial water during an increase in salinity, or as samples dried in the lab. Due to its high solubility and the saturation of the groundwater that currently feeds Lake Tyrrell (Macumber 1991), halite is usually deposited within sediments at the groundwater horizon. As this horizon moves up and down, halite may be deposited within layers that initially contained none. It also means that halite is selectively leached during times of lake freshening (due to increased precipitation or flow from Tyrrell Creek), such that palaeo-halite crusts, deposited under similarly arid conditions to those that predominate today, are not preserved in the sediment record (Bowler 1986). Therefore, the presence or absence of halite within sediments cannot be used to make reliable estimations of palaeo-salinity.

LT 4 contains a 1 cm layer of poorly-sorted quartz composed of larger, rounded grains and smaller, angular grains at the base, indicating a depositional sequence beginning with the accumulation of nearshore beach sands (Appendix 2, Figure A2.2 B). Different degrees of rounding of the quartz grains could reflect different modes of transport. Transition to clay layers implies rising lake levels due to greater runoff or discharge into the lake (Appendix 2, Figure A2.2 D). Overlying clays heavily stained with iron-oxides were most likely deposited during a deeper water phase (Appendix 2, Figures A2.2 F and G). The absence of ripple marks is also consistent with a deeper depositional environment, but these and other textural indicators may have been destroyed by post-depositional soil formation or by bioturbation by benthic organisms. The latter is more likely, as the sample displays multiple indicators of post-depositional alteration. These include quartz sand grains exhibiting clay cutans (Appendix 2, Figure A2.2 A), iron oxide staining of clays (Appendix 2, Figures A2.2 C and G), oriented clay haloes along cracks (Appendix 2, Figure A2.2 F) and other features common to the initial phase of soil development. No pollen were found in this sample, and solvent-extractable lipid content was low compared to the other subsamples (Table 2.3). These characteristics indicate that oxidation of the sediment initially deposited as a lacustrine sequence occurred during a subsequent lake-dry phase of sufficient duration for soil development to begin.

The mineralogy of LT 4 is also consistent with an interpretation of intensive post-depositional alteration: it contains a high percentage of clays and quartz; however, dolomite comprises approximately one quarter of the total weight of the sample. Dolomite is often found in the sediments of salt lakes of thalassohaline composition, where its presence has typically been attributed to the high Mg:Ca ratios of interstitial water generated by gypsum precipitation (Bowler and Teller 1986) and by the metabolic activities of mat-building organisms and sulfate-reducing bacteria (refer to Chapter 4). Based on the textural evidence for pedogenic processes contained in this sample, and on the micritic nature of the dolomite therein, it is more likely that this evaporite formed as a result of linked sequential post-depositional processes. First, calcium and carbonate ions within the dry lakebed sediment were mobilized by meteoric waters, and transported and deposited at horizons within the developing soil. This process occurs widely in regions where evaporation exceeds precipitation (Sehgal and Stoops 1972). Subsequently, during a lacustrine phase when the

proto-soil was bathed in saline waters with a high Mg:Ca ratio, the carbonate was dolomitized (the calcium was partially replaced with magnesium).

The suite of lipids in LT 4 are consistent with the sample's history as derived from mineral and textural data: the lipids seem to have been deposited by plants and microorganisms present during pedogenesis, as opposed to having been re-worked from the lake. The presence of 5α-cholestan-3-one (**27**) in addition to cholesterol (**1**) is consistent with post-depositional oxidation of the sample (Robinson *et al.* 1984). While β-sitosterol (**8**) is found in *D. salina*, as previously discussed, it is usually a marker for higher plants, especially when found in conjunction with taraxerol (**62**), as it is here (Koch *et al.* 2003) (Figure 2.3A).

Tetrahymanol (**60**) is primarily found in bacterivorous ciliates (Harvey and McManus 1991), and is usually taken to be an indicator of a stratified, saline environment (Peters and Moldowan 1993; Venkatesan *et al.* 1990). However, it is also found in a phototrophic alpha-*Proteobacteria, Rhodopseudomonas palustris* (Kleemann *et al.* 1990). *R. palustris* is a gram-negative bacteria commonly found in soil and sediment (Bent *et al.* 2003). If the tetrahymanol in LT 4 derived from a ciliate and is remnant in the soil from the previously existing lakebed, we would expect to find gammacer-3-one (**61**) co-occuring (ten Haven *et al.* 1989). Gammacer-3-one is the oxidation product of tetrahymanol, and would be expected to form during pedogenesis. The conspicuous absence of this compound indicates that it is likely that this tetrahymanol was emplaced post-diagenetically, during the "soil-building" phase, and so derives from *R. palustris* instead. Thus, in this layer tetrahymanol may be evidence of soil formation rather than salinity stratification.

In contrast to LT 4, LT 7 and 10 contain undisturbed sediment laminae and show relatively little evidence of post-depositional oxidation or pedogenesis. In addition, these samples contain pollen (Table 2.2) and marginally larger quantities of TOC (Table 2.3) than did LT 4.

LT 7 was perhaps deposited during a relatively wet time, as indicated by the extensive wash-in of clays and quartz (comprising > 50% of this sample). The presence of evaporites in the sample – gypsum and a small quantity of dolomite – is mostly due to post-depositional alteration of primary components. Based on the lenticular morphology of the gypsum crystals (Appendix 2, Figures A2.6 D and G), it is likely that groundwaters at gypsum saturation deposited gypsum displacively (Magee 1991), leading to high Mg:Ca ratio in groundwaters. Dolomitization of primary carbonate followed.

Deposition over the interval spanned by LT 7 commenced with deeper water clays, followed by the emplacement of displacive gypsum. The presence of the gypsum indicates a dryer lake phase, when surface water was absent and the capillary fringe of the groundwater was below the sediment surface. The imputation of this sequence of events is further supported by the presence of polygonal clay peds and iron-oxide blebs within the clay layer (Appendix 2, Figures A2.6 A-C), which indicate that drying occurred prior to further deposition.

Above the displacive gypsum layer are the gypsum/clay couplets, containing a layer of fecal pellets (Appendix 2, Figures A2.6 E and F). Based on the size (~100 μM in length) and shape (ovoid) of the pellets, it is possible that they derive from the gastropod *Coxiella*, an organism with a salinity tolerance of 10-100 g/L (Bowler and Teller 1986). This is slightly below the value accorded for gypsum saturation, but fits with the hypothesis of a sulfate saturated basin experiencing periodic, possibly seasonal, freshening, which would have washed in the clays and allowed colonization by organisms such as *Coxiella*. Orientation of the clay layers argues against significant benthic populations, however, so that the fecal pellets may derive from a planktonic organism, or may represent only a small population of grazers. Emplaced above these couplets is a thick (6 mm) layer of primary gypsum (Appendix 2, Figure A 2.6, ~415 cm depth), of a size (average grain size 40 μM) and shape

suggesting that it is 'settled' gypsum (Magee 1991) forming in waters supersaturated in sulfate (~120 g/L TDS (Bowler and Teller 1986)).

Overlying this layer are more massive clays, suggesting fresher and deeper waters returned to the lake. These clays include another lens of displacive gypsum, the sub-parallel orientation of which suggests emplacement along a more porous layer of sediments. Above this lens is a sub-vertical quartz lens, suggestive of the filling of a sub-vertical crack formed during a drying event. The quartz grains, which are rounded and poorly-sorted, likely derive from a beach sand. Further evidence for the drying event appears in the clay layer, in which polygonal cracking – the initial step in ped formation – can be seen (Appendix 2, Figure A2.6 H).

The most abundant compounds in LT 7 are 4-methyl sterols (**2, 10, 11, 12**), stanols (**21, 25, 26**), and stanones (**28, 29**) (Figure 2.3B), which derive primarily from dinoflagellates. The high abundance and variety of compounds, taken together with the relatively low abundance of archaeols (both $C_{20,20}$ (**35**) and $C_{20,25}$ (**36**)), points to a lacustrine system dominated by dinoflagellates. While some hypersaline dinoflagellates do exist (Alexander *et al.* 2009), most dinoflagellates live at fresh to marine salinity (Brand 1984). While 4,24-dimethlycholestanol (**21**), dinosterol (**10**), dinostanol (**26**), 4α-methyl, 24-ethylcholestan-3β-ol (**25**) and lophenol (**2**) are produced by a number of dinoflagellate species, 5-dehydrodinosterol (**12**) and 4α-methyl-24-ethyl-5α-cholest-22E-en-3β-ol (**11**) are only known to be produced by *Gymnodinium* species of dinoflagellates (Withers 1983, 1987). Gymnodinoid dinoflagellates are a large, polyphyletic group; however, all described species are marine (http://www.tolweb.org/Dinoflagellates/2445). The salinity tolerance of *G. simplex* ranges from 15 – 45 parts per thousand (ppt), with optimal growth at 33 ppt, which is the salinity of surface marine water (Brand 1984).

Not all of the sterols in the sample are unique to dinoflagellates: some diatoms have also been shown to produce dinosterol (Volkman *et al.* 1998); however they have not been shown to produce other 4-methyl sterols. In any case, most diatom taxa have salinity optima of < 3 g/L TDS (Wilson *et al.* 1994), which is fresh to subsaline, so that the environmental interpretation is unchanged. Moreover, it is likely that dinoflagellates, rather than diatoms, are the source of the dinosterol in this sample, due to the presence of dihydrolanosterol (**13**). Dihydrolanosterol (hydrogenated form of lanosterol) is an intermediate in sterol biosynthesis for the pathway shared by animals, fungi and dinoflagellates (Scallen *et al.* 1971), while higher plants, microalgae and protozoans utilize a pathway in which cycloartenol, instead of lanosterol (Volkman 2003). As no other sterols that are unique to diatoms are present, and the intermediate for sterol synthesis by dinoflagellates is present, it is safe to assert that this system was dominated by dinoflagellates.

In addition to the unaltered stenols, products of oxidation (stanones) and reduction (stanols) are also present. The high quantities of 4α,24-dimethylcholestan-3-one (**28**) and 4α-methyl, 24-ethylcholestan-3-one (**29**) relative to their precursor stanols (Figure 2.3B) indicate that post-depositional oxidation of the sample occurred; this interpretation is supported by the presence of gammacer-3-one (**61**) in addition to tetrahymanol (**60**). Biohydrogenation of indigenous stenols in sediments is indicated by the presence of all four stereoisomers of cholestanol (**14-17**), derived from hydrogenation of cholesterol; two stereoisomers of 24-methylenecholestanol (**20, 87**), derived from hydrogenation of the sterol produced by dinoflagellates or diatoms; and ergostanol (**19**) and stigmastanol (**24**), derived from the hydrogenation of the higher plant sterols (campesterol (**6**), stigmasterol (**7**) and β-sitosterol (**8**)) present in the sample.

Overall, the lipid suite of this sample is consistent with a lake at marine salinity, in which bottom-sediments were reducing and dinoflagellates were the major source of autochthonous lipids. Subsequent to deposition, the lakebed dried sufficiently for oxidation

of surficial sediments to occur. These interpretations are consistent with those derived from the mineralogy and pedology of this sample.

LT 10 was deposited under the highest salinity regime of any of the subsamples examined: the presence of primary gypsum indicates a TDS value between 120-150g/L (Bowler and Teller 1986). A small quantity of clays and quartz are also present, and are likely derived from runoff. The low quantity of these components indicates that runoff did not contribute significantly to the water budget of the lake at the time the sample was deposited. This mineral assemblage – primarily evaporites, with some clays and detrital minerals – is very similar to that seen in the modern lakebed (Bowler and Teller 1986) (Table 5.1). If LT 10 is analogous to the modern system, then it represents a groundwater fed lake of less than 1 m depth dominated by microbial mats and planktonic halophiles.

As LT 10 also contains the least evidence of post-depositional alteration, interpretations based on the mineralogy are robust. Laminae within the sections are undisturbed and iron-oxide staining is completely absent. In addition, nearly all gypsum crystals present in the laminae appear to be primary – crystals are prismatic and there is little evidence of re-working – so that salinity values based on gypsum precipitation represent those of the lake during the time of deposition. Both oriented and non-oriented clay layers alternate with primary gypsum laminae (Appendix 2, Figures A2.9 A-C), and many of the clay layers contain large (~250 μM width) syneresis cracks (see for example Appendix 2, Figure A2.9 at ~522.5 cm). These cracks are the result of contraction or shrinkage of clay layers due to changes in the salinity of the water overlying or bathing the clays (Burst 1965). Taken together, the primary gypsum and clay layers represent an evaporitic regime interrupted periodically by freshening.

This interpretation is supported by reverse grading in some of the gypsum layers (Appendix 2, Figure A2.9 A): such a sequence indicates rapid precipitation from water super-saturated with sulfate, followed by slower growth of larger crystals in a saline lake. The putative fecal pellets that appear in one of the gypsum layers appear to have been compressed, perhaps by post-depositional crystal growth. Based on the size of the pellets and their presence within primary gypsum layers, it is possible that these derive from the ostracod *Diacypris*, which has a salinity tolerance of up to 200 g/L (DeDeckker 2009). Therefore, LT 10 was deposited by a primarily hypersaline lake in which periodic freshening events occurred.

The suite of lipids in LT 10 is broadly similar to that in LT 7: many of the same compounds are present; however, relative abundances are quite different (Figures 2.3B and C). Stanols are more prevalent, while stanones are less abundant, indicating that biohydrogenation in sediments was the dominant diagenetic pathway for sterols. This is consistent with the lack of pedological evidence for post-depositional oxidation. Some dinoflagellate sterols are present, including the gymnodinoid sterols 5-dehydrodinosterol (**12**) and 4α-methyl-24-ethyl-5α-cholest-22E-en-3β-ol (**11**), dinosterol (**10**), 4,24-dimethlycholestanol (**21**) and dinostanol (**26**); however, they are in lower abundance relative to the sterols (and stanols) derived from higher plants. In addition, stigmast-7-en-3β-ol (**9**), a marker for green algae and a sterol of *D. salina* is present. This compound is absent in LT 1, 4, 7 and 20, but is found in the modern lake (Figures 2.2A and B). This supports the interpretation that LT 10 is analogous to the modern system.

The dominant compounds in this sample are the archaeols (both $C_{20,20}$ (**35**) and $C_{20,25}$ (**36**)), indicating an abundance of halophilic archaea in the lake during the time of deposition. While the $C_{20,20}$ diether core lipid is ubiquitous among extreme halophiles (Kamekura and Kates 1988), the $C_{20,25}$ moiety is less common, as described in section 2.5.1. It is unlikely that the $C_{20,25}$ lipid in this sample derives from haloalkaliphiles, as the mineral assemblage does not indicate an alkaline environment. *Halococcus* and *Halobacterium* species are found in the

modern lake, and the core isoprenoidal lipid $C_{20,25}$ is found in abundance in modern lake sediments (Figure 2.4). Based on the mineral assemblage, geochemical conditions in the modern lake (described in chapter 1) are similar to those that predominated during deposition of LT 10. Therefore it is reasonable to suppose that the $C_{20,25}$ archaeol in LT 10 derives from similar sources.

Archaeol may therefore be a reliable indicator of salinity when preservation is taken into account: its presence and abundance scale with salinity (as represented by the percent of evaporites by weight in a sample) as well as preservation (Figure 2.5). In samples deposited under approximately equal salinity regimes (as determined from evaporite abundance), post-depositional processes such as oxidation and soil formation can destroy archaeol (Figure 2.5, LT 4 vs. LT 7). Therefore, when preservation is accounted for, the presence of archaeol may be an 'indicator lipid', pointing to salinity values in excess of ~175 g/L, the minimum salinity tolerance of many halophilic archaea (Javor 1989). Due to the high solubility and consequent mobility of halite, as discussed previously, halite crusts are not preserved at depth. However, archaeol is preserved, and so can assist in placing constraints on salinity where minerals are not preserved.

The pollen spectra of LT 7 and LT 10 are similar: each is dominated by dryland taxa (>70% of the total pollen in the sample, Table 2.2), which is consistent with the semi-arid geographic setting of the lake. Pollen abundance information suggests that dryland woody vegetation dominated by Casuarinaceae (a type of drought-resistant evergreen tree), with an understory dominated by Poaceae (grasses) and Asteraceae (asters or daisies), surrounded the lake. The understory has more grass than in LT 20 (Table 2.2), reflecting a more open structure to the vegetation consistent with increased aridity (Luly 1993). It is likely that the pollen from *Cyathea*, Gleicheniaceae and *Milfordia homeopunctata* pollen in LT 7 and 10 are re-worked from outcrops of Blanchetown Clay, which form cliffs around the northern and western margins of the playa basin. These taxa have affinities with Tertiary age palynofloras in the Murray Basin and elsewhere (Hill 1994), and have previously been described in the Blanchetown Clay pollen assemblage (Luly 1990). Chenopodiaceae pollen representation remains consistent with the occurrence of scattered chenopod communities rather than the occurrence of extensive chenopod dominated shrublands (Luly 1990).

Neither LT 7 nor 10 contains *Pediastrum* or *Botryococcus* and there is little chance that whatever influx of freshwater entered the basin was of enduring importance to the lake ecosystem. Pollen spectra in both subsamples from the Tyrrell Bed sequence (LT 7 and 10) differ from those of the Holocene section of the Tyrrell Beds sequence in their relative lack of pollen from either *Eucalyptus* (the dominant trees in the region today) or *Callitris*, which was the overwhelmingly dominant tree of mid-Holocene times (Luly 1993). Instead, these subsamples contain Casuarinaceae as the dominant tree pollen, which might be interpreted to indicate that semi-arid conditions prevailed when these samples were deposited. Pollen assemblages representing Early Holocene communities at Lake Tyrrell are enriched in *Allocasuarinas,* and are associated with a semi-arid period in the lake's history (Bowler *et al.* 2006; Luly *et al.* 1986). Modern communities dominated by this tree are found in drier areas than those dominated by *Eucalyptus* (Luly 1993).

It is not unusual, on the other hand, for Casuarinaceae to dominate the woody component of pollen spectra in samples older than latest Pleistocene times, so over-interpretation must be guarded against. Overall, regional vegetation retained much of its essential character at Lake Tyrrell from the time of deposition of LT 20 (older than 700 ka (An *et al.* 1986; McLaren *et al.* 2009)) to the mid-Holocene. In particular, the subsamples from the Tyrrell Bed sequence containing pollen (LT 7 and 10) are similar with regard to types of pollen present and relative proportions of each. This indicates that while geochemical conditions within the lake may have differed between intervals represented by

LT 7 and 10, the regional conditions that prevailed at each were largely similar. Thus, palynological data provides a valuable constraint on palaeo-climatic interpretations based on sediment textures, sample mineralogy and biomarker assemblages. Local conditions, as indicated by the latter types of data, must be placed into a regional context provided by the former.

2.5.3 Lunette and Blanchetown Clay samples

In addition to being compared with the Tyrrell Bed samples as controls for contamination, LT 1 (from the lunette) and LT 20 (from the Blanchetown Clay) were analyzed for their mineral, textural, pollen and lipid content, in order to place constraints on the lacustrine environment during the last glacial maximum (LGM, ~22 ka) and during the early Pleistocene (>700 ka), respectively.

LT 1, a sample of the lunette taken from 20 cm depth, is composed primarily of clays (~75%) and quartz (~20%), with only trace amounts of evaporites. These values are typical of many Australian lunette sediments (Bowler 1973), and correspond to expected values for sediments sourced from Lake Tyrrell (Bowler and Teller 1986) and the nearby Mallee Dunefields (Pell *et al.* 2001). Although lunette building occurs during dry phases, so that it would seem logical that salts from the lakebed be incorporated into the lunette, salts are subsequently leached by meteoric waters (halite) or may be mobilized during soil formation (gypsum and calcite) (Bowler 1973). As gypsum content is low (Table 2.1) and textural indications point to limited matrix reorganization, typical of the early stages of soil formation (Appendix 2, Figure A2.1) – it is likely that the lake was at halite saturation when the lunette was formed, and this halite was subsequently leached from the lunette.

The most recent episode of major lunette building at Lake Tyrrell coincides with the LGM, and lasted from 17.5 to 15 ka (Bowler 1970). During this period, clay pellets formed in the lakebed due to drying and the resultant efflorescence of salts within the lake sediment (Bowler 1973). Pellets were transported by the prevailing west-southwesterly winds (Luly 1990) to the east-northeastern shore of Lake Tyrrell, from which our lunette sample derives. The rounded, fractured appearance of the quartz grains scattered throughout this section is indicative of long-range, aeolian transport, and it is likely that these quartz grains are sourced from the Lowan and/or Woorinen Formations of the Mallee Dunefield west of Lake Tyrrell (Pell *et al.* 2001). This sample was not analyzed for pollen content, although sediments of similar age from the lake bed contain pollen derived primarily from dryland taxa, broadly consistent with that found in the Tyrrell Beds, as described above (Luly 1990, 1993).

The lipid suite of this sample is consistent with the mineralogy and pedology. Lipids are derived from higher plants and other eukaryotes – cholesterol (**1**), campesterol (**6**), stigmasterol (**7**) and β-sitosterol (**8**) – and from the diagenetic products – 5α-cholestanol (**17**) and three isomers of stigmastanol (**22-24**) – of those lipids. The presence of diploptene (**58**) is indicative of active soil bacteria. Due to the high levels of oxidation that typically occur in shallow dune sediments, and to the presence of diploptene, a reasonable interpretation is that these lipids are mostly representative of modern, active organisms, not of the palaeo-communities that existed during lunette formation at the LGM.

LT 20, from the Blanchetown Clay, is relatively uniform, comprised of clays containing very fine, silt-sized quartz throughout. Some coarse quartz sand layers at the base of the section indicate fluvial activity. Laminae of fine sand/medium silt grading to silt-clay couplets, known as 'flood couplets', appear at the top of this section (Appendix 2, Figures A2.13 E-F). Flood couplets are diagnostic of discrete influxes of water, such as through increased river flow, to a deeper, clay-depositing water body. Taken together, these features are indicative of continuous deeper water deposition, but at a location close to an inflowing source of water due to the amount of fluvially-derived silt, quartz lenses, and flood couplets.

Minor iron-oxide staining of the clays is present throughout the section, pointing to post-depositional weathering of Lake Bungunnia/Blanchetown clay deposits.

This sample represents the freshest depositional regime of any discussed heretofore. The small quantities of feldspar are likely detrital, sourced fluvially from the Eastern Highlands (An *et al.* 1986; Cupper *et al.* 2003). This would also have been the source of the quartz sand that dominates this sample. The Blanchetown clay is typically described as a "… micaceous, sandy clay, commonly laminated" (An *et al.* 1986), so that the relatively small amount of clay in this sub-sample may be attributed to its geographic location within the lake. LT 20 likely represents deposition at the near the juncture of the lakeshore and an inflowing river or stream. As the flow velocity of the incoming water decreased, sand-size particles dropped out. The presence of clay may be interpreted as times when the volume of water in the river was lower, indicating decreased precipitation in the Eastern highlands or increased evaporation nearer the lake. Again, the trace amount of halite in this sample, along with the absence of any other evaporitic component, indicates that the halite is a feature of secondary, not primary, deposition, probably from modern, saline porewaters.

The pollen spectrum recovered from LT 20 is similar to that obtained from a long core collected from the western side of the lake by the Victorian Mines Department (Luly 1990) and it is likely that remnants of the Tertiary flora remained in the landscape at the time the sample was deposited. The small number and low abundance of aquatic taxa indicate that it is unlikely that the source plants grew close to the site. Instead, they may have been washed in during a particularly wet episode. The presence of the micro alga *Pediastrum* suggests that water salinity had an upper limit of 3.5 parts per thousand, at least episodically (Yedzani 1970). There is an abundance of the alga *Botryococcus* in the sample, which has a wider range of salinity tolerance than does *Pediastrum* and is indicative of fresh to brackish water (Rao *et al.* 2007). Pollen from *Milfordia hypolaenoides*, a form taxon referable to Restionaceae or Centrolepidaceae families, is also present. These families are typically associated with oligotrophic sandy soils in modern landscapes (Hill 1994). In comparison to the Tyrrell Beds samples, LT 20 contains relatively greater proportions of Tertiary and aquatic taxa relative to dryland taxa, consistent with wetter climatic conditions during deposition of Blanchetown clay unit in Lake Bungunnia. The presence of relatively larger amounts of Chenopodiaceae pollen is therefore surprising, as chenopod shrubs typically grow on saline soils in areas where precipitation is low (Luly 1990). However, the presence of *Pediastrum* and *Botryococcus* remains, in conjunction with pollen from remnant Tertiary flora, possibly indicates that the chenopods of this environment grew on clay dominated or calcareous rather than saline soils.

The lipid suite of LT 20 is dominated by diols (**69-71**) and keto-ols (**72-73**) (Figure 2.3D). C_{30} and C_{32} diols and keto-ols have been found in marine sediments (de Leeuw *et al.* 1981) and in freshwater micro- and macroalgae, and may indicate fresh to brackish salinity levels in the lake at the time of deposition of this sample. This interpretation is supported by the presence *Botryococcus* and *Pediastrum* remains (see pollen results above).

Two species of freshwater eustigmatophyte microalgae have been shown to produce a higher quantity of the C_{30} 1,15 diol than of either the 1,14 or 1,13 positional isomers (Volkman *et al.* 1999). A predominance of the C_{30} 1,14 isomer in a marine setting is indicative of diatomaceous input (Sinninghe Damste *et al.* 2003); by contrast, the mass spectrum of the mixture of positional isomers of the C_{30} diols (**70**, see Appendix 4) in LT 20 shows that the 1,15 and 1,13 isomers predominate in roughly equal amounts, with the 1,14 isomer present in only trace amounts. The abundance of the C_{32} 1,15 diol (**71**) is 35x that of the C_{30} diol mixture (**70**) (see Chapter 3, Figure 3.7, compounds 71 and 70), possibly indicating that a eustigmatophyte similar to modern marine species is the source of these lipids (Rampen *et al.* 2007).

The C_{32} 1,15 keto-ol (**73**) is present in ~7x abundance of the C_{30} 1,13 keto-ol (**72**) (see Chapter 3, Figure 3.7, compounds 73 and 72), which is consistent with the keto-ol profile of a number of species of the marine eustigmatophyte *Nannochloropsis* (Mejanelle *et al.* 2003; Volkman *et al.* 1992). The major sterols of *Nannochloropsis* are cholesterol (**1**) and β-sitosterol (**8**) (Mejanelle *et al.* 2003); these are also the dominant sterols in LT 20. Therefore, it seems likely that eustigmatophyte algae are the source of the dominant lipids in this sample, and that salinity, based on the lipid content, the mineralogy, and the pollen, was fresh to brackish.

2.6 Conclusions

Despite the oxidizing, hypersaline nature of the Lake Tyrrell sediments, solvent extractable lipids are present at depth. These lipids are indigenous to the sediments in which they are found; the original signal has neither been over-printed by contamination from modern sources, such as reflux brines, algal mats or higher plants growing on the lake margins, nor has it been destroyed by bacteria reworking in the sediment. While preservation of biomarkers is related to the extent of preservation of sediments, the lipid suite appears to remain intact unless soil formation occurs. The biomarkers within the sediments provide information about the community structure within the lake, and about organisms growing around the lake through the mid- to late-Pleistocene. Now that the syngeneity and extractability of biomarkers has been established, compound-specific radiocarbon dating can be used to construct a timeline of deposition for the late-Pleistocene/Holocene sequence of lake sediment. By combining this information with that gained from mineral and pollen assemblages and sedimentary textures, we can constrain the evaporitic and precipitation regimes affecting the lake through time. Ultimately, these data can assist in palaeo-climate reconstructions for the region.

2.7 Acknowledgements

I thank the Australian Research Council (ARC S47070 25), the American Society for Engineering Education (NDSEG graduate fellowship), the University of California, Berkeley Graduate Division (Berkeley Graduate Fellowship) and the Larsen Fund grant (1-55000-36567-12998-44-PG1JL) for financial support. We also thank the following people for input and assistance with various aspects of the project, including fieldwork, laboratory analyses, and research discussions: Jon Luly, Janet Hope, Damien Kelleher, Nigel Craddy, Phil Macumber, Ursula Pietrzak, Ulrike Troitzsch, John Vickers, Patrick De Deckker, Emmanuelle Grosjean, the Centre for Palynology and Palaeoecology at Monash University and Geotechnical Services, Inc. We thank Cheetham Salt Works, the Department of Planning and Community Development of Victoria and the Aboriginal Affairs Victoria Heritage Services for providing us with access and permission to collect at the sampling sites.

2.8 References

Alexander E, Stock A, Breiner H-W, Behnke A, Bunge J, Yakimov MM, Stoeck T (2009) Microbial eukaryotes in the hypersaline anoxic L'Atalante deep-sea basin *Environmental Microbiology* 11: 360-381

An Z, Bowler JM, Opdyke ND, Macumber PG, Firman JB (1986) Palaeomagnetic stratigraphy of Lake Bungunnia: Plio-Pleistocene precursor of aridity in the Murray Basin, southeastern Australia *Palaeogeography, Palaeoclimatology, Palaeoecology* 54: 219-239

Banfield JF, Allen E, Heidelberg K, "Comprehensive Genomic Analysis of Salt-impacted Microbial Communities in their Environmental Context" (National Science Foundation, 2009)

Bannon CD, Craske JD, Hai NT, Harper NL, O'Rourke KL (1982) Analysis of Fatty Acid Methyl Esters (FAME) with high accuracy and reliability: II. Methylation of fats and oils with boron trifluoride-methanol *Journal of Chromatography* 247: 63-69

Barbe A, Grimalt JO, Pueyo JJ, Albaiges J (1990) Characterization of model evaporitic environments through the study of lipid components *Organic Geochemistry* 16: 815-828

Bekele T (2000) "Plant Population Dynamics of Dodonaea angustifolia and Olea europaea ssp. cuspidata in Dry Afromontane Forests of Ethiopia", doctoral dissertation, Plant Ecology, Uppsala University

Bent SJ, Gucker CL, Oda Y, Forney LJ (2003) Spatial distribution of *Rhodopseudomonas palustris* ecotypes on a local scale *Applied Enviromental Microbiology* 69: 5192-5197

Bligh EG, Dyer WJ (1959) A rapid method of total lipid extraction and purification *Canadian Journal of Biochemistry and Physiology* 37: 911-917

Bowler JM (1970) "Late Quaternary environments: a study of lakes and associated sediments in south-eastern Australia", doctoral dissertation, The Australian National University

Bowler JM (1973) Clay dunes: their occurrence, formation and environmental significance *Earth Science Reviews* 9: 315-338

Bowler JM (1976) Aridity in Australia: age, origins and expression in aeolian landforms and sediments *Earth Science Reviews* 12: 279-310

Bowler JM (1986) Spatial variability and hydrologic evolution of Australian lake basins: analogue for Pleistocene hydrologic change and evaporite formation *Palaeogeography, Palaeoclimatology, Palaeoecology* 54: 21-41

Bowler JM, Teller JT (1986) Quaternary evaporites and hydrological changes, Lake Tyrrell, north-west Victoria *Australian Journal of Earth Sciences* 33: 43-63

Bowler JM, Kotsonis A, Lawrence CR (2006) Environmental evolution of the Mallee region, Western Murray Basin *Proceedings of the Royal Society of Victoria*: 161-210

Brand LE (1984) The salinity tolerance of forty-six marine phytoplankton isolates *Estuarine, Coastal and Shelf Science* 18: 543-556

Brocks JJ, Love GD, Summons RE, Knoll AH, Logan GA, Bowden SA (2005) Biomarker evidence for green and purple sulphur bacteria in a stratified Palaeoproterozoic sea *Nature* 437: 866-870

Brothers L, Engel MH, Krooss BM (1991) The effects of fluid flow through porous media on the distribution of organic compounds in a synthetic crude oil *Organic Geochemistry* 17: 11-24

Burst JF (1965) Subaqueously-formed shrinkage cracks in clay *Journal of Sedimentary Petrology* 35: 348-353

Calvo E, Pelejero C, Logan GA (2003) Pressurized liquid extraction of selected molecular biomarkers in deep sea sediments used as proxies in paleoceanography *Journal of Chromatography A* 989: 197-205
Carlson RMK, Chamberlain DE (1986) Steroid biomarker-clay mineral adsorption free energies: Implications to petroleum migration indices *Organic Geochemistry* 10: 163-180
Cupper ML, White S, Neilson JL, in *Geology of Victoria*, Birch WD, Ed. (Geological Society of Australia, 2003), pp. 337-360
de Leeuw JW, Rijpstra WIC, Schenck PA (1981) The occurrence and identification of C30, C31 and C32 alkan-1,15-diols and alkan-15-one-1-ols in Unit I and Unit II Black Sea sediments *Geochimica et Cosmochimica Acta* 45: 2281-2285
DeDeckker P, in *Lacustrine Petroleum Source Rocks*, Fleet AJ, Kelts K, Talbot MR, Eds. (Geological Society, 1988a), vol. 40 pp. 45-58
DeDeckker P (1988b) Biological and sedimentary facies of Australian salt lakes *Palaeogeography, Palaeoclimatology, Palaeoecology* 62: 237-270
DeDeckker P, Jones C, Brocks JJ, Eds. (Canberra, 2008)
DeDeckker P, Jones C, Ed. (Canberra, 2009)
Dyall-Smith MKM (1995) Taxonomy of the family Halobacteriaceae and the description of two new genera *Halorubrobacterium* and *Natrialba Journal of General and Applied Microbiology* 41: 333-350
Fitzsimmons K, Jones C, Ed. (Canberra, 2009)
Gaskell SJ, Eglinton G (1976) Sterols of a contemporary lacustrine sediment *Geochimica et Cosmochimica Acta* 40: 1221-1228
Gillespie R, Magee JW, Luly JG, Dlugokencky E, Sparks RJ, Wallace G (1991) AMS radiocarbon dating in the study of arid environments: Examples from Lake Eyre, South Australia *Palaeogeography, Palaeoclimatology, Palaeoecology* 84: 333-338
Harvey HR, McManus GB (1991) Marine ciliates as a widespread source of tetrahymanol and hopan-3B-ol in sediments *Geochimica et Cosmochimica Acta* 55: 3387-3390
Herczeg AL, Chapman A (1991) Uranium-series dating of lake and dune deposits in southeastern Australia: a reconnaissance *Palaeogeography, Palaeoclimatology, Palaeoecology* 84: 285-298
Hill RS, Ed., *History of the Australian vegetation: Cretaceous to recent,* (Cambridge University Press, Cambridge, 1994)
Ichihara K, Shibahara A, Yamamoto K, Nakayama T (1996) An improved method for rapid analysis of the fatty acids of glycerolipids *Lipids* 31: 535-539
Jahnke LL, Orphan VJ, Embaye T, Turk KA, Kubo MD, Summons RE, Des Marais DJ (2008) Lipid biomarker and phylogenetic analyses to reveal archaeal biodiversity and distribution in hypersaline microbial mat and underlying sediment *Geobiology* 6: 394-410
Javor B, *Hypersaline Environments: Microbiology and Geochemistry*. Brock TD, Ed., Brock/Springer Series in Contemporary Bioscience (Springer-Verlag, Berlin, 1989)
Jiang H, Dong H, Yu B, Liu X, Li Y, Ji S, Zhang CL (2007) Microbial response to salinity change in Lake Chaka, a hypersaline lake on Tibetan Plateau *Environmental Microbiology* 9: 2603-2621
Kamekura M, in *The Biology of Halophilic Bacteria,* Vreeland RH, Hochstein LI, Eds. (CRC Press, Inc., Boca Raton, 1993)
Kamekura M, Kates M, in *Halophilic Bacteria,* Rodriguez-Valera F, Ed. (CRC Press, Boca Raton, 1988), vol. 2 pp. 25-54

Kashirtsev VA, Kontorovich AE, Moskvin VI, Kuchkina AY, Kim VE (2008) Biomarker hydrocarbons in the organic matter of Paleogene sediments in southern West Siberia *Petroleum Chemistry* 48: 269-276

Kleemann G, Poralla K, Englert G, Kjøsen H, Liaaen-Jensen S, Neunlist S, Rohmer M (1990) Tetrahymanol from the phototrophic bacterium *Rhodopseudomonas palustris*: first report of a gammacerane triterpene from a prokaryote *Journal of General Microbiology* 136: 2551-2553

Koch BP, Rullkotter J, Lara RJ (2003) Evaluation of triterpenols and sterols as organic matter biomarkers in a mangrove ecosystem in northern Brazil *Wetlands Ecology and Management* 11: 257-263

Krooss BM, Leythaeuser D (1988) Experimental measurements of the diffusion parameters of light hydrocarbons in water-saturated sedimentary rocks---ll. Results and geochemical significance *Organic Geochemistry* 12: 91-108

Luly JG (1990) "A pollen analytical investigation of Holocene palaeoenvironments at Lake Tyrrell, semi-arid northwestern Victoria, Australia", doctoral dissertation, Department of Biogeography & Geomorphology, Research School of Pacific Studies, Australian National University

Luly JG (1993) Holocene palaeoenvironments near Lake Tyrrell, semi-arid northwestern Victoria, Australia *Journal of Biogeography* 20: 587-598

Luly JG, Bowler JM, Head MJ (1986) A radiocarbon chronology from the playa Lake Tyrrell, northwestern Victoria, Australia *Palaeogeography, Palaeoclimatology, Palaeoecology* 54: 171-180

Mackenzie AS, Maxwell JR, in *Organic Maturation Studies And Fossil Fuel Exploration* Brooks J, Ed. (Academic Press, 1981), pp. 239-254

Macnaughton SJ, Jenkins TL, Wimpee MH, Cormier MR, White DC (1997) Rapid extraction of lipid biomarkers from pure culture and environmental samples using pressurized accelerated hot solvent extraction *Journal of Microbiological Methods* 31: 19-27

Macumber PG (1991) "Interaction between groundwater and surface systems in Northern Victoria", doctoral dissertation, Geology Department, School of Earth Sciences, Melbourne University

Magee JW (1991) Late Quaternary lacustrine, groundwater, aeolian and pedogenic gypsum in the Prungle Lakes, southeastern Australia *Palaeogeography, Palaeoclimatology, Palaeoecology* 84: 3-42

Mayberry WR, Lane JR (1993) Sequential alkaline saponification/acid hydrolysis/esterification: a one-tube method with enhanced recovery of both cyclopropane and hydroxylated fatty acids *Journal of Microbiological Methods* 18: 21-32

McLaren S, Wallace MW, Pillans BJ, Gallagher SJ, Miranda JA, Warne MT (2009) Revised stratigraphy of the Blanchetown Clay, Murray Basin: age constraints on the evolution of paleo Lake Bungunnia *Australian Journal of Earth Sciences* 56: 259-270

Mejanelle LM, Sanchez-Gargallo A, Bentaleb I, Grimalt JO (2003) Long chain *n*-alkyl diols, hydroxy ketones and sterols in a marine eustigmatophyte, *Nannochloropsis gaditana*, and in *Brachionus plicatilis* feeding on the algae *Organic Geochemistry* 34: 527-538

Meyers PA (2003) Applications of organic geochemistry to paleolimnological reconstructions: a summary of examples from the Laurentian Great Lakes *Organic Geochemistry* 34: 261-289

Meyers PA, Ishiwatari R (1993) Lacustrine organic geochemistry - an overview of indicators of organic matter sources and diagenesis in lake sediments *Organic Geochemistry* 20: 867-900

Moore DM, Reynolds RC, in *X-Ray Diffraction and the Identification and Analysis of Clay Minerals*. (1997)
Morita M, Yamaguchi N, Eguchi T, Kakinuma K (1998) Structural diversity of the membrane core lipids of extreme halophiles *Bioscience, Biotechnology and Biochemistry* 62: 596-598
Mullakhanbhai MF, Francis GW (1972) Lipid constituents of a moderately halophilic bacterium *Acta Chemica Scandinavica* 26: 1399-1410
Nanson GC, Price DM, Short SA (1992) Wetting and drying of Australia over the past 300 ka *Geology* 20: 791-794
Nanson GC, Price DM, Short SA, Young RW, Jones BG (1991) Comparative uranium-thorium and thermoluminescence dating of weathered Quaternary alluvium in the tropics of northern Australia *Quaternary Research* 35: 347-366
Nishimura M (1977) Origin of stanols in young lacustrine sediments *Nature* 270: 711-712
Nishimura M, Koyama T (1976) Stenols and stanols in lake sediments and diatoms *Chemical Geology* 17: 229-239
Nishimura M, Koyama T (1977) The occurrence of stanols in various living organisms and the behavior of sterols in contemporary sediments *Geochimica et Cosmochimica Acta* 41: 379-385
Nissenbaum A, Baedecker MJ, Kaplan IR (1972) Organic geochemistry of Dead Sea sediments *Geochimica et Cosmochimica Acta* 36: 709-727
Oldenburg TBP, Rullkotter J, Bottcher ME, Nissenbaum A (2000) Molecular and isotopic characterization of organic matter in recent and sub-recent sediments from the Dead Sea *Organic Geochemistry* 31: 251-265
Ourisson G, Albrecht P, Rohmer M (1979) The hopanoids: palaeochemistry and biochemistry of a group of natural products *Pure & Applied Chemistry* 51: 709-729
Ourisson G, Rohmer M, Poralla K (1987) Prokaryotic hopanoids and other polyterpenoid sterol surrogates *Annual Reviews in Microbiology* 41: 301-333
Pancost RD, Boot CS (2004) The palaeoclimatic utility of terrestrial biomarkers in marine sediments *Marine Chemistry* 92: 239-261
Payne T, Kuwahara SS (1972) Sterols of the brine shrimp, *Artemia salina*, from Mono Lake, California *Experientia* 28: 1022-1023
Pearson EJ, Juggins S, Farrimond P (2008) Distribution and significance of long-chain alkenones as salinity and temperature indicators in Spanish saline lake sediments *Geochimica et Cosmochimica Acta* 72: 4035-4046
Peeler TC, Stephenson MB, Einspahr KJ, Thompson GAJ (1989) Lipid characterization of an enriched plasma membrane fraction of *Dunaliella salina* grown in media of varying salinity *Plant Physiology* 89: 970-976
Pell SD, Chivas AR, Williams IS (2001) The Mallee Dunfield: development and sand provenance *Journal of Arid Environments* 48: 149-170
Peters KE, Moldowan MJ, *The Biomarker Guide: Interpreting Molecular Fossils in Petroleum and Ancient Sediments*. (Prentice-Hall, Inc., Englewood Cliffs, ed. 1st, 1993)
Quirk MM, Wardroper AMK, Wheatley RE, Maxwell JR (1984) Extended hopanoids in peat environments *Chemical Geology* 42: 25-43
Rampen S, Schouten S, Wakeham SG, Sinninghe Damste JS (2007) Seasonal and spatial variation in the sources and fluxes of long chain diols and mid-chain hydroxy methyl alkanoates in the Arabian Sea *Organic Geochemistry* 38: 165-179
Rao AR, Dayananda C, Sarada R, Shamala TR, Ravishankar GA (2007) Effect of salinity on growth of green alga *Botryococcus braunii* and its constituents *Bioresource Technology* 98: 560-564

Reed WE (1977) Biogeochemistry of Mono Lake, California *Geochimica et Cosmochimica Acta* 41: 1231-1245
Rhead MM (1971) "The fate of biolipids in aquatic sediments", doctoral dissertation, Chemistry, University of Bristol
Robinson N, Cranwell PA, Finlay BJ, Eglinton G (1984) Lipids of aquatic organisms as potential contributors to lacustrine sediments *Organic Geochemistry* 6: 143-152
Rohmer M, Dastillung M, Ourisson G (1980) Hopanoids from C30 to C35 in recent muds: chemical markers for bacterial activity *Naturwissenschaften* 67: 456-458
Ryves DB, Battarbee RW, Juggins S, Fritz SC, Anderson NJ (2006) Physical and chemical predictors of diatom dissolution in freshwater and saline lake sediments in North America and West Greenland *Limnological Oceanography* 51: 1355-1368
Scallen TJ, Dhar AK, Loughran ED (1971) Isolation and characterization of C-4 methyl intermediates in cholesterol biosynthesis after treatment of rat liver *in vitro* with cholestan-3β,5α,6β-triol *Journal of Biological Chemistry* 246: 3168-3174
Sehgal JL, Stoops G (1972) Pedogenic calcite accumulation in arid and semi-arid regions of the Indo-Gangetic alluvial plain of erstwhile Punjab (India) - their morphology and origin *Geoderma* 8: 59-72
Sinninghe Damste JS, Rampen S, Rijpstra WIC, Abbas B, Muyzer G, Schouten S (2003) A diatomaceous origin for long-chain diols and mid-chain hydroxy methyl alkanoates widely occurring in Quaternary marine sediments: Indicators for high-nutrient conditions *Geochimica et Cosmochimica Acta* 67: 1339-1348
Teller JT, Bowler JM, Macumber PG (1982) Modern sedimentation and hydrology in Lake Tyrrell, Victoria *Journal of the Geological Society of Australia* 29: 159-175
ten Haven HL, Rohmer M, Rullkotter J, Bisseret P (1989) Tetrahymanol, the most likely precursor of gammacerane, occurs ubiquitously in marine sediments *Geochimica et Cosmochimica Acta* 53: 3073-3079
Torgersen T, Deckker PD, Chivas AR, Bowler JM (1986) Salt Lakes: A discussion of processes influencing palaeoenvironmental interpretation and recommendations for future study *Palaeogeography, Palaeoclimatology, Palaeoecology* 54: 7-19
Toste AP (1976) "The Sterol Molecule: Its Analysis and Utility as a Chemotaxonomic Marker and a Fine Geochemical Probe into Earth's Past", doctoral dissertation, Comparative Biochemistry, UC Berkeley
Venkatesan MI, Ruth E, Kaplan IR (1990) Triterpenols from sediments of Santa Monica Basin, Southern California Bight, U.S.A. *Organic Geochemistry* 16: 1015-1024
Volkman JK (1986) A review of sterol markers for marine and terrigenous organic matter *Organic Geochemistry* 9: 83-99
Volkman JK (2003) Sterols in microorganisms *Applied Microbiology and Biotechnology* 60: 495-506
Volkman JK, Barrett SM, Blackburn SI (1999) Eustigmatophyte microalgae are potential sources of C29 sterols, C22-C28 *n*-alcohols and C28-C32 *n*-alkyl diols in freshwater environments *Organic Geochemistry* 30: 307-318
Volkman JK, Gillian FT, Johns RB, Eglinton G (1981) Sources of neutral lipids in a temperate intertidal sediment *Geochimica et Cosmochimica Acta* 45: 1817-1828
Volkman JK, Burton HR, Everitt DA, Allen DI (1988) Pigment and lipid compositions of algal and bacterial communities in Ace Lake, Vestfold Hills, Antarctica *Hydrobiologia* 165: 41-57
Volkman JK, Barrett SM, Dunstan GA, Jeffrey SW (1992) C30-C32 alkyl diols and unsaturated alcohols in a microalgae of the class Eustigmatophyceae *Organic Geochemistry* 18: 131-138

Volkman JK, Farmer CL, Barrett SM, Sikes EL (1997) Unusual dihydroxysterols as chemotaxonomic markers for microalgae from the order Pavlovales (Haptophyceae) *Journal of Phycology* 33: 1016-1023

Volkman JK, Barrett SM, Blackburn SI, Mansour MP, Sikes EL, Gelin F (1998) Microalgal biomarkers: A review of recent research developments *Organic Geochemistry* 29: 1163-1179

Wilson SE, Cumming BF, Smol JP (1994) Diatom-salinity relationships in 111 lakes from the Interior Plateau of British Columbia, Canada: the development of diatom-based models for paleosalinity reconstructions *Journal of Paleolimnology* 12: 197-221

Withers N, in *Marine Natural Products: Chemical and Biological Perspectives*, Scheuer PJ, Ed. (Academic Press, Inc., New York, 1983), vol. 5

Withers N, in *The Biology of Dinoflagellates*, Taylor FJR, Ed. (1987)

Yedzani GH (1970) "A study of the Quaternary vegetation history in the volcanic lakes region of western Victoria", doctoral dissertation, Monash University

Chapter 3.

Reconstruction of organismal communities within and around Lake Tyrrell through the late-Pleistocene using a multi-proxy approach

3.1 Abstract

The reconstruction of palaeoenvironments from saline sediments in arid locales is plagued by three problems: the lack of proxies sufficiently robust to withstand the excessive drying and oxidation of the arid sediments of hypersaline playas, the controversy over which biomarkers function as indicators of palaeo-salinity, and the difficulty of dating discontiguous sediment sequences. Many reconstructions drawn from the semi-arid and arid regions of Australia are based solely on sedimentary characteristics and pollen assemblages, which provide incomplete information where sedimentary textures or pollen are not well preserved or where provenance of the pollen is not well constrained.

As a new approach for palaeoenvironmental reconstruction from arid, saline lacustrine sediments, we used ordination methods to classify sections of a core from Lake Tyrrell, Victoria, based on their mineralogy and lipid content. The core transected sediments deposited by a deep, freshwater megalake and sediments of an ephemeral, shallow, saline playa lake. We used sedimentary textural analyses and trends in pollen content to provide an independent check on the classification scheme derived from the mineralogy and lipid content, so that samples that had been heavily altered after deposition would not skew the analysis. After clustering samples, sub-sets of the lipids present were employed to reconstruct the palaeo-community of organisms within the lake, the existence and timing of temperature fluctuations associated with glacial-interglacial cycles, and the water level and approximate salinity within the lake over an estimated ~400 ka.

From these analyses, we have determined that Lake Tyrrell sediments preserve evidence of three glacial-interglacial cycles. Some sections contain high quantities of primary evaporites, for which lake level models suggest an ephemeral lake containing less than 1 meter of water, that was often completely dry. The presence of archaeol, phytol, ergosterol, ergost-7-en-3β-ol, and stigmast-7-en-3β-ol, as well as the sedimentary structures, suggest that the biota within the lake was similar to that of the modern lake: microbial mats grew at the interface of the sediment and the overlying halite crust, and waters at halite saturation promoted the growth of halophilic archaea, bacteria and algae. Layers of clay rich sediment containing fecal pellets indicate that periodic freshening events, likely associated with floods, decreased salinity enough that ostracods such as *Diacypris* could intermittently inhabit the lake. Though the timing of deposition is imprecise, we believe that these ephemeral lake episodes during glacial intervals (~20 ka, 140 ka, 260 or 340 ka).

By contrast, other sediment sections contain fewer evaporites but more detrital quartz and clays; lake level models associate these with water depths of 5-10 m and a lake poised at lower salinity. The presence of a large suite of dinoflagellate sterols, including dinosterol, in addition to terminal diols, suites of stanols (biohydrogenated sterols) and intermittent layers of distinctive fecal pellets demonstrate that the lake was colonized by dinoflagellates, eustigmatophyte algae, and occasionally by the gastropod *Coxiella*. The stanols specifically point to anaerobic bacteria

inhabiting the sediments. We believe these sections were deposited during interglacial intervals (modern, 120 ka, 220 or 320 ka), when the climate was wetter.

Pollen data from the same sections show that large fluctuations in lake level, salinity, and biota are set against a more gradual change within the catchment: from the deepest section of the Lake Tyrrell core to the more recent sediments, the dominant pollen shifts from eucalypt and casuarina to that of grasses and asterids. This indicates that between the oldest glacial maxima recorded and the last glacial maximum (LGM), casuarina and eucalypt woodland was gradually replaced by a somewhat more open, grassy structure. Overall, until the return to slightly wetter conditions in the early Holocene (~10 ka), dryland taxa such as casuarina, eucalypts and grasses remained the dominant members of the terrestrial plant community, with only slight shifts in the abundance of community members. This demonstrates that the composition of communities of terrestrial vegetation in arid areas is relatively resistant to environmental change, so that palaeoenvironmental reconstructions based solely on pollen assemblages may underestimate the severity of regional climatic shifts.

3.2 Introduction

3.2.1 Long-term trends in late-Pleistocene climate on the Australian continent

Climatic variability on the Australian continent over the past 350 ka is defined by both the 100 ka periodicity of glacial-interglacial cycles and a long-term trend toward drier and more variable regional climates (Kershaw *et al.* 2003). During glacial maxima, lower sea levels and reduced seasonal precipitation led to intensified atmospheric circulation over the Australian landmass, so that conditions were cold and dry (Bowler 1976; Petit *et al.* 1999). Interglacial intervals are characterized by warmer and wetter climatic conditions. The amplitude and frequency of these fluctuations increased through the Quaternary (1.8 Ma – present) (Cupper *et al.* 2003). The long-term drying trend superimposed on this cyclicity was a result of changes in atmospheric and ocean circulation resulting from Australia's continued migration northward into the southern Pacific ocean, and to the development of El Niño-Southern Oscillation (ENSO) weather patterns, which contributed to a decrease in summer monsoons (Kershaw *et al.* 2003). Modeling these changes requires detailed palaeoenvironmental reconstructions, typically generated from data gleaned from continuous marine sediment sequences. Although valuable in the context of global climate reconstructions, these data often do not reflect the timing and extent of climatic changes at a regional level (Gibbard and van Kolfschoten 2004; Kershaw *et al.* 2003).

Within southeastern Australia, increasing rates of evaporation coupled with a decrease in overall precipitation resulted in falling lake levels and the formation of clay dunes (Bowler *et al.* 2006; Cupper *et al.* 2003). Decreasing lake volumes led to an increase in the salinity of surface waters (Magee 1991), such that most lakes within southeastern Australia are saline (DeDeckker 1983). These lakes contain sediment sequences that represent a valuable repository of palaeoenvironmental data, although interpretation of data gathered from these sequences has proven difficult (see chapter 2, introduction). The salinity of these depositional environments contributes to the dissolution of micro-fossils (Ryves *et al.* 2006), and post-depositional oxidation and secondary mineral formation can destroy or alter pollen and sedimentary textures (Luly 1993; Torgersen *et al.* 1986). In addition, gaps in sediment sequences caused by deflation (Bowler 1970; Bowler and Teller 1986) combined with a lack of dateable materials (An *et al.* 1986; Luly *et al.* 1986) have made it difficult to place regional climate records within the context of global climate change.

3.2.2 Previous uses of the multiple-proxy approach to climate reconstruction

In the preceding chapter, we presented preliminary results of an analysis of lipid biomarkers contained in a core of the sediments of a hypersaline lake in northwestern Victoria, Lake Tyrrell. We were able to show that despite the adverse conditions described above, lipid biomarkers were preserved to depth, were syngenetic within the sediments from which they were extracted, and could be interpreted alongside conventional palaeoenvironmental proxies, such as mineral and pollen content and sedimentary textures, to generate a more complete picture of ecosystem change at a local and regional level. In this chapter, we expand this approach using ordination methods to classify samples within the core based on their mineral content and on the suite of biomarkers contained within each sample.

The strength of ordination methods lies in their ability to expose trends and clusters within datasets containing a large number of parameters. A variety of multivariate statistical approaches, including principal component analysis, non-metric multi-dimensional scaling analysis, and partial least squares path modeling, have already been employed in other studies to relate lipid biomarker suites to the environmental conditions under which they were deposited (Brassell *et al.* 1986b; Brassell *et al.* 1986a; Didyk *et al.* 1978; Irwin and Meyer 1990; Pearson *et al.* 2007; Yunker *et al.* 1995). Two of these studies were performed using modern sediment samples, where preservation is not an issue and where the values of environmental parameters at the time of deposition, such as temperature and salinity, can be directly measured (Pearson *et al.* 2007; Yunker *et al.* 1995). One study on older material examined rocks from oil-generating facies where thermal maturity was independently established (Irwin and Meyer 1990), so that the conditions that lipids had experienced after deposition were well established. A study on marine sediment sequences measured geochemical parameters and used published palaeo-temperature and chronological data in order to determine the conditions experienced by lipid biomarkers during and after deposition (Brassell *et al.* 1986b). In these studies, the environmental conditions that prevailed at the time of biomarker deposition could either be directly measured (for modern sediments), indirectly worked out from an assemblage of biomarkers that had undergone well understood diagenetic reactions (thermally-mature, oil-generating rocks), or indirectly established on the basis of previous, independent work (marine sediments).

Previous estimates of palaeo-salinity have been based on both mineral content and lipid biomarkers. However, as mentioned above, post-depositional oxidation and secondary mineral formation can alter both the minerals and organics within sediments. This means that mineral content is not a reliable indicator of salinity for sediments in which secondary minerals have overgrown primary ones (Schreiber and El Tabakh 2000). Palaeo-salinity estimates based on biomarkers have generally relied on observations on the association of particular compounds, such as docosane, phytane, and squalane, with saline facies (Peters and Moldowan 1993; ten Haven *et al.* 1988; Volkman 1988; Wang 1998). However, these compounds are not consistently found in saline environments (Barbe *et al.* 1990; Javor 1989), or have subsequently been shown to be of equivocal significance in the reconstruction palaeoenvironmental parameters (Peters *et al.* 2005; ten Haven *et al.* 1987). In addition, the lipid biomarker assemblage within highly-oxidized sediments (e.g. those that have undergone the initial stages of soil formation) is reflective of post-depositional processes as opposed to primary sources (see for example discussion of LT 4, chapter 2).

3.2.3 An expansion of the multiple-proxy approach applied to saline lake sediments deposited through the late-Pleistocene to the present

In order to overcome some of the difficulties described above, the current study employs pedological analyses to determine which sediments are best preserved, and may be most useful for palaeoenvironmental reconstruction. As salinity cannot be directly measured, palaeo-salinity for unaltered sediments is then approximated based on the mineral content and on the known salinity tolerance of organisms from which the lipid biomarkers preserved within the sediments are derived. Multivariate regression techniques are employed to identify lipid biomarkers that are consistently associated with hypersaline conditions within the core, so that clusters of like samples are evident.

Water levels for Lake Tyrrell through time are predicted from estimated palaeo-salinity using models accounting for basin geometry, precipitation and evaporation levels, (Bowler 1981, 1986; Bowler and Teller 1986), and surface-groundwater interactions (Macumber 1991). When combined with pollen data, lake level curves assist in the reconstruction of regional precipitation patterns (Singh 1981; Singh and Luly 1991).

Finally, we use certain classes of lipid biomarkers to gain information on palaeo-temperatures and chronology of deposition during the mid- to late-Pleistocene (~400 ka – 18 ka). We compare a curve generated from sterol/stanol ratios within the Tyrrell sediments, palaeo-temperatures calculated from the relative abundances of di- and tri-unsaturated alkyl ketones, a lake level curve generated from biomarkers and mineral assemblages within the Tyrrell sediments, and $\delta^{18}O$ curves from the Indian Ocean and the Australian Bight, in order to reconstruct the fluctuations in regional climate recorded at Lake Tyrrell over the past ~350 ka. This approach has allowed us to create a tentative chronology for deposition within a previously un-dated sequence (the Tyrrell Beds), a sequence which includes the “greatest environmental transformation of the last 20 Ma” (Bowler *et al.* 2006).

3.3 Samples and methods

3.3.1 Study sites and sample collection

The study site and sample collection are described in section 2.3.1.

3.3.2 Mineralogical analysis

Methods for mineralogical analysis are described in section 2.3.2.

3.3.3 Thin section analysis

Methods for thin section analysis are described in section 2.3.3.

3.3.4 Total organic carbon (TOC) analysis of sediments

Methods for TOC analysis are described in section 2.3.4.

3.3.5 Palynological analysis of sediments

Methods for palynological analysis are described in section 2.3.5.

3.3.6 Lipid extraction and fractionation

Methods for lipid extraction and fractionation are described in section 2.3.6. Sequential alkaline saponification/acid hydrolysis was not performed on additional samples presented here.

50% of the underivatized total lipid extract of each of five samples (LT 8, 12, 27, 35 and CJ07_026; this last is a sample from the shallow core described in chapter 5) was processed to identify glycerol dialkyl glycerol tetraethers (GDGTs). These samples were selected to represent the range of depth and mineralogy found in the Lake Tyrrell cores (see Tables 3.1A – C and 5.1). Extracts were saponified using the method of Volkman *et al.* (1998), dried under a stream of pure N_2 gas, and stored at 4°C prior to shipping.

3.3.7 Instrumental analysis and compound quantification

Analysis of lipid fractions was performed in an identical manner to that described in section 2.3.7.

GDGTs were analyzed in the laboratory of and by Emma Pearson at the School of Geography, Politics and Sociology, Newcastle University, United Kingdom. Instrumentation and conditions for analysis are described in Pearson *et al.* (2011).

3.3.8 Statistical analysis: multi-variate ordination and classification of samples

A comparison of principal component analysis (PCA) and non-metric multi-dimensional scaling (NMS) ordination techniques did not show any significant differences in representation of the data. For lipid analyses, we elected to perform NMS analysis for the following reasons: it employs a dissimilarity measure more suited to geochemical data than the Euclidean distance measure inherent in PCA; it does not assume a linear relationship between variables; and it represents inter-sample distances more faithfully than PCA (Clarke 1993). The starting configuraton of the standard MatLab algorithm was not altered.

3.4 Results

The drill core retrieved from Folly Point contained three primary sedimentary units: lunette, Tyrrell beds and Blanchetown clay. The lunette sediments, which comprise the top 2 m of the core, are composed primarily of sandy clay. The lunette is underlain by 4 m of Tyrrell beds, composed of evaporites and clays. From beneath the Tyrrell beds we recovered 7 m of Blanchetown clay, which is a massive clay unit containing intermittent sand lenses. Contacts between the units were clearly defined, and the broad characteristics of each have been described in Teller *et al*. 1982. An overview of the core with sampling locations marked may be found in Appendix 1.

3.4.1 Results of thin section analysis

Results of thin section analysis for samples LT 2, 4, 7, 10 and 20 may be found in section 2.4.1 of this work. These samples broadly cover the range of sedimentary units present in the core. Images of all thin sections, along with images and descriptions of relevant features, appear in Appendix 2. Interpretation of textural features into indices of preservation appear in Appendix 3.

LT 2 (192.5 – 200 cm) is composed of lunette sediments. This unit is an aeolian unit, composed of un-bedded clay interspersed with rounded quartz grains, some of which are fractured. Argillans surround many of the quartz grains. Partially degraded clay pellets, approximately 0.5 mm in diameter, appear at 195 cm depth (Appendix 2, Figure A2.1 D).

In order of depth, LT 4, 5, 30, 32, 7, 9, 34, 10, 35_36, and the top part of LT 11_12 are thin sections taken from the Tyrrell Beds unit of the core. Sections 4, 5 and 7 contain very little primary or secondary gypsum, and are mostly composed of clays, present either as oriented or non-oriented beds, or as blocky peds. LT 5 (280 – 287 cm) is the most altered of these sections, as it contains no bedding, and instead has iron oxide spherules and dendrites scattered throughout and reorganization of clays along cracks and edges of peds (Appendix 2, Figure A2.3 B through F). LT 4 (234 – 241 cm) is also relatively poorly preserved, although it contains some remnant microbialite layers (Appendix 2, Figure A2.2 D) in addition to joints with oriented clays, iron oxides cementing voids, and quartz sand lenses. Best preserved of these three sections is LT 7 (412 – 419 cm), which, in addition to blocky clay peds and secondary (displacive) gypsum, contains relatively undisturbed layers of oriented clays, putative fecal pellets and primary 'seed' gypsum (Appendix 2, Figure A2.6).

Sections 30 (312 – 319 cm) and 32 (360 – 367 cm) show extensive evidence of post-depositional alteration by groundwater, as bedding is chaotic or absent due to secondary gypsum growth (Appendix 2, Figures A2.4 and A2.5). This non-oriented, displacive gypsum has almost completely overgrown both of these sections, so that clays appear as discrete beds or small peds interrupted by syneresis cracks and cross-cutting structures (Appendix 2, Figure A2.5 A, D, and G). In addition, staining of clays by iron oxides (Appendix 2, Figure A2.5 E and F) and oriented clays within maturing peds (Appendix 2, Figure A2.4 H) indicate initial soil development prior to groundwater alteration. Although some remnant microbialites (Appendix 2, Figure A2.4 C) and primary gypsum (Appendix 2, Figure A2.4 B and C) remain, these sections are of limited use in a textural analysis.

Sections 9 (467 – 474 cm) and 34 (503 – 510 cm) are both less altered and more saline in character than those described above. Each contains minimal amounts of iron oxides, evidence of preserved bedding layers, primary 'settled' gypsum, and microbialite mat layers. The top of section 9 (467 – 469.5 cm) contains clay peds bordered by cutans (Appendix 2, Figure A2.7) and containing scattered iron oxide spherules (Appendix 2, Figures A2.7 G and H). By contrast, beneath this portion of the thin section primary settled gypsum crystals are interspersed with microbialite layers (Appendix 2, Figure A2.7 F), and some of the gypsiferous layers show reverse grading (Appendix 2, Figure A2.7 E) of crystals from ~100 μm – 40 μm diameter. Displacive or secondary gypsum dominated the section beneath the mat layers; its growth has destroyed any primary textures for this portion of the thin section (Appendix 2, Figure A2.7 D). At the very base of the section, layers which appear to be remnant mats are interspersed with oriented clay layers (Appendix 2, Figures A2.7 A and B) and layers composed of quartz sand (Appendix 2, Figure A2.7 C).

Mat layers (Appendix 2, Figures A2.8 C and H) are more clearly visible in section 34: 'tear-up' structures (Appendix 2, Figures A2.8 E and F) appear along planes of separation between mat and clay layers. Such separation would have occurred as a result of drying, though it is unclear whether during natural diagenesis or incidentally during the sample preparation process. Most of the gypsum in this section is primary, though a zone of displacive gypsum (100 – 500 μm diameter) is present near the top of the section (Appendix 2, Figure A2.8 G). The parallel orientation of the crystals in this layers are worth noting: they indicate that the displacive crystals grew within the confines of settled gypsum and oriented clay layers (Appendix 2, Figure A2.8 at 504 cm, 505 cm). The bottom half of the section contains oriented clay layers (Appendix 2, Figure A2.8 D) and larger gypsum crystals (>1 mm diameter) floating in a matrix of smaller (~200 μm), settled gypsum crystals. The larger crystals are equant as opposed to lenticular in

shape, and some of them show evidence of re-dissolution and minimal transport (Appendix 2, Figure A2.8 A).

Sections 10 (519 – 526 cm) and 35_36 (552 – 559 cm) are the least altered and the most saline of any of the Tyrrell Bed sections. Neither section contains any clay cutans, peds or polygons, or iron oxide spherules or dendrites (see Appendix 3). Nearly all of the gypsum in both sections appears to be primary: displacive gypsum is confined to several narrow bands between 521.5 – 522.5 cm in section 10. At the base of this region, displacive crystals up to 1 mm in diameter are sub-parallel to parallel in orientation and cracked along cleavage planes (Appendix 2, Figures A2.9 D and E) due to secondary crystal growth within a confined region. At the top of this region, these larger crystals have disrupted the primary matrix of dolomitic microbialites and are emplaced in random orientation (Appendix 2, Figures A2.9 F and G). Outside this region, gypsum in both section 10 and 35_36 is primary, settled gypsum. While some re-dissolution of crystals has occurred, this is localized along cleavage planes (Appendix 2, Figure A2.10 F) and associated with iron sulfide (Appendix 2, Figures A2.10 A, B, C, G and H) or iron oxide deposition (Appendix 2, Figure A2.10 E). This phenomenon is discussed in chapter 4 of this work. Overall, both section 10 and 35_36 are composed of layers of settled gypsum (some of which show reverse grading; Appendix 2, Figures A2.9 A and A2.10 F) interspersed with mat/microbialite layers (Appendix 2, Figuress A2.9 B and C, and A2.10 A, B and F).

The top of section 11_12 (from 591.5 – 597 cm) appears to be a less-preserved analog of section 35_36. Sulfidized gypsum crystals with partial re-dissolution along cleavage planes are present at the base of the section (Appendix 2, Figure A2.11 E); however, the interspersal of mat and gypsiferous layers has been completely destroyed by secondary gypsum growth Appendix 2, Figures A2.11 F and G). In addition to secondary, lenticular gypsum, rounded quartz crystals with partial clay argillans appear at the top of the section (Appendix 2, Figure A2.11 H), indicating allochthonous input.

The base of LT 11_12, and LT 13 and 20 are sections of the Blanchetown Clay unit. The base of LT 11_12 (591.5 – 599.5 cm) contains extensive iron oxides, present as horizons within some clay beds and haloes around voids likely created by rootlets. Some clay lenses are oriented, other beds contain more quartz grains (see Appendix 2, Figures A2.11 A and C). LT 13 (649 – 656 cm) contains hardly any bedding, and more quartz lenses, indicative of higher energy depositional conditions. Voids are all cemented by iron oxides, indicating post-depositional oxidation; however, the presence of organic debris limits the extent of this alteration (see Appendix 2, Figures A2.12 A through G). In contrast, LT 20 (1014 – 1021 cm) contains normally graded couplets of quartz sand and clay (see Appendix 2, Figure A2.13 E), indicative of episodes of more and less energetic deposition. In addition, oxidation is much less extensive, indicating less post-depositional alteration.

3.4.2 Results of mineralogical analysis

Results of mineralogical analysis for samples LT 1, 4, 7, 10 and 20 may be found in section 2.4.2 and Table 2.1 of this work. The mineral types in the core fall into three groups: evaporites (Table 3.1A), including halite, dolomite, calcite, gypsum, magnesite, celestite; clays (Table 3.1B), including illites (both pure and containing smectite), vermiculite, kaolinite, and montmorillonite (a group name for an unidentified clay component); and detrital or oxide minerals (Table 3.1C), including quartz, hematite, muscovite, and plagioclase and alkali feldspars.

Table 3.1A Evaporite mineralogy[a,b] of Lake Tyrrell S12 core samples

Sample name	Depth (cm)	TOC[c]	Halite	Gypsum	Celestite	Calcite	Dolomite	Magnesite
LT 1	20	0.22	2	1	nd	1	nd	nd
LT 2	190	0.06	3	nd	nd	nd	nd	nd
LT 3	203	0.09	5	nd	nd	nd	<1	nd
LT 4	223	0.10	3	nd	nd	nd	26	nd
LT 27	230	0.10	6	nd	nd	nd	7	nd
LT 28	240	0.04	3	nd	nd	nd	7	nd
LT 5	289	0.12	6	nd	nd	nd	<1	nd
LT 6	336	0.14	4	26	nd	nd	nd	nd
LT 7	411	0.14	7	23	nd	nd	1	nd
LT 8	429	0.27	4	17	nd	nd	nd	nd
LT 9	476	0.19	3	68	nd	nd	17	nd
LT 10	519	0.16	<1	91	nd	nd	nd	nd
LT 35	560	2.28	4	50	1	nd	nd	31
LT 36	561	0.45	4	65	1	nd	nd	3
LT 11	593	0.05	1	97	nd	nd	nd	nd
LT 12	603	0.06	4	nd	nd	nd	nd	nd
LT 13[d]	*663*	*0.15*	*4*	*63*	*nd*	*nd*	*nd*	*nd*
LT 26	745	0.05	4	<1	nd	nd	nd	nd
LT 20	1013	0.18	5	nd	nd	nd	nd	nd

[a]All mineral amounts in weight %, errors are <1% by weight; mineral amounts normalized to eliminate amorphous content - see explanation in text (section 2.4.2)

[b]nd = not detected

[c]Total organic carbon (TOC) reported as wt% of sediment, measurement error 0.01%

[d]Mineralogy does not match thin section, which contains quartz, mica, clays and iron oxides. Thin section was taken below grey lens in Blanchetown clay proper, whereas lipid and mineral samples come from the grey lens, which is probably Tyrrell bed contamination

Table 3.1B Clay mineralogy[a,b] of Lake Tyrrell S12 core samples

Sample name	Depth (cm)	TOC[c]	Montmorillonite	Illite	Kaolinite	Vermiculite
LT 1	20	0.22	17	38	20	nd
LT 2	190	0.06	16	35	33	nd
LT 3	203	0.09	15	45	25	nd
LT 4	223	0.10	7	34	12	1
LT 27	230	0.10	19	34	19	nd
LT 28	240	0.04	10	12	1	nd
LT 5	289	0.12	10	44	31	nd
LT 6	336	0.14	12	29	22	nd
LT 7	411	0.14	nd	37	24	nd
LT 8	429	0.27	23	32	10	nd
LT 9	476	0.19	7	1	1	nd
LT 10	519	0.16	nd	6	1	nd
LT 35	560	2.28	5	7	nd	nd
LT 36	561	0.45	11	11	1	nd
LT 11	593	0.05	nd	nd	nd	nd
LT 12	603	0.06	15	3	14	nd
LT 13[d]	*663*	*0.15*	*4*	*12*	*4*	*nd*
LT 26	745	0.05	3	6	12	nd
LT 20	1013	0.18	3	16	5	nd

[a]All mineral amounts in weight %, errors are <1% by weight; mineral amounts normalized to eliminate amorphous content - see explanation in text (section 2.4.2)

[b]nd = not detected

[c]Total organic carbon (TOC) reported as wt% of sediment, measurement error 0.01%

[d]Mineralogy does not match thin section, which contains quartz, mica, clays and iron oxides. Thin section was taken below grey lens in Blanchetown clay proper, whereas lipid and mineral samples come from the grey lens, which is probably Tyrrell bed contamination

Table 3.1C Detrital/other mineralogy[a,b] of Lake Tyrrell S12 core samples

Sample name	Depth (cm)	TOC[c]	Quartz	Hematite	Plagioclase feldspar	Alkali feldspar	Muscovite
LT 1	20	0.22	20	nd	nd	nd	nd
LT 2	190	0.06	13	nd	nd	nd	nd
LT 3	203	0.09	9	nd	nd	nd	nd
LT 4	223	0.10	17	nd	nd	nd	nd
LT 27	230	0.10	14	nd	0	nd	nd
LT 28	240	0.04	67	nd	nd	nd	nd
LT 5	289	0.12	8	nd	nd	nd	nd
LT 6	336	0.14	7	nd	nd	nd	nd
LT 7	411	0.14	8	nd	nd	nd	nd
LT 8	429	0.27	13	nd	nd	nd	nd
LT 9	476	0.19	3	nd	nd	nd	nd
LT 10	519	0.16	2	nd	nd	nd	nd
LT 35	560	2.28	2	nd	nd	nd	nd
LT 36	561	0.45	5	nd	nd	nd	nd
LT 11	593	0.05	1	nd	nd	nd	nd
LT 12	603	0.06	35	0	nd	nd	28
LT 13[d]	*663*	*0.15*	*13*	*nd*	*nd*	*nd*	*nd*
LT 26	745	0.05	63	nd	4	nd	8
LT 20	1013	0.18	64	nd	6	1	nd

[a]All mineral amounts in weight %, errors are <1% by weight; mineral amounts normalized to eliminate amorphous content - see explanation in text (section 2.4.2)

[b]nd = not detected

[c]Total organic carbon (TOC) reported as wt% of sediment, measurement error 0.01%

[d]Mineralogy does not match thin section, which contains quartz, mica, clays and iron oxides. Thin section was taken below grey lens in Blanchetown clay proper, whereas lipid and mineral samples come from the grey lens, which is probably Tyrrell bed contamination

Figure 3.1 shows the relative dominance of each mineral group within the three stratigraphic units: lunette sediments are composed primarily of clays, Tyrrell Bed samples of clays in the upper ~2.5 m and evaporites in the lower ~1.5 m, and samples from the Blanchetown Clay unit (with the exception of the anomalous sample LT 13 at 663 cm) are dominated by detrital and other minerals (mostly quartz).

The Blanchetown Clay sediments (603-1013 cm) are distinct in composition both from the lunette (<200 cm) and the Tyrrell bed (203-593 cm) sediments: LT 12 is the only sample to contain hematite (0.4%). It also contains ~30% muscovite; LT 26 (beneath LT 12, within the Blanchetown Clay) is ~8% muscovite. Feldspars are present at <6% abundance in LT 26 and LT 20. The major component of all of the Blanchetown Clay samples is quartz.

The evaporite signal is dominated by gypsum throughout the core, except in LT 4, 27 and 28, which have hardly any gypsum and 5-25% dolomite. LT 9 contains >60% gypsum, but also ~17% dolomite. LT 35 and LT 36 contain magnesite: 30% in LT 35, 3% in LT 36. However, gypsum is still the dominant evaporite in these samples: ~50% in LT 35, ~65% in LT 36. With the exception of the Blanchetown Clay samples, detrital minerals other than quartz make up only a small fraction of each sample.

TOC content varies with mineral content, and while higher TOC values are generally associated with greater evaporite content, the correlation is imperfect (Figure 3.1).

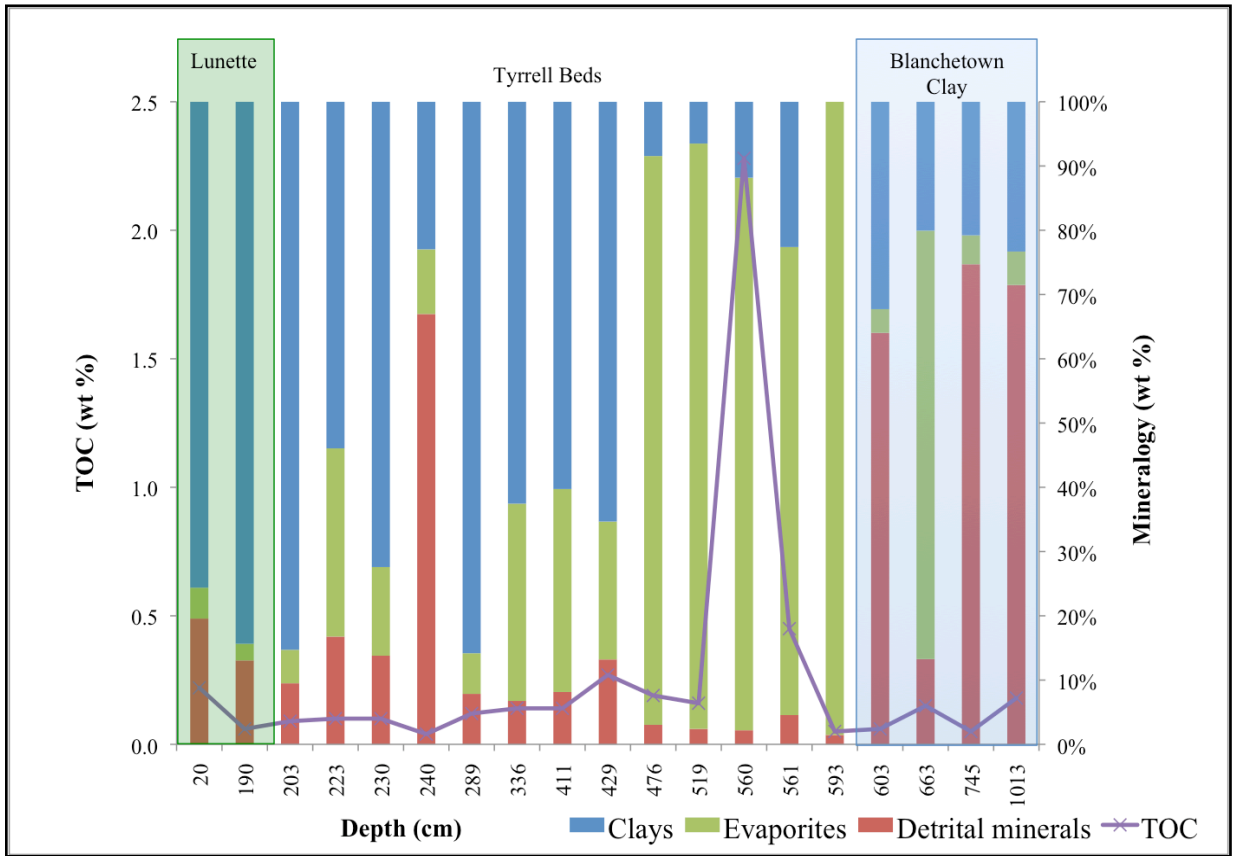

Figure 3.1 Variations in total organic carbon (TOC) content with mineralogy for LT S12 core

Total organic carbon (TOC) reported as wt% of sediment, measurement error 0.01%. Mineralogy is calculated as sum of minerals in Tables 3.1A (evaporites), 3.1B (clays) and 3.1C (detrital and other minerals).

3.4.2.1 Treatment of data from a contaminated sediment

LT 13, which at 663 cm lies within the Blanchetown Clay, is thought to be contamination from overlying Tyrrell beds. The mineralogy of this sample is dominated by evaporites (Tables 3.1A – C and Figure 3.1), and does not match that seen in the thin section, which is composed of quartz, mica, and clays with iron oxide staining (Appendix 2, Figure A2.12). This is because the thin section was taken below the grey lens from which mineral and lipid samples derived. This lens may be contamination from the overlying Tyrrell Beds. Such contamination could have occurred during the coring process, as some sediment may have fallen into the auger between the removal of one coring tube and the insertion of the next. Therefore, while the results of analysis of this sample will be presented, they will not be used further for reconstructions of palaeo-environment.

3.4.3 Results of palynological analysis

Results of palynological analysis for samples LT 4, 7, 10 and 20 may be found in section 2.4.3 and Table 2.2. Three additional samples were collected, corresponding to LT 30 from within the Tyrrell Beds, and LT 11 and LT 12, from above and below the Tyrrell Beds – Blanchetown Clay contact, respectively. Pollen were found only in LT 11, and relative abundances of major taxa present are listed in Table 3.2.

Table 3.2 Major taxa represented in additional Tyrrell Bed and Blanchetown Clay samples[a]

		LT 11 (601 – 602.5 cm)		
	Major taxa present	# grains	% total sample	grains per cc sample
Dryland taxa[b]	Poaceae	40	10.6	351
	Casuarinaceae	185	49.2	1625
	Asteraceae (Tubuliflorae)	21	5.6	185
	Chenopodiaceae	37	9.8	325
	Brassicaceae	nd[c]	-	-
	Callitris	4	1.1	35
	Eucalyptus	44	11.7	387
	Dodonaea	24	6.4	211
Aquatic taxa	Cyperaceae	3	0.8	26

[a]No pollen were detected in slides prepared from LT 30 (320 – 322.5 cm) or LT 12 (603 – 604.5 cm)
[b]Other dryland taxa present in <1% abundance include *Beyeria*, Gyrostemonaceae, Myrtaceae, Aizoaceae, *Plantago* sp., *Acacia*, *Haloragodendron*, Proteaceae and Legume sp.
[c]nd = not detected

3.4.4 Results of lipid biomarker analysis

Preliminary results of lipid biomarker analysis for samples LT 1, 4, 7, 10 and 20, as well as the neutral fractions of S12 salt and S12 mats, may be found in Chapter 2: section 2.4.4, Figures 2.2, 2.3, 2.4 and 2.5 and Table 2.4. Further results, as well as results for other subsamples from the core, are presented here.

n-alkanes, *n*-alkanols, steroids and acyclic isoprenoids were the dominant lipid classes in most samples (Table 3.3). No clear patterns emerged correlating class abundance with depth, stratigraphic unit, or extract yield. Total lipid extract (TLE) showed some correlation with total organic carbon (TOC) content (Figure 3.2), though the quantity of TOC was up to 1000x higher than the amount of TLE in any given sample.

Table 3.3 Relative abundance of lipid classes (as % of total) within LT S12 surface and core samples

Sample name	Depth (cm)	TLE (ug/g sample extracted)	*n*-alkanes (nC_{14}-nC_{35})	*n*-alkanols (nC_{12}-nC_{34})	*n*-alkanoic acids (nC_5-nC_{30}, nC_{32}, nC_{34})	steroids	hopanoids	alkyl ketones	triterpenoids[a]	isoprenoids[b]	diols, keto-ols and enols	misc and unidentified
S12 salt (TSN)[c]	0	1.2	1.2	1.7	nm	1.4	0.1	0.0	0.1	95.2	0.1	0.2
S12 mats (TSN)[c]	1	57.1	1.7	3.2	nm	1.8	0.1	0.0	0.1	92.3	0.6	0.3
LT 1	20	5.7	75.2	20.6	0.1	3.9	0.2	0.0	0.0	0.0	0.0	0.1
LT 2	190	0.2	37.9	5.2	19.0	0.1	0.0	0.0	0.0	37.8	0.0	0.0
LT 3	203	1.8	91.6	7.3	0.4	0.3	0.4	0.0	0.1	0.0	0.0	0.0
LT 4	223	1.4	80.5	10.7	0.9	0.9	0.0	0.0	6.9	0.1	0.0	0.0
LT 27	230	0.7	66.7	17.9	0.0	1.9	1.7	0.0	11.8	0.0	0.0	0.1
LT 28	240	0.9	90.0	3.8	0.0	0.5	2.3	0.0	3.4	0.0	0.0	0.0
LT 5	289	2.6	64.4	13.2	0.7	0.6	0.5	0.0	4.3	16.4	0.0	0.1
LT 6	336	2.3	82.9	8.2	0.0	3.2	2.3	0.9	2.1	0.1	0.0	0.3
LT 7	411	2.8	27.4	6.3	0.3	37.4	2.4	0.0	1.6	22.2	0.0	2.5
LT 8	429	15.5	9.9	6.7	0.0	9.0	1.3	0.0	0.8	68.6	0.0	3.7
LT 9	476	0.5	50.0	8.6	1.1	5.9	0.3	0.5	2.1	30.7	0.0	0.8
LT 10	519	8.9	15.8	2.9	22.1	8.2	1.8	0.0	3.3	45.1	0.0	0.9
LT 35	560	10.6	19.6	4.7	0.5	9.7	1.5	0.0	2.4	57.8	0.4	3.4
LT 36	561	18.1	9.1	2.8	0.6	4.8	1.5	0.0	1.9	76.5	0.2	2.8
LT 11	593	3.0	5.8	2.1	0.1	6.5	2.2	0.0	0.5	80.9	0.0	2.0
LT 12	603	2.9	27.8	3.4	0.1	5.7	0.7	0.0	0.7	59.1	0.0	2.5
LT 13	663	10.4	9.0	2.0	0.2	11.9	2.1	0.7	2.8	69.9	0.0	1.5
LT 26	745	0.3	94.7	5.1	0.0	0.3	0.0	0.0	0.0	0.0	0.0	0.0
LT 20	1013	4.9	43.5	13.3	23.2	1.7	5.6	0.0	1.4	3.8	7.4	0.0

[a]Triterpenoids included are tetrahymanol (gammaceran-3β-ol), gammacerone (gammacer-3-one), taraxerol (taraxer-14-en-3β-ol), germanicol (olean-18-en-3β-ol), lupeol (lup-20(29)-en-3β-ol), friedelan-3-one

[b]Isoprenoids included are $C_{20,20}$ archaeol (bis-O-phytanyl glycerol), $C_{20,25}$ archaeol (O-phytanyl-O-sesterpanylglycerol), phytol, phytanol (dihydrophytol), phytone (6,10,14-trimethyl-pentadecan-2-one), phytanic acid, squalene, dihydrosqualene

[c]*n*-alkanoic acids are not present, as extracts were saponified prior to analysis. TSN stands for total saponified neutrals

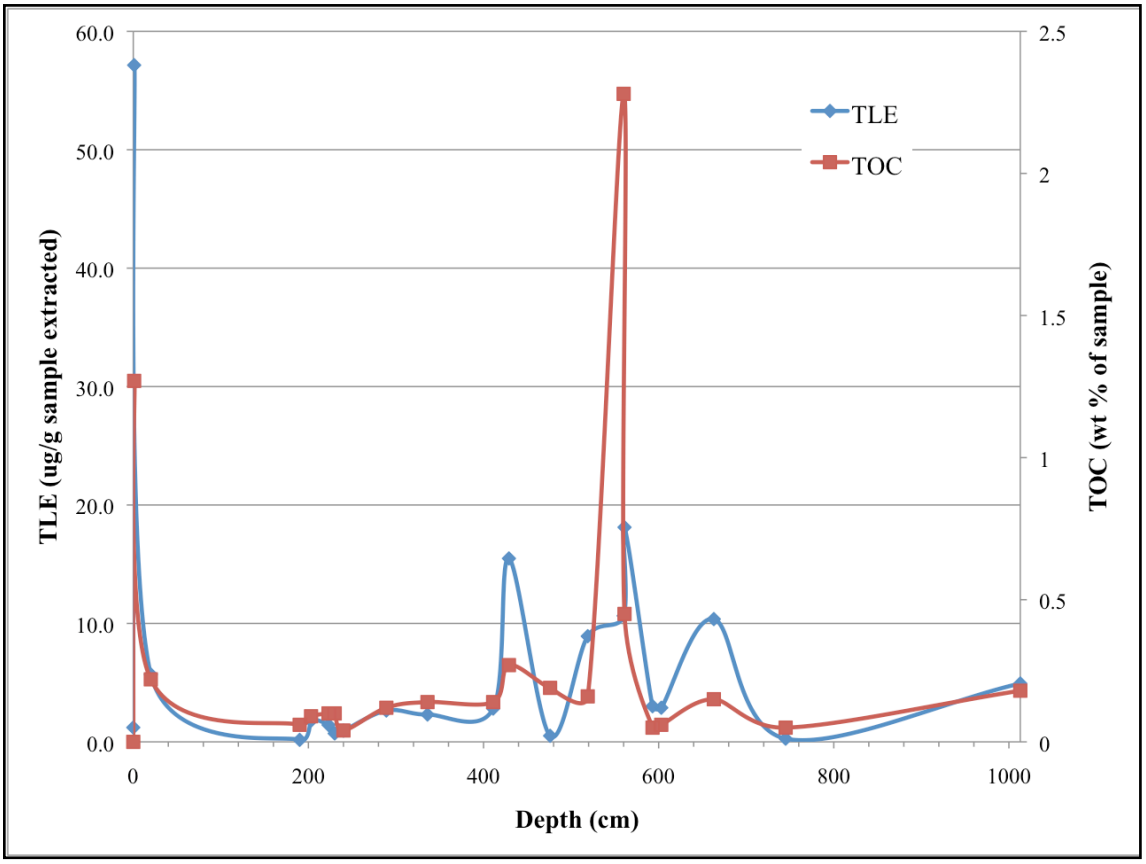

Figure 3.2 Quantities of TOC vs. TLE for samples from the LT S12 deep core

TLE is presented as a concentration, but can be converted to weight % with the addition of "x10^{-4}" to values along its axis. Thus it is evident that TOC content (wt%) for each sample is 100x – 1000x that of TLE (wt%).

Individual lipids across all classes were examined both as binary quantities (presence or absence) and as relative concentrations (as a percentage of the total quantity of lipids). A binary scatter plot of all lipids (Figure 3.3) shows that while nearly all samples contain the full suite of *n*-alkanes (nC_{14}-nC_{35}) and *n*-alkanols (nC_{12}-nC_{34}), only some contain *n*-alkanoic acids (nC_5-nC_{30}, nC_{32}, nC_{34}), most of which are of even C number (Figure 3.3). Complex lipids (those numbered in Table 2.4) are present in the surface material and throughout the core, although sediments from the lunette (LT 1 and 2), from the top of the Tyrrell Beds (LT 3 and 4) and one sample from the Blanchetown Clay (LT 26) contain fewer than 10 different complex compounds (Figure 3.3).

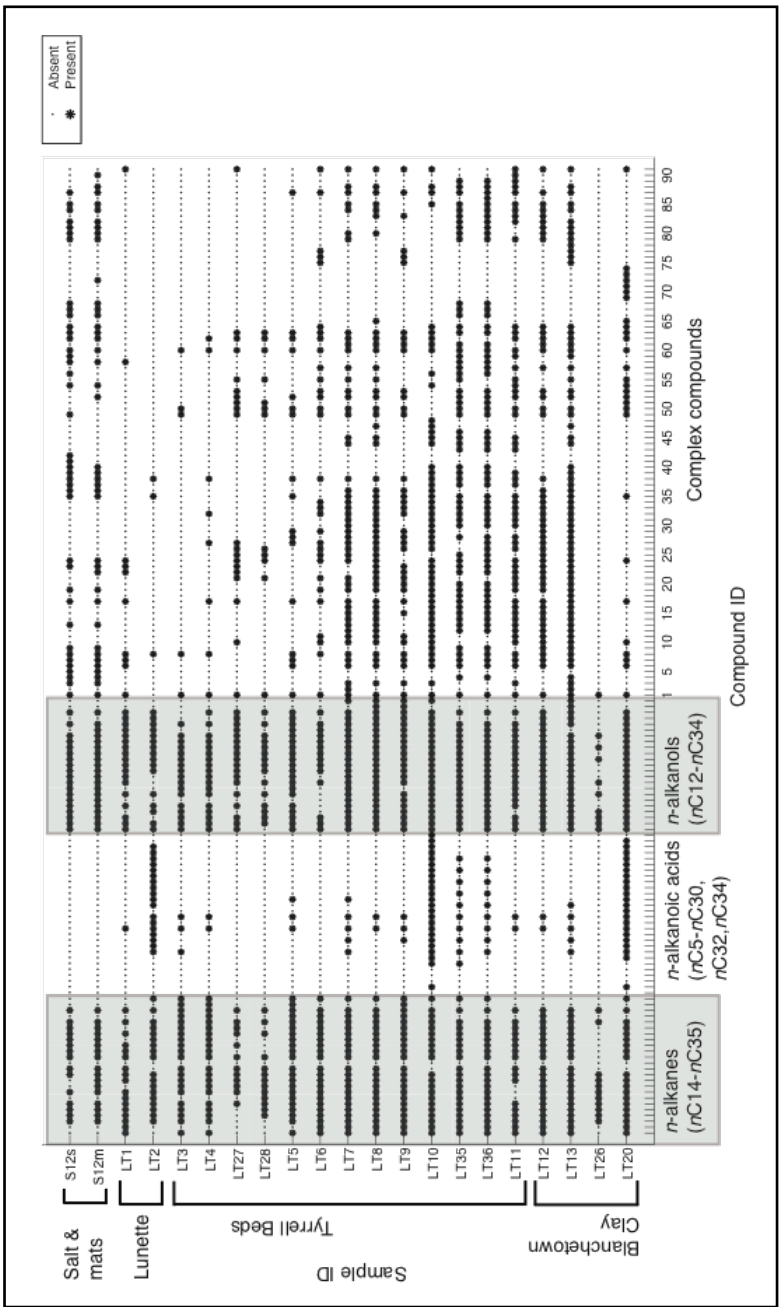

Figure 3.3 Presence/absence of lipid compounds by sample

Detection limit for compounds is ~20 ng per compound per extract; however, it may be higher if there is co-elution of compounds. Complex compound numbers and names are given in Table 2.4. *n*-alkanoic acids are not present in salt and mat samples (S12s and S12m) as these extracts were saponified prior to analysis and the acidic fraction was not analyzed. nC_{24} is masked by the standard, so is marked as absent in all samples. Samples are listed in order of depth, from the surface (0 cm) to the deepest sample (1013 cm) near the base of the core.

Relative concentrations of both simple lipids (*n*-alkanes, *n*-alkanoic acids, and *n*-alkanols) and complex lipids (steroids; hopanoids; alkyl ketones; triterpenoids; isoprenoids; diols, keto-ols and enols; and miscellaneous and unidentified lipids) change between individual samples; however, no obvious pattern with depth is apparent in the scatter plots (Figures 3.4 and 3.5).

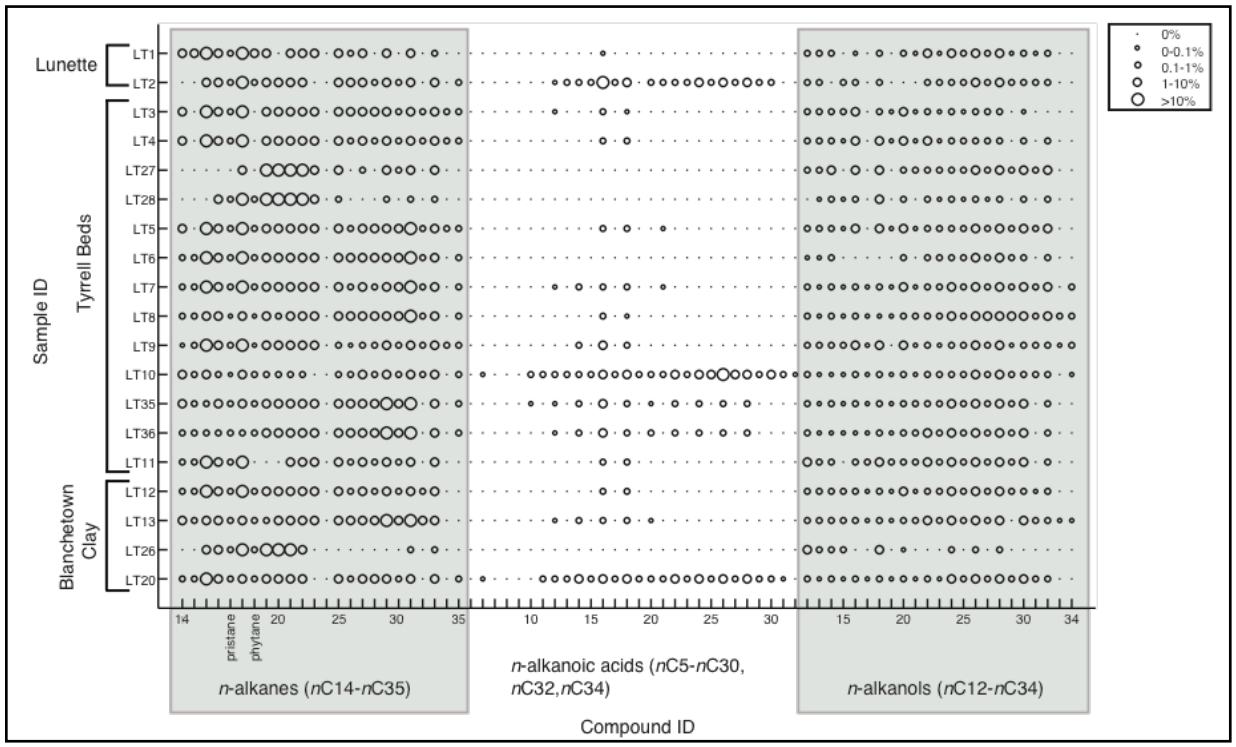

Figure 3.4 Relative abundances of simple lipids by sample

Relative abundances of individual lipids are given as percentages, calculated as µg/g lipid / total µg/g simple lipids; percent abundance is denoted by symbol size (see legend). Salt and mat samples are not included as these extracts did not contain *n*-alkanoic acids (due to saponification). nC_{24} is masked by the standard, so is marked as absent in all samples. Samples are presented in order of depth.

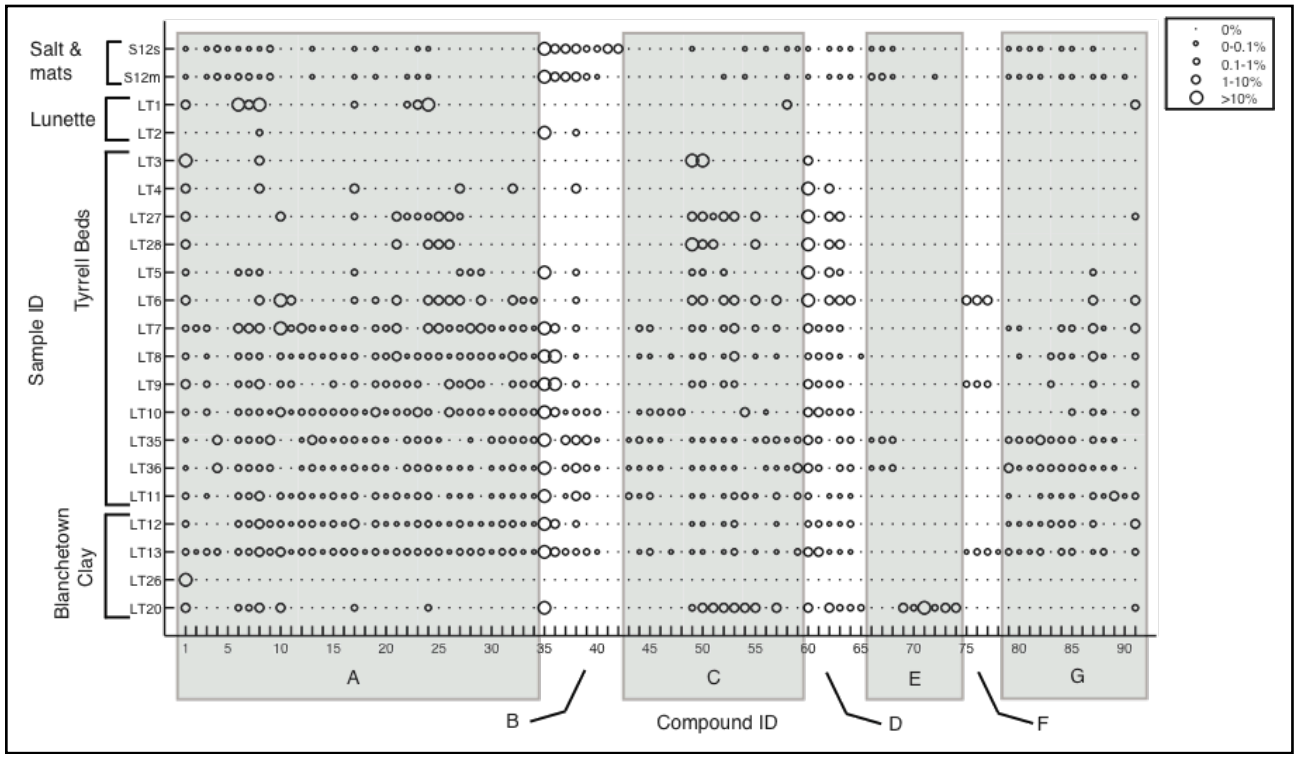

Figure 3.5 Relative abundances of complex lipids by sample

Relative abundances of individual lipids are given as mass percentages relative to total lipids, calculated as µg/g lipid / total µg/g complex lipids; percent abundance is denoted by symbol size (see legend). Complex lipid groups are alternately shaded to emphasize groupings, which are as follows: steroids (A), isoprenoids (B), hopanoids (C), triterpenoids (D), diols, keto-ols and enols (E), alkyl ketones (F), miscellaneous and unidentified complex lipids (G). Individual compounds are numbered as in Table 2.4. Samples are presented in order of depth.

GDGTs were detected in only one of the five samples analyzed: LT 35. This sample contained measurable quantities of GDGT V, GDGT VI and GDGT VII (Figure 3.6). Two additional isomers of GDGT VI with *m/z* 1300 were present, as well as the isomer typically seen in lake sediments (Pearson 2010). No branched tetraethers, nor any of the other GDGTs necessary for calculation of the TEX_{86} palaeothermometer (GDGTs VIII and IV', (Pearson *et al.* 2011)), were detected.

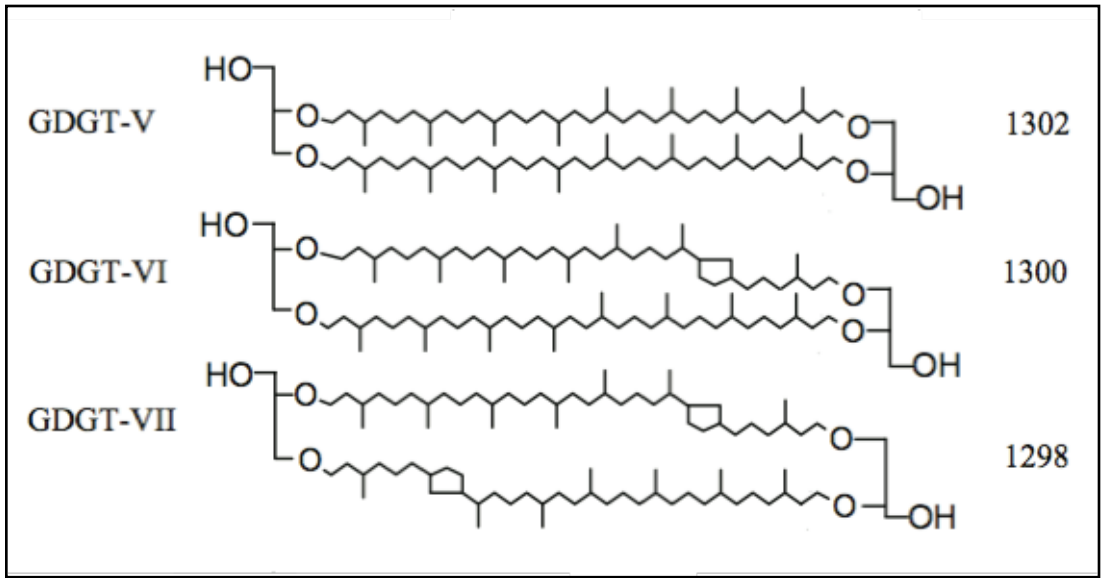

Figure 3.6 Molecular structures and masses of GDGTs found in LT 35
Figure is adapted from Pearson *et al.* (2011)

3.5 Discussion

In order to interpret lipid biomarker data in conjunction with traditional palaeo-environmental proxies such as mineral content, sedimentary textures, and pollen content, one needs to know what environmental factors control the composition of the lipid assemblage. The two most important controls on the composition of the biomarker suite of a given sample are input and diagenesis (Peters and Moldowan 1993). Input refers to changes in the source of lipid biomarkers, such as would occur during changes in the community composition of source organisms with time. Diagenesis refers to post-depositional changes to biomarker suites as a result of abiotic and biotic oxidation and reduction, soil formation, or chemical changes such as sulfurization or polymerization. If we can isolate the factors that influence input and diagenesis, we may be able to relate changes in biomarker composition to specific changes in the environment.

The most obvious factor controlling input is the salinity of the lake water. By determining the mineral composition of core samples, and relating these to an assessment of primary vs. secondary mineral formation based on thin section analysis, we can separate high from low salinity sediments to track relative change in salinity with time. Sedimentary textures seen in thin section provide information about diagenetic processes that have taken place in addition to secondary mineral formation, such as oxidation and soil formation. We can use these observations to contextualize biomarker assemblage data, and create a picture of the lake that includes the organismal assemblage, lake salinity and water level, and the abiotic and biotic processes affecting the chemistry of the water and sediments.

3.5.1 Analysis of mineral contents of core sediments

Information gained from thin section analyses and from analyses of mineral content were combined in order to assess the relative salinity and the extent of preservation of core sediments. Preservation indices were assigned as described in Appendix 2; samples for which there was no

accompanying thin section were assigned an index based on the initial core and sub-sample descriptions (Appendix 3), as compared with those for the nearest thin section of similar mineralogy. Values assigned ranged from 1 to 5, with 1 being best-preserved, and 5 least-preserved.

Assigning relative salinity was more problematic, as secondary mineral formation and post-depositional mineral dissolution can extensively alter the mineral content of a sample. However, evidence of such processes appears as disruptions to sedimentary texture as seen in thin section (Brewer 1964; Magee 1991; Poch *et al.* 2009). Relative salinity was tentatively ascribed based on the mineral content of the sediment, and checked against the textural analysis (see section 3.4.1 and Appendix 2) to ensure that relative salinity assignments were not skewed by extensive secondary mineral formation. It must be emphasized that relative salinity assignments are tentative, as they were made without reference to lipid biomarker content. Therefore, although mineral assemblages appear to reflect palaeo-salinity, they will be described as mineral groups, to avoid over-interpretation.

Results from mineralogical analysis demonstrated that the samples fell into three distinct groups, and were dominated by clays, evaporites, or other minerals (mostly quartz) (Figure 3.1). In order to determine whether relative dominance of these classes adequately reflected sample clustering, the ordination technique of non-metric multi-dimensional scaling (NMS) was employed. Figure 3.7A shows three distinct sample groups based on mineralogy; Figure 3.7B shows how much influence each mineral has on the distance between samples and between groups. The blue group is dominantly influenced by quartz (QUA). Since we know this is present as a beach sand and is representative of deeper water (see discussion in chapter 2), we tentatively assigned this group the lowest salinity value, and refer to it as mineral group 1 (MG1). The purple group is dominantly influenced by clays, specifically illite (ILL) and kaolinite (KAO). Clays can enter the Lake Tyrrell basin through run-off, however they are usually found in clay-gypsum couplets. These couplets are typically indicative of fluctuating salinity values of marine and greater salinity (see discussion in chapter 2). Therefore, this group was tentatively assigned an intermediate salinity value, and is referred to as mineral group 2 (MG2). It should be noted here that the assignment of a higher salinity value to clay dominated samples and a lower value to samples dominated by detrital minerals is supported by previously published material on the provenance and transport of sedimentary components within the lake beds of southeastern Australia (Bowler 1970, 1973, 1976; Bowler *et al.* 2006; DeDeckker 1988; Macumber 1991; Magee 1991; Pell *et al.* 2001). Finally, the red group is dominantly influenced by gypsum (GYP); deposition of primary gypsum indicates salinity values of >120 g/L (Bowler and Teller 1986). Therefore, this group was tentatively assigned the highest salinity value, and is referred to as mineral group 3 (MG3).

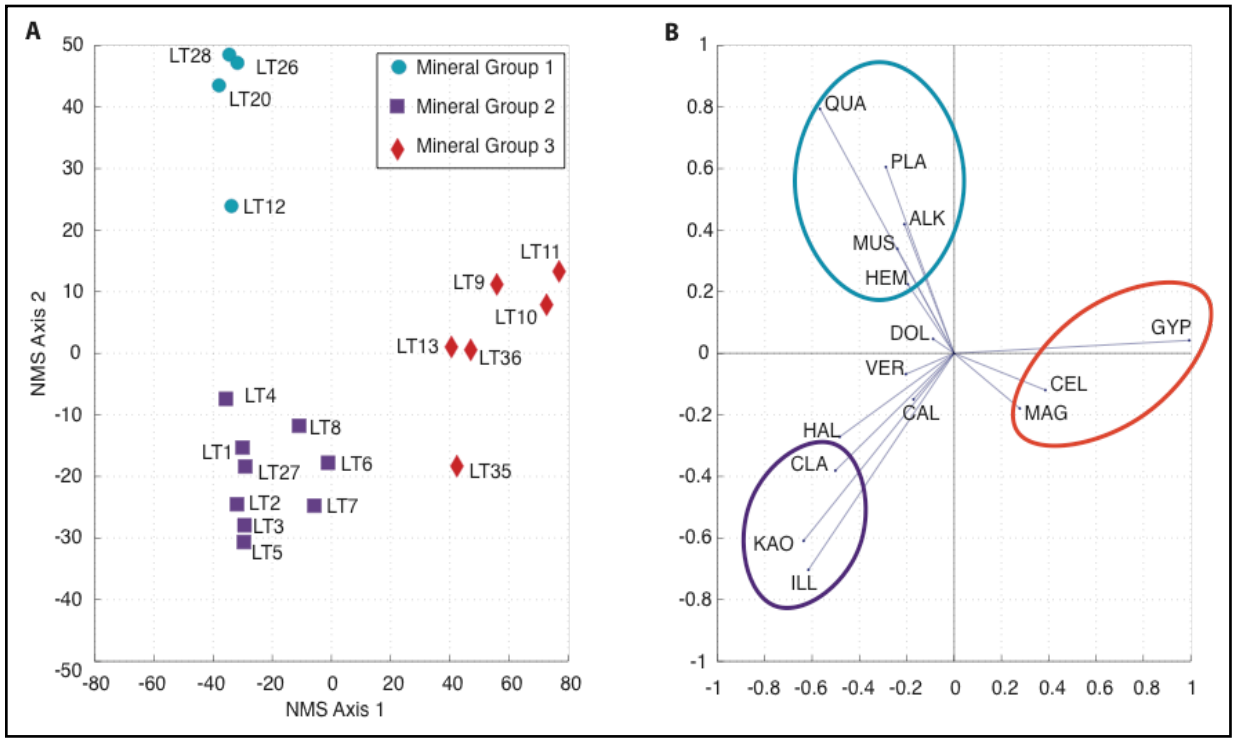

Figure 3.7 NMS plot of samples by dominant mineral group

Correlations between samples in plot A were calculated using Euclidean distance. Plot B shows the loading (relative influence) of each component (mineral) on the clustering of samples in plot A. Mineral groupings in plot B are as follows: the red group is composed of evaporite minerals - gypsum (GYP), celestite (CEL) and magnesite (MAG). The purple group is composed of clay minerals - an unidentified clay component/montmorillonite (CLA), kaolinite (KAO) and illite (ILL). The blue group is composed of detrital and oxide minerals - quartz (QUA), plagioclase feldspar (PLA), alkali feldspar (ALK), muscovite (MUS) and hematite (HEM). Dolomite (DOL), calcite (CAL) and halite (HAL) do not cluster within the evaporite minerals, probably because they typically form diagenetically (as secondary minerals) in the lake sediments and so are not indicative of salinity at the time of deposition. Vermiculite (VER) is present as a trace component (<1% by weight) in only one sample, so its loading is extremely low. Principal component analysis of these data yielded the same groupings, and the first two axes explain ~90% of the variability in the data.

As would be expected, three of the four samples in the blue (likely freshest) group are derived from the Blanchetown Clay. The salinity of this megalake has been estimated as fresh to marine, with increased salinity values assigned to the youngest samples of the facies, which were presumably deposited as Lake Bungunnia began to dry out (An *et al.* 1986; McLaren *et al.* 2009; Stephenson 1986). LT 20 and LT 12 do not appear to have undergone extensive post-depositional alteration (see section 3.4.1 and Appendix 2, Figures A2.11 and A2.13), so that the assessment of low salinity based on mineral content grouping is probably accurate. No thin section was taken for LT 26, so no assessment of the syngeneity of minerals is attempted.

LT 28, despite its location within the Tyrrell Beds, groups with these Blanchetown Clay samples. This is likely due to the anomalously high amount of quartz in LT 28 relative to other Tyrrell Bed sediments (Tables 3.1A – C and Figure 3.1), as the loadings assigned in Figure 3.7B show quartz to be the most significant variable in the clustering of MG 1. While there is no thin section for LT 28, it lies just below LT 4 (Appendix 1, Figure A1.1), the bottom of which section is composed largely of clays and iron oxides (Appendix 2, Figures A2.2 F and G). The base of LT 4 appears to have undergone extensive oxidation, possibly as a result of soil formation

(Brewer 1964). It was observed during core sub-sampling that LT 27 and LT 28 appeared to be part of a soil layer, and that both samples contained ~4% dolomite (DOL), a common secondary mineral in saline soils (Magee 1991). It is likely that both samples fall within a pedogenic zone, and the low quantity of quartz in LT 27 places it (possibly incorrectly) within the sample group of medium salinity, while LT 28 is dominated by quartz sand, and so groups with the fresher samples. As it is not possible to determine whether LT 27 and LT 28 originally contained primary evaporites, they are not utilized in further discussions of salinity in the absence of biomarker analysis.

The lunette samples (LT 1 and LT 2) cluster with the samples from the Tyrrell Beds containing approximately 5-30% evaporites (Figure 3.1), and Figure 3.7B shows kaolinite and illite content to be most significant in clustering MG2. As there are few igneous or metamorphic minerals within the Tyrrell Basin (Bowler 1970, 1979; Macumber 1991), clays cannot form secondarily in this system, so that we may be confident that primary sample mineralogy is preserved. Since the lunette formed as a result of deflation of the dry lakebed at the height of the LGM (Bowler 1973, 1976), it is not surprising that its mineralogy should be quite similar to that of the upper Tyrrell Beds.

For more saline samples from the deeper portion of the Tyrrell Beds, gypsum content is clearly the most significant variable in controlling the clustering (Figure 3.7B). Gypsum readily forms as a secondary mineral in saline sediments, and thin sections of LT 30, 32, 34, 10, and 11_12 contain varying quantities of displacive (secondary) gypsum (Appendix 2, Figures A2.4, A2.5, A2.8 G, A2.9 F, and A2.11 E – G). Sections LT 30 (312 – 319 cm), 32 (360 – 367 cm) and 34 (503 – 510 cm) were not assessed for mineral content nor for lipid biomarker content, as they demonstrated significantly altered mineral fabric, to the extent that primary mineralogy was difficult or impossible to determine.

Finally, LT 13, despite its location within the Blanchetown Clay, groups closely with the highly saline Tyrrell Bed samples. This is likely due to the fact that LT 13 actually derives from the Tyrrell Beds, and became incorporated into the Blanchetown Clay as contamination during the coring process, as described in section 3.4.2.1. Ordination techniques can therefore assist in identifying contamination in sample sets with many variables.

Table 3.4 below provides a summary of samples used in palaeoenvironmental reconstruction based on extent of preservation or post-depositional alteration. Explanations for samples not used in palaeoenvironmental reconstructions, for samples for which the extent of post-depositional alteration could not be assessed, and for the utility modern samples are given.

Table 3.4 Summary of sections from the LT S12 core used in palaeoenvironmental reconstruction

Sample facies	Sample name	Sample depth (cm)	Preservation index (1 – 5, where 1 is well-preserved and 5 is poorly-preserved)	Mineral Group (1, 2 or 3)	Used in palaeo-environmental reconstruction? (Y/N)	Explanation
Modern	S12 salt	0	1	na	Y	Basis for comparison
	S12 mats	1	1	na	Y	Basis for comparison
Lunette	LT 1	20	3.5	2	Y	As comparison from Ch. 2
	LT 2	190	3	2	Y	
Tyrrell Beds	LT 3	203	3.5	2	Y	As a check on the placement of contact between lunette (LT 2) and Tyrrell Beds (LT 4)
	LT 4	223	4	2	Y	
	LT 27	230	4	2	Y	Only with reference to biomarker assemblage
	LT 28	240	4	1	Y	Only with reference to biomarker assemblage
	LT 5	289	5	2	Y	
	LT 30	312	4	na	N	Extensive secondary mineral formation
	LT 6	336	3.5	2	Y	Used as a check on LT 5 and LT 7
	LT 32	360	3.5	na	N	Extensive secondary mineral formation
	LT 7	411	2.5	2	Y	
	LT 8	429	2.5	2	Y	As basis of comparison for LT 7 and LT 9
	LT 9	476	2.5	3	Y	
	LT 34	503	2.5	na	N	Extensive secondary mineral formation
	LT 10	519	1.5	3	Y	
	LT 35	560	1	3	Y	
	LT 36	561	1	3	Y	
	LT 11	593	3	3	Y	
Blanchetown Clay	LT 12	603	3	1	Y	
	LT 13	663	2.5	3	N	contamination
	LT 26	745	2.5	1	Y	As basis of comparison for LT 12 and LT 20
	LT 20	1013	2	1	Y	

na = not assessed

3.5.2 Relationship of abiotic to biotic contents of sediment

If mineral groupings are, in fact, a reflection of salinity, we would expect that biomarker source would vary broadly with mineral grouping. TOC roughly tracks TLE downcore (Figure 3.2), but quantities are extremely variable. Such variability suggests large changes in either input or post-depositional sample alteration (diagenesis). Now that we have three groups of samples defined by mineralogy, and preservation values assigned to each sample, it remains to be tested whether there is a statistically significant correlation between mineral group and preservation index. A box-plot of preservation values by mineral group was created for salt, mat and core material (Figure 3.8). The inter-quartile ranges of preservation values for samples within mineral groups 1 and 2 overlap; however, samples within mineral group 3 seem to be much better preserved. An ANOVA F-test shows that the means of the 3 boxes are different at $p<0.1$, which is less rigorous than we would like. Student's t-tests show that the mean preservation in populations of samples within mineral groups 1 and 2 are essentially the same, but that those of mineral groups 1 and 3 ($p<0.06$) and 2 and 3 ($p<0.0004$) are significantly different.

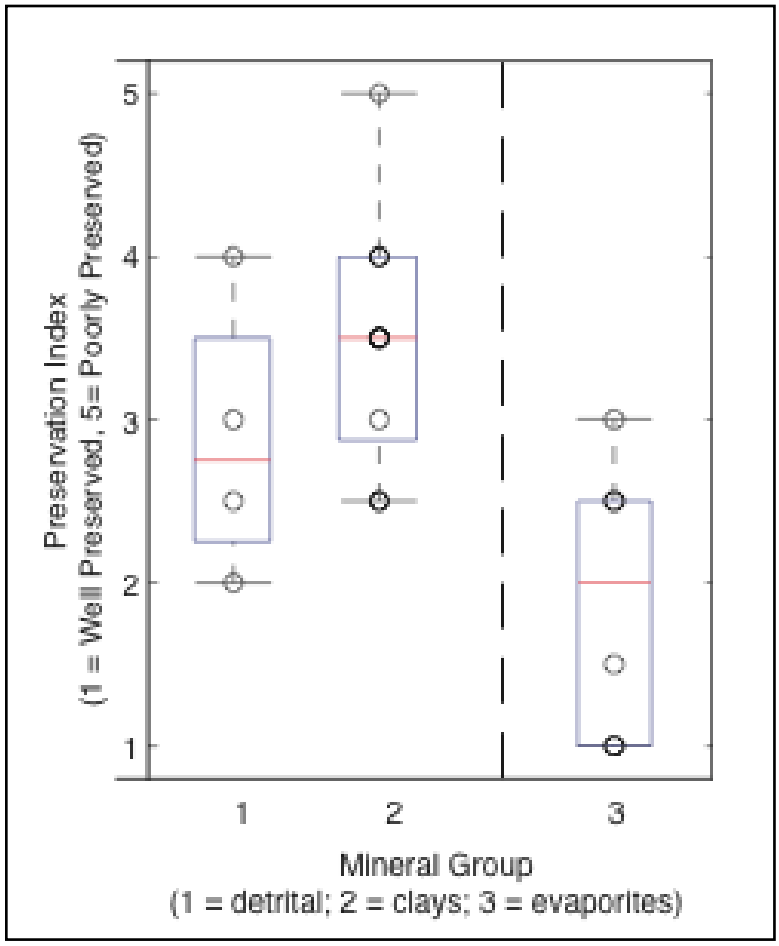

Figure 3.8 Box plot of preservation values by mineral group for surface and core samples

The top and bottom of each box represents the inter-quartile range (25-75%) around the median (red line in center of box) of the preservation values of samples within the mineral group. The minimum and maximum preservation values for the group are indicated by horizontal black lines above and below the box. For mineral group 1, n=4; for mineral group 2, n=9; for mineral group 3, n=8. The dotted line separates the mineral groups of low evaporite content on the left from that with high evaporite content on the right.

It appears that salinity and preservation are correlated, raising the question as to whether mineralogy, TOC or TLE, and preservation are related. It would seem obvious that better sample preservation (and therefore higher evaporite content) would correlate with higher TOC or even TLE; however, there is no statistically significant correlation between TOC or TLE and preservation or between TOC or TLE and evaporite content. Some other factor, then, is controlling TOC and TLE content – this could be biotic breakdown of sedimentary lipids (which process is difficult to infer from sedimentary textures), or changing wind regimes bringing more material into the lake at certain times (e.g., changes in input). It is encouraging that abiotic diagenetic processes, such as oxidation and soil formation, do not seem to alter the overall lipid content of samples. This reinforces the notion that even chemically hostile depostional environments, such as ephemeral saline lakes, may be valuable repositories of palaeo-climatic information.

3.5.3 Analysis of pollen contents of core sediments

Pollen content of lacustrine sediments provides information about the extent of post-depositional oxidation, the geographic range of allochthonous input, and the balance of precipitation and evaporation within a catchment. From Tables 2.2 and 3.2, it is clear that membership of the dryland community remains relatively constant throughout the time period covered by the deposition of the Tyrrell Beds. Poaceae (grasses) and Asteraceae (asterids or daisies) increase in relative abundance, while tree cover (Casuarinaceae, *Callitris* and *Eucalyptus*) decreases. This points to an overall increase in aridity over this time period (Luly 1990), which accords with accounts of the drying of Lake Bungunnia (An *et al.* 1986; Stephenson 1986) followed by the formation of salt lakes and dune fields (Bowler 1973, 1976, 1986; Pell *et al.* 2001).

Dodonea pollen is usually interpreted as evidence of disturbance within the plant community, typically ascribed to fire (Bekele 2000). The decrease in abundance in *Dodonea* pollen through time (Tables 2.2 and 3.2) indicates that the change in vegetation within the catchment was likely gradual, or at least was not a result of increased fire frequency. As fire frequency is controlled buy fuel supply as well as weather conditions (Bekele 2000; Luly 1993), the decrease in tree cover may have counter-balanced the increase in aridity.

The increased number of aquatic taxa and the presence of Tertiary pollen within LT 7 and LT 10 as compared to LT 11 may indicate changes in the sources of pollen to the sediments of Lake Tyrrell. Even as the overall landscape dried, episodic flooding causing increased amounts of run-off and erosion of the shoreline could have contributed small amounts of both Tertiary and aquatic pollen grains to the lake. As discussed in chapter 2, Tertiary pollen are typically absent (except as re-worked material) in Quaternary assemblages, but do appear in cores from Lake Tyrrell as re-worked components of the Blanchetown Clay.

The lack of pollen within and relatively poor preservation of LT 12 and 30 (preservation indices of 3 and 4, respectively) conforms with previous findings, which show heavily oxidized layers within the Tyrrell Beds (Luly 1993) and the upper 6 m of Blanchetown Clay (Luly 1990) as devoid of pollen. It is interesting to note that lipid biomarkers are preserved in the absence of pollen in both of these facies, re-affirming the importance of lipid biomarkers as palaeo-environmental proxies that may be preserved in the absence of other indicators.

3.5.4 Analysis of conventional indicator lipids

In addition to changes in concentration of TLE and TOC downcore, the lipid assemblage appears to change. As the mineral assemblage is partially a result of the salinity of the lake during deposition, it is possible that the lipid input is also controlled by salinity. Organic geochemists have analyzed the contents of oils and bitumens extracted from saline facies, and have identified certain biomarkers consistently associated with these facies as ‘indicators’ of saline depositonal conditions. For example, high abundance of docosane (nC$_{22}$), relative to C$_{21}$ and C$_{23}$ *n*-alkanes has previously been posited as an indicator for deposition under saline conditions (Haug and Sever 1971; Peters *et al.* 2005; ten Haven *et al.* 1985; ten Haven *et al.* 1988), although the reasons for its increased abundance are unknown. ten Haven *et al* (1988) calculated this ratio as:

Equation 3.1 $$R_{22} = 2*n\mathrm{C}_{22}/(n\mathrm{C}_{21} + n\mathrm{C}_{23})$$

Values of $R_{22} > 1.5$ were interpreted as evidence of deposition under hypersaline conditions (ten Haven *et al.* 1988). Table 3.5 contains R_{22} values, mineral groupings and evaporite content of

Tyrrell surface material and core sediments, from which it is evident that R_{22} and salinity proxies do not correlate in the Tyrrell core. Modern mats and salt contain comparatively little nC_{22}, suggesting either that nC_{22} is a product of diagenesis of some component of saline sediments, or that the Lake Tyrrell system is entirely different to those hypersaline facies previously described.

Table 3.5 R_{22} and phytane:pristane ratio compared to mineral content for salt, mat and S12 core samples

Sample facies	Sample name	Sample depth (cm)	Evaporites (wt %)[a]	Mineral group[b] (1=fresh, 2=medium, 3=saline)	R_{22}[c]	Phytane:Pristane ratio[d]
Modern	S12 salt	0	nm	3	0.5	nm
	S12 mats	1	nm	3	0.6	nm
Lunette	LT 1	20	4.81	2	1.4	4.3
	LT 2	190	2.58	2	2.5	2.0
Tyrrell Beds	LT 3	203	5.21	2	1.2	nm
	LT 4	223	29.29	2	1.5	nm
	LT 27	230	13.79	2	1.3	nm
	LT 28	240	10.06	1	1.0	1.1
	LT 5	289	6.32	2	1.2	2.0
	LT 6	336	30.69	2	1.2	0.4
	LT 7	411	31.59	2	1.0	2.0
	LT 8	429	21.46	2	1.0	0.4
	LT 9	476	88.51	3	1.2	0.3
	LT 10	519	91.09	3	2.2	1.5
	LT 35	560	85.99	3	0.9	0.2
	LT 36	561	72.83	3	0.6	0.2
	LT 11	593	98.54	3	1.3	nm
Blanchetown Clay	LT 12	603	3.68	1	1.3	2.7
	LT 26	745	4.51	1	0.9	0.6
	LT 20	1013	5.20	1	2.4	1.0

[a]Weight percent of evaporites is taken from Table 3.1; nm = not measured.

[b]Mineral groups are assigned as described in section 3.5.1.

[c]R_{22} is calculated as in Eqn 3.1.

[d]nm indicates not measured; samples in which pristane or phytane was absent.

In the Lake Tyrrell system, an elevated abundance of nC_{22} relative to all other *n*-alkanes seems to be associated with lower salinity samples, is any relationship exists at all (Figure 3.9). Therefore, docosane cannot be used as an indicator of palaeo-salinity in the Lake Tyrrell core.

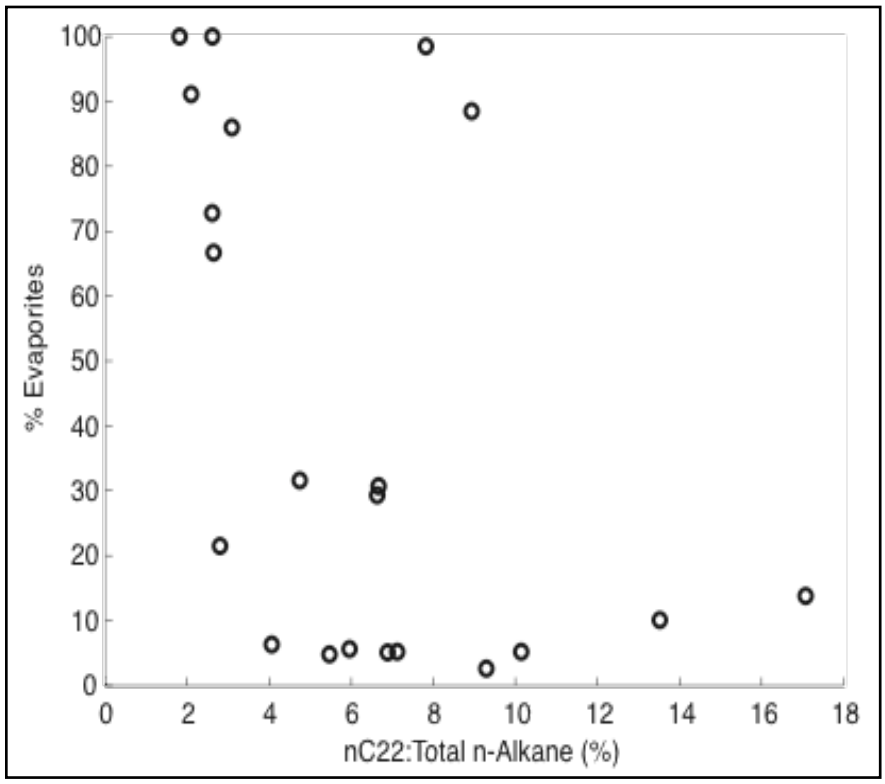

Figure 3.9 Relationship between relative dominance of *n*C22 and evaporite content
Relative nC_{22} dominance is calculated as a percentage: [(μg *n*C22/g sample extracted)/(μg *n*-alkanes/g sample extracted)]*100. Sample salinity is represented by the weight % of evaporite minerals in the sample, such that a greater evaporite content is a proxy for higher salinity.

High abundance of phytane (a C_{20} isoprenoid) relative to pristane (a C_{19} isoprenoid) has also been previously cited as indicative of a hypersaline depositional environment (ten Haven *et al.* 1988). This ratio was originally developed as an indicator of oxic vs. anoxic depositional environment, known as the pristane:phytane (Pr/Ph) ratio (Brooks *et al.* 1969; Didyk *et al.* 1978). Both compounds occur as diagenetic products of phytol, an isoprenoidal alcohol that forms the sidechain of chlorophyll (Rontani and Volkman 2003). As chlorophyll is degraded, sequential reduction of phytol produces phytane, whereas intermittent oxidation leads to the production of pristane (Didyk *et al.* 1978) (Figure 3.10). In light of this, values of the pristane:phytane ratio >1 were were thought to be indicative of oxic depositional regimes, and those less than 1 of anoxic ones (Peters *et al.* 2005).

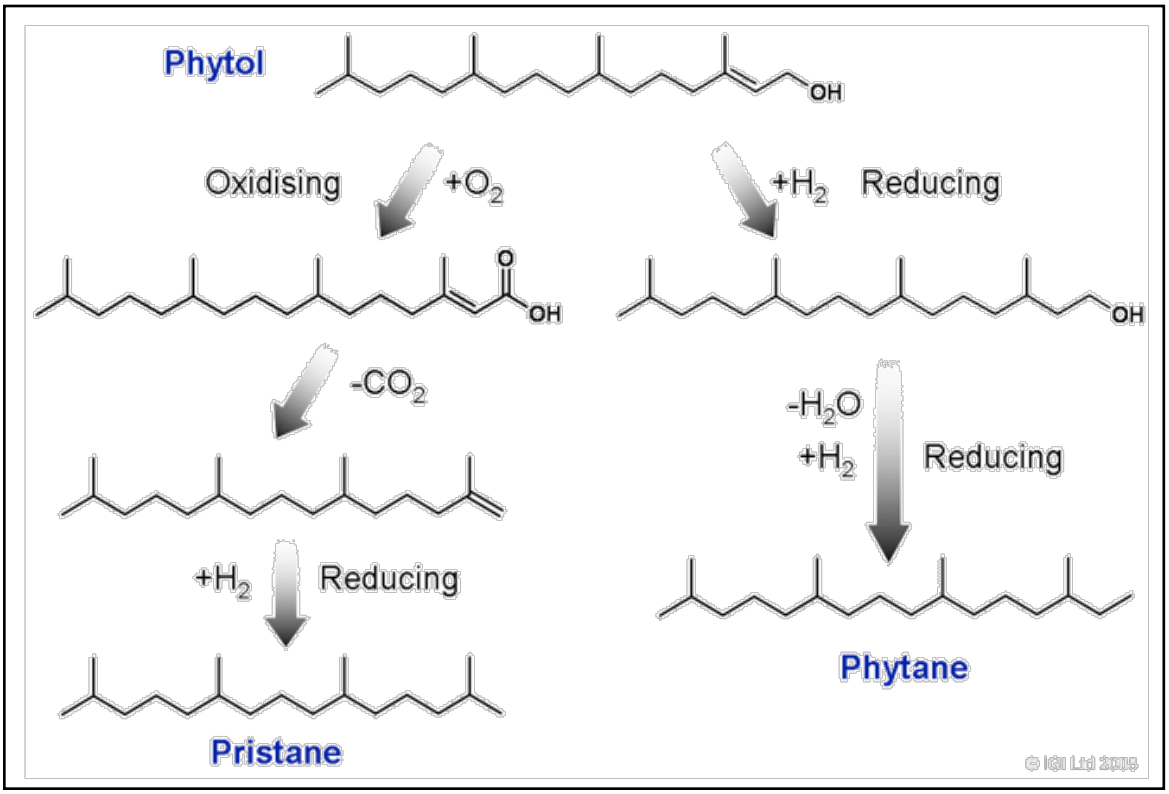

Figure 3.10 Phytol degradation pathways
Adapted from Didyk *et al* (1978); image source IGI Ltd (2008).

ten Haven *et al.* (1987) pointed out a number of problems with the use of the Pr/Ph ratio as an indication of anoxia. Firstly, the source of pristane and phytane is not limited to oxic or anoxic degradation of chlorophyll: phytol, the parent compound of both pristane and phytane, forms the phytanyl moiety of the ether lipids of archaea and methanogens (ten Haven *et al.* 1987), and pristane can also be generated by the degradation of tocopherols (Rontani *et al.* 1996). Subsequent investigations have demonstrated that phytol is degraded via multiple biotic and abiotic pathways, under both aerobic and anaerobic conditions, which produce a bewildering variety of isoprenoidal alcohols, acids, dienes, ketones, and alkanals (Rontani and Volkman 2003). Not all of the pathways ultimately produce pristane or phytane, and many involve a combination of biotic and abiotic steps at varying levels of O_2 saturation (Cox *et al.* 1971; Rontani and Volkman 2003).

The pristane:phytane ratio has been re-invented as the phytane:pristane ratio (Ph/Pr), and is currently mostly employed as an indicator of salinity, especially for younger (< 1 Ma) sediments (Peters *et al.* 2005). It is postulated that as halite saturation is approached, halophilic archaea, whose membrane lipids are largely composed of archaeol (mostly $C_{20,20}$, some $C_{20,25}$ (Javor 1989)) will dominate the ecosystem. The archaeols contain one or two C_{20} phytanyl moieties, so that they become the primary sources of phytol in saline environments (ten Haven *et al.* 1987). The extreme conditions restrict the membership of the microbial community, and saltern sediments are typically anoxic, at least at shallow depths (Javor 1989). This leads to a preponderance of phytane vs. pristane in biomarkers extracted from saline facies (Javor 1989; Moldowan *et al.* 1985; Peters *et al.* 2005; Robinson *et al.* 1984; ten Haven *et al.* 1987; ten Haven

et al. 1988; Wang 1998). Ph/Pr values within saline sediments typically range from 7-20, although values of Ph/Pr > 1.25 have been interpreted as evidence of deposition within a saline environment with reducing conditions in the sediments (Javor 1989; Robinson *et al.* 1984).

Values of Ph/Pr for salt, mats and core sediments from Lake Tyrrell do not seem to correlate with salinity in any meaningful way (Table 3.5). In fact, higher Ph/Pr values seem to be associated with a lower percentage of evaporites in samples (Figure 3.11). Interestingly, the highest value of Ph/Pr is found in lunette sediments (LT 1, Table 3.5), which are highly oxidized (see Appendix 2, A2.1 and Appendix 3 for descriptions of oxidized components of lunette sediments). These data indicate that the Ph/Pr ratio is indicative of neither salinity nor anoxia within the Lake Tyrrell system.

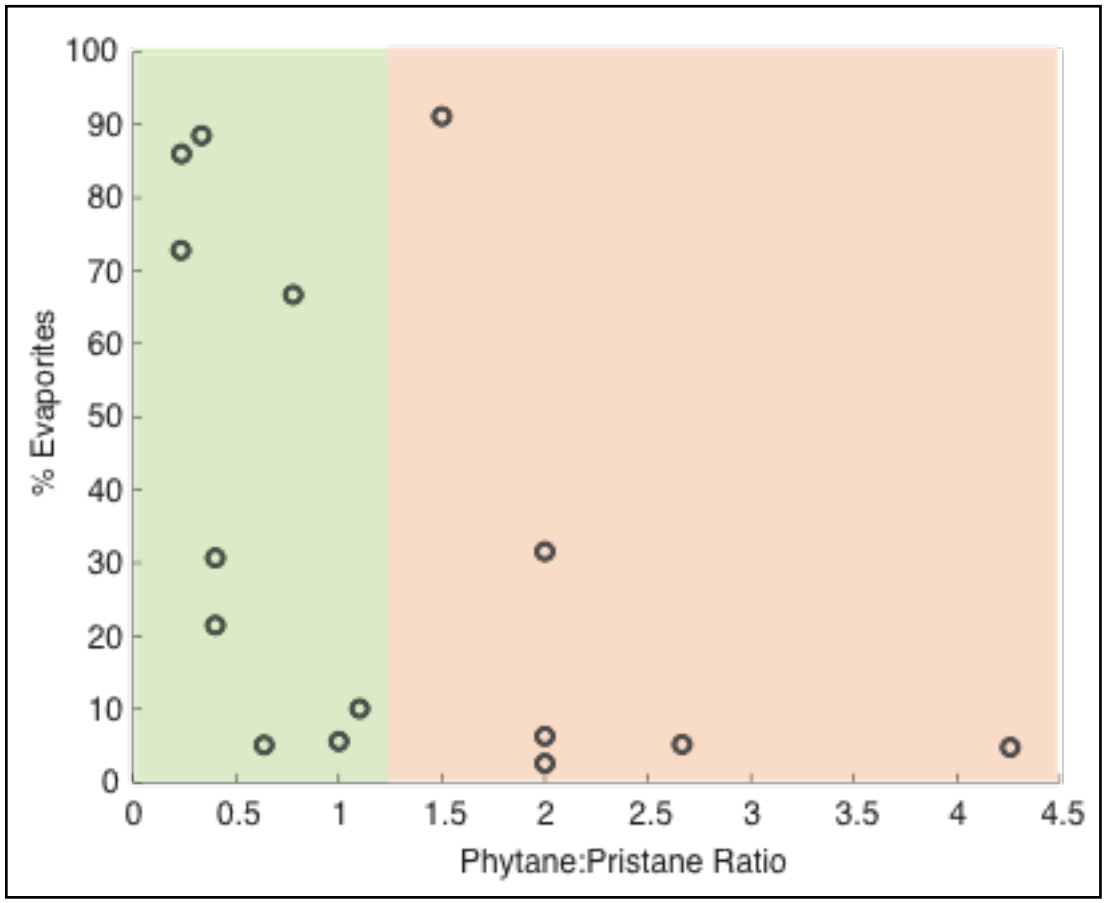

Figure 3.11 Relationship between relative dominance of phytane vs pristane and evaporite content

Relative dominance is calculated as [(μg phytane/g sample extracted)/(μg pristane/g sample extracted)]. Values > 1.25 are usually interpreted as evidence of a stratified, hypersaline environment and are shaded red. Values < 1.25 are shaded green, as they are typically associated with fresher, unstratified depositional regimes. Sample salinity is represented by the weight % of evaporite minerals in the sample, such that a greater evaporite content is a proxy for higher salinity.

3.5.5 Cluster analysis of lipids

From the data presented above, it is clear that individual biomarkers conventionally used as markers for hypersaline depositional regimes cannot be used as indicators of palaeo-salinity within the Lake Tyrrell system. However, as has been discussed in the preceding chapter, suites of biomarkers can provide information about organisms inhabiting the lake and its environs, and estimates of palaeo-salinity can then be made based on the known salinity tolerance of lacustrine organisms. Therefore, in order to constrain palaeo-salinity and associated lake levels, it is necessary to examine changes in the entire biomarker assemblage with depth. Over 160 compounds were quantified for each sample, so that in order to reveal trends, a visualization technique that reduces the dimensionality of the data is required. Ordination techniques, one of which is known as non-metric multi-dimensional scaling (NMS), were developed this express purpose. NMS allows us to look at the influence of all the lipids taken together on sample grouping, and to see if any particular lipid defines a group. In addition, we can overlay evaporite content to act as a proxy for salinity. This allows us to see whether sample groupings, as defined by lipid assemblage, are indeed the result of palaeo-salinity levels.

In addition, NMS was used in order to determine whether salinity of depositional environment, as represented by evaporite content, or post-depositional alteration of a sample exerted the greatest influence on the identities of lipids present in a sample, and whether "suites" of lipids remained constant between samples with similar evaporite contents. Lipid data were input both as relative abundances and as presence/absence, since differences in concentration between samples could be caused by differential allocthonous input as well as differential degradation rates between samples. Compositional differences were deemed of greater importance, as such differences would be more resistant to minor changes in input or depositional environment.

Figure 3.12A shows an NMS plot of salt, mat and core samples clustered according to the presence and absence of simple and complex lipids, where the loading of each lipid on sample clustering appears in Figure 3.12B. Evaporite content does not appear to strongly influence clustering: although samples with higher evaporite content appear on the left, and those with lower evaporite content are generally to the right, samples from the same facies with similar values for evaporite content are spread vertically across the plot (e.g. LT 9 and 10, or LT 20 and 12). It is possible that diagenesis is responsible for the spread between these samples, however, as preservation and evaporite content are correlated (see section 3.5.2 and Figure 3.8), this is unlikely. Instead, spread along the axes may be due to differential preservation of complex and simple lipids skewing the clusters. Stability of free lipids in sediments decreases in the order *n*-alkanes, alkanones, sterols, *n*-alkanoic acids, *n*-alkanols, and alkenoic acids, and shorter chain homologs have been shown to degrade completely in some lacustrine sediments after ~400 years (Cranwell 1981). By examining the loading of complex lipids only, it may be possible to eliminate the effect of differential diagenetic rates.

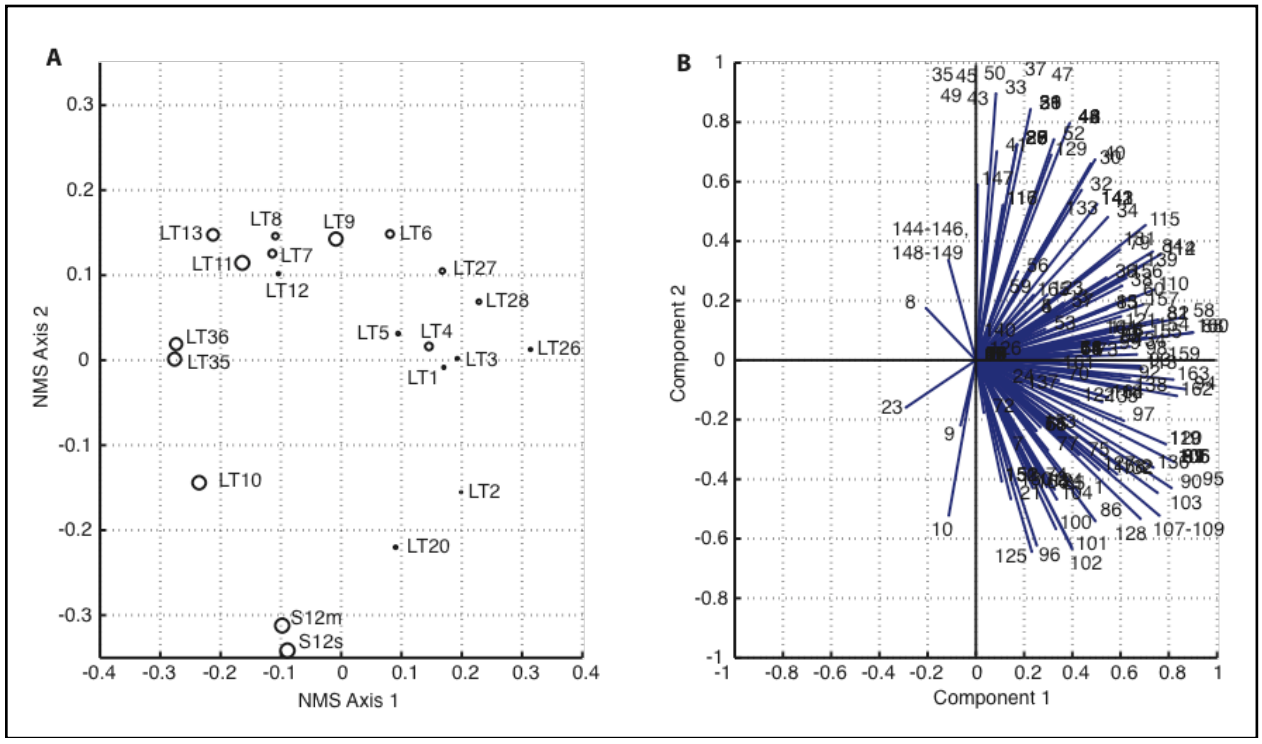

Figure 3.12 NMS plot of samples by lipid presence/absence and evaporite content
Distances between samples on plot A were calculated using hamming, which quantifies the extent of coordinates that are not alike. The size of the symbol (°) associated with each sample scales with evaporite content, such that larger circles are indicative of higher evaporite content. Plot B shows the loading (relative influence) of each component (individual lipid compound) on the clustering of the samples in plot A. Note that most compounds share similar loading, with the exception of numbers 8-10 (nC$_{19-21}$), 23 (nC$_{34}$), 144-146 (diols), 148 (a keto-ol),149 (an alkenol) and a cluster of fatty acids (33-50) at the top. These numbers are identical to those given in Figure 3.5.

Figure 3.13A shows an NMS plot of salt, mat and core samples clustered according to the presence and absence of complex lipids only, where the loading of each lipid on sample clustering appears in Figure 3.13B. Distinct sample groups appear to fall along a continuum within Figure 3.13A, with evaporite content generally increasing from left to right. Interestingly, the y-axis seems to correlate with preservation, since samples at more negative y-values are generally better preserved, and those at more positive y-values are generally less well preserved (see also Appendix 3 and Table 3.4). The spread in groupings is determined by only a few lipids: in Figure 3.13B, it is clear that certain groups of compounds heavily influence spread along both the x and y axes.

Groups of lipids influencing the loading along both the x and y axes (as seen in Figure 3.13B) confirm that samples in Figure 3.13A are clustering according to evaporite content (a proxy for salinity) and less strongly according to preservation (a proxy for diagenesis). Compounds **69-74** are diols, keto-ols, alkenols derived from freshwater and marine eustigmatophyte algae or diatoms (Sinninghe Damste *et al.* 2003; Volkman *et al.* 1999; Volkman *et al.* 1992; Wilson *et al.* 1994). Presence of these compounds within a sample pull it toward –x values, into the cluster of samples with lowest evaporite content. Compound **65** is friedelan-3-one, a triterpenoid ketone derived from higher plants (ten Haven *et al.* 1992). It is better preserved in fresher sediments (Killops and Frewin 1994), so its presence or absence should create spread along both the x (salinity) and y (preservation) axes. However as it is only present in two samples (LT 8 and 20), it is difficult to judge the extent of each effect.

Also present in only a couple of samples are compounds **41** (squalene) and **42** (dihydrosqualene). They are directly related to preservation, as they are fairly ubiquitous isoprene compounds that are readily degraded in sediments (Peters *et al.* 2005). The samples containing these compounds, S12 salt and mats, have extreme y values and cluster with well-preserved samples. The modern material are also the only samples to contain compound **5**, ergosterol. This C_{28} sterol is hydrogenated to ergostanol over time (Meyers and Ishiwatari 1993), so that its y-loading is indicative of preservation. It is usually interpreted as evidence of fungi (Volkman 1986); however it is also one of the primary sterols in the halophilic green alga *Dunaliella* (Peeler *et al.* 1989), so that its presence within the modern samples is indicative of both salinity and preservation.

Compound **12** is the dinoflagellate sterol 5-dehydrodinosterol, found in marine taxa such as *Scripsiella* and *Gymnodinium* (Brand 1984; Withers 1987). Its presence or absence would seem to be directly related to salinity, and indeed it appears in many of the more saline Tyrrell Bed samples (LT 7, 8, 10, 35, 36 and 11). Other steroids found exclusively in these samples, such as compounds **14** and **16**, are stanols derived from cholesterol hydrogenation, and **30** and **31** are oxidation products of sterols. Though grouped together with the dinoflagellate sterol, it would seem that their presence or absence should be influenced by preservation as well as salinity. Though absent from the most poorly-preserved samples, it is difficult to tell whether preservation is a key factor, as the best-preserved samples also have the highest evaporite content.

Overall, the relationship between evaporite content and position along the x-axis seems robust, whereas that between preservation and position along the y-axis is less clear. Despite this complication, groupings are relatively strong (Figure 3.13A) based on both evaporite content, and to some extent, preservation.

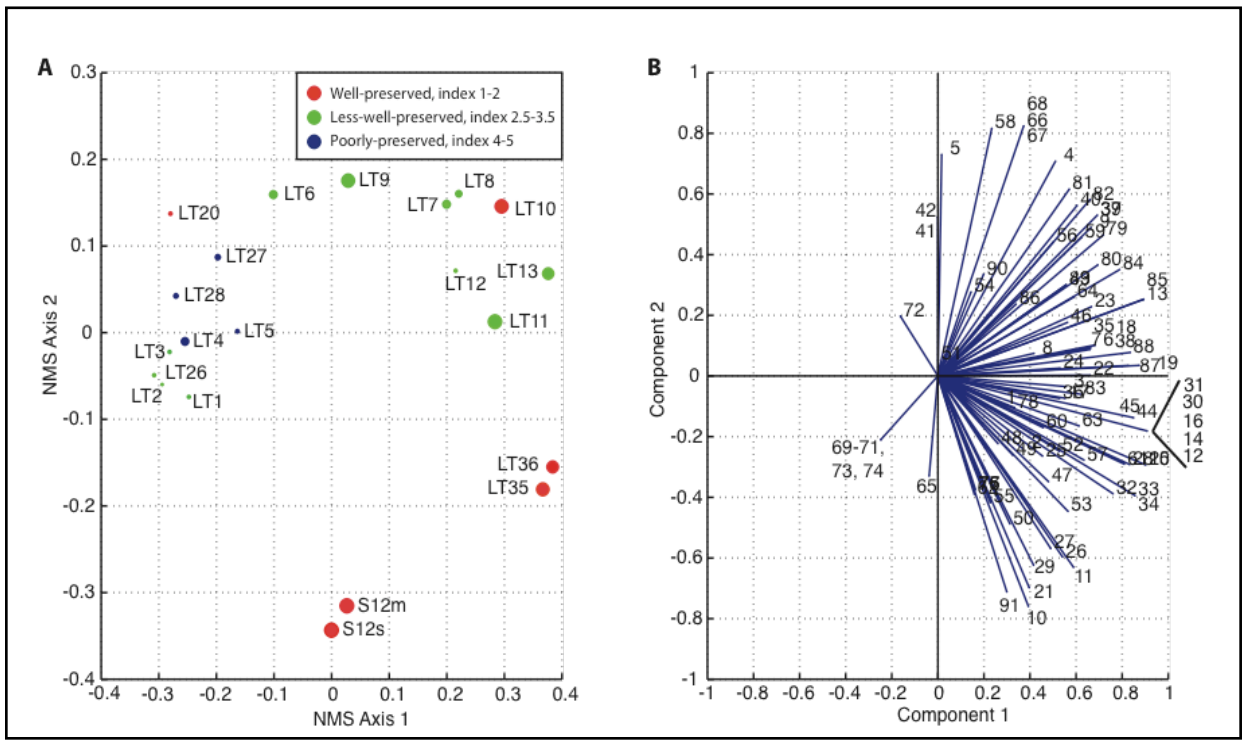

Figure 3.13 NMS plot of samples by complex lipid presence/absence, evaporite content and preservation index

Distances between samples in plot A were calculated using hamming, which quantifies the extent of coordinates that are not alike. The size of the symbol (°) associated with each sample scales with evaporite content, such that larger circles are indicative of higher evaporite content. Preservation index is indicated by the color of the symbol in plot A: red circles are well preserved (index 1 to 2), green circles are less well preserved (index 2.5 to 3.5), and blue circles are poorly preserved (index 4 to 5); where preservation indices are denoted in units of 0.5.
Plot B shows the loading (relative influence) of each component (individual lipid compound) on the clustering of the samples in plot A. Note that while many compounds share similar loading, some components (compounds) have greater influence. Compound numbers are identical to those presented in Table 2.4.

Samples can be grouped somewhat by lipid biomarker assemblage, and the biomarker suite of a sample seems to be influenced by both evaporite content and preservation. In order to understand the palaeoenvironmental significance of groupings, a technique that shows the mathematical distance between samples is needed. Hierarchical clustering is a good way to visualize this distance in a two-dimensional way. In Figure 3.14, nearest-neighbor analysis is used to divide the entire set of samples into six clusters based on the relative abundances of all complex lipids. The distance between samples within a cluster, and between clusters, is represented as a dendrogram at the right of the figure.

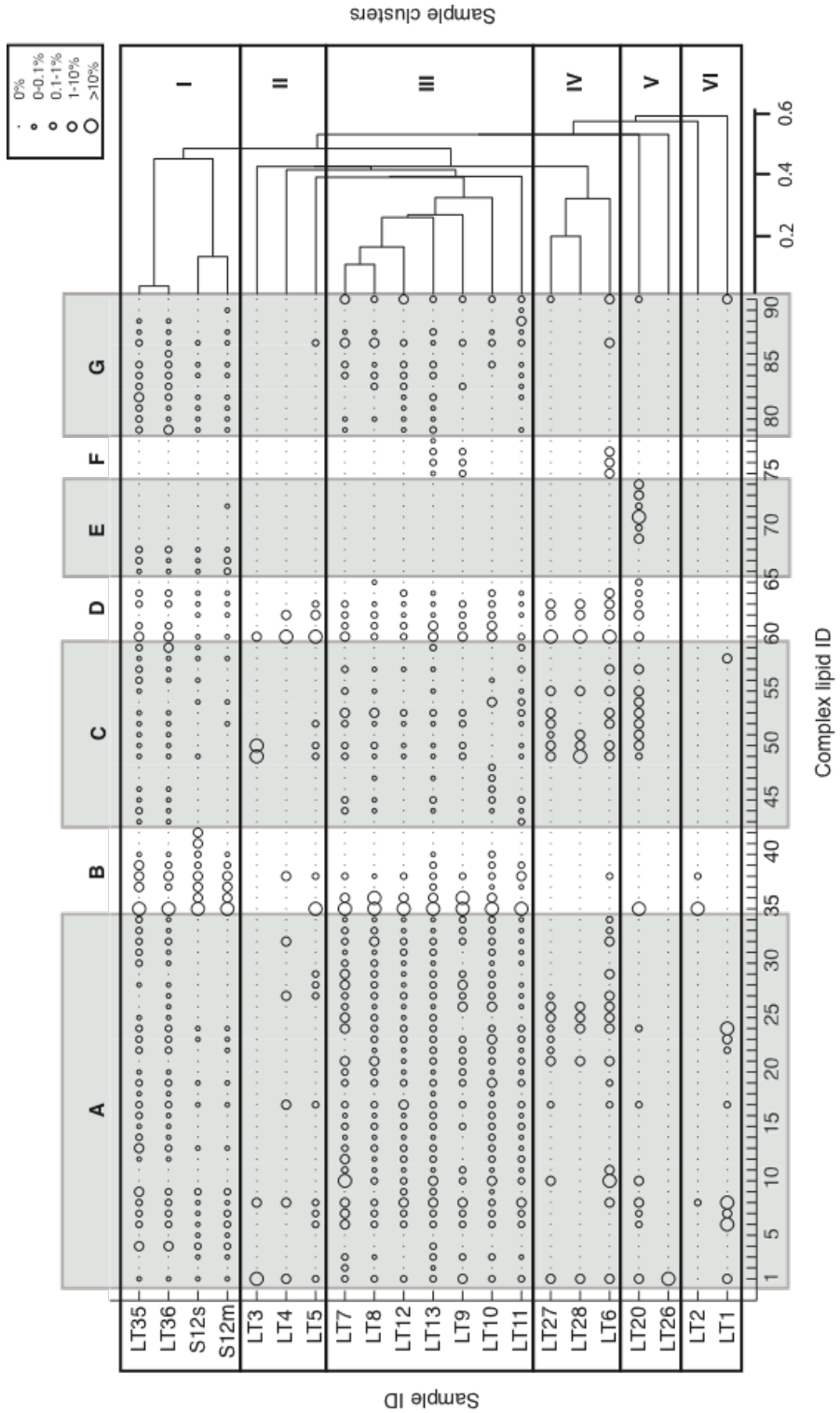

Figure 3.14 Cluster analysis of complex lipids in surface and core samples

Relative abundances of individual lipid compounds are given as percentages, calculated as (μg/g lipid / total μg/g complex lipids), and denoted by symbol size (see legend in figure). Complex lipid groups are shaded to emphasize groupings, which are as follows: steroids (A), isoprenoids (B), hopanoids (C), triterpenoids (D), diols, keto-ols and enols (E), alkyl ketones (F), miscellaneous and unidentified complex lipids (G); individual lipids are numbered as in

Table 2.4. Samples are presented as clusters (I-VI) determined by nearest-neighbor analysis; the distance between samples on the dendrogram is calculated based on the presence and absence of lipids using rank correlation.

Samples with similar mineral and lipid assemblages group together. Cluster I includes modern mats and salt (S12s and S12m) and samples from ~6 m depth (LT35 and 36). Both sets have high TOC (Table 3.1), are dominated by evaporites (Table 3.1 and assessments of modern lake salinity (Macumber 1991)), and are well-preserved (Figure 3.10). As discussed in chapter 2, modern salt and mats contain a number of compounds associated with a hypersaline depositional environment, such as ergost-7-en-3β-ol (**4**) and stigmast-7-en-3β-ol (**9**), which are the primary sterols found in the halophilic green alga *Dunaliella* sp. (Oldenburg *et al.* 2000). These compounds are also present in LT 35 and LT 36, but do not appear in any other samples. This may reflect preservation rather than input, as ergostanols (**18, 19**), which are generated by hydrogenation of ergostenols, are present in other core samples. The presence of terminal diols (**66-68**), which may also derive from algae (see discussion in section 2.5.1), further separate these samples from all others. High salinity during deposition is supported by the abundance of $C_{20,20}$ (**35**) and $C_{20,25}$ (**36**) archaeols, phytol (**37**) and phytanol (**38**). The biogenic precursors of these isoprenoids are produced in saline systems primarily by halophilic archaea (Mullakhanbhai and Francis 1972), or are diagenetic products of those isoprenoids (see section 3.5.5.3). Although both $C_{20,20}$ and $C_{20,25}$ archaeol are present in salt and mats, although only the $C_{20,20}$ homolog is present in LT 35 and 36. This may be due to a change in dominant species of haloarchaea within the lake, as only some taxa produce the $C_{20,25}$ homolog (Dyall-Smith 1995; Javor 1989; Kamekura and Kates 1988), or it could be that the $C_{20,25}$ homolog was below detection limits (this is unlikely as these samples have very high TLE, see Figure 3.2).

Halophilic archaea and *Dunaliella* both produce red pigments at high salinity, so that saline lakes are often pink. This coloration can raise the water temperature 3-6°C over that of waters that do not contain these organisms, thereby increasing evaporation (Schreiber and El Tabakh 2000). In a basin that is relatively closed to seepage/outflow of salts, such as the Tyrrell Basin, increased evaporation leads to halite saturation (Macumber 1979), where the modern lake is poised. Lipid and mineral data from LT 35 and 36 indicate deposition by an ephemeral salt lake, similar to the modern one. This interpretation is further supported by similar sample morphologies: the thin section covering LT 35 and 36 (Appendix 2, Figure A2.10) contains nearly undisturbed layers of primary gypsum, clays and what appear to be remnant microbial mats (Figures A2.10 A – C). The combination of lipids derived from *Dunaliella* and haloarchea, and the morphology of mats within gypsiferous sediments, indicate that the ecosystem present in the lake today may be a cyclic feature, and an ecosystem typical of an ephemeral salt lake. Bowler and Teller (1986) used models of surface-groundwater interactions (Torgersen *et al.* 1986) and the effects of increasing evaporation on water levels within lake basins (Bowler 1986) to create a lake level curve for Lake Tyrrell, where water depths are correlated with mineral assemblage. At halite saturation (>350 g/L TDS), lake depth is generally < 1m (Bowler and Teller 1986). Therefore we can see that during deposition of LT 35 and 36, the lake depth and ecosystem were similar to what is seen today.

Cluster II includes LT 3, 4 and 5, all of which derive from the upper meter of the Tyrrell Beds and are relatively poorly preserved (Appendix 3 and Figure 3.10). Thin sections show evidence of extensive post-depositional oxidation (e.g. Appendix 2, Figures A2.2 and A2.3) and TLE is much lower than TOC (Figure 3.2), indicating that lipids may have been destroyed. However, while the number of different complex lipids present in this cluster is relatively low

compared to clusters I, III and IV, the composition of the simple lipid assemblage is not noticeably different from other core samples (Figure 3.4). As simple lipids are generally less well preserved, it is possible that input, as opposed to diagenesis, is responsible for the lipid assemblage of cluster II. Triterpenoid biomarkers derived from soil bacteria or ciliates (tetrahymanol, **60**) and terrestrial plants (**62, 63**) are prominent, although the oxidation product of tetrahymanol, gammacerone (**61**), is absent. The presence of β-sitosterol (**8**) indicates terrestrial plant input, while the presence of 5α-cholestanol (**17**) and steroid ketones (**27-29**) point to sample diagenesis, such as would occur during soil formation (see discussion of LT 4, section 2.5.2). Cluster II likely represents a zone of pedogenesis, in which clay-rich sediments deposited by a lake of medium salinity (possibly poised at carbonate saturation, see LT 4 in Table 2.1) were the basis for soil building after the lake dried. At carbonate saturation (60-100 g/L TDS), for example during deposition of LT 4, lake depth would have been ~5-8 m (Bowler and Teller 1986).

Cluster III includes most of the remaining Tyrrell Bed samples, although LT 12, from the Blanchetown Clay, is also a member of this cluster. These samples have in common high abundances of archaeal isoprenoids (**35, 36, 38**), a full (or nearly full) complement of triterpenoids derived from soil bacteria or ciliated protists (**60, 61**) and terrestrial plants (**62-65**), and a large number of steroids derived from dinoflagellates (**2, 3, 11, 12, 17, 20, 21, 25, 26**). Samples with higher evaporitic mineral content – LT 9, 10, 11 and 13 (Table 3.1C and Figure 3.1) – are more closely related to each other than to samples of medium salinity – LT 7, 8 and 12 – within the larger cluster. This indicates that while the mineralogy may divide samples into discrete clusters based on salinity, lipid assemblages change along a continuum, so that only samples at halite saturation cluster separately (e.g. cluster I). Based on thin section analysis (Appendix 2, Figures A2.7, A2.9 and A2.11) and mineral content (Tables 3.1A – C), LT 9, 10, 11 and 13 were deposited between gypsum and halite saturation (120-350 g/L TDS), within a lake of 1-5 m depth (Bowler and Teller 1986). Fecal pellets likely deposited by the ostracod *Diacypris* are present in LT 10 (Appendix 2, Figure A2.9 B). As *Diacypris* has an upper salinity tolerance of 200 g/L TDS (DeDeckker 2009), the presence of its fecal pellets indicate periodic freshening events, likely associated with floods. LT 7, 8 and 12 (Appendix 2, Figures A2.6 and A2.11; Table 3.1) were deposited between carbonate and gypsum saturation, within a lake of 5-10 m depth (Bowler and Teller 1986). Ovoid fecal pellets in LT 7 (Appendix 2, Figures A2.6 E and F) were probably produced by the gastropod *Coxiella*, an organism with a salinity tolerance of 10-100 g/L TDS (Bowler and Teller 1986). This supports the assertion of lower salinity and increased water depth during deposition of these samples.

Cluster IV contains three samples (LT 6, 27, 28) from the upper portion of the Tyrrell Beds. Samples within this cluster are similar to those in cluster II, in that they contain abundant triterpenoids. Unlike cluster II samples, however, there are abundant C_{29}, C_{30}, and C_{31} hopanes (**49-57**) within this cluster. Hopanes are diagenetic products of bacteriohopanepolyols, compounds produced by many bacterial species for the purpose of membrane stabilization (Ourisson *et al.* 1979; Ourisson *et al.* 1987). The significance of these compounds is further discussed in section 3.5.5.2; briefly, the presence of hopanoids in the Tyrrell sediments bears no clear relationship to diagenesis within the sediment column. Instead, many of these hopanoids may have an allochthonous source, and their significance in cluster IV samples is largely a function of the lack of many other complex compounds in these samples. LT 6 contains alkenones (**75-78**), as do LT 9 and 13, from cluster III. Alkenones are produced by marine and lacustrine haptophyte algae and can be used for palaeo-temperature reconstructions.

Their significance within these samples is discussed in section 3.5.6. The mineral content of LT 6, 27 and 28 is indicative of a lake of marine or greater salinity (35-60 g/L TDS), wherein water levels fluctuated around 8-10 m depth (Bowler and Teller 1986). Overall, they are similar to cluster II, except that they lack evidence of pedogenesis.

Cluster V contains two samples from the Blanchetown Clay, LT 20 and 26. This cluster is somewhat arbitrary, as LT 26 contains only a single complex lipid, cholesterol (**1**), which is present in nearly all samples. The lipid assemblage of LT 20 has been discussed elsewhere (chapter 2, section 2.5.3). Briefly, it is dominated by diols, keto-ols and enols derived from eustigmatophyte algae, which typically have salinity tolerances of <35 g/L TDS. This accords with descriptions of Lake Bungunnia as a freshwater lake, with highstands of up to 30 m in places (An *et al.* 1986; McLaren *et al.* 2009). At Lake Tyrrell, Bowler and Teller (1986) calculated the depth of a lake of <30 g/L TDS as ~13 m. To maintain such a large, fresh lake, runoff (and therefore, precipitation) would have to be three times as great as it is today (Stephenson 1986). Large volumes of runoff probably contributed to the high proportions of detrital minerals (i.e. quartz sand) within these samples (Table 3.1C).

Finally, cluster VI includes both samples of lunette sediments, LT 1 and LT 2. Though they derive from the same sedimentary facies, the compositions of their complex lipid biomarker assemblages are quite dissimilar. The grouping is not entirely spurious, however, as the distributions and abundances of simple lipids (*n*-alkanes and *n*-alkanols) are similar between the samples (Figure 3.6). Lunettes are habitat for both soil bacteria and terrestrial plants, and lipid biomarkers for both types of organisms are present in lunette sediments (see chapter 2, section 2.5.3). LT 2 also contains $C_{20,20}$ archaeol, which in this context was probably deposited in lake sediments by halophilic archaea, and remained in the sediments even as they were deflated from the lake floor and blown onto the lunette. The most recent and extensive episode of lunette formation occurred at the height of the LGM, ~18-22 ka (Bowler 1973, 1976), when lake beds were completely dry; it is likely that the sediments within LT 1 and LT 2 were deposited during this episode.

3.5.6 Analysis of specific lipid classes

Clustering samples by lipid content is informative with regard to source similarity and sample salinity. More specific information can be gleaned by examination of compound distributions within certain classes of lipid biomarkers. These distributions are used to quantify autochthonous vs. allochthonous input, to compare levels of sample preservation, and to calculate salinity and temperature of sample deposition. The classes usually examined include the simple lipids, the hopanoids, the isoprenoids, and the alkenones; their presence and abundance within the Lake Tyrrell core is discussed here.

3.5.6.1 n-alkanes, n-alkanols and alkanoic acids as markers for terrestrial plant input

Input of terrestrial plants into lake sediments is typically estimated by examining quantities and distributions of lipids derived from epicuticular waxes (e.g. long-chain (>C_{25}) *n*-alkanes, *n*-alkanols, and alkanoic acids (Eglinton and Eglinton 2008). *n*-alkanes derived from plant waxes have chain lengths of C_{25}-C_{33}, with a distinct predominance of odd over even carbon number (Meyers 2003; Peters *et al.* 2005). Distributions typically peak at C_{27} or C_{29} if trees or shrubs are the dominant plants in the watershed, whereas C_{31} or C_{33} is most abundant when grasses dominate (Cranwell 1973). By contrast, *n*-alkanols of terrestrial plants have chain lengths

of C_{22}-C_{30} with a distinct predominance of even over odd carbon number (Meyers 2003). Distributions of terrestrially-derived *n*-alkanols peak at C_{26}, C_{28} or C_{30} (Meyers 2003; Volkman *et al.* 2008); a greater abundance of the C_{24} *n*-alkanol is usually interpreted to mean that cyanobacteria or submerged macrophytes, rather than terrestrial plants, are the source of the *n*-alkanols (Meyers 2003).

Alkanoic acids, while informative in recent sediments (tens to hundreds of years) (Volkman 1988), are highly sensitive to biotic and abiotic degradation (Meyers and Ishiwatari 1993). For sediments older than ~1000 years, they are generally better indicators of diagenetic conditions than of lipid provenance (Bourbonniere and Meyers 1996). Many of the $C_5 - C_{34}$ alkanoic acids are not present in most Lake Tyrrell core samples (Figures 3.3 and 3.4); those that are present are generally of even carbon number. Such a distribution is typical of higher plant input (Meyers and Ishiwatari 1993), but the dearth of alkanoic acids relative to *n*-alkanes could also be due to diagenetic effects. Decarboxylation reactions in sediment can lead to the production of *n*-alkanes of C_{n-1} relative to the parent alkanoic acid. Thus, in sediment initially containing mostly acids of even carbon number, diagenesis would lead to an abundance of odd carbon numbered *n*-alkanes, leading one to conclude that terrestrial plant input had been significant when in fact it had not. However, this degradation mechanism unlikely to be the dominant pathway; instead, alkanoic acids are more likely to be consumed by bacteria within the sediments (Meyers and Ishiwatari 1993).

In addition to the distribution of *n*-alkanes, the predominance of odd to even chain lengths of *n*-alkanes and *n*-alkanols can be used to confirm whether terrestrial (higher plant) or aquatic (algal) input is dominant. The odd/even preference (OEP) was developed by Bray and Evans (1961), and was computed by dividing the sum of the abundances of odd chain *n*-alkanes from $C_{25} - C_{33}$ by the sum of the abundances of even chain *n*-alkanes from $C_{26} - C_{34}$ or from $C_{24} - C_{32}$ (Bray and Evans 1961). Scalan and Smith (1970) altered the OEP ratio in order to account for the fact that weight percentage of *n*-alkanes tends to decrease with increasing chain length, thereby skewing the result (Scalan and Smith 1970). Following their method, the ratio is computed as:

Equation 3.2 $$OEP\ (1) = (C_{19}+6C_{21}+C_{23})/4(C_{20}+C_{22})$$

Equation 3.3 $$OEP\ (2) = (C_{27}+6C_{29}+C_{31})/4(C_{28}+C_{30})$$

Values >1 indicate a predominance chain lengths of odd carbon number, diagnostic of terrestrial plant input when *n*-alkanes are the compounds being examined (Scalan and Smith 1970). These ratios can equally well be used for *n*-alkanols and alkanoic acids, though for these compounds, even carbon number preference (OEP <1) is characteristic of terrestrial plant input (Meyers 1997).

As discussed in sections 2.4.4 and 2.5.1, *n*-alkanes and *n*-alkanols are produced by most organims. By including two separate ranges of carbon chain length in OEP calculations, it is possible to test whether odd over even preference within the *n*-alkanes is attributable to the input of terrestrial plants, or whether it is a result of input from aquatic algae (Bourbonniere and Meyers 1996; Meyers 1997). The OEP ratio is not an infallible indicator, as some algae (e.g. *Botryococcus braunii*) are known to produce *n*-alkanes in the same carbon range as terrestrial plants (Derenne *et al.* 1988; Moldowan *et al.* 1985). However, *B. braunii* generally produces distributions with peaks at C_{23}, C_{27} or C_{29} (Moldowan *et al.* 1985); for Lake Tyrrell core

samples, the most abundant long-chain *n*-alkanes are nC_{29} or nC_{31} (Figure 3.4). In addition, while *Botryococcus* remains were found in LT 20 (1013 cm), they were not present in any of the other samples examined for pollen and macerals (Tables 2.2 and 3.2). Therefore, long-chain ($>C_{25}$) *n*-alkanes in the Lake Tyrrell core are most likely to be sourced from terrestrial plants.

Figure 3.15 shows that odd carbon chain lengths dominate for longer chain *n*-alkanes ($C_{27} – C_{30}$) at all depths within the core. This includes modern salt and mat samples (0 and 1 cm depths), demonstrating that terrestrial plant lipids are an important component of organic matter in the lakebed even today. There is no pronounced odd-carbon number preference for shorter chain *n*-alkanes ($C_{19} – C_{23}$), re-affirming that algae (e.g. *Botryococcus*) do not significantly contribute to the pool of sedimentary *n*-alkanes, and that decarboxylation of alkanoic acids in this carbon range is not a significant diagenetic pathway. These shorter chain *n*-alkanes instead likely derive from microbial mat material, which is known to contain shorter chain *n*-alkanes ($C_{16} – C_{22}$) (Fourcans *et al.* 2004; Rontani and Volkman 2005). It is also possible that these shorter chain *n*-alkanes are sourced from more mature material that has washed into the lake, as thermally mature sediments and rocks contain *n*-alkane distributions with no odd-even preference (Peters and Moldowan 1993). Finally, it is worth noting that cyanobacteria are apparently not major contributors to the lipid pool, as nC_{17}, shown to be the most abundant hydrocarbon in cultures of the halotolerant cyanobacteria *Microcoleus, Oscillatoria,* and *Spirulina* (Allen *et al.* 2010), was not more abundant than either nC_{16} or nC_{18} (Figure 3.5).

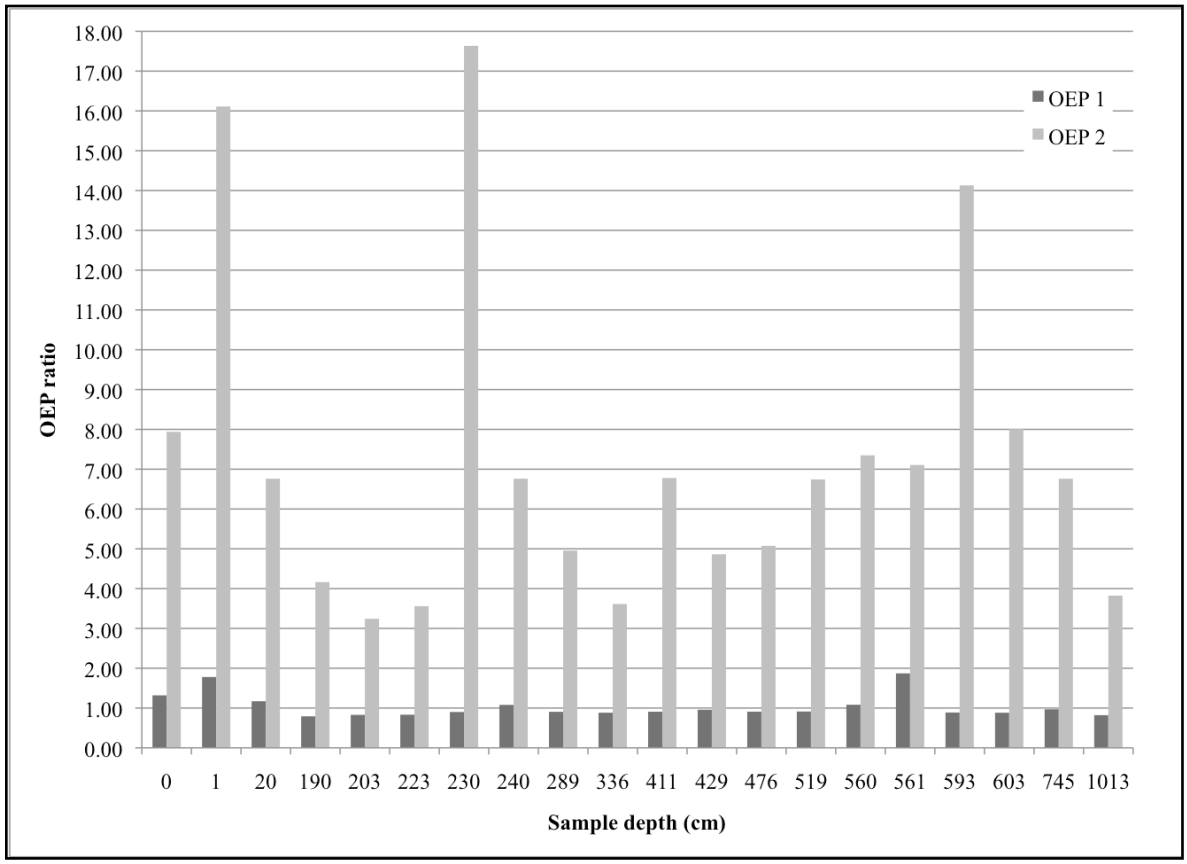

Figure 3.15 Odd-even preference index of long- and short-chain *n*-alkanes in salt, mat and core samples

OEP values for both shorter and longer chain *n*-alkanols at all sampled depths were <0.3. This confirms that higher plant waxes (longer chain *n*-alkanols, $C_{27} – C_{30}$) and algae (shorter chain homologs, $C_{19} – C_{23}$) have contributed consistently to the sedimentary lipid pool (Fourcans *et al.* 2004; Rontani and Volkman 2005).

3.5.6.2 Hopanes as indicators of diagenesis

As discussed in chapter 2, hopanoids are cyclic lipid compounds that are thought to regulate membrane stability and fluidity in bacteria. Hopanoids, including the sub-classes hopanoic acids, hopanols and hopanes, are formed through the degradation of biological bacteriohopanpolyols (BHPs). All of these sub-classes are present in Tyrrell sediments, though the distribution and abundance of compounds within each sub-class is unequal between samples (compounds **43-59**, Figure 3.5).

BHPs are converted to geohopanoids by both biotically-mediated and abiotic processes (Quirk *et al.* 1984; Saito and Suzuki 2007). Oxidative cleavage of the C-C bonds between hydroxylated carbons of the side chain, followed by reduction or oxidation, gives an alcohol or acid (respectively) of 31 – 35 carbons (Sandison *et al.* 2003). Hopanoids with fewer than 30 carbons are produced either from oxidation and/or reduction of the C_{30} hopanoid diploptene (**58**), which is produced by living cells, or by further diagenesis of BHPs (Barakat and Yen 1990; Ourisson *et al.* 1979; Sandison *et al.* 2003). The distribution of the hopanoids with respect to the number of carbon atoms has been interpreted as indicative both of biological source and of

diagenetic history (Sandison *et al.* 2003). For example, shorter side chains have been linked to oxidative, microbially-mediated degradation in marine sediments (Koster *et al.* 1997). Although certain chain lengths seem to be associated with particular types of environments (Moldowan *et al.* 1985; Peters and Moldowan 1993), at the present time there is no clear link between the carbon number of a hopanoid and the organism that produced it. This is because many taxa have yet to be evaluated for BHP content (Ourisson *et al.* 1987), and because diagenetic processes effect the carbon number of the hopanoid (Sandison *et al.* 2003).

In addition to carbon number, the configuration of the hydrogen atoms (either above or below the molecular plane) at positions 17 and 21 within the hopanoid skeleton is significant. It is usually interpreted as a diagenetic signature (Peters *et al.* 2005): although some soil bacteria have been shown to biosynthesize hopanoids with 17β, 21α (β,α) and 17α, 21β (α,β) stereochemistry (Rosa-Putra *et al.* 2001), most BHPs have 17β, 21β stereochemistry (Mackenzie and Maxwell 1981; Ourisson *et al.* 1987). β,α and α,β diastereomers are produced by diagenesis (Rohmer *et al.* 1980), and are conventionally referred to as moretanes and fossil hopanes respectively when discussing the hydrocarbon hopanoids (Peters *et al.* 2005). Thermal stability of the diastereomers is α,β > β,α > β,β (Peters *et al.* 2005), so that the process of diagenesis ultimately produces suites of hopanes dominated by the α,β isomer. In addition, at higher temperatures, conversion of the β,α to the α,β epimer through a β,β intermediate occurs, although the converse reaction does not (Peters *et al.* 2005). Therefore, a higher abundance of the α,β relative to the β,α isomer is interpreted as a marker for maturity (diagenesis) of the source sediment (Seifert and Moldowan 1980). This relative abundance calculation, referred to as the moretane/hopane ratio, is calculated as below for hopanes of a given carbon number:

Equation 3.4 $\beta,\alpha/(\beta,\alpha + \alpha,\beta)$ (Peters *et al.* 2005)

This ratio decreases as diagenesis – specifically thermal maturity – proceeds, e.g. it is usually ~0.8 – 1 in immature sediments (Larcher *et al.* 1988; Seifert and Moldowan 1980) and decreases to <0.15 in thermally mature rocks (Peters *et al.* 2005). More saline depositional environments tend to produce slightly lower moretane/hopane ratios than less saline environments (Rullkotter and Marzi 1988).

One other stereocenter, at the 22 carbon, is present in the hopanoid skeleton. BHPs all have the *R* configuration (Ourisson *et al.* 1987), and epimerization to the *S* configuration is an indicator of maturity (Mackenzie and Maxwell 1981; Rohmer *et al.* 1980). As all compounds discussed here have the *R* configuration, this indicator will not be discussed further.

Hopanes of 29-31 carbons (**49-57**) are present in the Tyrrell sediments, and to a lesser extent in the modern salt and mats (Figures 3.3 and 3.5). With the exception of the C_{30} β,β hopane (**54**), the quantities of hopanes are negligible. Values of the moretane/hopane ratio for Tyrrell samples range from ~0.35-0.8 for C_{29} hopanes, 0.35-1 for C_{30} hopanes, and 0.9-1 for C_{31} hopanes, and there does not seem to be any correlation between the evaporite content or the depth (age) of a sediment and the value of the moretane/hopane ratio. These data indicate that hopanes may derive from partially from degradation of BHPs formed in saline mats, and partially from allochthonous sources. The OEP values of ~1 for shorter chain *n*-alkanes within Lake Tyrrell sediments (Figure 3.15) suggest that allochthonous input of mature material may be contributing to the pool of sedimentary hydrocarbon compounds, and some of the hopanes may share a similar, allocthonous source.

Although there are no trends within the hopane distributions related to diagenesis or salinity, some information regarding possible mechanisms of formation may be gained by examining the ratios of various isomers in comparison with the mineral content of sediments. Figure 3.16 shows the ratios of β,β; β,a; and α,β diastereomers of C_{29}, C_{30}, and C_{31} hopanes compared with clay content of sediments.

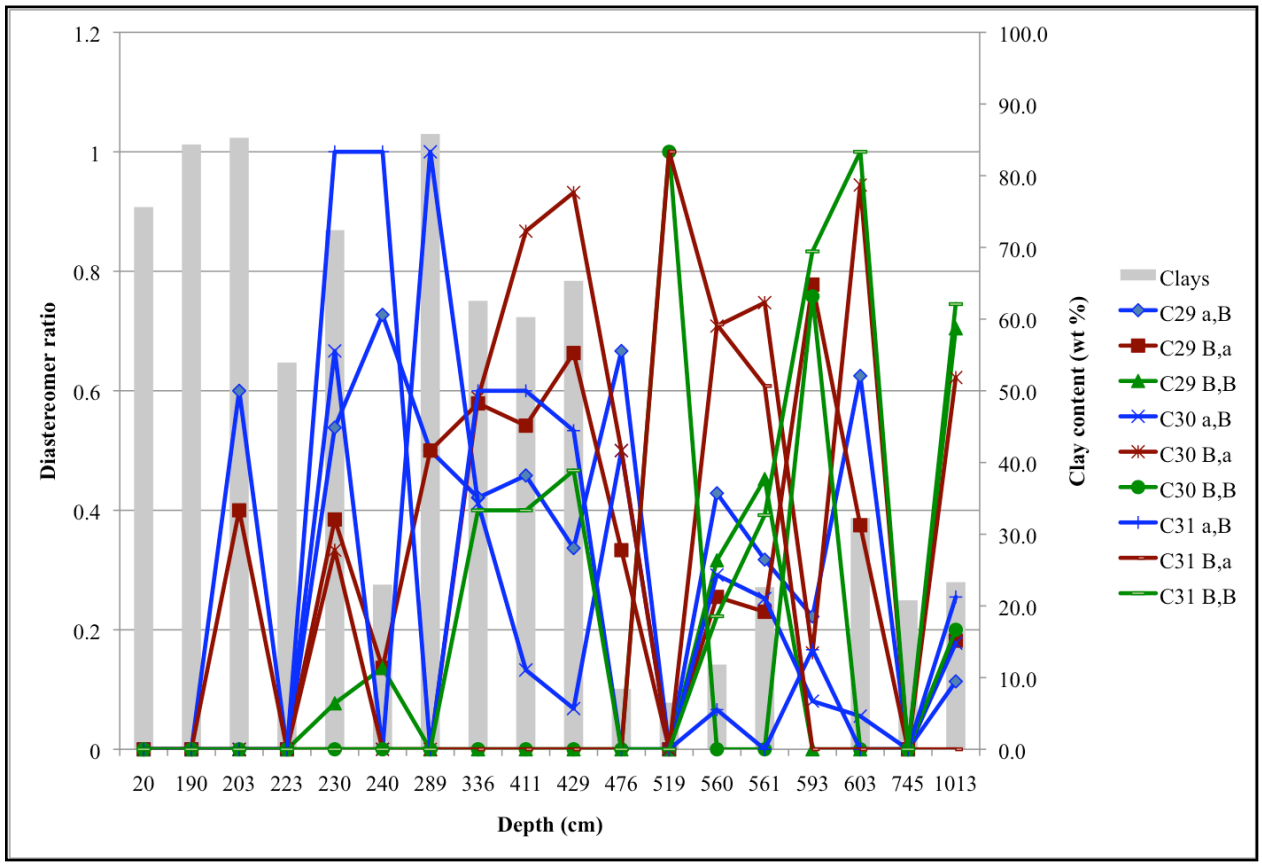

Figure 3.16 Distribution of C_{29} – C_{31} hopane diastereomers with depth and clay content
Hopane diastereomer ratio is calculated as C_n *x,y*/(C_n α,β + C_n β,α + C_n β,β), where n = number of carbons in the hopane. α,β ratios are in blue, β,α ratios are in red, and β,β ratios are in green. Zero values within series indicate that the ratio could not be calculated as the diastereomer was not present at that depth.

The patterns of abundance of the C_{29} and C_{31} homologs are similar throughout the core, possibly because they share a source. The β,β isomers of C_{29} (**51**) and C_{31} (**57**) seem to increase down core, which is the opposite pattern to what one would expect if the compounds were autochthonous. One possible explanation for the lower abundances of β,β hopanes (**51, 54, 57**) from 20 – 429 cm depth lies in the mineralogy of the samples. These depths include samples LT 1 through LT 8, as well as LT 27 and LT 28, all but one of which are composed primarily of clays (Table 3.1B and Figures 3.1 and 3.16). Clays have been shown to selectively react with the β,β diastereomers of hopanes in the carbon range C_{29}-C_{32} (Larcher *et al.* 1988). Specifically, the positions of the hydrogens in the β,β diastereomer allow closer interaction with the clay surface than for either of the other isomers, leading to the formation of highly reactive carbocations, which are further transformed to alkenes, aromatic hydrocarbons, or functionalized compounds

(Larcher *et al.* 1988). This may explain why the α,β and β,α diastereomers are present in greater relative abundances at these depths. The C_{31} β,β diastereomer does not conform to this pattern, which may indicate that it has a different source to the C_{29} and C_{30} homologs.

Beneath the clay-rich portion of the core (i.e., from 476 – 1013 cm), the β,β and β,α stereoisomers of the C_{29} - C_{31} hopanes are generally more abundant than the α,β isomer; however, there is no clear pattern of isomer type with depth, such as would be expected if *in situ* diagenesis of autochthonous compounds were the source of the hopanes. Therefore, the hopanes are likely sourced at least in part from allochthonous input, and without further data, it is not possible to assess the extent of this input. It must be noted, then, that hopanes cannot reliably be used as a proxy for maturity within the Lake Tyrrell sediments.

Functionalized hopanoids included hopanoic acids, hopanols, hopenes and hopanones. The only hopanoic acid detected was the C_{32} β,β acid (**46**, Figure 3.3). Carbon number distributions of hopanoic acids detected in both modern sediments and ancient (~65 Ma) sedimentary rocks typically maximizes at C_{32} (Farrimond *et al.* 2002), so that it is unsurprising that this acid should be detected in Lake Tyrrell sediments. In addition, hopanoic acids seem to be more resistant to isomerization than either hopanols or hopanes (Farrimond *et al.* 2002), so the presence of only the β,β isomer, even in sediments containing α,β and β,α isomers of hopanols and hopanes, is not unusual. It is present only in three samples from the core (LT 10, 35 and 36), all of which have high evaporite content (Figure 3.1). Its presence, taken together with the high salinity of the depositional environment, may indicate that oxidative degradation is an important process in the saline sediments of an ephemeral lake.

Hopanols with 31, 32 and 33 carbon atoms (**43-45, 47-48**) are present, though there does not seem to be a pattern in the distribution of either carbon numbers or diastereomers. As with the hopanoic acid (**46**), hopanols are present only in sediments with high evaporite content (LT 7, 8, 10, 35, 36 and 11, see Figure 3.3). These compounds are probably derived from isomerization of BHPs produced in mats; hopanoids present in modern material are discussed below.

Two additional hopanoids are present in the modern mats and salt, as well as in some samples from the core: diploptene (**58**) and 22,29,30-trinorhopan-21-one (**59**). As discussed in the preceding chapter, diploptene is a biosynthetic precursor to the BHP diplopterol, a common bacterial hopanoid (ten Haven *et al.* 1989), and 22,29,30-trinorhopan-21-one is one of diagenetic products of diploptene (Kashirtsev *et al.* 2008). Diploptene is readily converted to various hopenes (e.g. hop-17(21)-ene) both biotically and abiotically, while 22,29,30-trinorhopan-21-one has only been shown to be produced by abiotic oxidation of hop-17(21)-ene (Tritz *et al.* 1999).

Within Lake Tyrrell, diploptene is found only in the modern salt (S12s) and mats (S12m), in the shallow lunette (LT 1) sediments (compound **58**, Figure 3.3 and section 2.5.1), and in LT 35 and LT 36 (compound **58**, Figure 3.3), which are extremely well-preserved samples within the Tyrrell Beds (Table 3.4). 22,29,30-trinorhopan-21-one appears in the modern salt, in LT 35 and 36, and also in the saline samples LT 11 and LT 13 (compound **59**, Figure 3.3). The presence of diploptene in modern material is easily explained, as living bacterial communities in these samples would be expected to produce the compound. The associated 22,29,30-trinorhopan-21-one in the salt is also unsurprising, as ephemeral saline lakes are known to be oxidative depositional environments (refer to chapter 2 for a discussion of this assessment). The reason for its absence in the lunette sediments (compound **59**, Figure 3.3) is unknown, although it may indicate that bacterial re-working is a more important process than abiotic oxidation in these sediments.

The presence of both compounds within LT 35 and LT 36 confirms the assertion that these are extremely well-preserved samples, that underwent only slight oxidation and did not experience extensive bacterial re-working. The presence of 22,29,30-trinorhopan-21-one and the absence of diploptene in samples LT 11 and LT 13 (compounds **59** and **58**, Figure 3.3) supports the lower levels of preservation assigned to these samples (Table 3.4), and indicates that the process of abiotic oxidation was a significant factor at some time points in the lake's history.

3.5.6.3 Isoprenoid lipids: markers for archaeal input and diagenetic conditions

As discussed in the preceding chapter, the $C_{20,20}$ (**35**) and $C_{20,25}$ (**36**) archaeols are diagnostic markers for the presence of archaea. As their relative concentrations fluctuate broadly with evaporite content (Figure 3.17) in the Lake Tyrrell core, the most likely source organisms are halophilic archaeal species. The correlation between evaporite content and archaeol concentration is not perfect, such that some sediments with lower evaporite content possess higher concentrations of archaeols than sediments with higher quantities of evaporites (e.g. 190, 289, 336, 476 and 603 cm depth, Figure 3.17). This may be due to post-depositional alteration of primary sample mineralogy, for example by dissolution of primary evaporites during porewater freshening or soil formation, or the formation of secondary evaporites in sediments deposited by fresher waters. However, some of the anomalous sediments do not show any evidence of post-depositional mineral dissolution or formation (e.g. LT 9, 467-474 cm depth, see Appendix 2, Figure A2.7 and Appendix 3). An alternative explanation for the low abundance or total absence of archaeols in lunette sediments (20 cm and 190 cm depth) and those at the top of the Tyrrell Beds (203 – 336 cm depth) may be the poor overall preservation of these samples (Table 3.4). Post-depositional oxidation may have destroyed archaeal lipids that were originally present; this interpretation is supported by the low TOC values (Figure 3.2) and relative absence of complex lipids (Table 3.3) in these sediments.

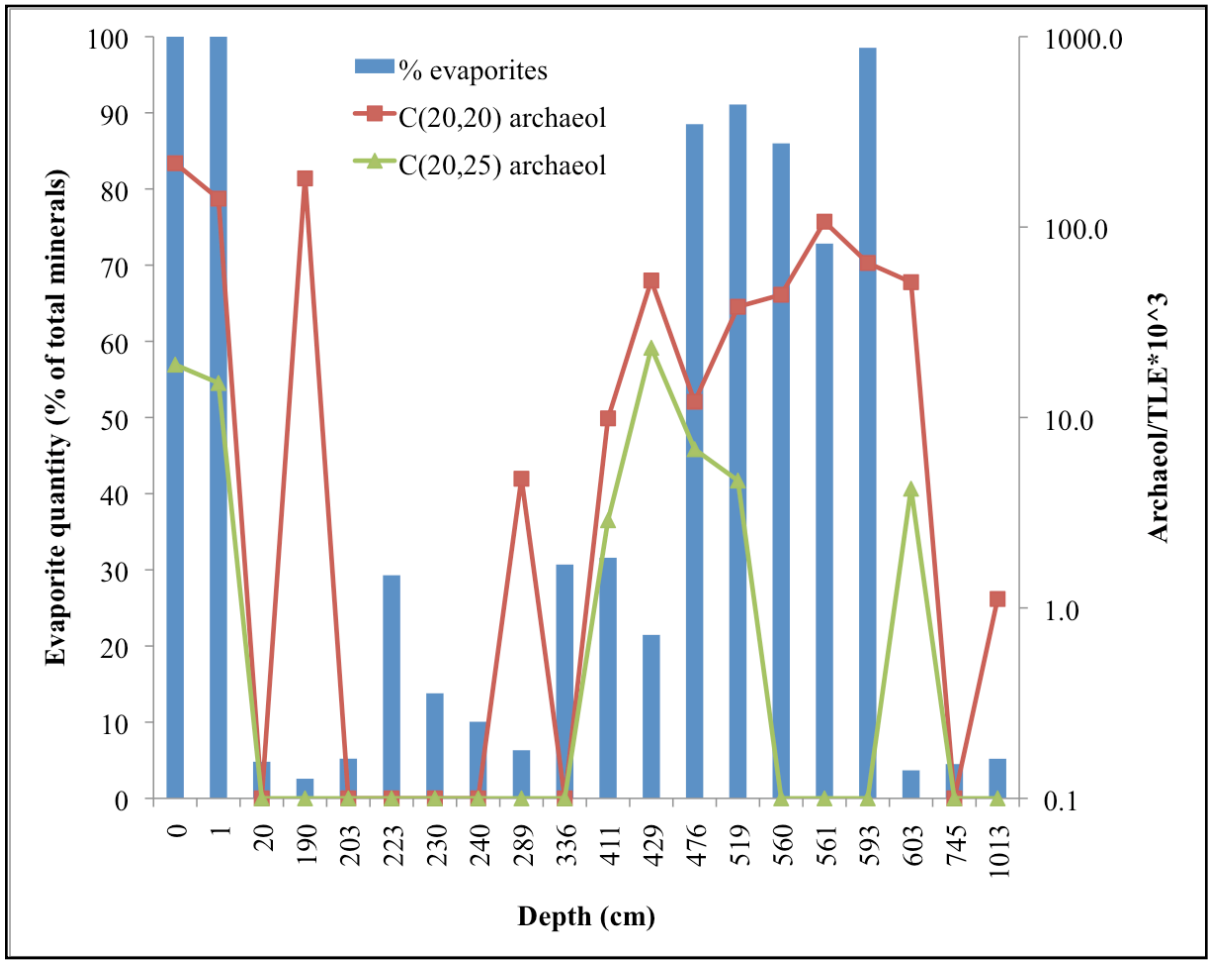

Figure 3.17 Variations in the abundance of archaeal isoprenoids with depth and evaporite content

Archaeol concentrations are on a $\log_{10}$ scale. Values <1 for the archaeols indicate samples in which they were not detected; dummy values were selected as zero values cannot be plotted on a $\log_{10}$ scale.

In better-preserved samples, such as LT 9 (476 cm), the low relative abundance of archaeols is mirrored by a low abundance of hopanoids, steroids and other complex lipids (Table 3.3) as compared to proximitous samples. Instead, *n*-alkanes are present in relatively greater abundance (Figure 3.4), suggesting increased input from higher plants. These data highlight the importance of considering abundances of multiple lipid classes when seeking to assign palaeo-environmental significance to a single compound. The archaeols may be used as a rough guide to palaeo-salinity, providing sample preservation and varying inputs are accounted for.

In addition to the archaeols, phytol (**37**), phytanol (**38**), phytone (**39**) and phytanic acid (**40**) – all C_{18} or C_{20} isoprenoids – were detected in the Lake Tyrrell core sediments. Phytol forms the sidechain of chlorophylls *a*, *b*, *c* and *d*, from which it is released by autooxidation and hydrolysis, by macrofaunal grazing or by clay-catalyzed hydrolysis (Rontani and Volkman 2003). Chlorophyll *a*, common to all terrestrial plants and many other phototrophs, is generally the major source of phytol in sediments, although tocopherols, wax esters, carotenoids, bacteriochlorophyll and archaeal ether lipids also contribute (Rontani *et al.* 1990). Free phytol

(**37**) is degraded to the C_{20} compounds phytanol (**38**) and phytanic acid (**40**) and to the C_{18} compound phytone (**39**) through aerobic and anaerobic biodegradation, grazing, autooxidation, the photooxidation of chlorophylls, and the clay catalyzed degradation of phytol (Cox *et al.* 1971; Ikan *et al.* 1973; Rontani *et al.* 1990; Rontani and Grossi 1995; Rontani *et al.* 1996; Rontani and Volkman 2003).

In hypersaline sediments, phytol has been shown to derive primarily from $C_{20,20}$ and $C_{20,25}$ archaeol. Diagenesis results in the breaking of the ether bond, and biotic and abiotic redox reactions lead to the production of the corresponding hydrated alcohol, the ketone and the acid. In such environments, these products are usually interpreted as evidence of the presence of halophilic archaea (Javor 1989). However, as phytol is also the side-chain of chlorophyll, as mentioned above, it is necessary to test whether its presence in the Tyrrell core is evidence for halophilic archaea or for allochthonous plant input.

Within core sediments from Lake Tyrrell, the relative concentrations of phytol, phytanol, phytone and phytanic acid closely track the concentrations of the archaeols (Figure 3.18). Further, abundance of isoprenoids (**37-40**) does not seem to correlate with abundance of plant-derived compounds, such as triterpenoids (**62-65**) (Table 3.3, Figure 3.5). Therefore it seems reasonable to conclude that the acyclic isoprenoids in the Tyrrell core derive from archaeal ether lipids, as opposed to deriving from chlorophylls of algae or higher plants.

Abundances of phytol, phytanol, phytone and phytanic acid seem correlated (Figure 3.29), although phytanol is uniformly in highest abundance. Phytanol forms by reduction of phytol (first reduction product, Figure 3.10). This indicates that within Lake Tyrrell sediments, post-depositional biotic and abiotic reduction are significant diagenetic processes, despite the pedological evidence for oxidative degradation.

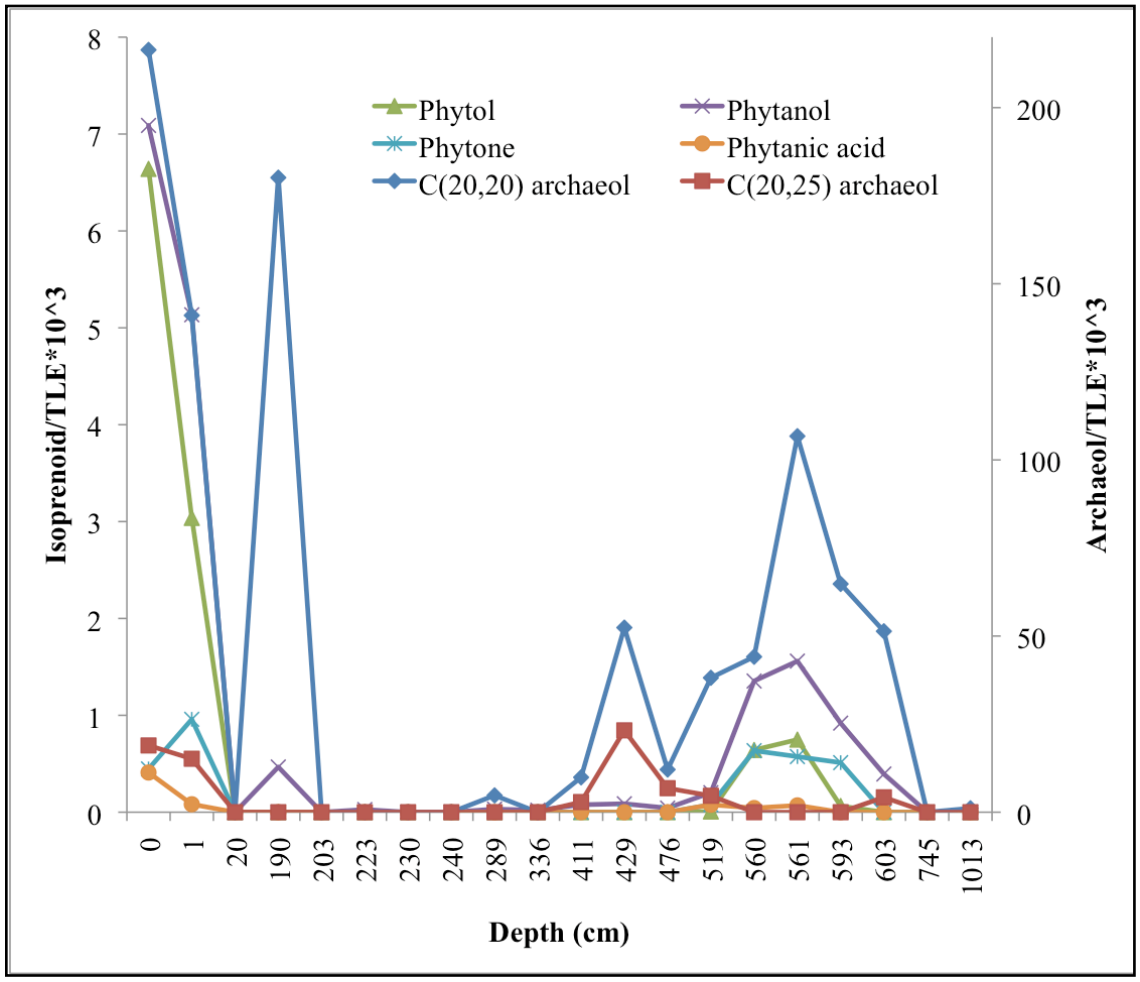

Figure 3.18 Variations in the abundance of acyclic isoprenoids with depth

3.5.6.4 Individual lipids as indicators of salinity

As demonstrated in section 3.5.4, lipid biomarkers conventionally used as indicators of palaeo-salinity do not serve this function within the Lake Tyrrell core. However, this does not mean that indicator lipid biomarkers do not exist for these samples. In order to determine the identities of such indicator biomarkers, an empiric process relating biomarker presence/absence with evaporite content is needed. One such method is the multivariate decision classification (MDC) tree. This method is a non-parametric decision tree learning technique that produces a classification tree where the dependent variable is discrete (categorical). The rules that govern the tree shape are based on the values of independent variables, where splits are chosen to minimize the dissimilarity of samples within a cluster (De'ath 2002). The procedure is recursive, so that the same rules are applied to each child node, producing leaves on the tree defined by the categorical dependent variable (De'ath 2002). Splitting ceases once the tree algorithm decides that no further gains can be made (Rencher 2002). The strength of this method is that it can be applied ot complex environmental data that may include imbalance, missing values, higher-order interactions, and non-linear relationships between variables (De'ath 2002). In addition, it can be

used to predict the value of the categorical (dependent) variable for samples for which only the values of the independent variables are known (De'ath 2002).

Figure 3.19 shows a tree in which the dependent variable is evaporite content represented as salinity, and the independent variables are the presence or absence of a lipid compound. The tree contains 21 samples, and has 3 nodes (boxed) and 4 leaves (within ellipses). The first split is by phytol (**37**), from which it is clear that the presence of phytol is correlated with high salinity. This seems to support the assertion of section 3.5.6.3, that phytol is derived from haloarchaeal lipids. The second split is by an alkane, nC$_{27}$. As described in section 3.5.6.1, nC$_{27}$ is a significant component of both terrestrial plant waxes (Eglinton and Eglinton 2008) and algae such as *Botryococcus braunii* (Moldowan *et al.* 1985). Here, samples with low salinity seem either to lack nC$_{27}$, or to contain both it and lupeol (**64**), another compound derived from terrestrial plants (Killops and Frewin 1994). This may be because the *n*-alkane is in fact derived from terrestrial plants, but oxidation of some samples (LT 26 and LT 28, neither of which contain nC$_{27}$) has led to the removal of many lipid compounds (Figures 3.3 and 3.4).

The final bifurcation in the tree is by the presence or absence of lupeol (**64**), a triterpenoid. Samples with low salinity contain it, while samples with medium salinity do not. One explanation could be that within the medium salinity samples, primary productivity within the lake diluted the allochthonous input, so that lupeol, which is not present in high abundance in many samples (Figure 3.5), was not preserved in sediments. Low salinity samples include those deposited by a fresher lake, but also record episodes of soil formation. As both lupeol and nC$_{27}$ derive from higher plants, the 3 samples that contain both compounds may be evidence of such episodes.

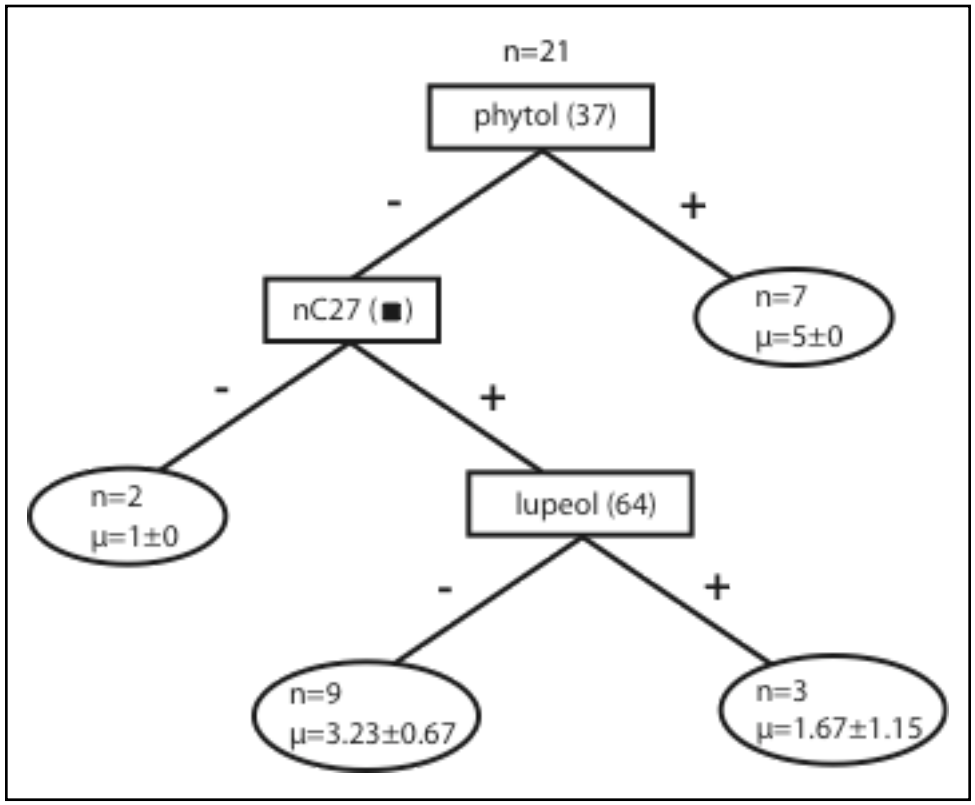

Figure 3.19 Using indicator lipids to cluster samples by salinity
This MDC tree clusters mat, salt and core samples (n=21). Each box is a node containing the name and number of a lipid compound (as given in Table 2.4), the presence (+) or absence (-) of which caused the split. Each ellipse shows the number of samples in that leaf of the tree (n=#), and the mean (μ) and standard deviation of the salinity value for the samples in that leaf. Salinity values (1=low salinity; 3=medium salinity; 5=high salinity) were assigned to mineral groups 1, 2, and 3, respectively. Mineral groupings are those described in section 3.5.1.

According to De'ath (2002), it should be possible to predict the salinity of sample of known lipid composition where mineral content and textures have been extensively altered by post-depositional processes. Within Lake Tyrrell, the presence of phytol seems to be a reliable indicator of high salinity, whereas the presence of terrestrial plant lipids is more equivocal. Further investigations are warranted to determine why archaeol is not a prominent node in the tree, as its abundance is correlated with salinity as described in section 3.5.6.3.

It is important to remember that the presence or absence of these compounds is determined not only by input, but also by the preservation of the sample. Therefore, while indicator lipids are useful guides for further investigation, they are not conclusive where diagenetic processes have destroyed indigenous lipids, for example during soil formation (refer to discussion of LT 4, chapter 2, section 2.5.2). Lipids do survive secondary mineral formation (e.g. indigenous lipids are present in LT 10 despite the presence of displacive gypsum), so for samples affected by secondary gypsum formation, lipid content could be used to predict palaeo-salinity.

3.5.7 Long chain alkenones (LCAs) and glycerol dialkyl glycerol tetraethers (GDGTs): lipids as palaeothermometers

Certain types of lipid biomarkers can yield direct information on some of the physical characteristics of a palaeoenvironment, as well on the organisms that lived within it. Long chain alkenones (LCAs) and glycerol dialkyl glycerol tetraethers (GDGTs) are two classes of lipid biomarkers whose distributions have been demonstrated to be related to palaeo-temperatures. LCAs are produced by lacustrine and marine haptophyte algae (also known as prymnesiophyte algae), and are composed of keto-functionalized alkyl chains of 37-39 carbon atoms in length (Brassell *et al.* 1986a; Cranwell 1985). The alkyl chains contain 2-4 unsaturated carbon-carbon bonds, with the abundances of the tri- and tetra-unsaturated LCAs increasing relative to the di-unsaturated homologs as the temperature of the water decreases (Brassell *et al.* 1986a; Prahl and Wakeham 1987). Brassell *et al* (1986) created an equation, known as the alkenone unsaturation index (U^{k}_{37}), which directly related the proportions of the LCAs to mean annual sea surface temperature at the time of deposition. However, as many sediments lack the tetra-unsaturated homolog(s), this equation was simplified by Prahl and Wakeham (1987) to include only the di- and tri-unsaturated molecules, and a calibration equation of improved accuracy was presented:

Equation 3.5 $U^{k'}_{37} = C_{37:2}/(C_{37:3} + C_{37:2})$ (Prahl and Wakeham 1987)

where $C_{x:y}$ indicates an alkyl chain of length x containing y unsaturations, and

Equation 3.6 $U^{k'}_{37} = 0.033T + 0.043 \quad (r^2 = 0.997)$ (Prahl and Wakeham 1987)

where T is temperature in degrees Celsius.

It should be noted that early efforts concentrated entirely on marine species, and that not all species respond to temperature shifts to the same extent (Sun *et al.* 2007). In addition, LCA distributions in lacustrine sediments are quite different to those from marine sediments in that they often contain a prodigious quantity of the tetra-unsaturated alkenone (Liu *et al.* 2008; Pearson *et al.* 2008; Thiel *et al.* 1997; Volkman *et al.* 1988; Zink *et al.* 2001). Such a pattern has been suggested as both a marker for lacustrine environments (Thiel *et al.* 1997) and as an indicator of salinity in those environments, such that its abundance decreases as salinity increases (Liu *et al.* 2008). In lake sediments that did not contain the $C_{37:4}$ compound, marine temperature calibrations, such as those given by Prahl and Wakeham (1987), were found to give results in accordance with independent indicators of palaeo-temperature, such as $\delta^{18}O$ (Theissen *et al.* 2005; Zink *et al.* 2001).

Three sub-samples of Lake Tyrrell core sediments contain LCAs (Table 3.6), though the distribution of unsaturated homologs is more similar to published data from marine, rather than limnic, sediments. Only di- and tri- unsaturated homologs are present, and $C_{37:2}$ (**76**) and $C_{38:2}$ (**77**) are more abundant than $C_{37:3}$ (**75**) (Figure 3.5). Since $C_{37:4}$ is absent, palaeo-temperatures were calculated as in Equations 3.5 and 3.6, after Prahl and Wakeham (1987). Higher temperatures were generally associated with higher evaporite content (Table 3.6), although the precision of such measurements is lacking. First, very few calibration studies for halophilic haptophytes have been completed (Pearson *et al.* 2008; Sun *et al.* 2007; Thiel *et al.* 1997), so that exact interpretation is problematic. Second, there are only three sample points, which is insufficient to plot a trend. And third, LT 13 has been previously discussed as out of place with

regard to depth – its likely source is the Tyrrell Beds, so that it cannot be interpreted as part of a temperature trend with depth.

At most, it is possible to assert that the temperature assignments are likely to be directionally correct (e.g. temperature of deposition at LT 6 was cooler than that at LT 9). While the modern lake experiences high temperatures and is poised at halite saturation, Pleistocene aridity (and decreased lake levels, leading to increased salinity) in Australia is associated with glacial maxima, when temperatures were lower. It may be that LT 6 and LT 9 were deposited during transitions from glacial to interglacial (or vice versa) periods, and that there is some time lag between changes in temperature, evaporation rate, and organismal biochemistry. Further, it is not possible to rule out changes in the species from which the LCAs are sourced. Species shift may be related to changes in salinity, and skews the signal such that $U^{k'}_{37}$ is a reflection of both changing salinity and temperature. Such cross-correlations in saline lacustrine LCA distributions have been previously noted (Liu *et al.* 2008).

Table 3.6 Alkenone unsaturation indices for Lake Tyrrell S12 core[a]

Sample name	Sample depth (cm)	Evaporite content (wt%)	37:3 (**75**)[b] concentration (ug/g sample extracted)	37:2 (**76**)[b] concentration (ug/g sample extracted)	$U^{k'}_{37}$	Palaeo-temperature (°C)
LT 6	336	31	0.000152306	0.000152306	0.50	13.8
LT 9	476	89	1.78263E-05	8.91315E-05	0.83	23.9
LT 13	663	67	0.000839731	0.002536331	0.75	21.5

[a] $U^{k'}_{37}$ is calculated as in Equation 3.5, and palaeo-temperature as in Equation 3.6.

[b] LCA concentration is determined by integration of *m/z* 81, as indicated in Table 2.4

Some GDGTs are also used to calculate palaeo-temperatures. Archaeal GDGTs are isoprenoid compounds containing up to 8 cyclopentane and cyclohexane rings, which are produced to regulate membrane fluidity (Wuchter *et al.* 2005). As temperature increases, so do the relative abundances of GDGTs with > 1 cyclopentane ring (Wuchter *et al.* 2005). These lipids were first described in marine sediments (Schouten *et al.* 2002), where they derive primarily from the membranes of Crenarchaeota. The composition of cell membrane GDGTs in the marine crenarchaea was shown to be strongly dependent on growth temperature, a relationship quantified by the TEX_{86} index (Schouten *et al.* 2002). In lacustrine and near-shore settings, however, non-isoprenoidal GDGTs have been found to derive from soil bacteria, and therefore are generally not predictive of palaeo-temperatures in such settings, unless a local calibration is known (Bechtel *et al.* 2010; Sinninghe Damste *et al.* 2009; Weijers *et al.* 2006; Weijers *et al.* 2007).

Unfortunately, only one of the Lake Tyrrell core samples (LT 35) tested for GDGTs contained detectable quantities of these compounds (see section 3.4.4 and Figure 3.6), and it did not contain any GDGTs more than 2 rings. Therefore, TEX_{86} could not be calculated for any Lake Tyrrell core samples. However, the absence of any of the branched non-isoprenoidal GDGTs known to derive from soil bacteria, the lack of isoprenoidal GDGTs with more than 2 rings, and the extremely high quantity of evaporites and level of preservation of the sample (Figure 3.1, Table 3.4) may indicate that lower temperatures prevailed when this sample was deposited. A highly-saline, shallow lake fits within a Pleistocene arid, glacial landscape, and high primary productivity within microbial mats growing at the salt-sediment interface (see

section 3.5.5 and Figure 3.12) would dilute any allochthonous contribution, possibly explaining the lack of non-isoprenoidal GDGTs. The distribution of GDGTs present in LT 35 (Figure 3.6) are not unlike those observed in other saline lakes, although it does not resemble distributions found in freshwater lakes (Pearson 2010; Pearson *et al.* 2011). As with other lipids, salinity may be the controlling physical factor, though the extremely high TLE yield of LT 35 compared to other core sediments is likely the reason that GDGTs were found in this sediment and in no others (Figure 3.2).

3.5.8 Lipids correlated with sedimentary minerals and textures to constrain palaeotemperatures, lake levels and timing of deposition

Curves generated from the computation of stanol/stenol ratios within lake cores have been shown to follow closely those generated from $\delta^{18}O$ measurements of planktonic foraminifera tests preserved in marine sediment cores (Toste 1976). The correlation between fluctuations in palaeo-temperatures and changes in $\delta^{18}O$ signatures in these tests (Emiliani 1970; Imbrie *et al.* 1984) and in bulk- and fine-fraction carbonate marine sediments (Andres and McKenzie 2002) has been well established. Further, it is known that the timing of these temperature fluctuations is controlled by the periodicity of global glacial-interglacial cycles (Imbrie *et al.* 1984; Martinson *et al.* 1987; Petit *et al.* 1999).

Steroid distributions within sediments are typically analyzed in order to gain information on eukaryotic organisms that were present in a particular environment at the time of deposition (Volkman 2003; Volkman *et al.* 1998), to differentiate between terrestrial and aquatic inputs to coastal or lacustrine sediments (Volkman 1986; Volkman *et al.* 1987; Volkman *et al.* 1981; Volkman *et al.* 2008), and/or to assess the extent of abiotic and biotic oxidation and reduction of a sample (Gaskell and Eglinton 1975; Meyers and Ishiwatari 1993; Nishimura and Koyama 1977). In 1976, however, researchers at the University of California, Berkeley, noted that the relative proportions of sterols to stanols within the sediments of a saline, alkaline lake were directly related to the temperature at which the sample was deposited (Toste 1976). The temperature curve to which Toste compared the curve of his stanol/stenol ratio was derived from $\delta^{18}O$ measurements of tests of planktonic foraminifera within cores taken from the seafloor in the Caribbean, the equatorial Pacific and the north Atlantic (Emiliani 1970). The temperature fluctuations were due to glacial-interglacial cycles, and Toste was able to match his steroid curve to the palaeotemperature curve from the present to 200 ka, capturing two glacial-interglacial cycles (Toste 1976).

Although LCAs have provided some information on palaeo-temperatures within the Tyrrell core, they are present in only a few samples. More temperature points would be advantageous. In addition, if it is possible to generate a curve in the manner of Toste (1976), it might be possible to match the curve with $\delta^{18}O$ curves from the southern hemisphere, and so obtain rough time constraints for the core. The dearth of dateable materials in the Tyrrell sediments has been previously discussed (see chapter 2 introduction), and at present, only the ages of the lunette (~18-22 ka, (Bowler 1970; Luly *et al.* 1986)) and youngest Blanchetown Clay (0.7-1.2 Ma (An *et al.* 1986; McLaren *et al.* 2009)) are roughly constrained. Thus, the utility of steroids as palaeo-temperature, and by extension age, indicators, if found to be suitable in such an environment, could hardly be over-stated.

In order to apply Toste's method, it is necessary to determine whether the conditions that prevailed at Mono Lake, his study site, also occur at Lake Tyrrell. The major assumption in the method is that stanols are generated from biotically-mediated hydrogenation of stenols (a/k/a

sterols) within sediments, and that this rate increases as temperature increases (Toste 1976). In most environments, including Mono Lake, stanols are products of the biotic (or rarely, abiotic) reduction of stenols (Nishimura 1977, 1982; Reed 1977; Rontani and Volkman 2005). However, some microalgae have also been shown to biosynthesize stanols (Nishimura and Koyama 1976, 1977; Robinson *et al.* 1984), which may be incorporated within sediments following cell death. The production of stanols by microalgae has not been shown to vary with temperature (Toste 1976), but an abundance of biological stanols in sediments (due to a change in abundance of microalgae) would skew the ratio stanol/stenol ratio, rendering it useless in the determination of palaeo-temperatures.

Although some stanols within Lake Tyrrell sediments are presumed to derive directly from microalgae, including 4,24-dimethylcholestanol (**21**), 5α-cholestanol (**17**), dinostanol (**26**) and 4α-methyl, 24-ethylcholestan-3β-ol (**25**), others are known to be produced through biotic reduction of stenols (see Table 2.4, compounds **14-20, 22-24**). Fortunately, of the stanols that may be produced directly by microalgae, only 5α-cholestanol is included in Toste's stanol/stenol curve. Its production by dinoflagellates may be low enough that the ratio is not drastically affected; we tested this by plotting the stanol/stenol ratio both with and without the inclusion of 5α-cholestanol. As the inflection points remain constant, it is unlikely that dinoflagellates contribute the major portion of 5α-cholestanol in sediments.

Additional considerations are that redox reactions in sediments can interconvert steroid ketones and stanols, and that clays can dehydrate stanols to sterenes (Robinson *et al.* 1984). To test whether these additional sources and sinks of stanols are significant, we plotted the relative abundances of $C_{27} - C_{30}$ sterols, stanols, steroid ketones and sterenes as a percentage of total steroids within the modern mats and salt, as well as the core sediments (Figure 3.20). It appears that that sterol abundance varies inversely with stanol abundance, and that sterenes and steroid ketones are present at only low abundance. This indicates that the biotic production of stanols, redox interconversions, and clay-catalyzed dehydration reactions are probably not significant enough to overprint the temperature signal.

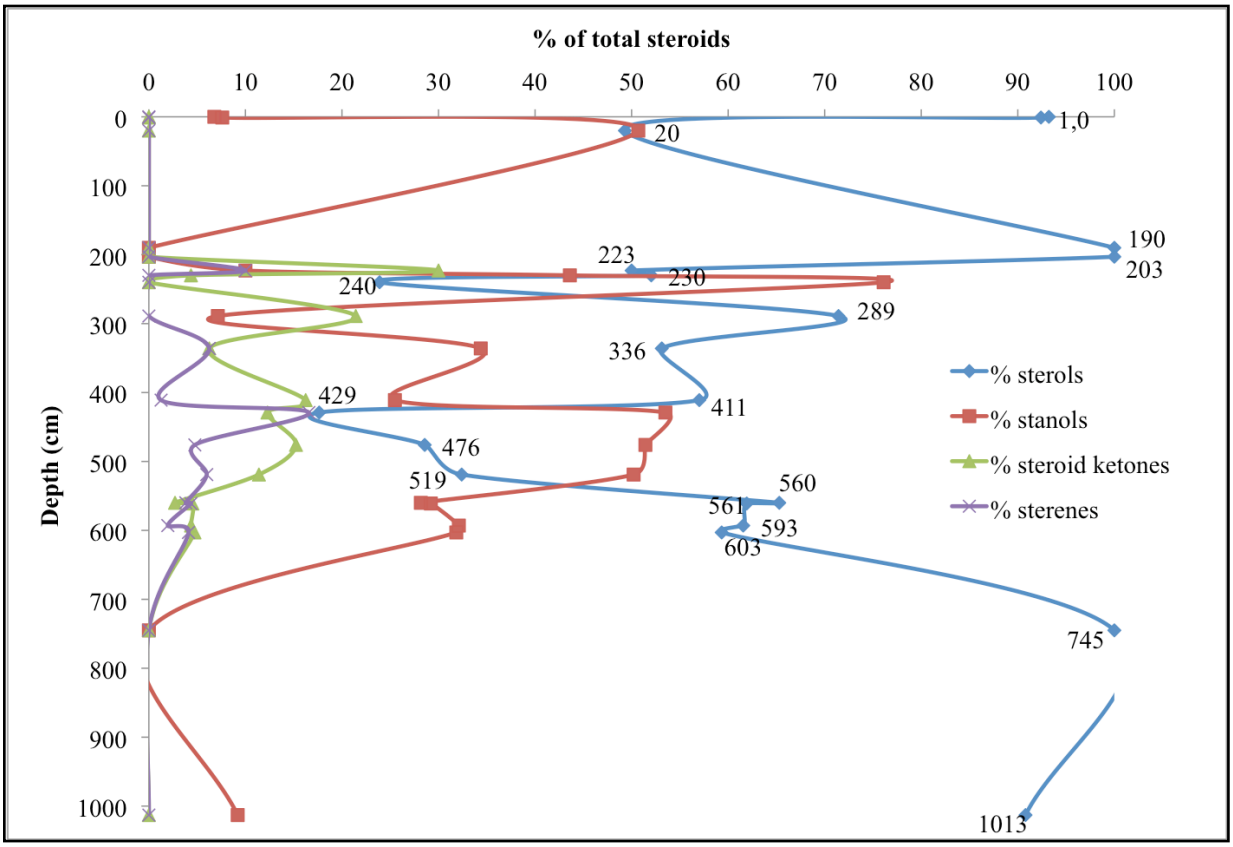

Figure 3.20 Variations in the relative abundances of steroid sub-classes with depth
Percentage of steroid classes is calculated as the abundance of a class relative to the sum of all classes. Depths (cm) of sampling points are given along sterol curve for reference.

Although steroid ketones and sterenes are present as only minor sub-classes, still, interconversion between these sub-classes and stanols may occur. To test whether the steroid suite of a sample is correlated with preservation (a proxy for post-depositional oxidation and reduction), or with clay content, we plotted the relative abundance of steroid ketones and sterenes against preservation values and clay content for Tyrrell core sediments. As no trend was evident, we were able to establish that post-depositional processes do not seem to overly influence steroid composition, so that a sterol/stanol ratio can be computed and used to estimate palaeo-temperature.

In Figure 3.21, the stanol/sterol ratio is computed as described by Toste (1976) (see caption to figure), and is plotted alongside a lake level curve generated from that given in Bowler and Teller (1986). Water depths from the Bowler and Teller (1986) curve were assigned to samples as described in section 3.5.5, based on mineral assemblage and textural analysis, and checked against the suite of biomarkers present.

An increase in the relative abundance of stanols is ascribed to an increase in palaeo-temperature, interpreted as an interglacial interval. Lower values are ascribed to the lower temperatures experienced during glaciation. As would be expected, lake levels are positively correlated with the stanol/sterol ratio, so that arid glacial intervals coincide with decreased water volume in the lake, and wetter interglacial intervals coincide with increased lake depths.

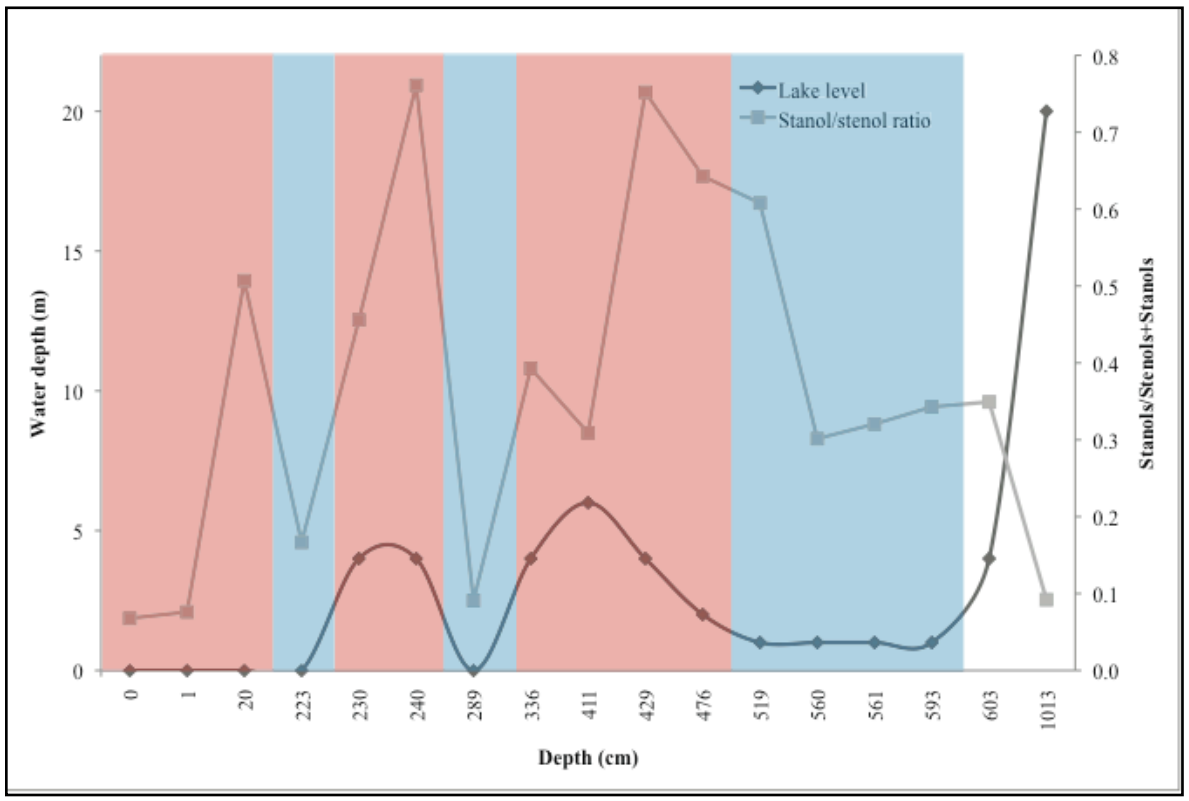

Figure 3.21 Correlation of stanol/stenol ratio with lake water levels

Stanol/stenol ratio is calculated as described by Toste (1976) with the addition of the C_{30} sterols: sum of concentrations of $C_{27} - C_{30}$ stanols divided by the sum of concentrations of $C_{27} - C_{30}$ stenols and stanols. Colored boxes denote temperatures inferred from the stanol/stenol ratio, with warmer (red) periods associated with increasing stanol/stenol ratios, and cooler (blue) periods associated with decreasing stanol/stenol ratios. Lake water level is estimated by correlating salinity tolerance of organisms present in the lake during sample deposition (as indicated by lipid biomarker assemblage) with salinity-lake level curve for Lake Tyrrell calculated by Bowler and Teller (1986). Stanol/stenol ratios calculated based on samples of modern material (0-1 cm depth) and from the Blanchetown Clay (>600 cm depth) are included as comparative values, and do not have palaeo-environmental significance in this context. However, the lake level curve for these samples was created independently, and does have significance (Bowler and Teller 1986).

Finally, the stanol/sterol curve can be plotted against a $\delta^{18}O$ curve generated from the tests of planktonic foraminifera within cores of marine sediments recovered in the Indian Ocean (Imbrie *et al.* 1984; Martinson *et al.* 1987), and against a $\delta^{18}O$ curve generated from bulk- and fine-fraction (<38 µm) sediment of the late Pleistocene succession from Hole 1127B drilled on IODP leg 182, in the Great Australian Bight (Figure 3.22) (Andres and McKenzie 2002).

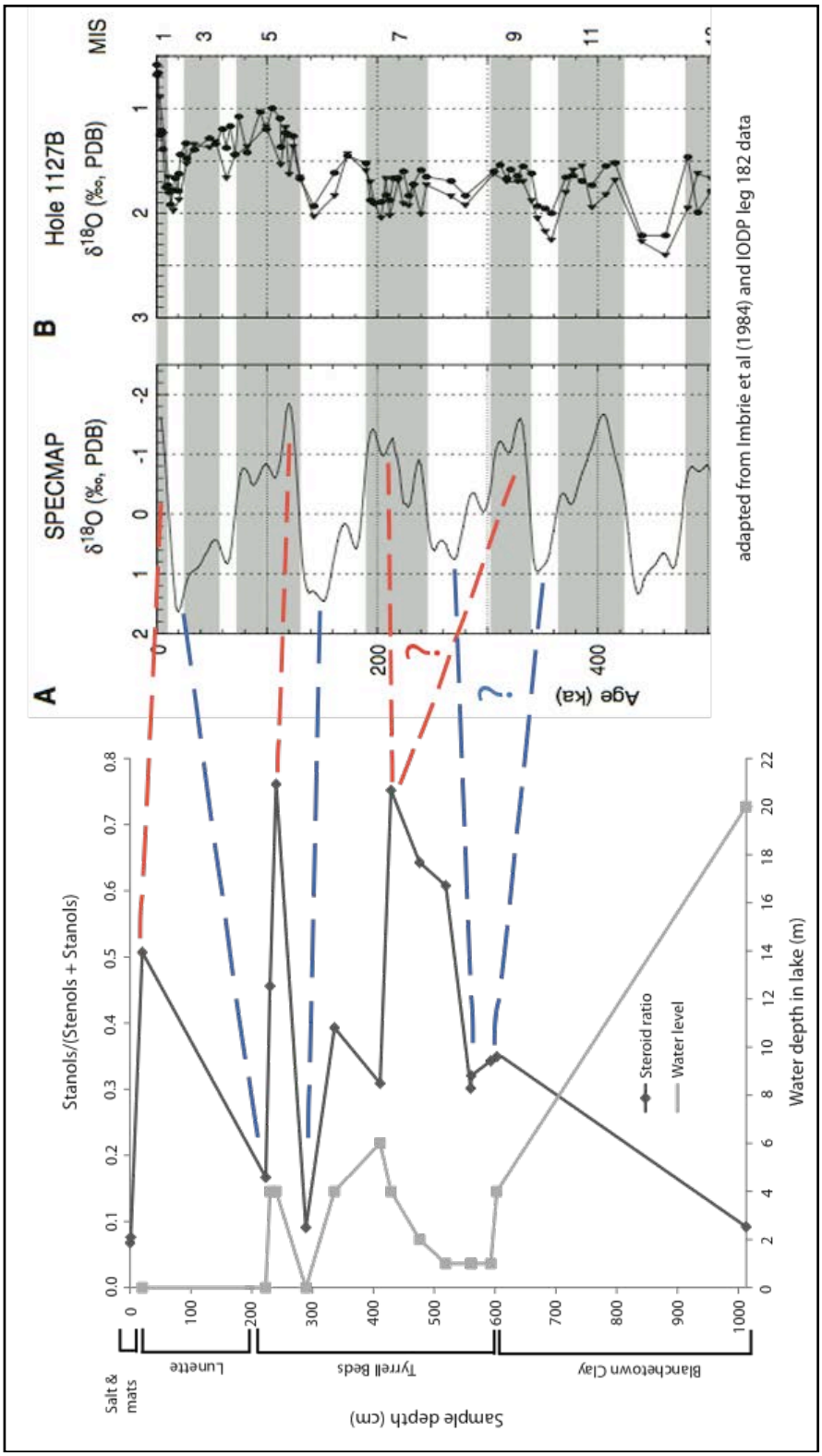

Figure 3.22 Fluctuations in palaeo-temperature and precipitation at Lake Tyrrell record three glacial-interglacial cycles during the last ~400 ka

Plot A shows the stanol/stenol ratio and lake water depth curves from Figure 3.21 plotted against sample depth. Sample stratigraphy is noted along the depth axis.
Red dashed lines denote warmer (interglacial) periods; blue dashed lines denote colder (glacial) periods. Bifurcated lines with question marks indicate uncertainty regarding the age of the sample.
Timescale is based on correlation of palaeo-temperature fluctuations at Lake Tyrrell with the $\delta^{18}O$ curves in Plot B. The curve on the left is SpecMap (spectral mapping) data from Imbrie *et al.* (1984) and Martinson *et al.* (1987), and is based on the $\delta^{18}O$ of plankton fossils in deep sea sediments tuned to the astronomical timescale of Earth's orbital cycles. The curve on the right comes from the $\delta^{18}O$ of bulk- and fine-fraction (<38 μm) sediments of the late Pleistocene succession from Hole 1127B drilled on the Great Australian Bight, IODP leg 182 (Andres and McKenzie 2002). Negative isotopic excursions are indicative of warmer (interglacial) periods, and positive isotopic excursions are indicative of colder (glacial) periods.

It can be seen from Figure 3.22 that at least two, and possibly three glacial-interglacial cycles are recorded in the sediments of Lake Tyrrell, as revealed by steroid sub-class abundance. During glacial intervals (~20 ka, 140 ka, 260 or 340 ka), the lake was ephemeral: it contained less than 1 meter of water, and was often completely dry. During interglacial periods (modern, 120 ka, 220 or 320 ka), water depth reached 5-10 m, and the lake was relatively fresher. The Tyrrell Beds are at least 260 ka, and possibly as old as 340 ka. Despite episodic deflation and the lack of dateable materials, an extension of this method to additional samples may render possible the assignment of ages to sediments within the Tyrrell core.

3.6 Conclusions

Post-depositional processes play a significant role in determining the composition of biomarker assemblages and mineral suites. Pedogenic horizons and secondary mineral growth destroy sedimentary textures, rendering traditional pedological investigations moot. However, lipid biomarkers remain intact up to a preservation index of 3, so that information about organismal assemblages, and by proxy, palaeoenvironmental conditions, can be gleaned unless oxidation is fairly complete.

Evaporite content exerts the most stringent control on input of lipids, and samples cluster strongly according to similarities in their biomarker assemblages. From this clustering, it is evident that deposition at Lake Tyrrell is cyclical through the late Pleistocene up to the present. Mats are high in TOC and remain so over long timescales; a perfect mineral, textural, and lipid complement to the modern lake exists at 560 cm depth, within the oldest Tyrrell Beds. Indicator lipids are of varied utility: lipids conventionally used to gauge sample salinity fail to function in this manner within the Tyrrell Beds. However, multivariate treeing techniques have the potential to identify, *de novo*, lipid biomarkers that could be used in this fashion. Further examination and application of this method is necessary to establish its robustness and applicability outside of the Tyrrell system.

Palaeo-temperature fluctuations recorded in varying abundances of algal lipids (stanols/stenols) are correlated with those deduced from changes in the abundances of various steroid sub-classes, and are attributed to glacial-interglacial cycles. Lake water levels can be estimated from known shoreline morphology, as reported by Bowler and Teller (1986), in combination with mineral assemblages, preservation data, and biomarker suites. Although lake water levels have fluctuated in accordance with glacial-interglacial cycles, broadly, the catchment has experienced a gradual drying through the late Pleistocene and Holocene.

3.7 Acknowledgements

We thank the Australian Research Council (ARC S47070 25), the American Society for Engineering Education (NDSEG graduate fellowship), the University of California, Berkeley Graduate Division (Berkeley Graduate Fellowship) and the Larsen Fund grant (1-55000-36567-12998-44-PG1JL) for financial support. We also thank the following people for input and assistance with various aspects of the project, including fieldwork, laboratory analyses, and research discussions: Andrew Pike, Emma Pearson, Jon Luly, Janet Hope, Damien Kelleher, Nigel Craddy, Phil Macumber, Ursula Pietrzak, Ulrike Troitzsch, Emmanuelle Grosjean, the Centre for Palynology and Palaeoecology at Monash University and Geotechnical Services, Inc. We thank Cheetham Salt Works, the Department of Planning and Community Development of Victoria and the Aboriginal Affairs Victoria Heritage Services for providing us with access and permission to collect at the sampling sites.

3.8 References

Allen MA, Neilan BA, Burns BP, Jahnke LL, Summons RE (2010) Lipid biomarkers in Hamelin Pool microbial mats and stromatolites *Organic Geochemistry* 41: 1207-1218

An Z, Bowler JM, Opdyke ND, Macumber PG, Firman JB (1986) Palaeomagnetic stratigraphy of Lake Bungunnia: Plio-Pleistocene precursor of aridity in the Murray Basin, southeastern Australia *Palaeogeography, Palaeoclimatology, Palaeoecology* 54: 219-239

Andres MS, McKenzie JA, in *Proceedings of the Ocean Drilling Program, Scientific Results*, Hine AC, Feary DA, Malone MJ, Eds. (IODP, 2002), vol. 182 pp. 1-13

Barakat AO, Yen TF (1990) Distribution of pentacyclic triterpenoids in Green River oil shale kerogen *Organic Geochemistry* 15: 299-311

Barbe A, Grimalt JO, Pueyo JJ, Albaiges J (1990) Characterization of model evaporitic environments through the study of lipid components *Organic Geochemistry* 16: 815-828

Bechtel A, Smittenberg RH, Bernasconi SM, Schubert CJ (2010) Distribution of branched and isoprenoid tetraether lipids in an oligotrophic and a eutrophic Swiss lake: Insights into sources and GDGT-based proxies *Organic Geochemistry* 41: 822-832

Bekele T (2000) "Plant Population Dynamics of *Dodonaea angustifolia* and *Olea europaea* ssp. *cuspidata* in Dry Afromontane Forests of Ethiopia", doctoral dissertation, Plant Ecology, Uppsala University

Bourbonniere RA, Meyers PA (1996) Sedimentary geolipid records of historical changes in the watersheds and productivities of Lakes Ontario and Erie *Limnological Oceanography* 41: 352-359

Bowler JM (1970) "Late Quaternary environments: a study of lakes and associated sediments in south-eastern Australia", doctoral dissertation, The Australian National University

Bowler JM (1973) Clay dunes: their occurrence, formation and environmental significance *Earth Science Reviews* 9: 315-338

Bowler JM (1976) Aridity in Australia: age, origins and expression in aeolian landforms and sediments *Earth Science Reviews* 12: 279-310

Bowler JM, in *Aeolian Landscapes in the Semi-Arid Zone of SE Australia* Storrier RR, Stannard ME, Eds. (Australian Soc of Soil Science, Riverina Branch, Mildura, VIC, 1979), vol. 1980, pp. 17-36

Bowler JM (1981) Australian salt lakes: A palaeohydrological approach *Hydrobiologia* 82: 431-444

Bowler JM (1986) Spatial variability and hydrologic evolution of Australian lake basins: analogue for Pleistocene hydrologic change and evaporite formation *Palaeogeography, Palaeoclimatology, Palaeoecology* 54: 21-41

Bowler JM, Teller JT (1986) Quaternary evaporites and hydrological changes, Lake Tyrrell, north-west Victoria *Australian Journal of Earth Sciences* 33: 43-63

Bowler JM, Kotsonis A, Lawrence CR (2006) Environmental evolution of the Mallee region, Western Murray Basin *Proceedings of the Royal Society of Victoria*: 161-210

Brand LE (1984) The salinity tolerance of forty-six marine phytoplankton isolates *Estuarine, Coastal and Shelf Science* 18: 543-556

Brassell SC, Eglinton G, Marlowe IT, Pflaumann U, Sarnthein M (1986a) Molecular stratigraphy: a new tool for climatic assessment *Nature* 320: 129-133

Brassell SC, Brereton RG, Eglinton G, Grimalt JO, Liebezeit G, Marlowe IT, Pflaumann U, Sarnthein M (1986b) Palaeoclimatic signals recognized by chemometric treatment of molecular stratigraphic data *Organic Geochemistry* 10: 649-660

Bray EE, Evans ED (1961) Distribution of *n*-paraffina as a clue to recognition of source beds *Geochimica et Cosmochimica Acta* 22: 2-15
Brewer R, *Fabric and Mineral Analysis of Soils*. (John Wiley & Sons, New York City, 1964)
Brooks JD, Gould K, Smith JW (1969) Isoprenoid hydrocarbons in coal and petroleum *Nature* 222: 257-259
Clarke KR (1993) Non-parametric multi-variate analyses of changes in community structure *Australian Journal of Ecology* 18: 117-143
Cox RE, Maxwell JR, Ackman RG, Hooper SN (1971) The isolation of a series of acyclic isoprenoidal alcohols from an ancient sediment: approaches to a study of the diagenesis and maturation of phytol *Advances in Organic Geochemistry*: 263-276
Cranwell PA (1973) Chain length distribution of *n*-alkanes from lake sediments in relation to post-glacial environmental change *Freshwater Biology* 3: 259-265
Cranwell PA (1981) Diagenesis of free and bound lipids in terrestrial detritus deposited in a lacustrine sediment *Organic Geochemistry* 3: 79-89
Cranwell PA (1985) Long-chain unsaturated ketones in recent lacustrine sediments *Geochimica et Cosmochimica Acta* 49: 1545-1551
Cupper ML, White S, Neilson JL, in *Geology of Victoria*, Birch WD, Ed. (Geological Society of Australia, 2003), pp. 337-360
De'ath G (2002) Multivariate regression trees: a new technique for modeling species-environment relationships *Ecology* 83: 1105-1117
DeDeckker P (1983) Australian salt lakes: their history, chemistry and biota - a review *Hydrobiologia* 105: 231-244
DeDeckker P (1988) Biological and sedimentary facies of Australian salt lakes *Palaeogeography, Palaeoclimatology, Palaeoecology* 62: 237-270
DeDeckker P, Jones C, Ed. (Canberra, 2009),
Derenne S, Largeau C, Casadevall E, Connan J (1988) Comparison of torbanites of various origins and evolutionary stages. Bacterial contribution to their formation. Cause of the lack of botryococcane in bitumens *Organic Geochemistry* 12: 43-59
Didyk BM, Simoneit BRT, Brassell SC, Eglinton G (1978) Organic geochemical indicators of paleoenvironmental conditions of sedimentation *Nature* 272: 216-222
Dyall-Smith MKM (1995) Taxonomy of the family Halobacteriaceae and the description of two new genera *Halorubrobacterium* and *Natrialba Journal of General and Applied Microbiology* 41: 333-350
Eglinton T, Eglinton G (2008) Molecular proxies for paleoclimatology *Earth and Planetary Science Letters* 275: 1-16
Emiliani C (1970) Pleistocene paleotemperatures *Science* 168: 822-825
Farrimond P, Griffiths T, Evdokiadis E (2002) Hopanoic acids in Mesozoic sedimentary rocks: their origin and relationship with hopanes *Organic Geochemistry* 33: 965-977
Fourcans A, Garcia de Oteyza T, Wieland A, Sole A, Diestra E, van Bleijswijk J, Grimalt JO, Kuhl M, Esteve I, Muyzer G, Caumette P, Duran R (2004) Chartacterization of functional bacterial groups in a hypersaline microbial mat community (Salins-de-Giraud, Camargue, France) *FEMS Microbiology Ecology* 51: 55-70
Gaskell SJ, Eglinton G (1975) Rapid hydrogenation of sterols in a contemporary lacustrine sediment *Nature* 254: 209-211
Gibbard P, van Kolfschoten T, in *A Geologic Time Scaleq*, Gradstein FM, Ed. (Cambridge University Press, Cambridge, 2004)

Haug P, Sever JR (1971) A study of the mechanism of formation of the acids in a marine sediment: acids of the Excello Shale and Surtsey lagoonal sediment *Advances in Organic Geochemistry*: 293-303
Ikan R, Baedecker MJ, Kaplan IR (1973) C18-isoprenoid ketone in recent marine sediment *Nature* 244: 154-155
Imbrie J, Hays JD, Martinson DG, McIntyre A, Mix AC, Morley JJ, Pisias NG, Prell WL, Shackleton NJ, in *Milankovitch and Climate, Part I*, Berger A, Ed. (D. Reidel, Hingham, MA, 1984), vol. 1 pp. 269-305
Irwin H, Meyer T (1990) Lacustrine organic facies. A biomarker study using multivariate statistical analysis *Organic Geochemistry* 16: 197-210
Javor B, *Hypersaline Environments: Microbiology and Geochemistry*. Brock TD, Ed., Brock/Springer Series in Contemporary Bioscience (Springer-Verlag, Berlin, 1989)
Kamekura M, Kates M, in *Halophilic Bacteria*, Rodriguez-Valera F, Ed. (CRC Press, Boca Raton, 1988), vol. 2 pp. 25-54
Kashirtsev VA, Kontorovich AE, Moskvin VI, Kuchkina AY, Kim VE (2008) Biomarker hydrocarbons in the organic matter of Paleogene sediments in southern West Siberia *Petroleum Chemistry* 48: 269-276
Kershaw P, Moss P, van der Kaars S (2003) Causes and consequences of long-term climatic variability on the Australian continent *Freshwater Biology* 48: 1274-1283
Killops SD, Frewin NL (1994) Triterpenoid diagenesis and cuticular preservation *Organic Geochemistry* 21: 1193-1209
Koster J, van Kaam-Peters HME, Koopmans MP, de Leeuw JW, Sinninghe Damste JS (1997) Sulfurisation of homohopanoids: effects on carbon number distribution, speciation, and 22S/22R epimer ratios *Geochimica et Cosmochimica Acta* 61: 2431-2452
Larcher AV, Alexander R, Kagi RI (1988) Differences in the reactivities of sedimentary hopane diastereomers when heated in the presence of clays *Organic Geochemistry* 13: 665-669
Liu W, Liu Z, Fu M, An Z (2008) Distribution of the C37 tetra-unsaturated alkenone in Lake Qinghai, China: A potential lake salinity indicator *Geochimica et Cosmochimica Acta* 72: 988-997
Luly JG (1990) "A pollen analytical investigation of Holocene palaeoenvironments at Lake Tyrrell, semi-arid northwestern Victoria, Australia", doctoral dissertation, Department of Biogeography & Geomorphology, Research School of Pacific Studies, Australian National University
Luly JG (1993) Holocene palaeoenvironments near Lake Tyrrell, semi-arid northwestern Victoria, Australia *Journal of Biogeography* 20: 587-598
Luly JG, Bowler JM, Head MJ (1986) A radiocarbon chronology from the playa Lake Tyrrell, northwestern Victoria, Australia *Palaeogeography, Palaeoclimatology, Palaeoecology* 54: 171-180
Mackenzie AS, Maxwell JR, in *Organic Maturation Studies And Fossil Fuel Exploration* Brooks J, Ed. (Academic Press, 1981), pp. 239-254
Macumber PG, in *Aeolian Landscapes in the Semi-Arid Zone of SE Australia* Storrier RR, Stannard ME, Eds. (Australian Soc of Soil Science, Riverina Branch, Mildura, VIC, 1979), vol. 1980, pp. 67-84
Macumber PG (1991) "Interaction between groundwater and surface systems in Northern Victoria", doctoral dissertation, Geology Department, School of Earth Sciences, Melbourne University

Magee JW (1991) Late Quaternary lacustrine, groundwater, aeolian and pedogenic gypsum in the Prungle Lakes, southeastern Australia *Palaeogeography, Palaeoclimatology, Palaeoecology* 84: 3-42
Martinson DG, Pisias NG, Hays JD, Imbrie J, Moore TC, Shackleton NJ (1987) Age dating and the orbital theory of the ice ages: Development of a high-resolution 0 to 300,000-year chronostratigraphy *Quaternary Research* 27: 1-30
McLaren S, Wallace MW, Pillans BJ, Gallagher SJ, Miranda JA, Warne MT (2009) Revised stratigraphy of the Blanchetown Clay, Murray Basin: age constraints on the evolution of paleo Lake Bungunnia *Australian Journal of Earth Sciences* 56: 259-270
Meyers PA (1997) Organic geochemical proxies of paleoceanographic, paleolimnologic, and paleoclimatic processes *Organic Geochemistry* 27: 213-250
Meyers PA (2003) Applications of organic geochemistry to paleolimnological reconstructions: a summary of examples from the Laurentian Great Lakes *Organic Geochemistry* 34: 261-289
Meyers PA, Ishiwatari R (1993) Lacustrine organic geochemistry - an overview of indicators of organic matter sources and diagenesis in lake sediments *Organic Geochemistry* 20: 867-900
Moldowan MJ, Seifert WK, Gallegos EJ (1985) Relationship between petroleum composition and depositional environment of petroleum source rocks *The American Association of Petroleum Geologists Bulletin* 69: 1255-1268
Mullakhanbhai MF, Francis GW (1972) Lipid constituents of a moderately halophilic bacterium *Acta Chemica Scandinavica* 26: 1399-1410
Nishimura M (1977) Origin of stanols in young lacustrine sediments *Nature* 270: 711-712
Nishimura M (1982) 5B-isomers of stanols and stanones as potential markers of sedimentary organic quality and depositional palaeoenvironments *Geochimica et Cosmochimica Acta* 46: 423-432
Nishimura M, Koyama T (1976) Stenols and stanols in lake sediments and diatoms *Chemical Geology* 17: 229-239
Nishimura M, Koyama T (1977) The occurrence of stanols in various living organisms and the behavior of sterols in contemporary sediments *Geochimica et Cosmochimica Acta* 41: 379-385
Oldenburg TBP, Rullkotter J, Bottcher ME, Nissenbaum A (2000) Molecular and isotopic characterization of organic matter in recent and sub-recent sediments from the Dead Sea *Organic Geochemistry* 31: 251-265
Ourisson G, Albrecht P, Rohmer M (1979) The hopanoids: palaeochemistry and biochemistry of a group of natural products *Pure & Applied Chemistry* 51: 709-729
Ourisson G, Rohmer M, Poralla K (1987) Prokaryotic hopanoids and other polyterpenoid sterol surrogates *Annual Reviews in Microbiology* 41: 301-333
Pearson EJ, Jones C, Ed. (Canberra, 2010)
Pearson EJ, Farrimond P, Juggins S (2007) Lipid geochemistry of lake sediments from semi-arid Spain: Relationships with source inputs and environmental factors *Organic Geochemistry* 38: 1169-1195
Pearson EJ, Juggins S, Farrimond P (2008) Distribution and significance of long-chain alkenones as salinity and temperature indicators in Spanish saline lake sediments *Geochimica et Cosmochimica Acta* 72: 4035-4046

Pearson EJ, Juggins S, Talbot HM, Weckström J, Rosén P, Ryves DB, Roberts SJ, Schmidt R (2011) A lacustrine GDGT-temperature calibration from the Scandinavian Arctic to Antarctic: renewed potential for the application of GDGT-paleothermometry in lakes *Geochimica et Cosmochimica Acta* in press

Peeler TC, Stephenson MB, Einspahr KJ, Thompson GAJ (1989) Lipid characterization of an enriched plasma membrane fraction of *Dunaliella salina* grown in media of varying salinity *Plant Physiology* 89: 970-976

Pell SD, Chivas AR, Williams IS (2001) The Mallee Dunfield: development and sand provenance *Journal of Arid Environments* 48: 149-170

Peters KE, Moldowan MJ, *The Biomarker Guide: Interpreting Molecular Fossils in Petroleum and Ancient Sediments*. (Prentice-Hall, Inc., Englewood Cliffs, ed. 1st, 1993)

Peters KE, Walters CC, Moldowan JM, *The Biomarker Guide: Biomarkers and Isotopes in Petroleum Exploration and Earth History* The Biomarker Guide (Cambridge University Press, Cambridge, 2005) vol. 2

Petit JR, Jouzel J, Raynaud D, Barkov NI, Barnola J-M, Basile I, Bender M, Chappellaz J, Davisk M, Delaygue G, Delmotte M, Kotlyakov VM, Legrand M, Lipenkov VY, Lorius C, Pe´pin L, Ritz C, Saltzmank E, Stievenard M (1999) Climate and atmospheric history of the past 420,000 years from the Vostok ice core, Antarctica *Nature* 399: 429-436

Poch RM, Thomas BP, Fitzpatrick RW, Merry RH (2009) Micromorphological evidence for mineral weathering pathways in a coastal acid sulfate soil sequence with Mediterranean-type climate, South Australia *Australian Journal of Soil Research* 47: 403-422

Prahl FG, Wakeham SG (1987) Calibration of unsaturation patterns in long-chain ketone compositions for palaeotemperature assessment *Nature* 330: 367-369

Quirk MM, Wardroper AMK, Wheatley RE, Maxwell JR (1984) Extended hopanoids in peat environments *Chemical Geology* 42: 25-43

Reed WE (1977) Biogeochemistry of Mono Lake, California *Geochimica et Cosmochimica Acta* 41: 1231-1245

Rencher AC, *Methods of Multivariate Analysis*. Wiley Series in Probability and Statistics (John Wiley & Sons, Inc., ed. 2nd, 2002)

Robinson N, Cranwell PA, Finlay BJ, Eglinton G (1984) Lipids of aquatic organisms as potential contributors to lacustrine sediments *Organic Geochemistry* 6: 143-152

Rohmer M, Dastillung M, Ourisson G (1980) Hopanoids from C30 to C35 in recent muds: chemical markers for bacterial activity *Naturwissenschaften* 67: 456-458

Rontani JF, Grossi V (1995) Abiotic degradation of intact and photooxidized chlorophyll phytyl chain under simulated geological conditions *Organic Geochemistry* 23: 355-366

Rontani JF, Volkman JK (2003) Phytol degradation products as biogeochemical tracers in aquatic environments *Organic Geochemistry* 34: 1-35

Rontani JF, Volkman JK (2005) Lipid characterization of coastal hypersaline cyanobacterial mats from the Camargue (France) *Organic Geochemistry* 36: 251-272

Rontani JF, Combe I, Giral PJ-P (1990) Abiotic degradation of free phytol in the water column: A new pathway for the production of acyclic isoprenoids in the marine environment *Geochimica et Cosmochimica Acta* 54: 1307-1313

Rontani JF, Raphel D, Cuny P (1996) Early diagenesis of the intact and photooxidized chlorophyll phytyl chain in a recent temperate sediment *Organic Geochemistry* 24: 825-832

Rosa-Putra S, Nalin R, Domenach A-M, Rohmer M (2001) Novel hopanoids from *Frankia* spp. and related soil bacteria. Squalene cyclization and significance og geological biomarkers revisited *European Journal of Biochemistry* 268: 4300-4306

Rullkotter J, Marzi M (1988) Natural and artificial maturation of biological markers in a Toarcian shale from northern Germany *Organic Geochemistry* 13: 639-645

Ryves DB, Battarbee RW, Juggins S, Fritz SC, Anderson NJ (2006) Physical and chemical predictors of diatom dissolution in freshwater and saline lake sediments in North America and West Greenland *Limnological Oceanography* 51: 1355-1368

Saito H, Suzuki N (2007) Distributions and sources of hopanes, hopanoic acids and hopanols in Miocene to recent sediments from ODP Leg 190, Nankai Trough *Organic Geochemistry* 38: 1715-1728

Sandison CM, Alexander R, Kagi RI, Boreham CJ (2003) Early diagenetic transformation of organic matter in a marine-influenced lignite *Organic Geochemistry* 34: 1081-1102

Scalan RS, Smith JE (1970) An improved measure of the odd-even predominance in the normal alkanes of sediment extracts and petroleum *Geochimica et Cosmochimica Acta* 34: 611-620

Schouten S, Hopmans EC, Schefuß E, Sinninghe Damsté JS (2002) Distributional variations in marine crenarchaeotal membrane lipids: a new tool for reconstructing ancient sea water temperatures? *Earth and Planetary Science Letters* 204: 265-274

Schreiber BC, El Tabakh M (2000) Deposition and early alteration of evaporites *Sedimentology* 47: 215-238

Seifert WK, Moldowan JM, in *Advances in Organic Geochemistry 1979,* Douglas AG, Maxwell JR, Eds. (Pergamon Press, Oxford, 1980), pp. 229-237

Singh G (1981) Late Quaternary pollen records and seasonal palaeoclimates of Lake Frome, South Australia *Hydrobiologia* 82: 419-430

Singh G, Luly JG (1991) Changes in vegetation and seasonal climate since the last full glacial at Lake Frome, South Australia *Palaeogeography, Palaeoclimatology, Palaeoecology* 84: 75-86

Sinninghe Damste JS, Ossebaar J, Abbas B, Schouten S, Verschuren D (2009) Fluxes and distribution of tetraether lipids in an equatorial African lake: constraints on the application of the TEX86 paleothermometer and BIT index in lacustrine settings *Geochimica et Cosmochimica Acta* 73: 4232-4249

Sinninghe Damste JS, Rampen S, Rijpstra WIC, Abbas B, Muyzer G, Schouten S (2003) A diatomaceous origin for long-chain diols and mid-chain hydroxy methyl alkanoates widely occurring in Quaternary marine sediments: Indicators for high-nutrient conditions *Geochimica et Cosmochimica Acta* 67: 1339-1348

Stephenson AE (1986) Lake Bungunnia - A Plio-Pleistocene megalake in southern Australia *Palaeogeography, Palaeoclimatology, Palaeoecology* 57: 137-156

Sun Q, Chu G, Liu G, Li S, Wang X (2007) Calibration of alkenone unsaturation index with growth temperature for a lacustrine species, *Chrysotila lamellosa* (Haptophyceae) *Organic Geochemistry* 38: 1226-1234

ten Haven HL, de Leeuw JW, Schenck PA (1985) Organic geochemical studies of a Messinian evaporite basin, northern Appenines (Italy) I: hydrocarbon biological markers for a hypersaline environment *Geochimica et Cosmochimica Acta* 49: 2181-2191

ten Haven HL, Peakman TM, Rullkotter J (1992) Early diagenetic transformation of higher-plant triterpenoids in deep-sea sediments from Baffin Bay *Geochimica et Cosmochimica Acta* 56: 2001-2024

ten Haven HL, de Leeuw JW, Rullkotter J, Sinninghe Damste JS (1987) Restricted utility of the pristane/phytane ratio as a palaeoenvironmental indicator *Nature* 330: 641-643

ten Haven HL, Rohmer M, Rullkotter J, Bisseret P (1989) Tetrahymanol, the most likely precursor of gammacerane, occurs ubiquitously in marine sediments *Geochimica et Cosmochimica Acta* 53: 3073-3079

ten Haven HL, de Leeuw JW, Sinninghe Damste JS, Schenck PA, Palmer SE, Zumberge JE, in *Lacustrine Petroleum Source Rocks,* Fleet AJ, Kelts K, Talbot MR, Eds. (Geological Society, 1988), vol. 40 pp. 123-130

Theissen KM, Zinniker DA, Moldowan JM, Dunbar RB, Rowe HD (2005) Pronounced occurrence of long-chain alkenones and dinosterol in a 25,000-year lipid molecular fossil record from Lake Titicaca, South America *Geochimica et Cosmochimica Acta* 69: 623-636

Thiel V, Jenisch A, Landmann G, Reimer A, Michaelis W (1997) Unusual distributions of long-chain alkenones and tetrahymanol from the highly alkaline Lake Van, Turkey *Geochimica et Cosmochimica Acta* 61: 2053-2064

Torgersen T, Deckker PD, Chivas AR, Bowler JM (1986) Salt Lakes: A discussion of processes influencing palaeoenvironmental interpretation and recommendations for future study *Palaeogeography, Palaeoclimatology, Palaeoecology* 54: 7-19

Toste AP (1976) "The Sterol Molecule: Its Analysis and Utility as a Chemotaxonomic Marker and a Fine Geochemical Probe into Earth's Past", doctoral dissertation, Comparative Biochemistry, UC Berkeley

Tritz JP, Herrmann D, Bisseret P, Connan J, Rohmer M (1999) Abiotic and biological hopanoid transformation: towards the formation of molecular fossils of the hopane series *Organic Geochemistry* 30: 499-514

Volkman JK (1986) A review of sterol markers for marine and terrigenous organic matter *Organic Geochemistry* 9: 83-99

Volkman JK, in *Lacustrine Petroleum Source Rocks,* Fleet AJ, Kelts K, Talbot MR, Eds. (Geological Society, 1988), vol. 40 pp. 103-122

Volkman JK (2003) Sterols in microorganisms *Applied Microbiology and Biotechnology* 60: 495-506

Volkman JK, Farrington JW, Gagosian RB (1987) Marine and terrigenous lipids in coastal sediments from the Peru upwelling region at 15°S: Sterols and triterpene alcohols *Organic Geochemistry* 11: 463-477

Volkman JK, Barrett SM, Blackburn SI (1999) Eustigmatophyte microalgae are potential sources of C29 sterols, C22-C28 *n*-alcohols and C28-C32 *n*-alkyl diols in freshwater environments *Organic Geochemistry* 30: 307-318

Volkman JK, Gillian FT, Johns RB, Eglinton G (1981) Sources of neutral lipids in a temperate intertidal sediment *Geochimica et Cosmochimica Acta* 45: 1817-1828

Volkman JK, Burton HR, Everitt DA, Allen DI (1988) Pigment and lipid compositions of algal and bacterial communities in Ace Lake, Vestfold Hills, Antarctica *Hydrobiologia* 165: 41-57

Volkman JK, Barrett SM, Dunstan GA, Jeffrey SW (1992) C30-C32 alkyl diols and unsaturated alcohols in a microalgae of the class Eustigmatophyceae *Organic Geochemistry* 18: 131-138

Volkman JK, Revill AT, Holdsworth DG, Fredericks D (2008) Organic matter sources in an enclosed coastal inlet assessed using lipid biomarkers and stable isotopes *Organic Geochemistry* 39: 689-710

Volkman JK, Barrett SM, Blackburn SI, Mansour MP, Sikes EL, Gelin F (1998) Microalgal biomarkers: A review of recent research developments *Organic Geochemistry* 29: 1163-1179

Wang R (1998) Acyclic isoprenoids - molecular indicators of archaeal activity in contemporary and ancient Chinese saline/hypersaline environments *Hydrobiologia* 381: 59-76

Weijers JWH, Schouten S, Spaargaren OC, Sinninghe Damste JS (2006) Occurrence and distribution of tetraether membrane lipids in soils: Implications for the use of the TEX86 proxy and the BIT index *Organic Geochemistry* 37: 1680-1693

Weijers JWH, Schouten S, van den Donker JC, Hopmans EC, Sinninghe Damste JS (2007) Environmental controls on bacterial tetraether membrane lipid distribution in soils *Geochimica et Cosmochimica Acta* 71: 703-713

Wilson SE, Cumming BF, Smol JP (1994) Diatom-salinity relationships in 111 lakes from the Interior Plateau of British Columbia, Canada: the development of diatom-based models for paleosalinity reconstructions *Journal of Paleolimnology* 12: 197-221

Withers N, in *The Biology of Dinoflagellates*, Taylor FJR, Ed. (1987)

Wuchter C, Schouten S, Wakeham SG, Sinninghe Damste JS (2005) Temporal and spatial variation in tetraether membrane lipids of marine Crenarchaeota in particulate organic matter: Implications for TEX86 paleothermometry *Paleoceanography* 20: PA3013

Yunker MB, Macdonald RW, Veltkamp DJ, Cretney WJ (1995) Terrestrial and marine biomarkers in a seasonally ice-covered Arctic estuary - integration of multivariate and biomarker approaches *Marine Chemistry* 49: 1-50

Zink K-G, Leythaeuser D, Melkonian M, Schwark L (2001) Temperature dependency of long-chain alkenone distributions in Recent to fossil limnic sediments and in lake waters *Geochimica et Cosmochimica Acta* 65: 253-265

Chapter 4.

Utility of sedimentary sulfides as biosignatures in hypersaline lake sediments

4.1 Abstract

In the present study, we examine the morphology, chemical composition and sulfur-isotopic signature of sedimentary sulfates and sulfides in Pleistocene sediments from Lake Tyrrell in order to gain insight into the biogeochemical cycles influencing the lake's geochemistry during that time period. The morphology of the gypsum crystals and associated pyrites show that cyanobacterial mats colonized the sediment-water interface of a lake saturated with respect to gypsum, and that evaporative concentration of groundwater during periodic lake-dry phases indirectly drove precipitation of pyrites within the cleavage planes of gypsum. The extreme isotopic fractionation of sulfur between gypsum and pyrite points to an active oxidation-reduction cycle mediated by sulfate-reducing bacteria (SRB) and sulfur-disproportionating bacteria. In a sedimentary environment not amenable to the preservation of molecular biomarkers specific to sulfate-reducers, inorganic residues of microbial metabolic processes can be used to infer the existence of palaeo-communities of microbes analogous to those colonizing the modern lake sediments.

4.2 Introduction

4.2.1 The importance of inorganic residues of metabolic processes

Since the first microbes arose from the pre-biotic soup of early Earth some 3.5-3.8 billion years ago, life has altered its physical environment in order to create conditions more amenable to its continued existence. Prokaryotes are particularly adept at transforming their immediate environment, due to their wide range of metabolic capabilities. Bacteria and Archaea can derive energy and sustenance from catalyzing, or simply exploiting, oxidation-reduction (redox) reactions involving a large subset of elements. As a result, the chemistry and morphology of Earth's surface is a reflection of the interactions of biotic and abiotic processes. When investigated in this light, rock and mineral formations can provide information on the metabolic capabilities of members of the microbial community present when these formations were deposited (Douglas 2005). Such inorganic evidence is important as it often persists when organic indicators of the presence of past life, such as lipid biomarkers, cell remains, and microfossils containing indigenous organic matter, are absent or ambiguous (Douglas 2004; Frankel and Bazylinski 2003; Shen and Buick 2004). This is particularly true for environments where conditions are harsh or where the interval of time since the community of interest existed is very long – on the order of billions of years. Thus, the search for inorganic indicators of past life is central to the study of the origins of life on Earth, as well as to the search for life on other planets.

Inorganic evidence of past life includes characteristic mineral textures, chemical compounds, dissolution patterns, isotopic signatures within minerals, and the mineralized 'casts' of organisms (Canfield *et al.* 2004; Douglas 2004, 2005; Frankel and Bazylinski 2003; Rasmussen 2000). Unfortunately, mineral textures and dissolution patterns can be altered or eliminated by post-depositional processes, especially metamorphic processes (Seckbach 2006).

Minerals formed as by-products of microbial metabolism are often indistinguishable from their inorganically precipitated counterparts (Astafieva *et al.* 2005; Posfai and Dunin-Borkowski 2006; Seckbach 2006). Mineralized casts of individual cells or of communities thereof (i.e. stromatolites and 'rusticles') are also problematic, as they lack organic residues and so must be judged on morphology alone. Famously controversial are putative microfossils within the Pilbara craton of Western Australia. If they are of biotic origin, they represent some of the oldest known lifeforms (Awramika *et al.* 1983; Schopf 1993). However, in recent years, objects with varied morphologies mimicking established biotic structures have been created in the lab abiotically. The formation of these 'biomorphs', as they are termed, occurs under geochemical conditions commonly found at Earth's surface (Carnerup *et al.* 2005; Christy 2010). As a result, many researchers reject the notion that simple morphology is a sufficient condition for the imputation of biotic production (Carnerup *et al.* 2005; Seckbach 2006).

Isotopic signatures of a number of elements preserved in minerals are more promising, as the fractionation imparted by biotic processes generally exceeds that of abiotic ones, given that both are operating at similar temperatures and pressures (Valley and Cole 2001). Biotically-mediated mineral formation commonly yields compounds enriched in the lightest of the stable isotopes of the element in question, relative to the same compound when produced abiotically. Any interpretation of isotopic signatures must take into account the thermodynamic conditions of the system (Seckbach 2006) so that fractionation resulting from higher-temperature chemical disproportionation will not be mistaken for evidence of biotic processes. With this *caveat*, however, isotopic signatures provide strong evidence for the existence and metabolic capabilities of past life.

4.2.2 Biotic vs abiotic fractionation of stable S isotopes

As discussed in section 1.3.1.3 of this work, fractionation of sulfur during low-temperature abiotic gypsum and pyrite precipitation, protonation of HS^- and the volatilization of H_2S is an order of magnitude less than that imparted during biotically-mediated dissimilatory sulfate reduction (DSR), sulfide oxidation, and sulfur disproportionation. All three processes typically operate in the surficial, water-logged sediments of lakes, seas and swamps. The bacteria that are involved in these processes exploit the depth-associated redox gradients of the sediments in which they live, such that the products of the metabolism of one become the substrate for another. Thus, the isotopic fractionation of sulfur is amplified by 'recycling', and the sulfur-bearing compounds ultimately deposited are isotopically extremely light relative to those that are chemically-identical, yet abiotically precipitated. For example, pyrite found in marine sediments can have a $\delta^{34}S$ value up to 55‰ lighter than that of seawater sulfate, a value that is impossible to produce through either abiotic processes operating at surface temperatures and pressures or through DSR alone (Habicht and Canfield 2001; Ku *et al.* 1999; Valley and Cole 2001). Moreover, under the thermodynamic conditions prevalent at Earth's surface, abiotically precipitated sulfur-bearing minerals are either enriched in the heavy isotope, or only slightly depleted (<2‰) (Javor 1989; Raab and Spiro 1991), while those that are biotically precipitated are nearly always depleted in the heavy isotope, with the extent of depletion dependent upon the types of bacteria involved, the characteristic fractionations they impart, the rates of production of the compound in question, and the substrate upon which the bacteria feed (Bottcher *et al.* 2001; Detmers *et al.* 2001; Valley and Cole 2001).

4.2.3 Inorganic evidence of sulfate-reducing bacteria (SRB) through time

Both in modern natural systems and in cultivation experiments, SRB have been shown to mediate the production of a variety of iron sulfide minerals, including marcasite, mackinawite, greigite, pyrrhotite, framboidal pyrite and amorphous FeS (Frankel and Bazylinski 2003; Schoonen and Barnes 1991). While framboids have usually been interpreted as the product of dissimilatory sulfate reduction (Valley and Cole 2001), it has been shown experimentally that morphology is an insufficient criterion for distinguishing between biogenic and abiogenic iron sulfides in the fossil record (Frankel and Bazylinski 2003; Posfai and Dunin-Borkowski 2006). Other lines of evidence must be considered in conjunction with the existence of pyrite in order to definitively assert that the pyrite is the product of SRB.

The oldest evidence of SRB comes from microscopic sulfides deposited along the growth faces of ~3.47 Ga barites located at North Pole, Australia. These sulfides possess "fractionations relative to co-existing sulfate ranging from 21.1‰ to 7.4‰, with a mean of 11.6‰" (Shen and Buick 2004). Such fractionation could be attributed to hydrothermal activity, especially when the fractionation of ^{33}S was taken into account (Runnegar 2001; Runnegar *et al.* 2002). However, based on the geology of the formation, it was determined that the depositional environment was sedimentary, so that bacterial sulfate reduction was the only thermodynamically-feasible process that could have produced the measured fractionation (Shen *et al.* 2001). The isotopic signature of the sulfide is somewhat heavier than that measured in comparable modern systems (31-39‰). This was attributed to the fact that evidence of ancient bacterial sulfate reduction does not necessarily imply that the ancient SRB were identical to modern species, or to the existence of associated disproportionating bacteria like those found in modern systems (Canfield *et al.* 2004).

More recently, phyllosilicate minerals showing evidence of sequential pyritization have been found in Miocene (23 – 5.3 Ma) evaporite sequences in the Madrid Basin (Sanz-Montero *et al.* 2009). The presence and isotopic signatures of carbon within fossilized filaments of extracellular polysaccharides, the depleted $\delta^{34}S$ values of the pyrites, and the selective depletion of iron within the associated phyllosilicates all point to the existence of a microbial consortium that included both iron-reducers and sulfate-reducers. Pyrite crystals grew within the cleavage planes of the phyllosilicate, replacing it, instead of appearing in the commonly found framboidal form. Interestingly, the researchers interpreted the morphology of the iron sulfide as evidence that bacteria were responsible not only for the release of iron from the phyllosilicates and the production of sulfide ions, but also for localizing the precipitation of the iron sulfide by acting as organic templates (Sanz-Montero *et al.* 2009). Therefore, while morphology cannot be used alone as an indicator of biogenicity, it can be informative as to the mode of mineral precipitation once biogenicity has been established.

Iron sulfides are not the only minerals produced as a by-product of SRB metabolism. A series of papers published in the last ~15 years have asserted that dissimilatory sulfate reduction may be indirectly responsible for primary dolomite precipitation in saline lakes (Lith et al. 2002; Lith et al. 2003; Vasconcelos et al. 1995; Warthmann et al. 2000; Wright 1999; Wright and Wacey 2005). Dolomite solubility is exceeded in modern seawater as well as in saline lakes, so that one would expect dolomite to be the primary carbonate mineral found in such settings. However, calcite is the mineral most often precipitated (Javor 1989). This stands in direct contrast to evidence from the rock record: in the Proterozoic, for example, the ratio of dolomite: limestone was ~3:1 (Vasconcelos *et al.* 1995). In modern saline lakes where dolomite is forming, high rates of evaporation leading to high Mg/Ca ratios have been invoked to explain how kinetic barriers to primary dolomite precipitation are overcome (Wright 1999). However, due to

complexing between Mg^{2+} and the sulfate and carbonate ions, high rates of evaporation would be expected to enhance such barriers (Wright 1999). This effect could, in theory, be balanced by the decrease in hydration energies of magnesium and calcium at elevated salinities, such that there is an optimal salinity which favors dolomite precipitation (Lith et al. 2002).

Elevated salinity alone, however, has never been shown to directly promote dolomite precipitation (Javor 1989). During dissimilatory sulfate reduction, local levels of sulfate are drawn down; bicarbonate is released, increasing its concentration; pH rises; and negatively-charged cell surfaces act to concentrate Ca^{2+} and Mg^{2+} ions – all of which lower kinetic barriers to dolomite precipitation (Lith *et al.* 2003; Sanchez-Roman *et al.* 2009; Warthmann *et al.* 2000; Wright and Wacey 2005). Since SRB are heterotrophic, primarily anaerobic organisms, in lacustrine systems they colonize anoxic sediments underlying actively growing microbial mats (Bontognali *et al.* 2010; Canfield *et al.* 2004; Wright 1999). Such mats contain large amounts of organic carbon, and act as a food source for the SRB (Douglas and Yang 2002). Therefore, sedimentary assemblages containing primary dolomite, iron sulfides depleted in ^{34}S, and with high total organic carbon (TOC) values may be seen as "macrofossils" of metabolic webs, the products of which are dependent on community membership and local redox conditions.

4.2.4 Significance of SRB metabolism to Lake Tyrrell's geochemistry

The metabolic activities of SRB within modern Lake Tyrrell sediments have been implicated in metal sequestration (Fegan *et al.* 1992), alteration of pH, carbonate dissolution (Hines *et al.* 1992), and dolomitization of carbonates (Teller *et al.* 1982b) therein. In a low-temperature environment like Lake Tyrrell, the only mechanism by which sulfate can be reduced to sulfide is biotic (Schoonen and Barnes 1991; Shen and Buick 2004). Therefore, the sulfidic, reducing character of Tyrrell reflux brines is directly attributable to the activities of SRB in the sediments (Hines *et al.* 1992; Long *et al.* 2009).

Sulfide produced by SRB reduces iron present in highly reactive iron oxides such as goethite and ferrihydrite, thereby assisting in the dissolution of these minerals (Schoonen and Barnes 1991). Some of this reduced iron is re-oxidized through ferrolysis, which precipitates iron oxyhydroxide while acidifying the water (Long *et al.* 1992; Long *et al.* 2009). Some is precipitated as amorphous FeS, which is converted to pyrite by the further addition of sulfur (Posfai and Dunin-Borkowski 2006). When this pyrite is re-oxidized, sulfuric acid is produced, further acidifying pore waters (Long *et al.* 1992; Long *et al.* 2009). The acidity produced mobilizes metals including Fe, Al, base metals and Ra (Dickson and Giblin 2009). In addition, sulfides present in surficial salt lake sediments have been shown to accumulate metals such as copper and manganese (Fegan *et al.* 1992), such that salt lake deposits have been considered as sources of metal ores (DeDeckker 1988b, a).

On a lake-wide scale, acidity generated as an indirect result of bacterially-mediated sulfate reduction contributes to the dissolution of $CaCO_3$ within the sediments (Ku *et al.* 1999). By contrast, in the micro-environments inhabited by the SRB, bacterially-mediated changes in pH, ionic strength and ionic composition lead to the precipitation of carbonates with varying ratios of Mg:Ca, as discussed in section 4.2.3, above. Culturing experiments have demonstrated that the type of carbonate mineral precipitated is dependent on bacterial metabolism, activity, and rate of precipitation (Lith *et al.* 2003). In any case, the geochemical conditions within the lake, as well as the mineralogy of lake sediments, is intimately connected to, and to some extent controlled by, microbial metabolic processes, specifically those of SRB.

4.3 Methods

4.3.1 Sample collection and sub-sampling

Samples were collected from the Lake Tyrrell Folly Point core, as described in chapter 2.

4.3.2 Thin sections and light microscopy

Thin sections were prepared as described in chapter 2, and were examined under a petrographic microscope with both transmitted and reflected light. Areas that appeared dark in transmitted and bright under reflected light were postulated to be sulfides, and sub-samples from these thin section blocks were taken for further analysis. These sections – LT S12 samples 11_12 and 35_36 – appear in Appendix 2 as Figures A2.10 and A2.11, respectively.

4.3.3 Electron microscopy

Three sub-samples for examination with an electron microprobe were prepared using thin sections cut from the blocks prepared previously (see chapter 2 for notes on thin section block preparation). The sections were coated with carbon to the standard 25 nm thickness (Kerrick *et al.* 1973) and viewed, imaged and analyzed on a Cameca SX-100 electron microprobe equipped with an EDS detector. For quantitative determination of Fe and S atomic percentages, standards of troilite, FeS and Fe metal were measured during operation of the microprobe. The troilite and FeS standards contained atomic ratios of ~49:50, S:Fe. The microprobe was operated at an accelerating voltage of 15 kV with an initial beam current of ~100 nA.

Three sub-samples for SEM work were prepared by breaking clean surfaces from a pre-made thin section block (see chapter 2 for notes on thin section block preparation) of LT S12 sample 11_12. Each sub-sample was mounted on an SEM stub using carbon tape, and coated with a carbon evaporator to 25 nm thickness. Samples were analyzed on a Zeiss EVO 10 SEM equipped with an EDAX silicon-drift detector. Machine operation and imaging were performed with SMARTSEM v05.04 Spectra software. Spectra were processed with EDAX Genesis software. All analyses may be treated as semi-quantitative, as standards were not employed.

During operation, an accelerating voltage of ~20 kV and a beam current of 100 μA were maintained, while probe current was varied according to the type of analysis being performed. For chemical analysis, probe current was set initially at ~1 nA and adjusted for optimal count rate. For high-resolution imaging with both back-scattered and secondary electrons, the probe current was varied in the range of 60 pA to 10 nA, with lower current correlated to smaller spot size and higher resolution.

4.3.4 Isotopic measurements

Samples for isotopic analysis on a Sensitive High-Resolution Ion Microprobe (SHRIMP) were prepared from individual pyritized gypsum crystals picked from the core at a depth corresponding to that preserved in the thin section of LT S12 sample 11_12. Crystals were embedded in a 25 mm round epoxy disk, polished and coated with gold to prevent charging during analysis.

Sulfur isotope analyses were performed by Richard Armstrong on the multicollector SHRIMP II instrument at the Research School of Earth Sciences (RSES), The Australian National University. A Cs^+ primary beam was used as the primary ionization source, and for this session, an electron gun was employed to neutralize any charge build up on the surface of the mount when analyzing the sulfates. The Kimball Physics ELG-5 electron gun streams electron at a 45^o incidence angle to the mount at a working distance of 20 mm. The spot size was ~15um

in diameter. The multicollector arrangement on SHRIMP II for sulfur isotope analyses comprised two Faraday cups with a 10^{10} ohm resistor for the ^{32}S beam and a 10^{11} ohm resistor for the ^{34}S beam. Data were collected in four sets of 6 measurements each (with 10 second integration times per measurement), with baselines measured during the "burn-in" prior to analysis. Possible isobaric interferences were resolved by operating at a mass resolution of ~2500 (source slit = 150mm and collector slit = 300mm). Secondary beam focusing was done before data collection and between sets.

Data reduction was performed using the in-house program POXI written by Peter Lanc of the RSES. The reference pyrite used was Ruttan (+1.2‰ $\delta^{34}S$ (Crowe and Vaughan 1996)) and for the sulfate analyses an anhydrite (An-1; 10.0‰ $\delta^{34}S$) supplied by Martin Whitehouse of the Swedish Museum of Natural History, Stockholm. Although untested at this stage, any significant matrix-related fractionation between anhydrite and gypsum is not anticipated. SHRIMP measurements of $^{34}S/^{32}S$ ratios within pyrite are well-established, and analytical fractionation and matrix effects are known and can be corrected for (Eldridge *et al.* 1987). To date, however, no measurements of the stable S isotopic composition of gypsum using SHRIMP have been published. It is known that the sulfate matrix strongly alters fractionation factors when compared to those of sulfides, due to the strength of S-O bonds as compared to weaker S-metal bonds (Eldridge *et al.* 1987). This strong bonding environment also leads to enrichment of sulfates in the heavier isotope as a result of equilibrium processes during deposition (Valley and Cole 2001), and the effect is compounded during measurement. For example, SHRIMP measurement of S isotopic ratios in barite ($BaSO_4$) has yielded equilibrium-like distributions of ^{34}S and ^{32}S, due to inefficient bond breaking: all Ba-SO_4 bonds are broken, but not all ^{32}S-O_4 bonds, and only a very few ^{34}S-O_4 bonds (Eldridge *et al.* 1987), due to the differing bond strengths of the S isotopes. Preliminary analyses of gypsum and anhydrite yielded similar fractionation factors to that of barite (Eldridge *et al.* 1987), indicating that the effect is relatively constant across hydrous and anhydrous sulfates. Thus, the selection of anhydrite as a matrix-correction standard for gypsum is reasonable.

Unknowns were bracketed by regular analyses of the reference materials described above, and the session calibrations included corrections for instrumental drift, gain corrections and for electron-induced-secondary ion emission (EISIE (Ickert *et al.* 2008)) during analyses of the sulfates. All data are reported as ‰ (per mil) with the $\delta^{34}S$ notation, expressed as deviations from Canyon Diablo Troilite (CDT) from the Canyon Diablo meteorite, which has a $^{34}S/^{32}S$ value of 0.0450045 (Ault and Jensen 1963). Individual analyses yielded precisions of the order of ±0.15‰ $\delta^{34}S$ (1s) for the sulfides and ±0.3‰ $\delta^{34}S$ (1s) for the sulfates. The mean $\delta^{34}S$ values of standards for the session were 1.19 ± 0.29‰ $\delta^{34}S$ (1s) for the Ruttan pyrite standard and 10.0 ± 0.38‰ $\delta^{34}S$ (1s) for the sulfate An-1.

4.4 Results

4.4.1 Results of thin section analysis and light microscopy

Images of thin sections of LT samples 11_12 and 35_36 in plane light, along with close-ups of areas of interest in both plane and polarized light, may be found in Appendix 2 (Figures A2.10 and A2.11). Figures A2.10 A, B and F through H show iron sulfides in the cleavage planes of gypsum crystals. In some cases, the sulfide has completely replaced the gypsum, creating pseudomorphs. As can be easily seen in the image of the entire thin section, the sulfide-rich gypsum is closely associated with well-preserved, carbon-rich (Table 3.1) remnant microbial

mat layers. In Figure A2.10 E, oxidized iron can be seen within the gypsum crystal. IN principle, it could be hematite, as this is present in the core at greater depth (see section 3.4.2). However, more likely it is goethite, as this is the most abundant oxidized iron mineral in Lake Tyrrell surface sediments (Jones *et al.* 2006).

Figure A2.11 shows disrupted layers of black (apparently pyritized) gypsum from 595-597 cm depth. These were likely deposited as coherent layers (featured in Figure A2.11 E) that were subsequently disrupted by the growth of secondary, displacive gypsum (Figures A2.11 F and G). At the base of the section, at ~597 cm, is the contact between the largely evaporitic Tyrrell Beds and the fresher Blanchetown Clay. Figures A2.11 A, B and D show iron oxides deposited as layers and filling voids within the Blanchetown Clay.

4.4.2 Results of electron microscopy

4.4.2.1 Mineralogy (EM)

LT S12 sample 35_36, despite the appearance of large areas of pyritized gypsum, contains only small amounts of pyrite in the form of scattered framboids (~2 μM). The composition of these framboids ranges from $FeS_{1.45}$ to FeS_2, indicating that the conversion from mackinawite or greigite to pyrite is not complete. The dark material within the gypsiferous layers is composed primarily of clays containing sulfur and limited amounts of iron; the identity of this material is unclear at this time. However, its brightness under reflected light (see section 4.3.2, above) suggests that it is some form of metal sulfide, most likely amorphous FeS.

In contrast, the area of interest in LT S12 sample 11_12 is composed of gypsum crystals in a kaolinite matrix, with large areas of gypsum replaced by iron sulfides (Figure 4.1A). Some crystals are completely replaced, while others contain iron sulfides concentrated along cleavage planes (Figure 4.1B). These last appear to be growing into the gypsum crystals from the outer edges. Scattered framboids are also present in the matrix. All iron sulfides in this sample have the composition FeS_2, indicating that pyritization has proceeded to completion.

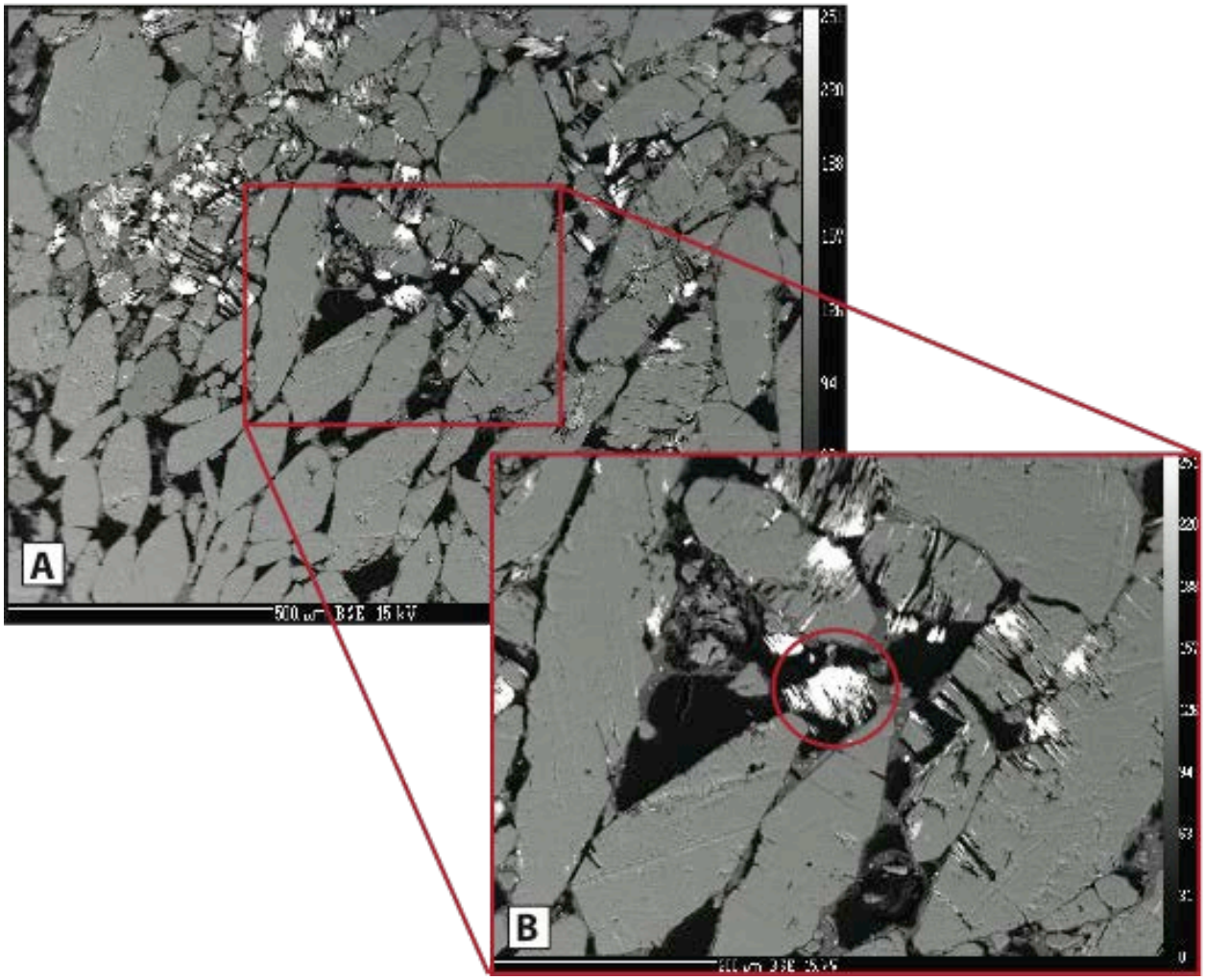

Figure 4.1 Back-scattered electron images of thin section of LT S12 sample 11_12
Bright areas are iron sulfides; grey, discoidal crystals are gypsum. A. Iron sulfides are growing into cleavage planes of gypsum crystals. B. Note iron sulfide pseudomorph after gypsum (circled) in center of image. Images taken by author.

4.4.2.2 Morphology and composition (SEM)

Of the three sub-samples prepared from LT S12 sample 11_12, only one (from the area between 595-596 cm, part of which is shown in Appendix 2, Figure A2.11E) contained appreciable quantities of iron sulfides. This was present both as scattered framboids within the clay and evaporite matrix, and as growths within the cleavage planes of gypsum crystals (Figure 4.2). Semi-quantitative EDAX analyses show that these iron sulfides have the stoichiometry of pyrite, with atomic ratios of 2:1, S:Fe. A typical spectrum appears in Figure 4.3 (quantification data not shown).

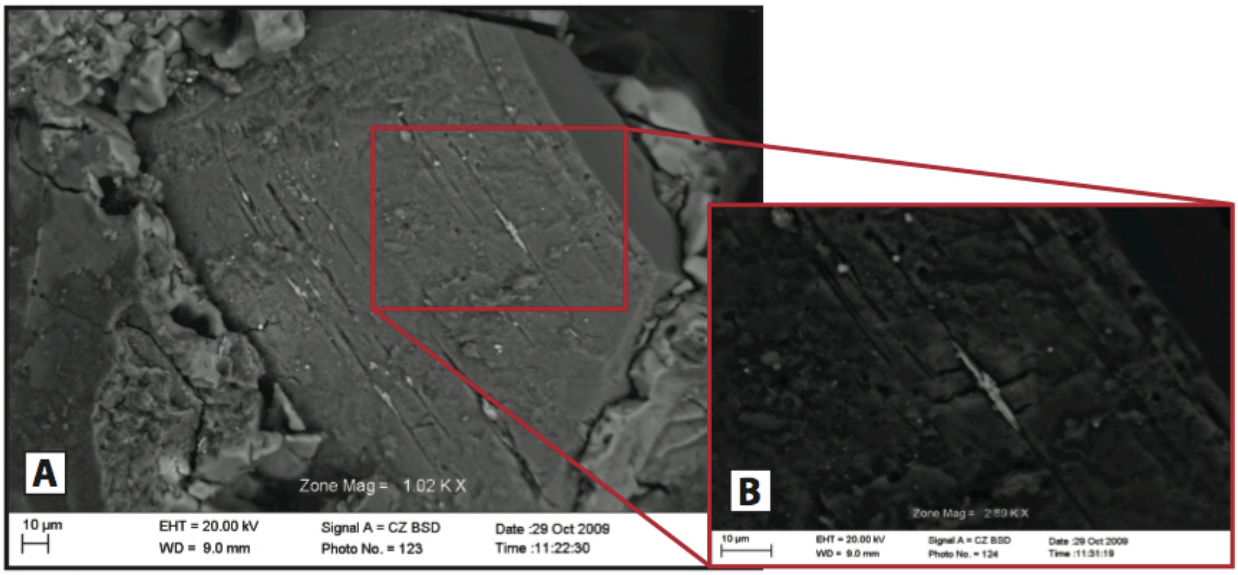

Figure 4.2 Back-scattered electron images of sulfides emplaced in cleavage planes of gypsum crystals

A. Bright areas within gypsum crystal are pyrite. Probe current = 61 pA.
B. Close-up of pyrite in cleavage plane of gypsum crystal – note that it appears to be growing along the cleavage plane. Probe current = 8.2 nA. Images taken by author.

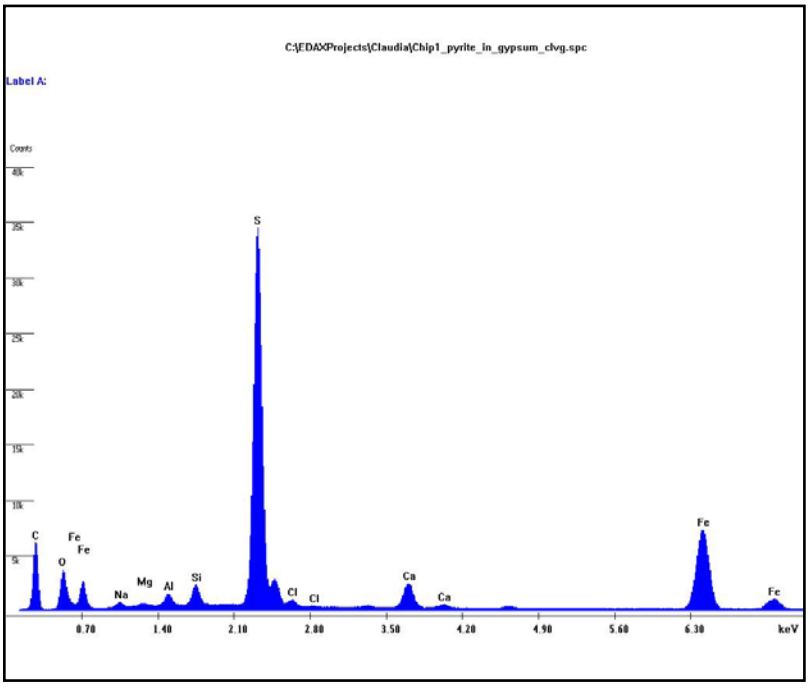

Figure 4.3 EDAX spectrum of pyrite

Pyrite analyzed appears in the center of Figure 4.2B. Probe current = 8.2 nA. Ca, O, Al, Si, Na, Mg and Cl peaks originate from surrounding gypsum crystal and surficial kaolinite and evaporite grains. C peak is due to sample coating. Small peak to the right of the large S peak is due to S Kb. Figure produced by author.

The morphology of the pyrite is variable: the size of the growths within cleavage planes ranges from 2 μM to >10 μM (compare Figures 4.2B and 4.4C), and that the pyrite appears to grow at the expense of the gypsum (Figures 4.4B and 4.4C). In addition, within this sub-sample, pyrite appears almost exclusively in association with 'etched' gypsum crystals, either as growths within the cleavage planes or as framboids in the surrounding matrix.

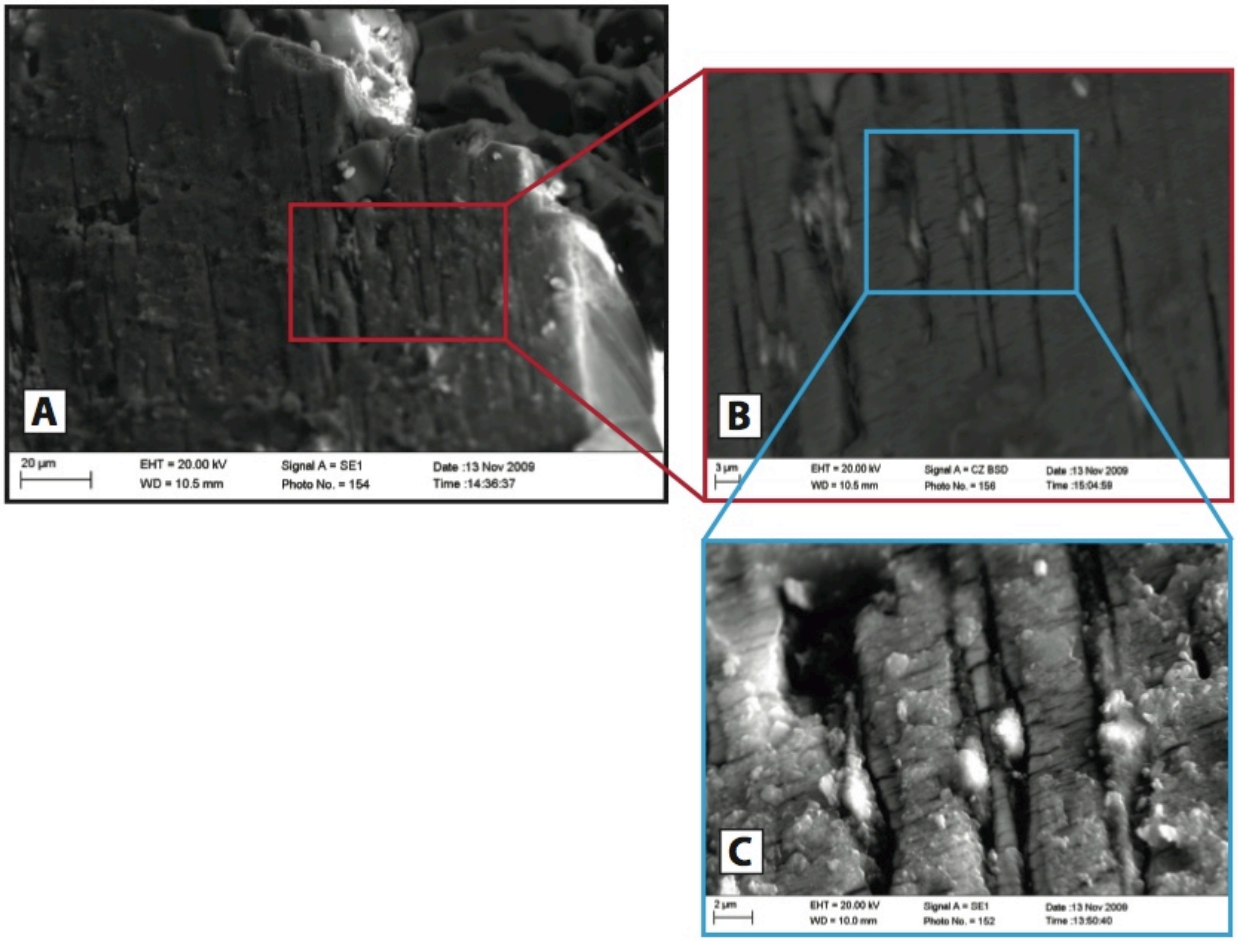

Figure 4.4 Pyrite blebs in the cleavage planes of gypsum crystals
A. Secondary electron image of gypsum crystal with partial dissolution along cleavage planes. Probe current = 10 nA.
B. Back-scattered electron image of pyrite blebs within cleavage planes of gypsum. Probe current = 670 pA.
C. Secondary electron image; close-up of pyrite blebs. Note that they appear to be growing down into the cleavage planes. Probe current = 603 pA. Images taken by author.

4.4.3 Results of S isotopic analysis

Isotopic analyses were performed on a subsample taken from the thin section LT S12 sample 11_12. Nine measurements of $^{34}S/^{32}S$ of gypsum and five measurements of $^{34}S/^{32}S$ of associated iron sulfides were made; results appear in Table 4.1 as $\delta^{34}S$ (per mil, ‰). Based on these measurements, the average value of $\delta^{34}S$ for gypsum is 10.99 ± 0.94‰, and for pyrite the average $\delta^{34}S$ is -37.34 ± 1.66‰. Total ε of pyrite relative to gypsum is ~53‰.

Table 4.1 Results of isotopic analyses of sulfur in gypsum and pyrite contained in LT S12 sample 11_12[a]

Sample number[b]	$\delta^{34}S$ (‰)	Measurement error (‰)
GYP-2	12.16	0.31
GYP-3	10.41	0.34
GYP-4	11.50	0.35
GYP-5	9.16	0.24
GYP-6	10.96	0.35
GYP-7	11.25	0.30
GYP-8	12.13	0.13
GYP-9	10.37	0.30
GYP-10	10.93	0.25
PYR-1	-34.76	0.15
PYR-2	-36.77	0.11
PYR-3	-38.27	0.05
PYR-4	-37.88	0.16
PYR-5	-39.04	0.15

[a]Refer to Appendix 2, Figure A2.11

[b]GYP indicates gypsum, PYR indicates pyrite

4.5 Discussion

Currently, sedimentation at Lake Tyrrell is dominated by aeolian quartz sands and clays, primary and secondary evaporites such as gypsum and halite, organic matter from microbial mats and black sulfidic material (Bowler and Teller 1986). Halite is precipitated from lake waters super-saturated with NaCl (Macumber 1991), forming a crust up to ~15 cm thick atop the lake sediments. Microbial mats grow at the sediment-salt crust interface (Figure 4.5), and preliminary genomic analyses have demonstrated that these mats contain a number of cyanobacterial species (data not shown). Finally, black, sulfidic material appears directly beneath the mat layer, and it is thought that this material is evidence of active sulfate reduction.

Figure 4.5 'Shovel section' of typical surface sediments found at Lake Tyrrell

Note the thin layer (<2 mm) of microbial mats between the sediments and the overlying salt (denoted by blue arrowhead). Primary production in these mats provides the carbon for heterotrophic SRB in the underlying black sediments. Black color is due to sulfides produced by SRB. Also note layers beneath black sediments, thought to represent buried mats. Image courtesy of J.J. Brocks.

Two lines of evidence support this assertion: first, TOC values decrease rapidly within the top 5 cm of sediment underlying the mats (Table 5.1). Both in coastal sediments and salterns, sulfate reducers have been shown to oxidize as much organic matter to CO_2 as all aerobic organisms, and have done so within the top 3 cm of sediment (Jorgensen 1982). Secondly, preliminary lipid biomarker analysis of FAMEs (fatty acid methyl esters, derived from the phospholipid fatty acids that make up the membranes of cells) in the sulfidic material (Figure 4.5) has yielded the fatty acid 10-methyl 16:0, a biomarker for members of the genus *Desulfobacter* (Allen *et al.* 2010; Oren *et al.* 2009; Orphan *et al.* 2001).

As discussed in section 4.2.4, active bacterially-mediated sulfate-reduction (BSR) at Lake Tyrrell considerably impacts the geochemistry and mineralogy of the waters and sediments. As one of the primary goals of this thesis is to reconstruct the evolution in the lake's chemistry through time, it is vital to ascertain whether intensive BSR has been ongoing throughout the lake's history, or whether it is a recent development. During initial characterization of sediments from the Folly Point (S12) core described in chapters 2 and 3, inspection of thin sections from ~560 cm (LT S12 sample 35_36) and ~590 cm (LT S12 sample 11_12) depth containing gypsum and iron sulfides showed that these layers were closely associated with what appeared to be remnant microbial mat layers. This was particularly evident in LT S12 sample 35_36, which is to be expected, as it was the better preserved of the two sections examined (refer to Appendix 3 for further information on preservation, and to chapter 3 for comparison of modern mats with LT 35_36). Thus, the morphology of the layers within the thin sections appeared to be analogous to that of the modern mat-sulfidic sediment system. If this were true, it would demonstrate that aspects of Lake Tyrrell's geochemistry are cyclic, with modern conditions approximating those in the mid- to late-Pleistocene (see chapter 3 for a discussion of assigning ages to depths within the S12/Folly Point core). To investigate the possibility that SRB had been active in Lake Tyrrell in the past, microscopic, chemical and isotopic analyses of the gypsum-sulfide layers within LT S12 samples 35_36 and 11_12 were performed.

As described in chapter 3, lipid biomarkers were extracted from each of these samples, and the identities and quantities of the lipids established using GC-MS. Unfortunately, unique lipid biomarkers for SRB are limited to a small number of fatty acids, all of which are branched, enoic, cyclized, or some combination thereof (Londry *et al.* 2004). The length of the primary carbon chain together with the positions of the branches and double bonds are indicative of the genus of SRB that produced the compound (Londry *et al.* 2004; Orphan *et al.* 2001). In order to determine the exact structure of such compounds, they must be present in sufficient quantities to be isolated from other lipid types and specially processed (Allen *et al.* 2010; Oren *et al.* 2009). Due to the extremely low concentrations of fatty acids present in the sediment sub-samples discussed here (Table 3.3), such analyses were not possible. It is for this reason that we sought to characterize inorganic residues attributable to the activity of SRB.

While not present in either LT S12 samples 35_36 or 11_12, dolomite does occur at various depths within the Folly Point core. LT S12 samples 4 (223 cm depth), 27 (230 cm depth), 28 (240 cm depth), 7 (411 cm depth) and 9 (476 cm depth) all contain dolomite at > 1% abundance (see section 3.4.2). In addition, the thin section of sample 4 contains remnant microbial mat layers (Figure A2.2 D) associated with iron oxides (Appendix 2, Figure A2.2 E) and sample 9 contains remnant mat layers interspersed with gypsiferous layers (Appendix 2, Figures A2.7 E and F). Sample 7 does not seem to contain mat material; however, putative fecal pellets (Appendix 2, Figure A2.6 E) could well have provided the carbon required by SRB. Sample 7 also contains gypsum crystals with evidence of dissolution along cleavage planes

(Appendix 2, Figure A2.6 D), which is known as 'etching' (Mbogoro *et al.* 2009). Etched gypsum crystals also appear in samples 11_12 (Figures A2.11 E and F) and 35_36. Taken together, the presence of dolomite, remnant mats, iron oxides and etched gypsum suggests that SRB have been active during deposition of these other samples, but that pyrite was not formed or was re-oxidized. For conclusive proof that SRB were active, an examination of samples containing amorphous FeS and pyrite associated with gypsum crystals was necessary. Sulfides are common components of saline lake sediments, but have been attributed at times to "the breakdown of sulfur-containing amino acids by putrefactive bacteria" (Javor 1989), as opposed to BSR. In order to establish that the pyritization of gypsum had been mediated by SRB, we examined the morphology and isotopic composition of the gypsum and associated iron sulfides in LT S12 samples 11_12 and 35_36.

The phenomenon of iron sulfides within evaporitic matrices is not unique to Lake Tyrrell: sediments from the Prungle Lakes, a part of the dry Willandra Lakes system in the semi-arid region of New South Wales, contain gypsum crystals with iron oxides deposited along the cleavage planes. The presence of these oxides has been attributed to the oxidation of iron sulfides produced as a result of colonization of sediments by SRB (Magee 1991). Iron sulfides associated with evaporitic sequences have also been detected as components of the sediment of the Basin Lakes, two saline volcanic maar lakes in Victoria (Last and DeDeckker 1990), and pyrite-rich laminae occur in the sediments of ephemeral saline lakes within the Coorong region of South Australia (Wright 1999; Wright and Wacey 2005). However, with the exception of the Prungle Lakes gypsum described above, no other examples of pyrites deposited along and within the cleavage planes of gypsum appear in the literature. Framboidal pyrite deposited along the growth faces of ~3.47 Ga baritized gypsum (Shen and Buick 2004; Shen *et al.* 2001) and pyritization along cleavage planes of phyllosilicates deposited under saline lacustrine conditions during the Miocene (Sanz-Montero *et al.* 2009) are the closest analogs – morphologically and geochemically – to the pyritized gypsum in the Lake Tyrrell sediments. In order to understand the cause of the difference in morphology between Prungle and Tyrrell pyrites and pyrites in other saline lake sediments, it is necessary to explore the mechanisms of pyrite formation and deposition in sediments.

Pyrite does not nucleate and precipitate directly from solution – it forms by the successive sulfidation of a series of metastable iron (II) sulfides (Langmuir 1997). Stepwise, it is as follows:

Equation 4.1 $(FeS_{0.9}$ to $FeS_{0.92})$ -> $(FeS_{0.93}$ to $FeS_{0.96})$ -> Fe_3S_4 -> FeS_2
FeS (amorphous) mackinawite greigite pyrite or marcasite

(Schoonen and Barnes 1991)

The initial step – the formation of amorphous FeS – occurs when reduced iron (Fe^{2+}) combines with aqueous sulfur species:

Equation 4.2 Fe^{2+} (aq) + H_2S (aq) -> FeS + $2H^+$ (Schoonen and Barnes 1991)

In order to generate amorphous FeS, sources of aqueous, reduced sulfur and dissolved, reduced iron are required. At Lake Tyrrell, sulfur is present primarily in oxidized form, as dissolved sulfate (SO_4^{2-}) and gypsum ($CaSO_4 * 2H_2O$) (Macumber 1991). SRB are heterotrophs, using dissolved sulfate (in excess) as an electron acceptor for the oxidation of organic matter such as

hydrocarbons, fatty acids, carbohydrates and amino acids. Hydrogen sulfide (H_2S) is a by-product of this reaction, as shown by an example reaction of the oxidation of lactic acid:

Equation 4.3 $2CH_3CHOHCOOH + SO_4^{2-} \rightarrow 2CH_3COOH + H_2S + 2HCO_3^-$

(Langmuir 1997)

In the Lake Tyrrell system, the dissolved, reduced iron can only come from iron oxides within the sediments. Figures A2.11 A, B, and D in Appendix 2 show iron oxides as laminations around voids and as horizons within clay-rich sediments. The morphology of the iron oxides indicates that they have been deposited by groundwater (Brewer 1964). When iron-rich groundwater invades gypsiferous layers, iron oxides form cutans (coatings) around gypsum crystals and other minerals, as seen in Appendix 2, Figure A2.10 E. The bound Fe^{3+} is converted to aqueous Fe^{2+} either through the reducing action of aqueous H_2S released by SRB, or via the activities of dissimilatory metal-reducing bacteria (Posfai and Dunin-Borkowski 2006). The reduced iron scavenges sulfide from the water very rapidly (Javor 1989), localizing the deposition of iron sulfides.

The mineral species that is ultimately formed through the progressive sulfidation of amorphous FeS changes with pH and Eh of environment, temperature, species of oxidizing and reducing agents present, and the iron source (Frankel and Bazylinski 2003). For example, marcasite is most stable at pH < 5, while pyrite is favored at pH > 6, when polysulfide anions are the major species present in solution (Langmuir 1997). Greigite may be absent under reducing conditions, whereas under slightly oxidizing conditions, it may be the only iron sulfide present (Langmuir 1997). The presence of pyrite within the gypsiferous layers in LT S12 samples 35_36 and 11_12 indicate that the pH of the pore waters was likely circumneutral during pyrite deposition, as it is today (Teller *et al.* 1982a).

In contrast, most of the iron sulfides in LT S12 sample 35_36 are amorphous. Taken together with the tight coupling of gypsiferous layers and TOC-rich remnant mat layers in this sample (Appendix 2, Figure A2.10), we may conclude that the rate of sulfidation was insufficient for pyritization to proceed to completion prior to burial of the iron sulfides below the zone inhabited by SRB. Previous studies have indicated that most sulfate-reduction occurs in the top 3 cm of sediment (Jorgensen 1982), so burial below this zone could occur within years assuming that mat growth and burial is a seasonal event. We have worked at Lake Tyrrell during both the wet and dry season, and have noted that microbial mats and associated sulfidic sediment seem most well-developed during the dry season, when a halite crust forms and groundwater is the primary source of water in the lake. During the wet season, precipitation and runoff contribute to the partial or total dissolution of the halite, and clays and quartz sands washed in from the lunette cover the mats. Thus it seems reasonable to assume that the development and burial of the mat-sulfidic sediment system is an annual occurrence in the modern lake, and may well have been so at the time the samples described here were deposited.

The rate of sulfidation of amorphous FeS depends heavily on the species of reduced sulfide present: if hydrogen sulfide or hydrogen bisulfide (HS^-) provides the sulfur, below 100°C reaction rates are so slow as to be insignificant (Schoonen and Barnes 1991). Rates are much faster if metastable sulfur species, such as polysulfides (S^{2-}_n), thiosulfate ($S_2O_3^{2-}$), and polythionate ($S_nO_6^{2-}$) ions, provide the sulfur (Langmuir 1997):

Equation 4.4 $FeS + S^{2-}_n \rightarrow FeS_2 + S^{2-}_{n-1}$

Equation 4.5 $FeS + S_2O_3^{2-} \rightarrow FeS_2 + SO_3^{2-}$

Equation 4.6 $FeS + S_nO_6^{2-} \rightarrow FeS_2 + S_{n-1}O_6^{2-}$

While H_2S and HS^- are the major species of reduced sulfur in organic rich, anaerobic water-logged soils and sediments (Langmuir 1997), elemental sulfur (S°) reacts readily with water to produce polysulfides (pH > 7), thiosulfate (pH > 6) and polythionates (pH < 6) (Schoonen and Barnes 1991). Experiments have demonstrated that elemental sulfur is produced in such sediments through the oxidation of H_2S or HS^- by amorphous iron oxides (FeOOH) (Bottcher *et al.* 2001; Thamdrup *et al.* 1993).

At Lake Tyrrell, goethite (α-FeOOH) is the primary crystal form of iron oxide (Jones et al. 2006). Compared to amorphous iron oxides, high sulfide concentrations are required to convert goethite to amorphous FeS (Langmuir 1997): $1.15x10^{-2}$ moles of FeOOH reduced per kg HS^- at pH 8 for goethite vs. $2.14x10^{-6}$ moles of FeOOH reduced per kg HS^- at pH 8 for amorphous iron oxides/oxyhydroxides. However, in the sulfide-rich zones created by SRB, goethite behaves as a highly reactive iron oxide, with a half-life (time for half of all goethite to be converted to amorphous FeS) of less than one year (Posfai and Dunin-Borkowski 2006). The reaction proceeds as follows:

Equation 4.7 $2\alpha\text{-FeOOH} + 3HS^- + 3H^+ \rightarrow 2FeS + S° + 4H_2O$ (Langmuir 1997)

It should be noted that this reaction produces both of the reactants for pyrite formation, amorphous FeS and elemental sulfur.

The transformation of amorphous FeS to pyrite appears to progress more efficiently in the presence of bacteria than it does under abiogenic conditions (Frankel and Bazylinski 2003). Typically, mineralization proceeds via the localization of amorphous FeS formation on cell surfaces. Ionic interactions between the cation Fe^{2+}, negatively charged (anionic) cellular membrane lipid residues (Douglas and Yang 2002; Frankel and Bazylinski 2003) and H_2S produced during sulfate reduction lead to the precipitation of amorphous FeS, which is then pyritized in the manner described above. These pyrites are found in sediments as framboids, mineralized organic structures such as diatom tests or worm tubes, and occasionally as 'casts' of individual bacterial cells or colonies (Astafieva *et al.* 2005; Douglas 2005; Frankel and Bazylinski 2003; Siesser and Rogers 1976). Pyrites and amorphous FeS within the Lake Tyrrell sediments appear primarily as growths within the cleavage planes of gypsum crystals as seen in Figures 4.1A, 4.2A, and 4.4C. Therefore, some additional process must be contributing to the localization of the iron sulfides within the gypsum crystals.

Gypsum crystals containing iron sulfides in LT S12 sample 35_36 exhibit morphologies consistent with primary deposition (precipitation from the water column, Figures A2.10 A-C and E-H in Appendix 2), while those in LT S12 sample 11_12 are more characteristic of secondary, displacive gypsum (precipitated from groundwaters super-saturated in calcium and sulfate due to evaporation at the capillary fringe of the water table, Figures A2.11 F and G, Appendix 2) (Magee 1991). In both cases, however, saturation of gypsiferous layers by iron-rich groundwater appears to have led to the formation of iron oxide coatings on crystals (Appendix 2, Figure A2.10 E) that were overgrown by subsequent gypsum precipitation. The location of the iron oxides is key to interpreting the morphology of the pyritized gypsum.

SRB have never been shown to scavenge sulfate directly from minerals via bacterially-mediated dissolution. However, both SRB and cyanobacteria, such as those that would have helped to form the remnant mat layers, alkalize their micro-environments to pH values above 8 (Douglas 2004; Douglas and Yang 2002). Above pH 7.9, gypsum is unstable, and dissolution is favored (Douglas 2002 and 2004). In addition, cyanobacteria actively exclude Ca^{2+} ions from their cells and concentrate them at the cell surface, producing microenvironments enriched in calcium on their cell surfaces (Thompson and Ferris 1990). These calcium ions bind with carbonate ions to precipitate carbonates, reducing Ca^{2+} activity to the point that dissolution of gypsum occurs (Thompson and Ferris 1990). The uptake of aqueous sulfate by SRB enhances this process by decreasing the activity of the sulfate ion in the pore water.

Gypsum has been previously shown to dissolve via the formation of 'etch pits' on the crystal's surface (Mbogoro *et al.* 2009). As dissolution proceeds, the size of the pits increases. Dissolution along cleavage planes exposes faces parallel to 010, which contain both ions, as opposed to pyramidal faces containing only Ca^{2+} ions (Magee 1991). In addition, iron oxides originally deposited as cutans around crystals, as described above, would be exposed along the etched cleavage planes. Sulfate ions released from the gypsum matrix would be utilized by the SRB for the oxidation of organics sourced from the overlying mats, and the resulting sulfide would reduce the iron, localizing the precipitation of amorphous FeS within the etched cleavages. Finally, successive sulfidation would lead to the formation of pyrite as previously described. Thus, the morphology of the samples described here may be an inorganic marker for the activity of SRB in neutral-to-acidic saline lakes with high iron content.

Morphology alone, however, does not provide a full picture of the microbial metabolic web that produced the pyrite. The stable sulfur isotope ratios of both the pyrite and the surrounding gypsum yield additional information regarding the types of microbes involved in the sulfur cycle and the geochemistry of the lake waters during precipitation. The average $\delta^{34}S$ of the gypsum in LT S12 sample 11_12 is ~8-10‰ lighter than the values of modern seawater and of gypsum precipitated during evaporative concentration thereof (Raab and Spiro 1991). This value is not unusual once placed in the context of the lake's hydrology and geochemistry. Lake Tyrrell is a closed system with regard to sulfates – they precipitate and re-dissolve, but once sulfate enters the lake water, it does not leave except as an evaporitic precipitate or a sulfide. As has been previously mentioned, the precipitation of gypsum from brine involves fractionation of ~1‰ (Holser and Kaplan 1966), so that the sulfur isotopic composition of gypsum approximates that of the brine from which it precipitated. Factors contributing to the light isotope signature of closed-basin non-marine vs. marine brines are: precipitation and dry fallout of sulfur from the atmosphere (average $\delta^{34}S$ 3-15‰), inflow from rivers which brings light sulfur from pre-modern evaporites or connate brines, and oxidation of pyrites during weathering of shale (Holser and Kaplan 1966). The values of $\delta^{34}S$ of gypsum measured here are very similar to those measured in Dead Sea sulfates (+13.7 to +15‰) (Javor 1989), and may be taken as relatively typical of closed hypersaline environments.

On average, the pyrites within the cleavage planes of gypsum in LT S12 sample 11_12 are ~53‰ lighter than the surrounding gypsum. This fractionation is considerably larger than that found in modern hypersaline environments (Canfield *et al.* 2004; Shen and Buick 2004), and exceeds the maximum fractionation (~45‰) measured in pure cultures and natural populations of 28 different genera of SRB within the delta-proteobacteria and Gram positive bacteria groups (Detmers *et al.* 2001; Frankel and Bazylinski 2003; Valley and Cole 2001). However, it is well within the range of fractionation between sedimentary sulfide and dissolved sulfate found in

contemporary marine and other sedimentary environments (Habicht and Canfield 2001). These extreme fractionations – up to ~60‰ in some environments – indicate that some process in addition to DSR is fractionating sulfur prior to the precipitation of pyrite. The fractionation associated with pyrite formation from dissolved sulfide is on the order of 1‰ (Valley and Cole 2001), so that it is unlikely that abiotic processes are responsible for the discrepancy between maximum measured fractionation by SRB and fractionation between sulfide and sulfate in natural sedimentary systems. It is necessary to invoke an additional biotically-mediated pathway in the sulfur cycle: sulfide oxidation and accompanying disproportionation.

It has been shown that up to 90% of sulfide produced in marine sediments is abiotically re-oxidized to sulfate (Jorgensen 1982). The reaction proceeds in a stepwise manner, resulting in the formation of a number of sulfur compounds of intermediate redox states (Langmuir 1997; Shen and Buick 2004):

Equation 4.8 $H_2S + ½\ O_2 \rightarrow S° + H_2O$

Equation 4.9 $S° + O_2 + H_2O \rightarrow SO_3^{2-} + 2H^+$

Equation 4.10 $SO_3^{2-} + S° \rightarrow S_2O_3^{2-}$

Equation 4.11 $SO_3^{2-} + ½\ O_2 \rightarrow SO_4^{2-}$

Under standard sedimentary conditions, thiosulfate ($S_2O_3^{2-}$) and sulfite (SO_3^{2-}) are metastable with respect to sulfate, and are most abundant near groundwater redox interfaces where they complex with metal cations (Langmuir 1997) or are transformed by microbial oxidation, reduction or disproportionation (Shen and Buick 2004). Microbially-mediated disproportionation reactions occur as follows:

Equation 4.12 $S_2O_3^{2-} + H_2O \rightarrow SO_4^{2-} + HS^- + H^+$ (Bak and Pfennig 1987)

Equation 4.13 $4S° + 4H_2O \rightarrow SO_4^{2-} + 3H_2S + 2H^+$ (Thamdrup et al. 1993)

Equation 4.14 $4SO_3^{2-} + 2H^+ \rightarrow 3SO_4^{2-} + H_2S$ (Valley and Cole 2001)

When iron oxides and oxyhydroxides are readily available, sulfides produced by disproportionation are efficiently removed, driving the reactions further (Bottcher et al. 2001; Thamdrup et al. 1993). The sulfides are depleted in ^{34}S relative to the parent compound by up to ~9‰ (Shen and Buick 2004) – a moderate amount of fractionation. However, it has been demonstrated that highly depleted sulfides are produced when initial DSR is followed by the oxidation of sulfide to intermediate sulfur compounds, which are subsequently disproportionated to sulfate and sulfide (Canfield and Thamdrup 1994). Eventually, extremely light sulfides are produced through sequential cycles of oxidation and disproportionation (Valley and Cole 2001).

As the supply of sulfate in Lake Tyrrell pore waters is effectively infinite (Jones *et al.* 1994), we cannot use a Rayleigh distillation model to explain isotopic compositions of sulfates and sulfides. Species of SRB do not have discrete associated fractionation values – instead, fractionation falls within a range determined by species-specific physiology, sulfate-reduction rate, identity of the electron donor, variable regulation of sulfate-transport across the cell

membrane, external sulfate concentrations, and growth temperature (Detmers *et al.* 2001; Valley and Cole 2001). In addition, as there are multiple disproportionation pathways, knowing the identity of the SRB and the associated fractionation would permit calculation of the extent to which the $\delta^{34}S$ signature of the pyrites is attributable to disproportionation, but would not assist in determining which pathway (and associated organism) is responsible.

4.6 Conclusions

An examination of the morphology, chemistry and isotopic composition of pyrite growths within etched gypsum crystals conclusively demonstrate the existence of an active microbially-mediated sulfur cycle within Lake Tyrrell sediments during the Pleistocene. When the samples examined were being deposited, the lake was hypersaline and likely ephemeral, as it is today. Lake waters saturated with calcium and sulfate precipitated gypsum during the wet season. During the dry season, evaporative concentration of iron-rich groundwaters at the capillary fringe within surficial sediments coated gypsum crystals therein with iron oxide cutans. As gypsum continued to precipitate in the wet season, these cutans were overgrown. Dissolution of gypsum in sediments was driven by the development of the mats: cyanobacteria in these mats concentrated calcium on their cell surfaces, thereby decreasing the ion's activity in pore waters.

As gypsum dissolved via the formation of etch pits along cleavage planes, SRB reduced the sulfate released to sulfide. Due to fractionation imposed by the SRB, the sulfide is depleted in ^{34}S with respect to the sulfate. This depleted sulfide reacts with the iron oxides exposed in the etch pits of the partially-dissolved gypsum crystals, generating Fe^{2+} and S^0. Sulfur-disproportionating bacteria then use the S^0, or the thiosulfate or sulfite produced when S^0 reacts with water (Eqns. 4.9-4.10), to produce sulfate and sulfide. The sulfate is slightly isotopically enriched when compared to the parent S species, whereas the sulfide is further depleted. This depleted sulfide can then become the substrate for another cycle of oxidation and disproportionation. Eventually, when all available iron oxides have been reduced, the isotopically light sulfide combines with reduced iron to precipitate amorphous FeS within etch pits along the cleavage planes of gypsum. Sulfurization of FeS by isotopically light S^0, or the products of its reaction with water (thiosulfate, polythionate or polysulfides, Eqns 4.4-4.6) ultimately produces pyrites heavily depleted in ^{34}S (Figure 4.6).

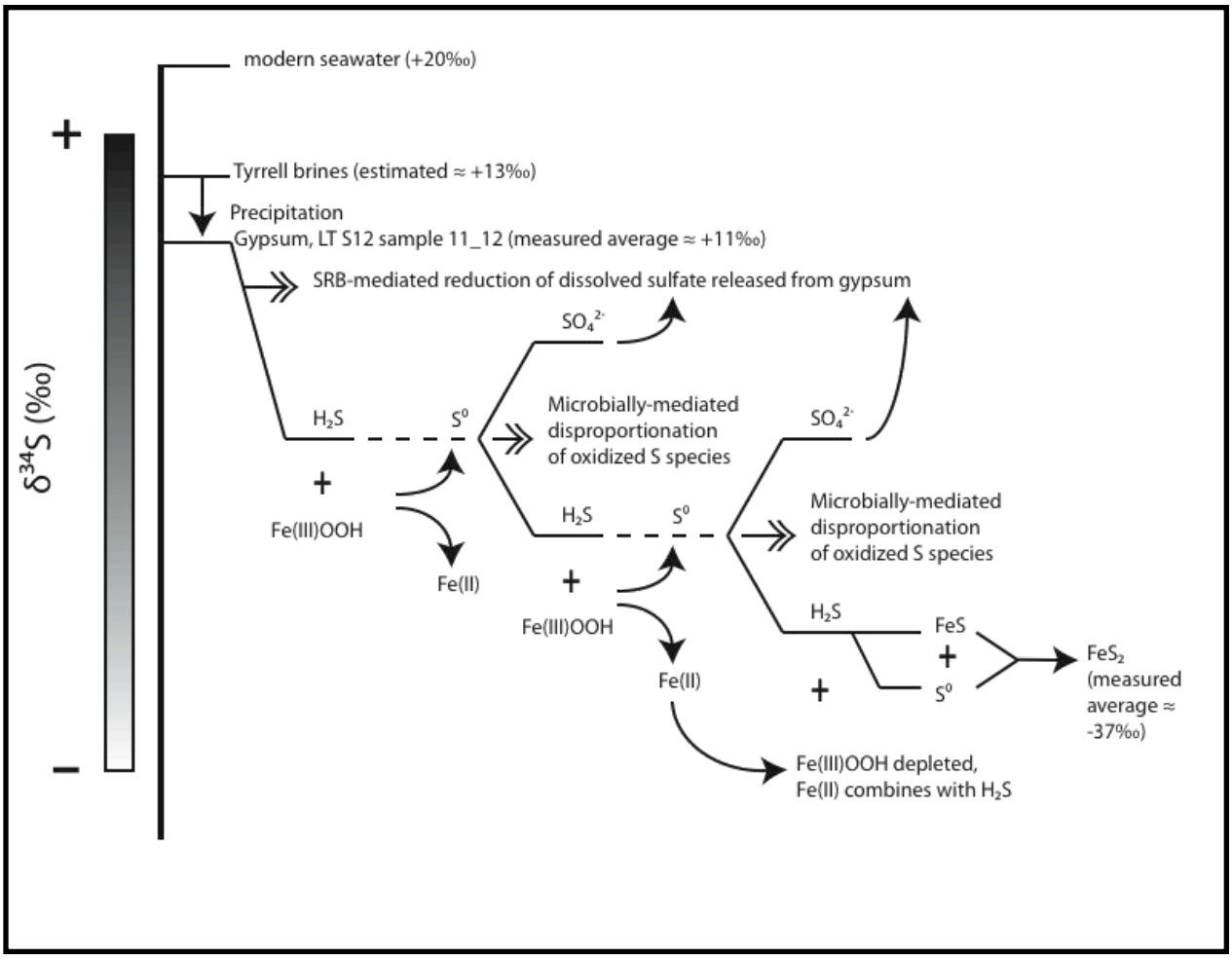

Figure 4.6 Schematic of sulfur cycle operating in Lake Tyrrell sediments during sample deposition

After the initial reduction of sulfate by SRB, isotopic depletion of sulfur species occurs via repeated cycles of abiotic oxidation and bacterially-mediated disproportionation. Single arrows indicate abiotic processes, double arrows indicate biotic processes, plus signs indicate reaction between compounds.

4.7 Acknowledgements

I thank Richard Armstrong for his time and expertise with sample preparation and operation of the SHRIMP for isotopic analyses of the sulfur in both the gypsum and pyrite. John Magee was instrumental in pointing out the existence and possible significance of the pyritized gypsum, specifically with regard to Australian salt lakes.

4.8 References

Allen MA, Neilan BA, B.P. Burns, Jahnke LL, Summons RE (2010) Lipid biomarkers in Hamelin Pool microbial mats and stromatolites *Organic Geochemistry* 41: 1207-1218

Astafieva MM, Rozanov AY, Hoover R (2005) Framboids: their structure and origin *Paleontological Journal* 39: 457-464

Ault WU, Jensen ML, paper presented at the Biogeochemistry of Sulfur Isotopes, Yale University, 1963

Awramika SM, Schopf JW, Walter MR (1983) Filamentous fossil bacteria from the Archean of Western Australia *Precambrian Research* 20: 357-374

Bak F, Pfennig N (1987) Chemolithotrophic growth of *Desulfovibrio sulfodismutans* sp. nov. by disproportionation of inorganic sulfur compounds *Archives of Microbiology* 147: 184-189

Bontognali TRR, Vasconcelos C, Warthmann RJ, Bernasconi SM, Dupraz C, Strohmenger CJ, McKenzie JA (2010) Dolomite formation within microbial mats in the coastal sabkha of Abu Dhabi (United Arab Emirates) *Sedimentology* 57: 824-844

Bottcher ME, Thamdrup B, Vennemann TW (2001) Oxygen and sulfur isotope fractionation during anaerobic bacterial disproportionation of elemental sulfur *Geochimica et Cosmochimica Acta* 65: 1601-1609

Bowler JM, Teller JT (1986) Quaternary evaporites and hydrological changes, Lake Tyrrell, north-west Victoria *Australian Journal of Earth Sciences* 33: 43-63

Brewer R, *Fabric and Mineral Analysis of Soils*. (John Wiley & Sons, New York City, 1964)

Canfield DE, Thamdrup B (1994) The production of 34S-depleted sulfide during bacterial disproportionation of elemental sulfur *Science* 266: 1973-1975

Canfield DE, Sorensen KB, Oren A (2004) Biogeochemistry of a gypsum-encrusted microbial ecosystem *Geobiology* 2: 133-150

Carnerup AM, Hyde ST, Larsson A-K, Christy AG, Gracía-Ruiz JM, in *Life in the Universe: From the Miller Experiment to the Search for Life on Other Worlds,* Seckbach J, Chela-Flores J, Owen T, Raulin F, Eds. (Springer, Berlin, 2005)

Christy AG, Jones C, Ed. (Canberra, 2010)

Crowe DE, Vaughan RG (1996) Characterization and use of isotopically homogeneous standards for *in situ* laser microprobe analysis of 34S/32S ratios *American Mineralogist* 81: 187-193

DeDeckker P, in *Lacustrine Petroleum Source Rocks,* Fleet AJ, Kelts K, Talbot MR, Eds. (Geological Society, 1988a), vol. 40 pp. 45-58

DeDeckker P (1988b) Biological and sedimentary facies of Australian salt lakes *Palaeogeography, Palaeoclimatology, Palaeoecology* 62: 237-270

Detmers J, Bruchert V, Habicht KS, Kuever J (2001) Diversity of sulfur isotope fractionations by sulfate-reducing prokaryotes *Applied and Environmental Microbiology* 67: 888-894

Dickson BL, Giblin AM (2009) Features of acid-saline systems of southern Australia *Applied Geochemistry* 24: 297-302

Douglas S (2004) Microbial biosignatures in evaporite deposits: evidence from Death Valley, California *Planetary and Space Science* 52: 223-227

Douglas S (2005) Mineralogical footprints of microbial life *American Journal of Science* 305: 503-525

Douglas S, Yang H (2002) Mineral biosignatures in evaporites: presence of rosickyite in an endoevaporitic microbial community from Death Valley, California *Geology* 30: 1075-1078

Eldridge CS, Compston W, Williams IS, Walshe JL (1987) *In situ* microanalysis for 34S/32S ratios using the ion microprobe SHRIMP *International Journal of Mass Spectrometry and Ion Processes* 76: 65-83

Fegan NE, Long DT, Lyons WB, Hines ME, Macumber PG (1992) Metal partitioning in acid hypersaline sediments - Lake Tyrrell, Victoria, Australia *Chemical Geology* 96: 167-181

Frankel RB, Bazylinski DA, in *Biomineralization*, Dove PM, DeYoreo JJ, Weiner S, Eds. (Mineralogical Society of America, Washington, D.C., 2003), vol. 54

Habicht KS, Canfield DE (2001) Isotope fractionation by sulfate-reducing natural populations and the isotopic composition of sulfide in marine sediments *Geology* 29: 555-558

Hines ME, Lyons WB, Lent RM, Long DT (1992) Sedimentary biogeochemistry of an acidic, saline groundwater discharge zone in Lake Tyrrell, Victoria, Australia *Chemical Geology* 96: 53-65

Holser WT, Kaplan IR (1966) Isotope geochemistry of sedimentary sulfates *Chemical Geology* 1: 93-135

Ickert RB, Hiess J, Williams IS, Holden P, Ireland TR, Lanc P, Schram N, Foster JJ, Clement SW (2008) Determining high precision, *in situ*, oxygen isotope ratios with a SHRIMP II: Analyses of MPI-DING silicate-glass reference materials and zircon from contrasting granites *Chemical Geology* 257: 114-128

Javor B, *Hypersaline Environments: Microbiology and Biogeochemistry*. Brock TD, Ed., Brock/Springer Series in Contemporary Bioscience (Springer-Verlag, 1989)

Jones BF, Hanor JS, Evans WR (1994) Sources of Dissolved Salts in the Central Murray Basin, Australia *Chemical Geology* 111: 135-154

Jones CM, Allen EE, Giska JR, Welch SA, Kirste D, Banfield JF, in *Goldschmidt*. (Geochimica et Cosmochimica Acta, Melbourne, Australia, 2006), vol. Suppl S70, pp. A297

Jorgensen BB (1982) Mineralization of organic matter in the sea bed - the role of sulphate reduction *Nature* 296: 643-645

Kerrick DM, Eminhizer LB, Villaume JF (1973) The role of carbon film thickness in electron microprobe analysis *American Mineralogist* 58: 920-925

Ku TCW, Walter LM, Coleman ML, Blake RE, Martini AM (1999) Coupling between sulfur recycling and syndepositional carbonate dissolution: evidence from oxygen and sulfur isotope composition of pore water sulfate, South Florida Platform, U.S.A. *Geochimica et Cosmochimica Acta* 63: 2529-2546

Langmuir D, in *Aqueous Environmental Geochemistry*, McConnin R, Ed. (Prentice-Hall, Inc., Upper Saddle River, NJ, 1997)

Last WM, DeDeckker P (1990) Modern and Holocene carbonate sedimentology of two saline volcanic maar lakes, southern Australia *Sedimentology* 37: 967-981

Lith YV, Warthmann R, Vasconcelos C, McKenzie JA (2003) Sulphate-reducing bacteria induce low-temperature Ca-dolomite and high Mg-calcite formation *Geobiology* 1: 71-79

Lith YV, Vasconcelos C, Warthmann R, Martins JCF, McKenzie JA (2002) Bacterial sulfate reduction and salinity: two controls on dolomite precipitation in Lagoa Vermelha and Brejo do Espinho (Brazil) *Hydrobiologia* 485: 35-49

Londry KL, Jahnke LL, Marais DJD (2004) Stable carbon isotope ratios of lipid biomarkers of sulfate-reducing bacteria *Applied and Environmental Microbiology* 70: 745-751

Long DT, Lyons WB, Hines ME (2009) Influence of hydrogeology, microbiology and landscape history on the geochemistry of acid hypersaline waters, N.W. Victoria *Applied Geochemistry* 24: 285-296
Long DT, Fegan NE, Lyons WB, Hines ME, Macumber PG, Giblin AM (1992) Geochemistry of acid brines - Lake Tyrrell, Victoria, Australia *Chemical Geology* 96: 33-52
Macumber PG (1991) "Interaction between groundwater and surface systems in Northern Victoria", doctoral dissertation, Geology Department, School of Earth Sciences, Melbourne University
Magee JW (1991) Late Quaternary lacustrine, groundwater, aeolian and pedogenic gypsum in the Prungle Lakes, southeastern Australia *Palaeogeography, Palaeoclimatology, Palaeoecology* 84: 3-42
Mbogoro MM, Edwards MA, Unwin PR, in *Goldschmidt*. (Geochimica et Cosmochimica Acta, Davos, Switzerland, 2009), vol. 73, pp. A854
Oren A, Sorensen KB, Canfield DE, Teske AP, Ionescu D, Lipski A, Altendorf K (2009) Microbial communities and processes within a hypersaline gypsum crust in a saltern evaporation pond (Eilat, Israel) *Hydrobiologia* 626: 15-26
Orphan VJ, House CH, Hinrichs KU, McKeegan KD, DeLong EF (2001) Methane-consuming archaea revealed by directly coupled isotopic and phylogenetic analysis *Science* 293: 484-487
Posfai M, Dunin-Borkowski RE, in *Sulfide Mineralogy and Geochemistry*, Vaughan DJ, Ed. (Geochemical Society/Mineralogical Society of America, 2006), vol. 61 pp. 679-708
Raab M, Spiro B (1991) Sulfur isotopic variations during seawater evaporation with fractional crystallization *Chemical Geology* 86: 323-333
Rasmussen B (2000) Filamentous microfossils in a 3,235-million-year-old volcanogenic massive sulphide deposit *Nature* 405: 676-679
Runnegar B, in *Geological Society of America Annual Meeting*. (GSA, 2001), pp. 166-170
Runnegar B, Coath CD, Lyons JR, McKeegan KD, in *Goldschmidt* GCA, Ed. (Geochimica et Cosmochimica Acta, 2002), vol. 66, pp. A655
Sanchez-Roman M, McKenzie JA, Wagener AdLR, Rivadeneyra MA, Vasconcelos C (2009) Presence of sulfate does not inhibit low-temperature dolomite precipitation *Earth and Planetary Science Letters* 285: 131-139
Sanz-Montero ME, Rodriguez-Aranda JP, Perez-Soba C (2009) Microbial weathering of Fe-rich phyllosilicates and formation of pyrite in the dolomite precipitating environment of a Miocene lacustrine system *European Journal of Mineralogy* 21: 163-175
Schoonen MAA, Barnes HL (1991) Reactions forming pyrite and marcasite from solution: II. Via FeS precursors below 100C *Geochimica et Cosmochimica Acta* 55: 1505-1514
Schopf JW (1993) Microfossils of the early Archean Apex Chert: new evidence of the antiquity of life *Science* 260: 640-646
Seckbach J, *Life As we Know It*. Seckbach J, Ed., Cellular Origins, Life in Extreme Habitats and Astrobiology (Springer, 2006) vol. 10
Shen Y, Buick R (2004) The antiquity of microbial sulfate reduction *Earth Science Reviews* 64: 243-272
Shen Y, Buick R, Canfield DE (2001) Isotopic evidence for microbial sulphate reduction in the early Archaean era *Nature* 410: 77-81
Siesser WG, Rogers J (1976) Authigenic pyrite and gypsum in South West African continental slope sediments *Sedimentology* 23: 567-577

Teller JT, Bowler JM, Macumber PG (1982a) Modern sedimentation in Lake Tyrrell, Victoria, Australia *Journal of the Geological Society of Australia* 29: 159-175
Teller JT, Bowler JM, Macumber PG (1982b) Modern Sedimentation and Hydrology in Lake Tyrrell, Victoria *Journal of the Geological Society of Australia* 29: 159-175
Thamdrup B, Finster K, Hansen JW, Bak F (1993) Bacterial disproportionation of elemental sulfur coupled to chemical reduction of iron or manganese *Applied and Environmental Microbiology* 59: 101-108
Thompson JB, Ferris FG (1990) Cyanobacterial precipitation of gypsum, calcite, and magnesite from natural alkaline lake water *Geology* 18: 995-998
Valley JW, Cole DR, Eds., *Stable Isotope Geochemistry*, vol. 43 (Mineralogical Society of America, Washington D.C., 2001)
Vasconcelos C, McKenzie JA, Bernasconi S, Grujic D, Tien AJ (1995) Microbial mediation as a possible mechanism for natural dolomite formation at low temperatures *Nature* 377: 220-222
Warthmann R, Lith Yv, Vasconcelos C, McKenzie JA, Karpoff AM (2000) Bacterially induced dolomite precipitation in anoxic culture experiments *Geology* 28: 1091-1094
Wright DT (1999) The role of sulphate-reducing bacteria and cyanobacteria in dolomite formation in distal ephermeral lakes of the Coorong region, South Australia *Sedimentary Geology* 126: 147-157
Wright DT, Wacey D (2005) Precipitation of dolomite using sulphate-reducing bacteria from the Coorong region, South Australia: significance and implications *Sedimentology* 52: 987-1008

Chapter 5.

An analysis of changes in plant communities in SE Australia through the late Pleistocene and Holocene using pollen, charcoal and $\delta^{13}C$ of plant biomarkers (long chain *n*-alkanes) from sediments of hypersaline Lake Tyrrell

5.1 Abstract

Climate change in south-eastern Australia over the past ~22 ka has been broadly characterized by increasing aridity. Since European colonization 200 years ago, climate-based changes to regional water budgets have been over-printed (and at times, exacerbated) by anthropogenic factors. Therefore, studies of ecosystem changes that occurred prior to modern settlement are valuable in that they can help us to determine the impact of climate change on a system in the absence of human intervention. In the current study, we use the pollen, charcoal, plant waxes, isotopic and mineralogical records of the top 135 cm of sediment deposited in the northern basin of Lake Tyrrell, Victoria, over the past ~10 ka to explore changes in a regional plant community caused by shifts in climate, and by modern land use. Two abrupt shifts in the isotopic signal of plant waxes, the first to heavier values and the second to lighter values, are correlated with changes in the mineralogy and lipid abundance patterns. The initial shift, at about 90 – 60 cm depth, may correspond to an increased dominance of C_4 shrubs during a wet period from 9.5 – 7.5 ka. The more recent shift, from 10 – 1 cm depth, is possibly due to the overwhelming predominance of C_3 plants in more modern times (<500 years BP) as a result of livestock grazing and farming.

5.2 Introduction

5.2.1 Reconstructing climate in Australia, Last Glacial Maximum (LGM) – present, through studies of changes in plant community composition

As discussed in chapter 2, many palaeo-climate reconstructions for Australia are biased toward data gathered from offshore marine sediment cores due to the paucity of inland sampling sites. In order to understand regional changes across the continent, terrestrial records are needed, and lake basins can be excellent repositories of such records (Magee *et al.* 2004). In addition to preserving information about conditions within the lake, lake-bed sediments contain material derived from the broader catchment, so that changes in regional conditions can be distinguished from those which are merely local (as discussed in chapter 2, also (Barnett 1994; Gell *et al.* 1994; Kershaw *et al.* 2003). Vascular plant communities composed of trees, shrubs and grasses, are useful proxies for regional climate: their composition reflects growth conditions, and they produce abundant organic matter which can be preserved over geologic time scales.

Species-level information is generally not preserved; however, the relative abundance of C_3 vs. C_4 plants in a community can provide valuable information on growth conditions. The primary factors controlling the distribution of C_3 vs. C_4 plants on the Australian continent are geographic – growth season temperature and light intensity (Kershaw 1986). C_3 plants, which include some grasses and nearly all trees, shrubs, and forbs (Johnson *et al.* 1999), favor the cool-temperate climes found south of the summer-winter rain boundary (Figure 1.2). By contrast, C_4 plants, which include most grasses and some sedges (Sage and Monson 1999), favor warm

growing seasons, moderate to high light intensity, and a summer monsoonal influence, such as that in the northern part of the continent (Johnson *et al.* 2005).

In addition to the primary controlling factors, there are secondary factors. These include climatic variables – precipitation variability (Kershaw 1986), drought – as well as soil characteristics, biotic disturbances (grazing pressure, disease) and frequency and intensity of fire (Johnson *et al.* 2005; Turney *et al.* 2001). When palaeo-climate studies are carried out, generally a single site with a known geographic location (relative to precipitation regimes) is reconstructed through time. Therefore, secondary factors become most influential in determining plant community composition. Extensive studies of plant community shifts at Lake Eyre, in the south-central part of the continent, have shown that the relative abundance of C_4 grasses can be correlated with the relative strength or weakness of the Australian (summer) monsoon (Johnson *et al.* 1999; Johnson *et al.* 2005). Johnson *et al* (1999) used the stable carbon isotope signature of plants preserved in emu eggshells to show that a near-total absence of C_4 grasses during the LGM is due to a pronounced weakening in the monsoon. More recently, Johnson *et al* (2005) found a 20% reduction in C_4 plant biomass in emu diets, as recorded in $\delta^{13}C$ signature of eggshells deposited over the last 200 years. At Lake Eyre, C_4 plants are mostly grasses, with some chenopods, and C_3 plants are the dominant chenopods, shrubs, trees and forbs. As the shift is large in magnitude and matches the timescale of European colonization, the authors concluded that over-grazing of C_4 grasses by kangaroos and livestock, drought, and changes in fire regimes in late 1890s (Johnson *et al.* 2005) caused the reduction in C_4 plant biomass. It is worth noting from these two studies that the magnitude of changes in plant communities at Lake Eyre over the past 200 years is analogous to that which occurred during LGM (~21000 years ago) (Johnson *et al.* 2005), indicating major changes in arid zone ecology after European settlement.

Thus, plant community shifts can point to changes in climate, or to the effects of human settlement and land use change.

5.2.2 Utility of stable carbon isotopic measurements of plant materials in palaeo-climate studies

The stable carbon isotopic signature of plant waxes records information about the temperature, aridity and wind strength of the environment in which the plant grew and in which the biomarker was transported and deposited (Eglinton and Eglinton 2008). In addition, $\delta^{13}C$ of plant waxes depends on the isotopic composition of atmospheric CO_2, the biosynthetic pathway employed during photosynthesis (C_3 or C_4), light intensity and edaphic properties (soil conditions: texture, whether nutrient rich or poor, TOC content, etc.) (Johnson *et al.* 2005).

In Australia, winter rains favor the growth of daisies and herbaceous C_3 plants, whereas summer rains favor the growth of C_4 grasses (Johnson *et al.* 1999). C_4 plants are adapted to lower pCO_2, higher temperatures and greater aridity (Eglinton and Eglinton 2008), so that a shift in dominance in a plant community from C_3 to C_4 (and *vice versa*) is a consequence of a shift in climate or weather patterns. Such a shift can be investigated using stable carbon isotope analysis of the residual plant material: average $\delta^{13}C$ values for lipids derived from C_4 grasses are -22‰ (±4‰), whereas for those derived from C_3 plants the values are nearer to -36‰ (±4‰) (Rommerskirchen *et al.* 2006). Plant tissue is isotopically heavier than plant lipids. The average plant tissue $\delta^{13}C$ for C_4 plants is -13‰ (±10‰); for C_3 plants it is -27‰ (±12‰) (Johnson *et al.* 2005).

5.2.3 Contributions of higher plants to the proxies used for climate reconstruction: lipids, pollen and charcoal

Plant leaf waxes can act as terrigenous biomarkers, recording changes in type of vegetation colonizing the land around a lake or marine basin. Plant waxes prominently include long-chain (24-36 C atoms) *n*-alkanes, *n*-alkanols, and *n*-alkanoic acids. Higher plants produce a strong odd C number preference in their alkanes, and a strong even C number preference for alkanols and alkanoic acids. This is because the *n*-alkanes are formed in the plant by the loss of a single C atom from the precursor *n*C+1 alkanoic acid in a decarboxylation reaction (Eglinton and Eglinton 2008).

n-alkanes, which are present in high abundance in the epicuticular waxy coatings of higher plants, make good biomarkers: they are water insoluble, not very volatile, chemically inert, and resistant to biodegradation (Eglinton and Eglinton 2008; Meyers and Ishiwatari 1993). They can also travel long distances as aerosols from fires, and on leaf fragments. In addition, the isotopic composition, particularly of the carbon, remains constant through time, since covalent C-C bonds are very difficult to break in the absence of large inputs of energy, radical attack or specific enzymatic action (Eglinton and Eglinton 2008). Due to their chemical stability, their abundance in Tyrrell sediments, and their ease of isolation and isotopic measurement as a compound class, long chain (>25 C atoms) *n*-alkanes were selected as the compounds for analysis in the current work.

In addition to lipids, plants produce pollen, which are transported by wind, water, or insect activity and are incorporated into sediments. Pollen are stable in sediments over thousands to millions of years (Luly 1990), and have been used in many palaeoenvironmental studies to track vegetation change through time (Kershaw *et al.* 2003; Luly 1993; Schwark *et al.* 2002). Furthermore, pollen type has been shown to correlate closely with the distribution of *n*-alkanes in sediments, such that mean carbon number of the *n*-alkane can be used to predict whether grasses or trees and shrubs have been the dominant source of material in sediments (Fishera *et al.* 2003; Meyers 2003; Schwark *et al.* 2002): C_4 plants (most of which, in Australia, are grasses or chenopods) produce a suite of odd C number *n*-alkanes with nC_{31} and nC_{33} in highest abundance, whereas C_3 plants (such as trees and shrubs, as well as some grasses) produce a suite of odd C number *n*-alkanes with nC_{29} and nC_{31} in highest abundance. At Lake Tyrrell, pollen input is dictated by wind regimes (which affect input) and rainfall (which affects the distribution of source plants) (Luly 1990).

Shifts in plant communities can occur gradually, as the result of climate change, or instantly, as the result of catastrophic events such as fire. Evidence of palaeo-fire in sediments includes charcoal and biomarkers generated during the combustion of vegetation. Charcoal particles are divided into two classes: macroscopic and microscopic. Macroscopic charcoal analysis provides information on fire regimes close to the source of the charcoal; in addition, it can provide information on the types of plants that have burned through analysis of fragment morphology (Conedera *et al.* 2009). Microscopic charcoal analysis is complementary in that it can provide information on fire regimes further from the sample location; thus it can be correlated to some extent with pollen analyses (depending on wind regime) and with biomarkers diagnostic for combustion (Conedera *et al.* 2009; Elias *et al.* 2001).

Biomarkers of burning include polycyclic aromatic hydrocarbons (such as retene), phenolic compounds and breakdown products of cellulose, such as levoglucosan and mannosan (Simoneit 2002). However, all of these except levoglucosan can be produced by methods other than burning of live plant material, for example by the combustion of coal, hydrolization of

original material in soils, and possibly by bacterial breakdown of some compounds (Masran and Pocock 1981; Simoneit 2002). Levoglucosan has been shown to correlate reliably with other markers of burning within sediments, such as charcoal, over timescales relevant for this study (LGM – present) (Elias et al. 2001). In addition, as previous work has shown the consistent presence of grasses within the catchment through the Holocene (Luly 1993), and as levoglucosan is sourced from the burning of cellulose (a primary component of grasses), then we may reasonably expect burning in the catchment to be reflected in the deposition of levoglucosan to the lake sediments.

5.2.4 Sedimentary sequences of Lake Tyrrell, LGM – present

Late Pleistocene and Holocene sedimentary sequences of Lake Tyrrell have been extensively described by previous workers (Bowler and Teller 1986; Luly 1993; Luly *et al.* 1986; Teller *et al.* 1982). Briefly, they are as follows: from 22 ka – 15 ka at the time of the last glacial maximum, deflation of the lakebed led to lunette building, so that there is a time gap in the lakebed sediment sequence at about 135 – 140 cm depth (Luly *et al.* 1986). Above this disconformity, there are broadly three sedimentary units. Unit 3 comprises ~5 cm of greenish sandy clay and detrital gypsum directly above the disconformity. It has been carbon dated to approximately 10 ka, though it may be older as the authors admitted the possibility of contamination of bulk-dated samples by young carbon (Luly *et al.* 1986). Unit 2 is the largest of the three units, extending from 20 – 120 cm depth and covering ~3 ka – 7 ka. It is composed of a laminated gypsum-clay unit, with textural indications of having been precipitated directly from lake water (Luly *et al.* 1986). Unit 1 extends from beneath the surface salt crust to ~20 cm depth, with a maximum age of ~2 ka, and is composed of grey clays containing large quantities of displacive gypsum (Luly *et al.* 1986).

Regrettably, Lake Tyrrell sediments are very low in organic carbon (typically less than 0.2% by weight), so that bulk carbon dating can be rendered inaccurate. Recently, more accurate carbon dates, obtained from lipids extracted from the lake sediment, have become available for the top 13 cm of sediment. These show that sediments from just below the surface salt to ~3.5 cm depth are modern (less than 500 years old), those from 4.5 – 7.5 cm are ~500 years old, and those at and below 8.5 cm rapidly increase in age with depth from ~1 ka to ~ 7 ka (Bray *et al.* 2010). The discrepancy between the dates obtained by Bray *et al* (2010) and those obtained by Luly *et al* (1986) may well be due to the difference in techniques, or to difference in sampling sites, as sedimentation across the basin is unlikely to be constant. As the samples used in the Bray *et al* (2010) study derive from the southern part of the lake basin, while those obtained by Luly *et al* (1986) derive from the northern part of the basin, near the sampling site discussed in this work, the Luly *et al* (1986) chronology and sedimentary descriptions will be used to provide context to the current study.

5.3 Samples and methods

5.3.1 Study sites and sample collection

A shallow (135 cm) sediment core was collected from the northern basin of the lake (Site 12 on Figure 2.1) during March 2006. Shallow coring was performed using a Dormer soil auger (stainless steel, 50 mm internal diameter; Dormer Soil Samplers, NSW Australia). The auger was twisted into the lakebed, and sediment retrieved was sub-sampled at 3 cm intervals for the top 6

cm, then at 5 cm intervals to 20 cm depth, and finally at 10 cm intervals to the base, in order to capture the full range of mineralogies present.

Samples of salt crust and microbial mats overlying the sediment were collected from Site 12 in August 2006 using metal spatulas cleaned with methanol. Samples were stored in baked glass jars, capped with baked aluminum foil, and kept at 4°C until processing.

5.3.2 Total organic carbon (TOC) analysis of sediments

Samples for TOC analysis were taken in parallel with lipid sub-samples. These were subsequently lyophilized in a freeze-drier, then crushed and homogenized in a mortar and pestle cleaned with 5% nitric acid. Carbonates were removed by sulfurous acid treatment and TOC analysis was performed on a Leco CS-444 (accuracy of +/- 0.01% in comparison to standards, detection limit of 0.05%, replicates run periodically to check for precision).

5.3.3 Analysis of charcoal in sediments

Sediment samples were lyophilized in a freeze-drier, then crushed and homogenized in a mortar and pestle cleaned with methanol. 4 mL of each sample was retained for pollen and charcoal analyses; the remainder was processed for lipid extraction (see below). Half of each 4 mL subsample was processed and analyzed for microscopic charcoal (defined as wood and plant materials smaller than 125 μm in diameter) and pollen, and half for macroscopic charcoal (defined as wood and plant materials larger than 125 μm in diameter). Analysis of microscopic charcoal and pollen slides is ongoing, and will not be discussed further.

Preparation of sub-samples for macroscopic charcoal analysis proceeded as follows: 2 mL of each sediment subsample was placed in a 50 mL falcon tube. To remove excess salt from samples, de-ionized water was added in excess, and tubes were inverted several times and allowed to sit overnight so that particulates would settle, after which the water was decanted. To remove carbonate particles, 5% sodium hexametaphosphate in de-ionized water was added in excess (>3:1 by volume) to each tube; tubes were inverted several times and the contents allowed to settle overnight. After decanting, sodium hypochlorite (NaClO or bleach) was added in excess (>3:1 by volume) to each tube to bleach out dark, non-charcoal particulates. Tubes were inverted several times and the contents allowed to settle overnight.

Sediments were washed through sequential 250 μm and 125 μm mesh filters with excess water, and the two size fractions of each sample were placed in separate petri dishes and examined with a standard binocular microscope at 125x magnification. After charcoal were counted in each of the two size fractions for each sample, the fractions were re-combined and retained in falcon tubes with a small amount of water.

5.3.4 Mineralogical analysis

Sediment samples were prepared for x-ray diffraction analysis as described in chapter 2.

5.3.5 Lipid extraction and fractionation

Sediment and algal mats were lyophilized in a freeze-drier, then crushed and homogenized in a mortar and pestle cleaned with methanol. Homogenized samples were extracted using a Dionex ASE (DCM:MeOH 9:1 v/v, 100°C, 1000 p.s.i., 5 cycles), as described in chapter 2. Salt was extracted using a modified Bligh-Dyer technique (Bligh and Dyer 1959; Volkman *et al.* 1997).

After passing extracts through pipette columns of activated copper to remove sulfur, extracts were evaporated to dryness under a stream of pure N_2 gas and re-dissolved in a known volume of DCM. An aliquot of 25% of each sediment extract was preserved as total lipid extract (TLE) for archival purposes at -20°C, and the remainder was used for subsequent analyses. To simplify the TLE of mat and salt extracts, 50% of the underivatized TLE was saponified using the method of Volkman *et al.* (1998). We aliquoted 25% of the saponified neutral lipid fraction (TSN) for further derivatization.

To separate *n*-alkanes from the TLE of sediment extracts and TSN of mat and salt extracts, extracts were passed through dry-packed silica gel columns using a solvent sequence of 1.5 dead column volumes (DV) of *n*-hexanes to elute the saturated lipids, 2 DV of 4:1 *n*-hexanes:DCM (v/v) to elute the aromatic lipids, and ~2.5 DV of 1:1 DCM/MeOH (v/v) to elute the polar lipids. An internal quantification standard (18-methyl eicosanoic acid methyl ester, 18-MEAME) was added to polar and aromatic fractions, which were subsequently derivatized with BSTFA. After examination on the GC-MS for the presence of levoglucosan, these fractions were retained at -20°C for archival purposes. Saturate fractions were evaporated to dryness under a stream of pure N_2 gas and re-dissolved in 35 μL of DCM. 3-methyl-heneicosane (aC_{22}) was added as a standard for quantification, and samples were analyzed by GC-MS.

Parallel to samples, five laboratory blanks were performed, two of which were solvent-only and three using combusted sand (baked at 450°C for 9 hours). These were carried through all steps, from lyophilization to GC-MS analysis.

5.3.6 Instrumental analysis and compound quantification

Lipid samples were analyzed using gas chromatography-mass spectrometry (GC-MS). An Agilent 6890 series gas chromatograph was coupled to a Micromass Waters Autospec Premier magnetic sector mass spectrometer. The MS source was operated at 260°C in EI+ mode at 70 eV ionization energy and with 8000 V acceleration voltage. Samples were injected at 40°C on a PTV injector for 0.1 minutes onto a DB-5 MS column (57.5 m x 0.25 mm i.d.; 0.25 μM film thickness), heated to 300°C at 10°C per second, and held at 300°C for 1.5 minutes. The GC oven temperature was programmed at 40°C (hold time 4 minutes), heated to 315°C at 4°C/minute, then held for 20 minutes. Helium was used as the carrier gas with a flow rate of 1 mL per minute for all samples.

Data acquisition on the mass spectrometer was performed in full scan mode (*m/z* 55-600, 0.7 s cycle time, interscan delay of 0.2 s). Compounds were identified by comparison with mass spectra and chromatographic data in the literature, and using the NIST 2.0 (2005) MS library. Individual compound concentrations were estimated using uncorrected GC-MS peak areas relative to aC_{22}. Total yields (of each extract) were estimated by summing the integration of all peaks in chromatogram. Absolute quantification was deemed unnecessary, as the purpose was to compare yields between samples and to determine whether samples contained sufficient quantities of compounds of interest to be amenable to isotopic analysis.

5.3.7 Isotopic analysis of individual n-alkanes

$\delta^{13}C$ values of individual *n*-alkanes were determined by gas chromatography-isotopic ratio mass spectrometry (GC-IRMS). The analytical system included an Agilent 6890 gas chromatograph interfaced via a Thermo Fisher Scientific GC Combustion III to a Thermo Fisher Scientific MAT 253 isotope-ratio mass spectrometer. All samples were dissolved in *n*-hexanes and injected on column in splitless mode. Helium was used as the carrier gas, and the GC

capillary column was a J&W Scientific DB-5 MS column (30 m x 0.25 mm i.d.; 0.25 μM film thickness). Samples were injected at 45°C on a Gerstel Cold Injection System CIS4 GC injector for 0.08 minutes, heated to 305°C at 10°C per second, and held at 305°C for 1.5 minutes. The GC oven was programmed at 60°C for 2 minutes, heated to 300°C at 3°C/minute, and held at the final temperature for up to 10 minutes. CO_2 gas pulses were introduced at the beginning and at the end of each GC run as a reference gas to determine the delta values of the samples. Calibration and correction for instrument drift was performed using Schimmelmanns' certified B2-Standard and a house standard mixture, which were measured between the runs. All isotopic ratios are expressed in per mil relative to the Vienna Pee Dee Belemnite (V-PDB) standard.

5.4 Results

5.4.1 Results of mineralogical and TOC analyses

Results of x-ray diffraction and total organic carbon analyses of shallow core sediments and surface samples are presented in Table 5.1. Unlike the deep core samples described in chapters 2 and 3, shallow core sediments did not contain detectable quantities of iron oxides, muscovite, magnesite or calcite. As with the deep core samples, evaporites were composed predominantly of gypsum and halite. Small quantities of dolomite (<7%) were present in samples CJ07_026 and CJ07_027; celestite appeared in minute amounts (1.5%) in one sample, CJ07_022. Detrital minerals comprised quartz, with minor amounts of alkali and plagioclase feldspars (<5% total). The clay component was primarily illite, with associated kaolinite and an unidentified clay component. Overall, clay content increases downcore as detritals decrease, and evaporite content ranges from ~20-80%.

Table 5.1 Mineralogy of Lake Tyrrell S12 shallow core samples[a]

Units	Sample name	Sample depth (cm)	TOC[b]	Evaporites	Other minerals (detrital)[c]	Clays
Unit 1	LT S12 salt	0	nm	nm	nm	nm
	B06015A	1	1.27	nm	nm	nm
	S12 Core 1A	1-3.5	nm	nm	nm	nm
	CJ07_020	3.5-6.5	0.07	59.1±0.7	33.9±0.8	7.0±1.5
	S12 Core 1B	6.5-10	nm	nm	nm	nm
	CJ07_021	10-15	0.05	64.7±0.6	27.9±0.3	7.5±1.3
	S12 Core 1C	15-21	nm	nm	nm	nm
	CJ07_022	21-30	0.05	79.7±1.4	14.4±0.3	6.0±1.7
Unit 2	S12 Core 1D	30-40	nm	nm	nm	nm
	CJ07_024	40-50	0.19	42.3±0.7	13.4±0.2	44.3±1.4
	S12 Core 1E	50-60	nm	nm	nm	nm
	CJ07_025	60-70	0.12	30.5±0.5	13.5±0.7	56.0±2.5
	S12 Core 1F	70-80	nm	nm	nm	nm
	CJ07_026	80-90	0.12	19.9±0.6	15.8±0.6	64.4±1.3
Unit 3	S12 Core 1G	90-100	nm	nm	nm	nm
	CJ07_027	100-110	0.21	39.9±0.7	12.7±0.7	47.4±1.9
	S12 Core 1H	110-120	nm	nm	nm	nm
	CJ07_028	120-135	nm	63.6±0.8	7.9±0.8	28.5±1.0

[a]All mineral amounts and errors in weight %, errors are 1 sigma (estimated standard deviation); normalized to eliminate amorphous content - see explanation in text, chapter 2

[b]TOC reported as wt% of sediment, measurement error 0.01%

[c]detrital minerals include quartz, plagioclase and alkali feldspars

nm = not measured

5.4.2 Results of charcoal analysis

No macroscopic charcoal particles were found in any of the sediment samples examined. Analyses of microscopic charcoal and pollen are ongoing.

5.4.3 Results of lipid biomarker analysis

n-alkanes of chain lengths > 25 carbons are present in both modern material (salt and mats) and sediments from the core, albeit in greater abundance in modern material than at depth (see Figure 5.1). As would be expected for samples experiencing input from higher plants, alkanes with an odd number of carbons are present in much greater abundance than those with an even number of carbons. In both the modern material and the core sediments, nC_{31} is the most abundant *n*-alkane (see Figures 5.1 and 5.2).

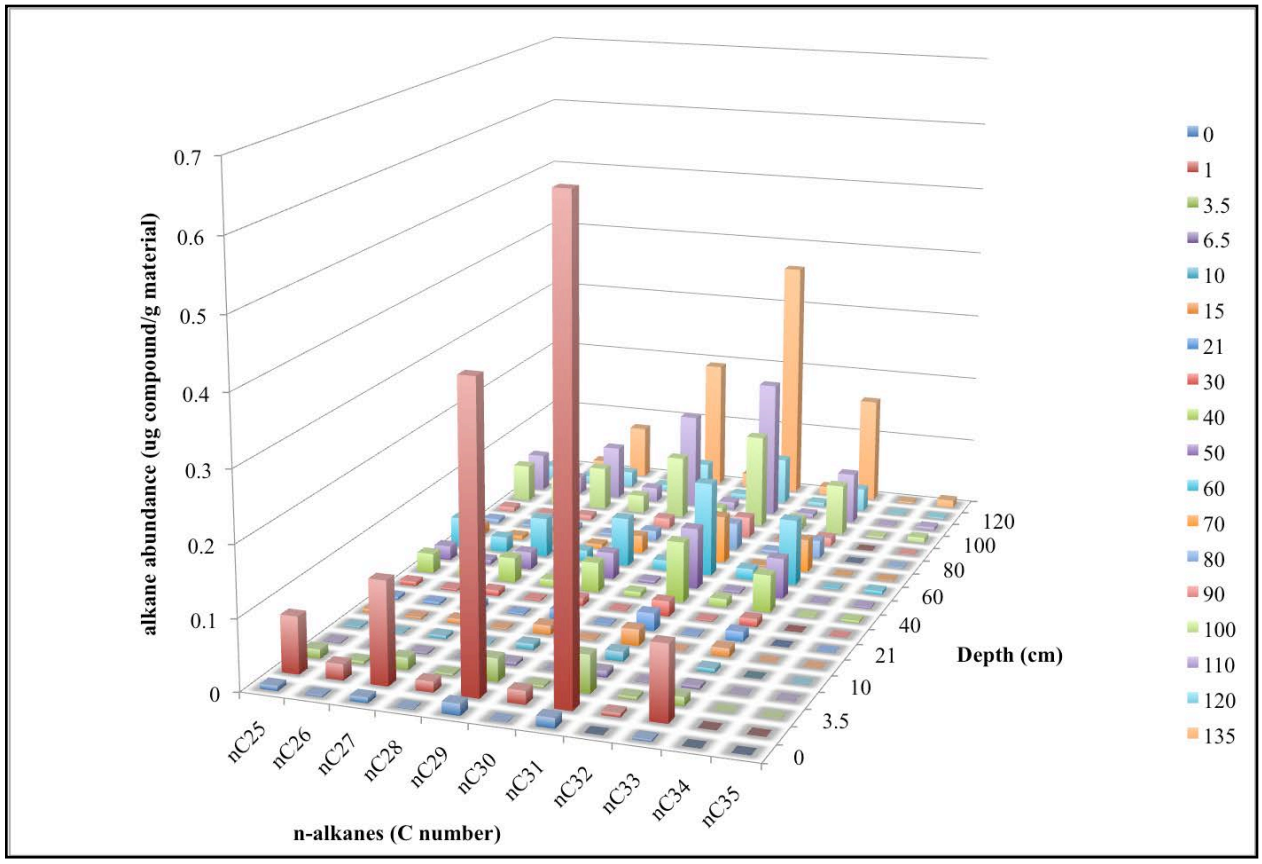

Figure 5.1 Abundance of long chain *n*-alkanes in salt, mats and sediments from Site 12 shallow core

Legend shows depth of sample in cm. Depths given are those at base of sample section; sampling is continuous.

5.4.4 Results of isotopic analysis

Stable C isotope values range from approximately -25‰ to -33‰ (Figure 5.2). Generally, values of nC$_{25}$, nC$_{27}$, and nC$_{29}$ track together, and those of nC$_{31}$ and nC$_{33}$ track together, with the second group possessing more negative values. Values are relatively constant, with the exception of two excursions: the first appears between 90 to 60 cm depth, where delta values of nC$_{25\text{-}29}$ become heavier by ~2‰ (Figure 5.2). Delta values of nC$_{31\text{-}33}$ remain relatively constant over this interval (-28 to -29‰). The second excursion appears between 10 cm depth and the surface, over which interval all compounds show an isotopic shift of negative 4-5‰. Although the concentration of individual compounds varies through the core (0.005 – 0.65 μg/g), the relative abundances of the *n*-alkanes with respect to each other remain constant, with the exception of a shift in abundance of nC$_{33}$ to nC$_{29}$ (Figure 5.2).

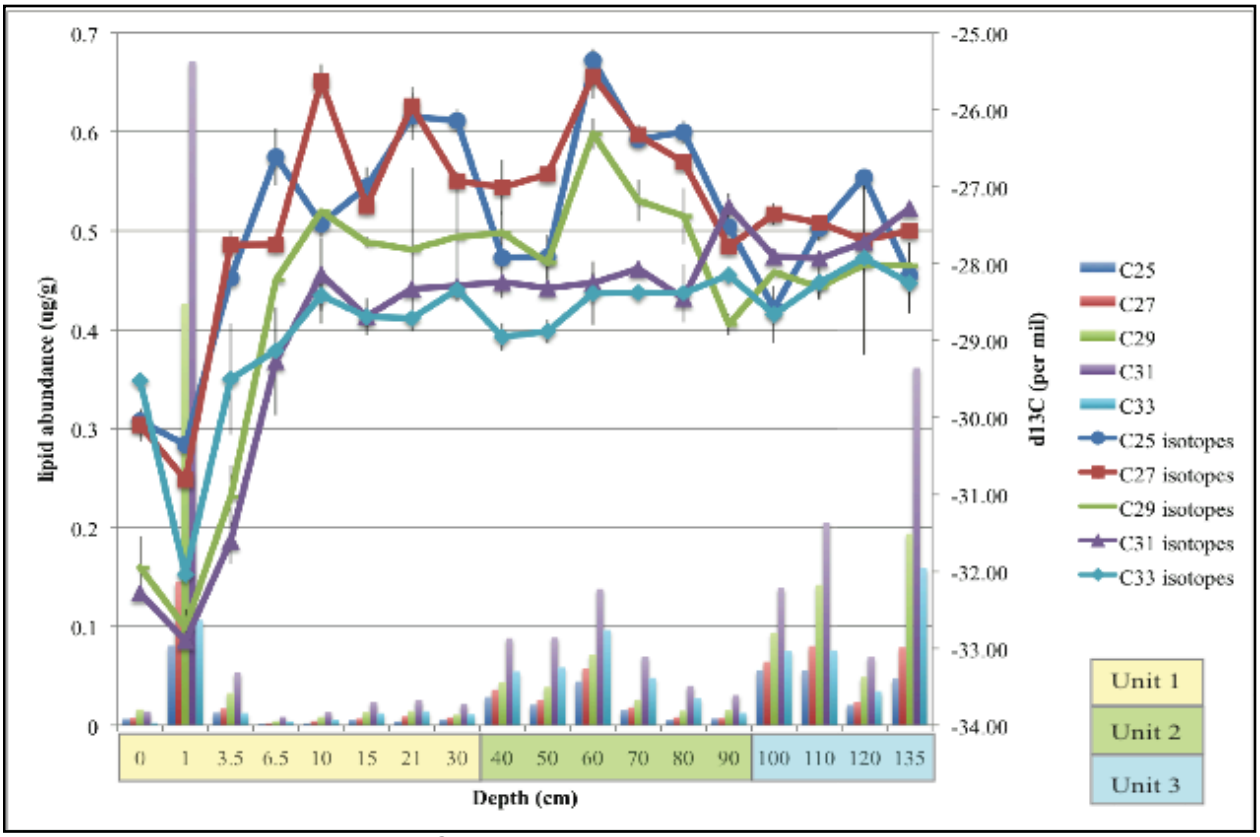

Figure 5.2 Abundance and $\delta^{13}C$ values of odd-carbon-number *n*-alkanes (nC_{25}-nC_{33}) in salt, mats and sediments from S12 shallow core

Stable carbon isotope values are averaged from two measurements; error bars are the standard deviations of these measurements. Depths given are those at base of sample section; sampling is continuous.

5.5 Discussion

The motivation for this work was to determine whether, by the integration of information gleaned from multiple proxies, it was possible to determine the relative dominance of C_3 vs. C_4 plants in the Lake Tyrrell catchment from the last glacial maximum to the present. In analyzing the abundance and distribution of long chain *n*-alkanes, the $\delta^{13}C$ values of these alkanes, the provenance and abundance of charcoal and pollen, and the mineral content of sediment samples, we would be able to distinguish changes resulting from catastrophic or discrete events, such as fire and/or human settlement, from those of a more gradual nature, such as those resulting from climate change.

As sub-samples for pollen and microscopic charcoal have not yet been analyzed, we must examine pollen and microscopic charcoal data from samples collected at corresponding depths and geographic locations (<2 km distance away) to those discussed here. Luly (1990,1993) extracted pollen and charcoal from 5 mm thick slices of a 132 cm long core taken at the center of Lake Tyrrell's northern basin. Sampling was continuous from 0 – 10 cm depth, and spaced in 5 mm intervals from 10 – 132 cm. He described four distinct pollen 'units' broadly correlated with sedimentary units that had been dated in a previous study (Luly *et al.* 1986). LT2-4, also referred to as Unit 3, extends from the base of the core to 100 cm depth. It was deposited between 10000

– 6600 years BP, and is composed of green massive clays from which charcoal and callitris pollen are absent. Casuarina and grass (Poaceae) pollen dominate this unit (Luly 1993) (Figure 5.3). LT2-3, also referred to as Unit 2, extends from 100 – 40 cm depth. It was deposited between 6600 – 2200 years before present, and is typified by primary gypsum-clay laminae, with a layer of massive selenite crystals at the base. The abundance of charcoal decreases from the bottom to the top of the unit. The pollen spectrum contains primarily callitris (a type of tree) and chenopod pollen, where the abundance of callitris increases as the charcoal abundance decreases. Smaller quantities of casuarina, eucalypt, grass and asterid pollen are also present (Figure 5.3). LT2-2, also referred to as Unit 1, extends from 40 – 10 cm depth. It was deposited between 2200 – 800 years BP, and is composed of pale, oxidized clays containing abundant displacive gypsum. Charcoal was present in only trace quantities, with pollen spectra dominated by casuarina and asterid (daisy) pollen (Luly 1993) (Figure 5.3). LT2-1, also referred to as Unit 1, extends from 10 cm depth to the surface. It was deposited over the last 800 years, and is composed of dark grey clays containing abundant sulfides, high quantities of microscopic charcoal and abundant grass and chenopod pollen, along with smaller quantities of eucalypt and casuarina pollen (both of which are trees) (Luly 1993) (Figure 5.3). For clarity of discussion, we have designated LT2-2 as Unit 1B, and LT2-1 as Unit 1A.

From these data, we can construct a model of local and regional rainfall and fire frequency, to provide context for the data gathered in the present study. According to Luly (1993), Unit 3 represents ephemeral lake conditions. The abundance of casuarina and grass pollen indicates an open woodland living under extremely dry conditions: in modern environments, casuarina colonize drier environments than do eucalypts. This stage of regional and local conditions likely represents a gradual return to lacustrine conditions following the extreme aridity that accompanied the LGM (Luly 1993).

Unit 2 was deposited during a period much wetter than that of today. According to Luly (1993), the lake would have been permanent (several meters in depth), requiring an annual volume of rainfall >2.5x that of today. Dense callitris thickets co-existed with Mallee eucalypt vegetation. Callitris is not very fire-tolerant, unlike the Mallee eucalypt; this may explain why its pollen increases in abundance as charcoal abundance decreases through time. As callitris is adapted to wetter soils than Mallee eucalypts, it is probable that the two tree types were geographically segregated, such that the callitris grew on lower, clay-rich soils nearer the lake, and the eucalypts colonized drier, sandy soils at greater distance from the lake (Luly 1993).

Unit 1B represents a dry lake phase, when conditions in lake bed sediments were oxidizing. Luly (1993) postulates that decreased rainfall favored colonization by drought-tolerant casuarina and eucalypts, creating a slightly denser woodland where asterids, as opposed to grasses, were the groundcover. Fire frequency was lower, despite the drier conditions, probably as a result of decreased fuel load. Unit 1A approximates modern conditions: chenopod shrubland covers the lunette that surrounds an ephemeral lake; Mallee eucalypts are the dominant tree, and woodland is fairly sparse so that grasses are abundant. These grasses create an abundant fuel load, so that fires are frequent (Luly 1993; Noble 1980).

The core from which samples were collected in this study covers approximately the same depth interval as Luly's (1993) core. Unit 3 extends from 135 – 90 cm and contains high quantities of both clays and evaporites (Table 5.1). Despite being deposited under drier conditions (as indicated by the relative abundance of evaporites to clays), Unit 3 contains both high quantities of TOC and high *n*-alkane abundances (Table 5.1 and Figure 5.1). However, if this unit corresponds to Luly's Unit 3 or to the selenite crystal layer at the base of his Unit 2, as it

seems to do, these values are not as surprising. Ephemeral lakes can be quite productive (see the TOC values for the modern mat sample, taken from the modern ephemeral lake, in Table 5.1), and if burial rate outstrips oxidation, the organic carbon would be preserved. Unit 2 extends from 90 – 30 cm and is dominated by clays (Table 5.1). Unit 2 has slightly lower TOC values and *n*-alkane abundances than Unit 3, but they are higher than those of Unit 1 (Table 5.1 and Figure 5.1). This may be attributable to wetter lake conditions (as indicated by the relative abundance of clays) providing an environment amenable to the preservation of organic carbon. This unit seems to correspond to Luly's Unit 2. As it was not possible to sub-divide more recent sediments based on mineralogy (Table 5.1), they are grouped together and termed Unit 1, extending from 30 cm depth to the surface. Unit 1 is dominated by evaporites and has, with the exception of the mat and salt samples at the surface, extremely low TOC values (Table 5.1) and correspondingly low abundances of *n*-alkanes (Figure 5.1). This is likely due to the effects of oxidation inherent in an ephemeral or dry lake setting (Johnson and Calder 1973; Meyers and Ishiwatari 1993). This unit likely corresponds to Luly's Units 1A and 1B.

In addition to lipid abundance shifts across the units, there are shifts in the distribution of lipids. Unit 3 contains *n*-alkane distributions and isotopic signatures characteristic of a relatively even mixture of C_3 and C_4 plants: alkane isotopic values of -28‰ are the average of C_3 (-34‰) and C_4 (-22‰) values, and remain fairly constant throughout the unit and for each *n*-alkane (Figure 5.2). As nC_{29} is present in greater abundance than nC_{33} (Figure 5.3), it is possible that there were slightly more C_3 plants relative to C_4. The pollen data support this: levels of eucalypt pollen are lower, and those of casuarina and grass pollen are higher (Figure 5.3). As previously described, C_3 plants are more adapted to a winter rain regime and cooler temperatures, comparable to conditions that prevailed toward the end of the last glacial period (18 – 16 ka (Bowler 1976)).

Although *n*C31 is always the most abundant *n*-alkane (Figures 5.1 and 5.2), the second most abundant compound changes. In Units 3 and 1, it is nC_{29}, while in Unit 2, it is nC_{33} (Figures 5.2 and 5.3). Another way to examine this shift is the nC_{33}/nC_{29} ratio: it shifts from <1 in Unit 3, to >1 in Unit 2, then returns to <1 in Unit 1 (Figure 5.3). As C_4 grasses are known to produce primarily nC_{31} and nC_{33}, and C_3 grasses preferentially produce nC_{29} and nC_{31} homologues (Rommerskirchen *et al.* 2006), it is likely that the change in the nC_{33}/nC_{29} ratio is the result of a change in the relative abundance of C_3 vs. C_4 grasses. Plant input into Lake Tyrrell is primarily windborne, so that grass blades (which are small and easily transported) are over-represented in lake sediments relative to other plant materials (Luly 1997). Further supporting the theory that grasses are the dominant signal is the stable isotopic data: delta values for the $nC_{25–29}$ alkanes become heavier by ~3‰ between 90 and 60 cm depth in Unit 2, while at the same time, the nC_{33}/nC_{29} ratio increases to >1 (Figures 5.2 and 5.3). Together, these data demonstrate the increased contribution of C_4 grasses to this pool of *n*-alkanes. As C_4 grasses are adapted to a summer rain regime, it is likely that the deposition of Unit 2 is correlated with a return to wetter conditions and a strengthened Australian monsoon subsequent to the LGM. Periods of increased rainfall in southeastern Australia since the LGM have been constrained as 13.5 – 11.5 ka (Gingele *et al.* 2007), 9.5 – 7.5 ka (Gingele *et al.* 2007) or alternately 10 – 6 ka (Bowler and Teller 1986). It is likely that Unit 2 represents this most recent wet period, since it is unclear that the core chronology would extend to the previous wet period.

While there is some 'spread' in the delta values of different *n*-alkanes in Unit 1, the most prominent feature of the record is the ~4‰ shift to lighter isotopic values between 10 – 1 cm depth. This shift affects all *n*-alkanes equally and without regard to concentration (Figure 5.2),

and indicates an extreme shift in favor of C_3 plants. The magnitude of this shift is likely due to a combination of a return to a natural dominance of C_3 grasses during a return to drier conditions and winter rain regimes, and to the more recent arrival of European settlers. Grazing pressure on C_4 grasses and the planting of C_3 crops may have exacerbated a climate-induced trend.

No macroscopic charcoal or levoglucosan was detected in any of the samples. This indicates that burning, at least in the immediate vicinity of the lake, is not a major factor in precipitating plant community change. Therefore, the isotopic shifts indicate changes in plant community structure that more likely resulted from climatic and anthropogenic factors. Further investigations of the microscopic charcoal and pollen content of the LT Site 12 shallow core samples should yield more complete information on the nature of these structural changes, as well as expanding the geographic range of the signal.

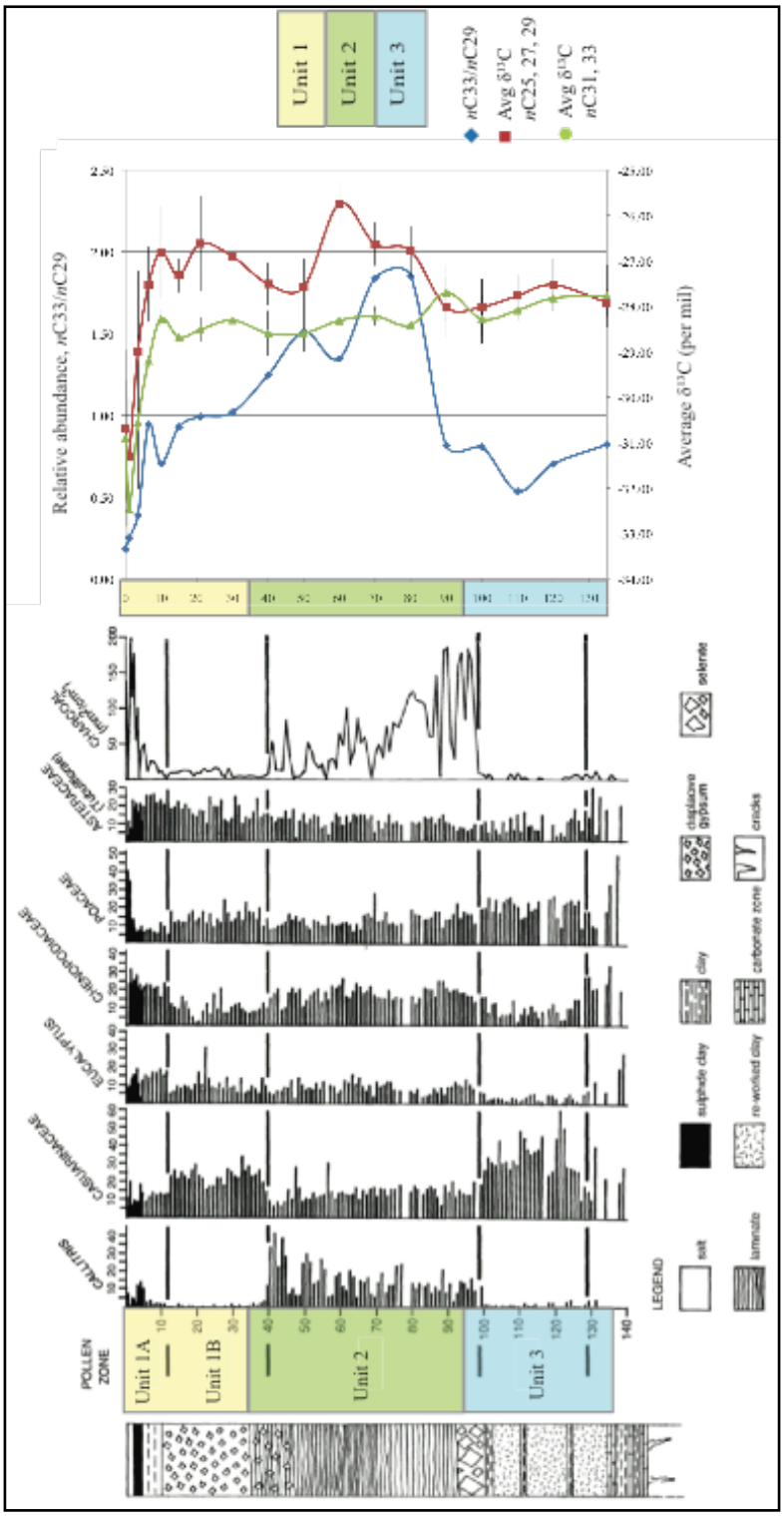

Figure 5.3 Shifts in lipid abundance and isotopic signature correlated with changes in the plant community at Lake Tyrrell over the past ~10 ka

Core schematic and pollen and charcoal abundances adapted from Luly, 1993. His core section numbers have been changed from LT 2-1, 2-2, 2-3 and 2-4 to Unit 1A, 1B, 2 and 3, respectively, in order to facilitate comparison with the core described in this work.

5.6 Conclusions

Changes in plant community structure in the vicinity of Lake Tyrrell can be described based on the integration of mineralogical, palynological, lipid and isotopic data. The relative abundance of C_3 vs. C_4 plants can be estimated from the delta values and distributions of individual *n*-alkanes. Shifts in abundance can be attributed to climatic or anthropogenic factors, based upon time constraints gleaned from the mineralogy of the samples and from correlation with other models of palaeo-climate. Thus, we can define three distinct depositional periods during the Holocene, corresponding to three different plant communities. Finally, we can see that anthropogenic alterations to the natural Holocene vegetation have exacerbated the ascendance of C_3 over C_4 plants, causing a change in the ecosystem that exceeds in magnitude that which occurred during the last major climate shift. Therefore, it is clear that land use practices must now take into account both the effects of climate change and of human habitation.

5.7 Acknowledgements

The author would like to thank Jon Luly for conversations about the pollen content of Lake Tyrrell's Holocene sediments, Mat Prebble for assistance with the preparation of samples for macroscopic charcoal analysis, Ulrike Troitzsch for assistance with preparation and analysis of samples for XRD analysis, Bernd Kopke and Juergen Rullkotter for stable carbon isotope analysis of alkanes, and Janet Hope for assistance with operation of the GC-MS for quantification of *n*-alkanes.

5.8 References

Barnett EJ (1994) A Holocene paleoenvironmental history of Lake Alexandria, South Australia *Journal of Paleolimnology* 12: 259-268

Bligh EG, Dyer WJ (1959) A rapid method of total lipid extraction and purification *Canadian Journal of Biochemistry and Physiology* 37: 911-917

Bowler JM (1976) Aridity in Australia: age, origins and expression in aeolian landforms and sediments *Earth Science Reviews* 12: 279-310

Bowler JM, Teller JT (1986) Quaternary evaporites and hydrological changes, Lake Tyrrell, north-west Victoria *Australian Journal of Earth Sciences* 33: 43-63

Bray PS, Jones CM, Fallon S, Brocks JJ, George SC, paper presented at the Australian Organic Geochemistry Conference, Canberra, Australia, 2010

Conedera M, Tinner W, Neff C, Meurer M, Dickens A, Krebs P (2009) Reconstructing past fire regimes: methods, applications, and relevance to fire management and conservation *Quaternary Science Reviews* 28: 555-576

Eglinton T, Eglinton G (2008) Molecular proxies for paleoclimatology *Earth & Planetary Science Letters* 275: 1-16

Elias VO, Simoneit BRT, Cordeiro RC, Turcq B (2001) Evaluating levoglucosan as an indicator of biomass burning in Carajas, Amazonia: A comparison to the charcoal record *Geochimica et Cosmochimica Acta* 65: 267-272

Fishera E, Oldfield F, Wake R, Boyle J, Appleby P, Wolff GA (2003) Molecular marker records of land use change *Organic Geochemistry* 34: 105-119

Gell PA, Barker PA, DeDeckker P, Last WM, Jelicic L (1994) The Holocene history of West Basin Lake, Victoria, Australia; chemical changes based on fossil biota and sediment mineralogy *Journal of Paleolimnology* 12: 235-258

Gingele F, Deckker PD, Norman M (2007) Late Pleistocene and Holocene climate of SE Australia reconstructed from dust and river loads deposited offshore the River Murray Mouth *Earth & Planetary Science Letters* 255: 257-272

Johnson BJ, Miller GH, Fogel ML, Magee JW, Gagan MK, Chivas AR (1999) 65,000 years of Vegetation Change in Central Australia and the Australian Summer Monsoon *Science* 284: 1150-1152

Johnson BJ, Miller GH, Magee JW, Gagan MK, Fogel ML, Quay PD (2005) Carbon isotope evidence for an abrupt reduction in grasses coincident with European settlement of Lake Eyre, South Australia *The Holocene* 15: 888-896

Johnson RW, Calder JA (1973) Early diagenesis of fatty acids and hydrocarbons in a salt marsh environment *Geochimica et Cosmochimica Acta* 37: 1943-1955

Kershaw AP (1986) Climatic change and Aboriginal burning in north-east Australia during that last two glacial/interglacial cycles *Nature* 322: 47-49

Kershaw P, Moss P, Van der Kaars S (2003) Causes and consequences of long-term climatic variability on the Australian continent *Freshwater Biology* 48: 1274-1283

Luly JG (1990) "A pollen analytical investigation of Holocene palaeoenvironments at Lake Tyrrell, semi-arid northwestern Victoria, Australia", Department of Biogeography & Geomorphology, Research School of Pacific Studies, Australian National University

Luly JG (1993) Holocene palaeoenvironments near Lake Tyrrell, semi-arid northwestern Victoria, Australia *Journal of Biogeography* 20: 587-598

Luly JG (1997) Modern pollen dynamics and surficial sedimentary processes at Lake Tyrrell, semi-arid northwestern Victoria, Australia *Review of Palaeobotany and Palynology* 97: 301-318

Luly JG, Bowler JM, Head MJ (1986) A Radiocarbon Chronology from the Playa Lake Tyrrell, Northwestern Victoria, Australia *Palaeogeography, Palaeoclimatology, Palaeoecology* 54: 171-180

Magee J, Miller G, Spooner N, Questiaux D (2004) Continuous 150 k.y. monsoon record from Lake Eyre, Australia: Insolation-forcing implications and unexpected Holocene failure *Geology* 32: 885-888

Masran TC, Pocock SAJ, in *Organic Maturation Studies and Fossil Fuel Exploration*, Brooks J, Ed. (Academic Press, New York, 1981), pp. 145-159

Meyers PA (2003) Applications of organic geochemistry to paleolimnological reconstructions: a summary of examples from the Laurentian Great Lakes *Organic Geochemistry* 34: 261-289

Meyers PA, Ishiwatari R (1993) Lacustrine organic geochemistry - an overview of indicators of organic matter sources and diagenesis in lake sediments *Organic Geochemistry* 20: 867-900

Noble JC, in *Aeolian Landscapes in the Semi-Arid Zone of South-Eastern Australia*, Storrier RR, Kelly ID, Eds. (Australian Soil Science Society, Riverina Branch, Wagga Wagga, 1980), pp. 143-144

Rommerskirchen F, Plader A, Eglinton G, Chikaraishi Y, Rullkoetter J (2006) Chemotaxonomic significance of distribution and stable carbon isotopic composition of long-chain alkanes and alkan-1-ols in C4 grass waxes *Organic Geochemistry* 37: 1303-1332

Sage RF, Monson RK, Eds., *C4 Plant Biology* (Elsevier, 1999)

Schwark L, Zink K, Lechterbeck J (2002) Reconstruction of postglacial to early Holocene vegetation history in terrestrial Central Europe via cuticular lipid biomarkers and pollen records from lake sediments *Geology* 30: 463-466

Simoneit BRT (2002) Biomass burning - a review of organic tracers for smoke from incomplete combustion *Applied Geochemistry* 17: 129-162

Teller JT, Bowler JM, Macumber PG (1982) Modern Sedimentation and Hydrology in Lake Tyrrell, Victoria *Journal of the Geological Society of Australia* 29: 159-175

Turney CSM, Kershaw AP, Moss P, Bird MI, Fifield LK, Cresswell RG, Santos GM, Di Tada ML, Hausladen PA, Zhou Y (2001) Redating the onset of burning at Lynch's Crater (North Queensland): implications for human settlement in Australia *Journal of Quaternary Science* 16: 767-771

Volkman JK, Farmer CL, Barrett SM, Sikes EL (1997) Unusual dihydroxysterols as chemotaxonomic markers for microalgae from the order Pavlovales (Haptophyceae) *Journal of Phycology* 33: 1016-1023

Appendix 1. Initial description of Lake Tyrrell S12 core/Folly Point core

A1.1 Summary stratigraphic cross-section of core with sample names and depths

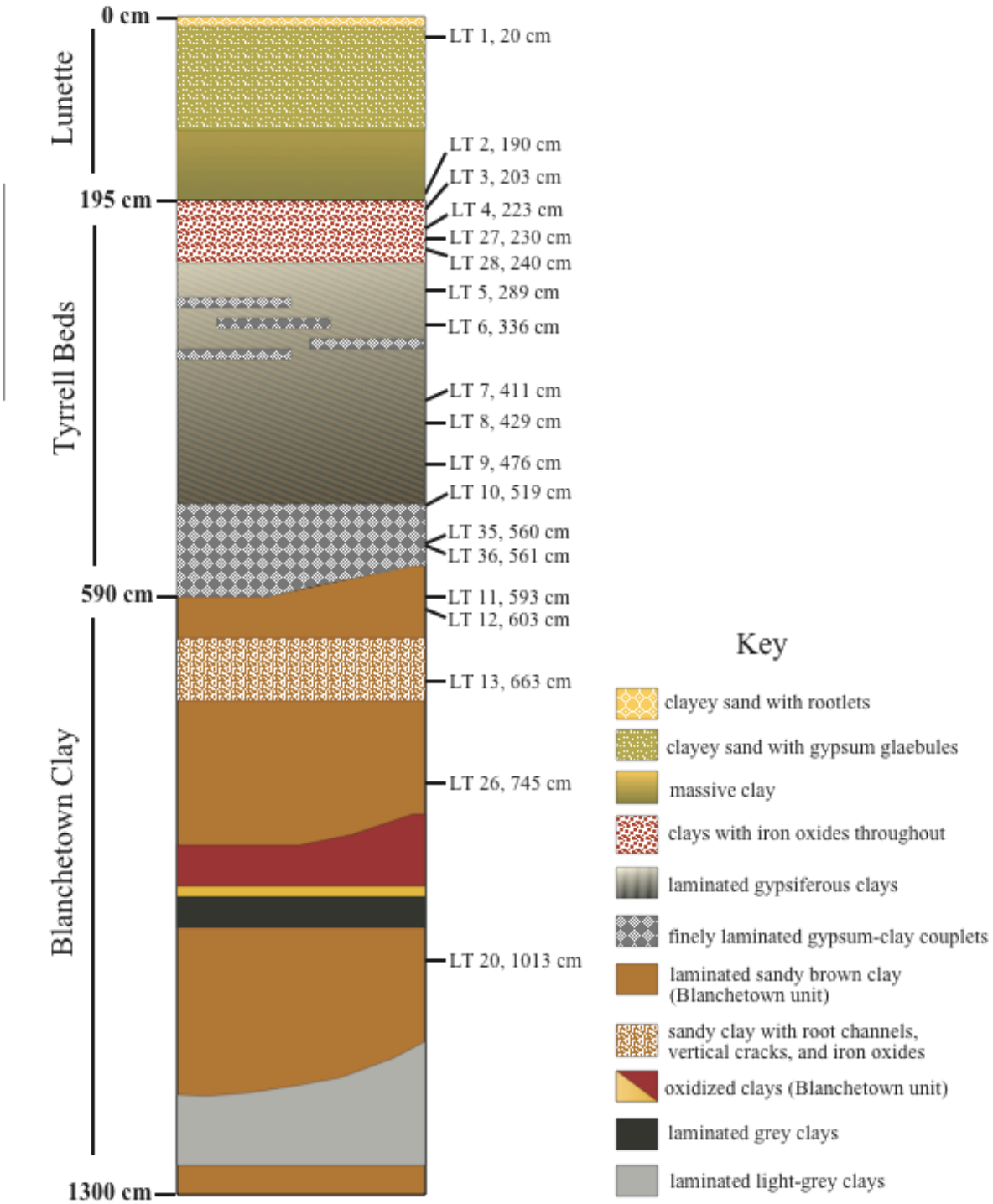

A1.2 Detailed core stratigraphy

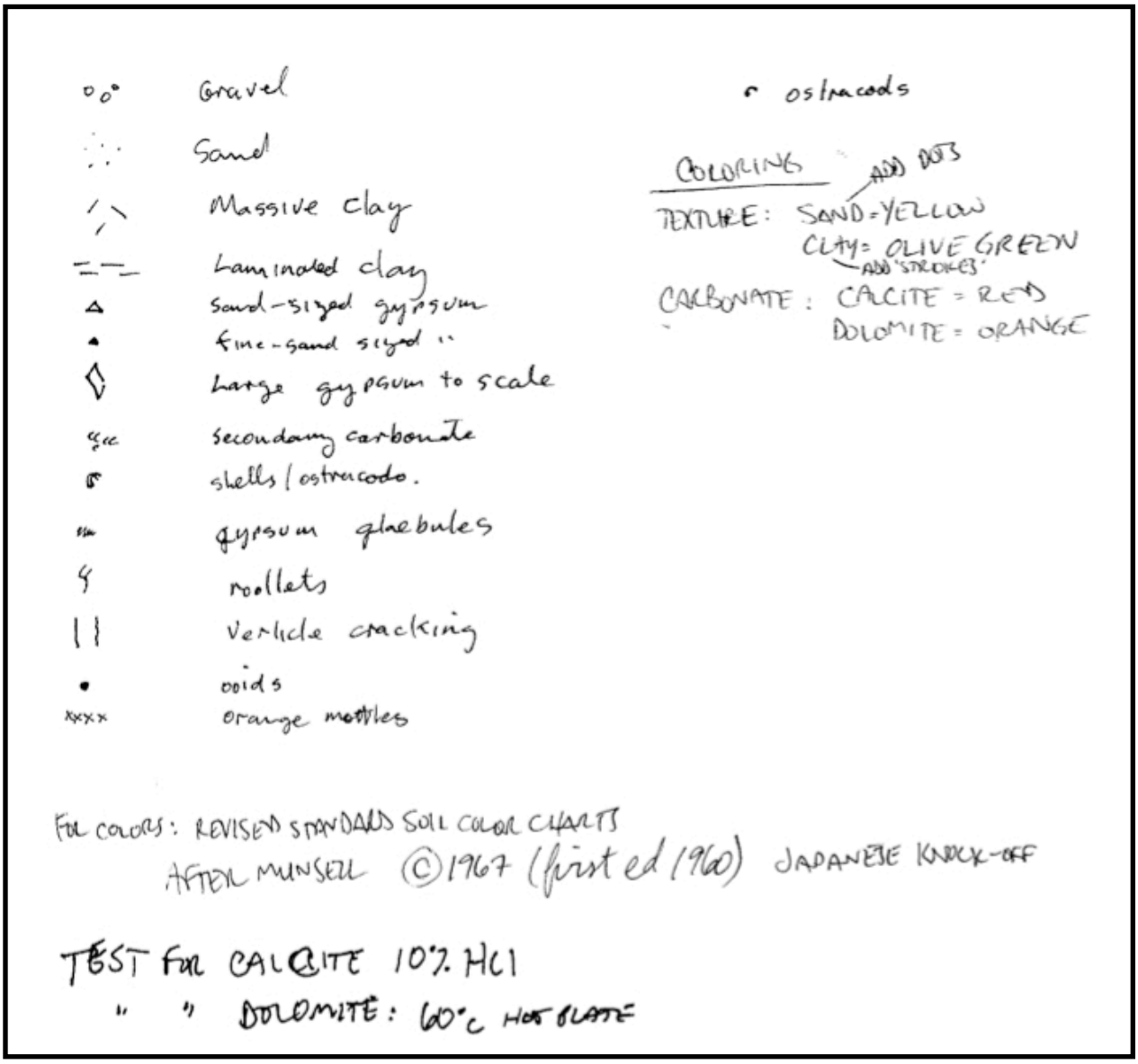

Note: sampling sites within core are indicated as follows*

Lipid sample – pink box
Total organic carbon sample – blue box
Thin section sample – orange box with diagonal blue stripe
Collaborator's sample – lime green box
Pollen sample – dark green box

*Dimensions of boxes relative to diagram approximately equal vertical and horizontal dimensions of subsample relative to the core. Depths (to left of core descriptions) are in cm.

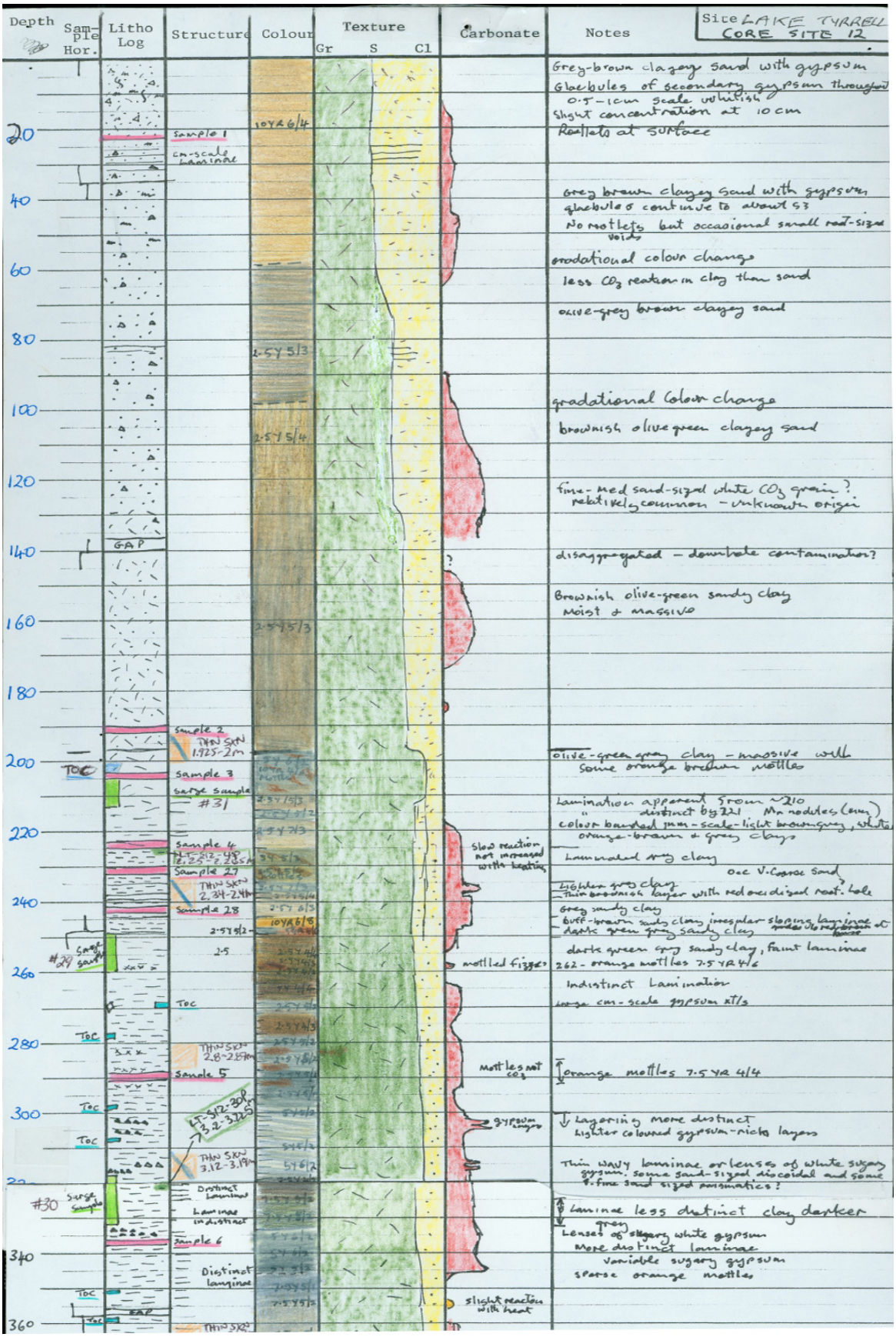
Depth
Sample Hor.
Litho Log
Structure
Colour
Texture
Gr S Cl
Carbonate
Notes
Site LAKE TYRRELL CORE SITE 12
Grey-brown clayey sand with gypsum
Glaebules of secondary gypsum throughout
0.5–1cm scale whitish
Slight concentration at 10 cm
Rootlets at surface
grey brown clayey sand with gypsum
glaebules continue to about 53
No mottles but occasional small root-sized voids
gradational colour change
less CO3 reaction in clay than sand
olive-grey brown clayey sand
gradational colour change
brownish olive green clayey sand
fine-med sand-sized white CO3 grain? relatively common – unknown origin
disaggregated – dominate contamination?
Brownish olive-green sandy clay
Moist & massive
olive-green grey clay – massive with some orange brown mottles
Lamination apparent from ~210
distinct by 221 Mn nodules (rare)
colour banded mm-scale light brown-grey, white orange-brown & grey clays
Laminated grey clay
one V. Coarse Sand
Lighter grey clay
Thin brownish layer with red oxidized root hole
Grey sandy clay
dark green grey sandy clay
dark green grey sandy clay, faint laminae
262 – orange mottles 7.5 YR 4/6
Indistinct Lamination
large cm-scale gypsum xtls
orange mottles 7.5 YR 4/4
Lamination more distinct
Lighter coloured gypsum-rich layers
Thin WAVY laminae or lenses of white sugary gypsum, some sand-sized discoidal and some fine sand sized prismatics?
laminae less distinct clay darker grey
Lenses of sugary white gypsum
More distinct laminae
variable sugary gypsum
sparse orange mottles
slow reaction not increased with heating
mottled fizzes
mottles not CO3
gypsum layers
slight reaction with heat
Sample 1
cm-scale laminae
Sample 2
Thin SKN 1.925-2m
Sample 3
Large sample #31
Sample 4
Sample 27
Thin SKN 2.34-2.4m
Sample 28
Large sample #29
Toc
Thin SKN 2.8-2.85m
Sample 5
Thin SKN 3.12-3.19m
Large sample #30
Distinct Laminae
Laminae indistinct
Sample 6
Distinct laminae
GAP
20
40
60
80
100
120
140
160
180
200
220
240
260
280
300
340
360

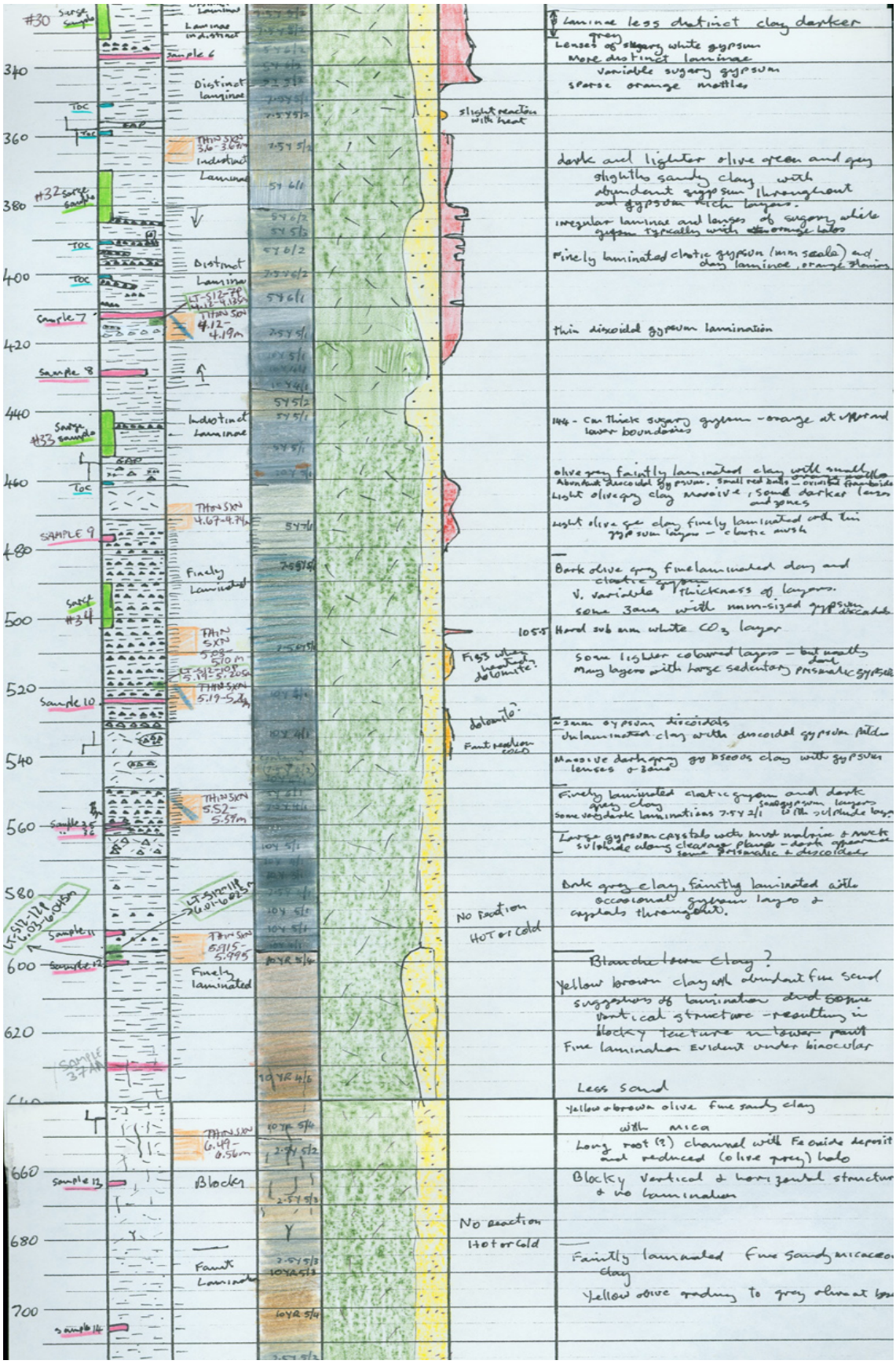
#30
Laminae less distinct clay darker grey
Lenses of sugary white gypsum
More distinct laminae
variable sugary gypsum
sparse orange mottles
340
Distinct laminae
slight reaction with heat
360
dark and lighter olive green and grey slightly sandy clay with abundant gypsum throughout and gypsum rich layers.
#32
380
irregular laminae and lenses of sugary white gypsum typically with orange halos
Finely laminated clastic gypsum (mm scale) and clay laminae, orange stains
400
Distinct Laminae
420
thin discoidal gypsum lamination
#33
440
Indistinct laminae
1cm - Cm thick sugary gypsum - orange at top and lower boundaries
olive grey faintly laminated clay with small
Abundant discoidal gypsum. Small red balls
460
Light olive grey clay massive, some darker layers and zones
light olive gr clay finely laminated with thin gypsum layers - clastic wash
480
Finely Laminated
Dark olive grey fine laminated clay and clastic gypsum
V. variable thickness of layers.
some 3cms with mm-sized gypsum discoids
#34
500
105-5
Hard sub cm white CO3 layer
Figs white banded dolomite.
some lighter coloured layers - but mostly dark
Many layers with large sedentary prismatic gypsum
520
dolomite
~3mm gypsum discoidals
Unlaminated clay with discoidal gypsum fillers
Fant reaction cold
540
Massive dark grey gypsiferous clay with gypsum lenses of 3cms
Finely laminated clastic gypsum and dark grey clay
some very dark laminations 7.5Y 2/1 to the subdivide layers
560
Large gypsum crystals with most halite & some sylvinite along cleavage planes - dark appearance
some prismatic & discoidals
580
Dark grey clay, faintly laminated with occasional gypsum layers & crystals throughout.
No reaction HOT or Cold
600
Finely laminated
Blandford loam clay ?
Yellow brown clay with abundant fine sand
suggestions of lamination and some vertical structure - resulting in blocky texture in lower part
620
Fine lamination evident under binocular
Less sand
Yellow brown olive fine sandy clay with mica
640
Long root (?) channel with Fe oxide deposit and reduced (olive grey) halo
660
Blocky
Blocky Vertical & horizontal structure & no lamination
680
No reaction Hot or Cold
Faint Laminae
Faintly laminated Fine sandy micaceous clay
Yellow olive grading to grey olive at base
700

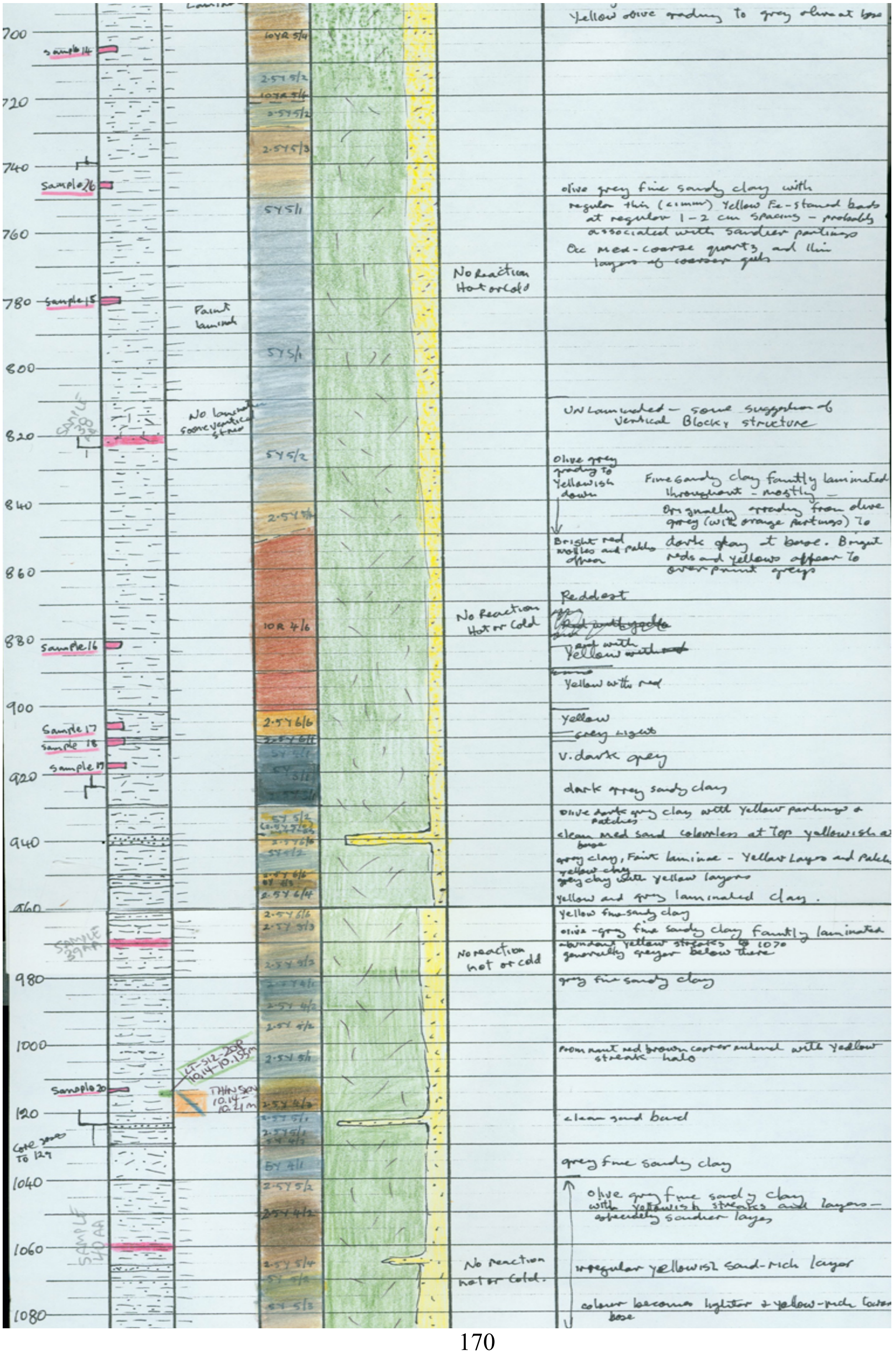
700
720
740
760
780
800
820
840
860
880
900
920
940
960
980
1000
120
1040
1060
1080
sample 14
sample 26
sample 15
sample 16
sample 17
sample 18
sample 19
sample 20
10YR 5/4
2.5Y 5/2
2.5Y 5/3
5Y 5/1
5Y 5/2
10R 4/6
2.5Y 6/6
2.5Y 5/2
5Y 4/1
2.5Y 4/2
5Y 5/3
Faint laminae
No Reaction Hot or cold
No Reaction Hot or Cold
No reaction hot or cold
No reaction hot or cold.
Yellow olive grading to grey olive at base
olive grey fine sandy clay with
Unlaminated – some suggestion of Vertical Blocky structure
Olive grey grading to Yellowish down
Fine sandy clay faintly laminated throughout
Bright red mottles and patches appear
Reddest
Yellow with red
yellow
V. dark grey
dark grey sandy clay
clean med sand colourless at Top yellowish at base
yellow and grey laminated clay.
yellow fine sandy clay
olive-grey fine sandy clay faintly laminated
grey fine sandy clay
clean sand band
grey fine sandy clay
olive grey fine sandy clay
irregular yellowish sand-rich layer
colour becomes lighter & yellow-rich towards base

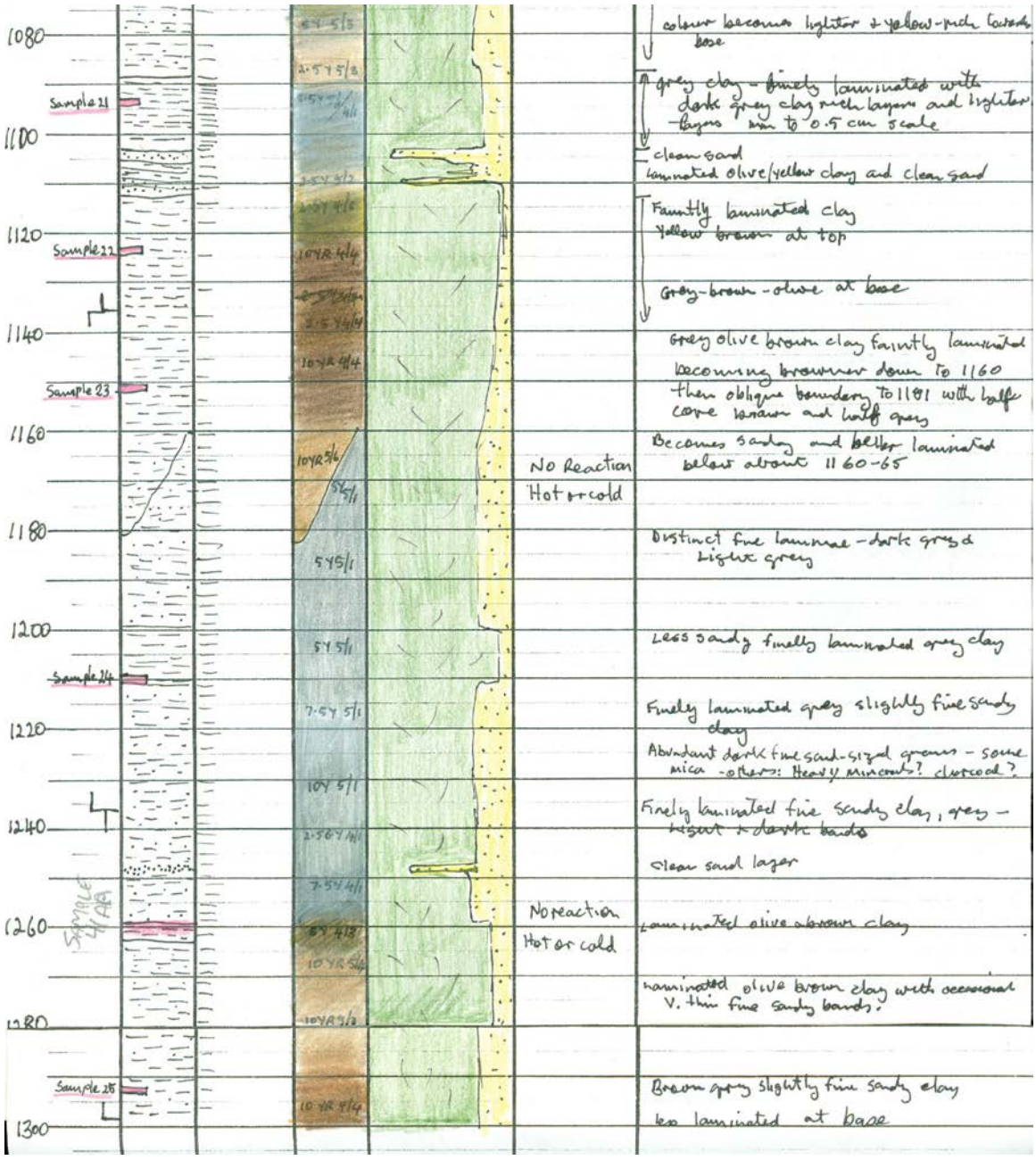
1080
1100
1120
1140
1160
1180
1200
1220
1240
1260
1280
1300
Sample 21
Sample 22
Sample 23
Sample 24
Sample 25
Sample 26
colour becomes lighter + yellow-ish towards base
grey clay - finely laminated with dark grey clay rich layers and lighter layers mm to 0.5 cm scale
clean sand
laminated olive/yellow clay and clean sand
Faintly laminated clay
Yellow brown at top
Grey-brown - olive at base
Grey olive brown clay faintly laminated becoming browner down to 1160
then oblique boundary to 1191 with half core brown and half grey
Becomes sandy and better laminated below about 1160-65
No Reaction
Hot or cold
Distinct fine laminae - dark grey & lighter grey
Less sandy finely laminated grey clay
Finely laminated grey slightly fine sandy clay
Abundant dark fine sand-sized grains - some mica - others: Heavy minerals? charcoal?
Finely laminated fine sandy clay, grey -
clean sand layer
No reaction
Hot or cold
laminated olive brown clay
laminated olive brown clay with occasional v. thin fine sandy bands.
Brown grey slightly fine sandy clay
less laminated at base

Appendix 2. Textural features of thin sections of Lake Tyrrell S12 core/Folly Point core

All thin section images taken in plane polarized light.
Close-ups in plane and crossed polars.
'Cutan' is a term connoting a modification in the texture, structure or arrangement of a pedological material along a soil surface – typically the coating of a clay ped, mineral grain or void by some other mineral or organic substance. When clays form such a coating, they are termed 'clay cutans' or 'argillans'.

Figure A2.1 LT S12 sample 2, 192.5 – 200 cm:

A. Orange-red iron oxides deposited along joints in clay matrix; tilted 40° right of vertical.

B. Well-developed joints in the clay matrix with oriented clay along the edges of the joints.

C. Oriented clay along joints, partial argillans around a rounded quartz grain, and brown iron oxide staining along the edges of the oriented clays. Tilted 50° right of vertical to show oriented clay along the joint.

D. Partially degraded clay pellets – these are losing their roundedness, and the edges are becoming blurred and conjoined.

E. Red and brown iron oxide staining of edges of clay pellets. These edges are developing into joints as the oxides become more extensive and the borders of the pellets more well-defined.

F. Sub-rounded, poly-crystalline quartz grain with partial clay cutan.

G. Rounded, well-preserved clay pellets. Note the steep slope of this layer: it likely formed when clay pellets were blown from the dry lakebed onto the side of the lunette, so that this layer represents a palaeo-surface.

Figure A2.1 LT S12 sample 2 thin section, 192.5 - 200 cm

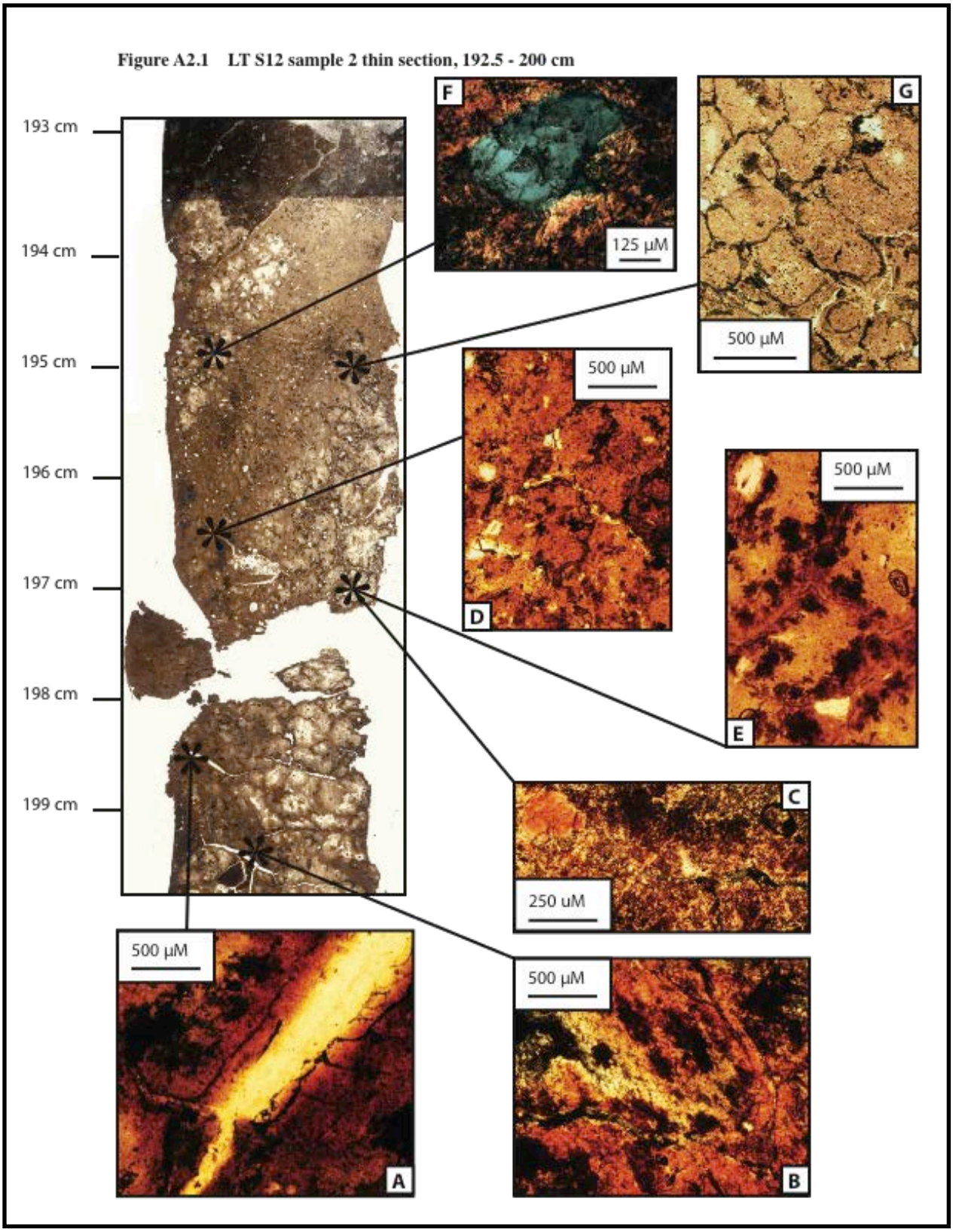

Figure A2.2 LT S12 sample 4, 234 – 241 cm:

A. Sub-angular quartz grain with partial clay cutan. Note also iron oxide staining and argillan along edge of joint in clay.

B. Lens of quartz sand with grains of diameter ranging from 200 μM to >1 mm. Large variation in roundedness of grains indicates sub-mature assemblage, probably transported by wind.

C. Cracks in clay beds cemented by iron oxides. Note also the ferri-argillan around the sub-angular quartz grain in the center right of the image.

D. Remnant mat layer composed of microbialites and clays. Cracking of the section has occurred along the contact between the microbialite and clay layers. Note reddish iron oxide staining and iron oxide blebs, showing that alteration by groundwater has occurred, though bedding structure is retained.

E. Iron oxides filling a void in the mat layers.

F. Oriented clays and reddish iron oxides arranged along well-developed joints in the clay matrix.

G. Large, brownish iron oxide blebs of 60 – 140 μM in diameter concentrated along cracks or joints in clay matrix.

Figure A2.2 LT S12 sample 4 thin section, 234 - 241 cm

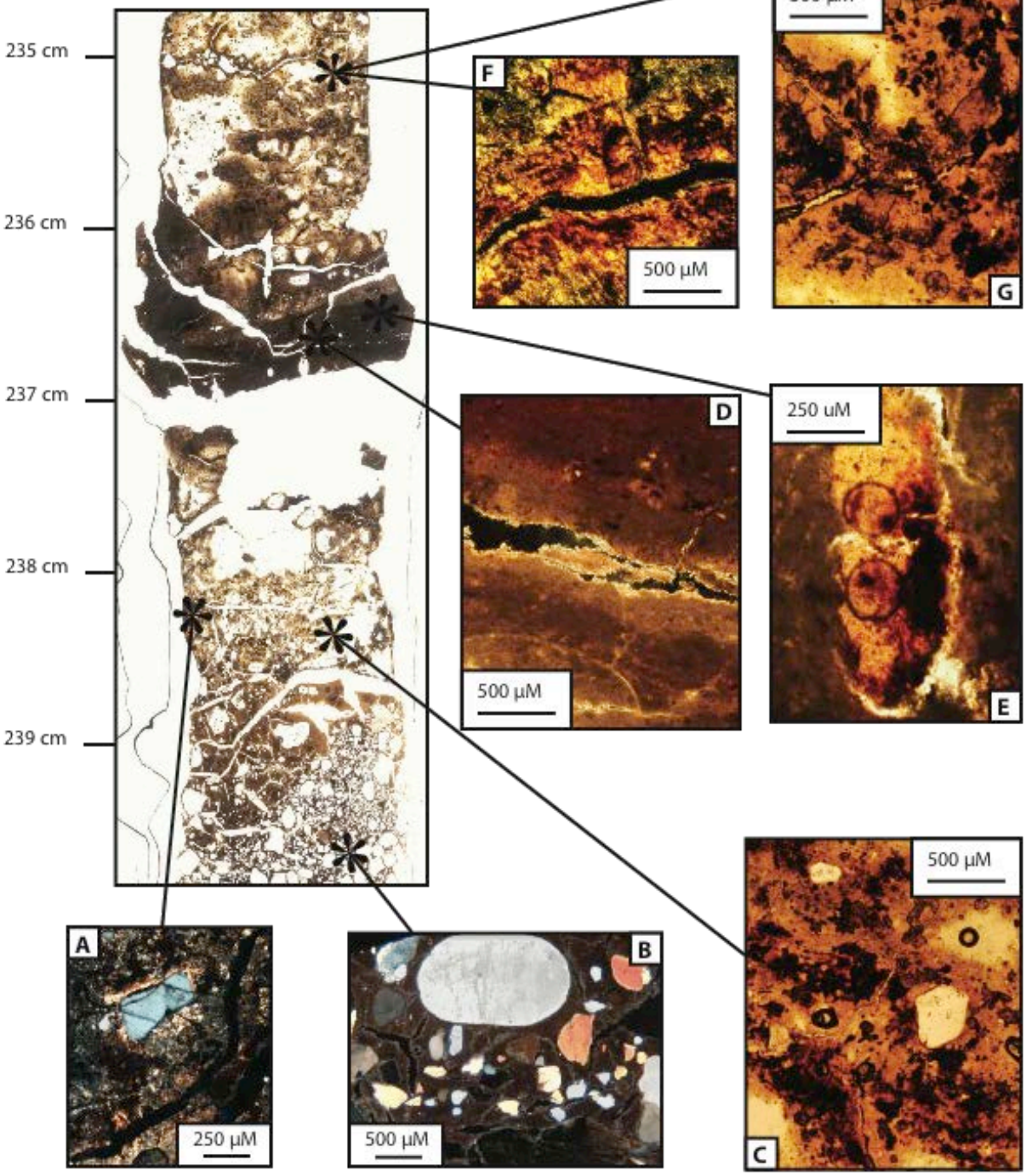

Figure A2.3 LT S12 sample 5, 280 – 287 cm:

A. Rounded quartz grain with partial argillan and associated iron oxides.

B. Blocky clay peds containing iron oxide spherules concentrated along cracks.

C. Iron oxide spherules scattered throughout the section. It is likely that these were deposited as pyrite framboids, and have been subsequently oxidized during pedogenesis or by groundwater.

D. Large dendritic structure composed of iron oxides. Note smaller iron oxide spherules scattered throughout clay matrix on either side of dendrite.

E. Clays re-organized along cracks between peds and along cross-cutting structures. Clay re-organization points to a maturing of sedimentary structures.

F. As above, rotated through 50° to show orientation of clays along cracks. White region of section just below this area is a gap filled with epoxy, where the section cracked during sample preparation.

Figure A2.3 LT S12 sample 5 thin section, 280 - 287 cm

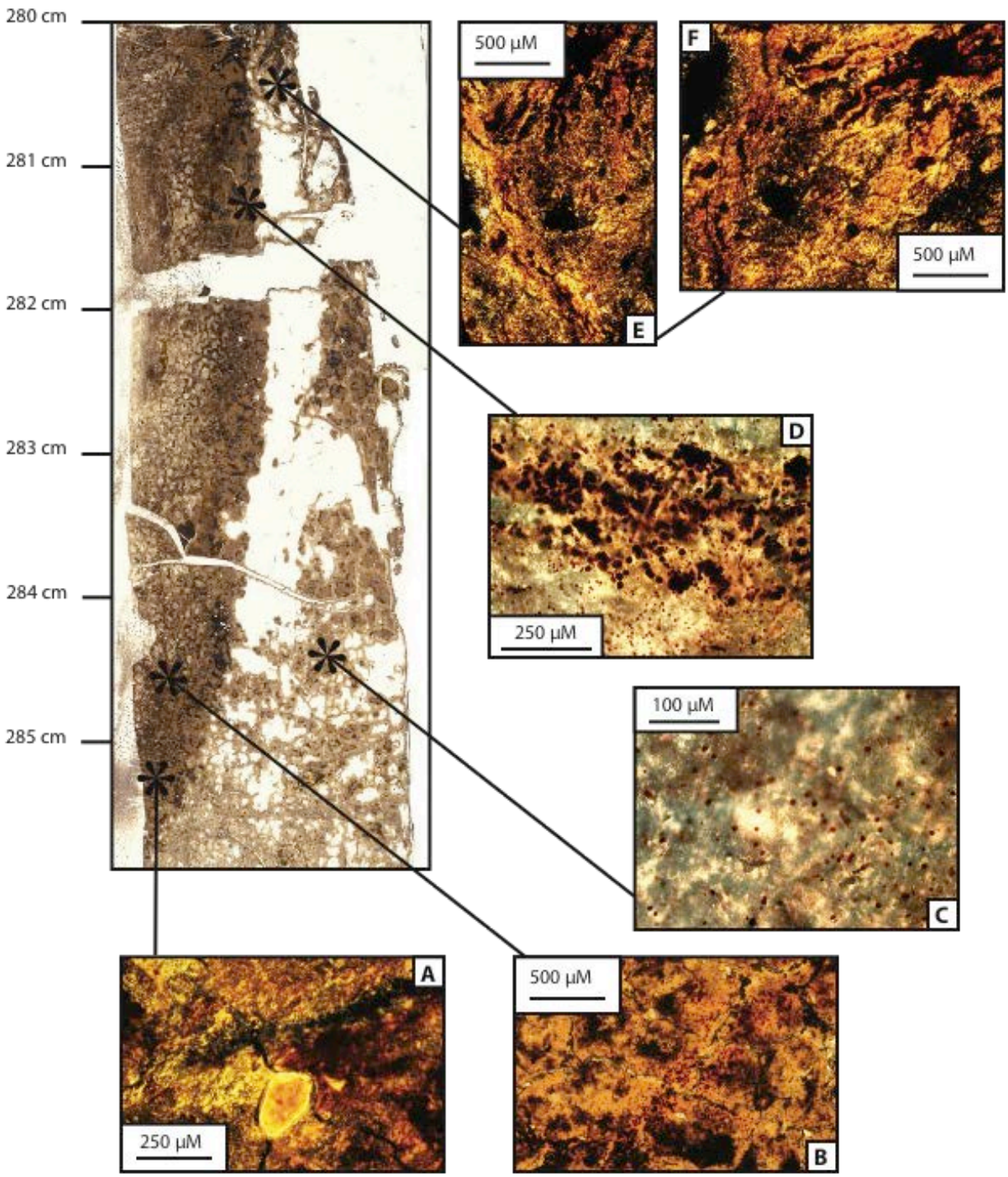

Figure A2.4 LT S12 sample 30, 312 – 319 cm:

A. Oriented clays containing displacive gypsum crystals. Gypsum crystals range from 100-500 μM in diameter, and are oriented parallel to the clay layers in which they have grown.

B. Rounded and partially re-dissolved gypsum crystals contained within a clay matrix. Rounding is likely due to saltation (erosive transport by wind; crystals become rounded due to friction between the surfaces of the crystal and the dry lakebed).

C. Remnant mat layers (composed of microbialites and clay) contained within matrix of settled gypsum crystals.

D. Settled gypsum crystals forming the matrix of image above. Crystals are ~20 μM in diameter.

E. Sub-angular to sub-rounded quartz grains with associated partial clay cutans.

F. Displacive gypsum crystals emplaced in parallel orientation within a matrix of settled gypsum crystals. Note larger size of displacive crystals relative to settled crystals.

G. Partially re-dissolved displacive gypsum crystals in random orientation. Diameter of crystals ranges from 200-1000 μM.

H. Cross-cutting structure with oriented clays along the edges of the crack. Orientation demonstrates maturity and development of this structure, which has formed during the initial phase of soil development.

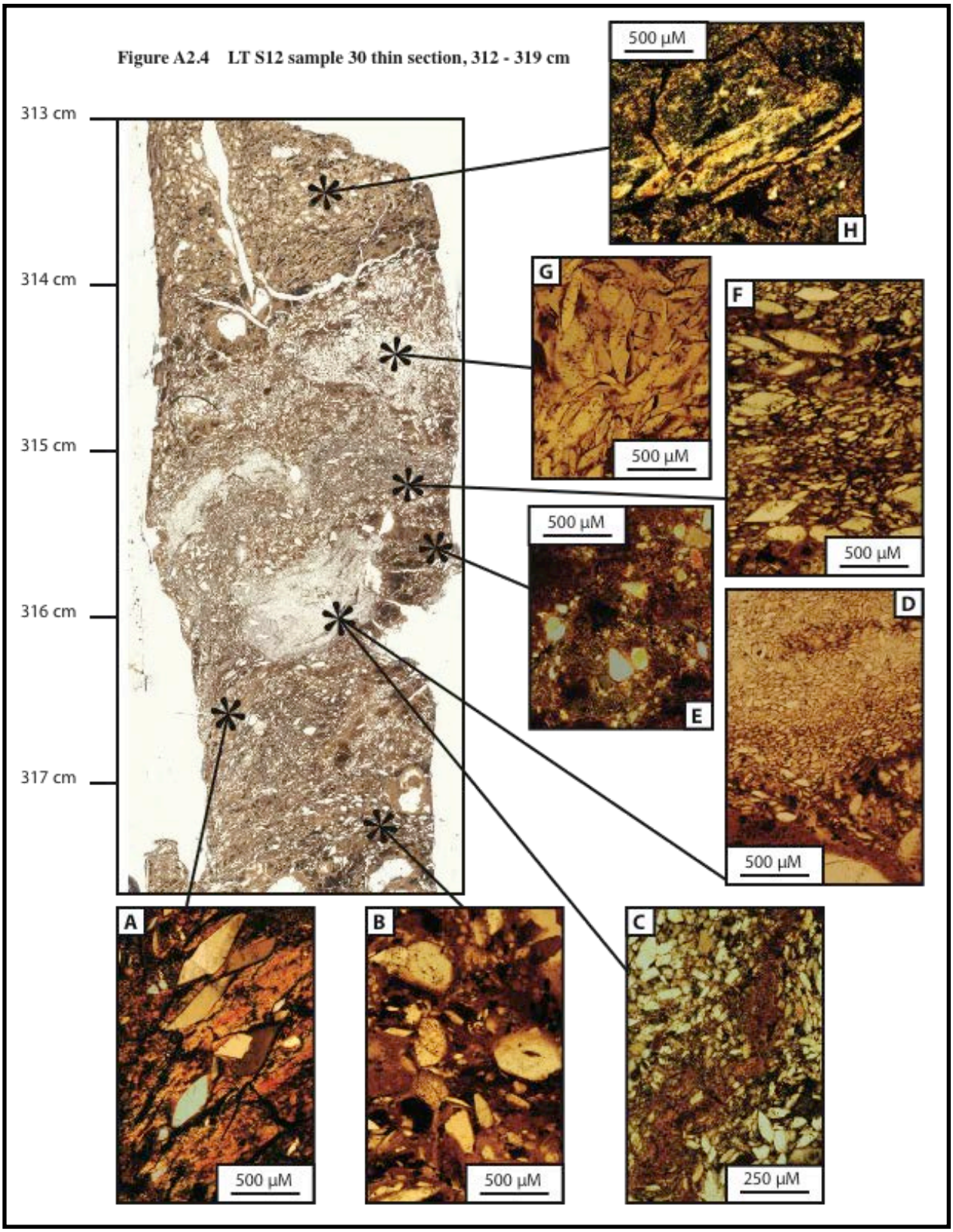
Figure A2.4 LT S12 sample 30 thin section, 312 - 319 cm
313 cm
314 cm
315 cm
316 cm
317 cm
500 µM
H
G
500 µM
F
500 µM
500 µM
E
D
500 µM
A
500 µM
B
500 µM
C
250 µM

Figure A2.5 LT S12 sample 32, 360 – 367 cm:

A. Clay ped (2 mm diameter) trapped in gypsiferous clay matrix. Note cross-cutting features within the ped, and orientation of clays along its edges.

B. Displacive gypsum crystals, in sub-parallel orientation within clay matrix. Note cutans around gypsum crystals.

C. Randomly oriented, displacive gypsum crystals of ~100-500 μM diameter. Note absence of clay in matrix. Possibly indicative of settled gypsum overgrown with larger, displacive crystals post-burial.

D. Clay beds disrupted by syneresis cracks (these form when secondary evaporite precipitation 'sucks' water from surrounding clays, causing them to shrink and crack), and containing displacive gypsum crystals. It is likely that the disruption of the layers as a whole (see larger thin section image) was a direct result of secondary gypsum growth.

E. Light orange iron oxide staining of clay layers.

F. As above. Note concentration of iron oxides along cracks within clay layers. Probably due to groundwater penetration of disrupted clay layers.

G. Oriented clays along syneresis cracks within clay layers.

Figure A2.5 LT S12 sample 32 thin section, 360 - 367 cm

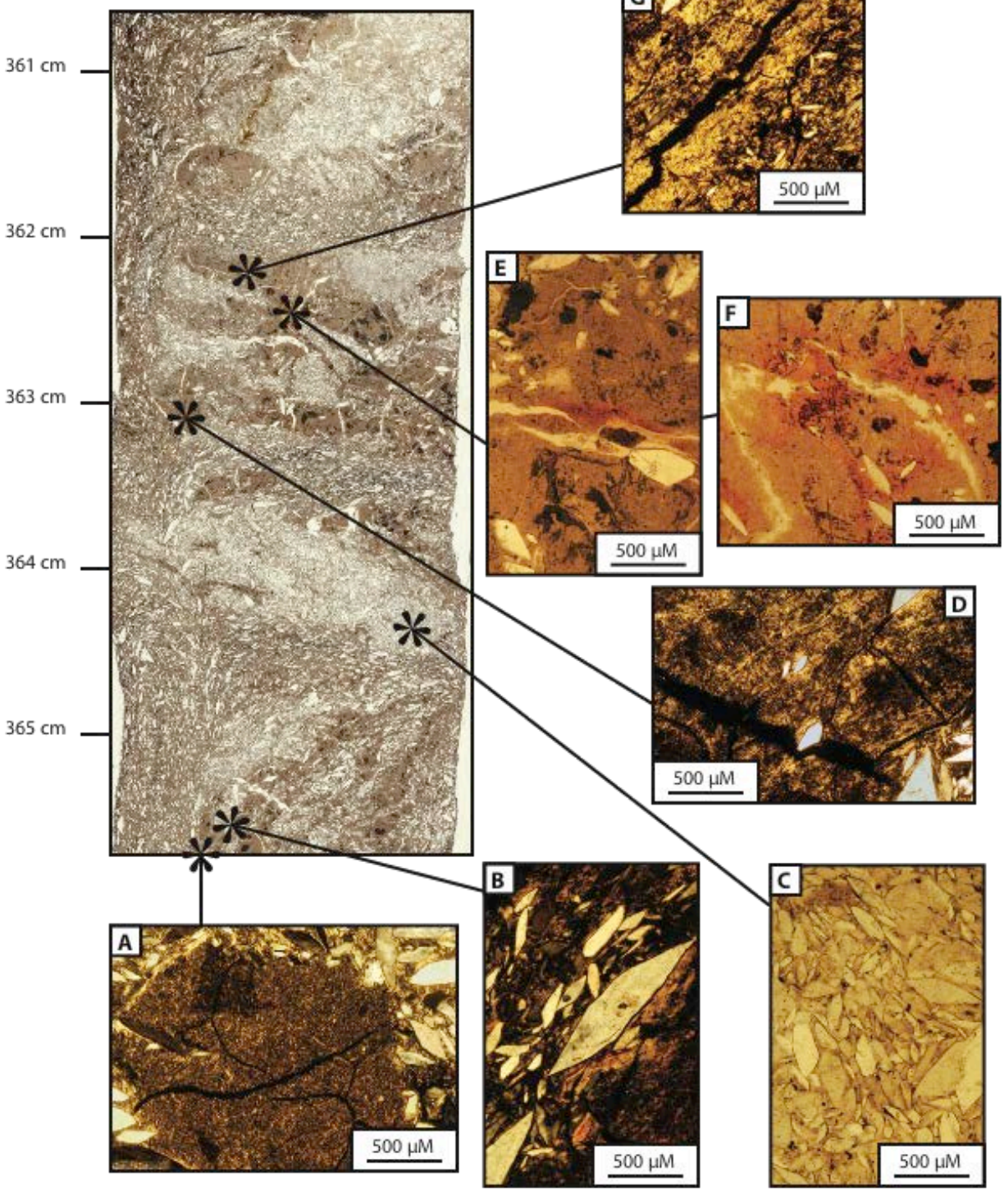

Figure A2.6 LT S12 sample 7, 412 – 419 cm:

A. Well-defined polygonal clay peds. Indicative of freshwater deposition and subsequent drying.

B. Large, brown iron oxide blebs within the clay matrix, indicating post-depositional oxidation.

C. Rounded quartz grain with continuous clay cutan and partial ferri-argillan.

D. Displacive gypsum horizon. Note partial dissolution of gypsum crystals along cleavage planes, indicating post-depositional freshening or microbially-mediated dissolution.

E. Putative fecal pellets of 120 – 200 μM diameter within settled gypsum layer. Below this layer is a clay layer, shown in F. If these are fecal pellets, they likely indicate slight freshening episodes.

F. Oriented clay layer (rotated through 50° to show orientation of clay layer) underlying settled gypsum layer containing putative fecal pellets (possibly derived from the gastropod *Coxiella*). Note that the putative pellets show no evidence of preferred orientation, and instead seem to be comprised of scattered carbonate grains and organics, as would be expected.

G. Partially re-dissolved displacive gypsum layer. Crystals display parallel to sub-parallel orientation to the bedding.

H. Clay polygons with no preferred orientation at the edges, indicating less well-developed peds. Rounded quartz grains are scattered throughout this layer.

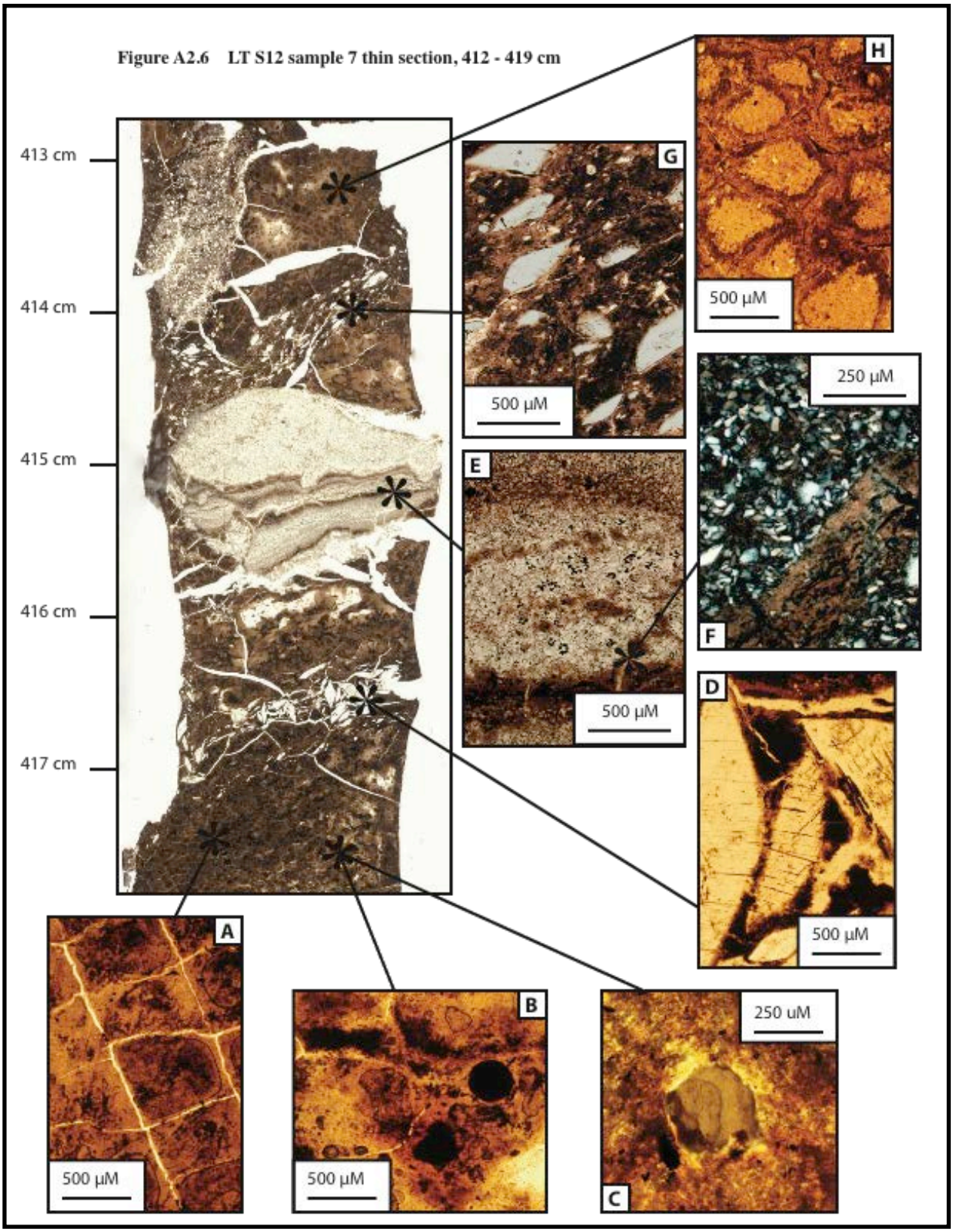

Figure A2.6 LT S12 sample 7 thin section, 412 - 419 cm

Figure A2.7 LT S12 sample 9, 467 – 474 cm:

A. Oriented clay layer overlain by organic-rich remnant mat layer and underlain by quartz-rich lens. Rotated 50° clockwise from bedding plane in order to show preferred orientation of clay layer.

B. As above, not rotated. Note high birefringence of grains in top left corner – these are microbialites, and point to organic origin of the layer.

C. Quartz-rich sand lenses within non-oriented clay matrix.

D. Randomly oriented displacive gypsum crystals, little to no matrix present.

E. Layers of settled gypsum crystals intercalated with microbialite mat layers. Note reverse grading in the gypsum, from ~40 μM diameter near the bottom to ~100 μM at the top.

F. Mat layers (200 – 500 μM thick) interspersed with settled gypsum crystals.

G. Clay and microbialite carbonate matrix including scattered iron oxide spherules. Rotated 50° counterclockwise in order to show preferred orientation in clays.

H. As above, not rotated.

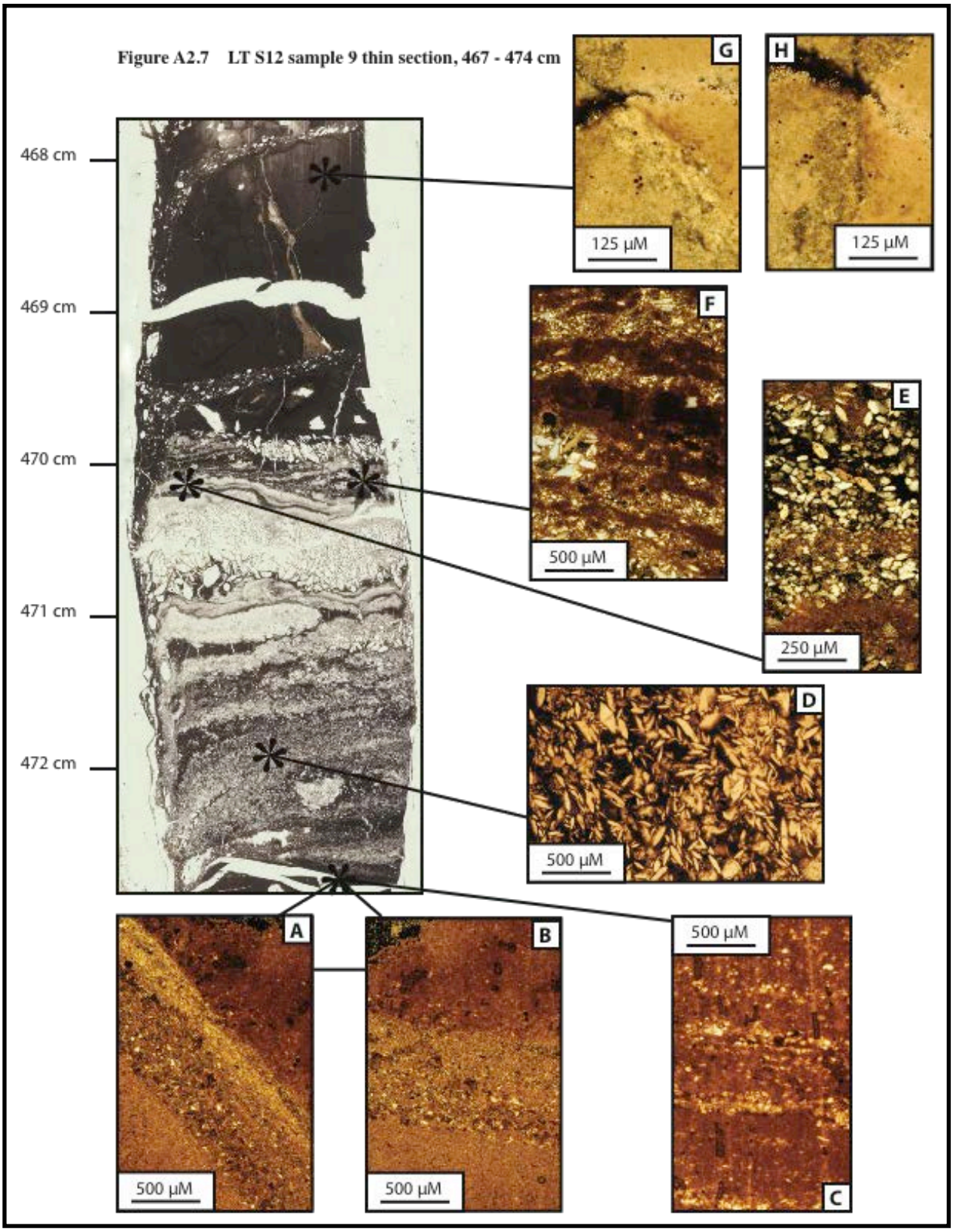
Figure A2.7 LT S12 sample 9 thin section, 467 - 474 cm
468 cm
469 cm
470 cm
471 cm
472 cm
G
H
125 µM
125 µM
F
500 µM
E
250 µM
D
500 µM
A
500 µM
B
500 µM
500 µM
C

Figure A2.8 LT S12 sample 34, 503 – 510 cm:

A. Transported gypsum of ~125-500 μM diameter, partially re-dissolved. Minimal clay matrix.

B. Zoned, blocky clays disrupted by syneresis cracks.

C. Oriented clay layer below microbialite layer. Rotated 50° from bedding plane in order to show preferred orientation in clays. Note layering within microbialites. Separation between the clay and mat layers likely occurred during drying (sample preparation).

D. Settled gypsum interspersed with oriented clay layer. Rotated 50° from bedding plane in order to show preferred orientation in clays.

E. Further image of clay layer overlain by mat layer. Note "tear-up" structure within mats adhering to top of clay layer. Black area is a void.

F. Close-up of "tear-up" feature in image described above. Note bright grains within mat layer – these are likely microbialites (carbonates precipitated by microbes, remarkable for their small size), which are commonly found associated with living and preserved microbial mats.

G. Displacive gypsum layer, with sub-parallel orientation of crystals. Lenticular, displacive crystals have grown within a primary settled gypsum layer.

H. Close-up of mat layers, so that layering within the larger structure can be discerned. Plane polarized light.

I. Strongly oriented clay layer containing some organics, overlain by settled gypsum. Rotated 50° from bedding plane in order to show preferred orientation in clays.

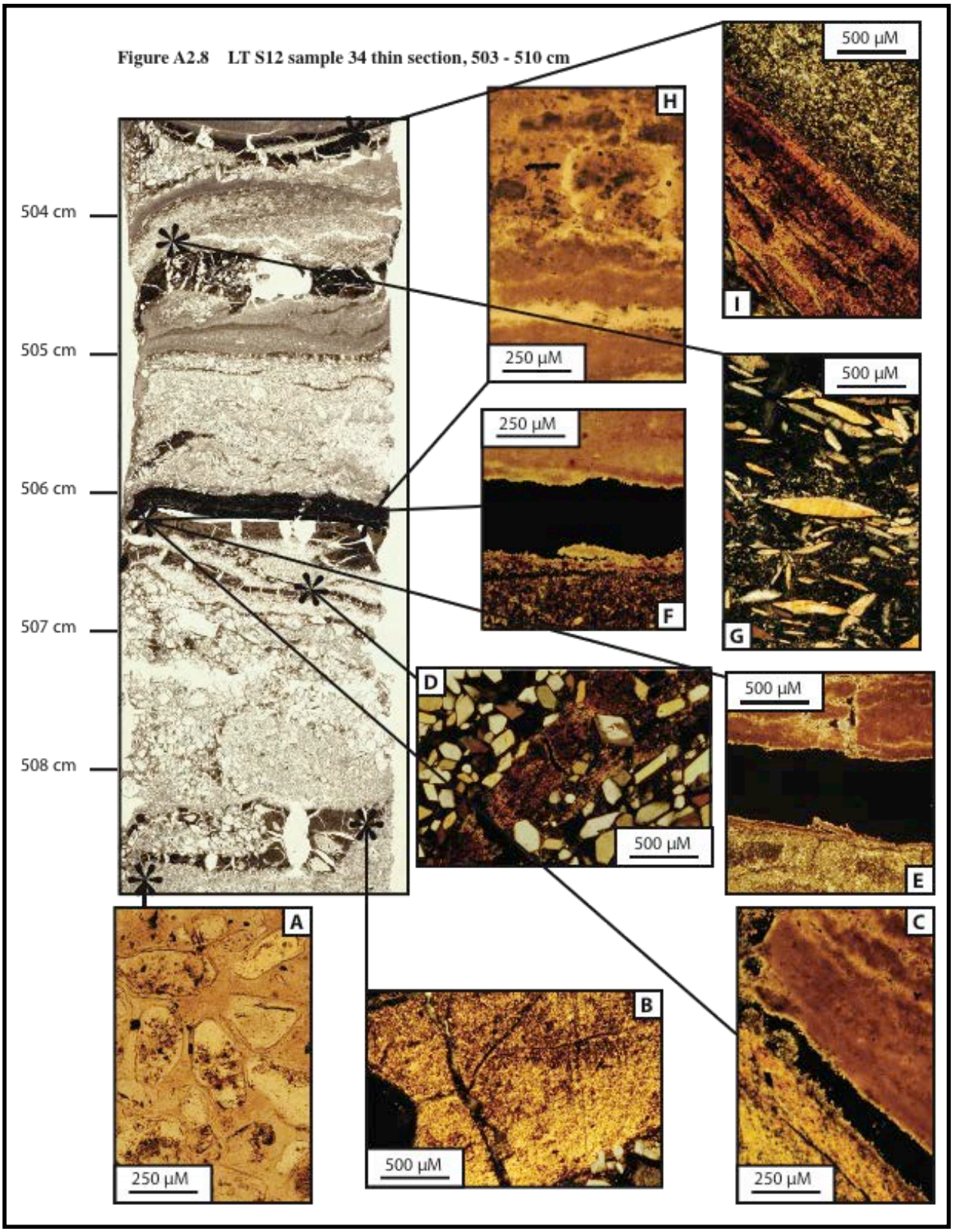
Figure A2.8 LT S12 sample 34 thin section, 503 - 510 cm
504 cm
505 cm
506 cm
507 cm
508 cm
A
250 µM
B
500 µM
C
250 µM
D
500 µM
E
500 µM
F
250 µM
G
500 µM
H
250 µM
I
500 µM

Figure A2.9 LT S12 sample 10, 519 – 526 cm:

A. Settled gypsum with reverse grading, from 80 to 200 μM. Not re-worked, indicative of deposition from water saturated in $CaSO_4$, below wave base.

B. Putative fecal pellets, possibly from *Diacypris* (up to 200 g/L salt tolerance), a genus of ostracod endemic in Australian saline lake systems.

C. As above, rotated through 50°

D. Sub-parallel displacive gypsum, partial re-dissolution, cracks in crystals due to pressure from growth of displacive crystals

E. As above.

F. Displacive, secondary gypsum, size ~20 μM to 1 mm, in random orientation.

G. >1mm lenticular, displacive gypsum floating in matrix of dolomitic microbialites and smaller, secondary gypsum crystals

Figure A2.9 LT S12 sample 10 thin section, 519 - 526 cm

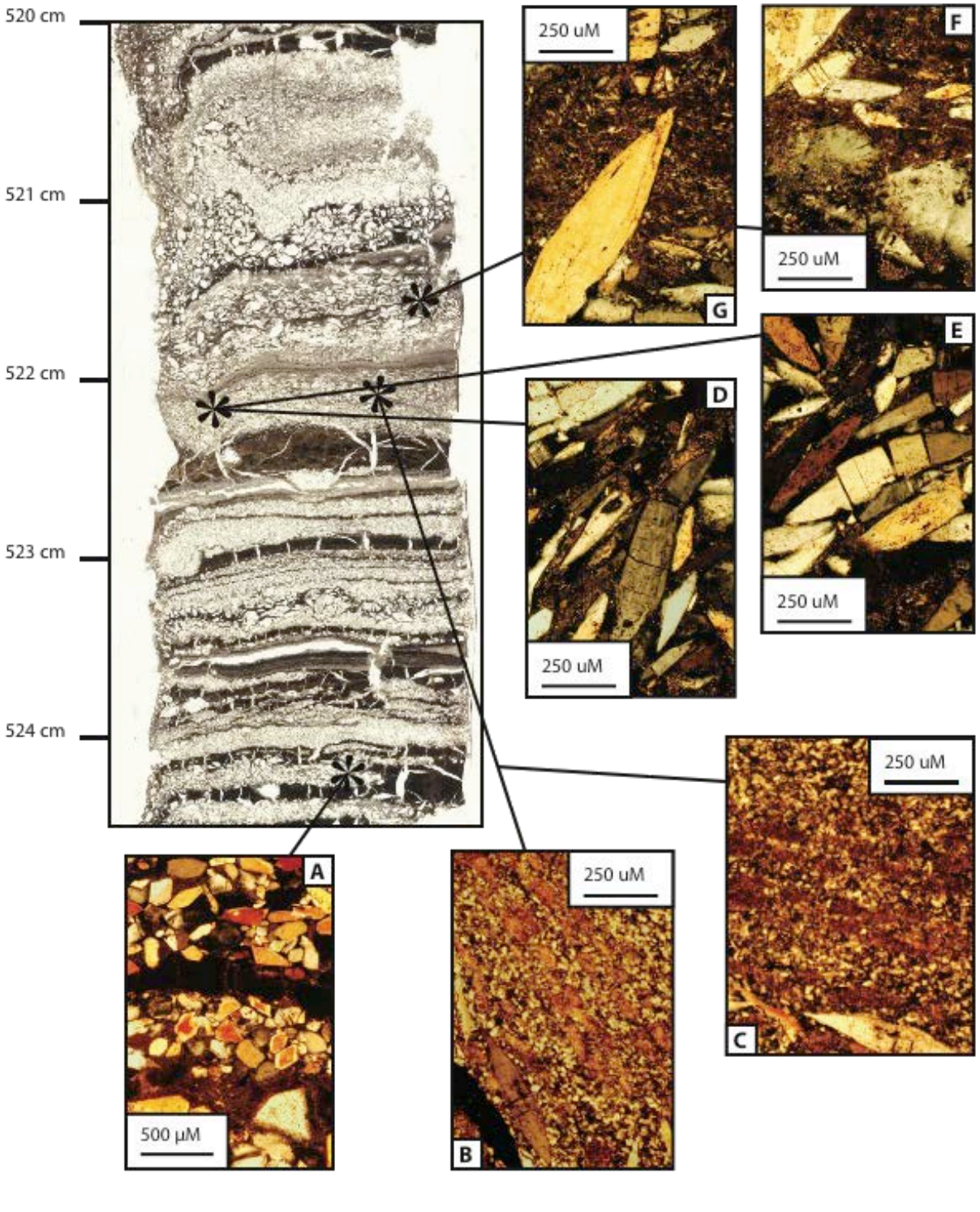

Figure A2.10 LT S12 sample 35_36, 552 – 559 cm:

A. Iron sulfides in gypsum, deposited between layers of preferentially oriented clays.

B. As above, including partially re-dissolved gypsum crystals.

C. Disruption of clay/remnant microbial mat layers and subsequent “pour-through” of gypsum crystals (note in image of entire thin section as well as in close-up provided by image C) through disrupted layers. Disruption possibly due to tearing of mat layers due to wave-action (note macroscopic ripple structure at top of thin section), or contraction of mat layers during drying. Note multiple syneresis cracks throughout layers in this section.

D. Reverse-grading in settled gypsum deposited between clay layers. Gypsum crystals increase in size from ~40 μM to ~200 μM from bottom to top of image.

E. Oxidized iron contained in gypsum crystals. The likely crystal form is either goethite or ferrihydrite; its presence in the etch pits of the gypsum crystal indicates the mechanism through which subsequent pyrite precipitation was localized along the cleavage planes of the gypsum.

F. Iron sulfide contained within the cleavage planes of gypsum overlain by microbial mat layers. Note close association of iron-sulfide rich gypsum with mat layers. It is likely that the activities of heterotrophic sulfate-reducing bacteria are responsible for the presence of the sulfides, and their proliferation at this depth is due to their use of the overlying mats as a carbon source.

G. Iron sulfide contained within cleavage planes of gypsum. Note that it seems to ‘invade’ from the outside of the crystal.

H. As above. Note some gypsum crystals have been nearly completely replaced by FeS, and have become pseudomorphs.

Figure A2.10 LT S12 sample 35_36 thin section, 552 - 559 cm

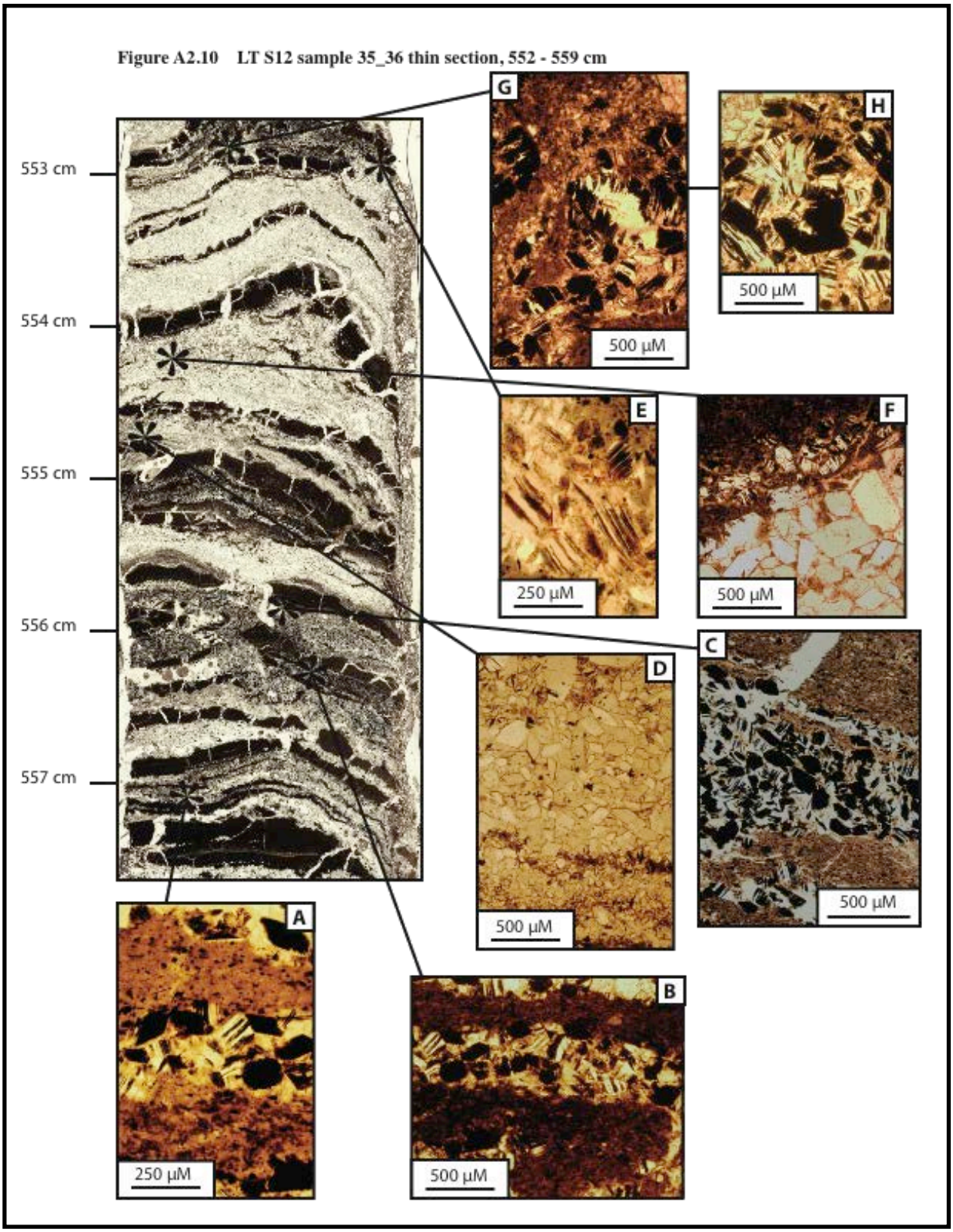

Figure A2.11 LT S12 sample 11_12, 591.5 – 599.5 cm:

A. Iron oxide horizon contained within Blanchetown Clay layers.

B. Void, possibly created by rootlet, filled with iron oxide and silicates.

C. Oriented clay layer surrounded by quartz lenses. Rotated 50° from bedding plane in order to show preferred orientation in clays.

D. Void laminated with iron oxides. Due to shape of void and build-up of laminations, it is likely that is void is evidence of the presence of a rootlet.

E. Disrupted layer of pyritized gypsum crystals. Note that pyrite seems to invade crystal from the outer edge. Disruption is likely due to secondary gypsum growth (non-pyritized, randomly oriented displacive crystals).

F. Displacive gypsum crystals with evidence of some dissolution along the cleavage planes.

G. Displacive and transported gypsum crystals – evidence of re-working and transport of some of the crystals is demonstrated by their lack of points. Displacive (non-reworked) crystals oriented sub-parallel to thin clay layer (~250 μM thick).

H. Rounded quartz grain (black shape in center of image, color is due to orientation in crossed polars) with partial argillan.

Figure A2.11 LT S12 sample 11_12 thin section, 591.5 - 599.5 cm

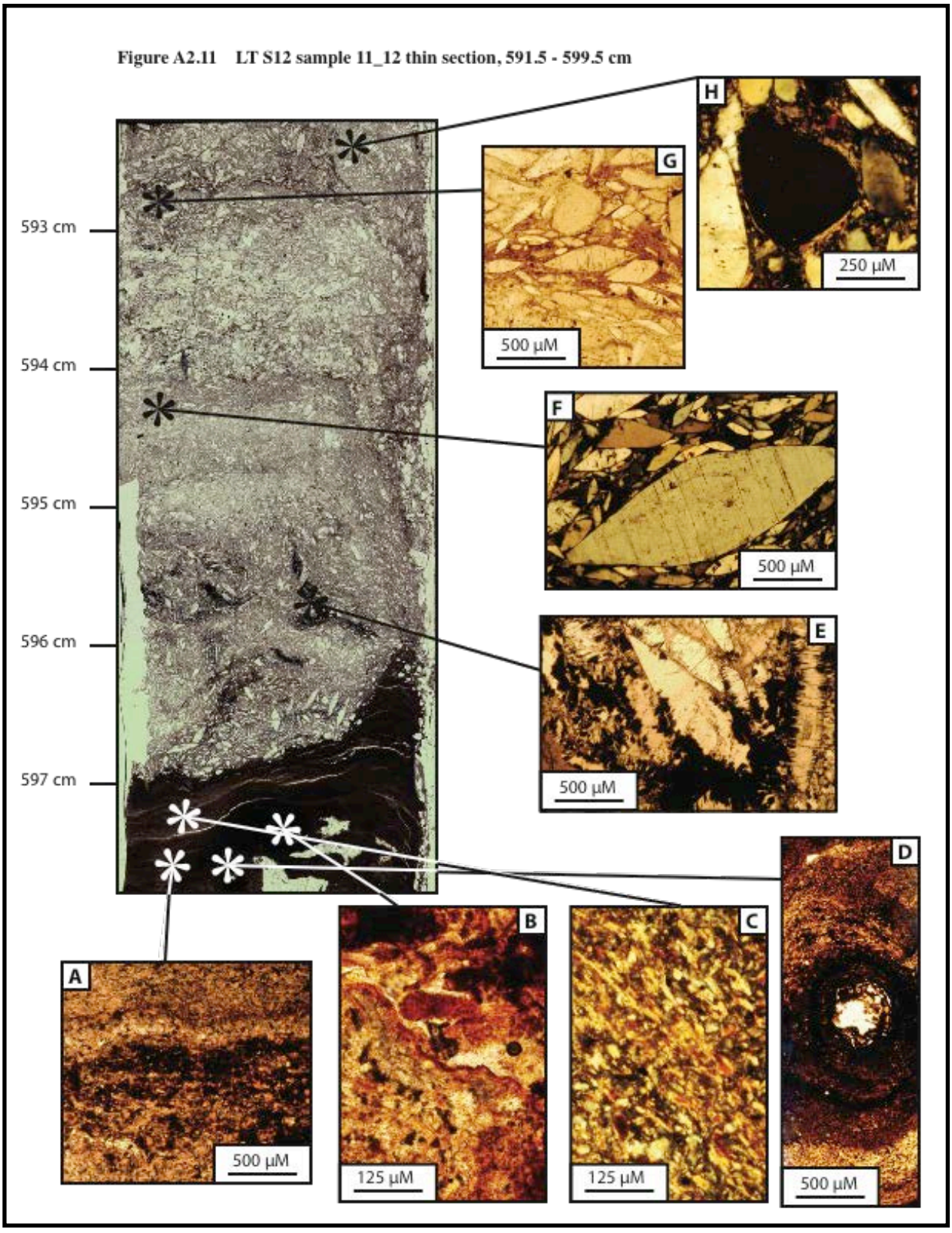

Figure A2.12 LT S12 sample 13, 649 – 656 cm:

A. Organic remnants – possibly plant fibers – contained within clay layers.

B. As above.

C. Dark grains of putative charcoal in clay matrix.

D. Void surrounded by iron oxide halo. Shape of void indicates that it may have been formed by a rootlet.

E. Quartz sand lens within clay matrix. These lenses are scattered throughout this section of the Blanchetown Clay, indicating periods of higher energy deposition.

F. Close-up of quartz sand layer. Note roundedness of quartz grains, indicating extensive transport from source.

G. Iron oxide haloes around voids partially filled with clays. The unusual shape of these voids may be attributed to organic matter – possibly plant matter.

Figure A2.12 LT S12 sample 13 thin section, 649 - 656 cm

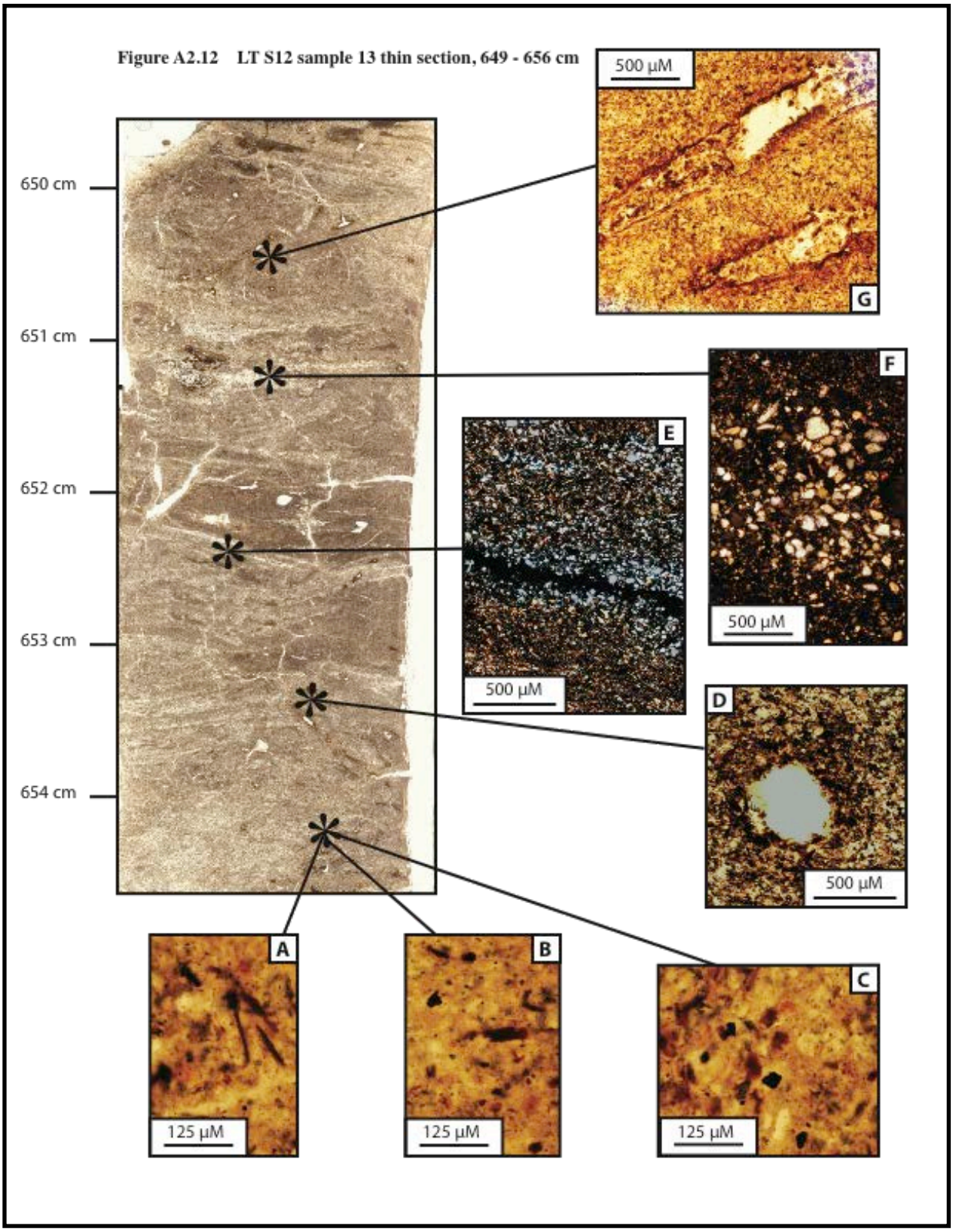

Figure A2.13 LT S12 sample 20, 1014 – 1021 cm:

A. Coarse-sized quartz sand layer within clay beds.

B. Fine, silt-sized quartz layer. Note, silt-sized quartz is scattered throughout this section, so that it may be described as a silty-clay.

C. Brownish-red iron oxide haloes around voids, and iron oxides filling voids within clays.

D. Scattered silt-sized quartz grains within clay matrix. Note indications of bedding in clay, and iron oxide horizon in bottom third of image.

E. Interspersed layers of coarser quartz and finer clays. Normal grading is evident within each couplet.

F. As above. Note syneresis crack in clay-rich layer.

Figure A2.13 LT S12 sample 20 thin section, 1014 - 1021 cm

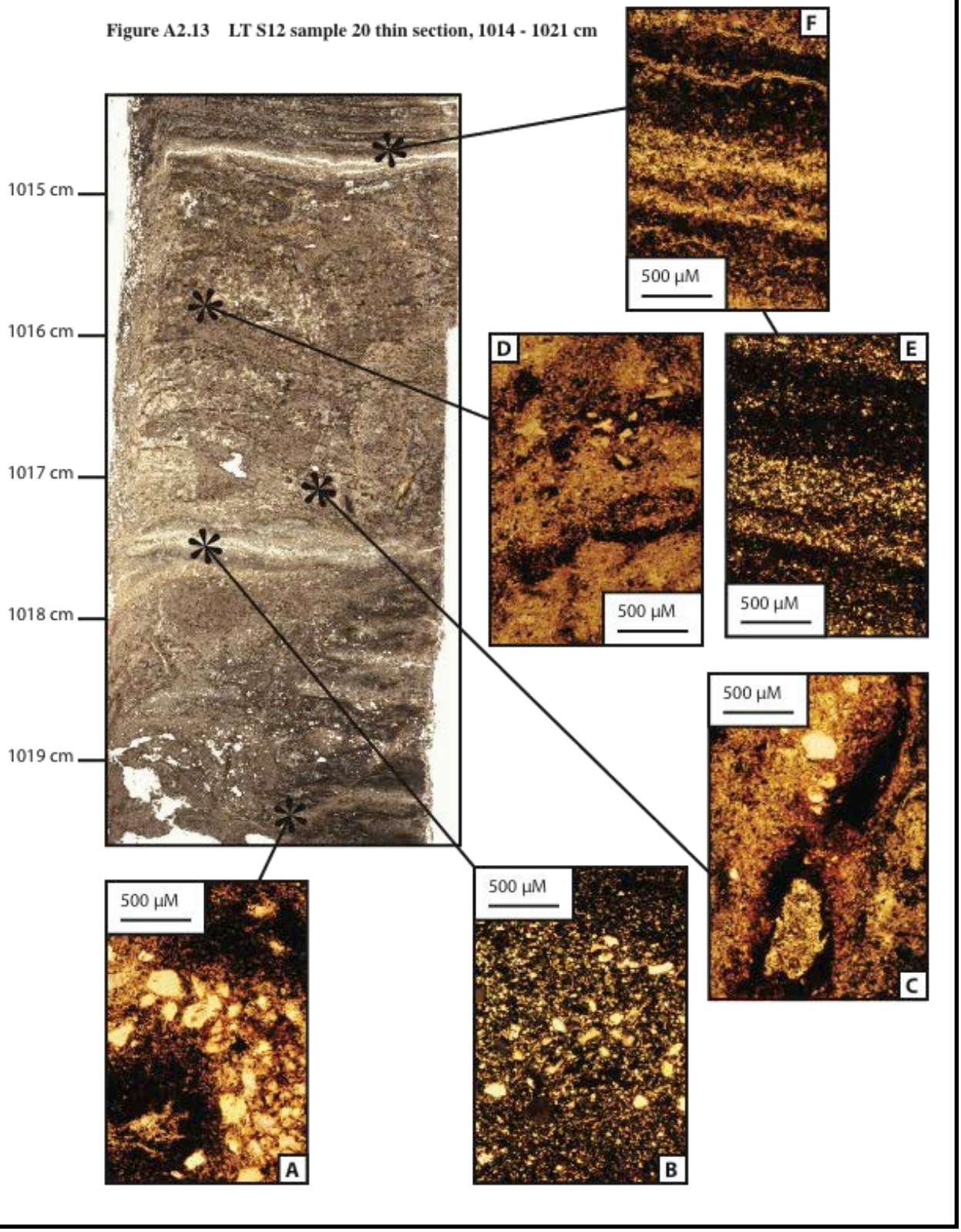

Appendix 3. Diagenetic ranking of Lake Tyrrell S12 core/Folly Point core samples

Composed with input from John Magee, August 2010

From 1 to 5: 1 indicating least extensive post-depositional alteration, 5 indicating most extensive post-depositional alteration

**NB: Nature of sample - lunette, Tyrrell Beds, or Blanchetown Clay – must be taken into consideration when assessing amount of post-depositional alteration

Characteristics on which assessment is based:

Cutans are indicative of actual soil formation – these happen as clays are leached out of upper A horizon by meteoric water and washed down into B horizon, where they coat grains or voids (illuviation). They are deposited on surfaces as water disappears/evaporates, and because of the tendency of clays to adsorb to surfaces.

rare (1) or ubiquitous (5)? Discontinuous (1) or continuous (5)? Thin (1) or thick (5)?

Clay pellets form on the surface of drier, groundwater fed lake bed. There is no real cementation of grains, so that pellets do not survive extensive transport. Rounding is due to aeolian transport from the lake bed to the lunette. Pellets break down in a soil environment due to wetting, drying and compaction – so pelletal structure disappears quite rapidly. This can also happen during reworking within the lake.

Perfectly preserved including borders and roundedness (1) or preferentially aligned but with boundaries beginning to merge – i.e. voids disappearing (3) or absent (in lunette only) (5)

Note: polygonal structures/peds are different from pellets.

Iron oxides are indicative of post-depositional oxidation, possibly by oxic groundwater or even by penetration of air (via plant roots, or animal burrows). Different colors are indicative of the extent of oxidation; with redder colors associated with more extensive oxidation. Note: many iron oxides found in Lake Tyrrell sediments are brown, indicating less extensive oxidation.

Absent (1), present but brown (3), present and red (5)

Ranking is not based on the morphology of the iron oxides: dendrites or framboids in place do not indicate better preservation than iron oxide coating a void; instead, morphology reveals how the iron oxide got there in the first place.

Instead, color of iron oxides within pedogenic features is compared: voids to voids, cutans to cutans.

Secondary carbonate and gypsum in pedogenic nodular form - these form as a result of dissolution and re-deposition by meteoric waters (evaporites are transported from the A to the B horizon, down the soil profile).

Absent (1) or common and large (5)

Miscellaneous features of interest: cross-cutting structures, disruption of bedding – perfect preservation (1) or no bedding (5)

Secondary precipitation of gypsum by groundwater: if there is no evidence of primary gypsum, and all gypsum is secondary (discoidal, displacive forms), then salinity of original sample cannot be inferred

NOTE: Descriptions of all of these features may be found in "Late Quaternary environments and palaeohydrology of Lake Eyre, arid central Australia" (1997), an unpublished Ph.D. thesis by J.W. Magee, in the Division of Archaeology and Natural History, Research School of Pacific and Asian Studies at the Australian National University, Canberra, Australia.

Abbreviated sample name*	Depth (cm)	Cutans	Pellets OR peds (specify)	Iron oxides	Miscellaneous	Overall
LT 2 (lunette)	192.5-200	3 common, fairly continuous; from ~60 um thick around grains up to 250 uM thick along cracks; more at base of section where other indicators of preservation are poorer	3 pellets relatively well preserved in top of section with clear boundaries, though not perfectly rounded - beginning to merge at base	2 orange-red to red at base of section; covering ~5% of section at base and only along cracks	3 Cross-cutting features at base of section, some clay re-organization along joints, plus iron-oxides cementing some joints	3
LT 4 (Tyrrell beds)	234-241	3 present, surrounding some quartz grains and along edges of peds and joints; some continuous, some discontinuous	4 Peds well developed; some cemented joints between peds; oriented clays along boundaries of many peds	4 Some brownish, some reddish, very widespread; includes staining along cracks, some spherules, cementing of cracks, and ferri-argillans around quartz grains, haloes around voids	4 Bedding absent, cross-cutting features and clay reorganization throughout section; area with putative microbialites full of red and brown iron oxides (possibly due to groundwater alteration)	4
LT 5 (Tyrrell beds)	280-287	5 cutans present along grains and peds	5 polygonal cracking with clay re-organization; well developed peds at	5 dendrites and very red spherules all through section; concentrated along	5 no bedding; evidence of extensive matrix reorganization	5

			base of section	cracks		
LT 30 (Tyrrell beds)	312-319	3 discontinuous clay cutans along gypsum crystals; continuous along cracks	3-4 Peds/polygonal cracking with clay reorganization along edges in all clay layers	3 Some brownish iron oxides along cracks	4 Cross-cutting structures in all clay layers; secondary gypsum growth has completely disrupted/destroyed all layers; initial soil formation at top of section	4
LT 32 (Tyrrell beds)	360-367	3 discontinuous clay cutans along gypsum crystals; continuous along cracks	3-4 Peds/polygonal cracking with clay reorganization along edges in all clay layers; some peds appear to be re-worked and have their own cutans	2.5 red iron oxide staining along cracks in small area of upper section	3-4 Cross-cutting structures in all clay layers; secondary gypsum growth has completely disrupted/destroyed most layers	3.5
LT 7 (Tyrrell beds)	412-419	2.5 Limited zoning in clay at base of section; small, discontinuous cutans on some quartz grains at base of section	2.5 Peds at top and base of section; no oriented clay or oxides along edges; joints not well developed	2 Some red iron oxides present in scattered locations among clay at base of section; most is brownish color	2.5 Bedding well preserved within gypsiferous/mat layers, though not within clay; some displacive gypsum present; primary gypsum and dolomite present; putative fecal pellets	2.5

LT 9 (Tyrrell beds)	467-474	2 cutans along some cracks at top of section	2.5 Peds/polygons present at top of section	1.5-2 Scattered brown spherules within microbialites at top of section	3 lots of displacive and re-worked gypsum disrupting bedding; also present are some undisturbed beds, primary gypsum, and dolomite	2.5
LT 34 (Tyrrell beds)	503-510	2 very small (~20uM), discontinuous cutans, not always present around gypsum crystals, around some voids	1 absent	1 absent	2-3 displacive gypsum growth has heavily disrupted primary layers including some mats; also present are many drying cracks	2.5
LT 10 (Tyrrell beds)	519-526	1 absent	1 absent	1 absent	2 sineresis cracks in some clay layers, other than this bedding is well preserved; however displacive gypsum has disrupted some bedding and overgrown some microbialites	1.5
LT 35_36 (Tyrrell beds)	552-559	1 absent	1 absent	1-1.5 absent Reduction is evident (FeS_2) but appears to be	1-1.5 Layers mostly well-preserved, some disruption due to secondary gypsum	1

				primary	growth	
LT 11_12 (across Tyrrell beds/Blanchetown clay contact; 11 is within Tyrrell beds, 12 is within Blanchetown Clay)	591.5-599.5	For LT 11: 2 Present in the small clay layers For LT 12: 1 absent	For LT 11: n/a No massive clay For LT 12: 1 absent	For LT 11: 3 Absent – though extensive evidence of *reduction* For LT 12: 3 Brownish- orange, around voids and in blebs throughout	For LT 11: 4 No bedding, microbialite and primary gypsum completely disrupted by secondary gypsum; even this is then disrupted by FeS_2 and re-dissolution For LT 12: 3.5 Some bedding, but massively oxidized	For LT 11: 3 For LT 12: 3
LT 13 (Blanchetown clay)	649-656	1 absent	2 some partially formed peds at top of section	2 Brownish-reddish, but present only in certain parts of section	3 some bedding preserved, some is destroyed by cross-cutting structures; organic fibers also present	2.5
LT 20 (Blanchetown clay)	1014-1021	1 absent	1 absent	3 Some brownish iron-oxide staining around voids and within layers throughout section	2 Bedding only at top of section - perhaps multitude of iron-oxides has disrupted bedding; also some quartz lenses disrupted	2

* All samples are from the core taken at Folly Point. Full names would read, for example, "LT S12 sample 2, 192.5 – 200 cm" for what is here denoted "LT 2"

Appendix 4:

Mass spectra of lipids extracted from Lake Tyrrell S12 core/Folly Point core and modern mat, water and sediment samples

Notes on terms in Appendix 4

- DBEs: double bond equivalents (a double bond = 1 DBE, a ring = 1 DBE)
- MW: molecular weight
- M+: molecular ion, total mass of ion carrying a positive charge; can assist in identification of molecule
- Me = methyl, Et = ethyl
- Δn: location of double bond, for example Δ5,22 means there are two double bonds, 1 between C5 and C6 and another between C22 and C23
- Δn(m): location of double bond if the carbons it joins are not sequential in the numbering scheme, for example Δ24(28) indicates that the double bond joins the C28 methyl to C24 in the skeleton; Δ24 would indicate that the double bond is in the side chain between C24 and C25
- β or B, α or a: stereochemistry of functional group; compounds that differ only in this are stereoisomers
- $C_{x:n}$: Number of carbons and number of double bonds in molecule

Notes on structures & fragmentation patterns

- For background information on the structure and nomenclature of simple lipids and terpenoids (including steroids, hopanoids, and triterpenoids), refer to:
- Analysis of Sterols, by L. John Goad and Toshihiro Akihisa; Blackie Academic & Professional (1997)
- LJ Goad (1991) *Methods in Plant Biochemistry* vol 7, pp 369-434
- "Mass Spectrometry of Lipids", by Richard P. Evershed; Chapter 8 of Lipid Analysis: a Practical Approach; ed. Hamilton & Hamilton (1992)
- The Mass Spectra of Organic Molecules, by JH Benyon, RA Saunders & AE Williams; Elsevier Publishing Company (1968)
- Topics in Lipid Chemistry, vol. 1, by FD Gunstone; Ed. Logos Press, Ltd. (1970)

Standards

Quantification standard: 18-methyl eicosanoic acid methyl ester (18-MEAME)

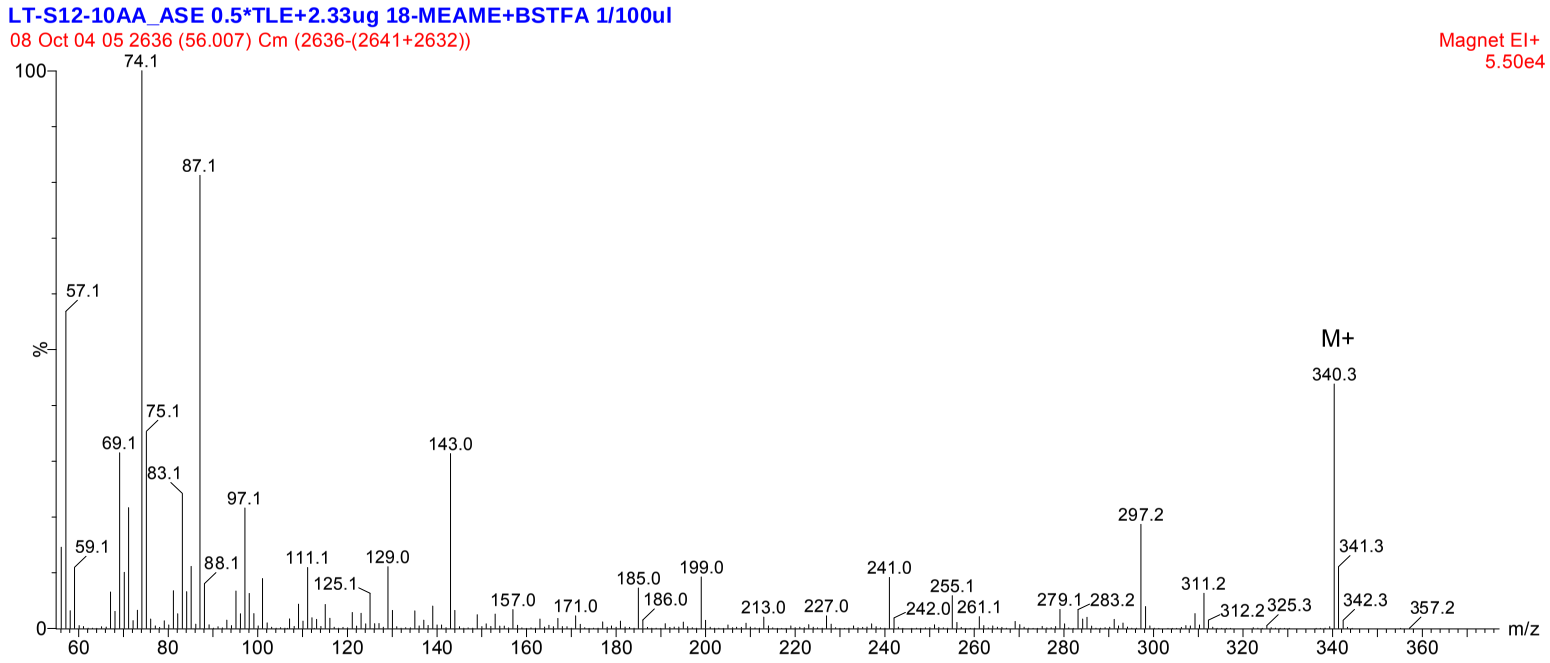

Formula: $C_{22}H_{44}O_2$

MW = 340

Alkane quantification standard: 3-methyl heneicosane (3-me-22)

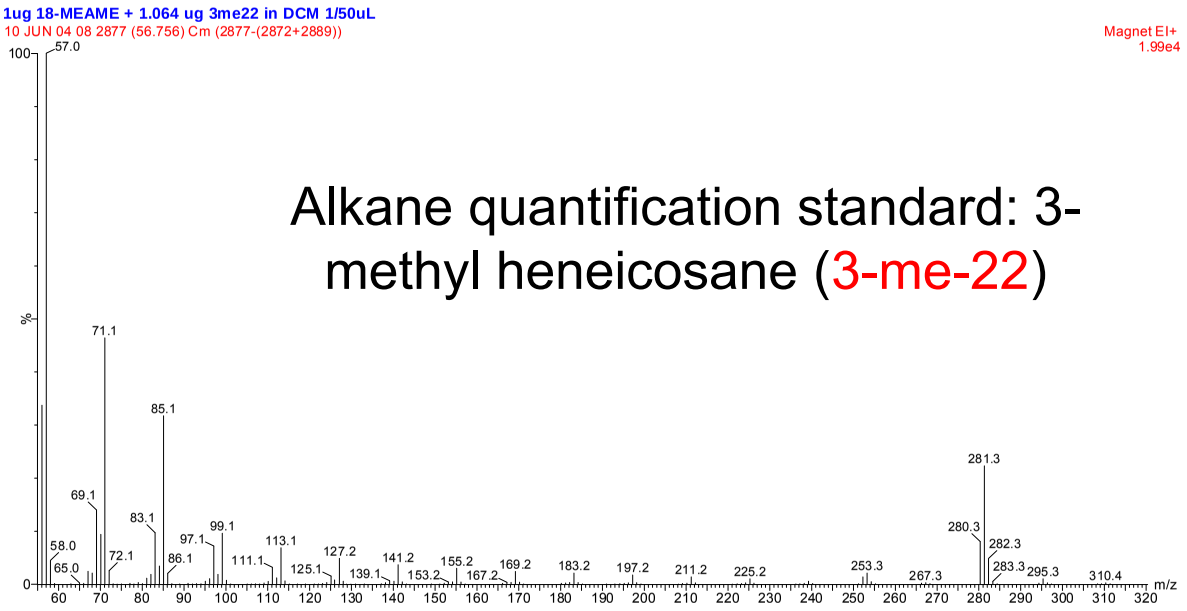

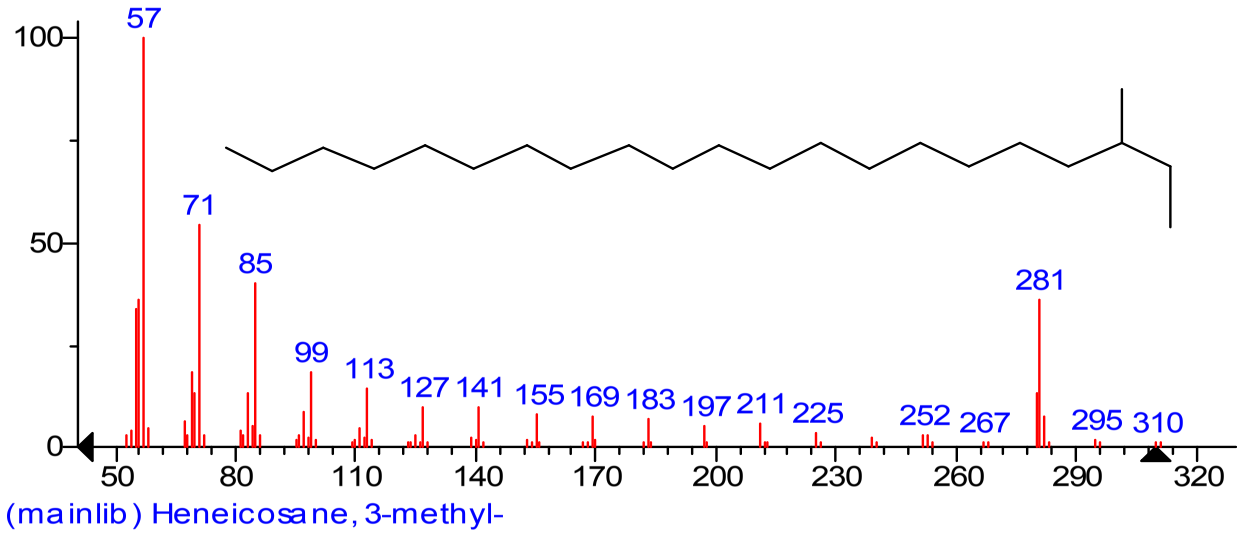

Formula: C22H46
MW = 310
Response factor relative to 18-MEAME: 0.684 (calculated June 2010)

Extraction efficiency standard: 1-Br-eicosane

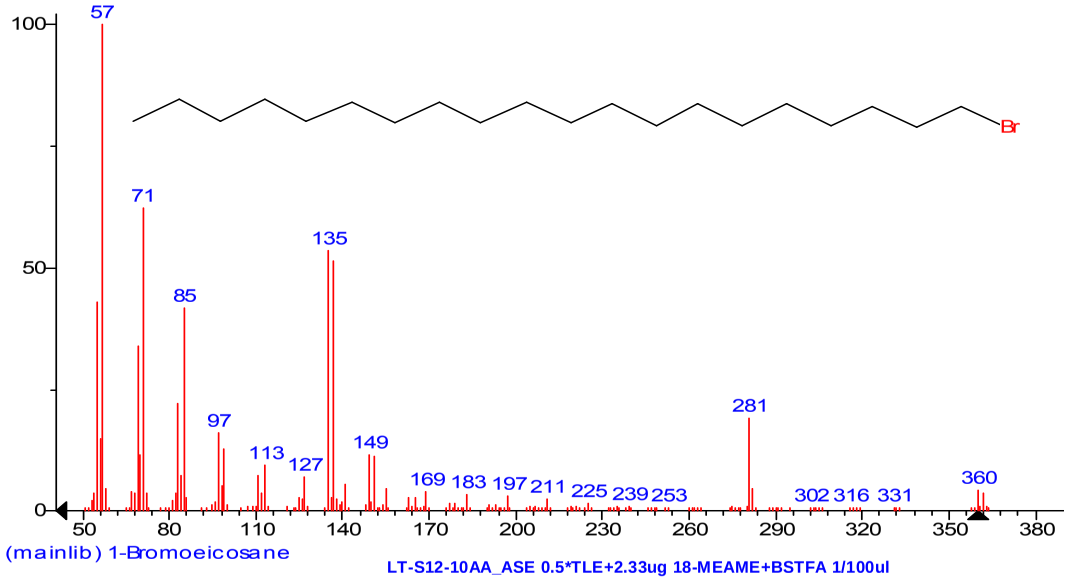

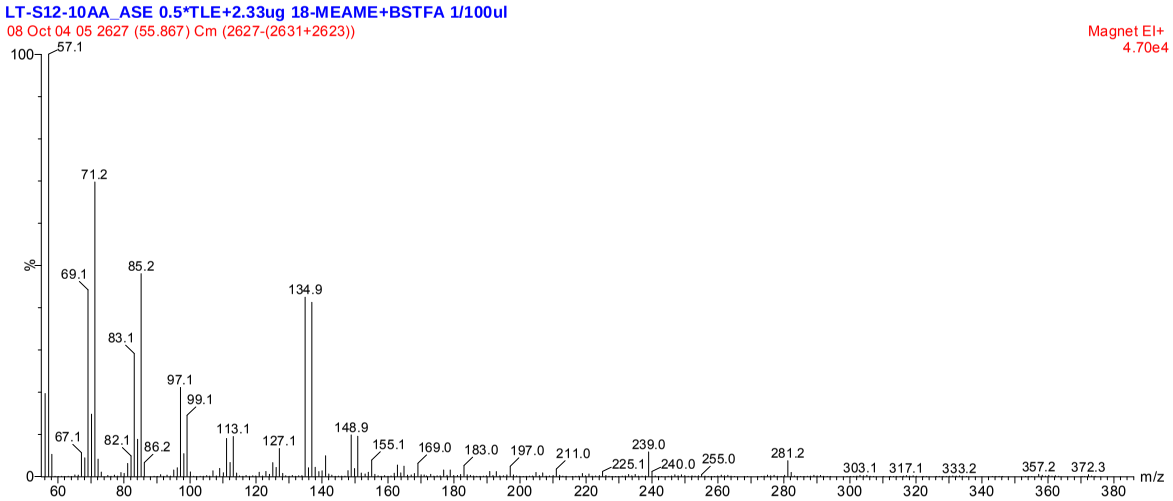

Formula: C20H41Br
MW = 360
Response factor relative
to 18-MEAME: 1.035

BSTFA (derivatization) standard: 12-Br-dodecan-1-ol

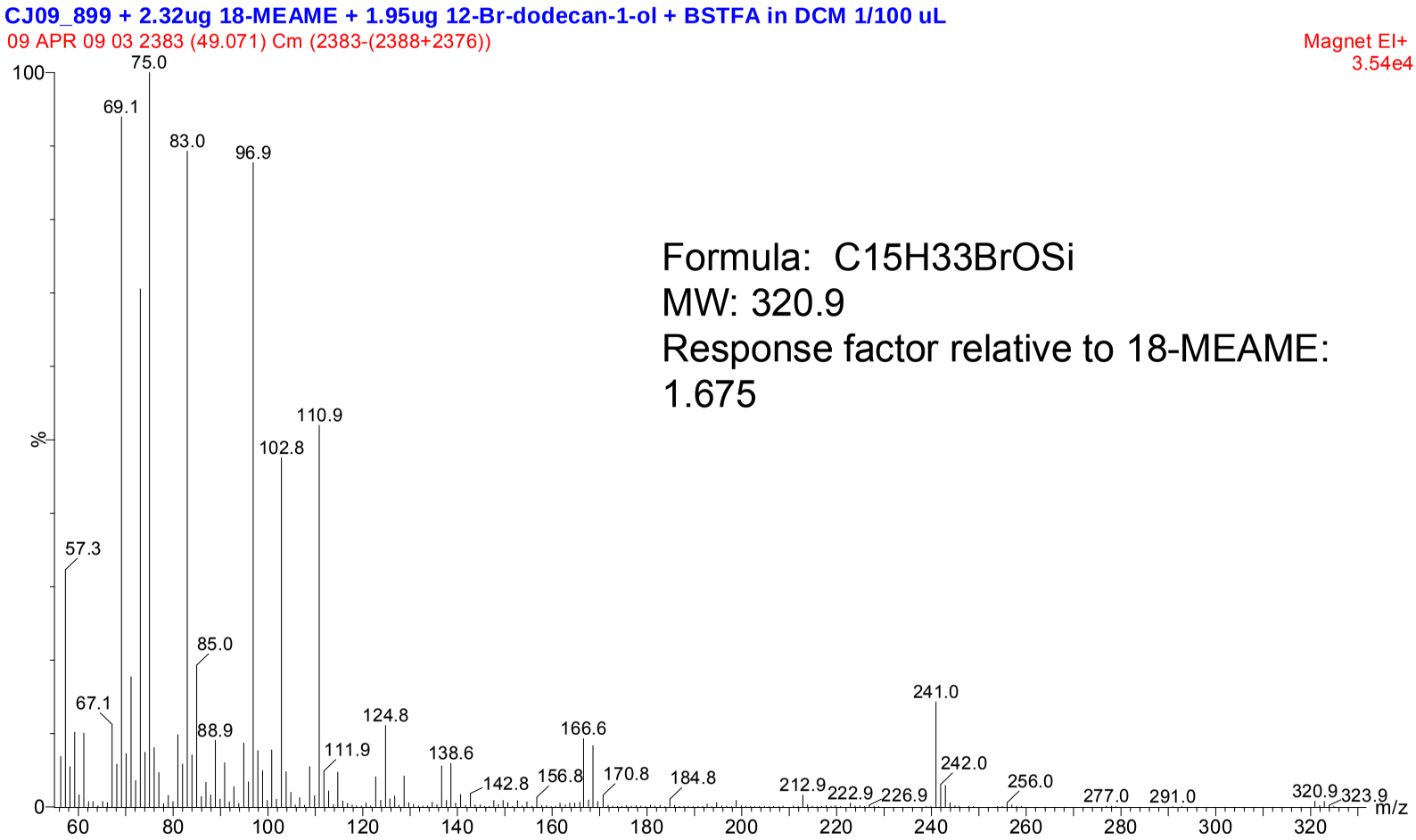

Formula: C15H33BrOSi
MW: 320.9
Response factor relative to 18-MEAME: 1.675

Sterols

General information about sterol sources based on carbon number:
C27: eukaryotes (animals)
C28: phytoplankton (including diatoms)
C29: green algae, higher plants
C30: dinoflagellates

1: Cholest-5-en-3B-ol TMS (Cholesterol); NIST library + samples

C27, 5 DBEs
C27 Δ5 Sterol
Source:
Ubiquitous
Algae,
Zooplankton,
phytoplankton

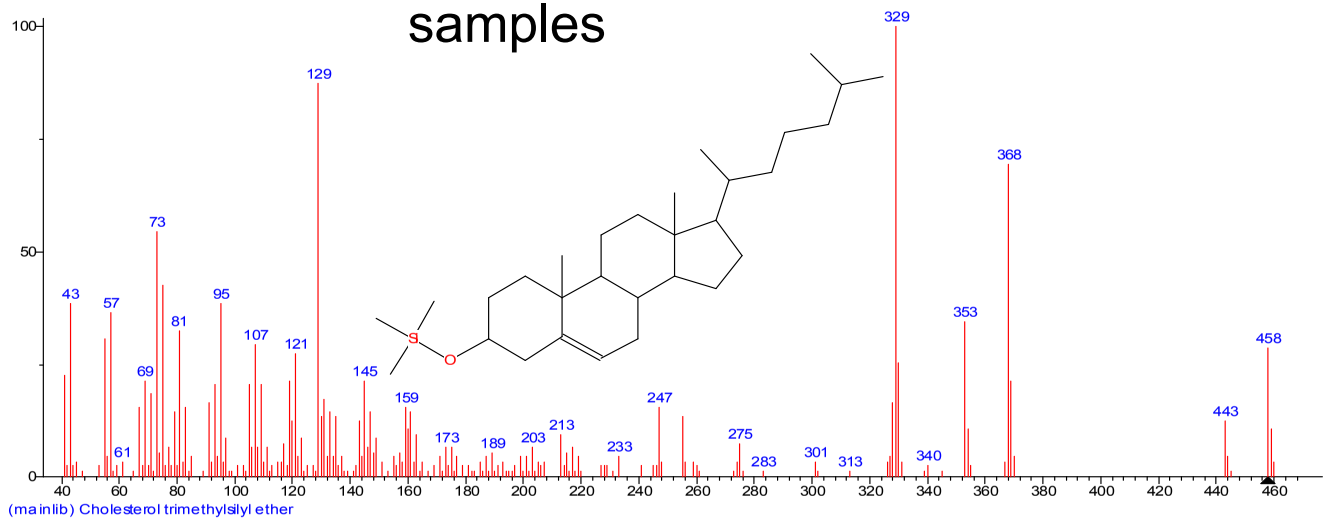

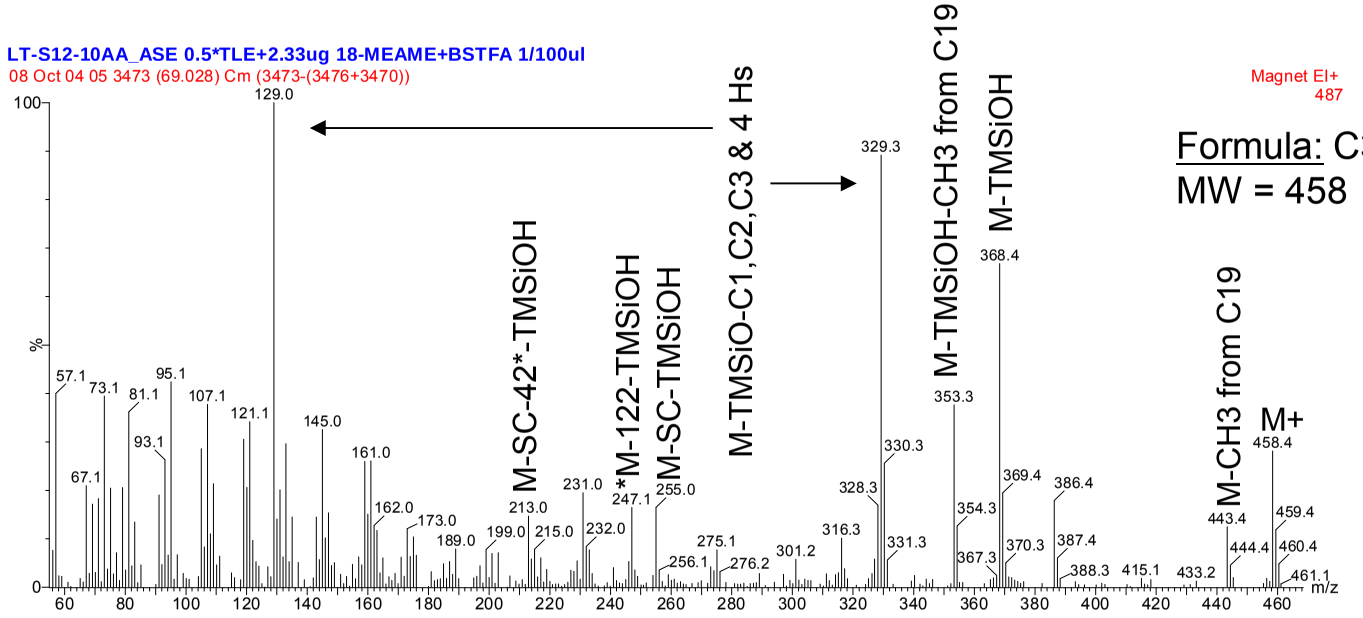

Formula: C30H54OSi
MW = 458

*42 is C15,
C16, C17, 6H

*C & D
Rings plus side chain

Lathosterol TMS

C27, 5 DBEs
C27 Δ7 Sterol

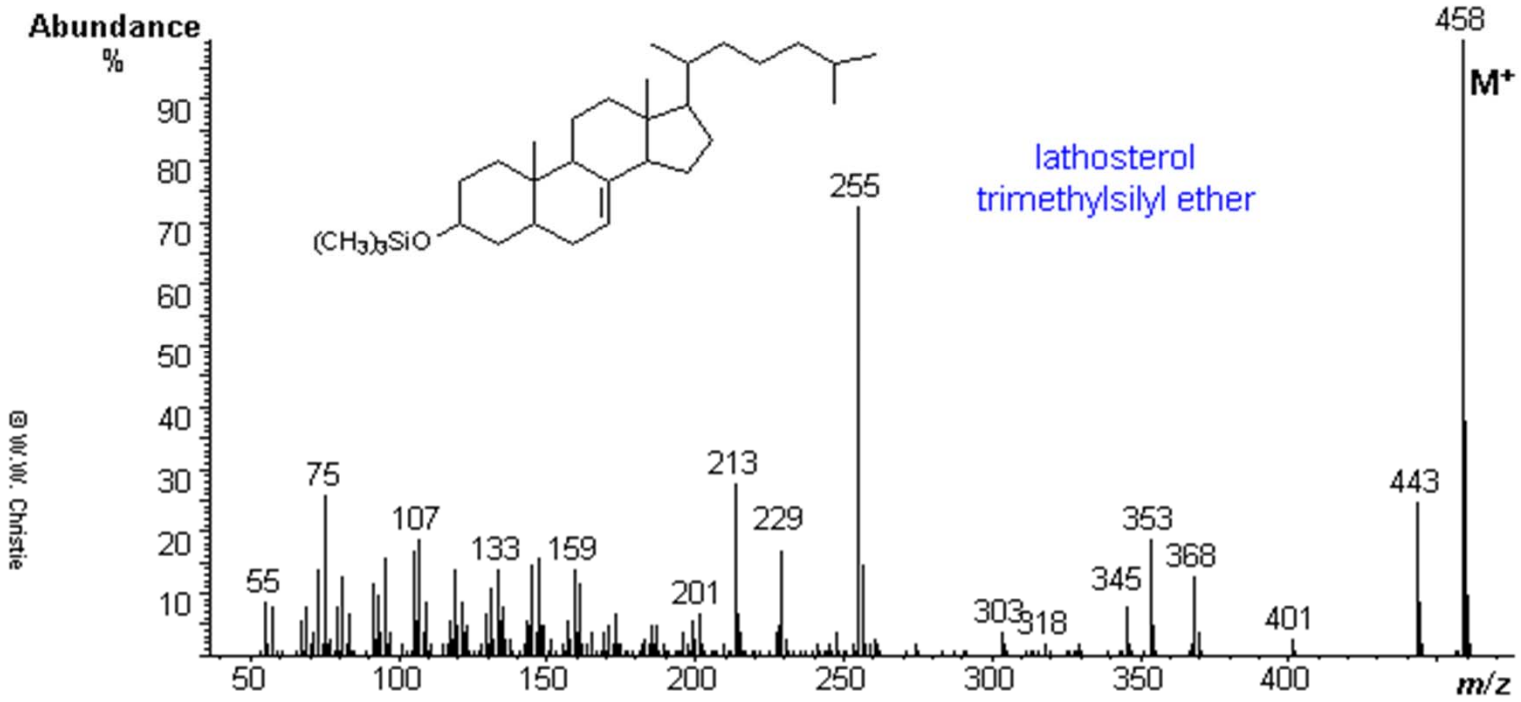

Identified from lipidlibrary.co.uk – W.W. Christie

Desmosterol TMS

C27, 6 DBEs
C27 Δ5, 24 Sterol

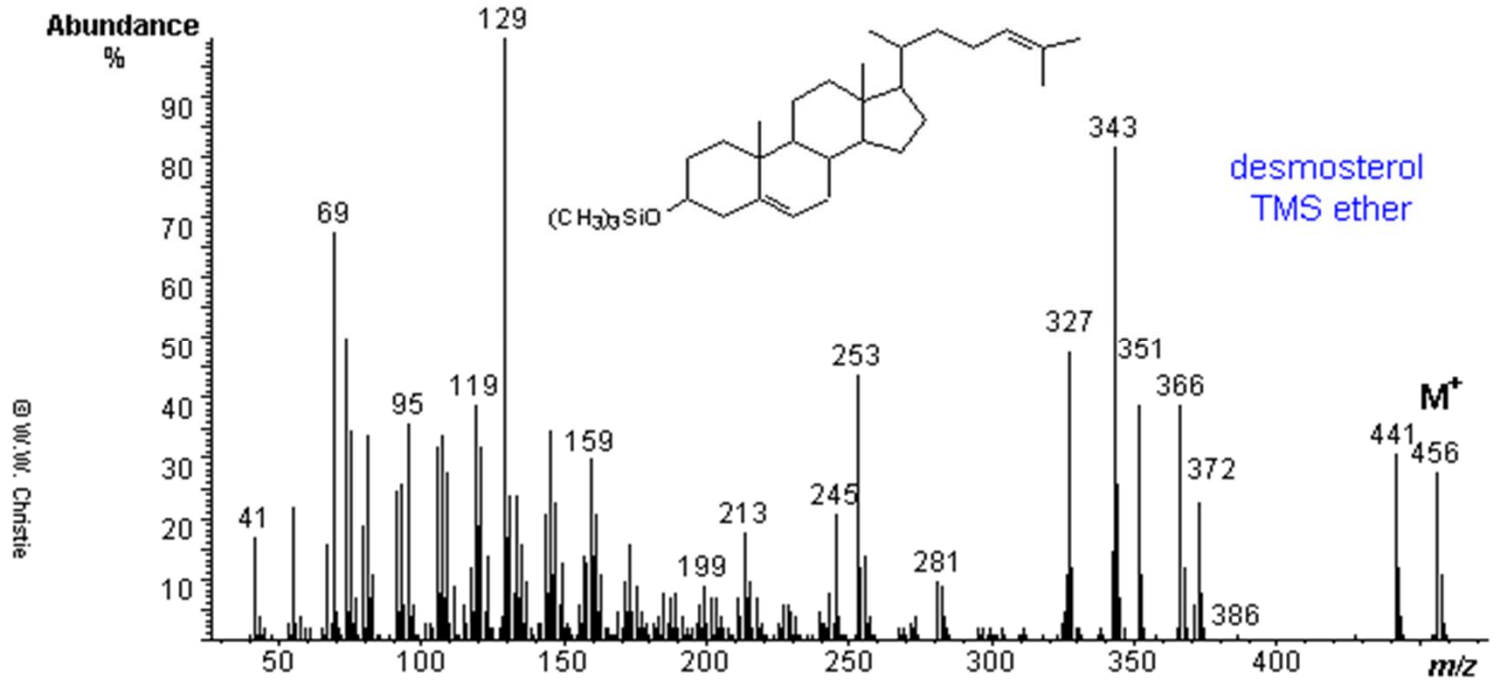

Identified from lipidlibrary.co.uk – W.W. Christie

Zymosterol TMS

C27, 6 DBEs
C27 Δ8, 24 Sterol

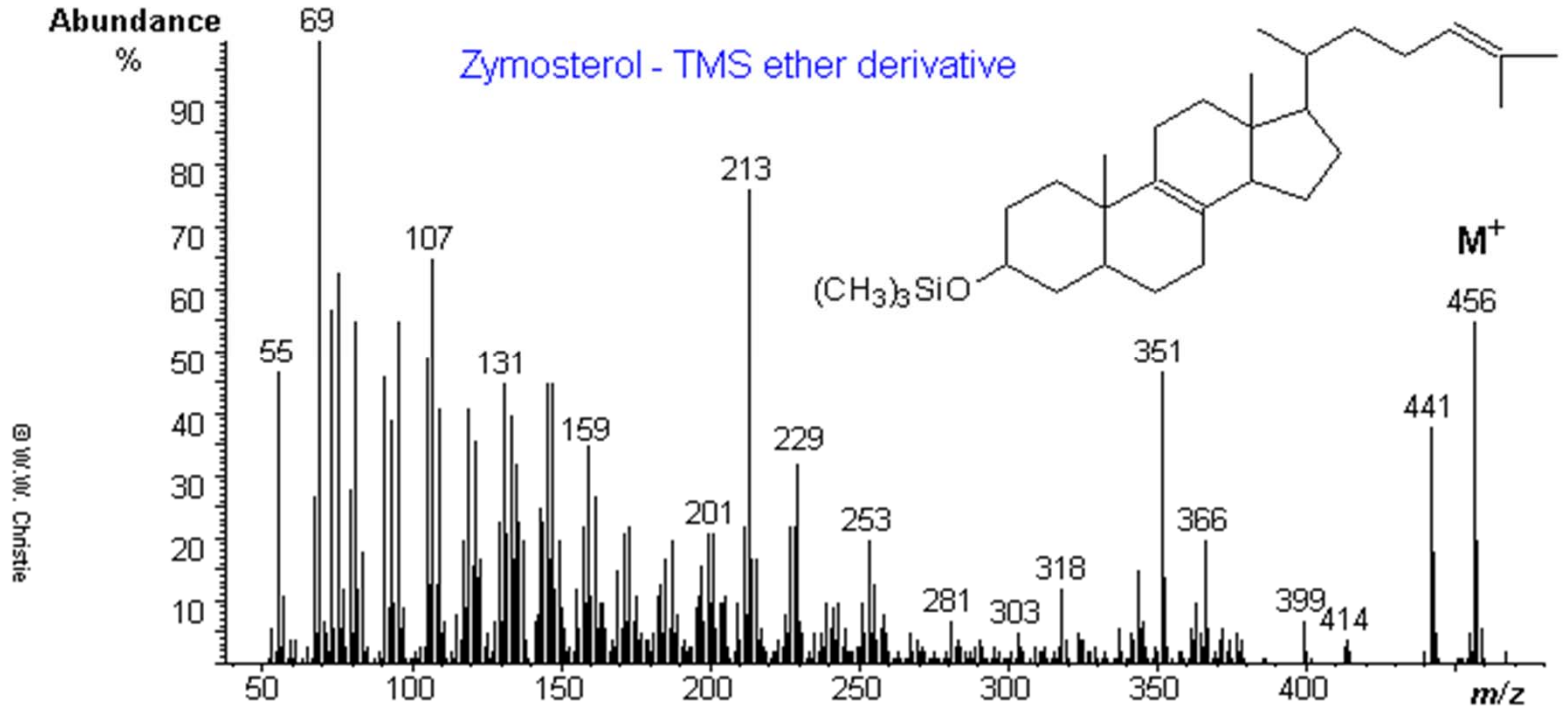

Identified from lipidlibrary.co.uk – W.W. Christie

2: 4a-methyl-5a-cholest-7-en-3B-ol (Lophenol); sample & reference below

C28, 5 DBEs

C28 Δ7 Sterol Sources: dinoflagellates, cacti, intermediate in sterol biosynthesis

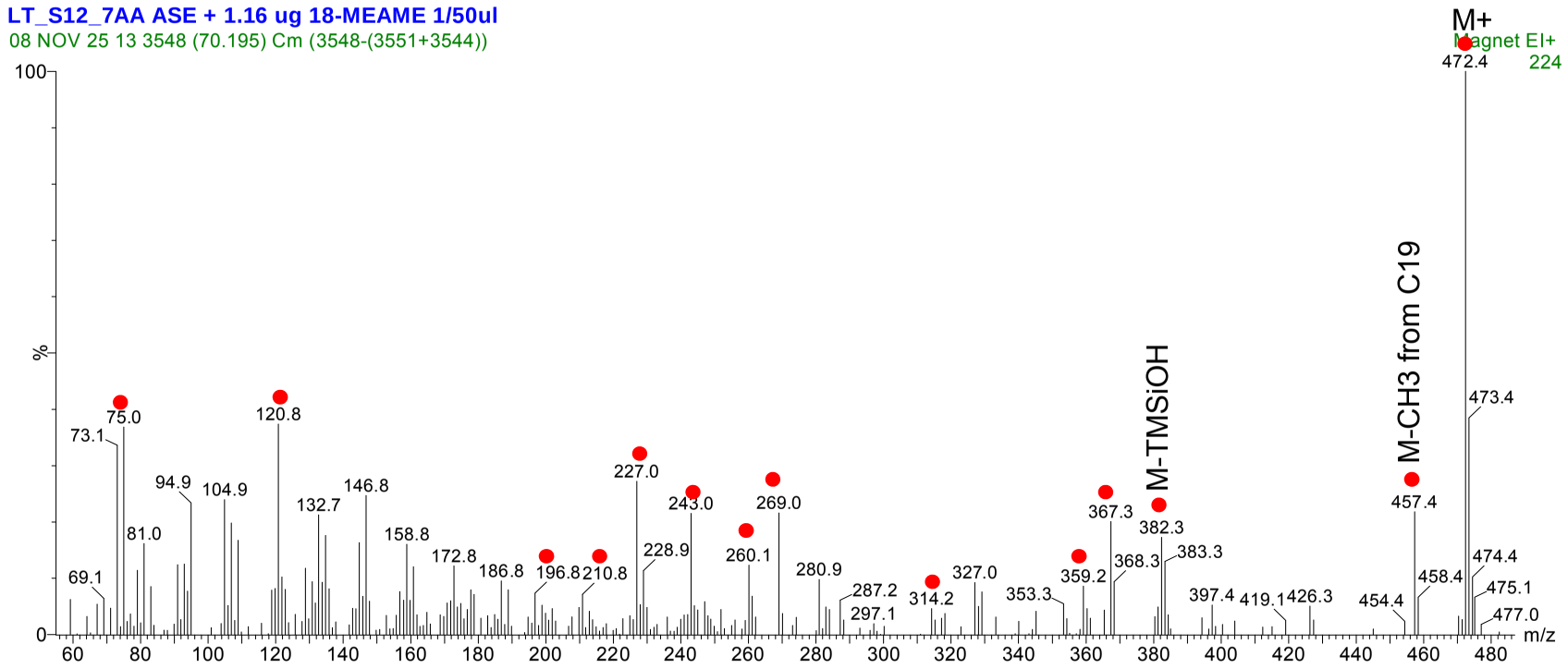

- Red dots indicate major ions id'd w NIST library

N. Withers (1987) *Dinoflagellate sterols*, pp 316-359
in The Biology of Dinoflagellates, ed. FJR Taylor, Botanical Monographs 21
sources listed: *Amphidinium carterae*, cactus, biosynthetic intermediate in mammalian cholesterol biosynthesis

2: Lophenol TMS (NIST library)

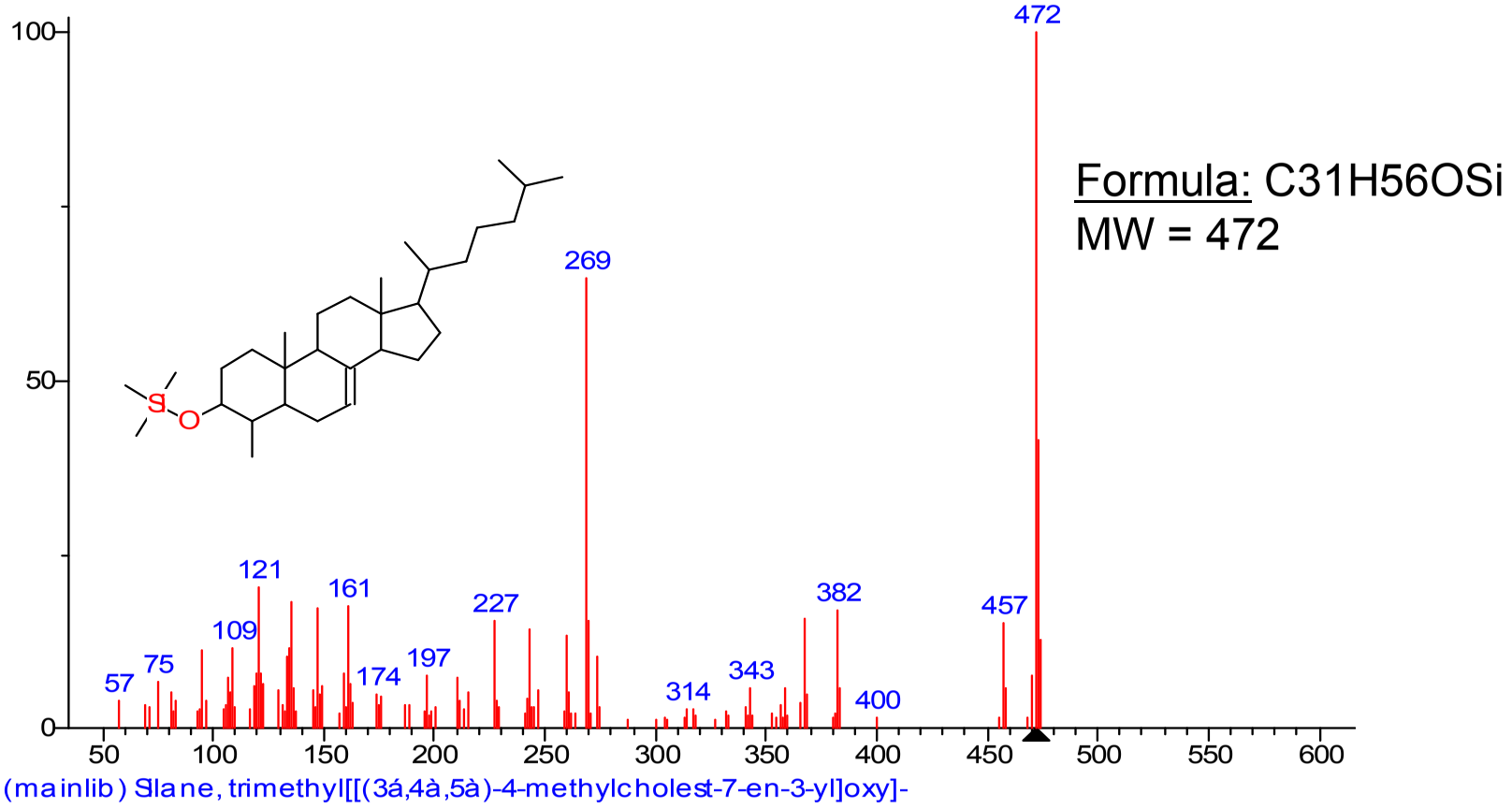

3: 24B-methylcholesta-5,22-dien-3B-ol TMS (Ergosta-5,22-dien-3B-ol; Brassicasterol); sample & reference below

C28, 6 DBEs

C28 Δ5,22 Sterol

Sources: haptophytes, cryptophytes, diatoms

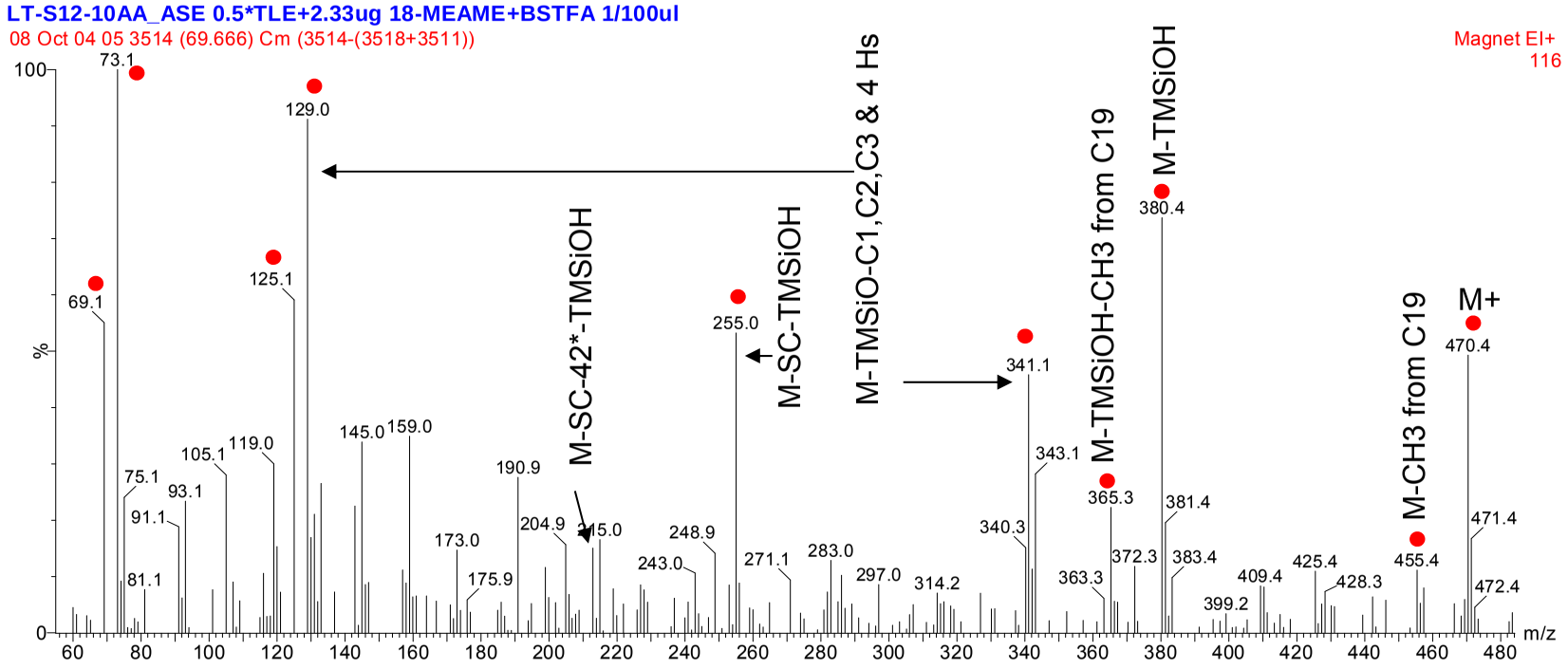

- Red dots indicate ions labeled in reference
  W. Henderson, W.E. Reed and G. Steel (1971) *Adv. Org. Geochem.* pp 335 – 352; Ed. H.R. v. Gaertner and H. Wehner Pergamon Press

*42 is C15, C16, C17, 6H

*C & D Rings plus side chain

4: 24-methylcholest-7-en-3B-ol TMS (Ergost-7en-3B-ol); reference spectrum

C28, 5 DBEs

C28 Δ7 Sterol Sources: algal sterol & hydrogenation of ergosterol

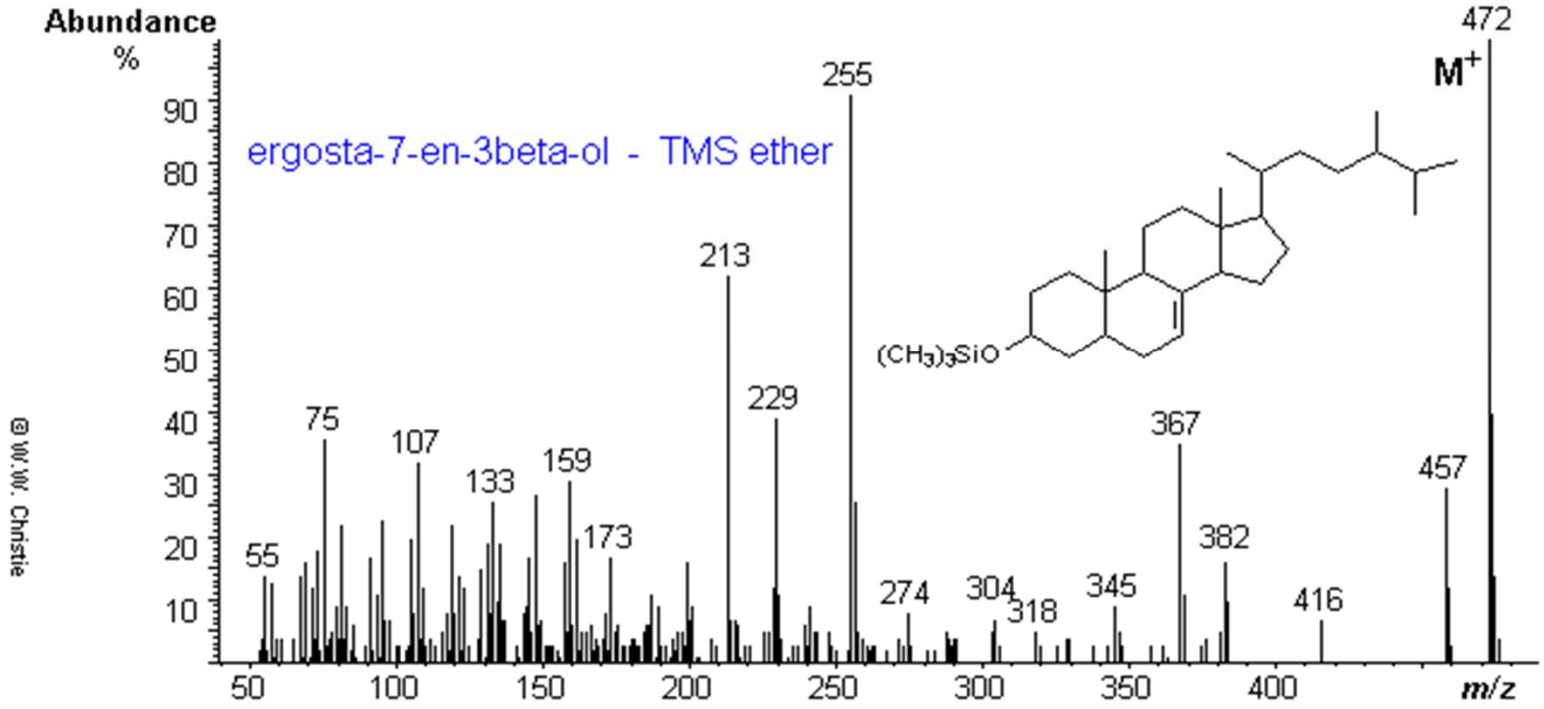

Identified from lipidlibrary.co.uk – W.W. Christie

4: 24-methylcholest-7en-3B-ol (Ergost-7en-3B-ol); sample and reference below

C28, 5 DBEs

C28 Δ7 Sterol Sources: algal sterol & hydrogenation of ergosterol

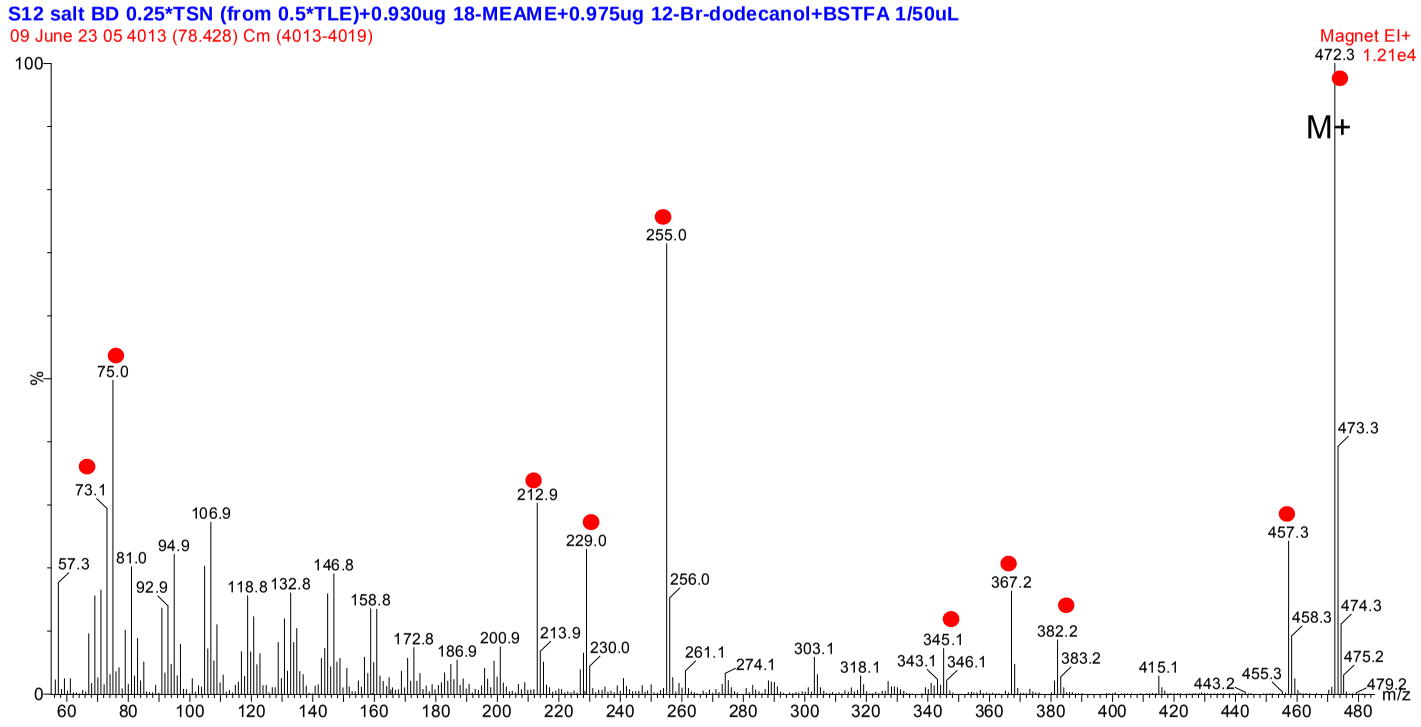

- Red dots indicate ions labeled in reference
  W. Henderson, W.E. Reed and G. Steel (1971) *Adv. Org. Geochem.* pp 335 – 352; Ed. H.R. v. Gaertner and H. Wehner Pergamon Press

*42 is C15, C16, C17, 6H

*C & D
Rings plus side chain

5: Ergosta-5,7,22-trien-3B-ol TMS (Ergosterol); reference spectrum

C28, 7 DBEs
C28 Δ5,7, 22 Sterol

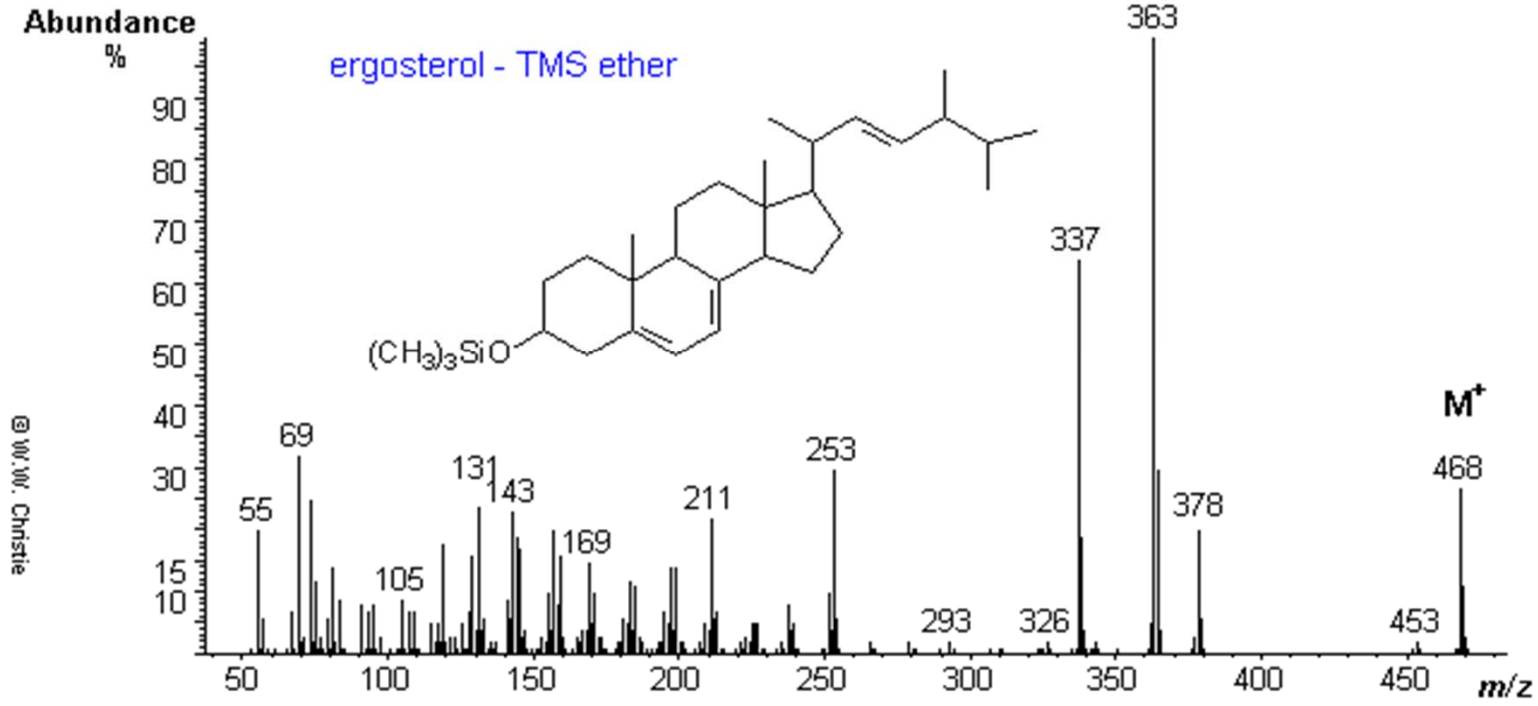

One of main sterols of *Dunaliella salina*
Zelazny *et al* (1995) *Plant Physiology* 109 pp 1395-1403
Identified from lipidlibrary.co.uk – W.W. Christie

Ergosta-7,22-dien-3B-ol TMS

C28, 6 DBEs
C28 Δ7, 22 Sterol

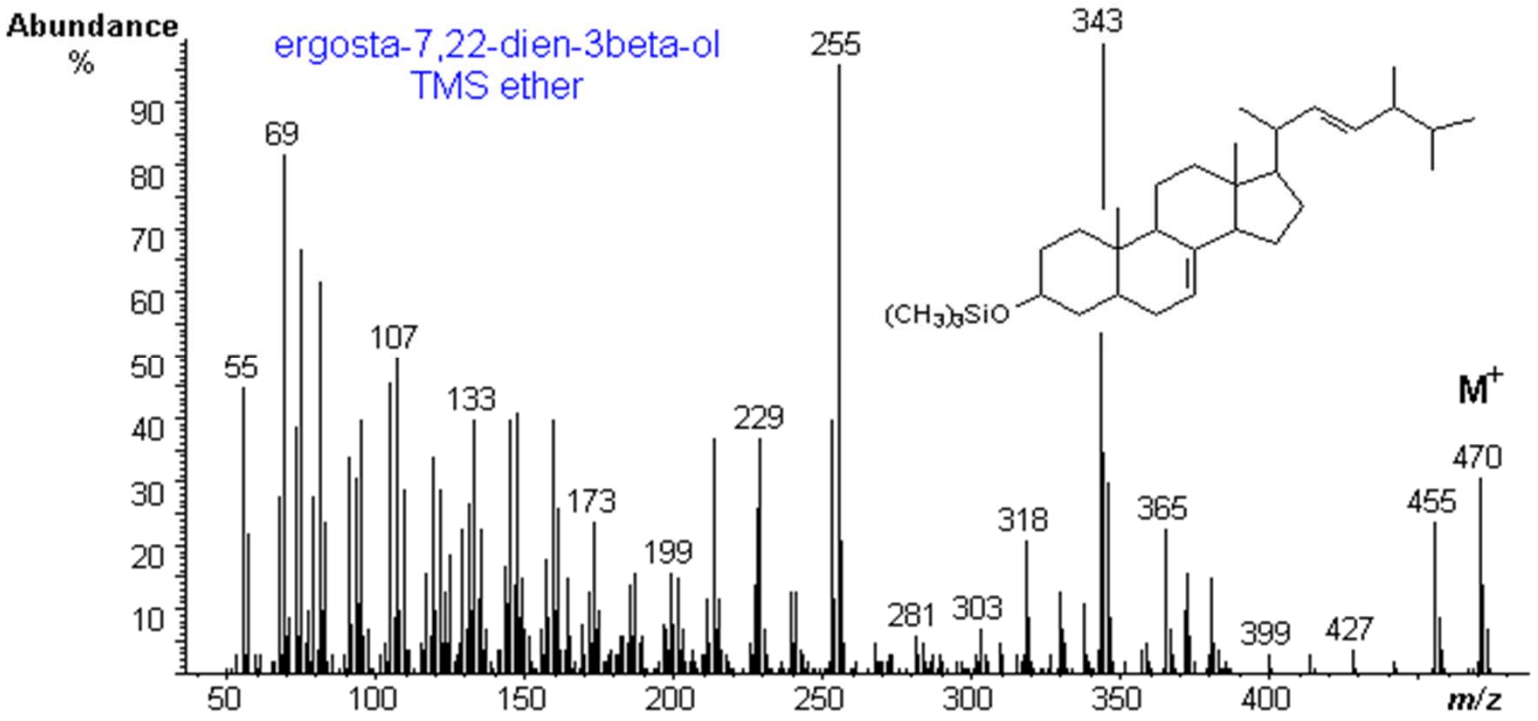

Identified from lipidlibrary.co.uk – W.W. Christie

Ergost-8(14)-en-3B-ol (?) (24-methylcholest-8(14)-en-3B-ol); sample spectrum or maybe DB is in a different spot; Δ8 sterol or perhaps Δ14 are likely

C28, 5 DBEs

C28 Δ? Sterol

Sources: SC=127 w/o H transfer

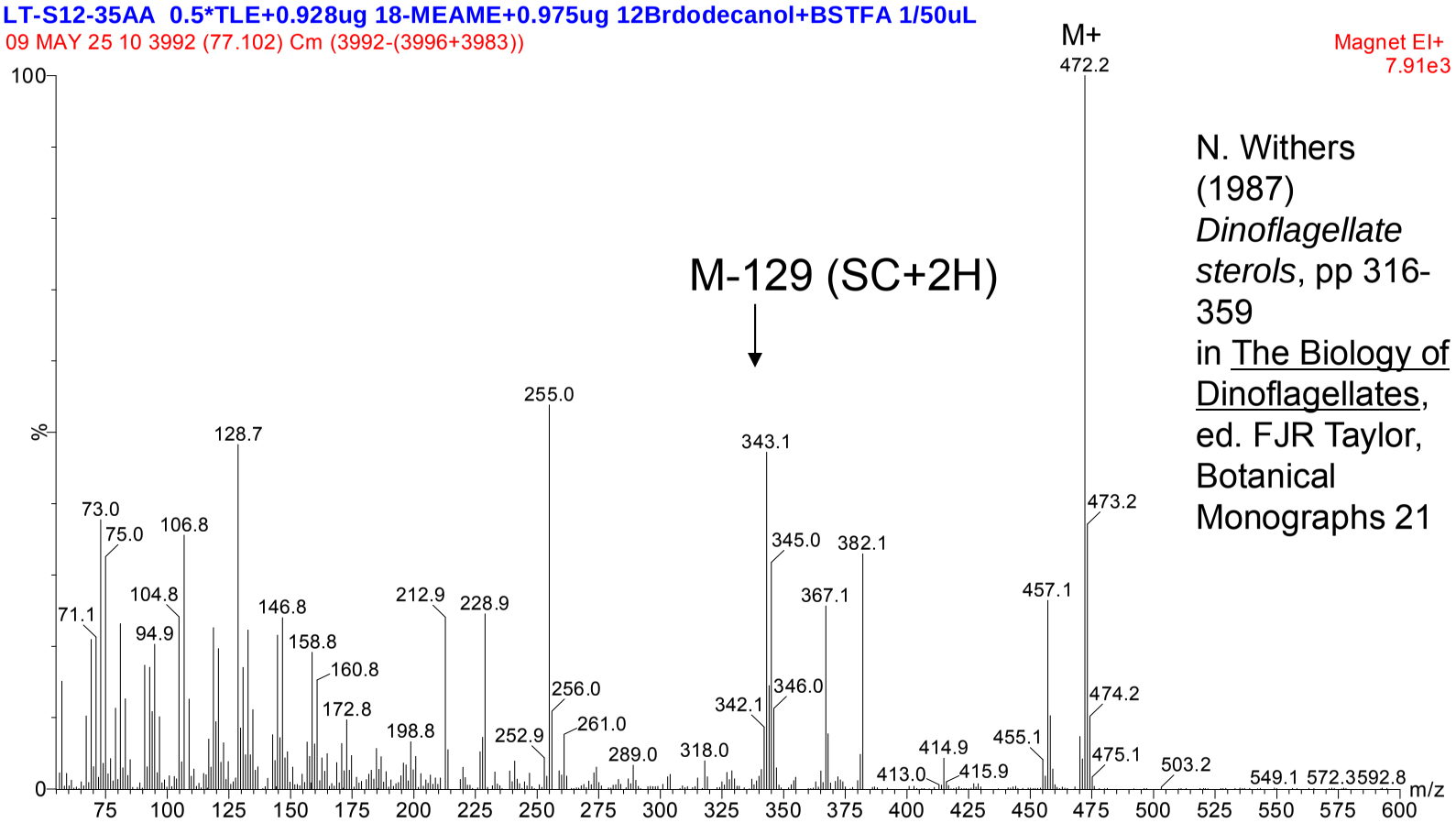

N. Withers (1987) *Dinoflagellate sterols*, pp 316-359 in The Biology of Dinoflagellates, ed. FJR Taylor, Botanical Monographs 21

Ergost-8(14)-en-3B-ol (reference spectrum, NIST library)

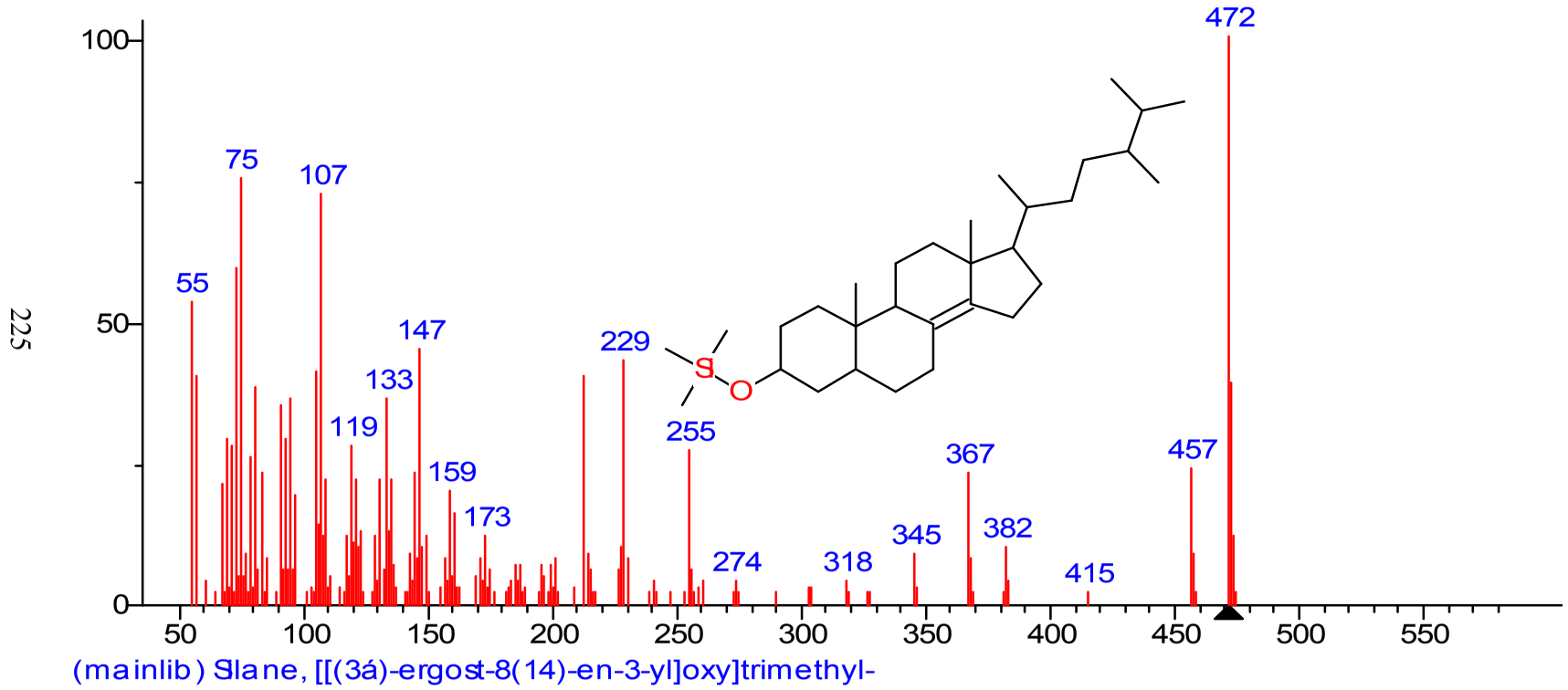

Ergosta-tetra-enol; reference spectrum

C28, 8 DBEs
C28 Δ5,7,9(11),22 sterol

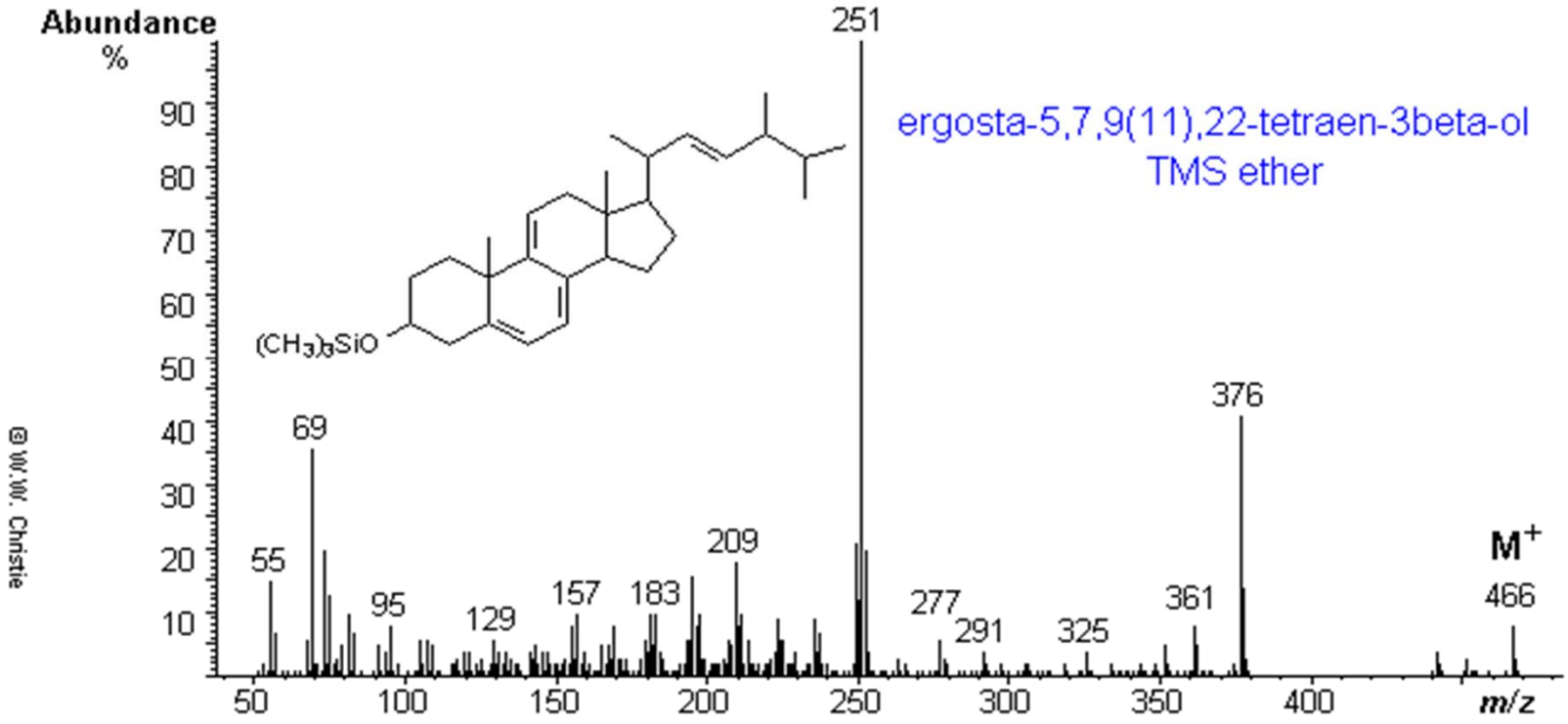

Identified from lipidlibrary.co.uk – W.W. Christie

6: 24a-methylcholesta-5-en-3B-ol TMS (Ergosta-5-en-3B-ol; Campesterol); sample & reference below

C28, 5 DBEs

C28 Δ5 Sterol

Sources: higher plants

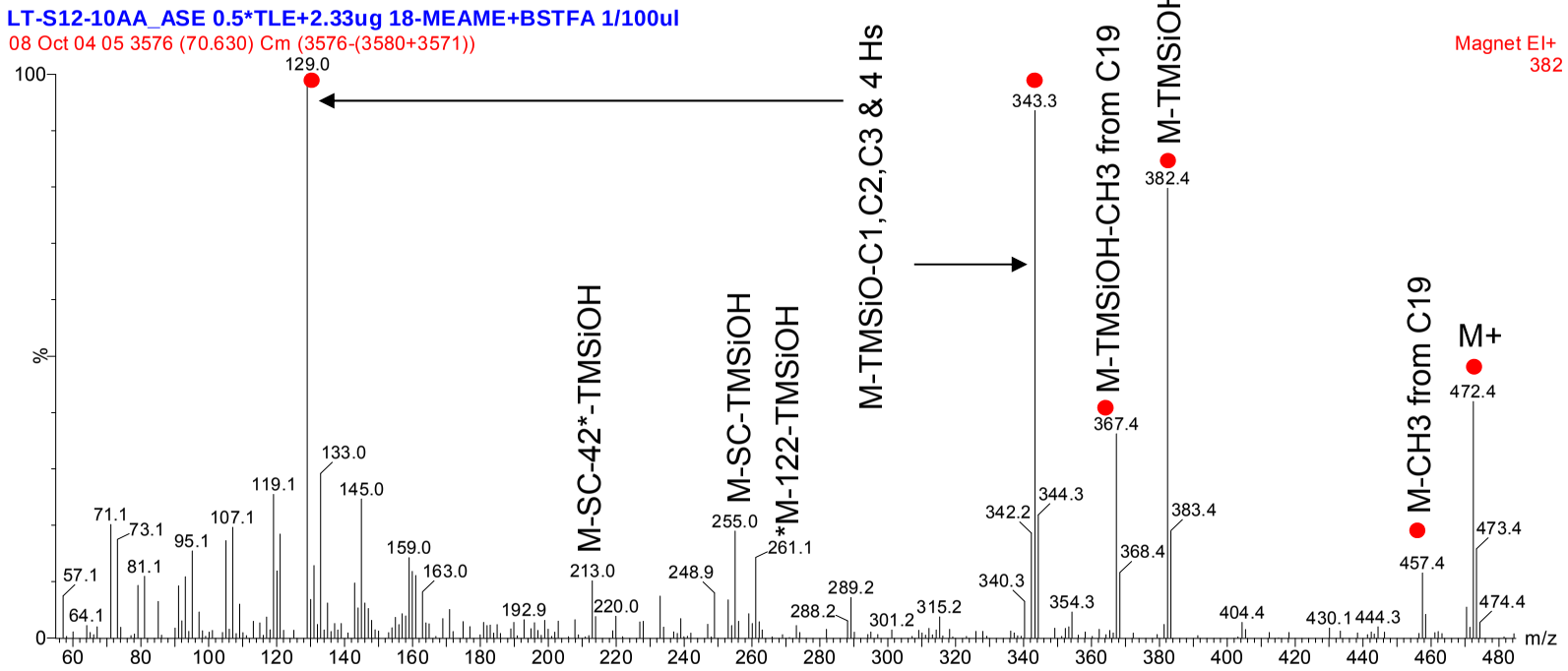

- Red dots indicate ions labeled in reference
  W. Henderson, W.E. Reed and G. Steel (1971) *Adv. Org. Geochem.* pp 335 – 352; Ed. H.R. v. Gaertner and H. Wehner Pergamon Press

*42 is C15, C16, C17, 6H

*C & D Rings plus side chain

7: 24a-ethylcholesta-5,22-dien-3B-ol TMS (Stigmast-5,22-dien-3B-ol; Stigmasterol); sample & reference below

C29, 6 DBEs

C29 Δ5,22 Sterol

Sources: higher plants

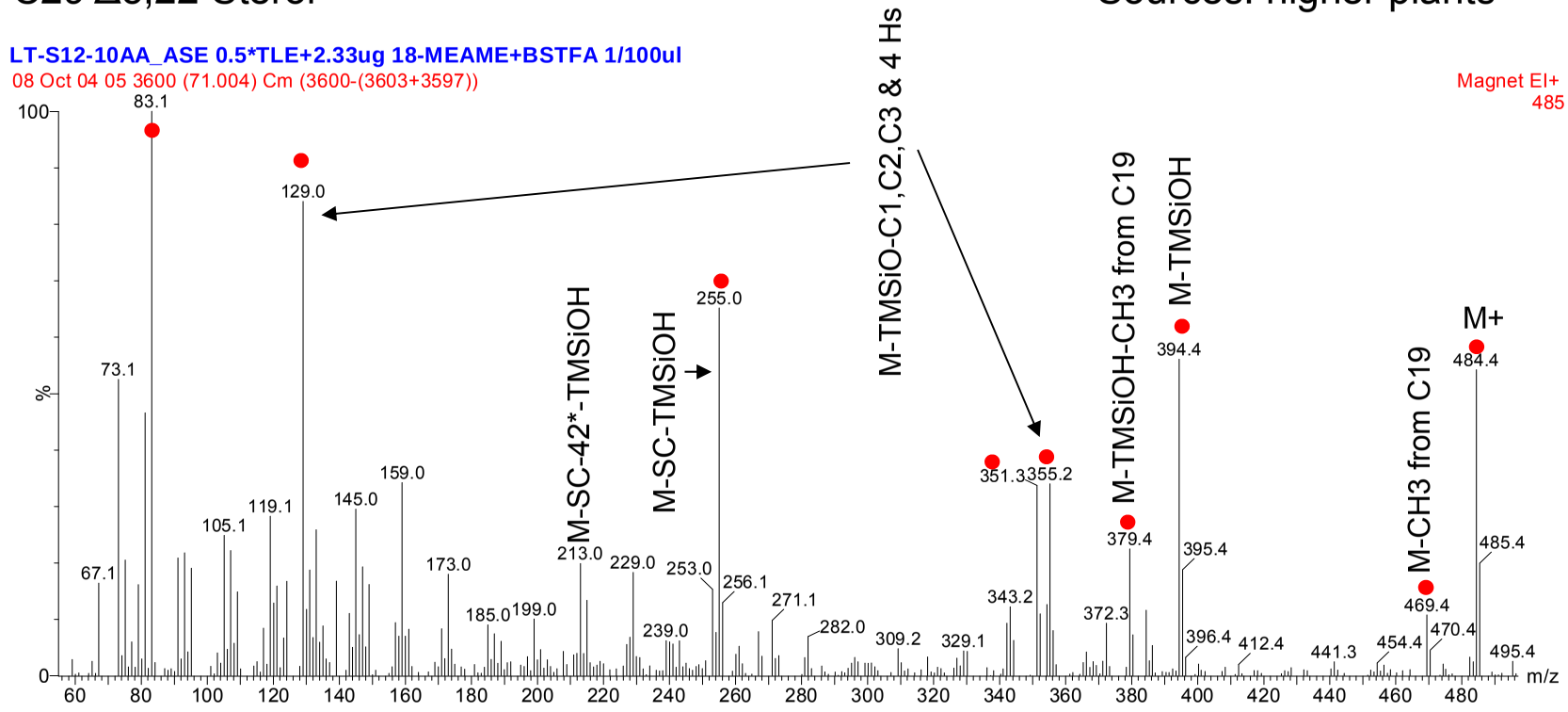

- Red dots indicate ions labeled in reference
  W. Henderson, W.E. Reed and G. Steel (1971) *Adv. Org. Geochem.* pp 335 – 352; Ed. H.R. v. Gaertner and H. Wehner Pergamon Press

*42 is C15, C16, C17, 6H

*C & D Rings plus side chain

7: Stigmasterol TMS (NIST library)

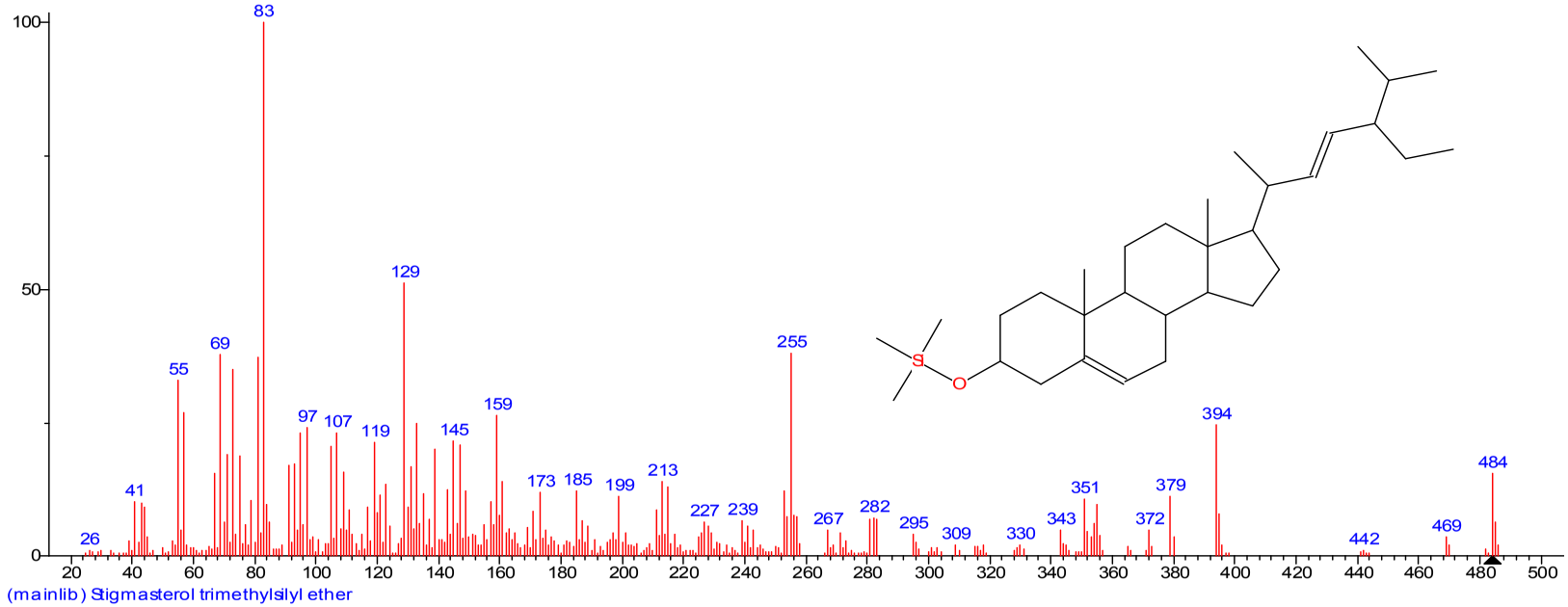

Formula: C32H56OSi

MW = 484

8: 24a-ethylcholesta-5-en-3B-ol TMS (Stigmast-5-en-3B-ol; B-Sitosterol); sample & reference below

C29, 5 DBEs

C29 Δ5 Sterol Sources: higher plants, *D. salina*

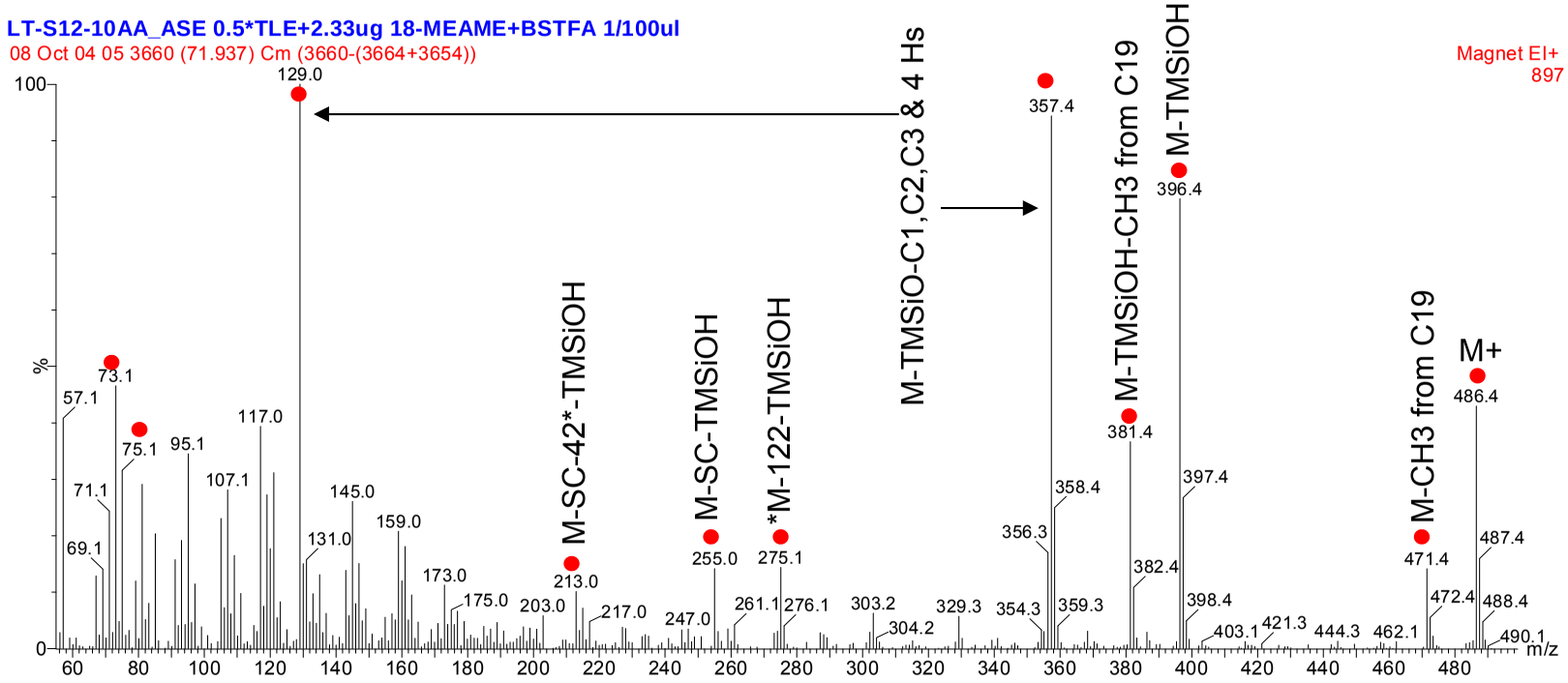

- Red dots indicate ions labeled in reference
  W. Henderson, W.E. Reed and G. Steel (1971) *Adv. Org. Geochem.* pp 335 – 352; Ed. H.R. v. Gaertner and H. Wehner Pergamon Press

*42 is C15, C16, C17, 6H

*C & D Rings plus side chain

8: B-sitosterol TMS (NIST library)

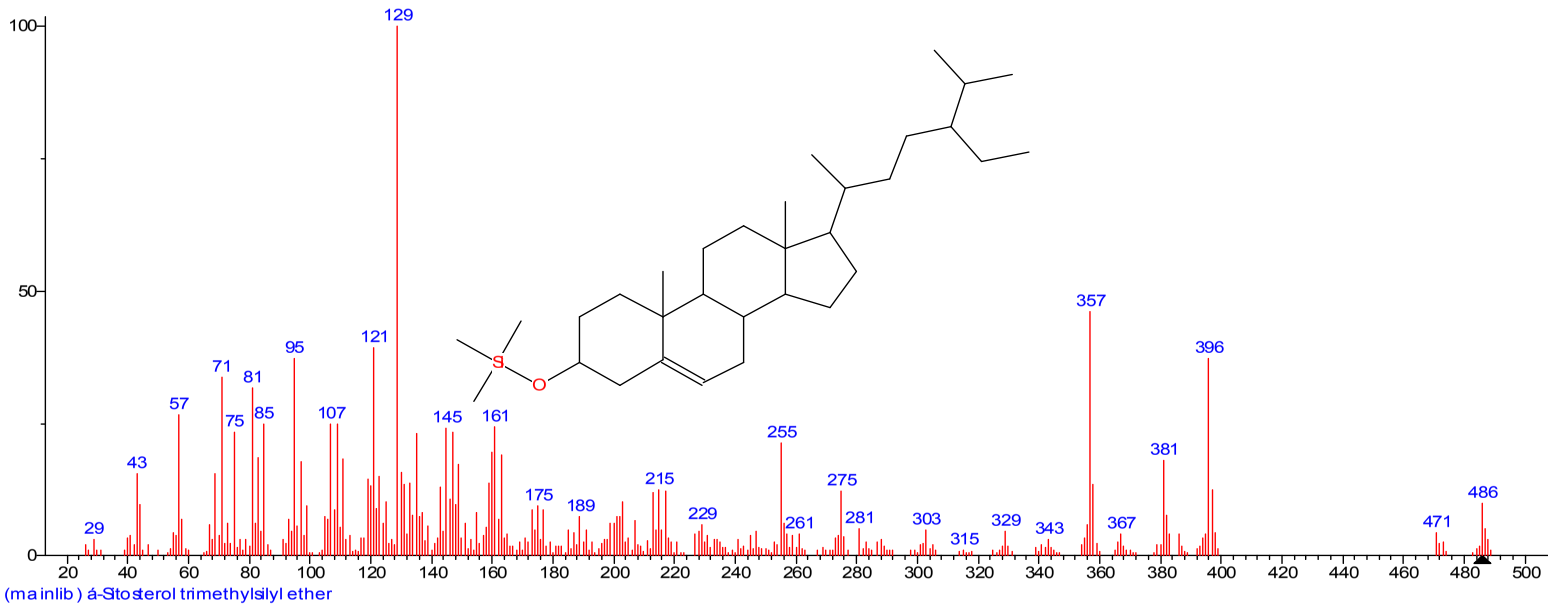

Formula: C32H58OSi

MW = 486

9: 24-ethylcholesta-7-en-3B-ol TMS (Stigmasta-7-en-3B-ol); sample & reference below

C29, 5 DBEs
C29 Δ7 Sterol

Sources: green algae

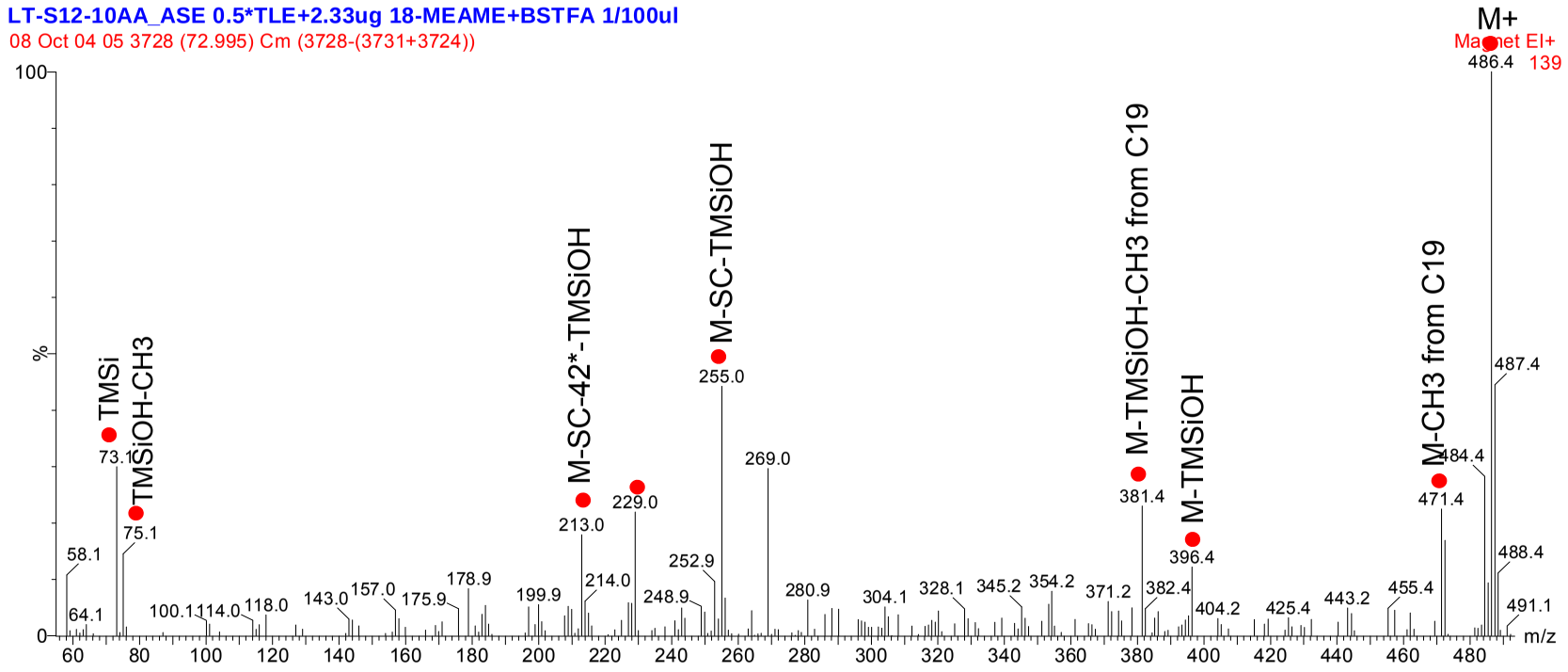

- Red dots indicate ions labeled in reference
  W. Henderson, W.E. Reed and G. Steel (1971) *Adv. Org. Geochem.* pp 335 – 352; Ed. H.R. v. Gaertner and H. Wehner; Pergamon Press

*42 is C15, C16, C17, 6H

10: 4a,23,24-trimethyl-5a (H)-cholest-22-en-3B-ol TMS (Dinosterol); sample & reference below

C30, 5 DBEs

C30 Δ22 Sterol Sources: dinoflagellates, some diatoms

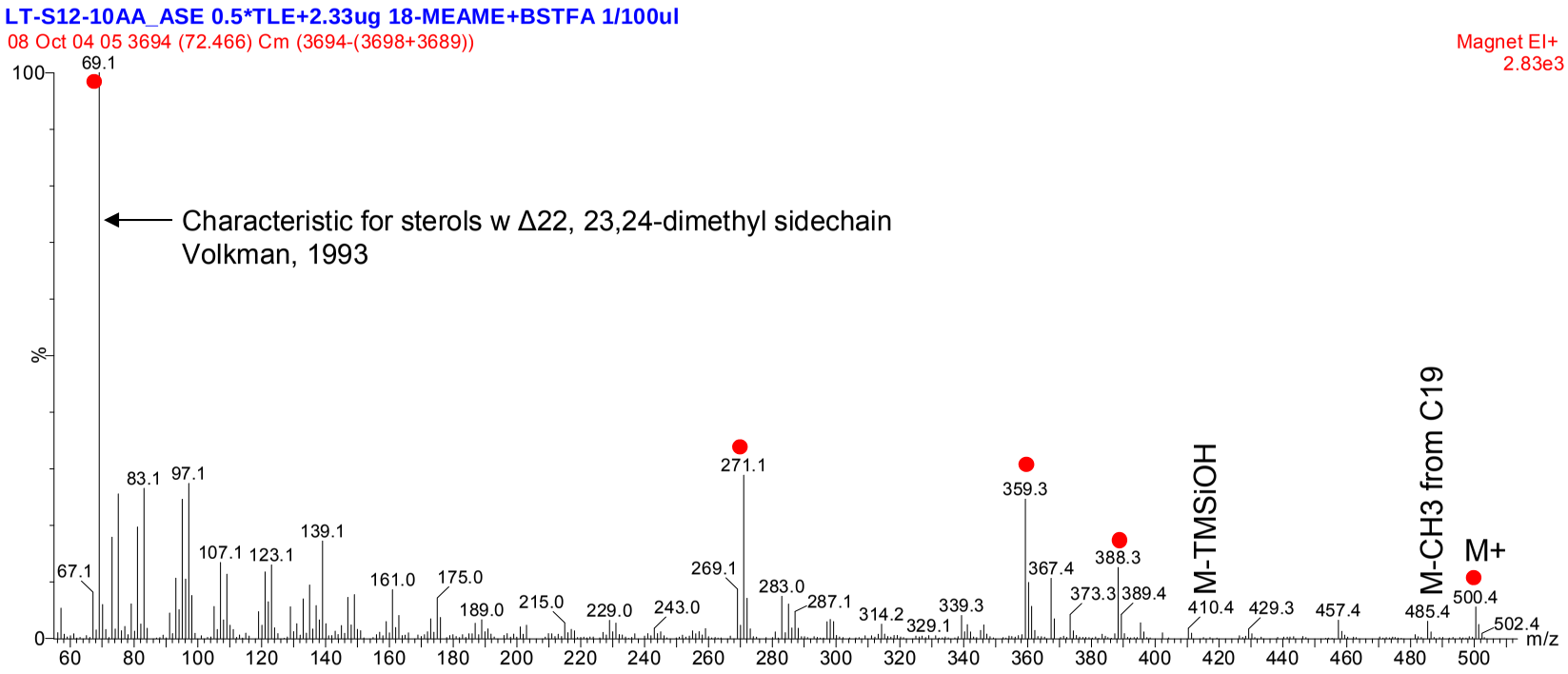

- Red dots indicate ions labeled in reference
  Harvey *et al* (1988) *Phytochemistry*, vol 27, no 6, pp 1723-1729; ions listed (no figure)

10: Dinosterol TMS (NIST library)

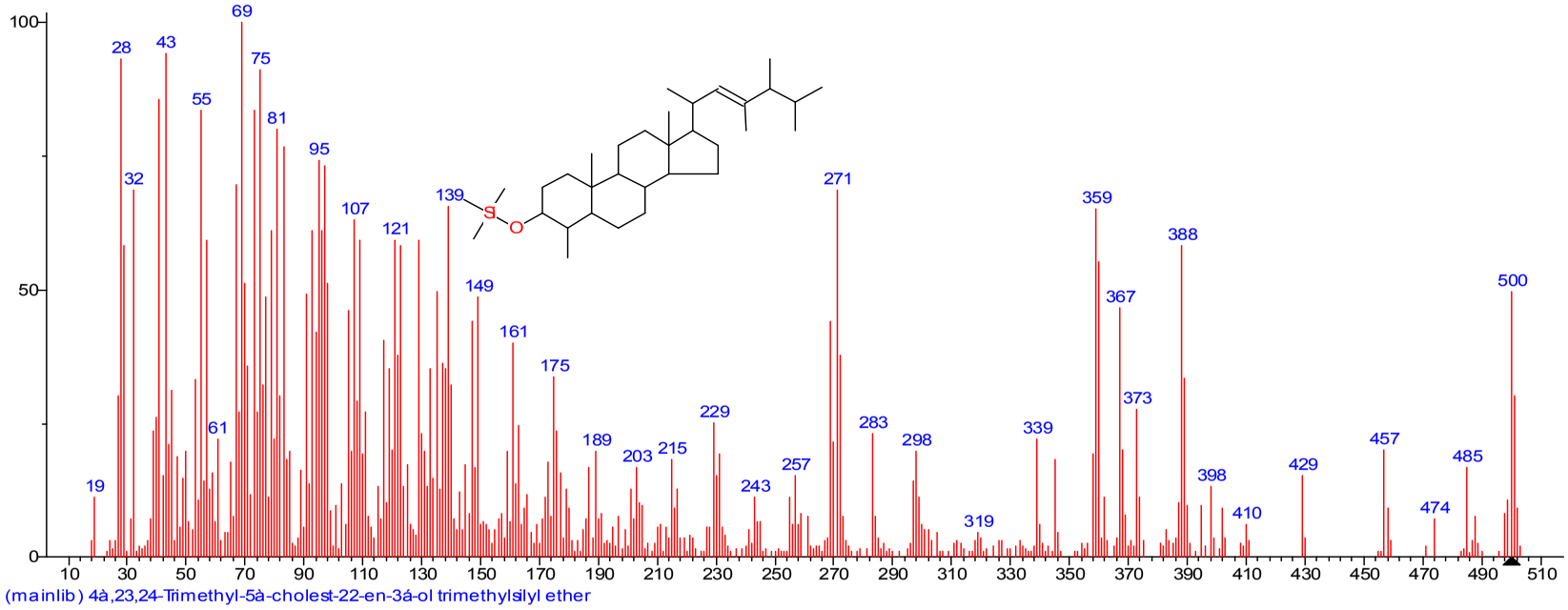

Formula: C33H60OSi

MW = 500

11: 4a-methyl-24-ethyl-5a-cholest-22E-en-3B-ol TMS; sample & reference below

C30, 5 DBEs
C30 Δ22 Sterol

Sources: gymnodinoid dinoflagellates

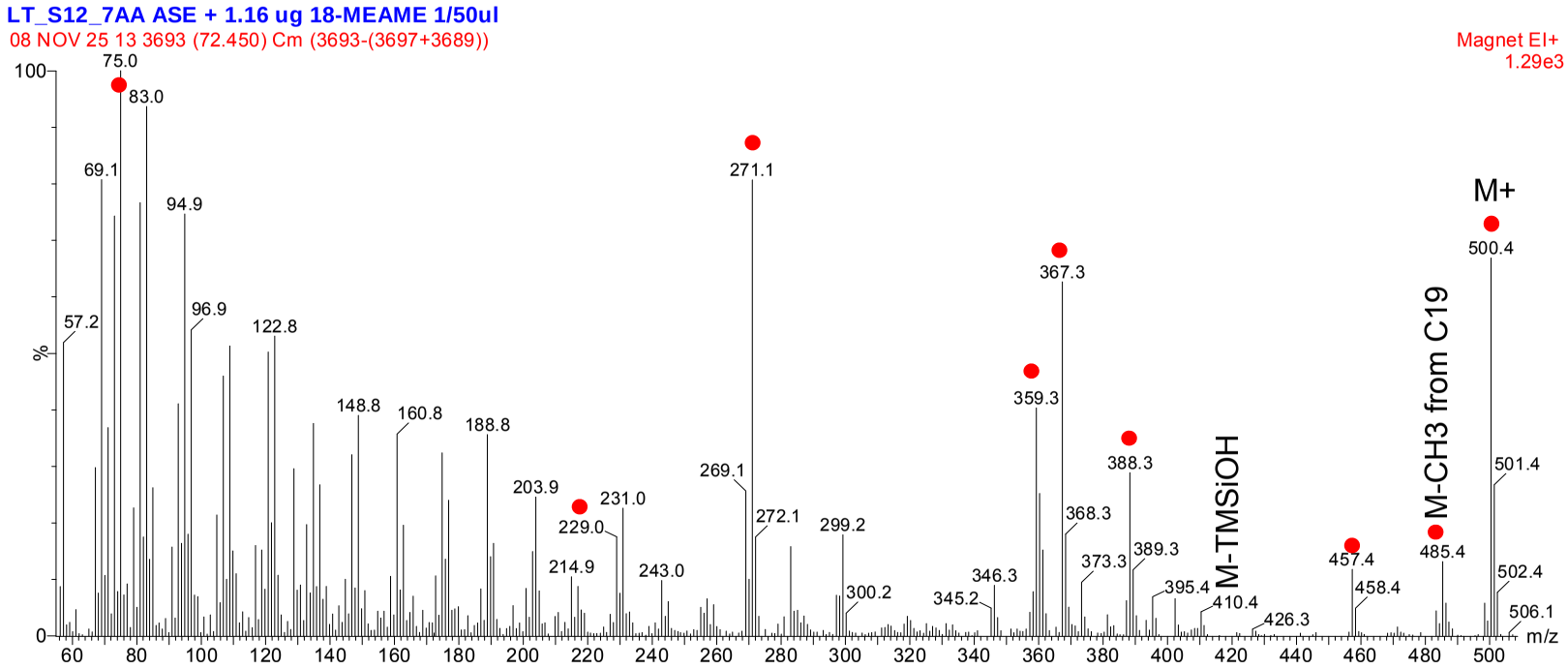

- Red dots indicate major ions

Mansour *et al* (1999) *Journal of Phycology*, vol 35, pp 710-720; source listed (*Gymnodinium sanguineum*); MS id'd by J. Volkman, pers.comm.

12: 4a,23,24-trimethylcholesta-5,22-dien-3B-ol TMS (5-dehydrodinosterol); sample & reference below

C30, 6 DBEs

C30 Δ5,22 Sterol Sources: dinoflagellates (*Scripsiella, Gymnodinium* species)

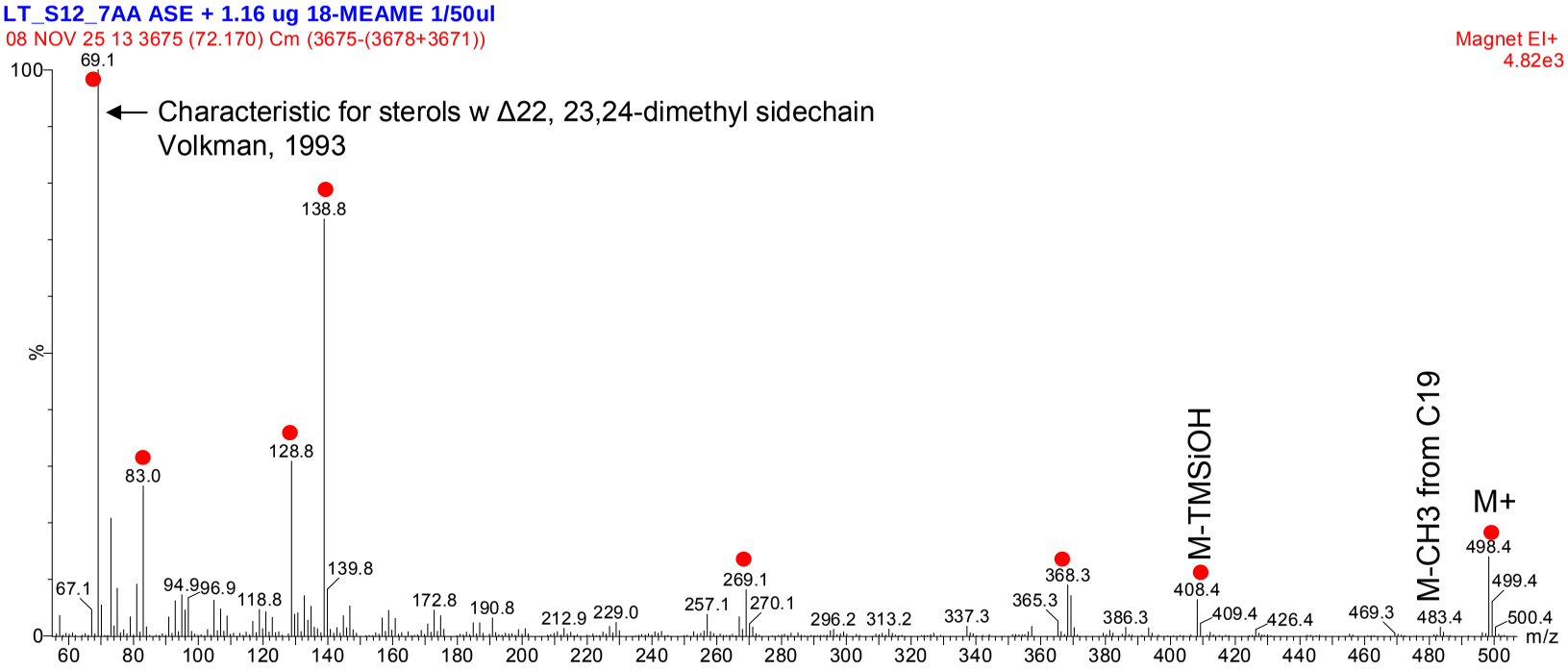

- Red dots indicate major ions

Mansour *et al* (1999) *Journal of Phycology*, vol 35, pp 710-720;
source listed (*Gymnodinium catenatum* & *Scripsiella trochoidea*);
MS id'd by J. Volkman, pers.comm. & Harvey *et al* (1988) *Phytochemistry*, vol 27 no. 6 (ions listed)
But these do not match Volkman ID…

13: Dihydrolanosterol (4,4,14 trimethylcholest-8-en-3B-ol)

C30, 5 DBEs
C30 Δ8 Sterol

Source: precursor to cholesterol, after hydrogenation of lanosterol

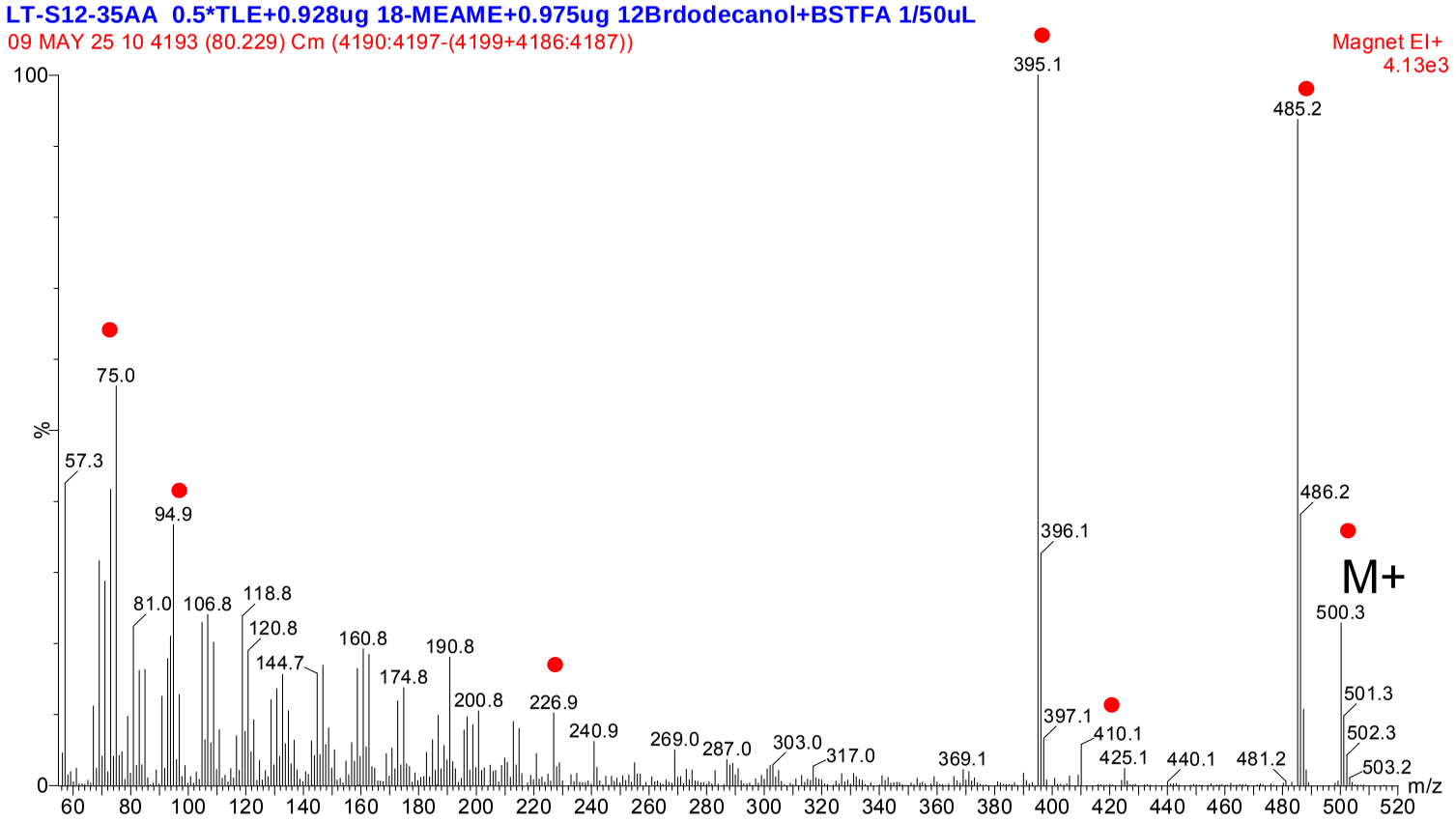

Identified from lipidlibrary.co.uk – W.W. Christie
Scallen *et al*, (1971) *J Biol. Chem.* vol 246, No 10, pp 3168-3174

Lanosterol TMS

C30, 6 DBEs
C30 Δ8,24 Sterol

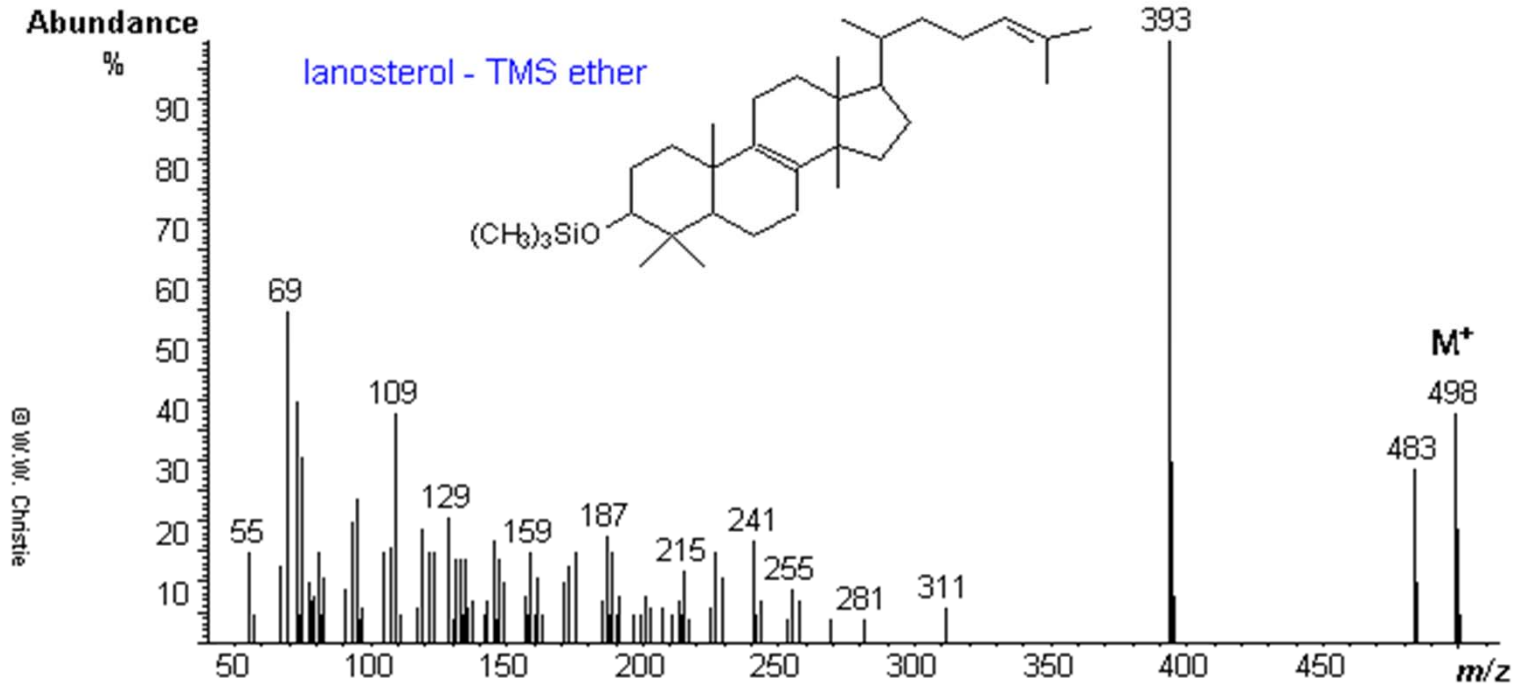

Identified from lipidlibrary.co.uk – W.W. Christie

Stanols

Some are directly generated by organisms,
Some are the result of biotic or abiotic hydrogenation of sterols (usually this occurs in sediments)

14: 5B-cholestan-3B-ol TMS (5B-coprostanol); NIST library + samples

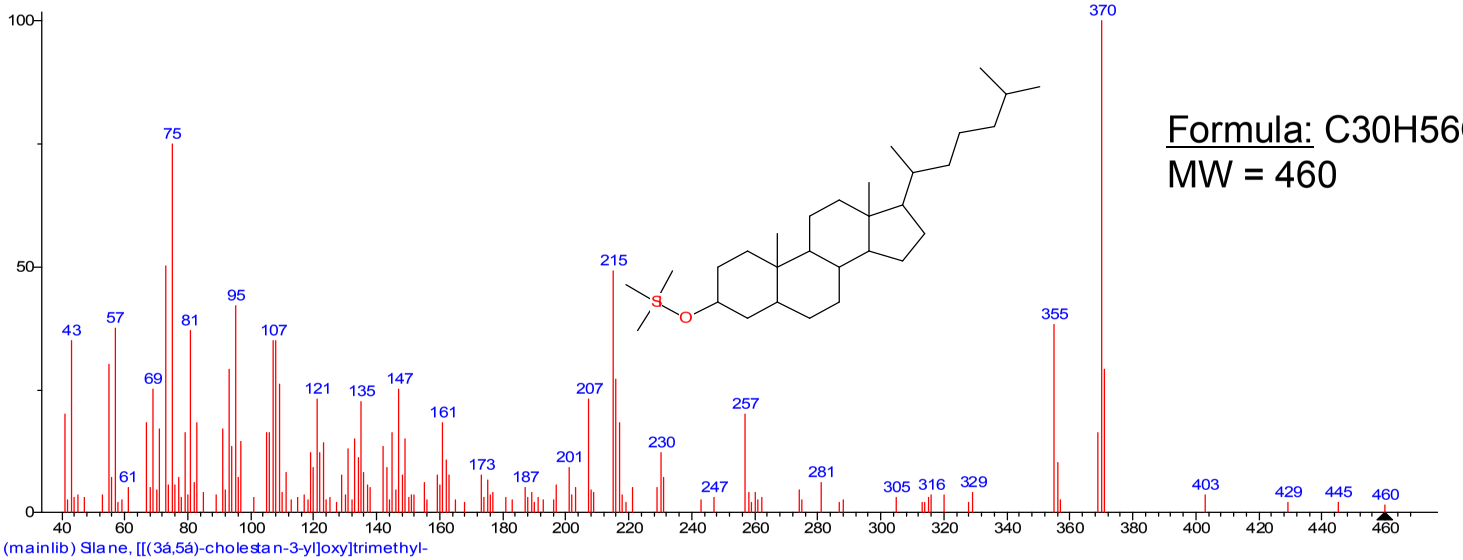

Formula: C30H56OSi
MW = 460

C27, 4 DBEs
C27 Δ0 Stanol

Sources: Formed by hydrogenation of cholesterol in guts of some animals and birds; can indicate fecal contamination

Gaskell and Eglinton (1975) *Nature* vol. 254 pp 209-211

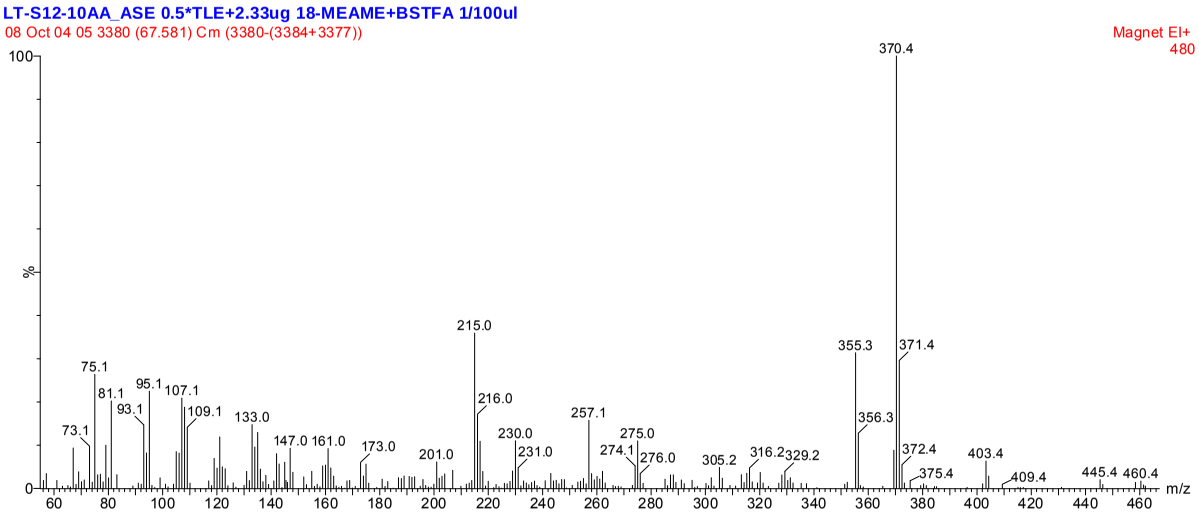

15: 5a-cholestan-3a-ol TMS (Epi-cholestanol); NIST library + samples

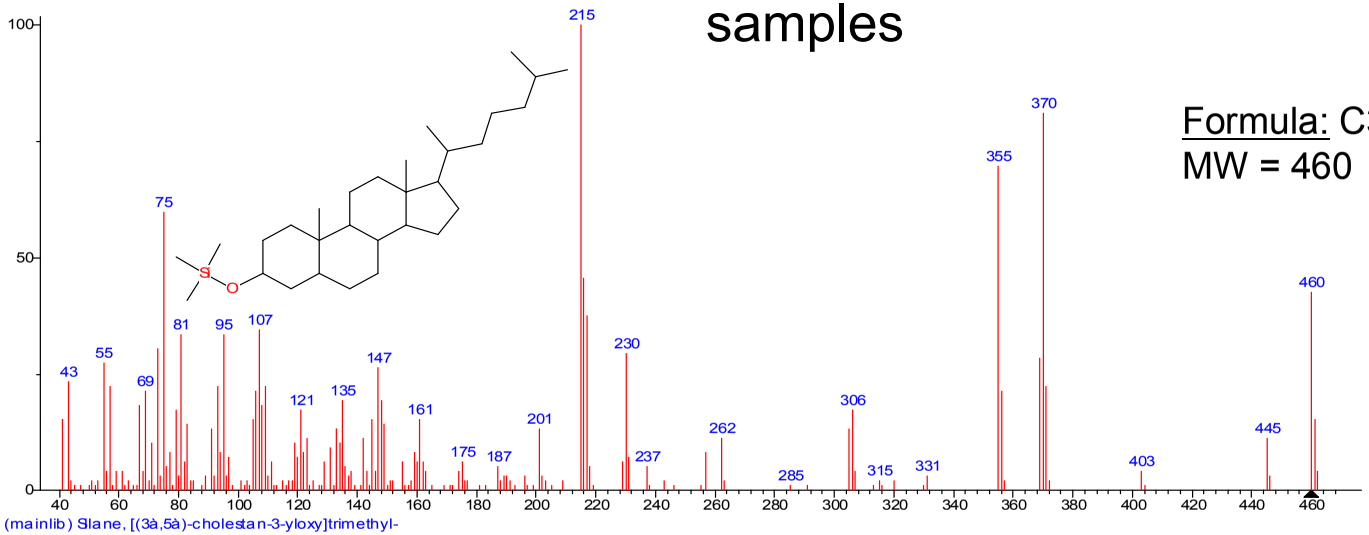

Formula: C30H56OSi
MW = 460

C27, 4 DBEs
C27 Δ0 Stanol

Sources: Formed by hydrogenation of cholesterol and isomerization of 5B-coprostanol

Gaskell and Eglinton (1975) *Nature* vol. 254 pp 209-211

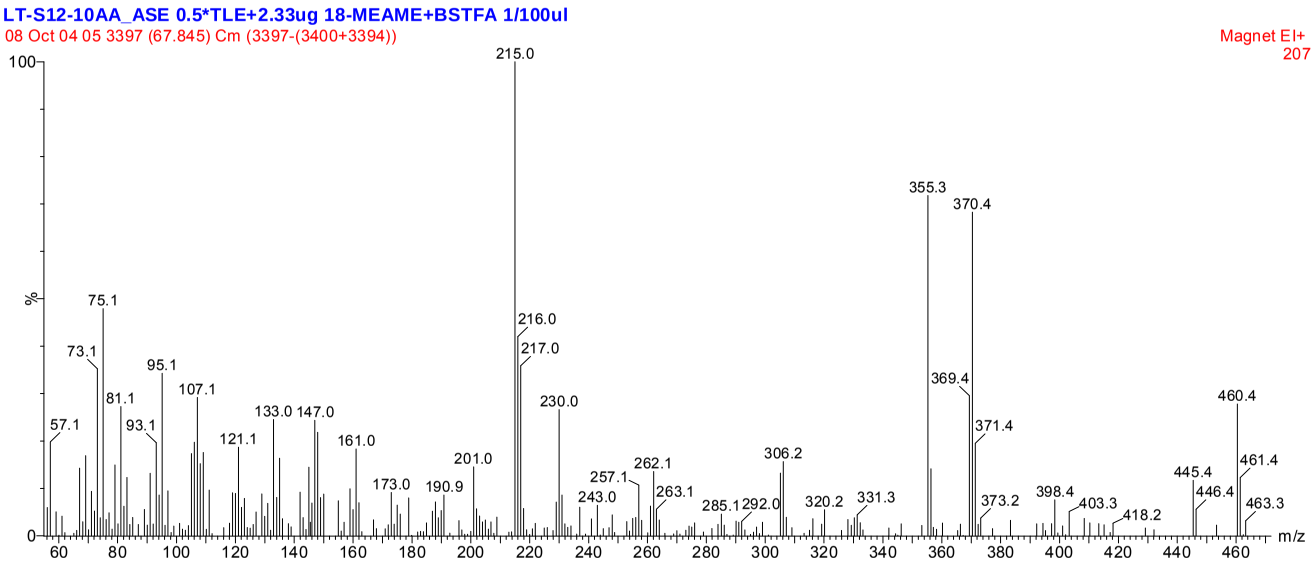

16: 5B-cholestan-3a-ol TMS (Epi-coprostanol); NIST library + samples

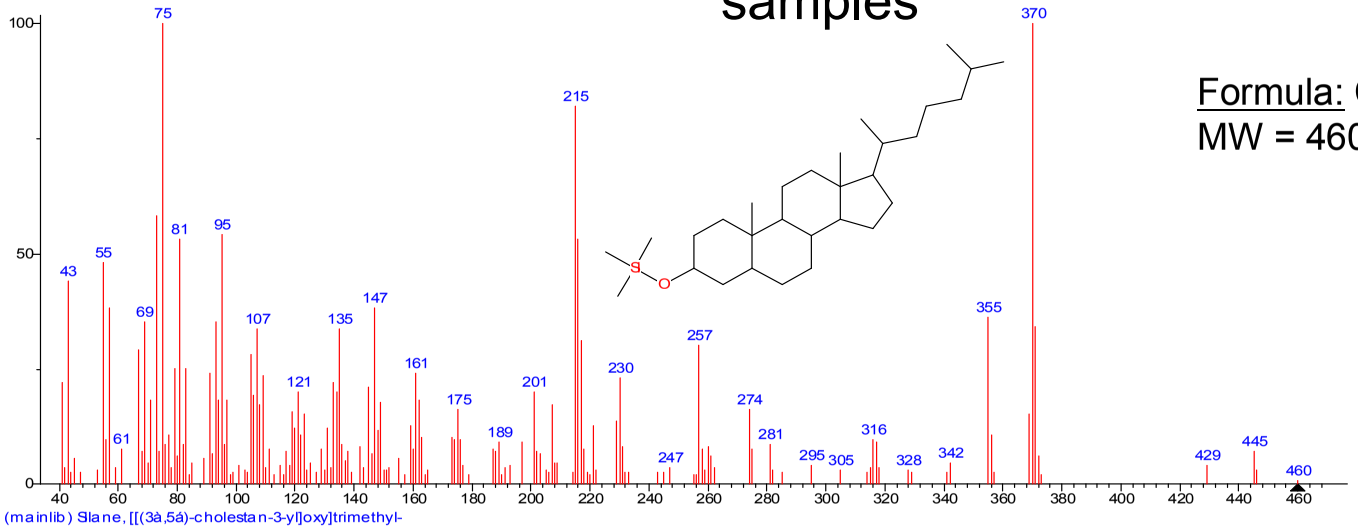

Formula: C30H56OSi
MW = 460

C27, 4 DBEs
C27 Δ0 Stanol

Sources: Formed by isomerization of 5B-coprostanol

Gaskell and Eglinton (1975) *Nature* vol. 254 pp 209-211

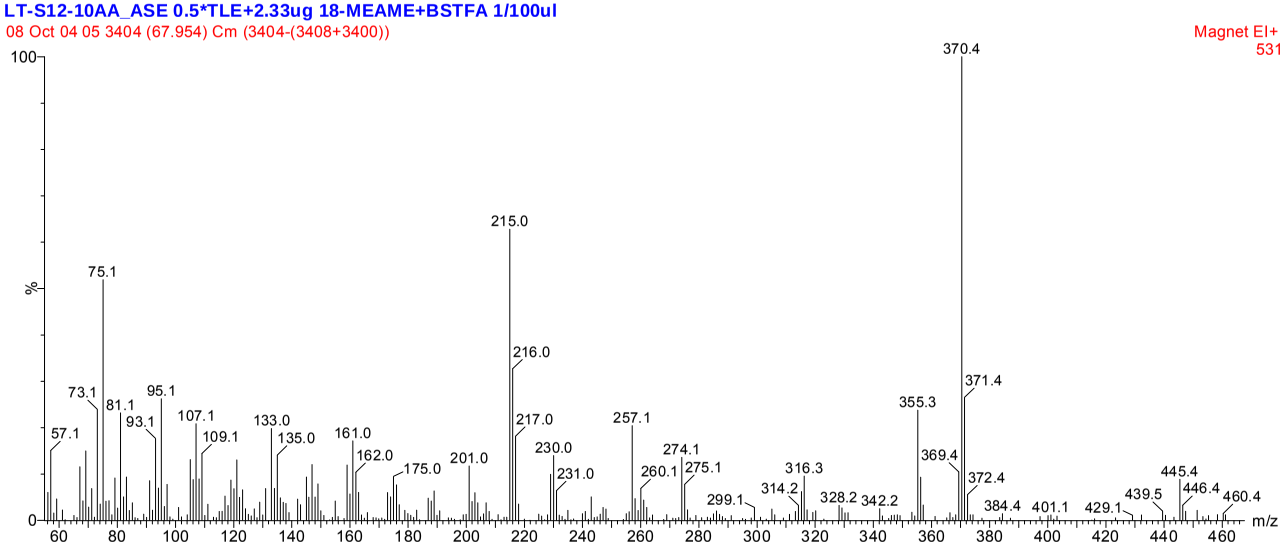

17: 5a-cholestan-3B-ol TMS (5a-cholestanol); NIST library + samples

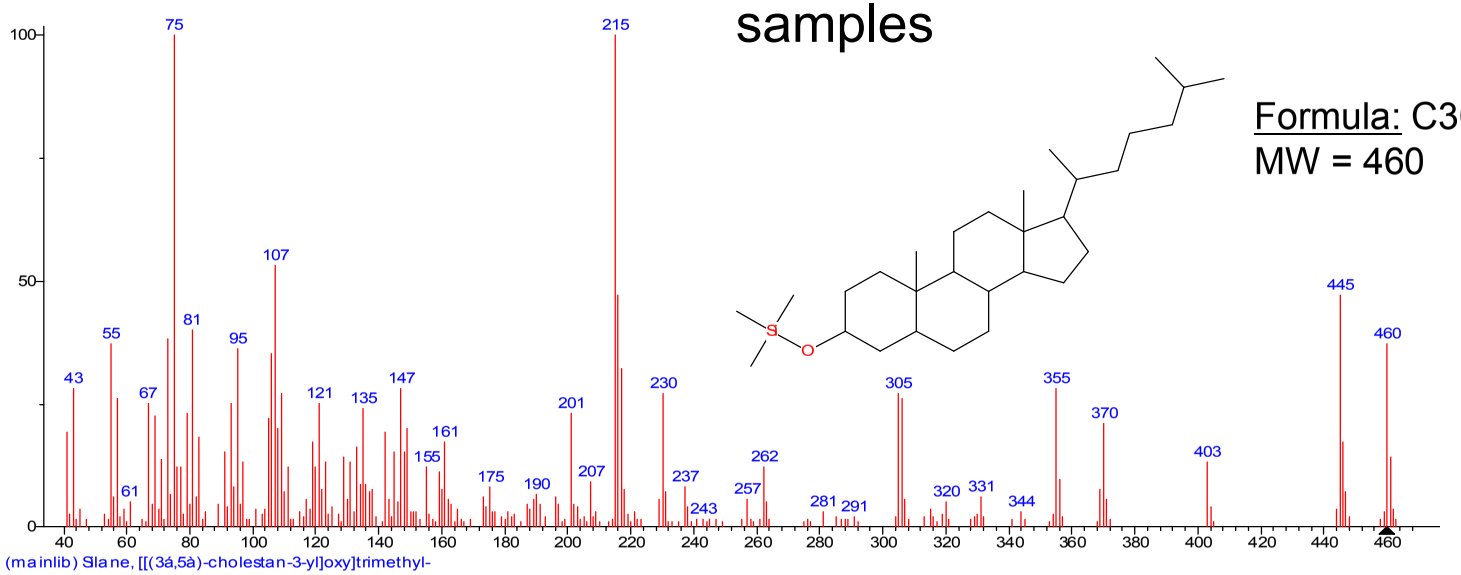

Formula: C30H56OSi
MW = 460

C27, 4 DBEs
C27 Δ0 Stanol

Sources: Formed in reducing/anaerobic sediments by biohydrogenation of cholesterol (preferentially formed over other isomers),
also in vivo by dinoflagellates

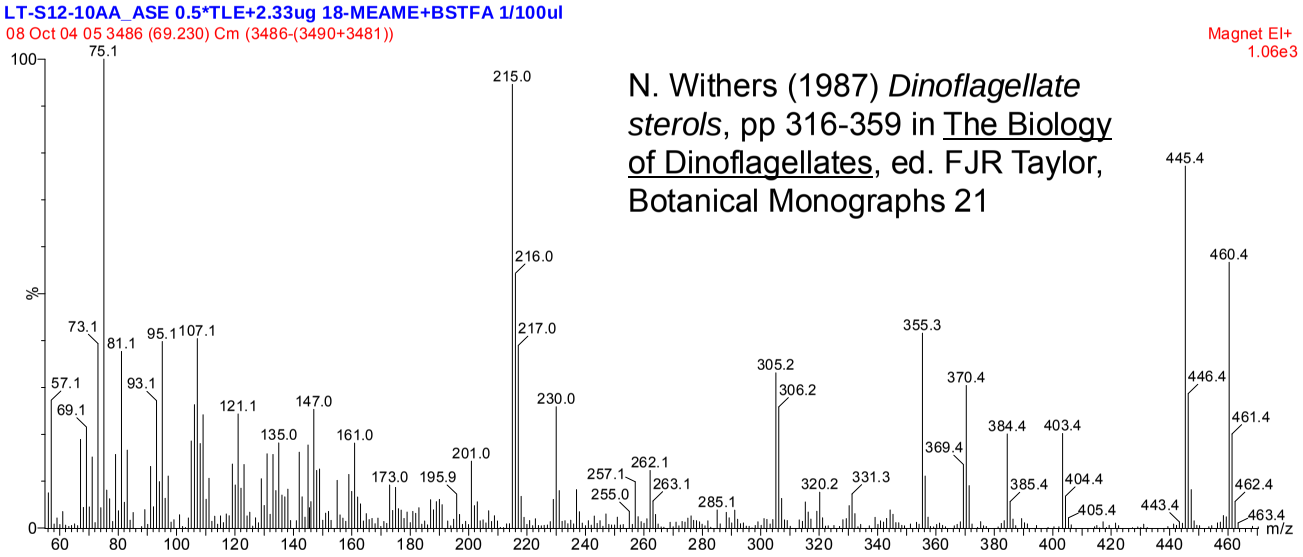

N. Withers (1987) *Dinoflagellate sterols*, pp 316-359 in The Biology of Dinoflagellates, ed. FJR Taylor, Botanical Monographs 21

18: 5B-ergostan-3a-ol TMS (5B-ergostanol), id'd by elution position in samples as series with ergostanol

C28, 4 DBEs
C28 Δ0 Stanol

Sources: biohydrogenation of ergosterol (and/or isomerization of ergostanol) produced by D. salina & other organisms

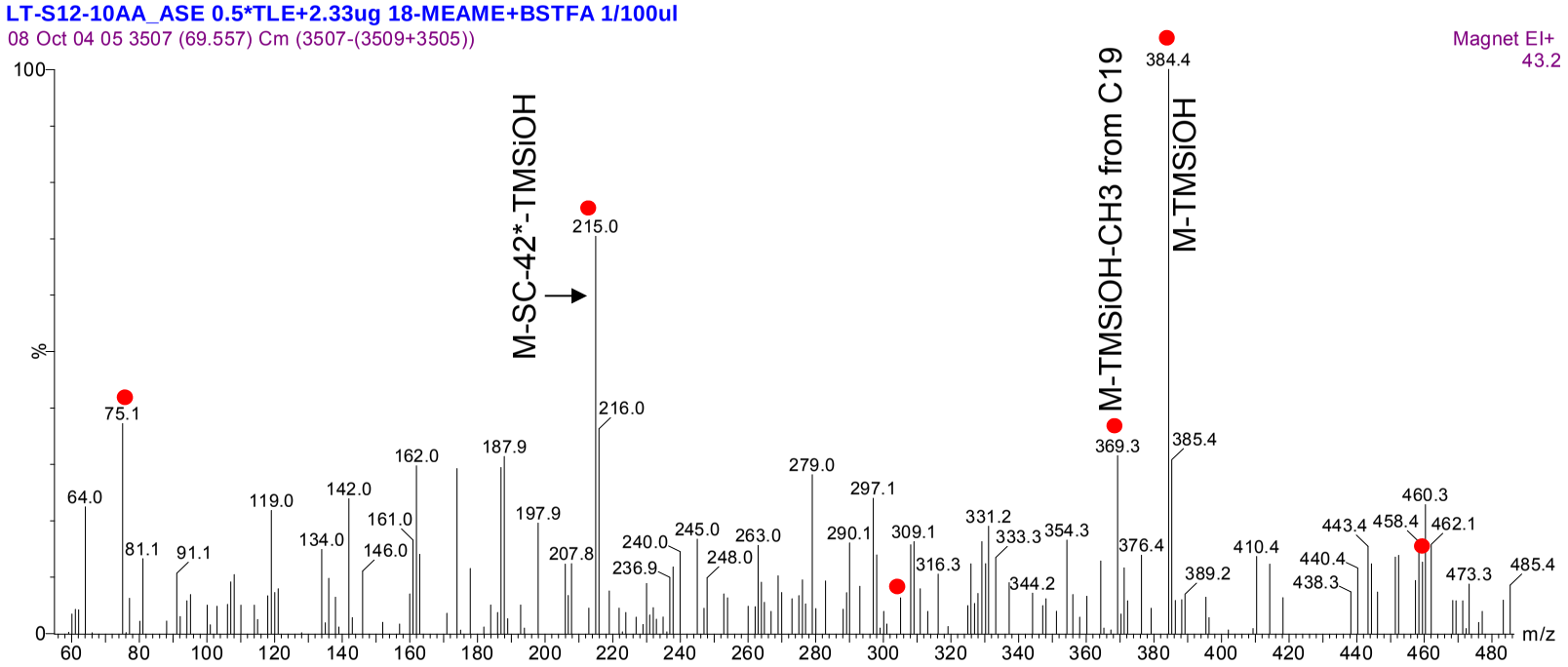

- Red dots indicate peaks in common w regular ergostanol
  Note peak is very small in sample so spectrum is messy

*42 is C15, C16, C17, 6H

19: 5a-ergostan-3B-ol TMS (ergostanol), samples & reference below

C28, 4 DBEs
C28 Δ0 Stanol

Sources: biohydrogenation of ergosterol
produced by D. salina & other organisms

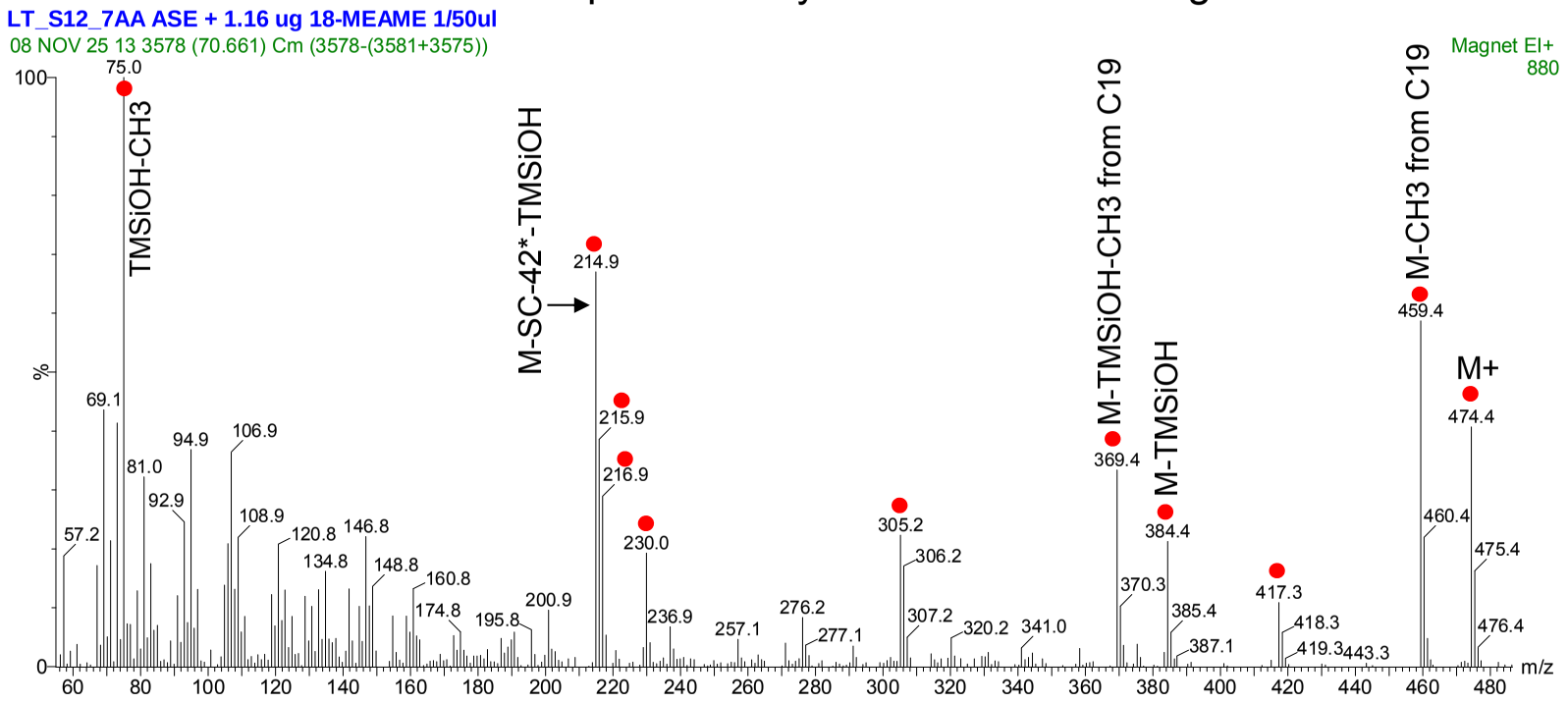

- Red dots indicate ions labeled in reference
  W. Henderson, W.E. Reed and G. Steel (1971) *Adv. Org. Geochem.* pp 335 – 352; Ed. H.R. v. Gaertner and H. Wehner Pergamon Press; also Harvey *et al* (1988) *Phytochemistry*, vol 27, no.6 pp 1723-1729 (ions listed)

*42 is C15, C16, C17, 6H

Campestanol TMS (NIST library)

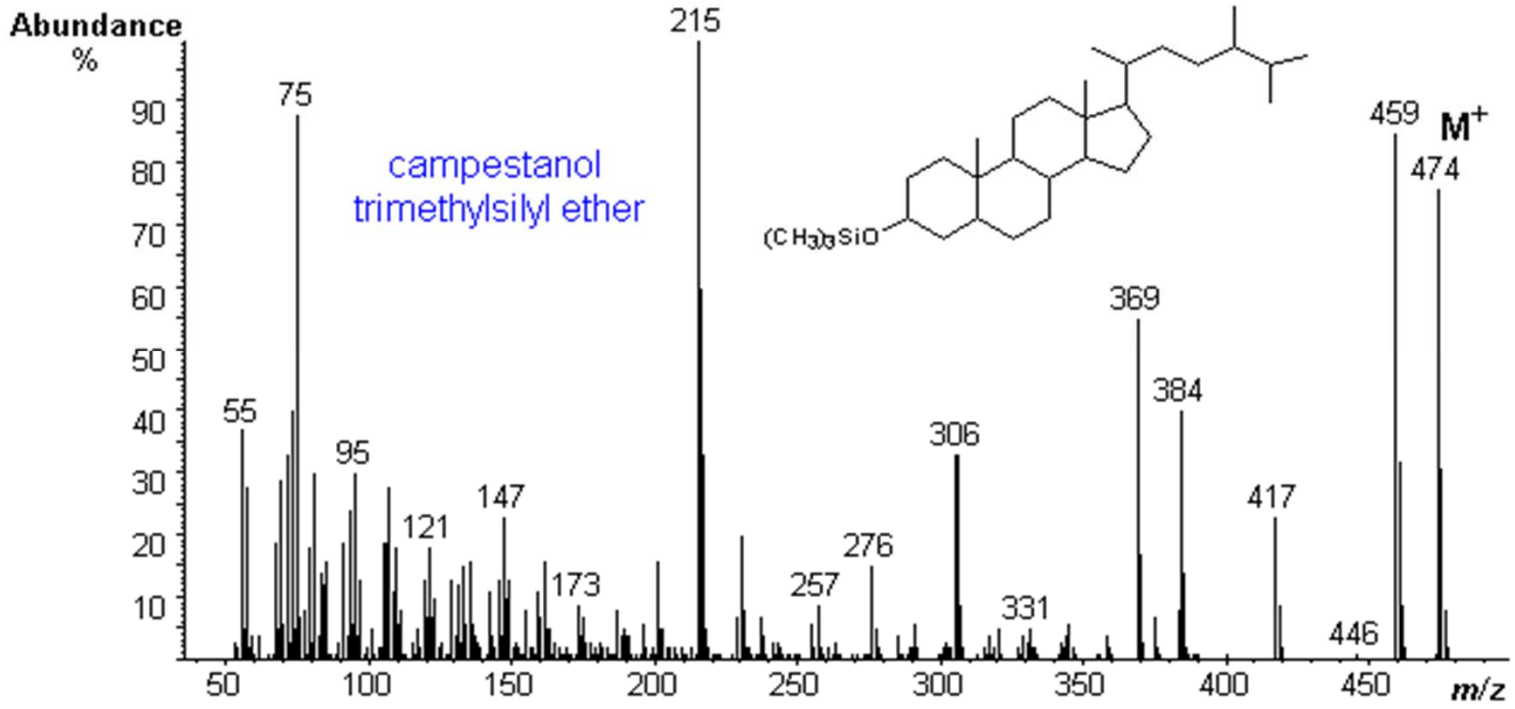

20: 24-methyl-5b-cholestan-24(28)-en-3B-ol TMS (24-methylenecholestanol); samples and reference below

C28, 5 DBEs Sources: biohydrogenation of regular 5a stanol or sterol
C28 Δ24(28) Stanol produced by dinoflagellates

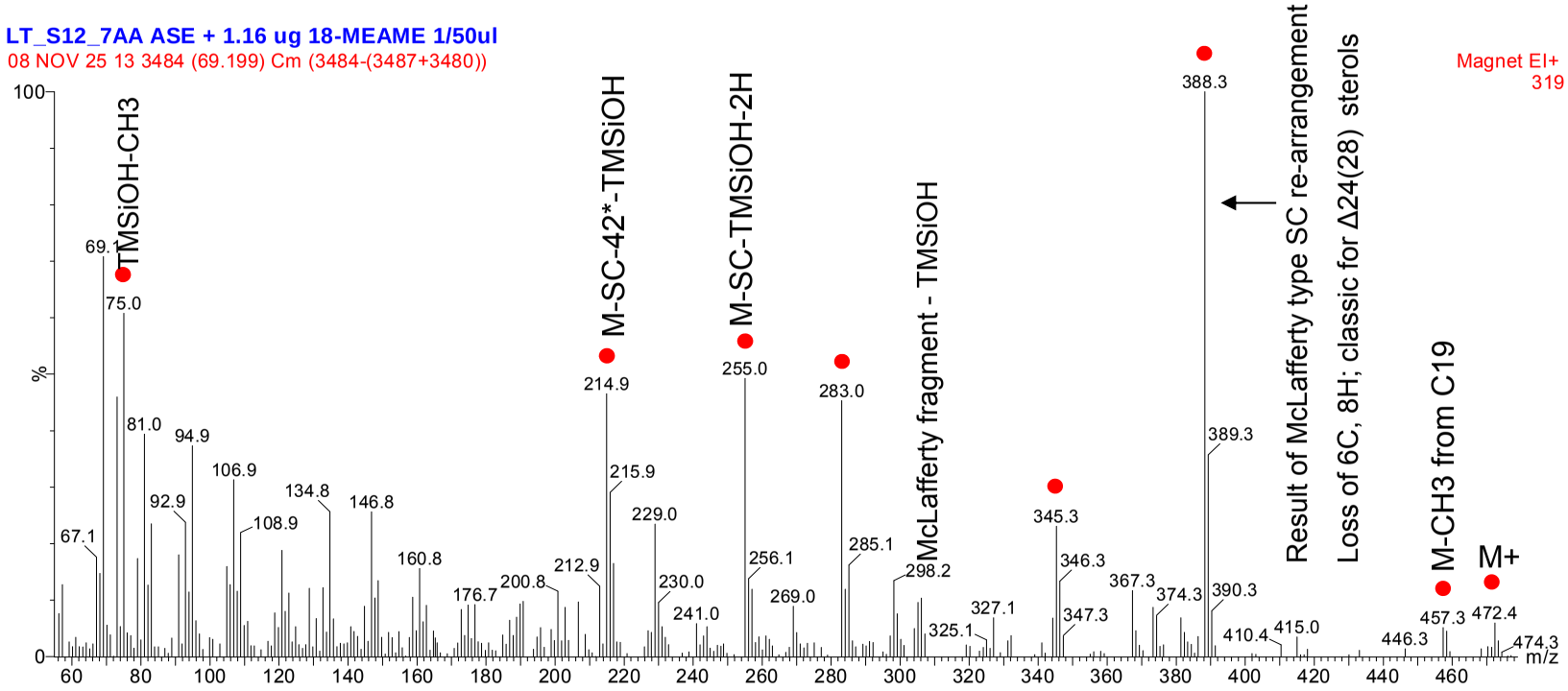

- Red dots indicate major ions

Mansour *et al* (1999) *Journal of Phycology*, vol 35 pp 710-720; source listed (*Gymnodinium sanguineum*);
MS id'd by J. Volkman, pers.comm.

*42 is C15, C16, C17, 6H

21: 4a, 24S-Dimethyl-5a-cholestan-3B-ol TMS (4,24 dimethylcholestanol), samples and reference, below

C29, 4 DBEs

C29 Δ0 Stanol (4methyl)

Sources: dinoflagellates

*42 is C15, C16, C17, 6H

**129 is TMSiOH + C1, C2, C3, 3Hs

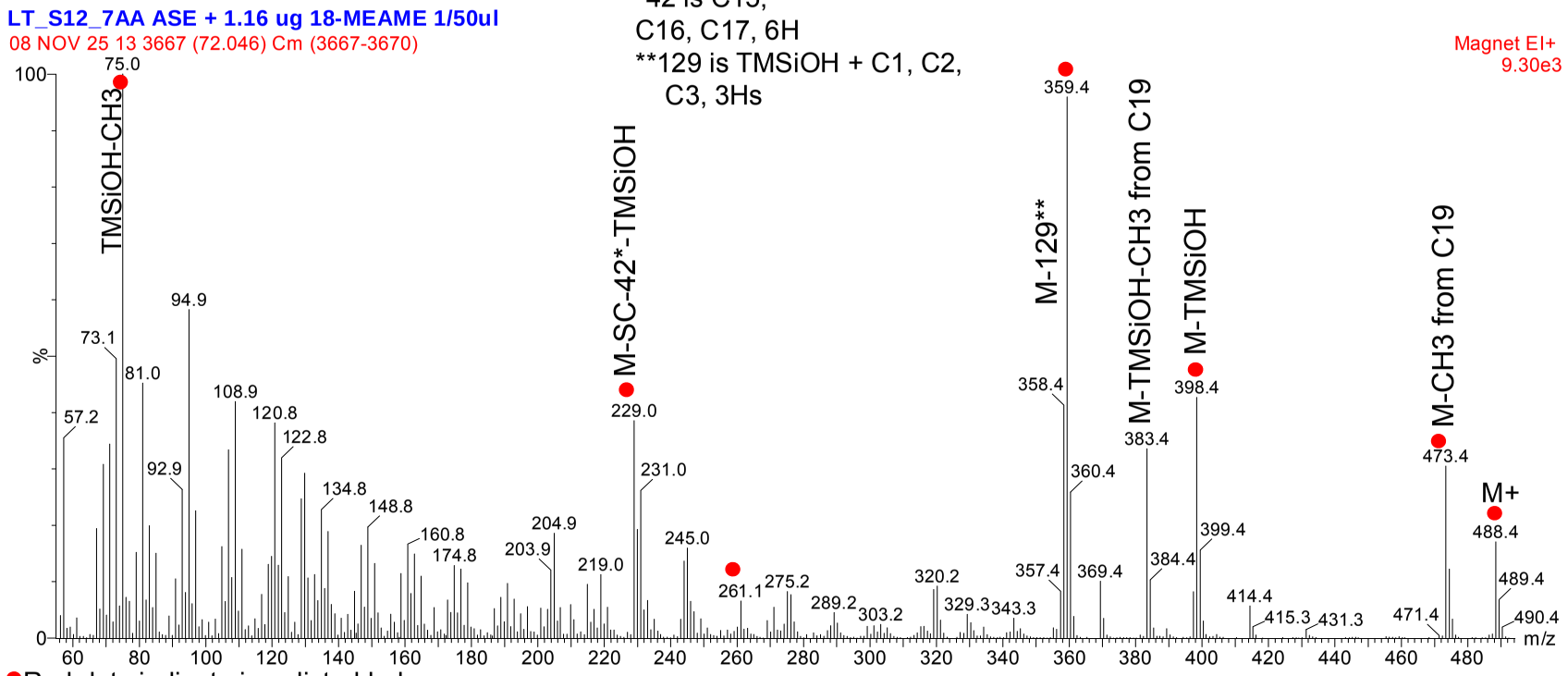

Red dots indicate ions listed below

Mansour *et al* (1999) *Journal of Phycology*, vol 35, pp 710-720; source listed (**Gymnodinium* sp., *Symbiodinium*, *Scripsiella* sp.);

Also Leblond & Chapman (2002) *Journal of Phycology*, vol 38, pp 670-682

And N. Withers (1987) *Dinoflagellate sterols*, pp 316-359 in The Biology of Dinoflagellates, ed. FJR Taylor, Botanical Monographs 21

Source noted that it is major stanol in *Gymnodinium simplex* sp.

MS id'd by J. Volkman, pers.comm. And Harvey *et al* (1988) *Phytochemistry*, vol 27, no 6, pp 1723-1729; ions listed (no figure)

22: 24-ethyl-5B-cholestan-3B-ol TMS (5B-stigmastanol), samples and reference, below

C29, 4 DBEs
C29 Δ0 Stanol

Sources: hydrogenation of stigmasterol produced by plants, or isomerization of regular 5a-stigmastanol

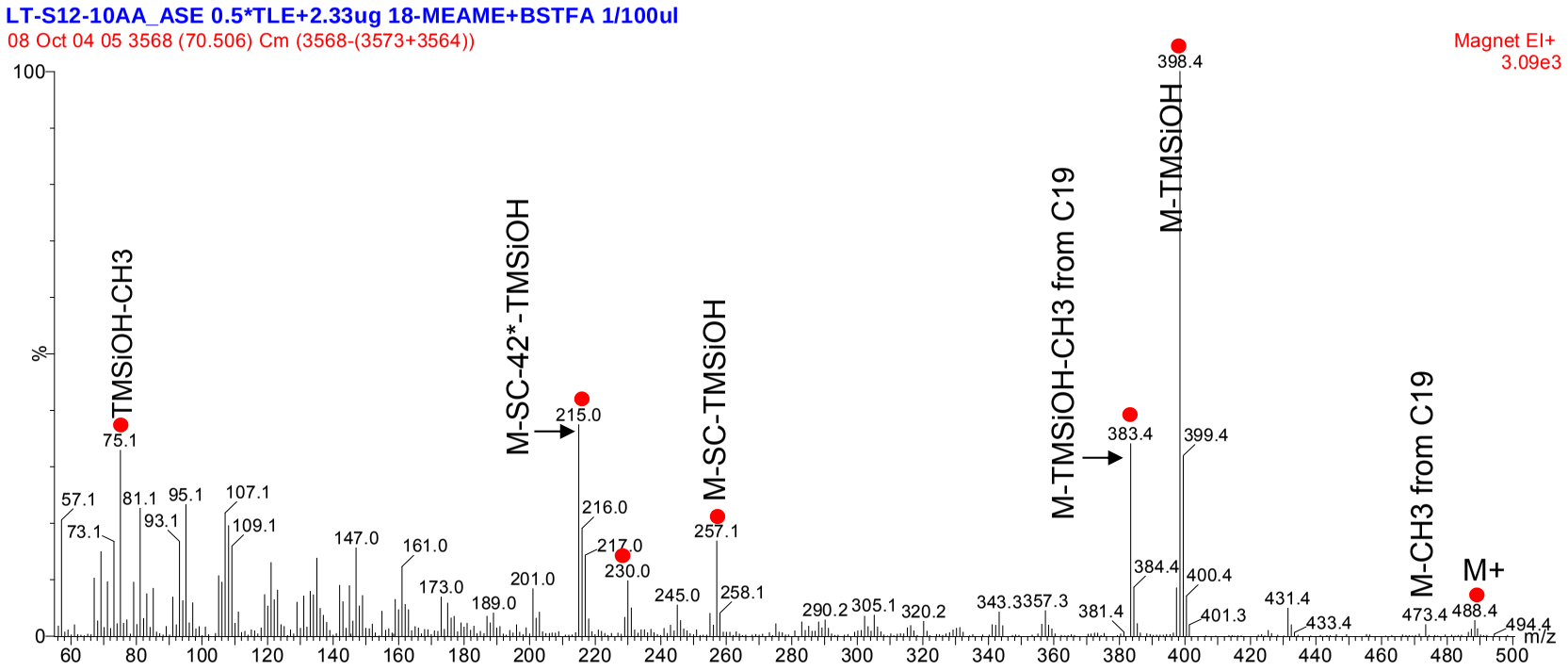

- Red dots indicate major ions
  Volkman *et al* (1999) *Journal of Phytochemistry*, vol 52
  pp 659-668; source of 5a-stigmastanol listed (*Prorocentrum micans*);
  ID based on elution position relative to 5a-stigmastanol and 5B-stigmastanol

*42 is C15, C16, C17, 6H

23: 24-ethyl-5a-cholestan-3a-ol TMS (5a,3a-stigmastanol), samples and reference, below

C29, 4 DBEs
C29 Δ0 Stanol

Sources: hydrogenation of stigmasterol produced by plants, or isomerization of regular 5a-stigmastanol

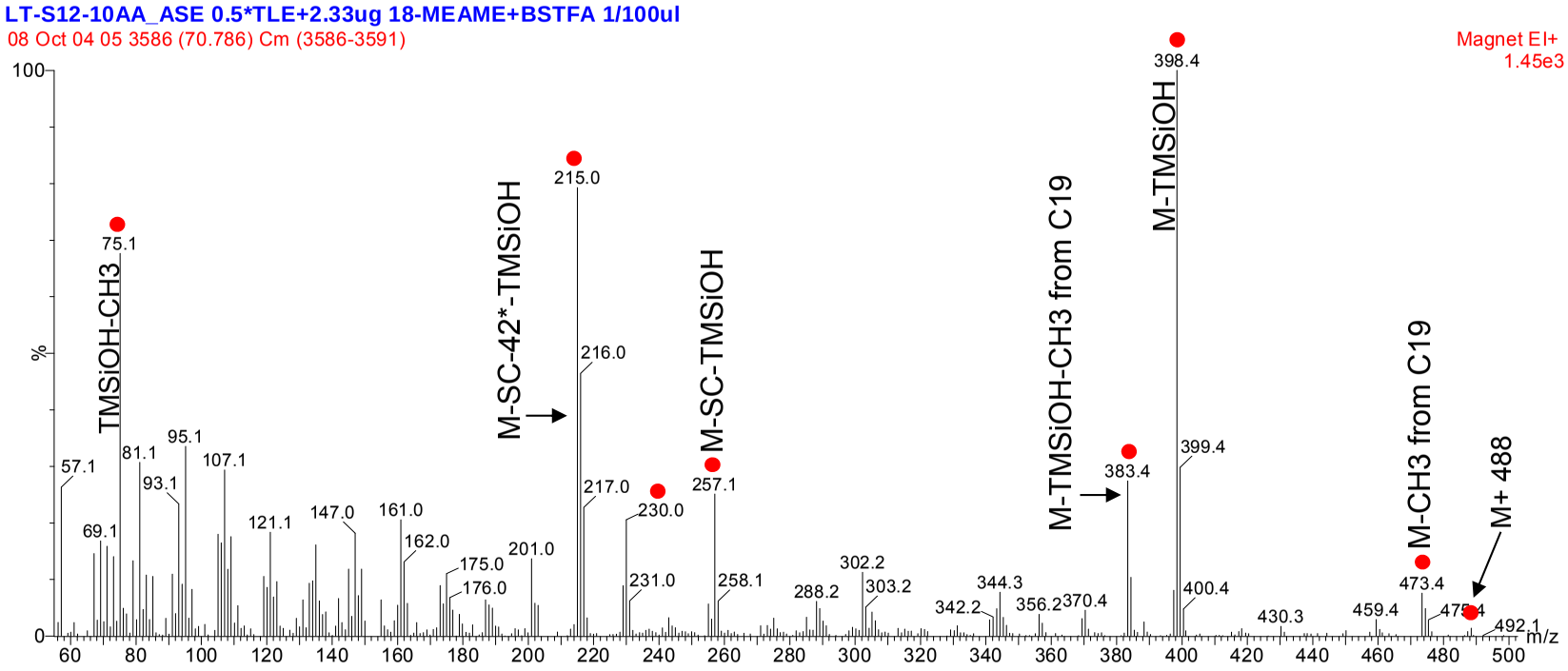

- Red dots indicate major ions

Volkman *et al* (1999) *Journal of Phytochemistry*, vol 52
pp 659-668; source of 5a-stigmastanol listed (*Prorocentrum micans*);
ID based on elution position relative to 5a-stigmastanol and 5B-stigmastanol

*42 is C15, C16, C17, 6H

24: 24a-ethyl-5a-cholestan-3B-ol TMS (Stigmastanol), samples and reference, below

C29, 4 DBEs
C29 Δ0 Stanol

Sources: hydrogenation of stigmasterol produced by plants, or stigmastanol from dinoflagellates

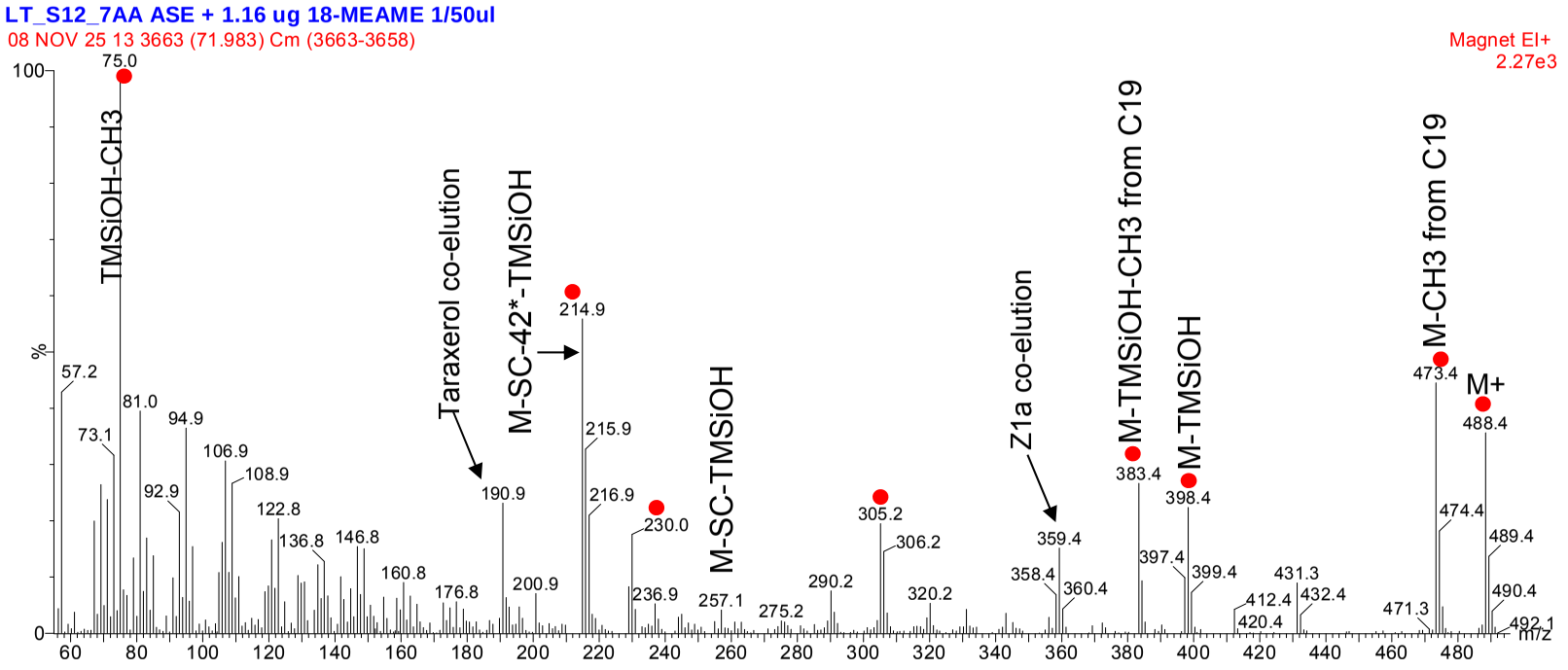

- Red dots indicate ions labeled in MS ref below

*42 is C15, C16, C17, 6H

Volkman *et al* (1999) *Journal of Phytochemistry*, vol 52 pp 659-668; source of stigmastanol listed (*Prorocentrum micans*); ID based on W. Henderson, W.E. Reed and G. Steel (1971) *Adv. Org. Geochem.* pp 335 – 352; Ed. H.R. v. Gaertner and H. Wehner, Pergamon Press

25: 4a-methyl, 24-ethylcholestan-3B-ol TMS, samples and reference, below

C30, 4 DBEs Sources: dinoflagellates (especially *Prorocentrum micans*)

C30 Δ0 Stanol (4-methyl)

*42 is C15,
C16, C17, 6H
**129 is TMSiOH + C1, C2,
C3, 3Hs

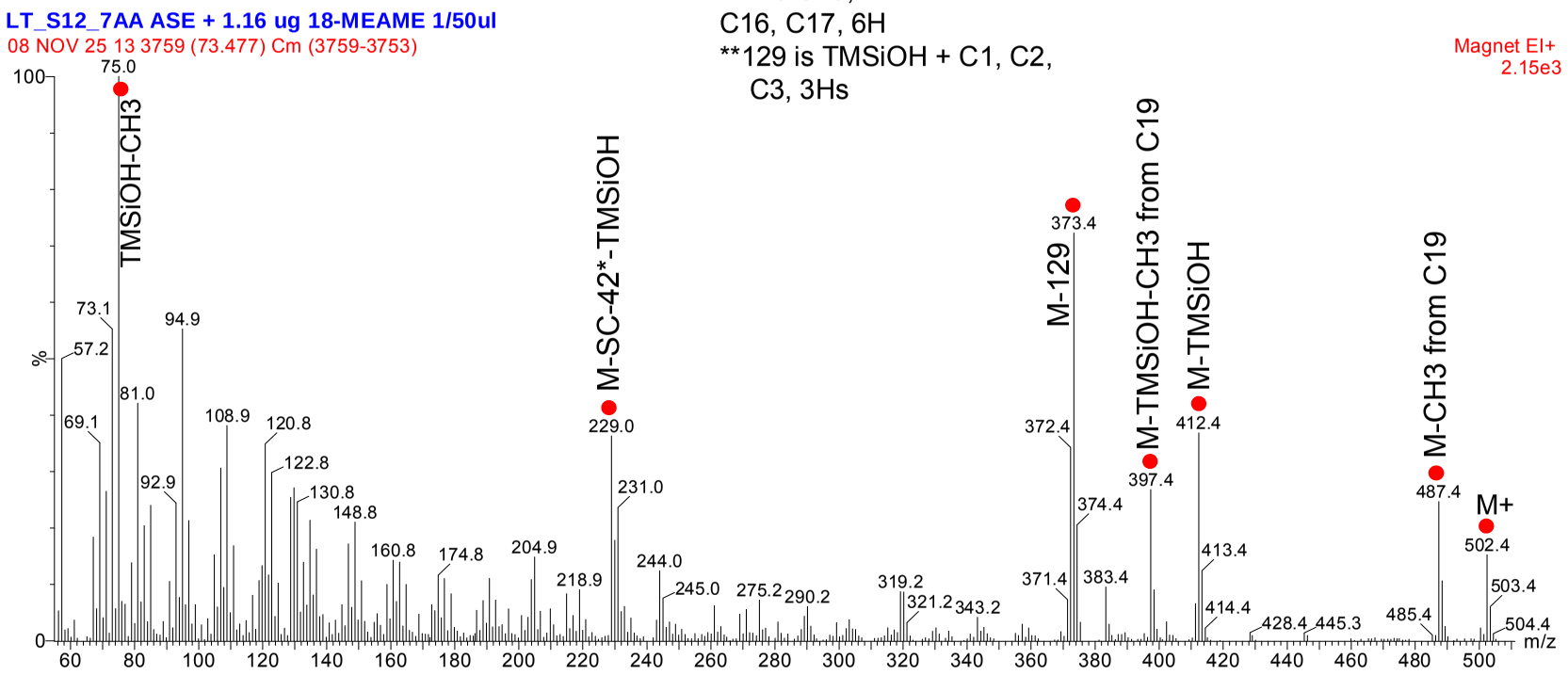

● Red dots indicate major ions

N. Withers (1987) *Dinoflagellate sterols*, pp 316-359 in The Biology of Dinoflagellates, ed. FJR Taylor, Botanical Monographs 21 & Volkman *et al* (1999) *Phytochemistry* vol 52 pp 659-668

Source noted that if its configuration is 24R, 5B, it was discovered in Glenodinium sp. as steryl ester

If it is 24S, 5a, it was isolated from cultured zooxanthellae of host gorgonians B. asbestinum & M. flavida

MS id'd by J. Volkman, pers.comm. – lack of m/z 261 indicates it's not 23S, 24R dinostanol

26: 4a, 23R, 24R-trimethyl-5a-cholestan-3B-ol TMS (Dinostanol (23R 24R)), samples and reference, below

C30, 4 DBEs

Sources: dinoflagellates

C30 Δ0 Stanol (4-methyl)

*42 is C15, C16, C17, 6H

**129 is TMSiOH + C1, C2, C3, 3Hs

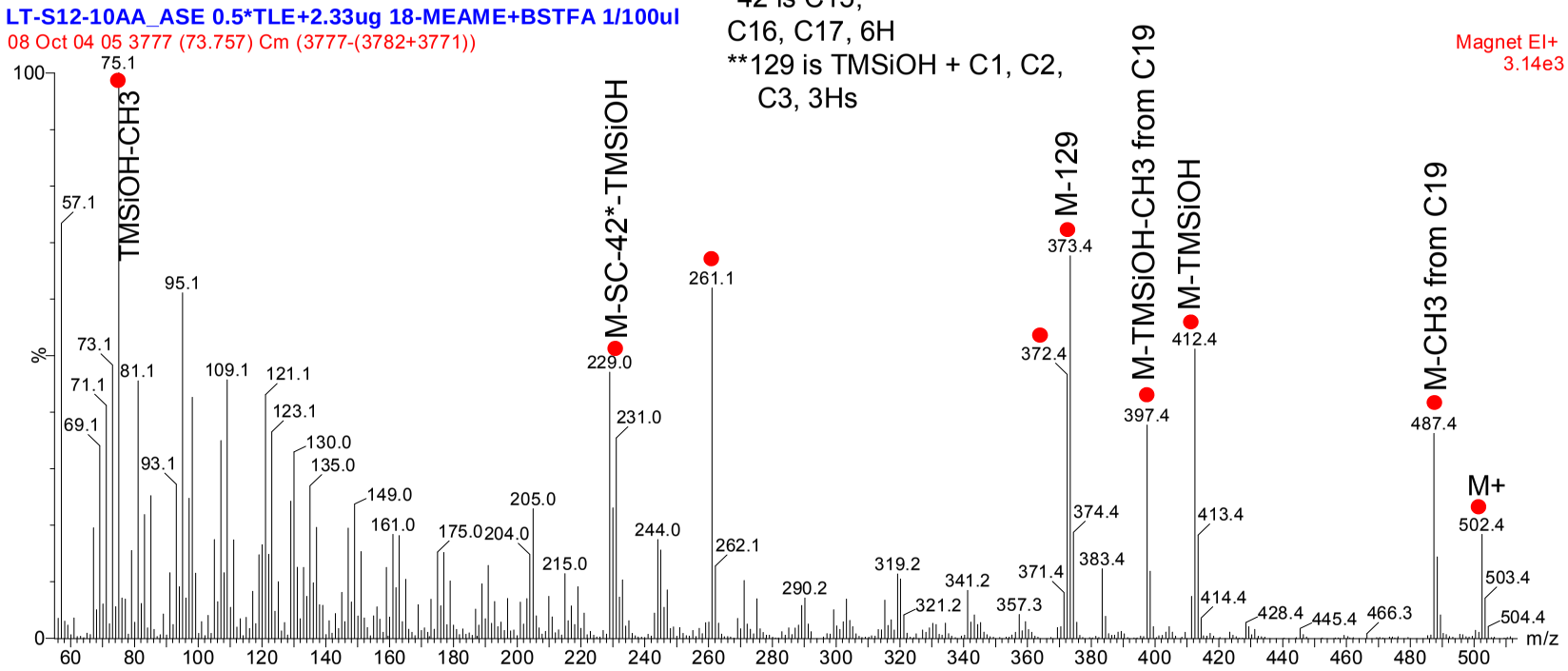

- Red dots indicate ions labeled in references

Harvey *et al* (1988) *Phytochemistry*, vol 27, no 6; pp 1723-1729; ions listed (no figure)

Note: to tell apart from 23S, 24R isomer, Volkman *et* al (1999) *Journal of Phytochemistry*, vol 52 on pp 662 notes 23S, 24R elutes first with ratio of m/z 229:261 = 1.31; 23R, 24R elutes second with ratio of m/z 229:261 = 0.96

Here, ratio is obviously <1, so this is 23R, 24R. ID'd by this method & J. Volkman, pers. comm.

Steroid ketones

Steroid ketones are the result of the oxidation (usually abiotic) of sterols that can occur in sediments during diagenesis

27: 5a-cholestan-3-one (cholestanone) (sample spectrum)

C27, 4 DBEs
C27 Δ0 Stanone

Sources: oxidation of cholesterol to cholestenone followed by hydrogenation to cholestanone in sediments**

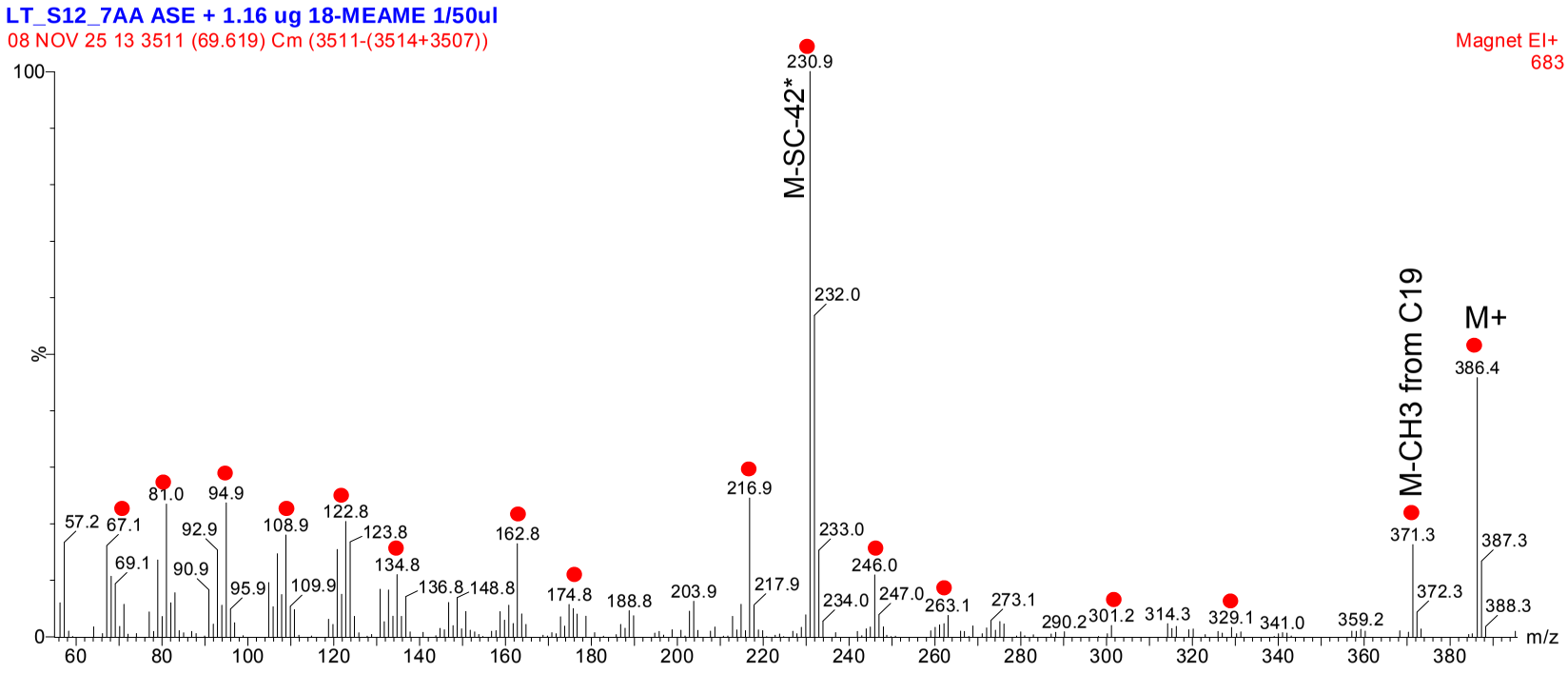

*42 is C15, C16, C17, 6H

- Red dots indicate ions labeled in library spectrum

**this process described in Gagosian & Smith (1979) *Nature* vol 277, pp 287-289
Ions listed in Mansour *et al* (1999) *Journal of Phycology* vol 35, pp 710-720
MS id confirmed by J. Volkman, pers. comm.

27: Cholestanone (NIST library)

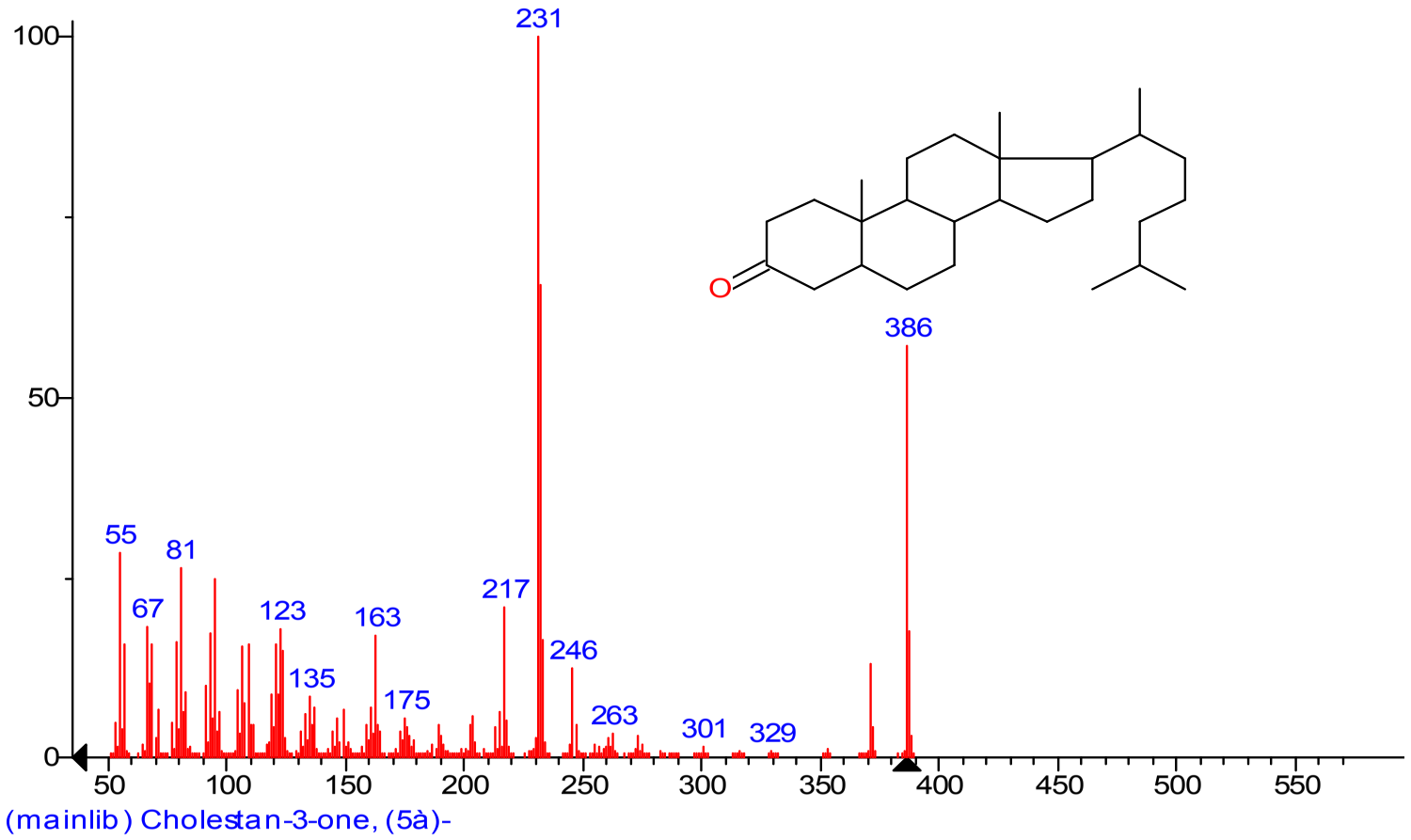

28: 4a,24-dimethylcholestan-3-one, samples & reference below

C29, 4 DBEs

C29 Δ0 Stanone

Sources: oxidation of 4,24-dimethylcholestanol in sediments

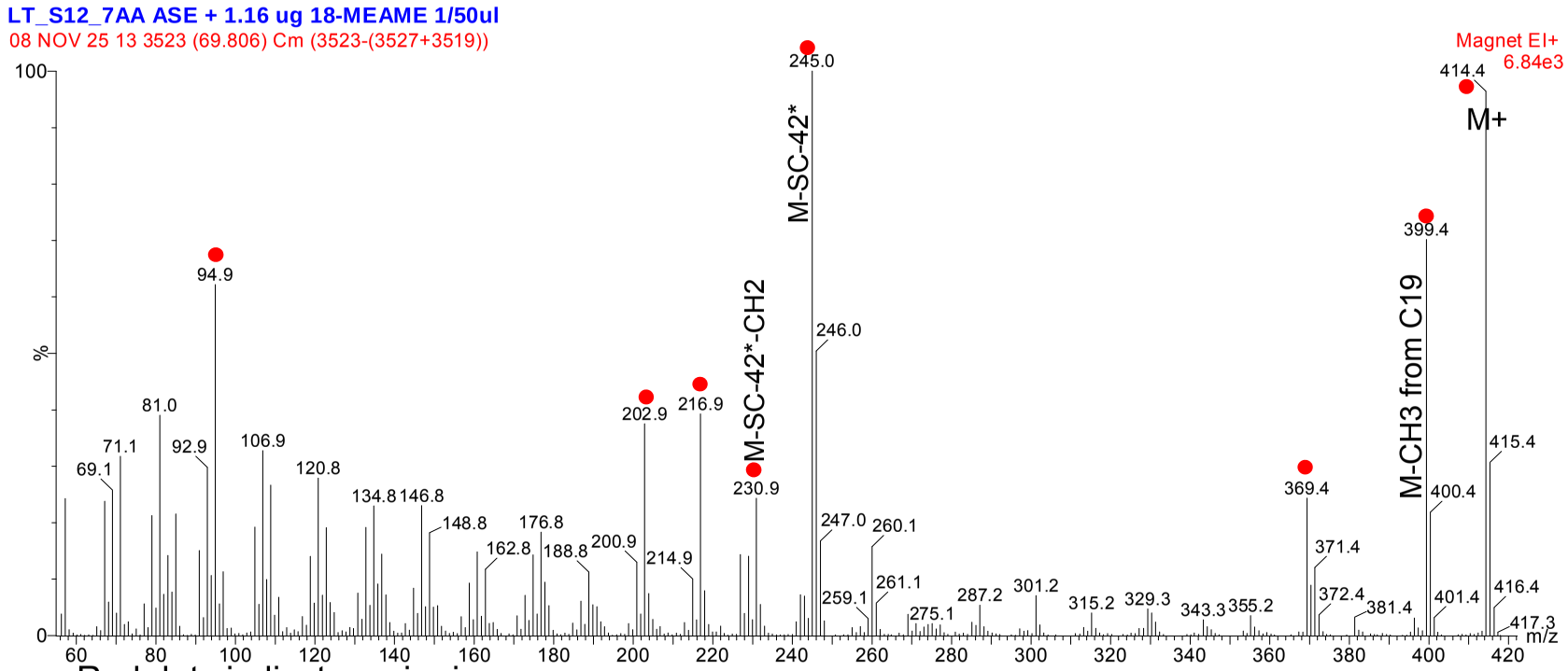

- Red dots indicate major ions

Compound described in N. Withers (1987) *Dinoflagellate sterols*, pp 316-359 in The Biology of Dinoflagellates, ed. FJR Taylor, Botanical Monographs 21

Source noted it appeared in bottom seds of eutrophic lake and in freshwater dinoflagellate Peridinium lomnickii

MS id'd by J. Volkman, pers. comm.

*42 is C15, C16, C17, 6H

29: 4a-methyl, 24-ethylcholestan-3-one, samples & reference below

C30, 4 DBEs
C30 Δ0 Stanone

Sources: oxidation of 4a-methyl-24-ethylcholestanol in sediments

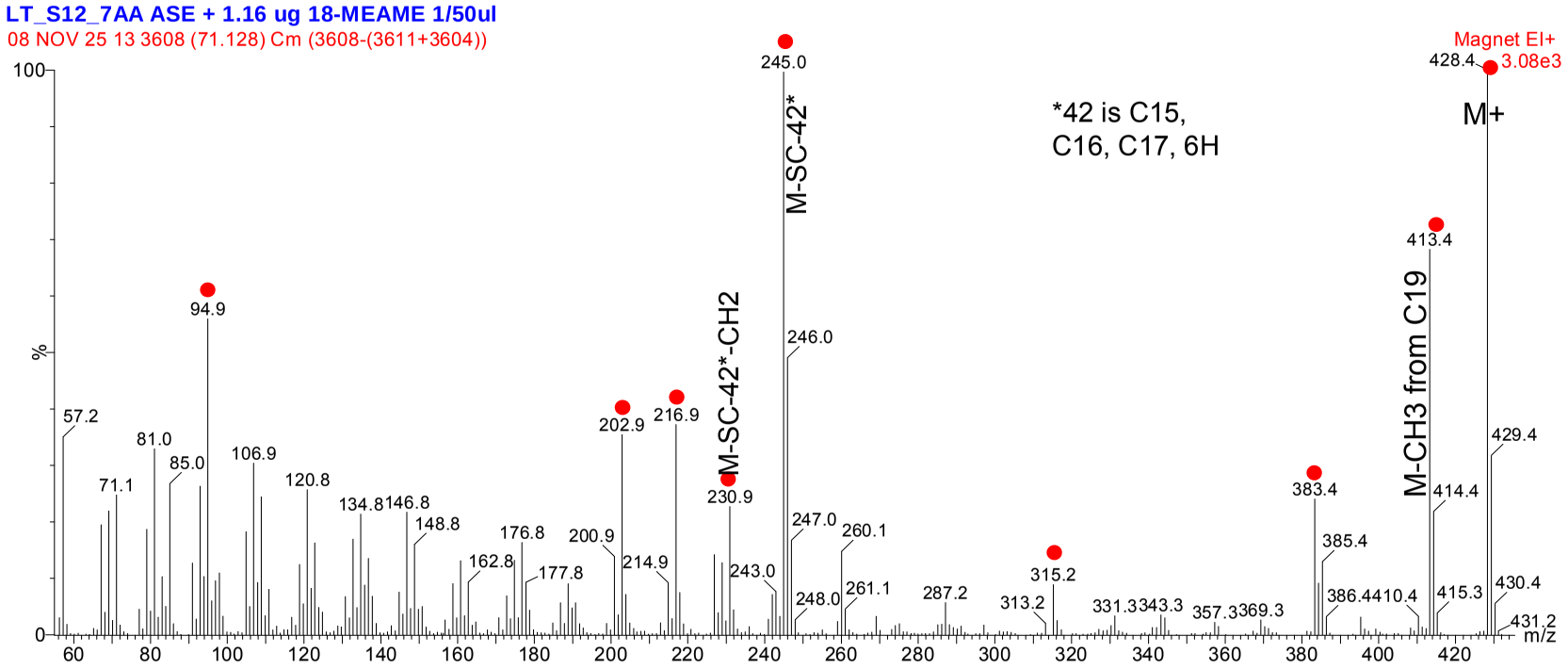

- Red dots indicate major ions

this compound (or dinostanone) described in Gagosian & Smith (1979) *Nature* vol 277, pp 287-289
Note difference to dinostanone ions provided in Mansour *et al* (1999) *Journal of Phycology* vol 35 pp 710-720; dinostanone contains m/z 281(12) & 207(27), which this compound does not
MS id'd by J. Volkman, pers. comm.

30: Cycloartan-3-one (sample spectrum)

C30, 5 DBEs
C30 Δ0 Stanone

Sources: oxidation of cycloartanol (part of biosynthetic pathway of sterol synthesis in higher plants, microalgae, protists) in sediment

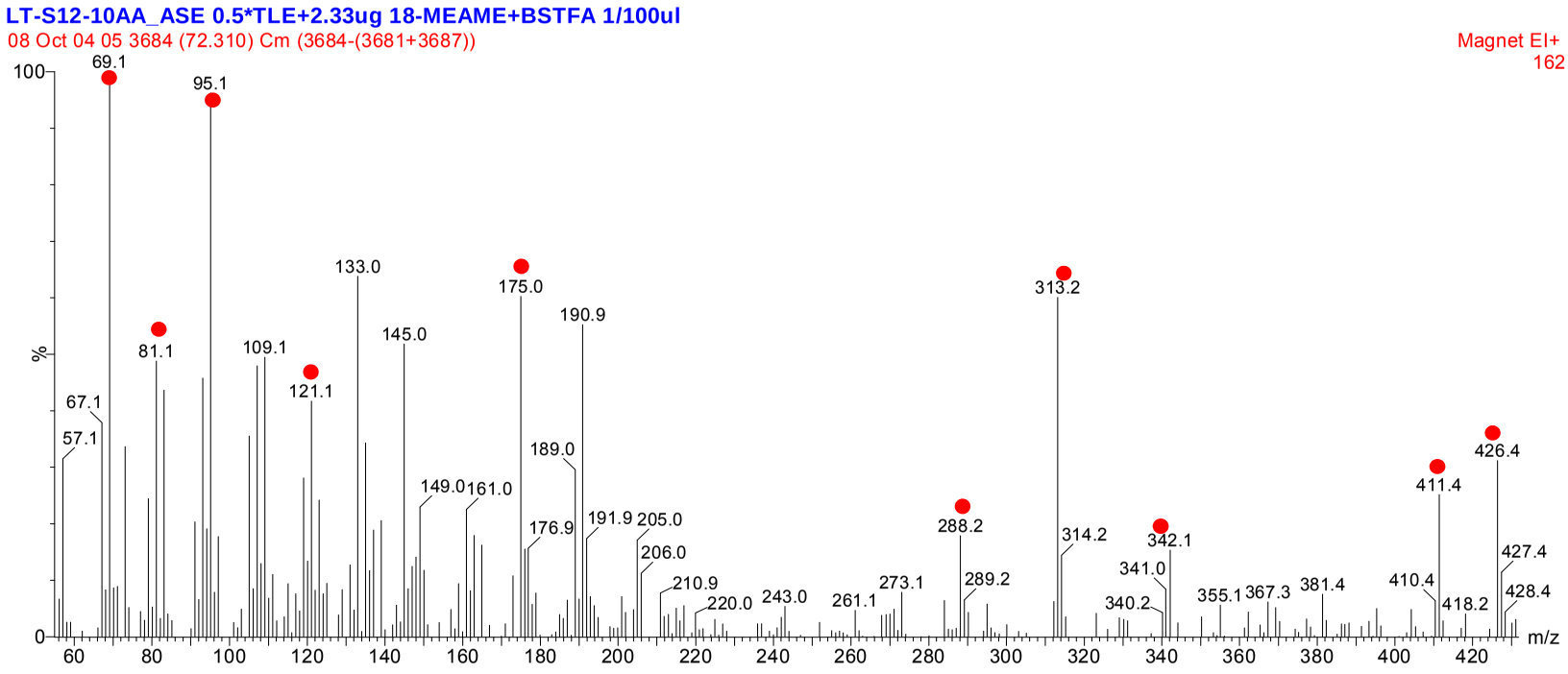

MS id'd using NIST library – not an exact match, but close considering co-elution with dehydrodinosterol and C_{31} B,a hopane

- Red dots indicate major ions

30: Cycloartanone, NIST library

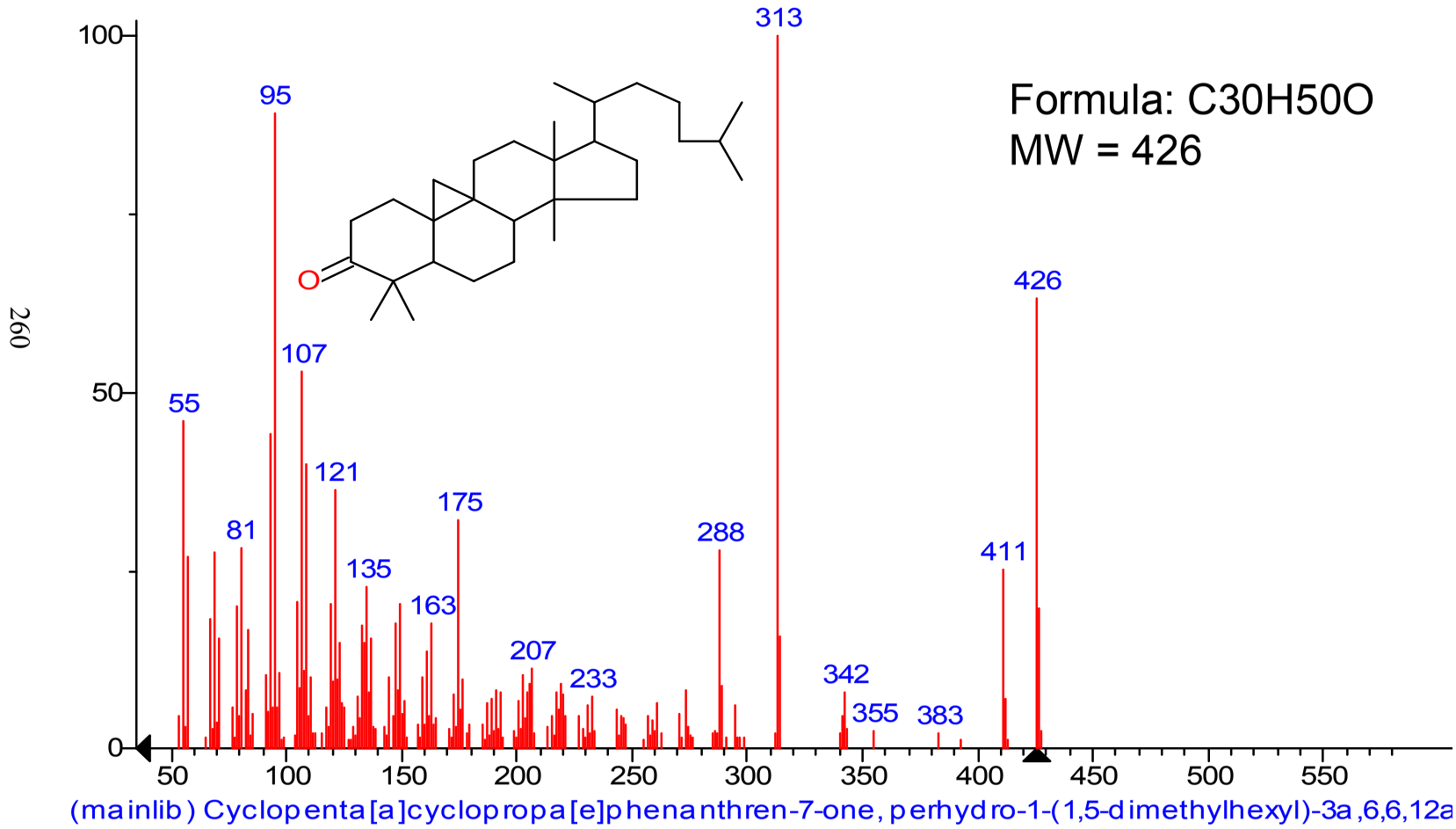

31: Stimast-4-en-3-one (stigmastenone), id'd based on NIST library

C29, 5 DBEs

C29 Δ1 Stenone

Sources: oxidation of stigmasterol in sediments

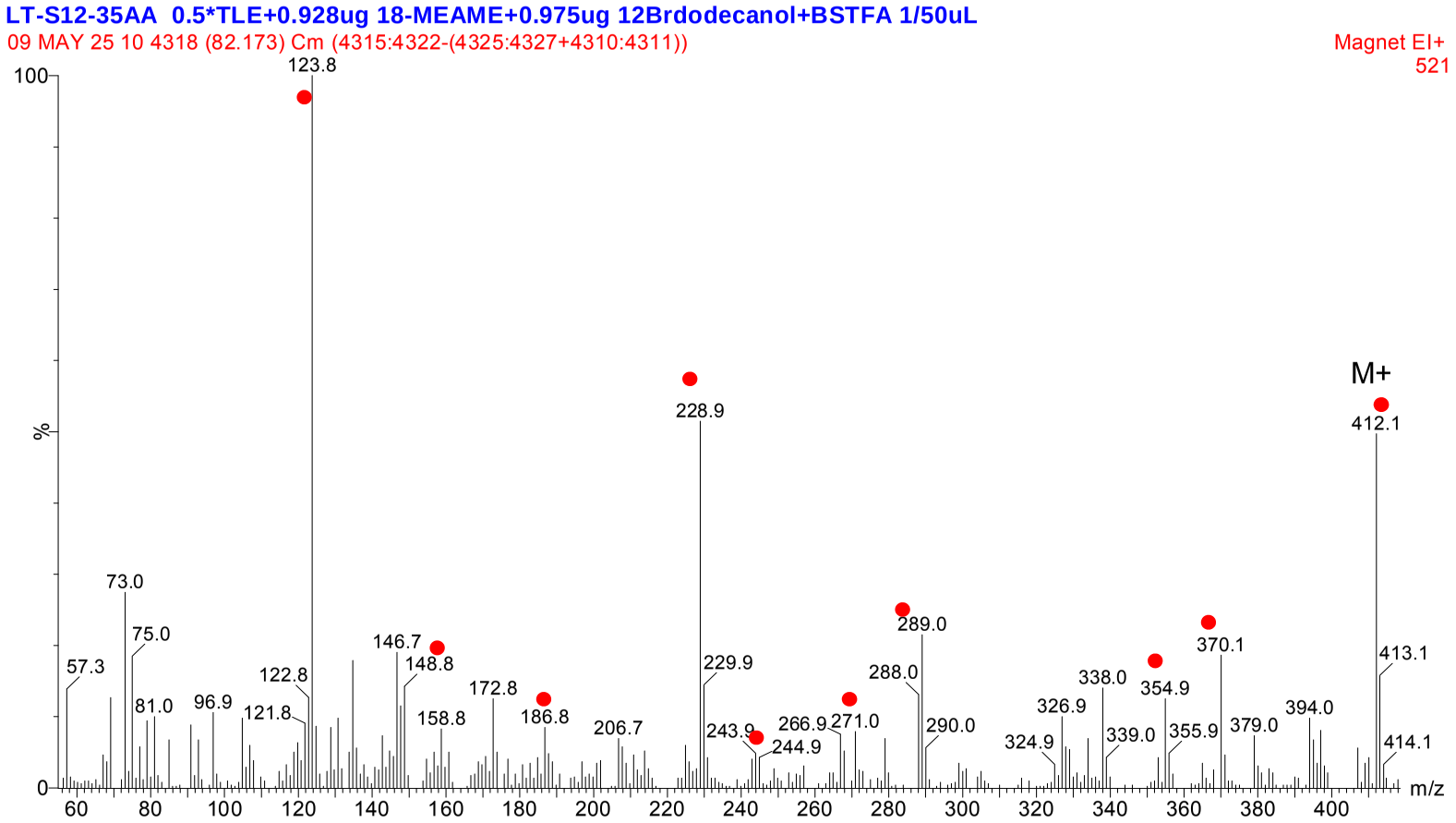

- Red dots indicate ions labeled in library spectrum
  **this process described in Meyer & Ishiwatari (1993) *Organic Geochemistry* vol 20 pp 867-900 and references therein (see sterol degradation references, pp 880)

31: Stigmastenone (NIST library)

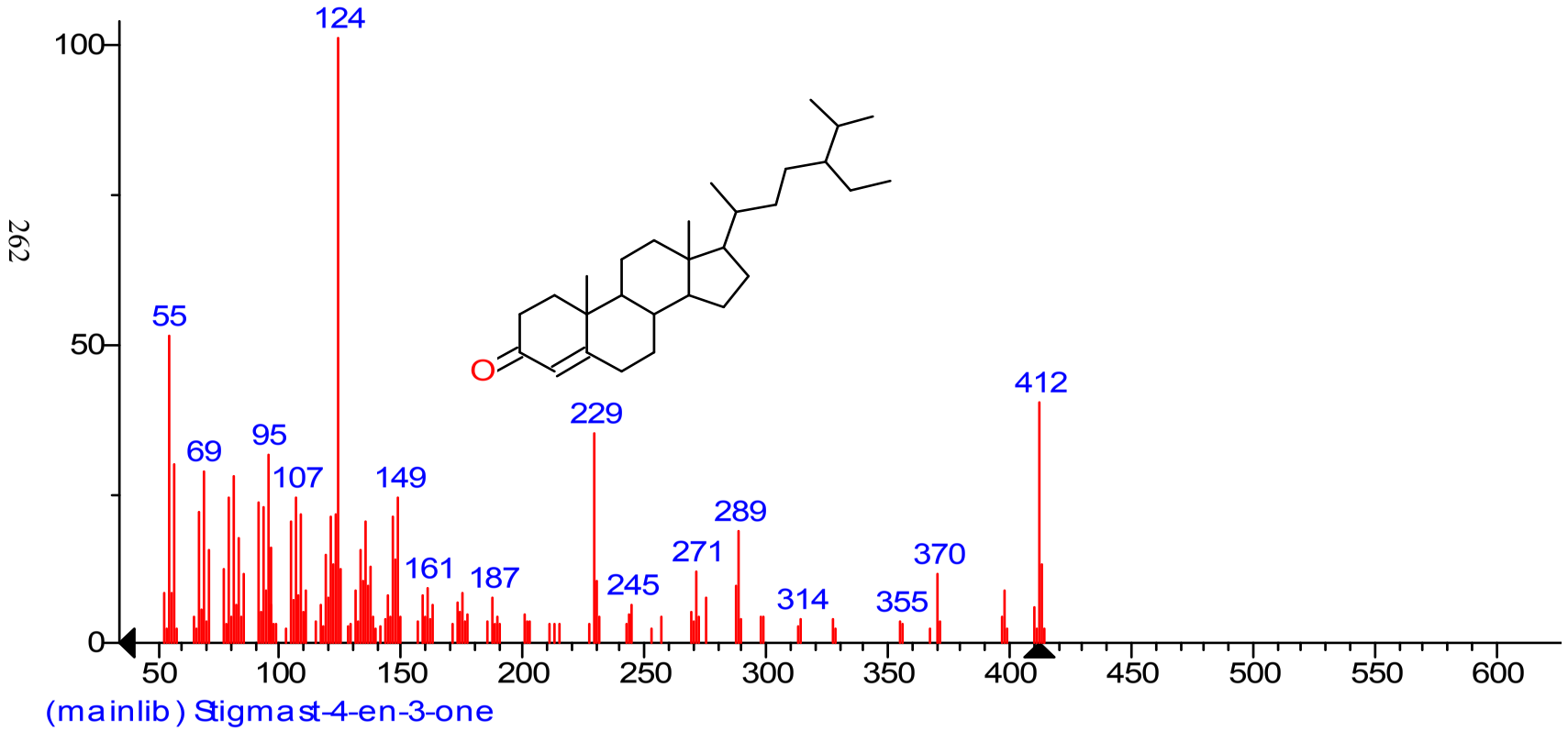

Sterenes

Sterenes are products of dehydration of parent sterols;
Typical of saline environments at gypsum saturation and above

See Barbe *et al* (1989) *Advances in Organic Geochemistry*
Vol 16 pp 815-828

32: 5a-cholest-2-ene (sample spectrum)

C27, 5 DBEs
C27 Δ2 Sterene

Sources: dehydration of cholestanol in sediments**

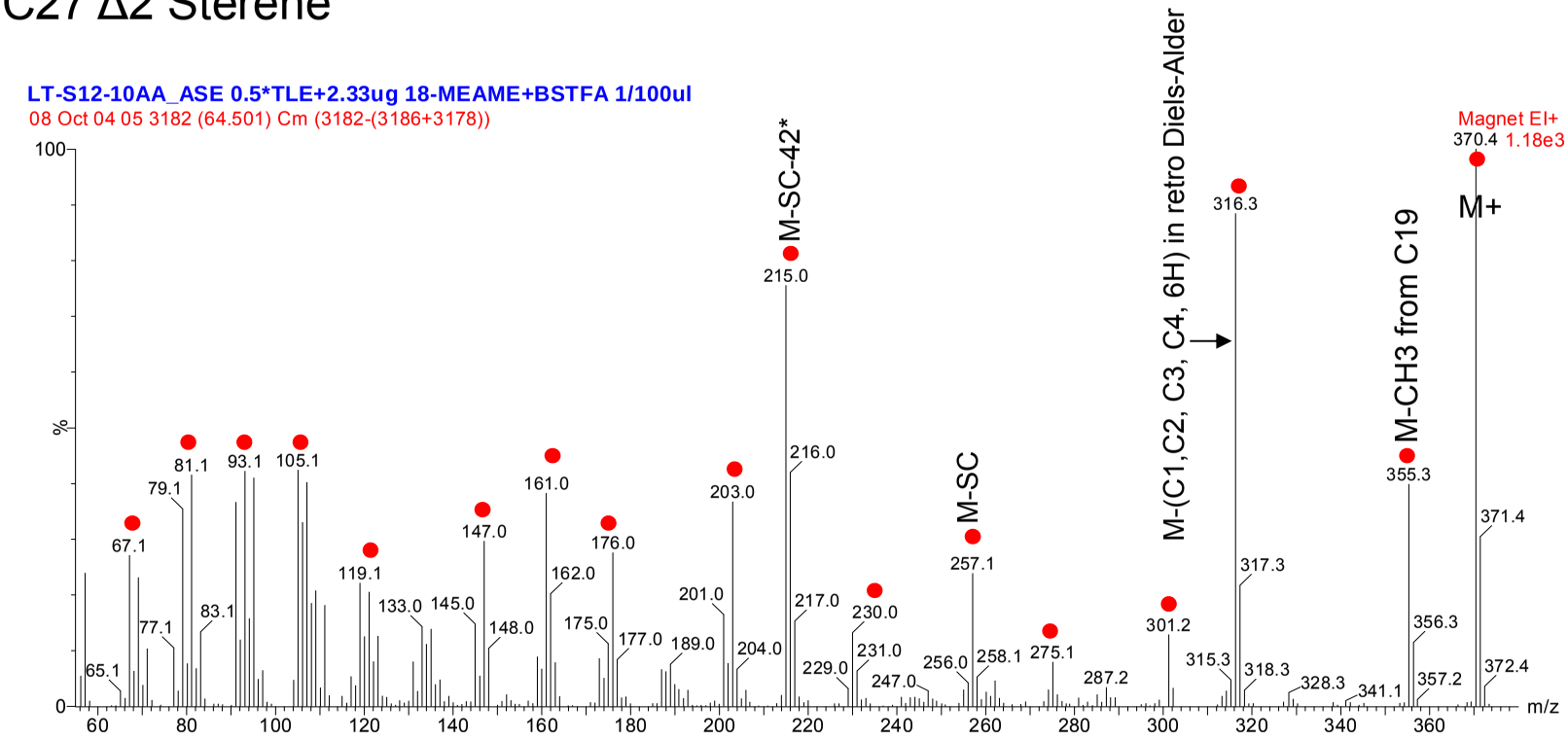

- Red dots indicate ions labeled in library spectrum

**this compound present in slightly higher concentration in sample 10AB, which was NOT freeze-dried & was extracted with Bligh-Dyer, NOT ASE, so dehydration was not due to lab technique

*42 is C15, C16, C17, 6H

32: 5a-cholest-2-ene (NIST library)

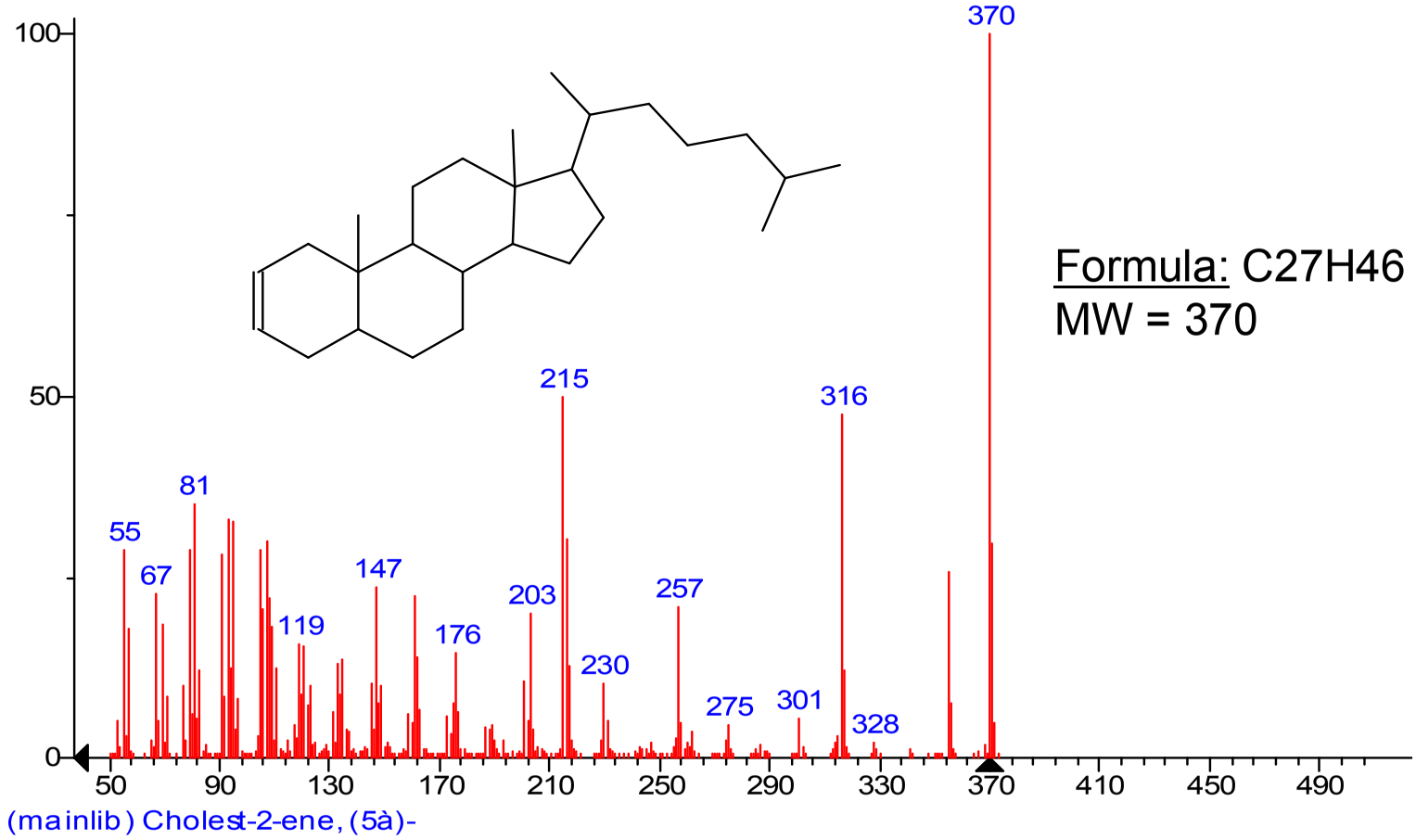

Formula: C27H46
MW = 370

33: 5a-ergost-2-ene, id'd based on series of sterenes

C28, 5 DBEs

C28 Δ2 Sterene

Sources: dehydration of ergostanol in sediments**

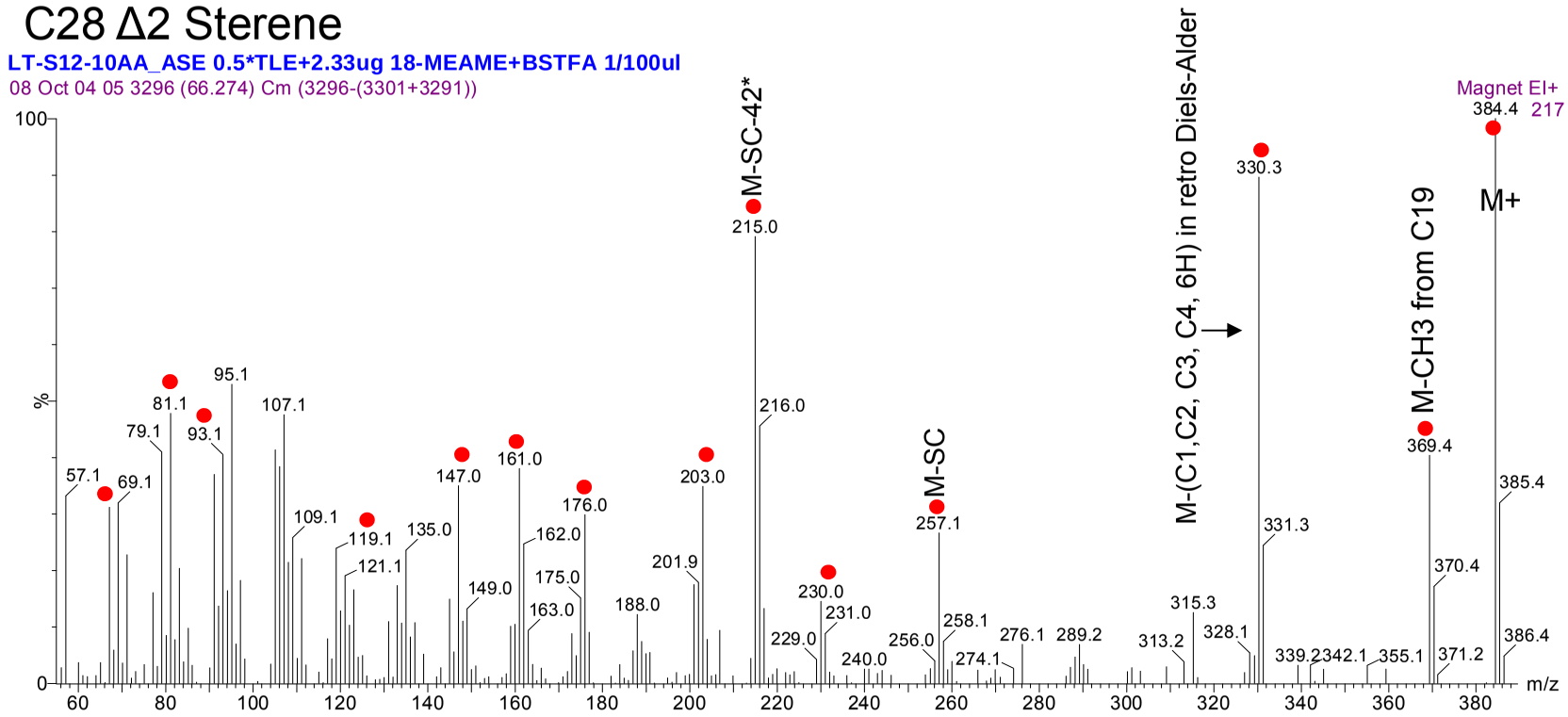

- Red dots indicate ions comparable to those in 5a cholestene

**this compound present in slightly higher concentration in sample 10AB, which was NOT freeze-dried & was extracted with Bligh-Dyer, NOT ASE, so dehydration was not due to lab technique

*42 is C15, C16, C17, 6H

34: 5a-stigmast-2-ene, id'd based on series of sterenes

C29, 5 DBEs Sources: dehydration of stigmastanol in sediments**

C29 Δ2 Sterene

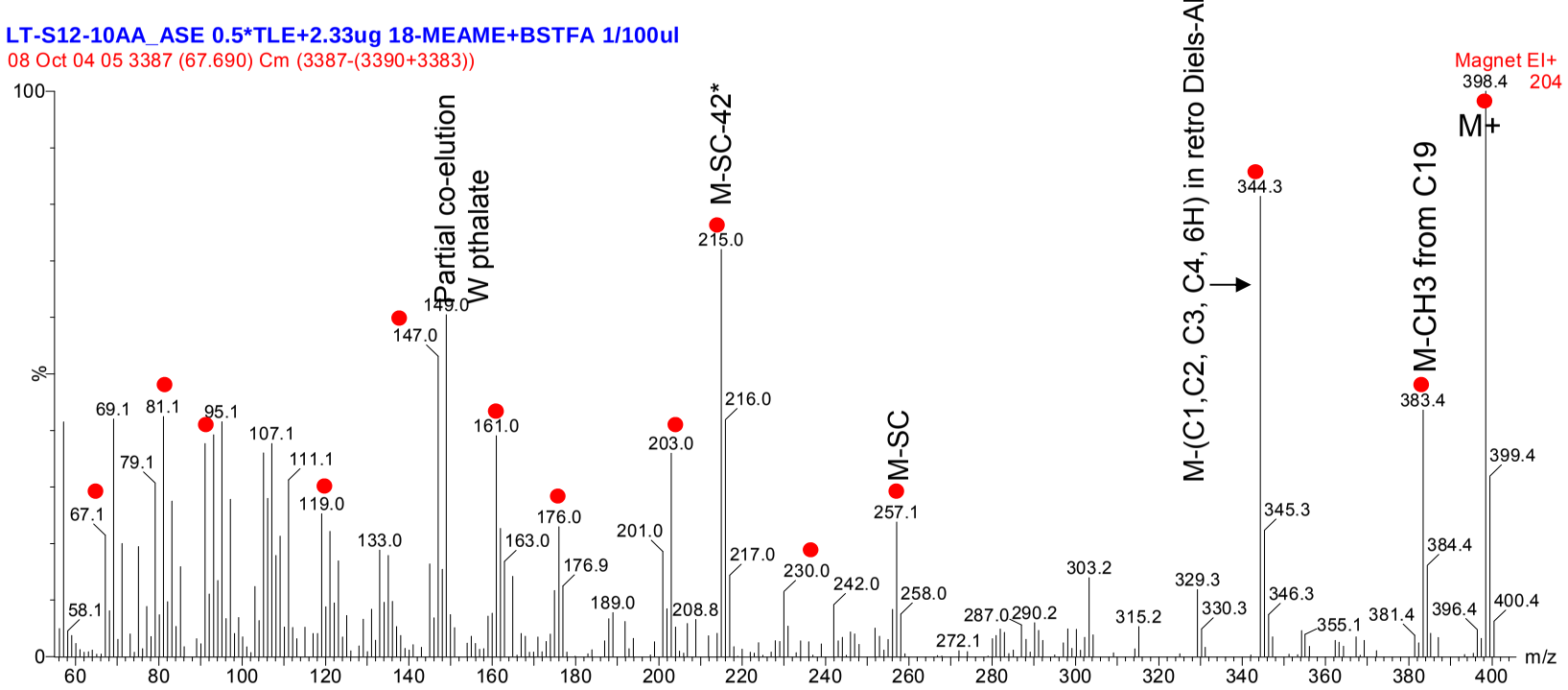

- Red dots indicate ions comparable to those in 5a cholestene

**this compound present in similar concentration in sample 10AB, which was NOT freeze-dried & was extracted with Bligh-Dyer, NOT ASE, so dehydration was not due to lab technique

*42 is C15, C16, C17, 6H

Isoprenoids

35: Archaeol ($C_{20,20}$) TMS
(bis-O-phytanyl glycerol) (MW = 724)

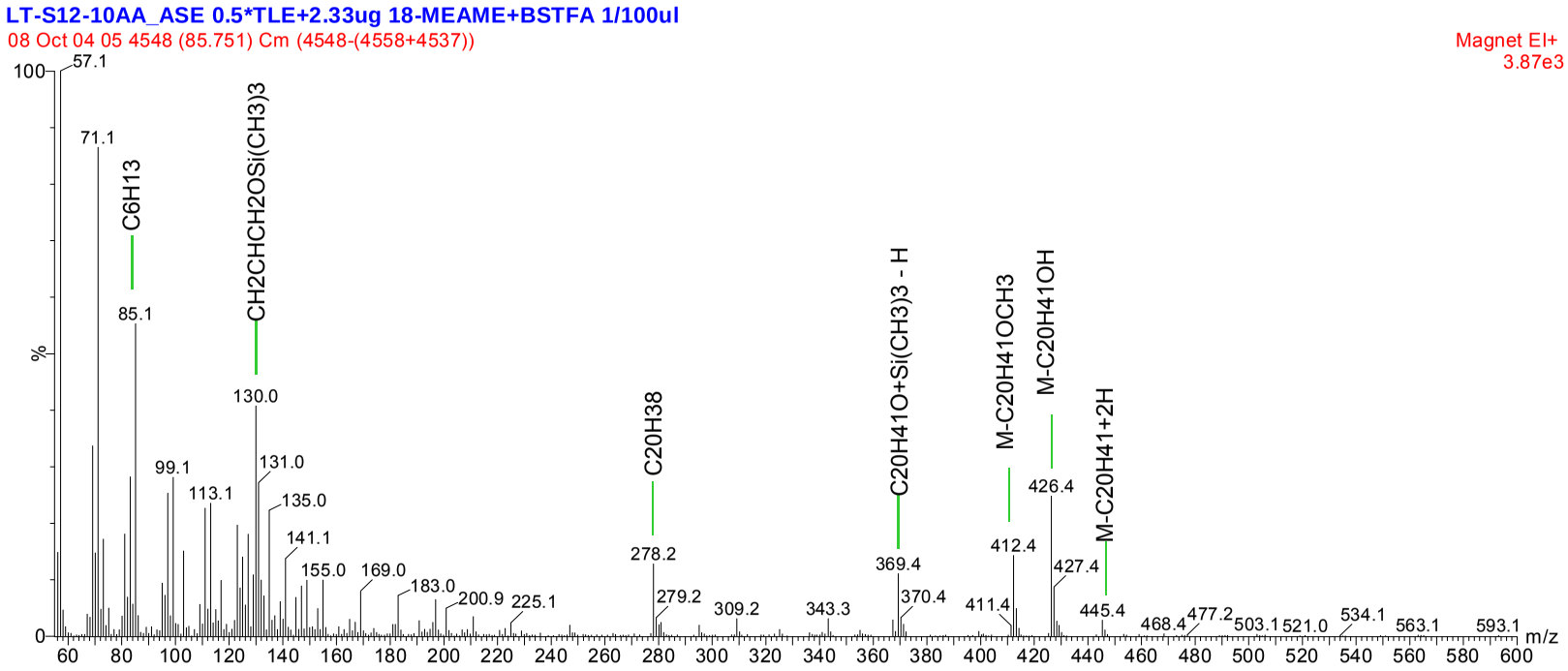

Reference: Teixidor *et al*, 1993 (*GCA* vol 57, pp 4479); structure & spectrum
& Teixidor *et al*, 1992 (*Journal of Chromatography* vol 607, pp 253); elution position & spectrum
Source: archaea, especially halophilic archaea, reference Javor B, *Hypersaline Environments: Microbiology and Geochemistry. Brock TD, Ed., Brock/Springer Series in Contemporary Bioscience (Springer-Verlag, Berlin, 1989).*

36: Archaeol ($C_{20,25}$) TMS
(O-phytanyl-O-sesterpanylglycerol) (MW = 794)

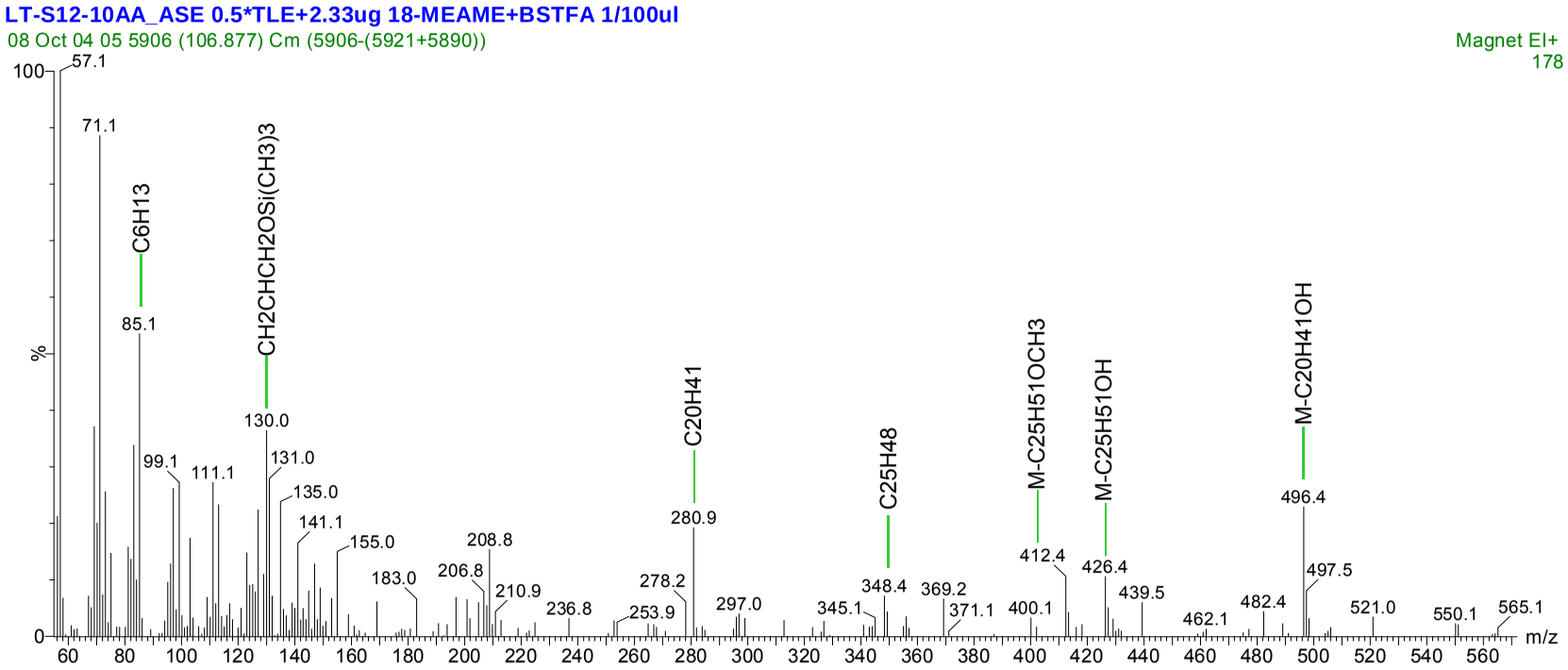

Reference: Teixidor *et al*, 1993 (*GCA* vol 57, pp 4479); structure & spectrum
& Teixidor *et al*, 1992 (*Journal of Chromatography* vol 607, pp 253); elution position & spectrum
Source: archaea, especially halophilic archaea, reference Javor B, *Hypersaline Environments: Microbiology and Geochemistry. Brock TD, Ed., Brock/Springer Series in Contemporary Bioscience (Springer-Verlag, Berlin, 1989).*

37: Phytol TMS (sample)

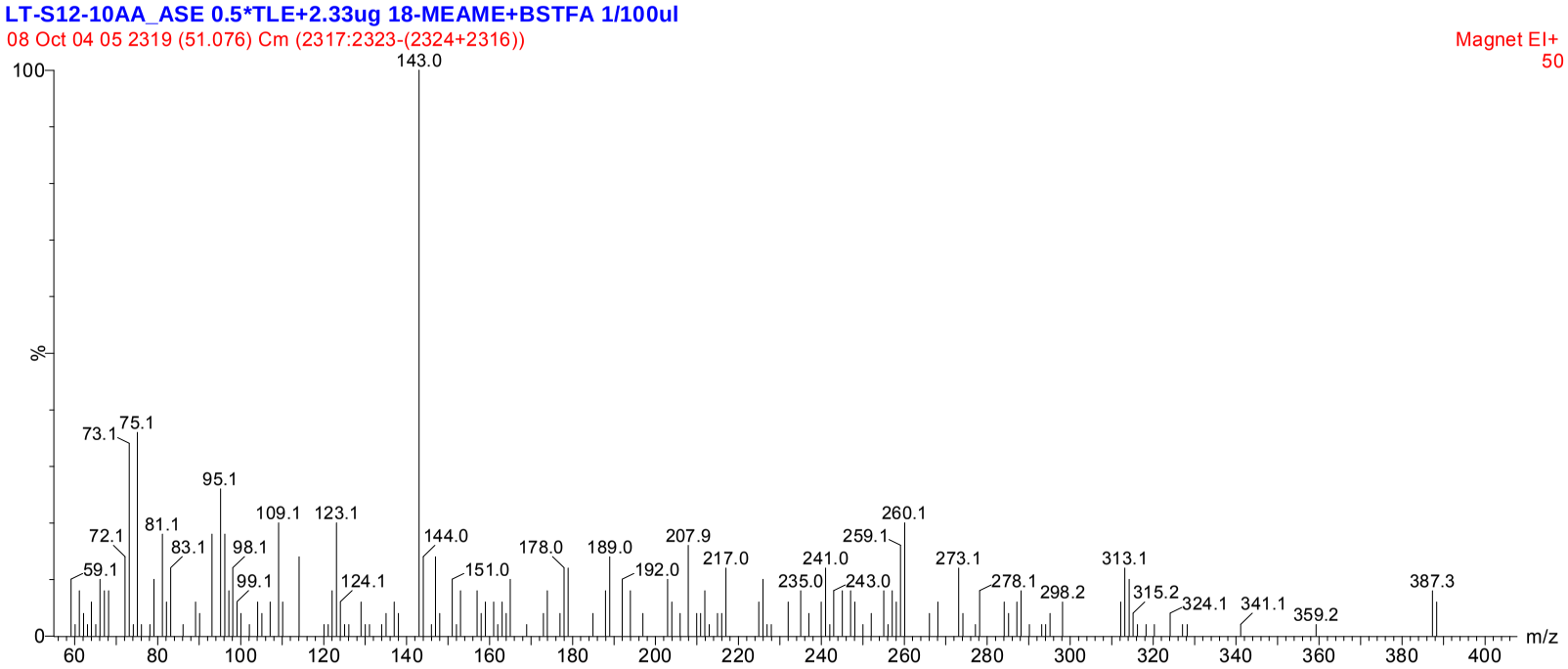

Source: side chain of Chlorophyll-a; Cox *et al* (1971)
Advances in Organic Geochemistry
pp 263-276

37: Phytol TMS (NIST library)

272

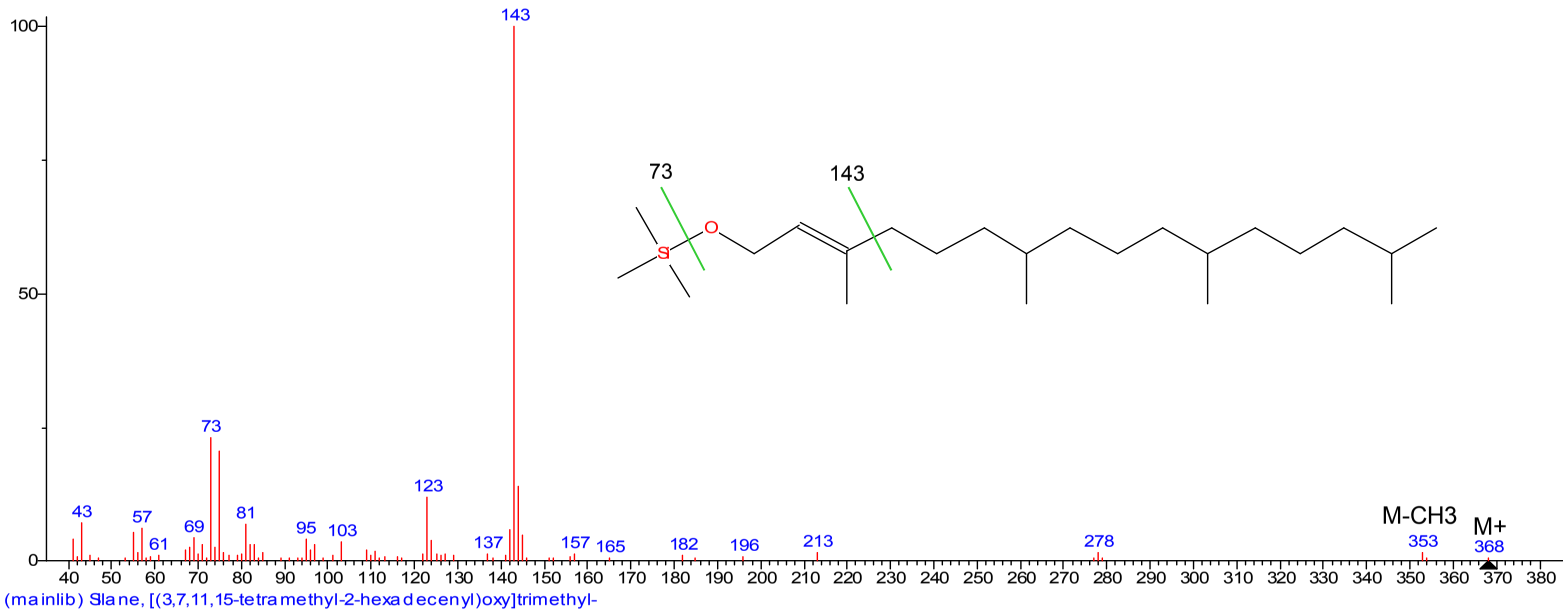

Formula: C23H48OSi
MW = 368

38: Phytanol TMS (sample)
(dihydrophytol)

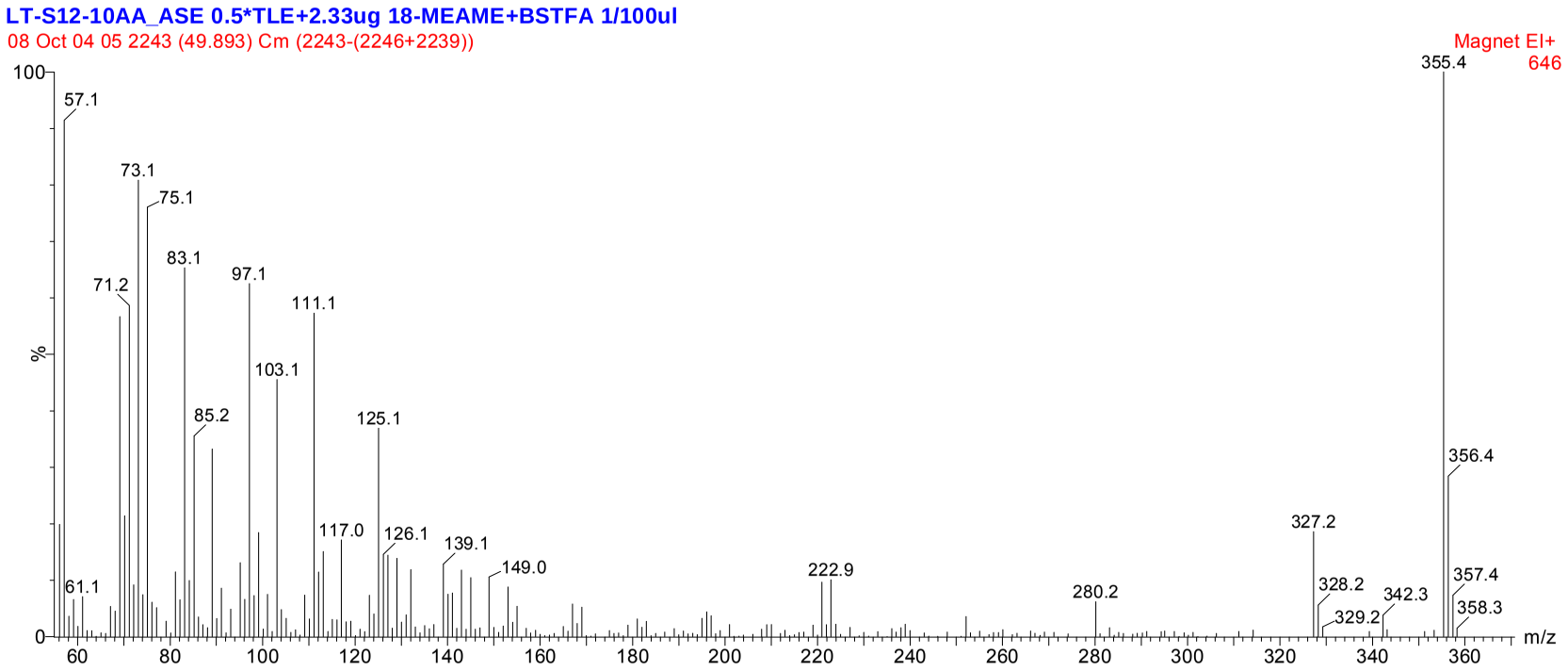

Source: Reduction of phytol;
Cox *et al* (1971) *Adv Org Geochem*, pp 263-276

38: Phytanol TMS (NIST library)

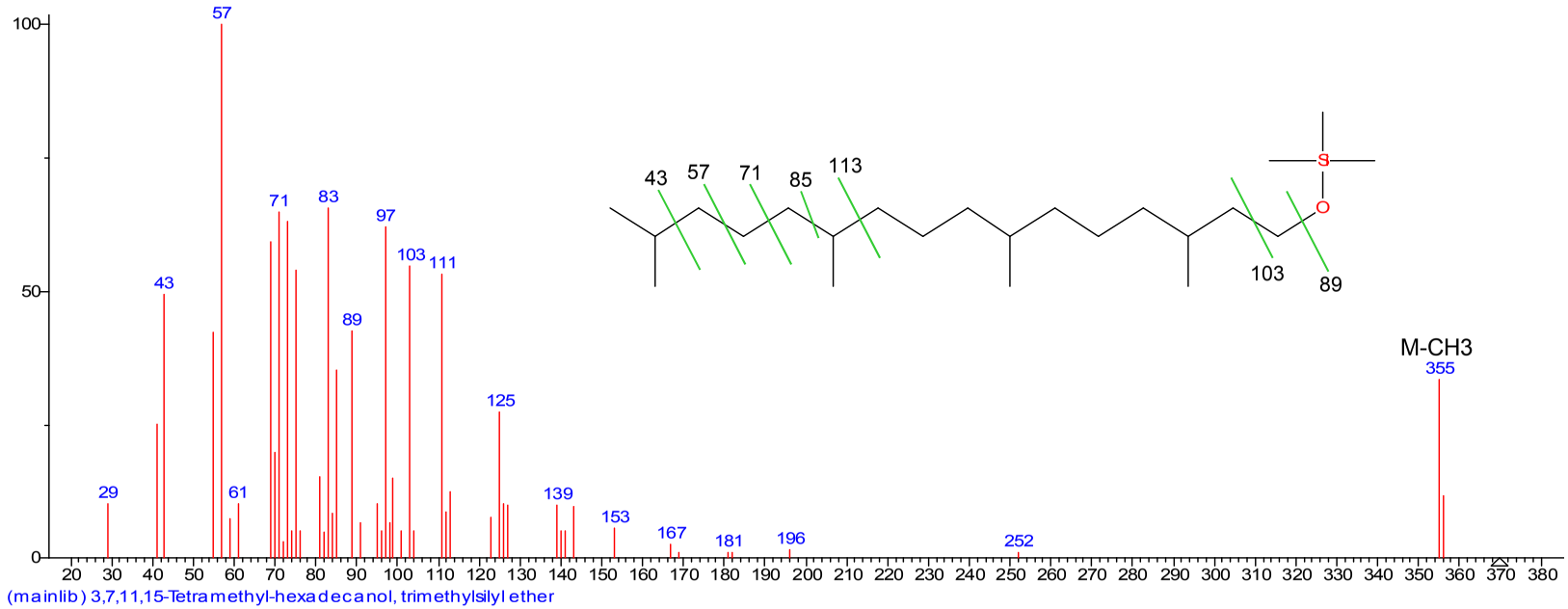

Formula: C23H50OSi

MW = 370

39: 6,10,14-trimethyl-pentadecan-2-one (phytone) (sample)

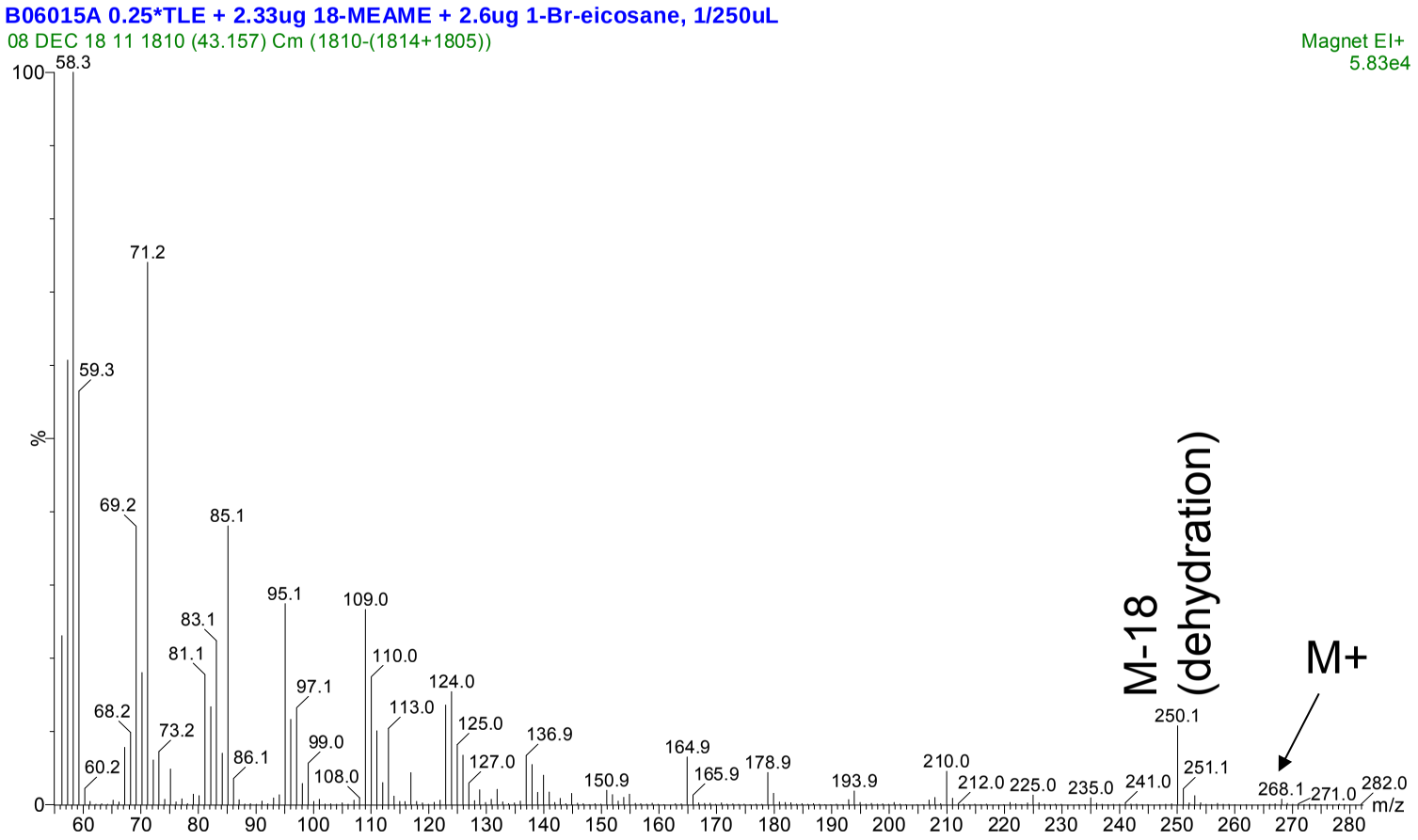

Source: oxidation of phytol – sometimes bacterially mediated?
See Simoneit & Burlingame (1973) *Adv Org Geochem*, pp 629-648
Also see Cox *et al* (1971) *Adv Org Geochem*, pp 263-276

39: Phytone, NIST library

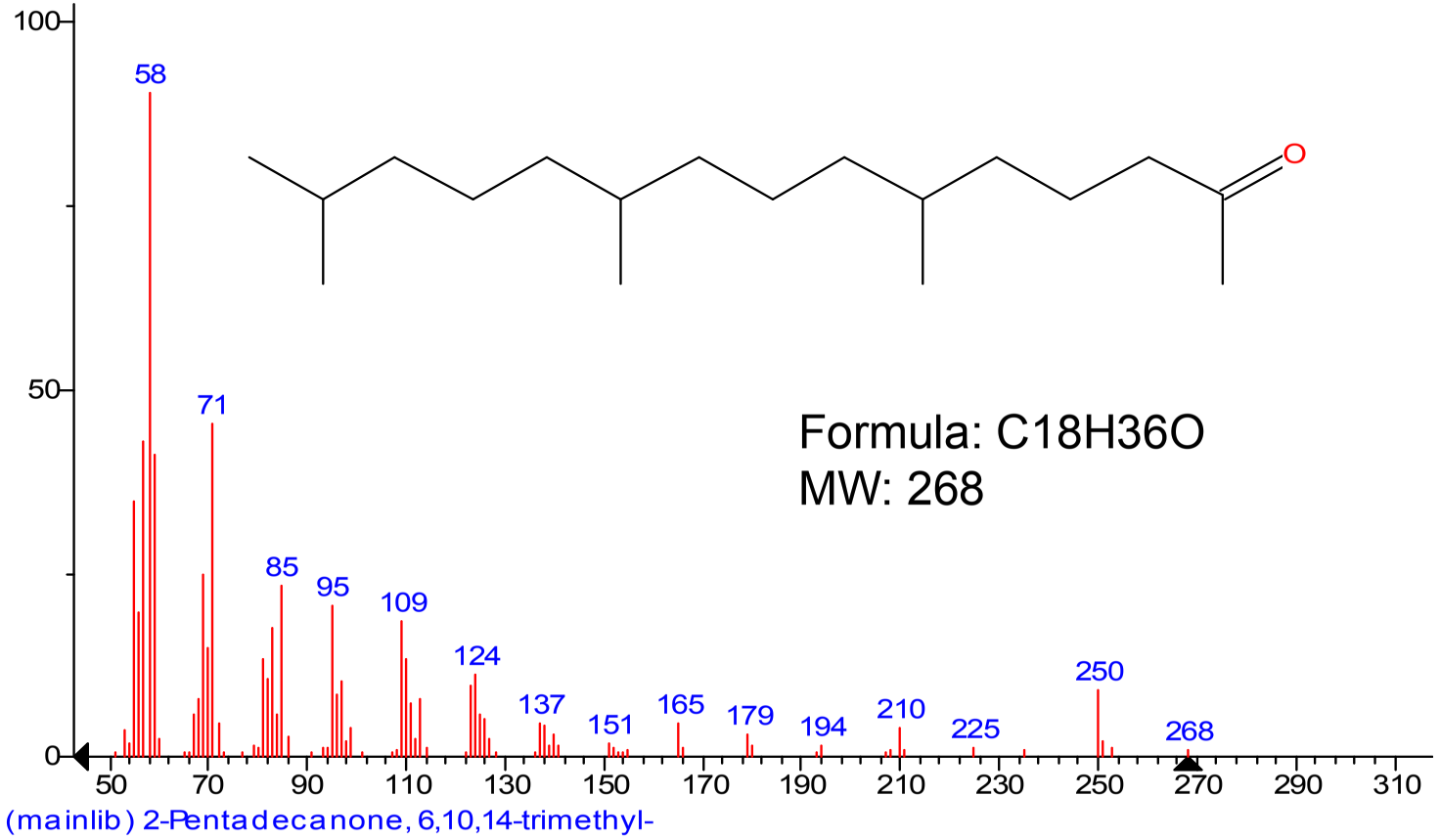

6,10-dimethyl-undecan-2-one, NIST library and samples

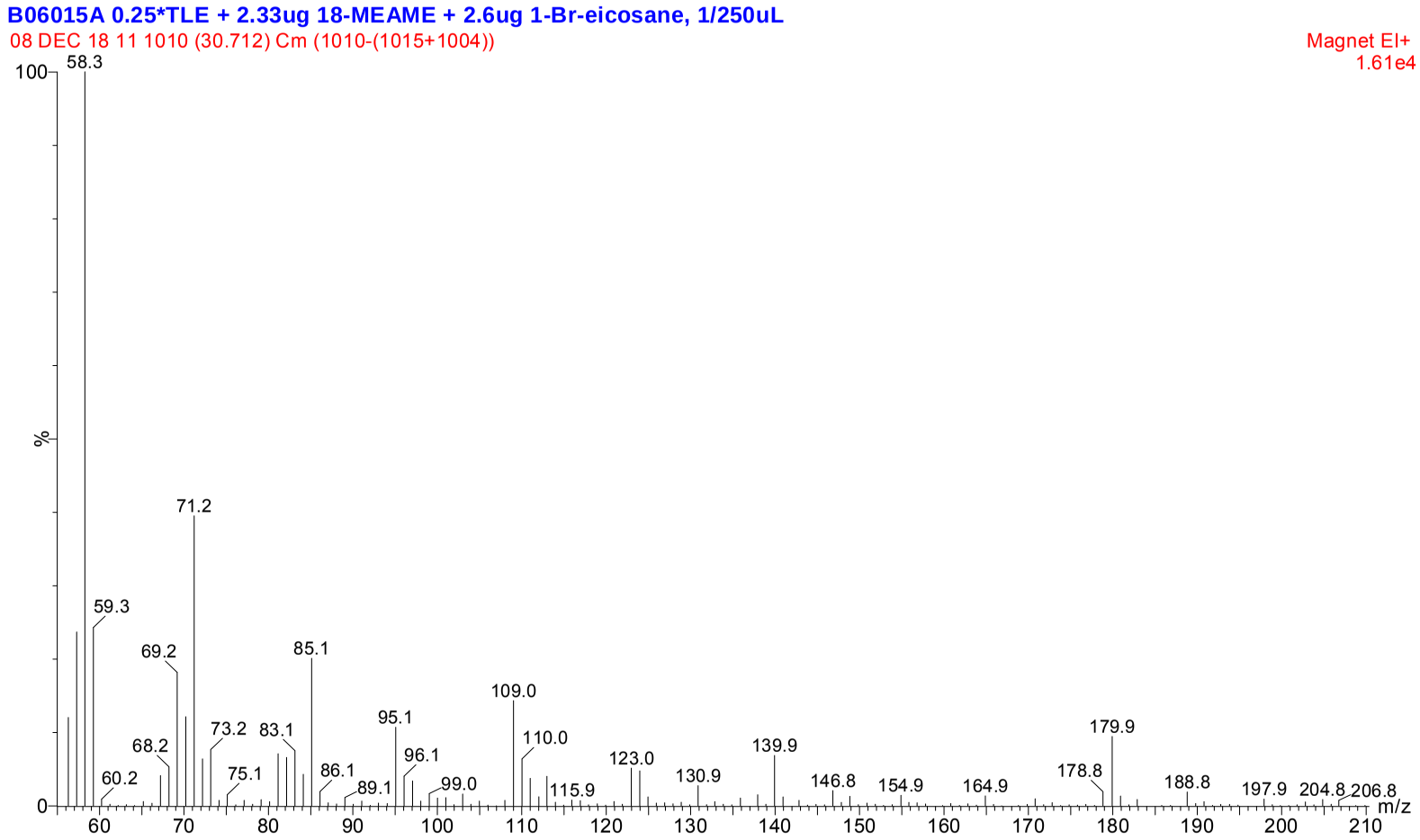

Source: oxidation of phytol & phytone (?) – sometimes bacterially mediated? see Cox *et al* (1971) *Adv Org Geochem*, pp 263-276

6,10-dimethyl-undecan-2-one (NIST library)

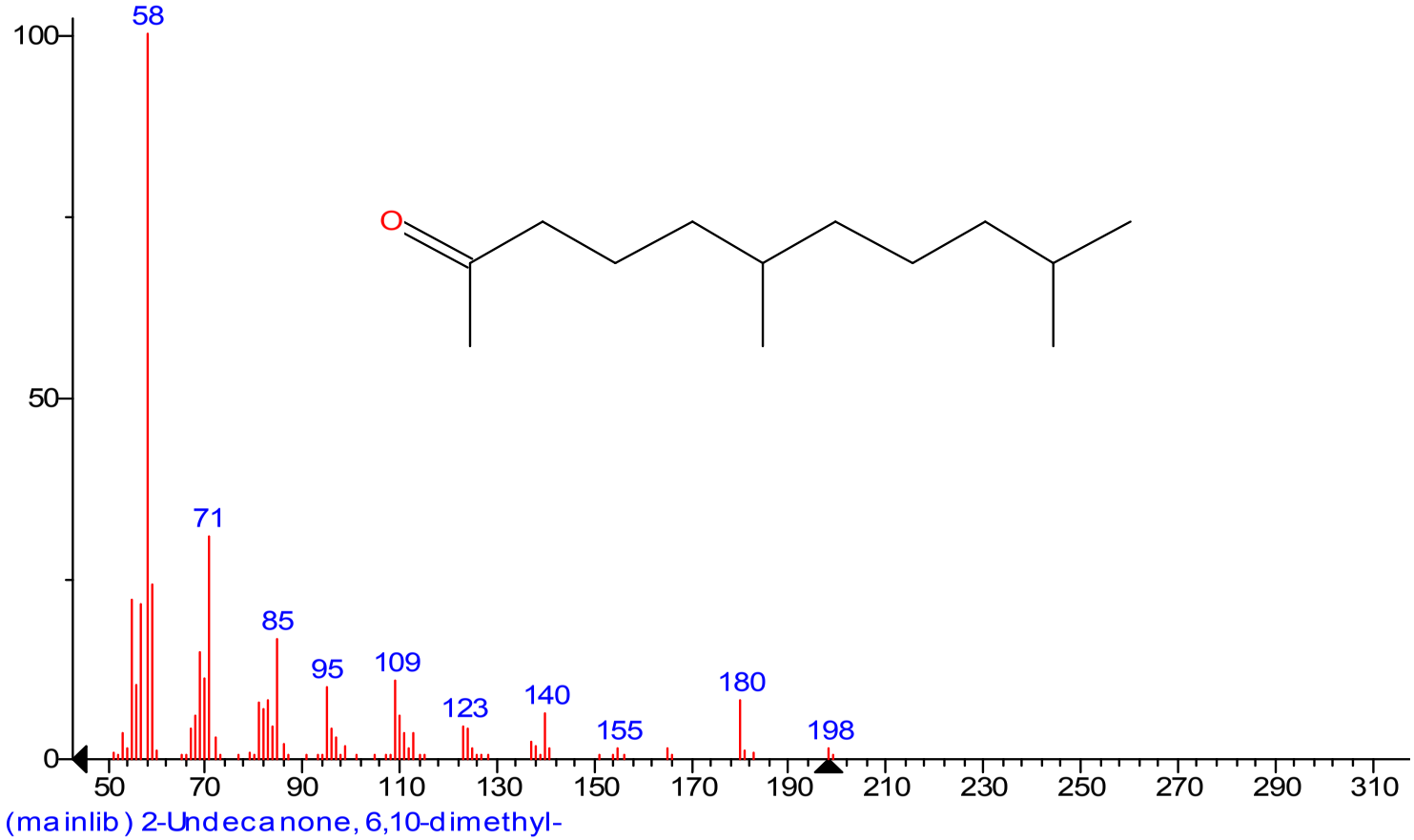

40: Phytanic acid TMS (sample)

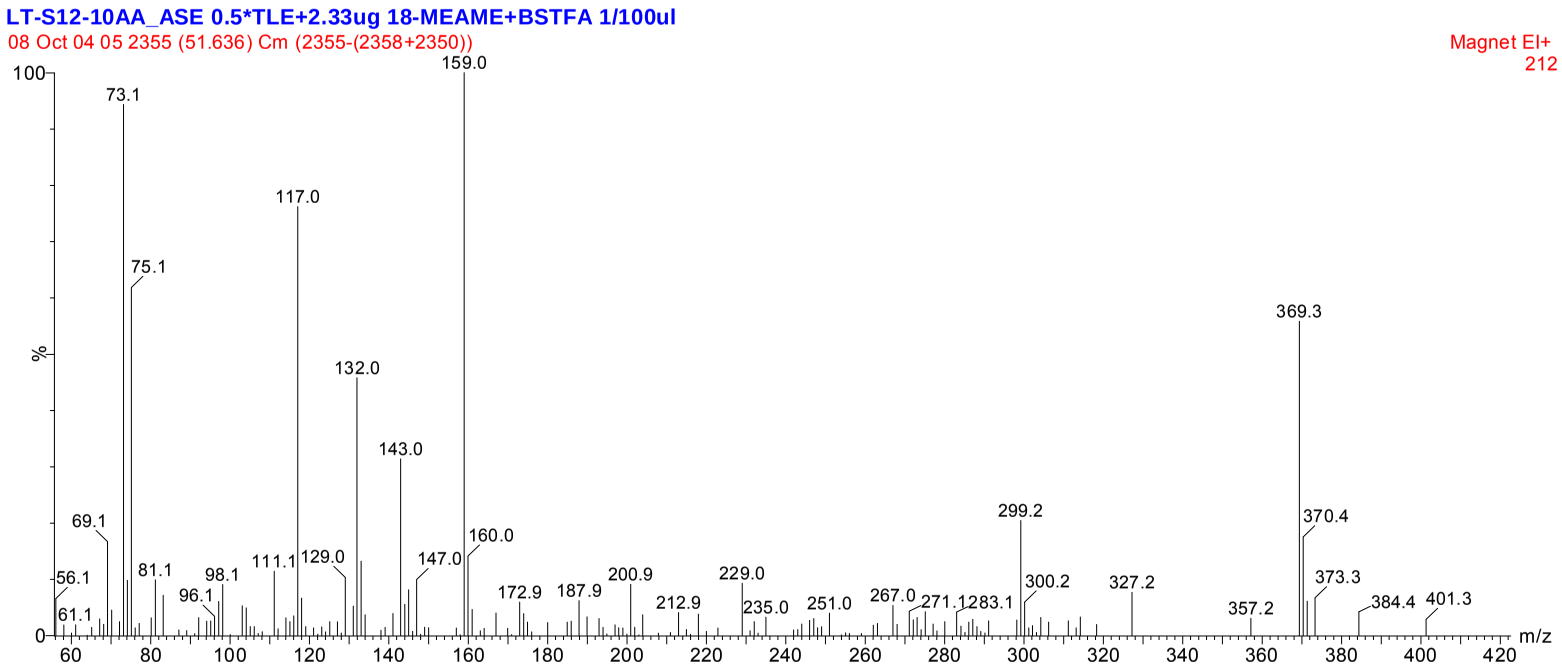

Source: oxidation of phytanol; Cox *et al* (1971)
Advances in Organic Geochemistry
Pp 263-276

40: Phytanic acid TMS (NIST library)

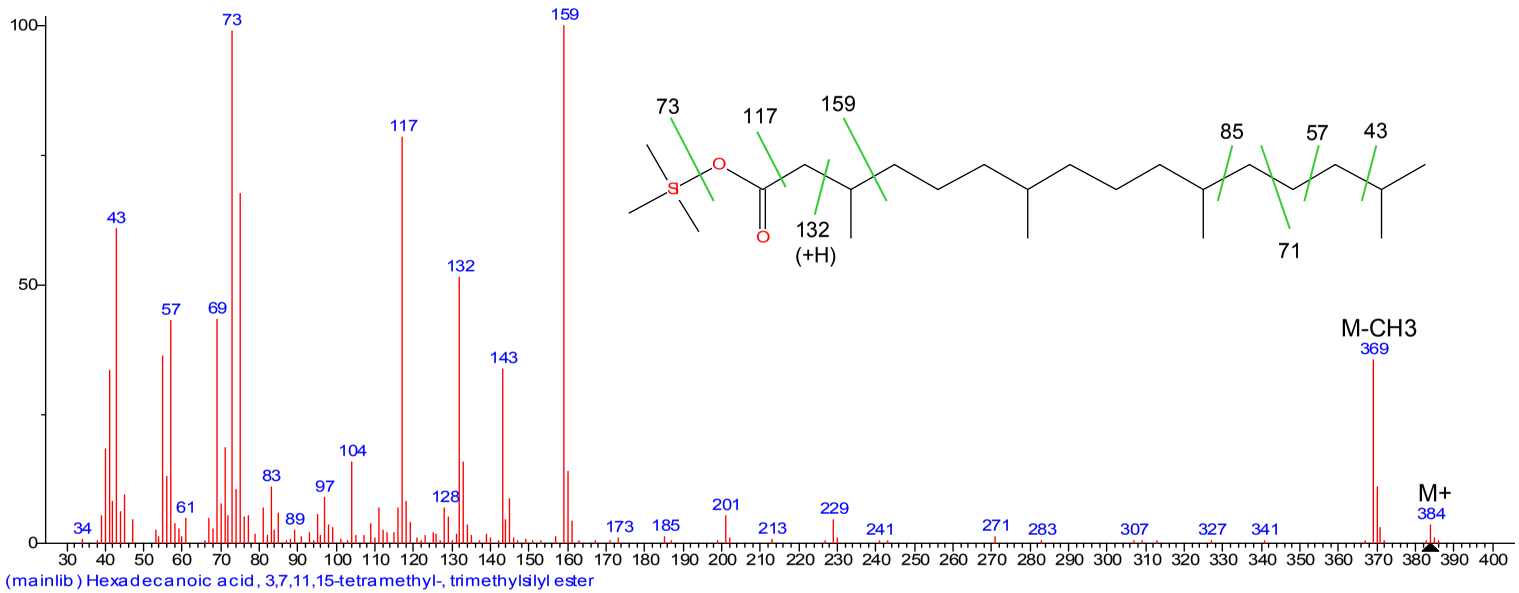

Formula: C23H48O2Si

MW = 384

Phytenic acid TMS (NIST library only)

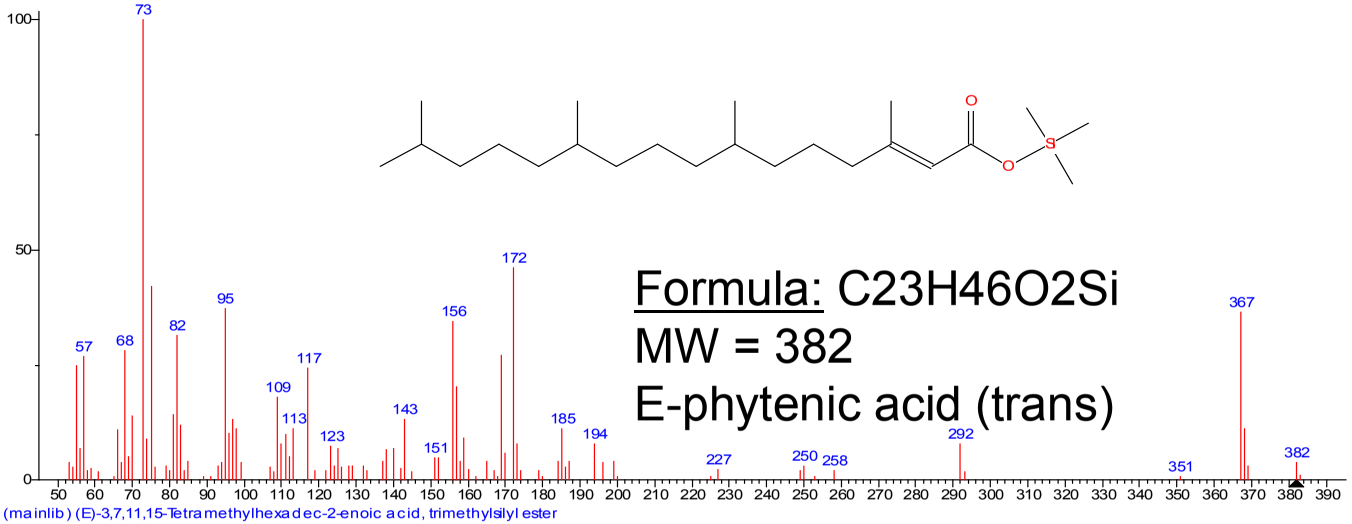

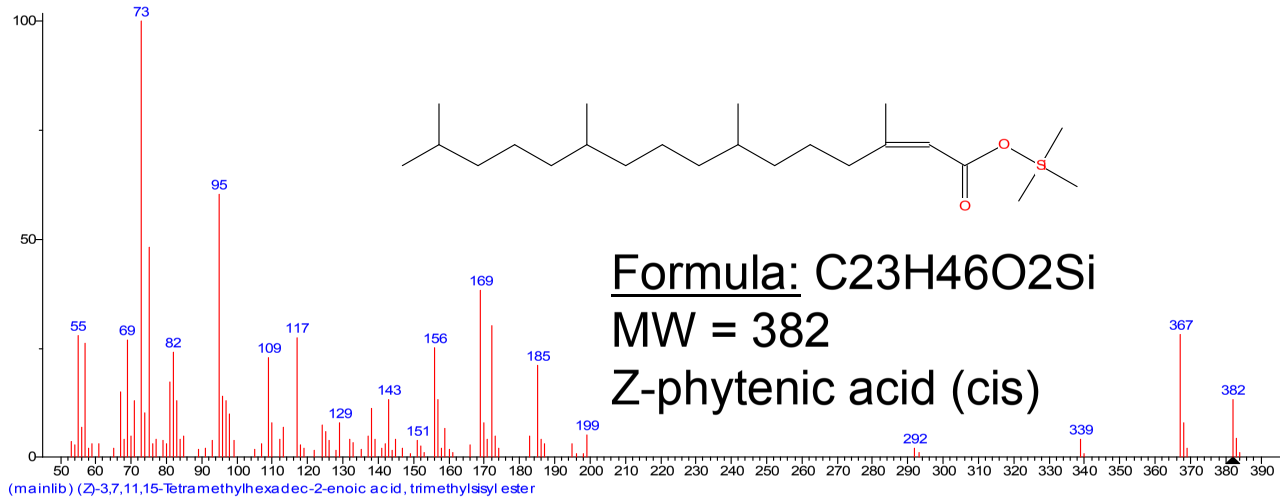

Pristane (co-elutes w nC17 on DB-5 MS column); NIST library + samples

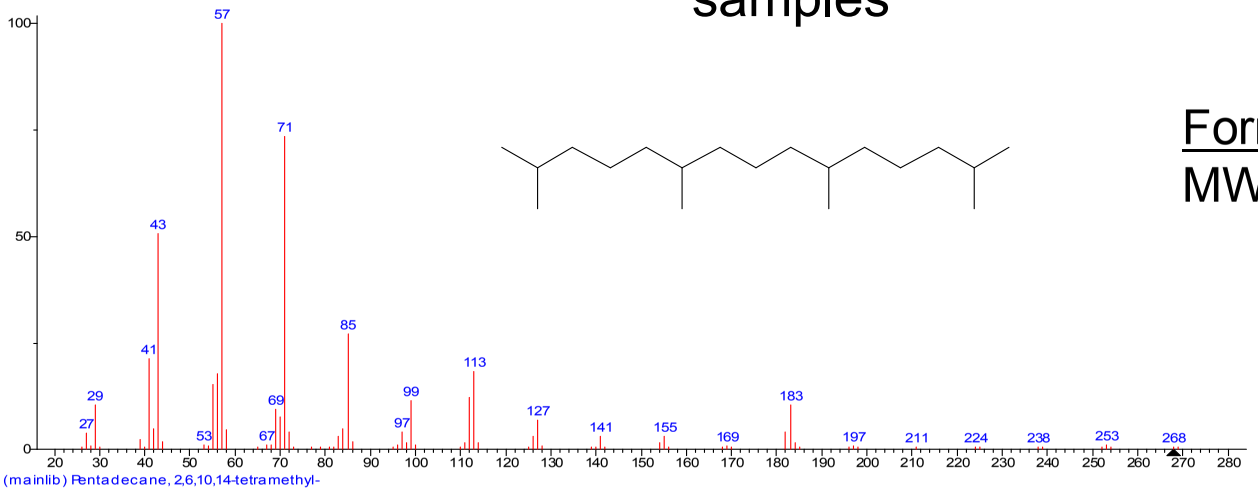

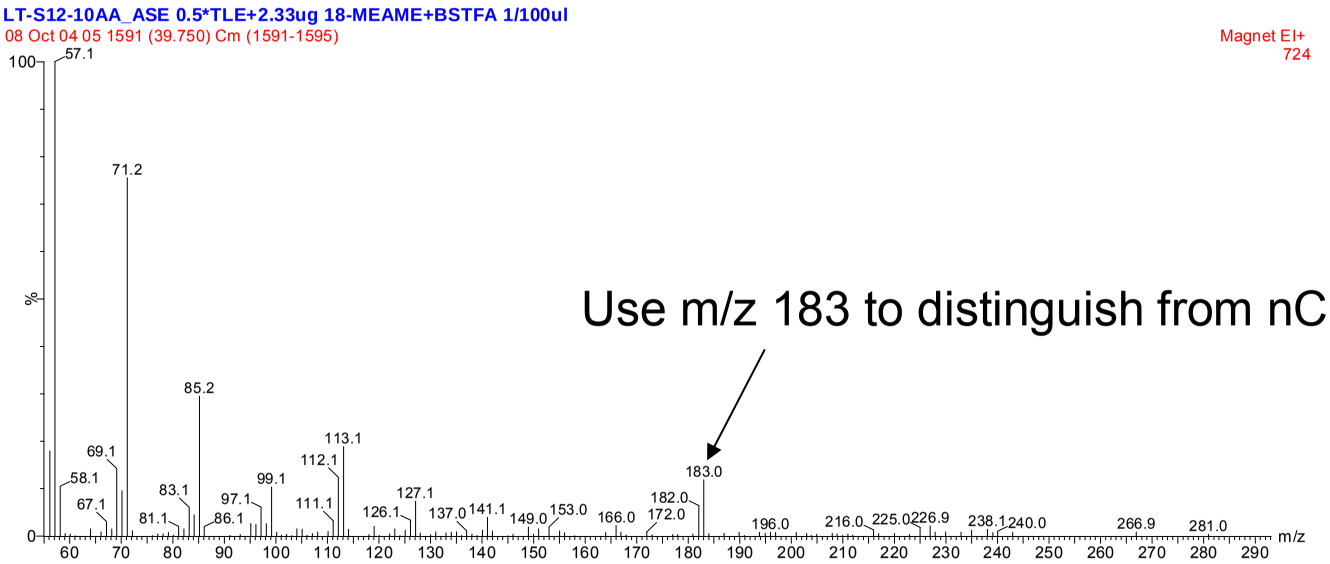

Formula: C19H40
MW = 268

Use m/z 183 to distinguish from nC17

Phytane (elutes just after nC18 on DB-5 MS column); NIST library + samples

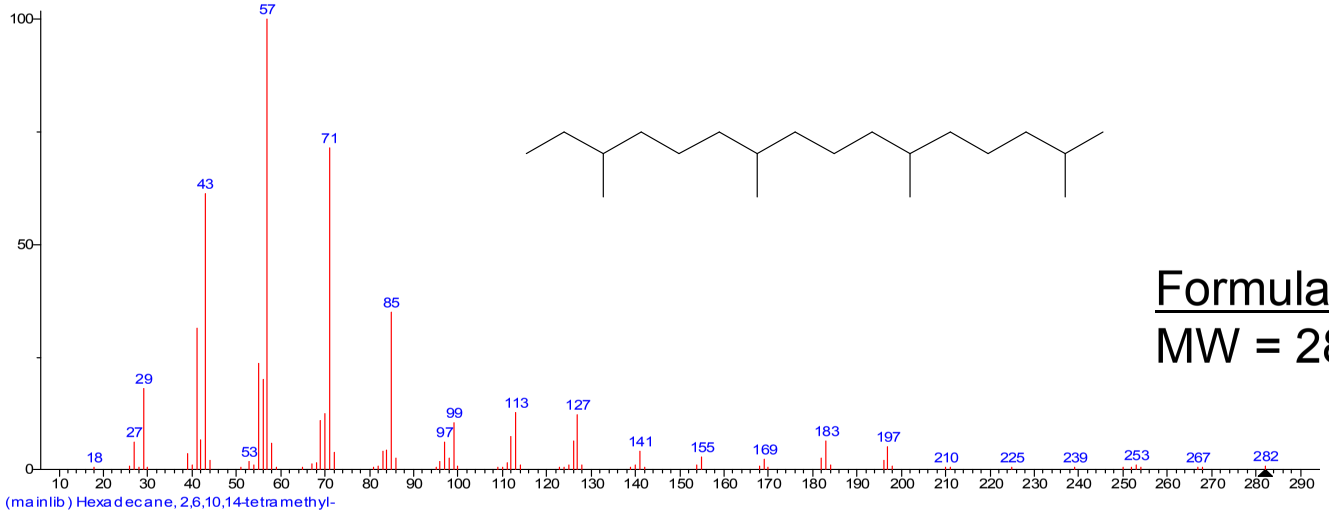

Formula: C20H42
MW = 282

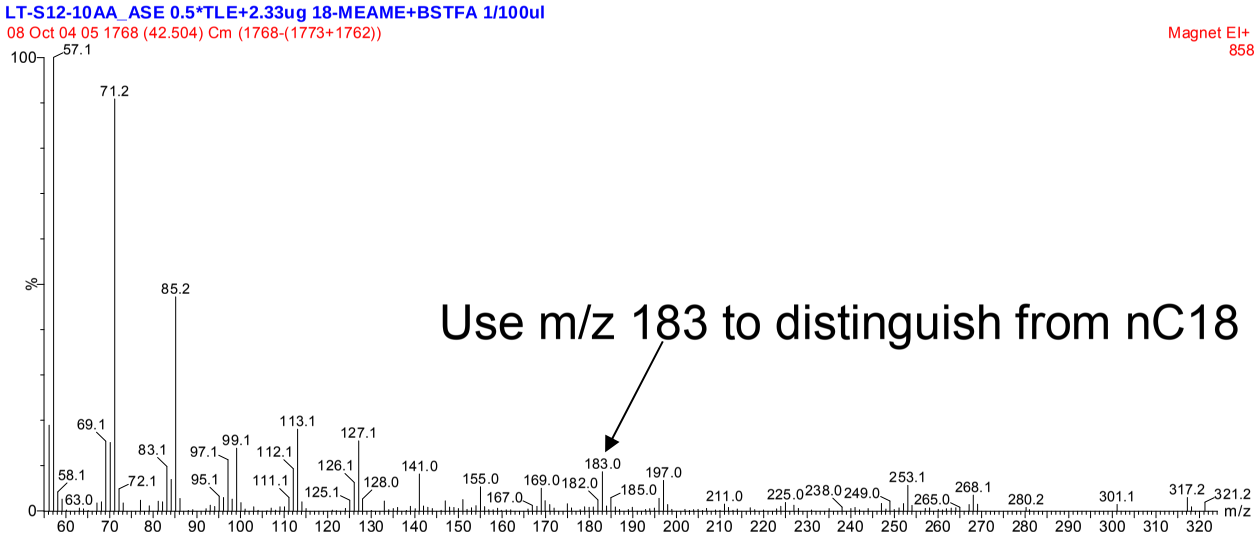

Use m/z 183 to distinguish from nC18

41: Squalene (all-trans, NIST library)

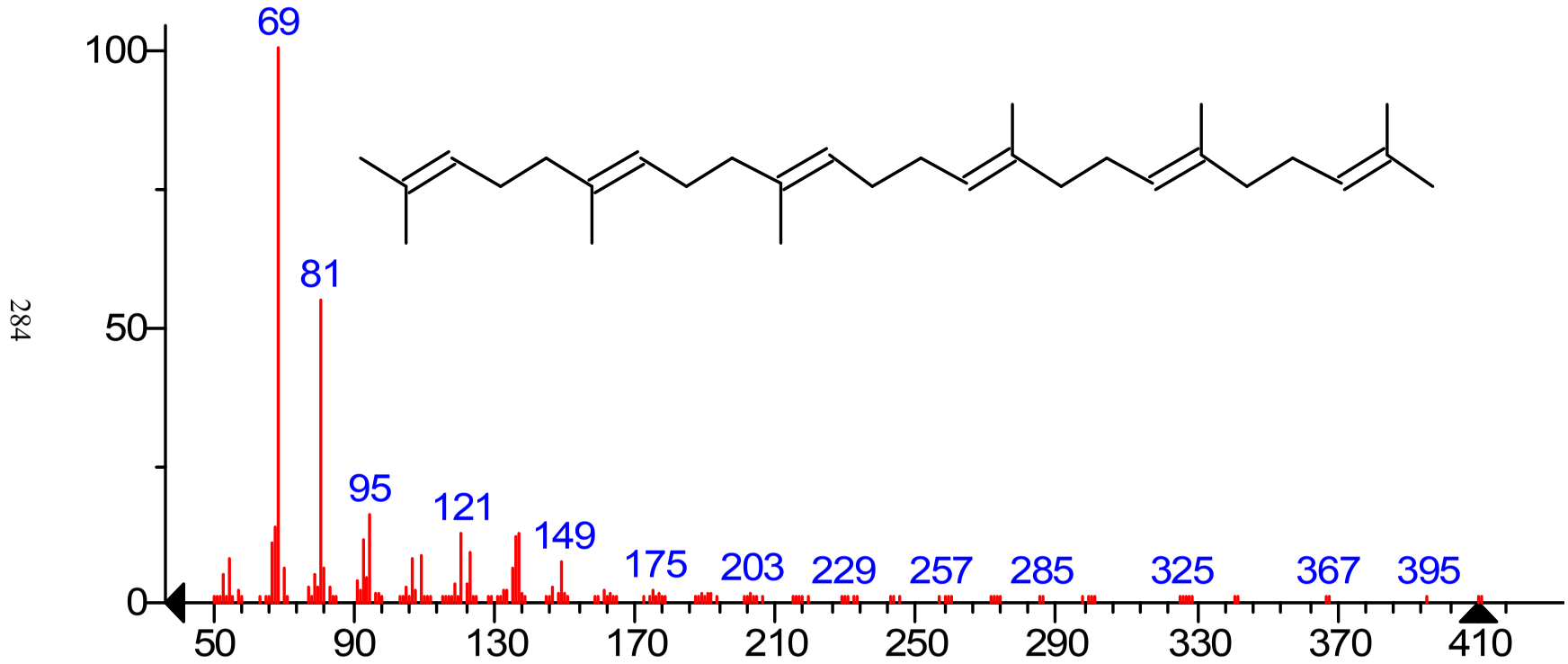

41: Normal squalene (NIST library)

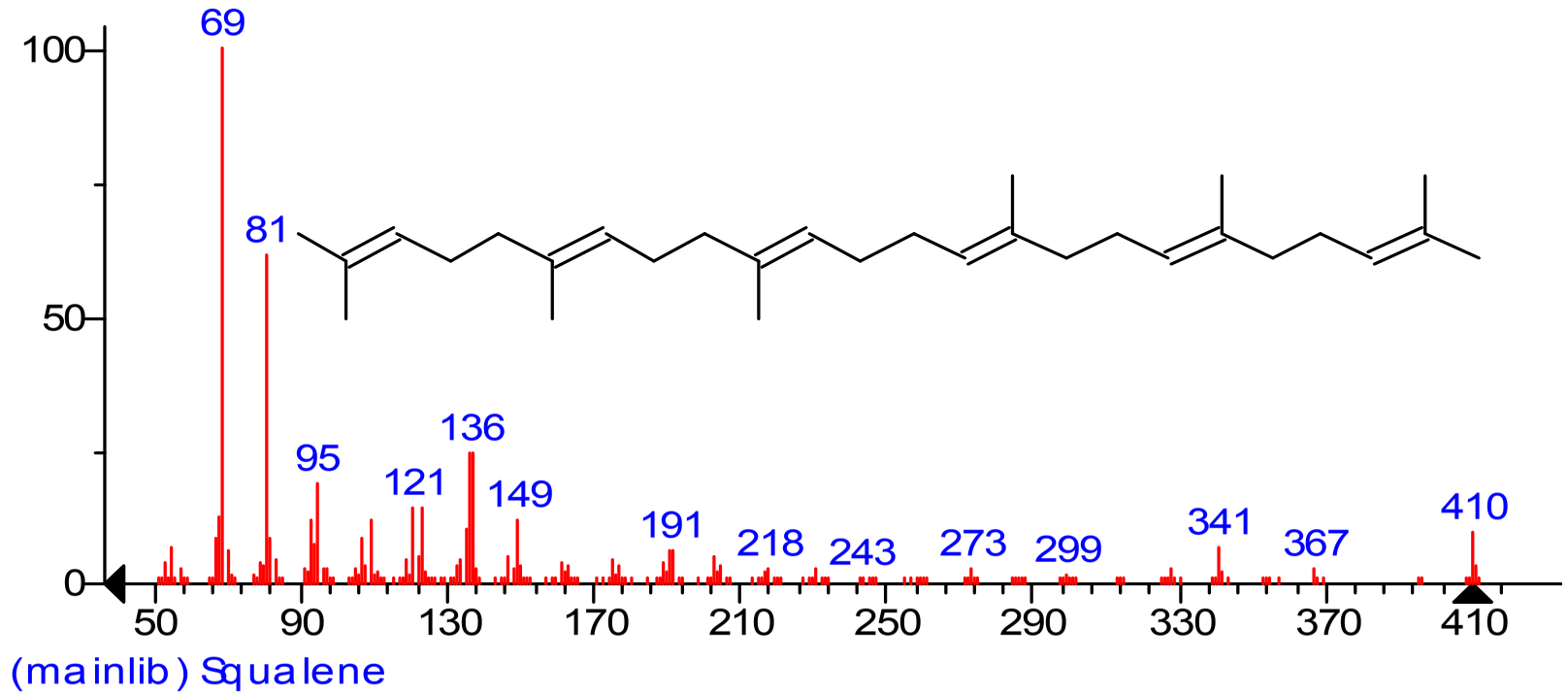

42: Dihydrosqualene (NIST library)

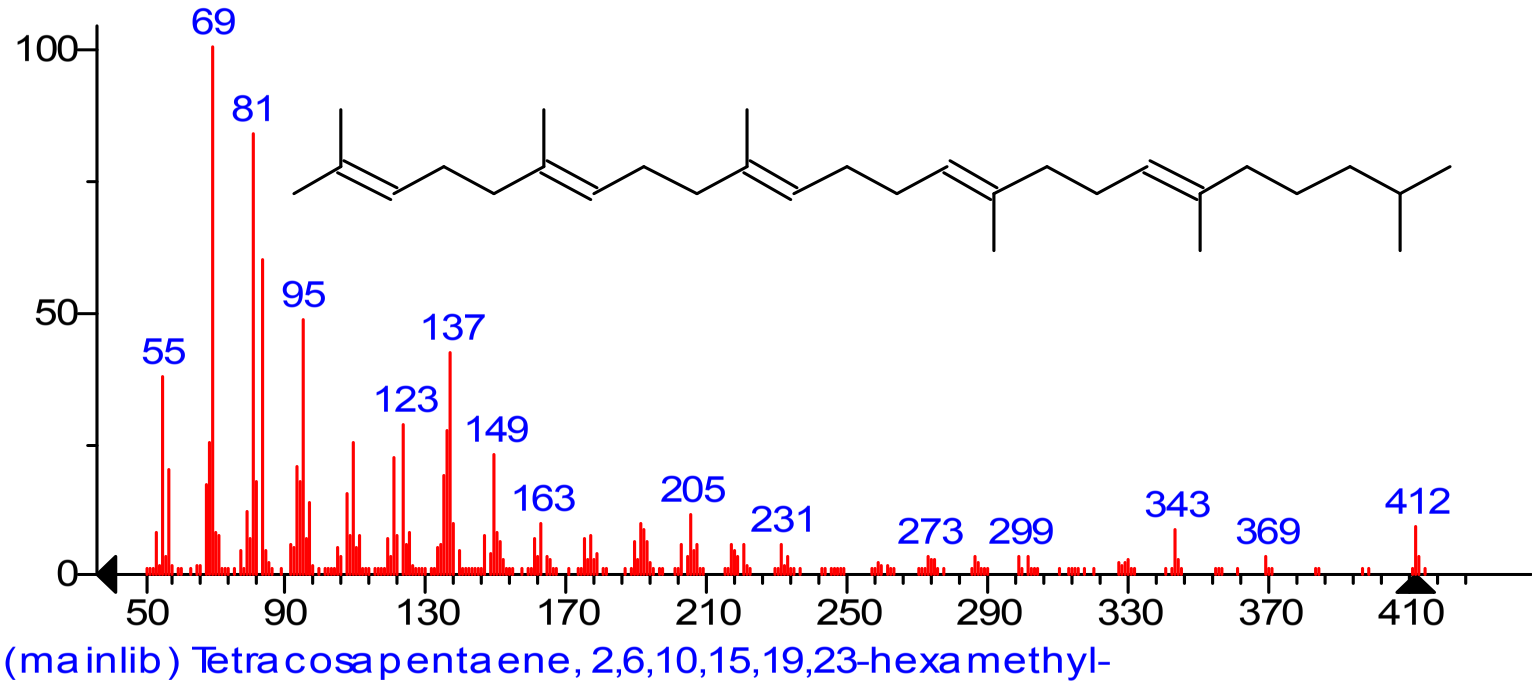

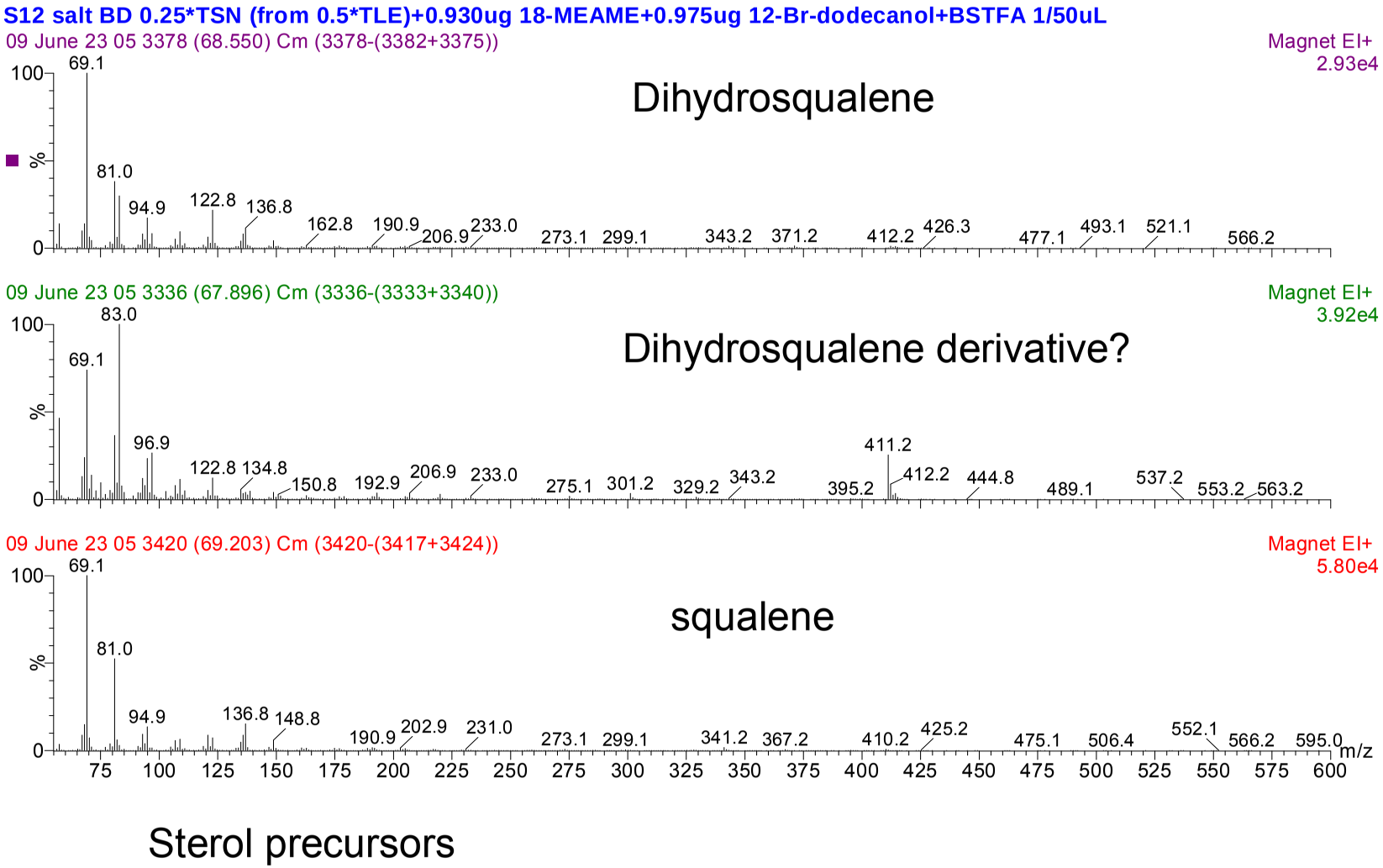

Sterol precursors

Hopanoids

Four 6C rings + one 5C ring

43: (22R)-17_(H), 21_(H)-homohopan-31-ol TMS (C_{31} hopanol): could be B,a or a,B

C31, 5 DBEs Sources: bacterial

C31 Δ0 hopanol (BB)

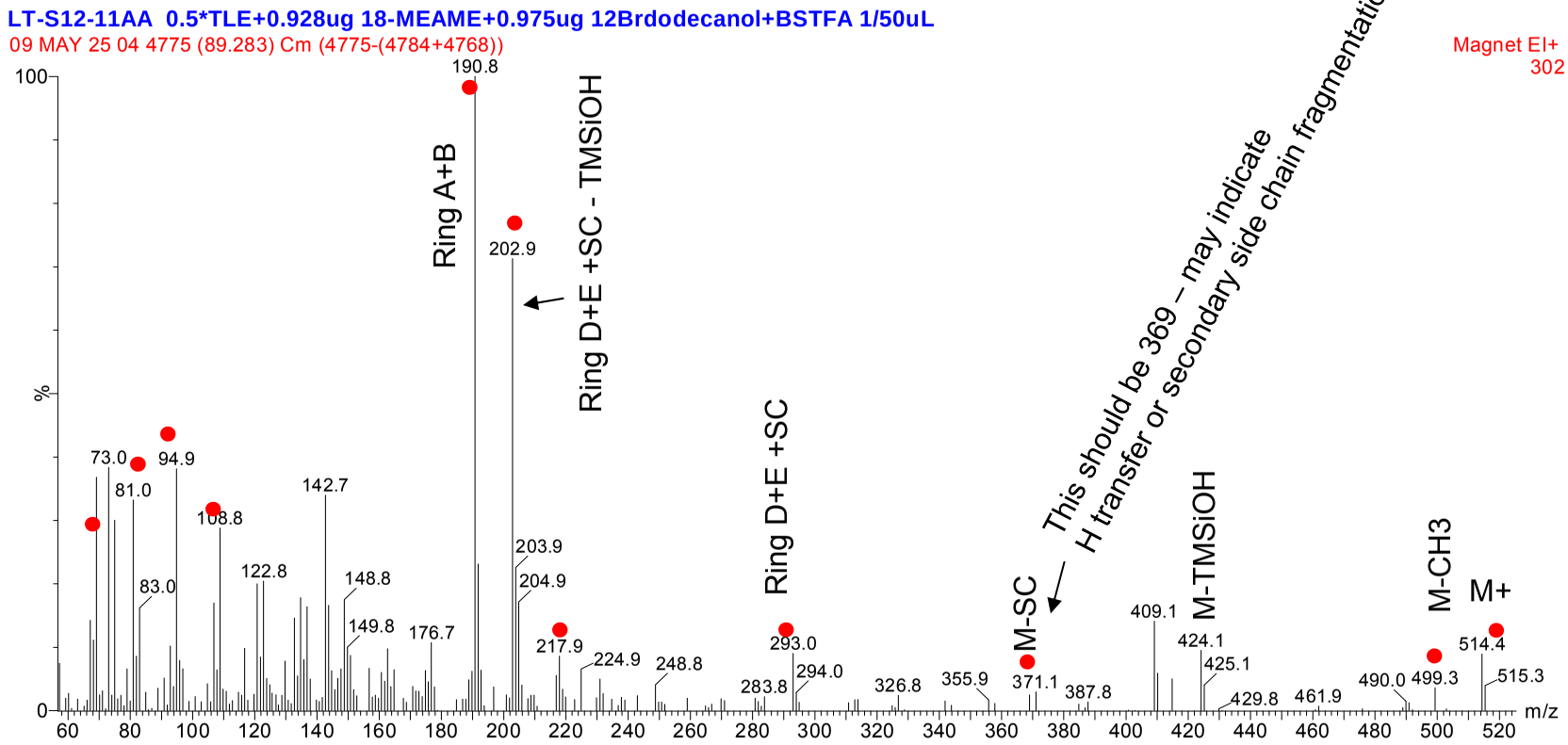

- Red dots indicate ions labeled in reference spectrum

Venkatesan *et al* (1990) *Organic Geochemistry* vol 16, nos 4-6, pp 1015-1024

MS id'd by comparison with C_{31} B,B hopanol

44: (22R)-17B(H), 21B(H)-homohopan-31-ol TMS (C_{31} hopanol), samples & reference below

C31, 5 DBEs Sources: bacterial

C31 Δ0 hopanol (BB)

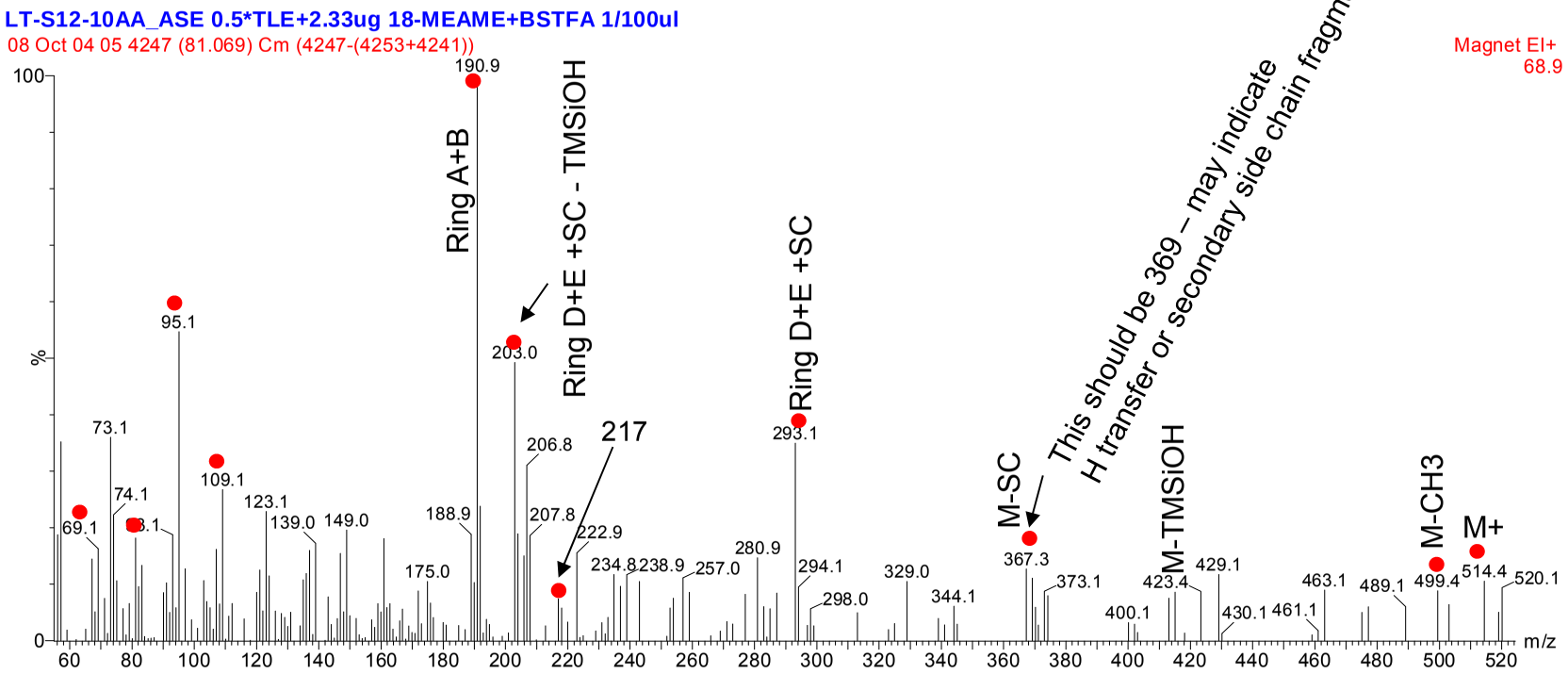

- Red dots indicate ions labeled in reference spectrum
  Venkatesan *et al* (1990) *Organic Geochemistry* vol 16, nos 4-6, pp 1015-1024
  MS id'd initially by Emmanuelle Grosjean, pers. comm.

45: (22R)-17B(H), 21B(H)-bishomohopan-32-ol TMS (C_{32} hopanol), samples & reference below

C32, 5 DBEs Sources: bacterial

C32 Δ0 hopanol (BB)

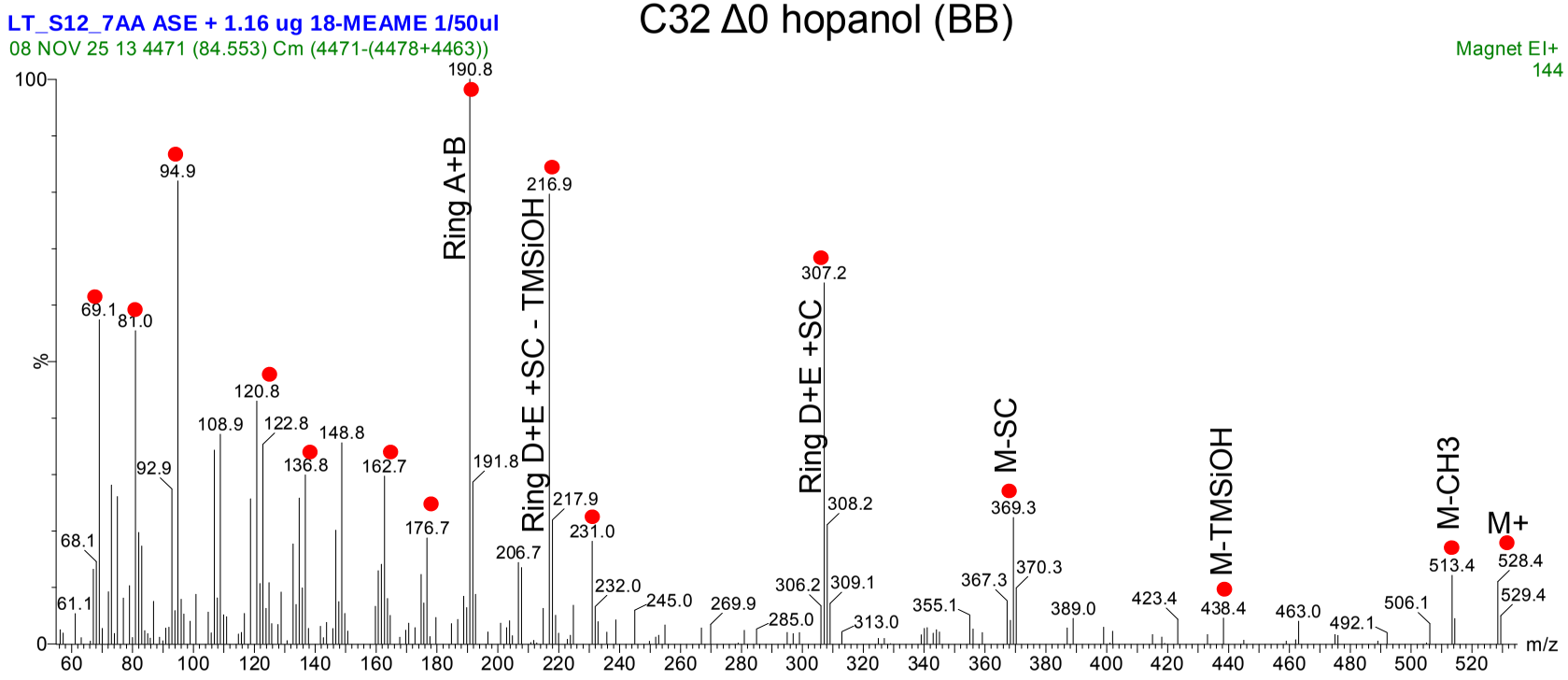

- Red dots indicate ions labeled in reference spectrum
  Venkatesan *et al* (1990) *Organic Geochemistry* vol 16, nos 4-6, pp 1015-1024
  MS id'd initially by Emmanuelle Grosjean, pers. comm.

46: (22R)-17B(H), 21B(H)-bishomohopan-32-oic acid TMS (C_{32} hopanoic acid), samples & reference below

C32, 5 DBEs Sources: bacterial

C32 Δ0 hopanoic acid (BB)

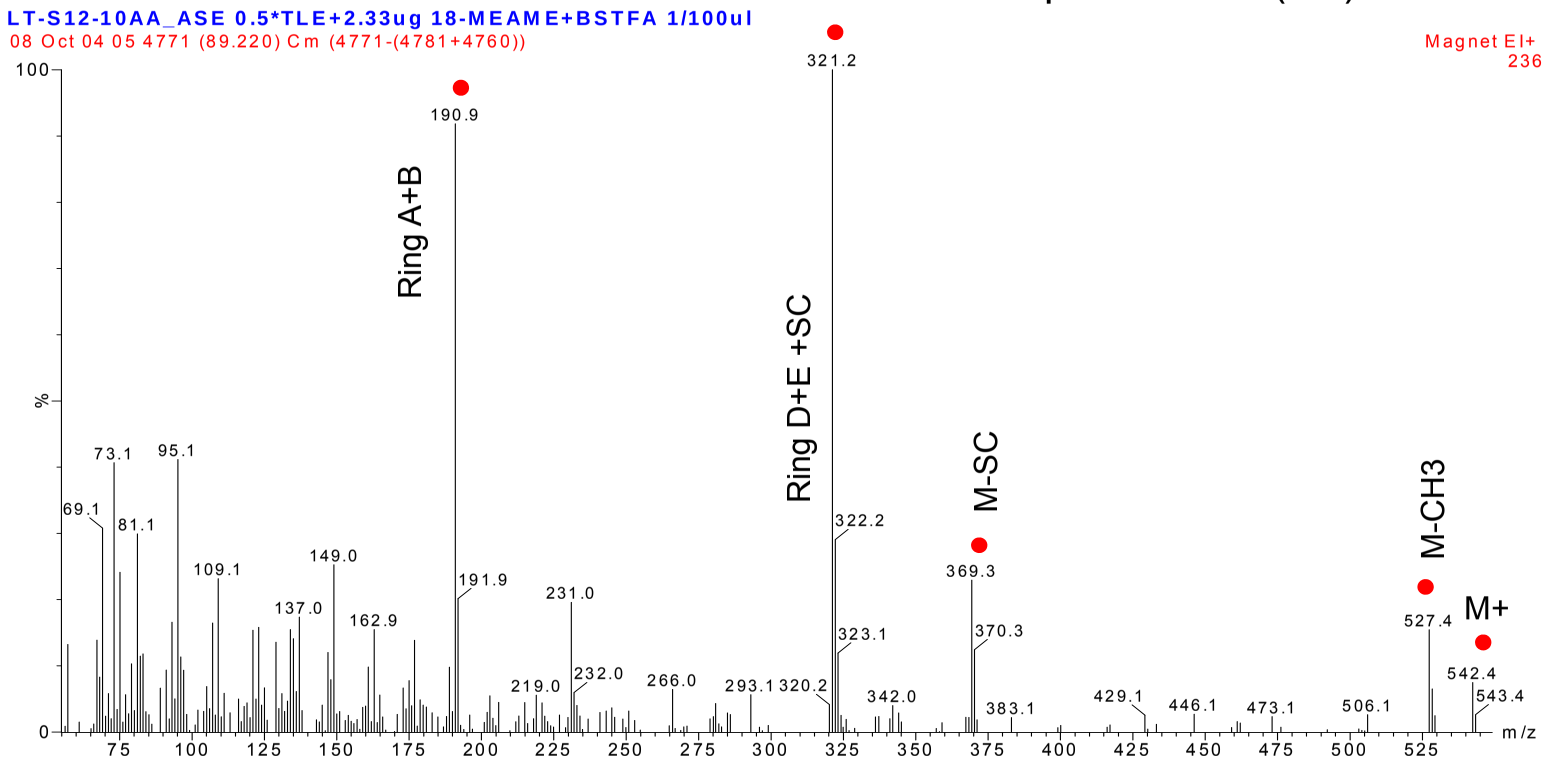

- Red dots indicate ions labeled in reference spectrum
  MS id'd by personal comm., Emmanuelle Grosjean. Compared to her sample spectra also (see binder); 321>191 indicates B,B acid vs C33 hopanol (if 191 ~ 321,may be B,a acid)

47: (22R)-17a(H), 21B(H)-trishomohopan-33-ol TMS (C_{33} hopanol), samples & reference below

C33, 5 DBEs

C33 Δ0 hopanol (aB)

Sources: bacterial

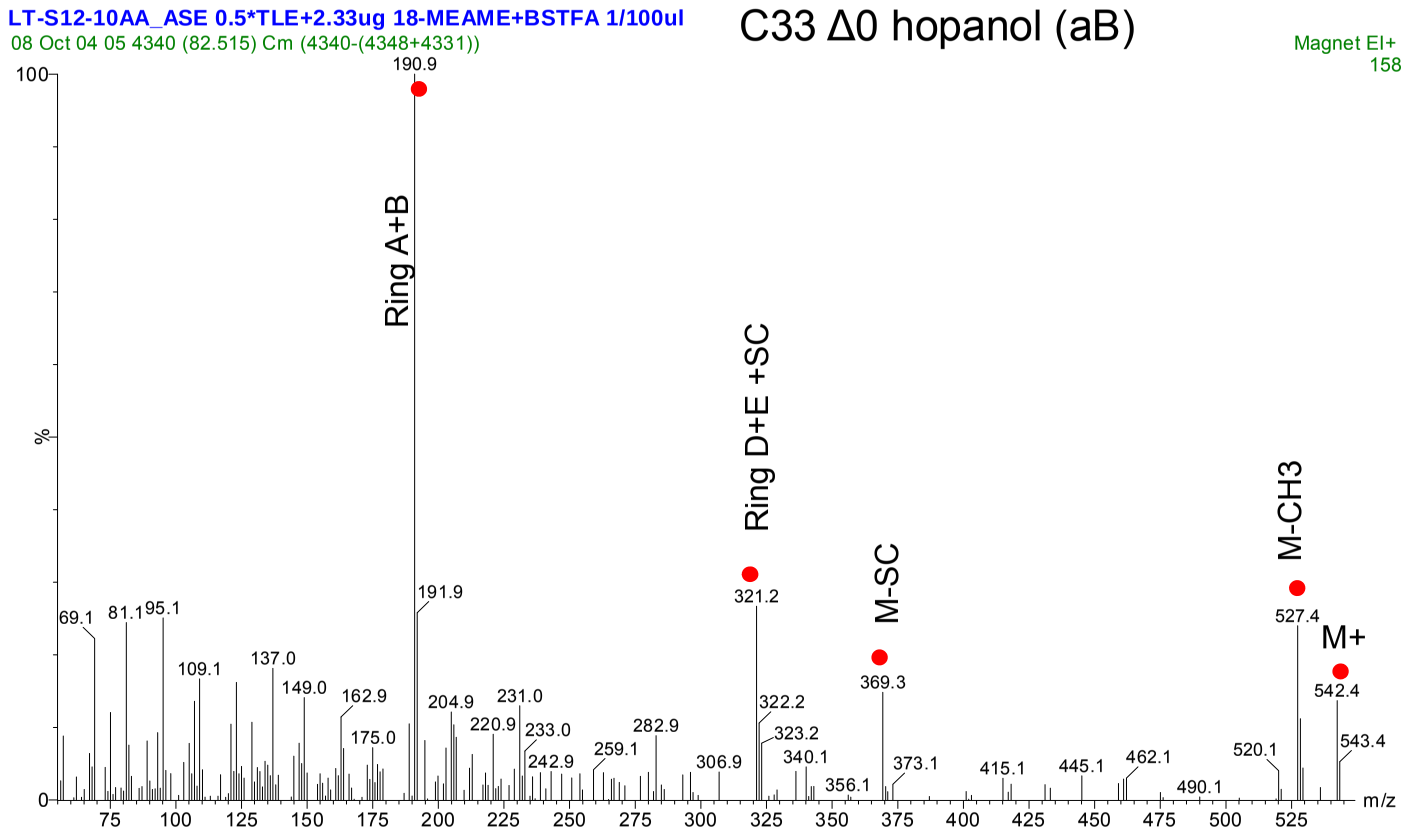

- Red dots indicate ions labeled in reference spectrum
  MS id'd by personal comm., Emmanuelle Grosjean. Compared to spectral info (see binder); 321<191 indicates a,B hopanol

48: (22R)-17B(H), 21a(H)-trishomohopan-33-ol TMS (C_{33} hopanol), samples & reference below

C33, 5 DBEs

C33 Δ0 hopanol (Ba)

Sources: bacterial

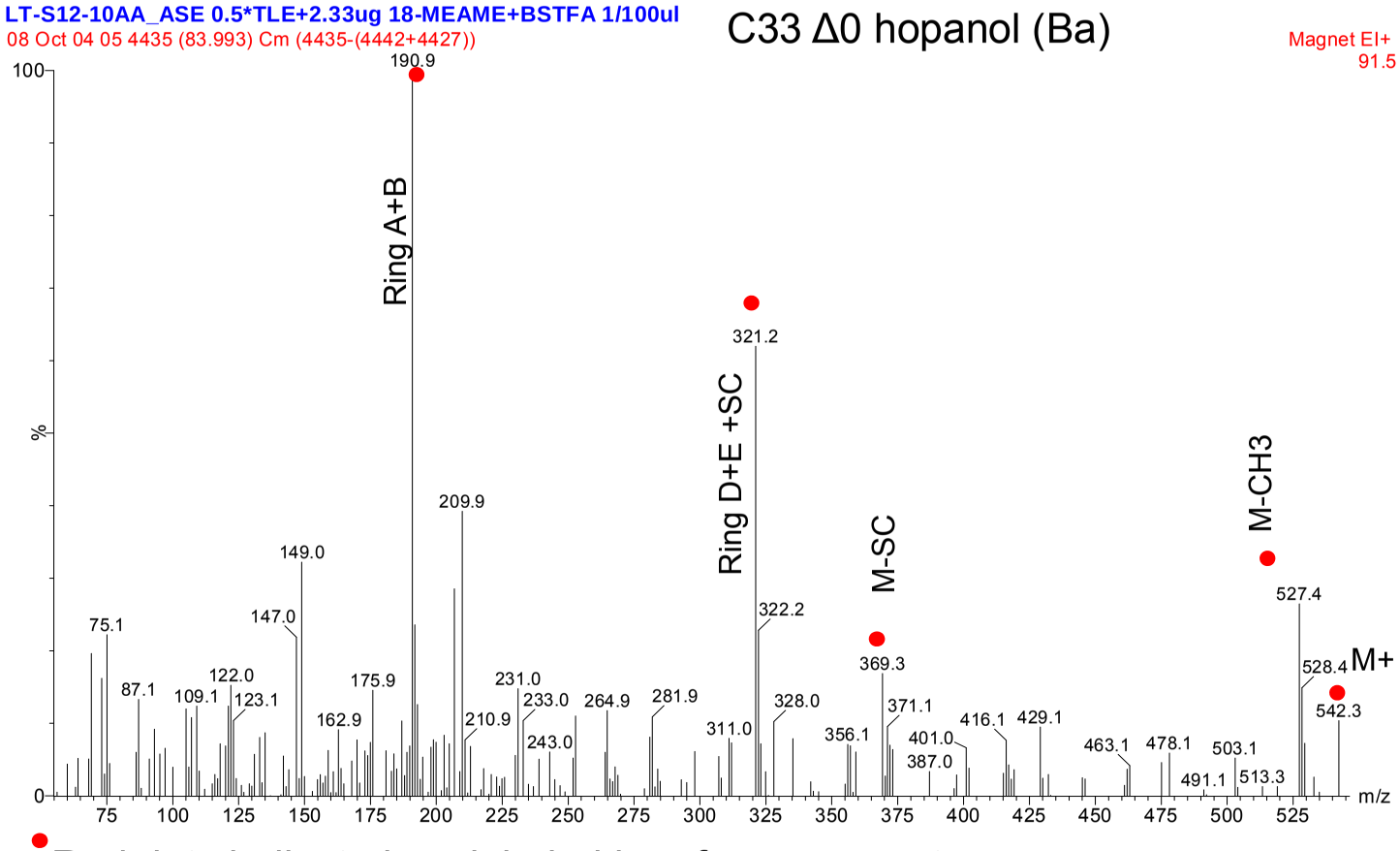

Red dots indicate ions labeled in reference spectrum

MS id'd by personal comm., Emmanuelle Grosjean. Compared to spectral info (see binder); 321 ~ 191 indicates B,a hopanol

49: 30-nor-hopane (a,B) (C_{29} hopane, a,B), samples & reference below

Source: degradation (biotic or abiotic) of functionalized hopanoids

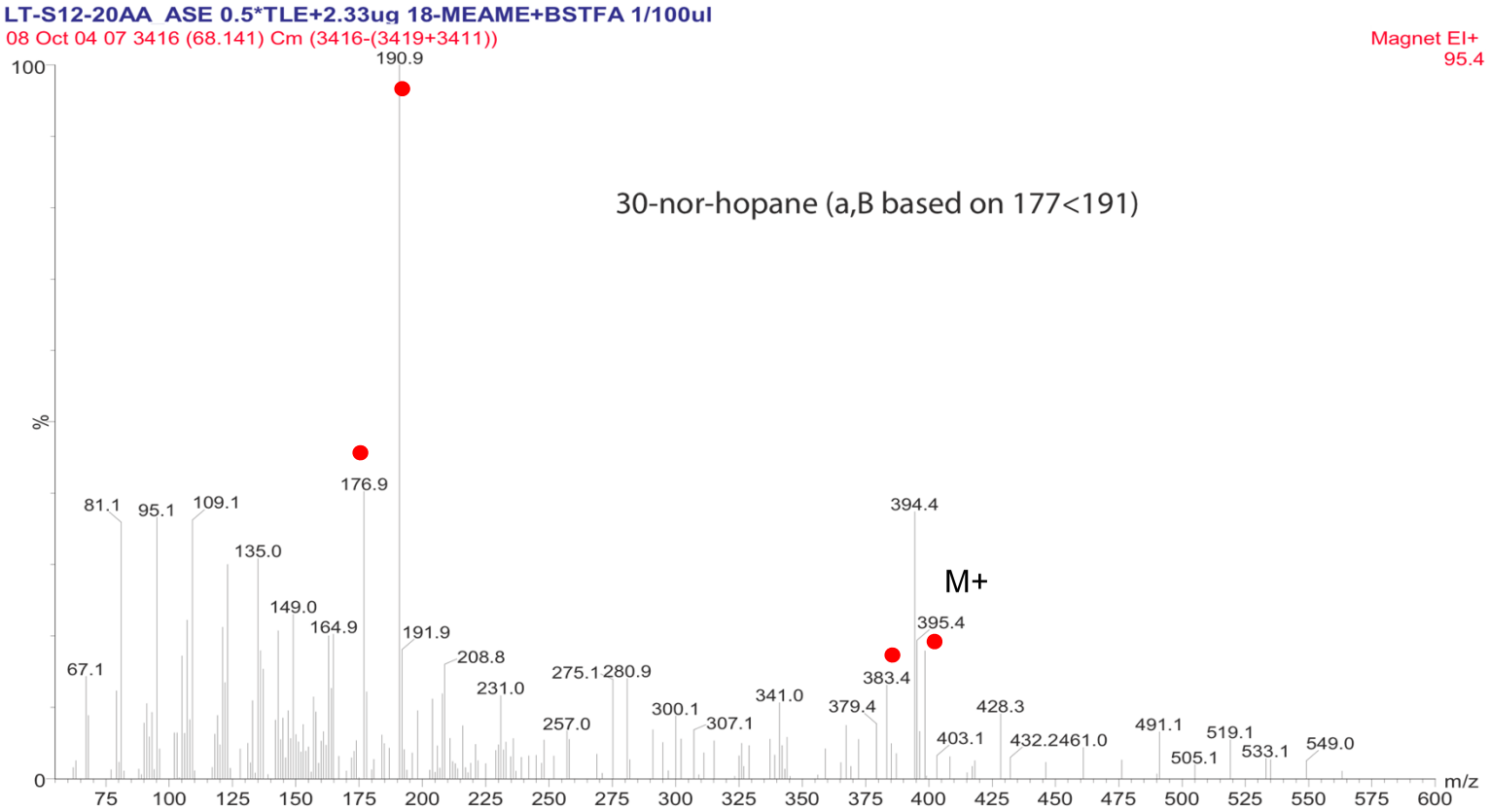

- Red dots indicate ions labeled in reference spectrum
  MS id'd by personal comm., Emmanuelle Grosjean. Compared to spectral info (see binder)
  also see Smittenberg *et al* (2004) *Palaeogeography, Palaeoclimatology, Palaeoecology* vol 202, pp 331-351

50: 30-nor-moretane (B,a) (C_{29} hopane B,a), samples & reference below

Source: degradation (biotic or abiotic) of functionalized hopanoids

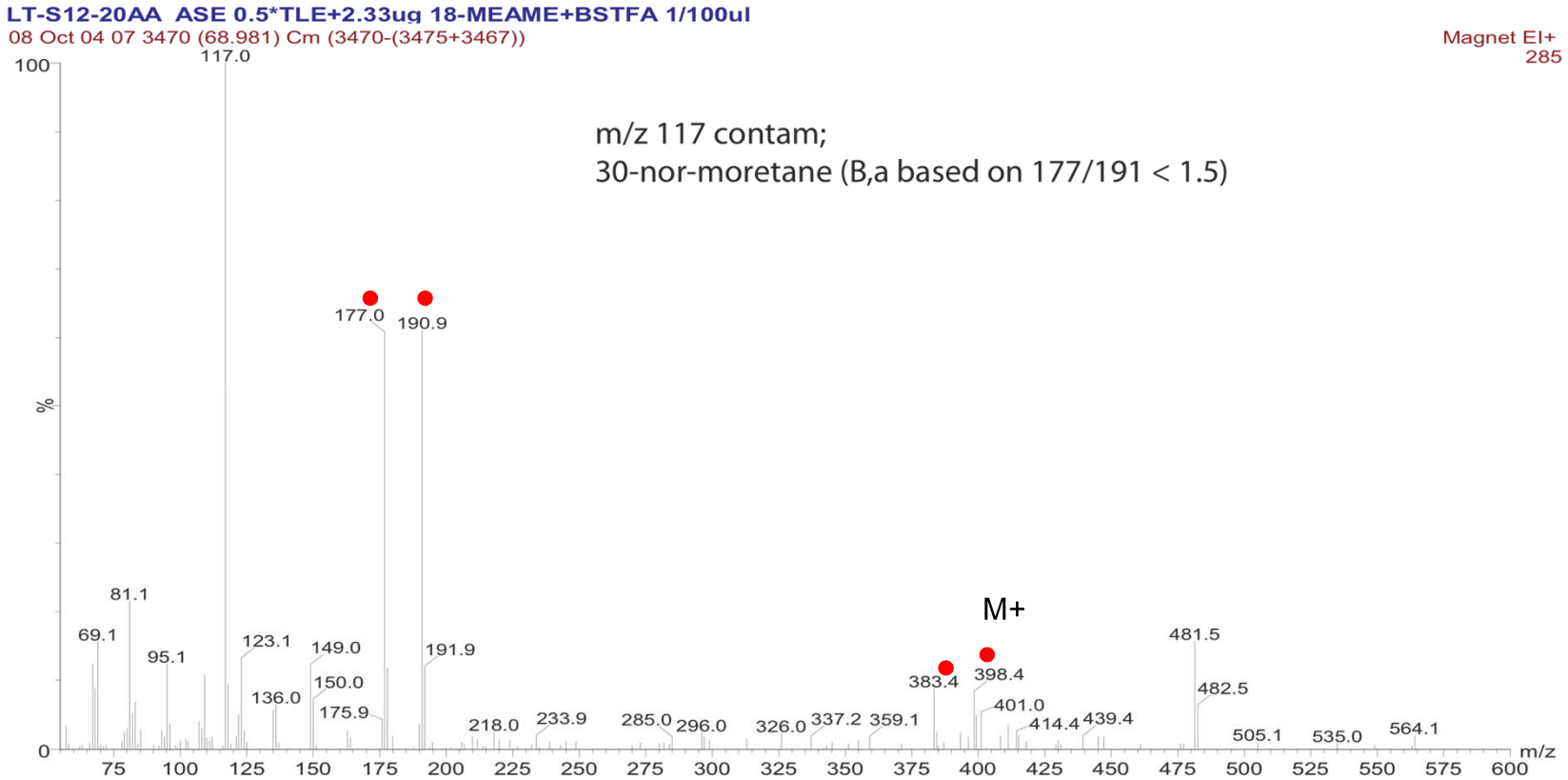

- Red dots indicate ions labeled in reference spectrum

MS id'd by personal comm., Emmanuelle Grosjean. Compared to spectral info (see binder) also see Smittenberg *et al* (2004) *Palaeogeography, Palaeoclimatology, Palaeoecology* vol 202, pp 331-351

51: 30-nor-hopane (BB) (C_{29} hopane B,B), samples & reference below

Source: degradation (biotic or abiotic) of functionalized hopanoids

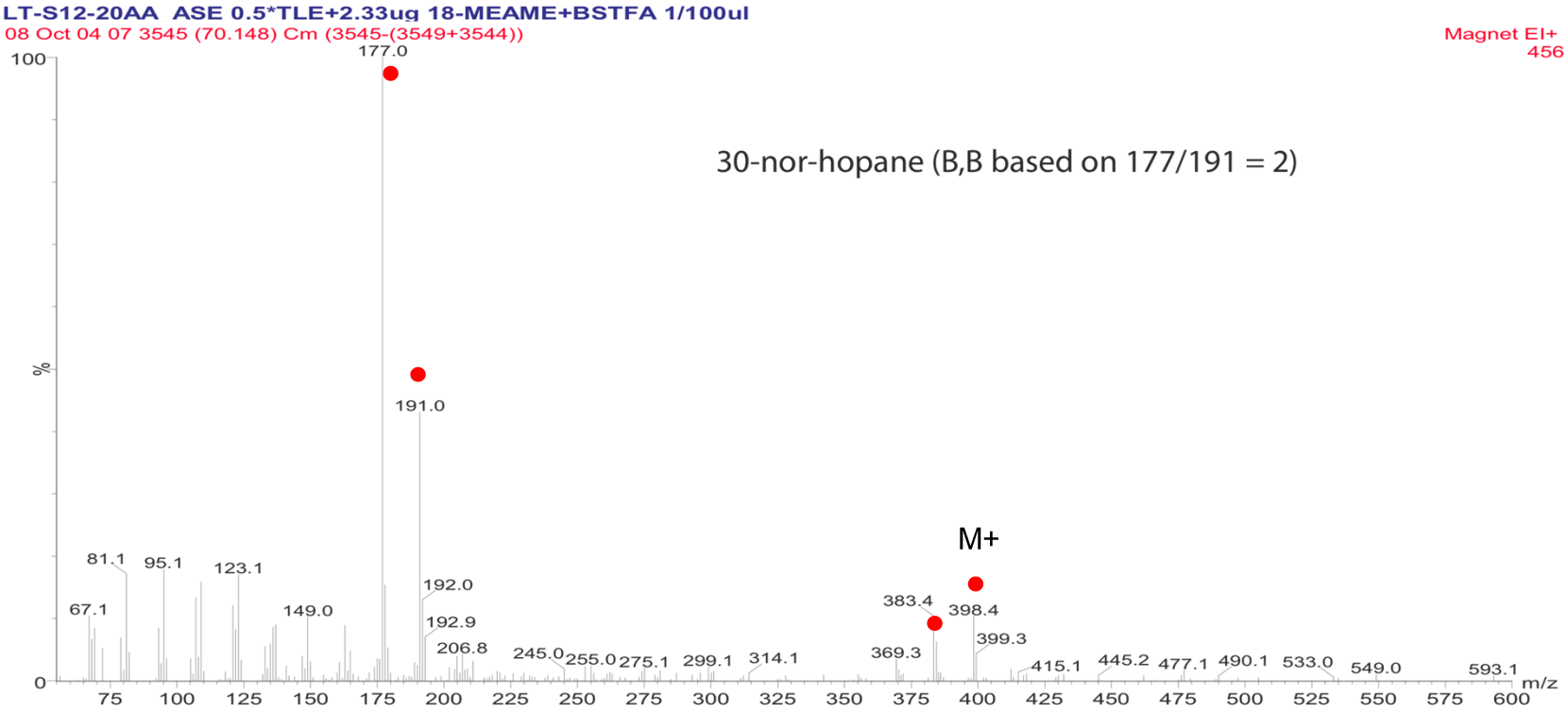

- Red dots indicate ions labeled in reference spectrum
  MS id'd by personal comm., Emmanuelle Grosjean. Compared to spectral info (see binder)
  also see Smittenberg *et al* (2004) *Palaeogeography, Palaeoclimatology, Palaeoecology* vol 202, pp 331-351

52: C_{30} hopane (a,B) , samples & reference below

Source: degradation (biotic or abiotic) of functionalized hopanoids

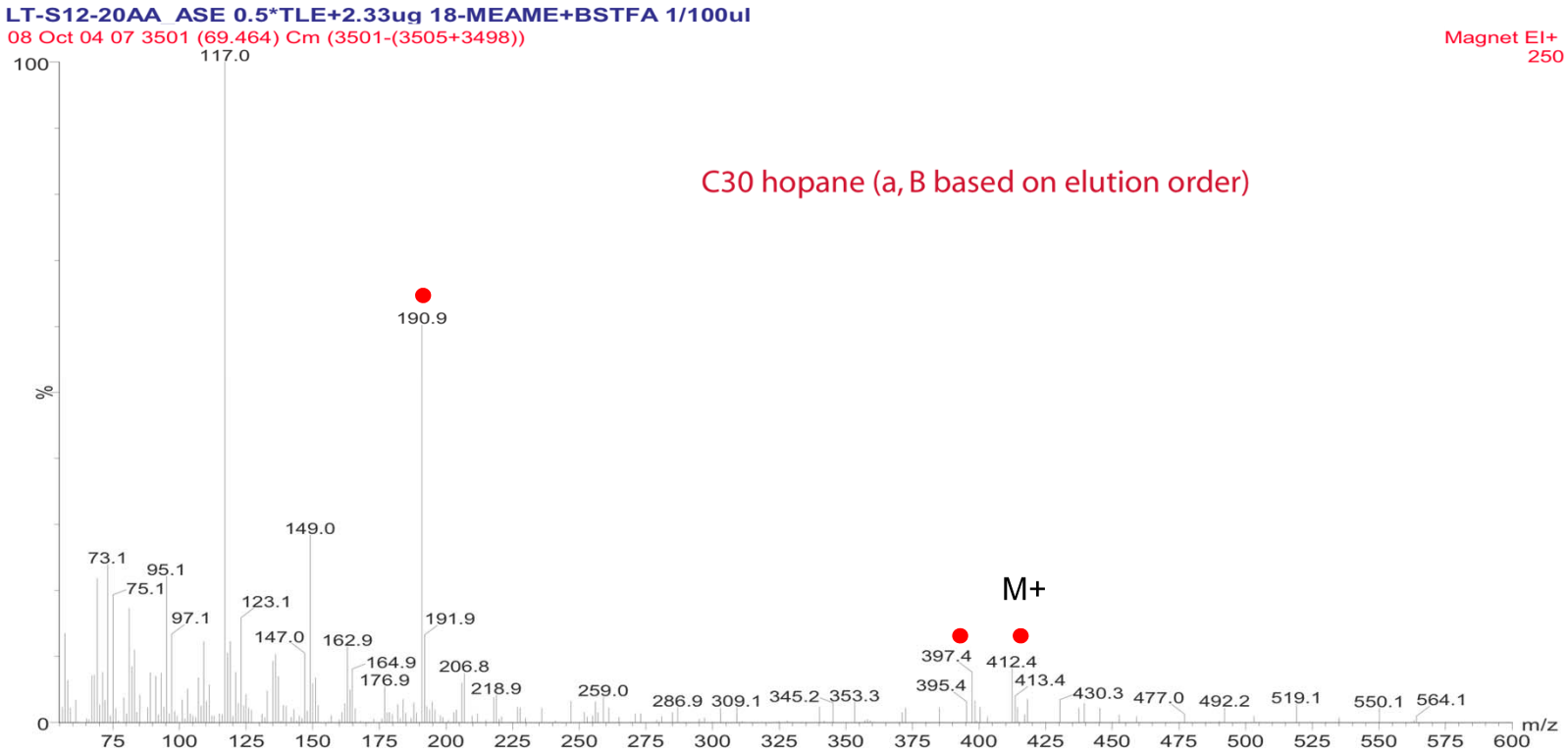

- Red dots indicate ions labeled in reference spectrum
  MS id'd by personal comm., Emmanuelle Grosjean. Compared to spectral info (see binder)
  also see Smittenberg *et al* (2004) *Palaeogeography, Palaeoclimatology, Palaeoecology* vol 202, pp 331-351

53: C_{30} hopane (B,a) , samples & reference below

Source: degradation (biotic or abiotic) of functionalized hopanoids

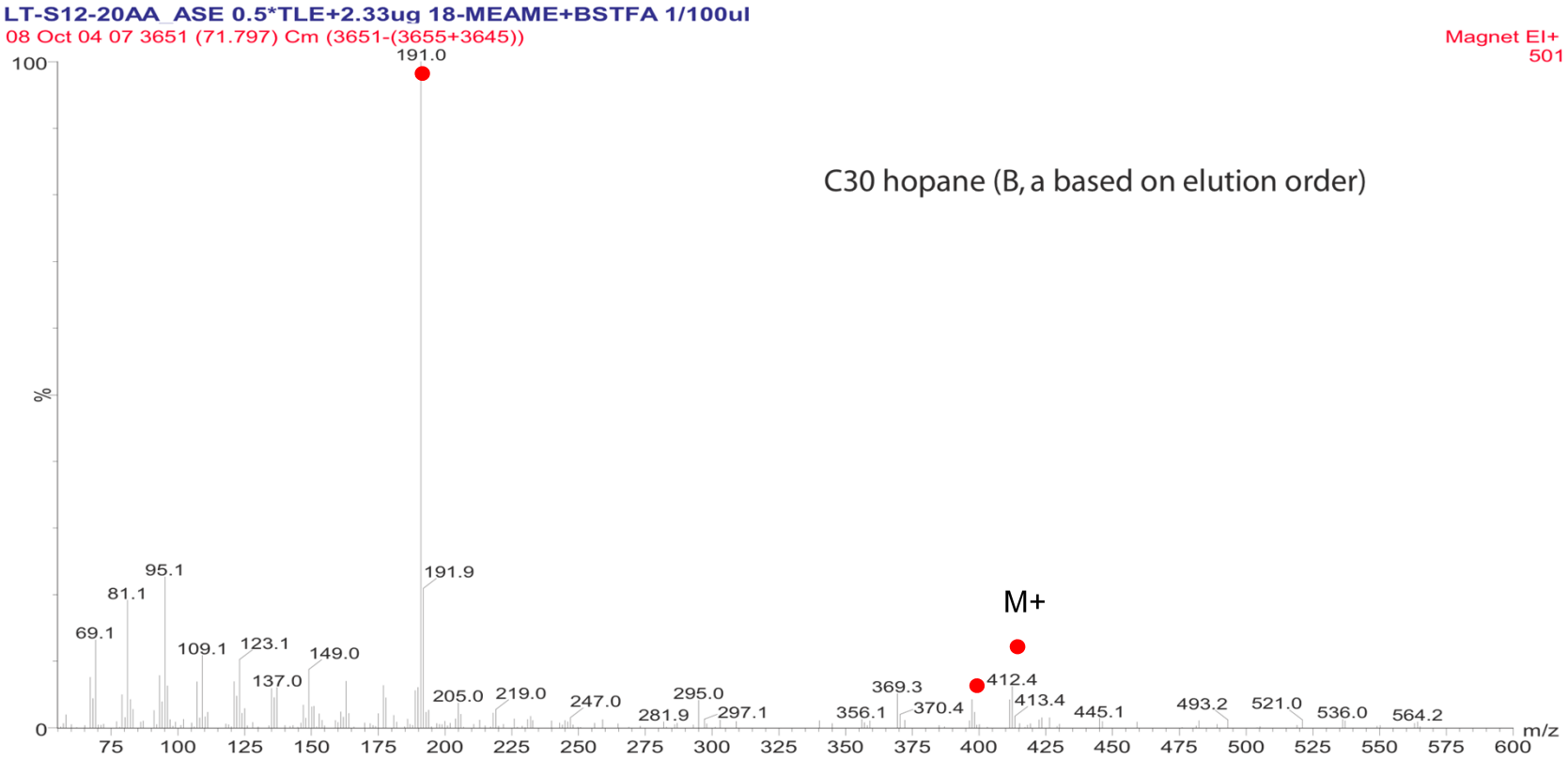

- Red dots indicate ions labeled in reference spectrum
  MS id'd by personal comm., Emmanuelle Grosjean. Compared to spectral info (see binder)
  also see Smittenberg *et al* (2004) *Palaeogeography, Palaeoclimatology, Palaeoecology* vol 202, pp 331-351

54: C_{30} hopane (B,B) , samples & reference below

Source: degradation (biotic or abiotic) of functionalized hopanoids

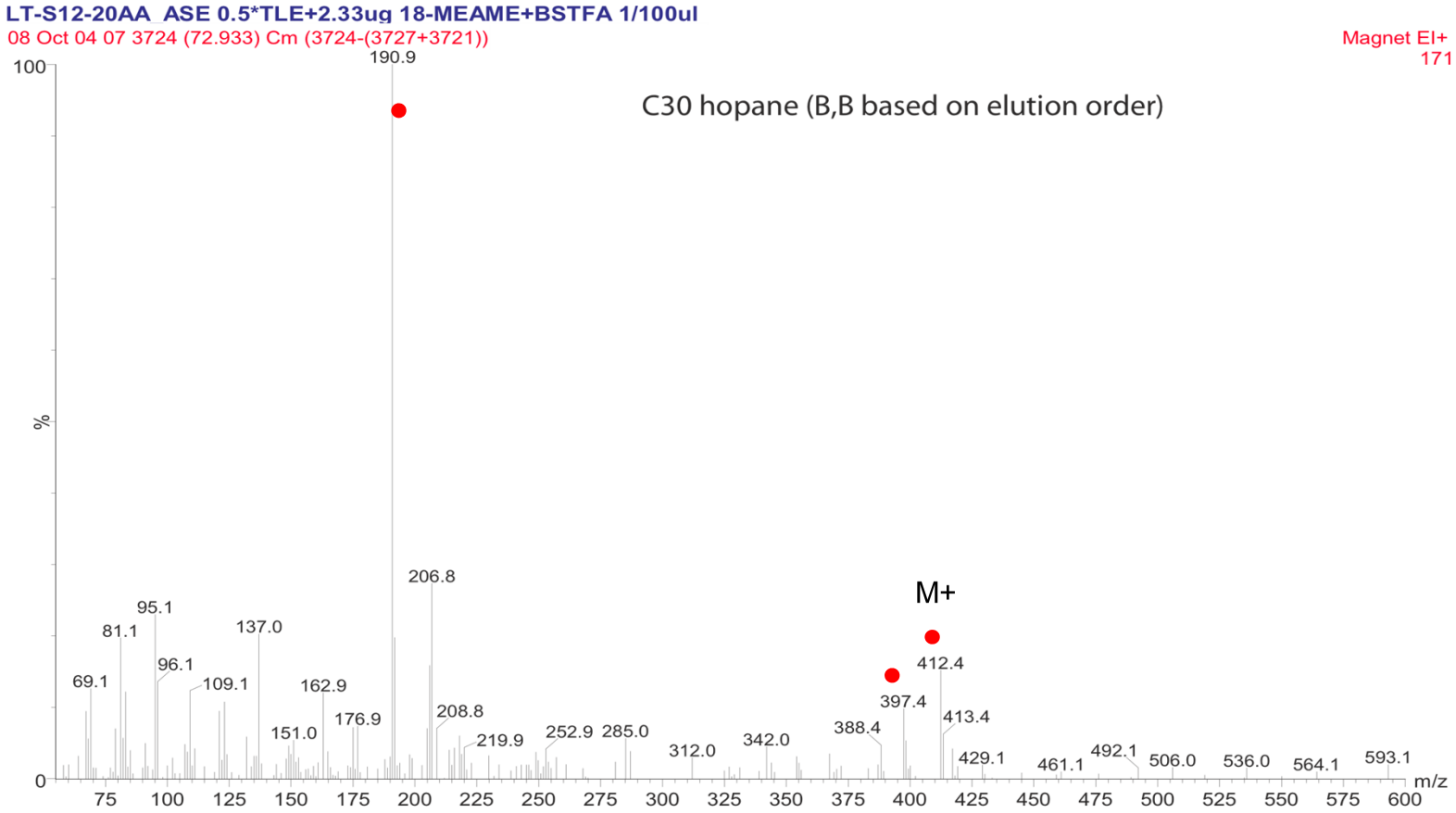

- Red dots indicate ions labeled in reference spectrum

MS id'd by personal comm., Emmanuelle Grosjean. Compared to spectral info (see binder) also see Smittenberg *et al* (2004) *Palaeogeography, Palaeoclimatology, Palaeoecology* vol 202, pp 331-351

55: C_{31} hopane (a,B) , samples & reference below

Source: degradation (biotic or abiotic) of functionalized hopanoids

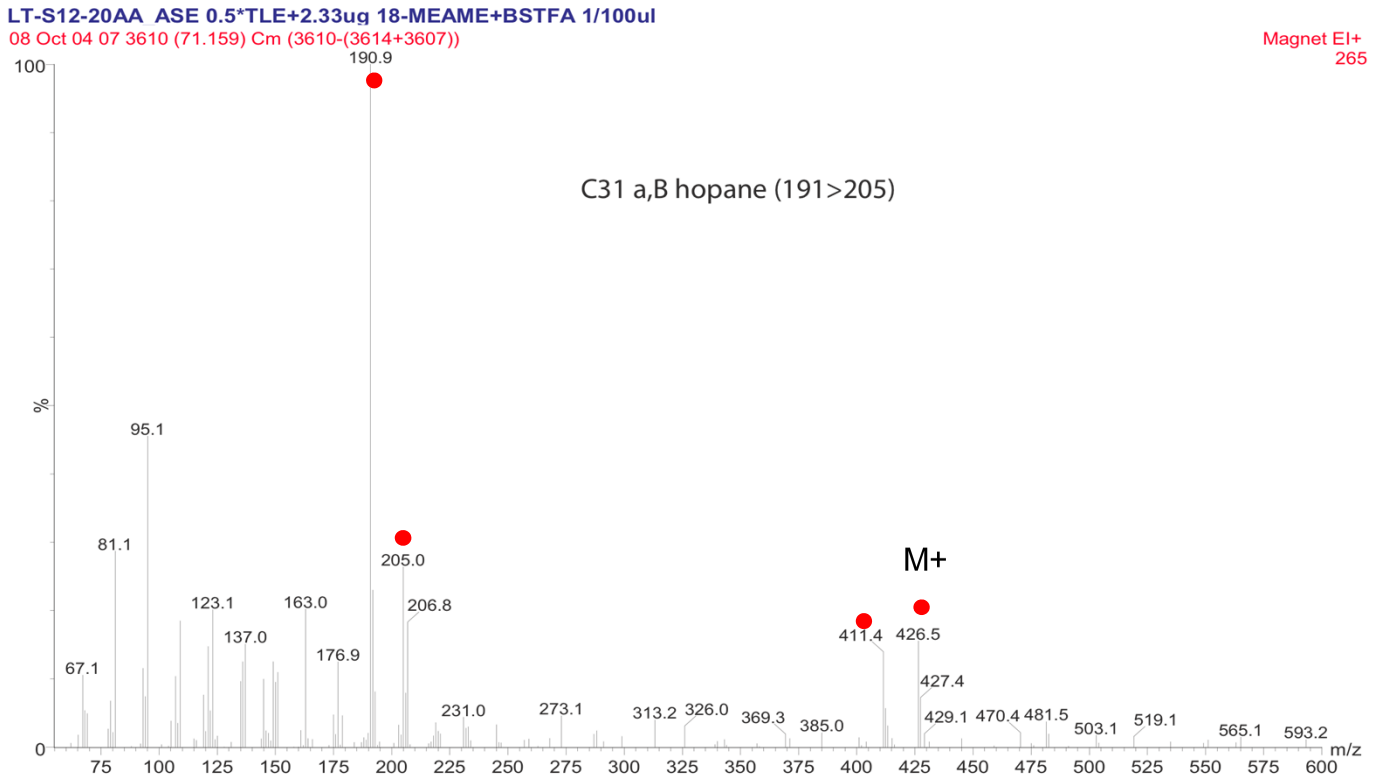

- Red dots indicate ions labeled in reference spectrum
  MS id'd by personal comm., Emmanuelle Grosjean. Compared to spectral info (see binder)
  also see Smittenberg *et al* (2004) *Palaeogeography, Palaeoclimatology, Palaeoecology* vol 202, pp 331-351

56: C_{31} hopane (B,a) , samples & reference below

Source: degradation (biotic or abiotic) of functionalized hopanoids

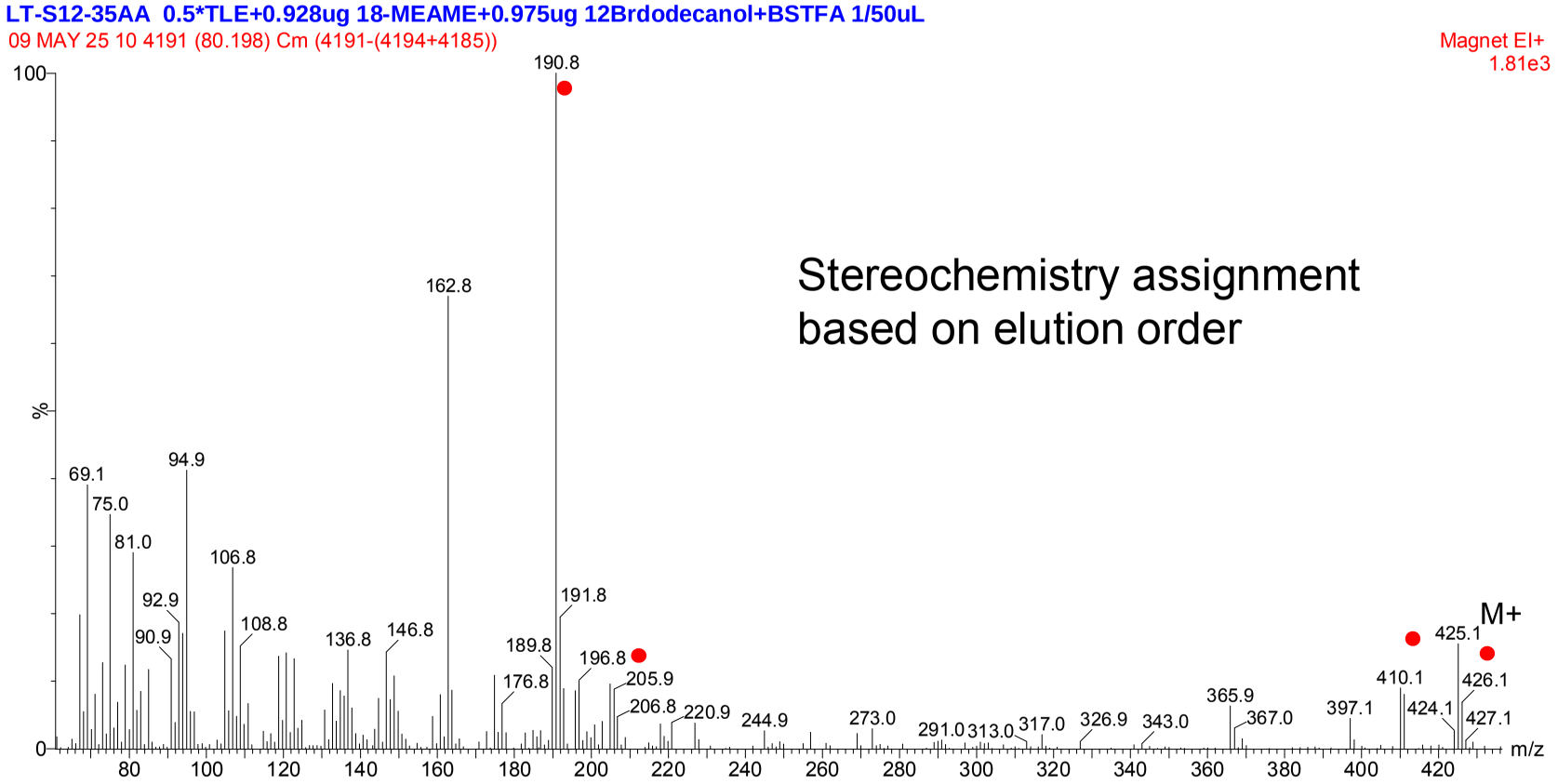

Stereochemistry assignment based on elution order

- Red dots indicate ions labeled in reference spectrum

MS id'd by personal comm., Emmanuelle Grosjean. Compared to spectral info (see binder) also see Smittenberg *et al* (2004) *Palaeogeography, Palaeoclimatology, Palaeoecology* vol 202, pp 331-351

57: C_{31} hopane (B,B) , samples & reference below

Source: degradation (biotic or abiotic) of functionalized hopanoids

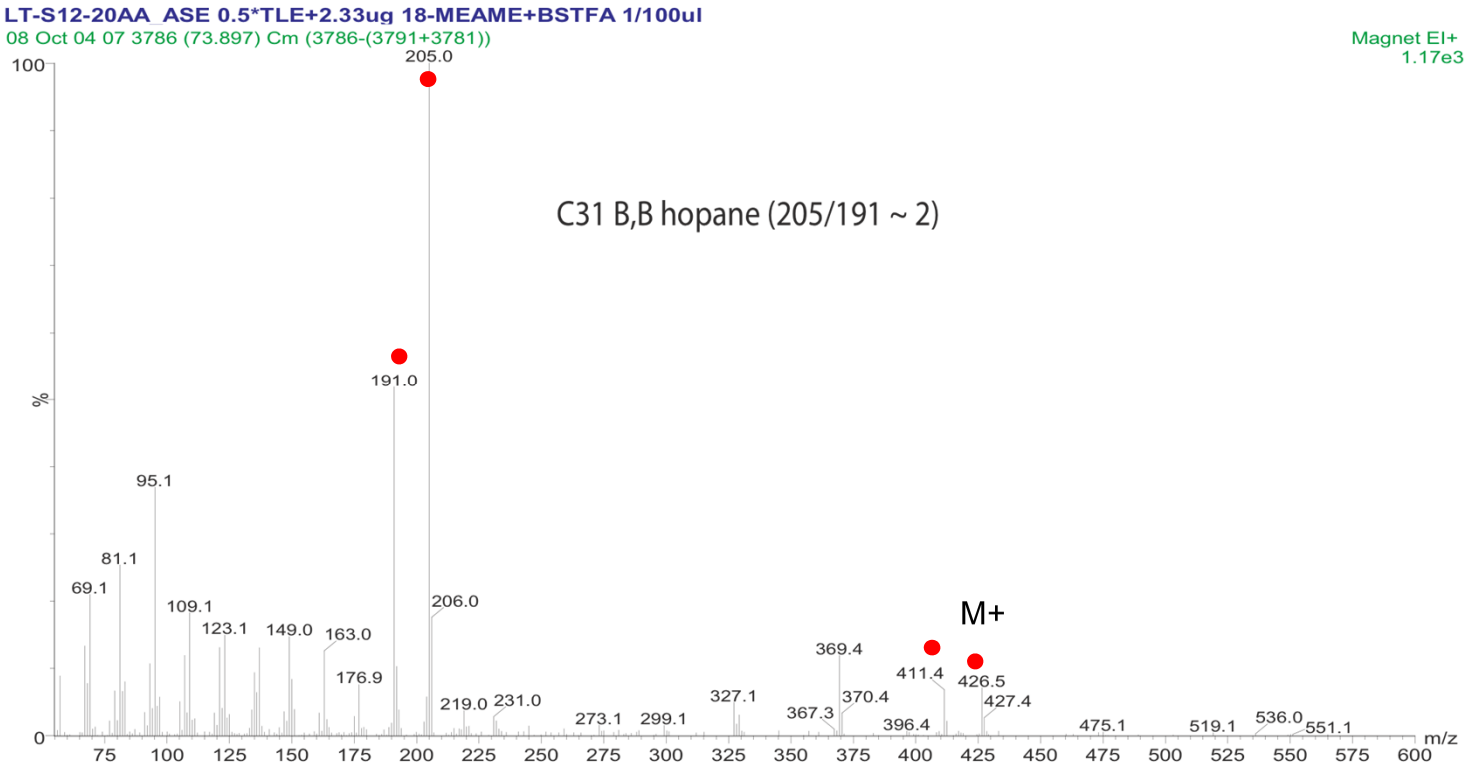

- Red dots indicate ions labeled in reference spectrum
  MS id'd by personal comm., Emmanuelle Grosjean. Compared to spectral info (see binder)
  also see Smittenberg *et al* (2004) *Palaeogeography, Palaeoclimatology, Palaeoecology*
  vol 202, pp 331-351

58: Diploptene (samples)

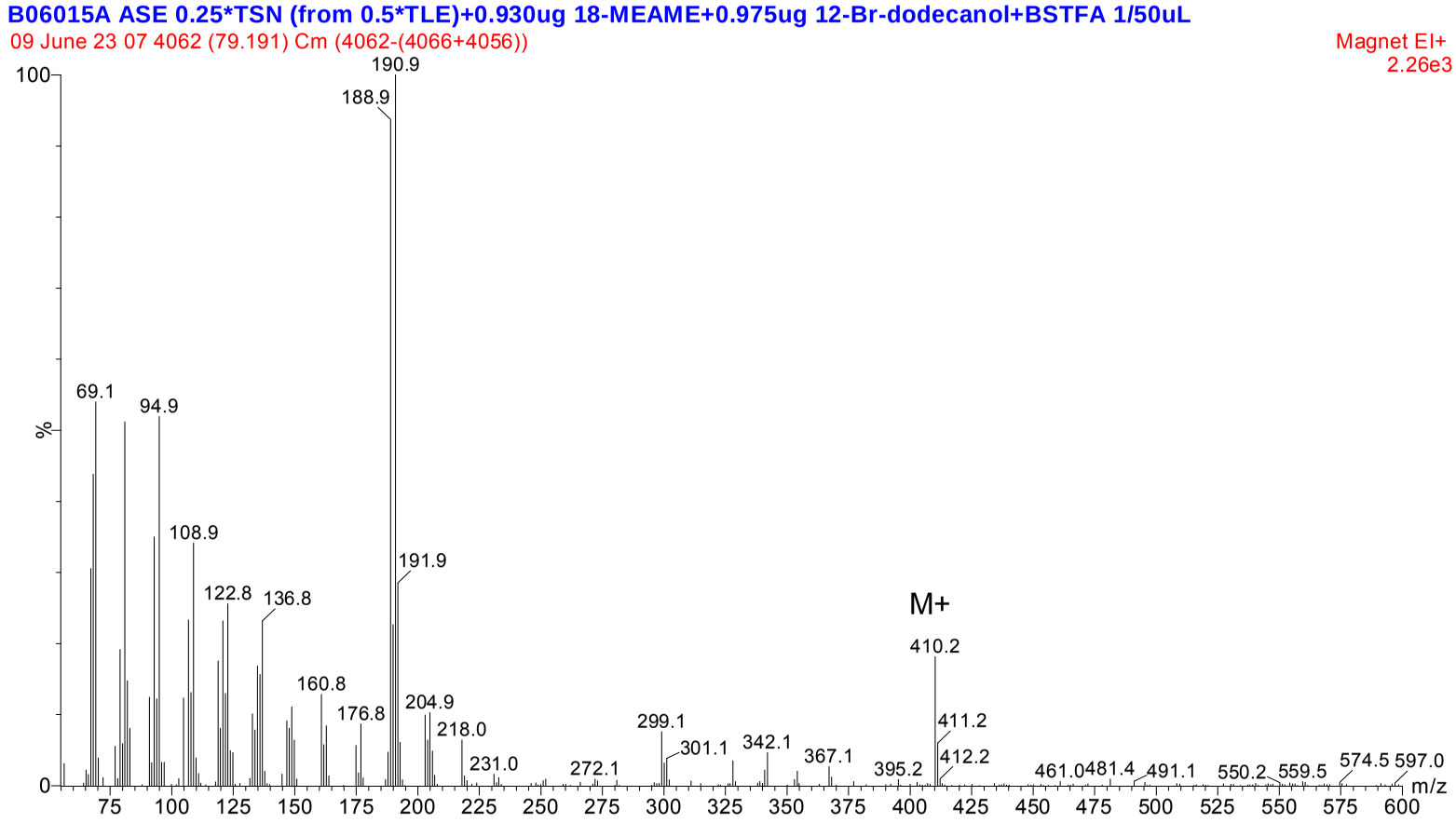

Diploptene – bacterial source, precursor to hopanoids “Diplopterol”
See ten Haven *et al* (1989) *GCA* 53, pp 3073-3079

58: Diploptene, NIST library

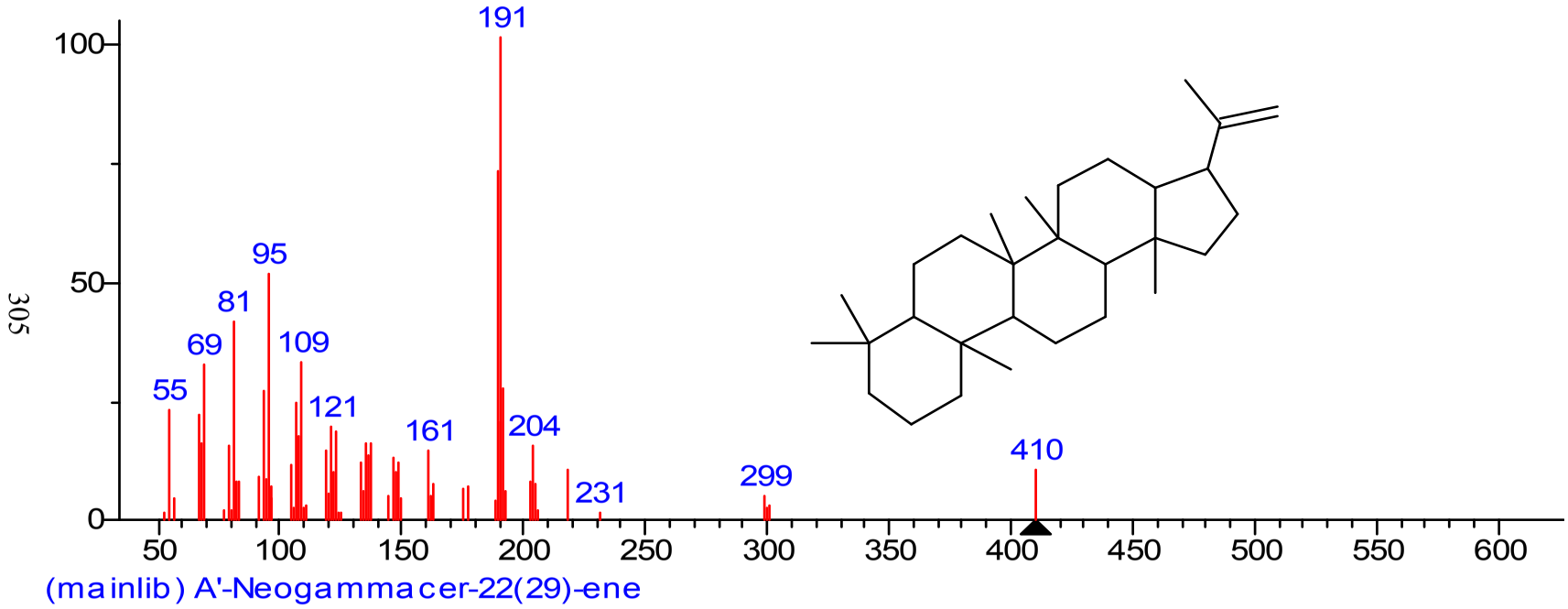

59: 22,29,30-trinorhopan-21-one (samples)

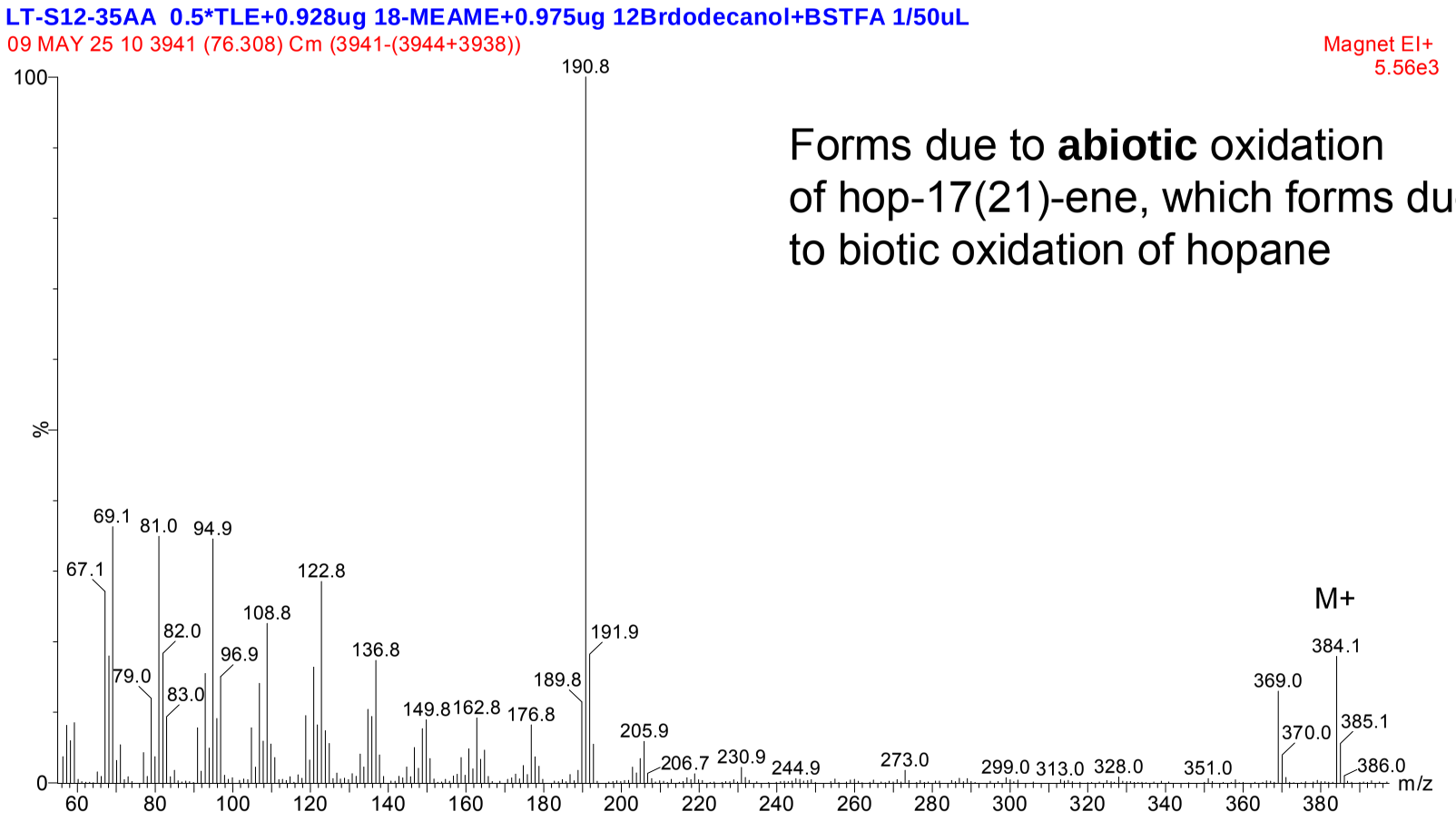

Forms due to **abiotic** oxidation of hop-17(21)-ene, which forms due to biotic oxidation of hopane

Spectrum identified from Barakat & Yen (1990) *Organic Geochemistry* vol 15 pp 299
Formation detailed in Tritz *et al* (1999) *Organic Geochemistry* vol 30, pp 499-514

Triterpenoids

Five 6C rings

60: Gammaceran-3B-ol TMS (tetrahymanol), samples & reference below

C30, 5 DBEs
C30 Δ0 triterpenol

Sources: ciliated protists (marine and fresh water, “scuticociliates”) incl. Tetrahymena, Pleuronema, Parauronema

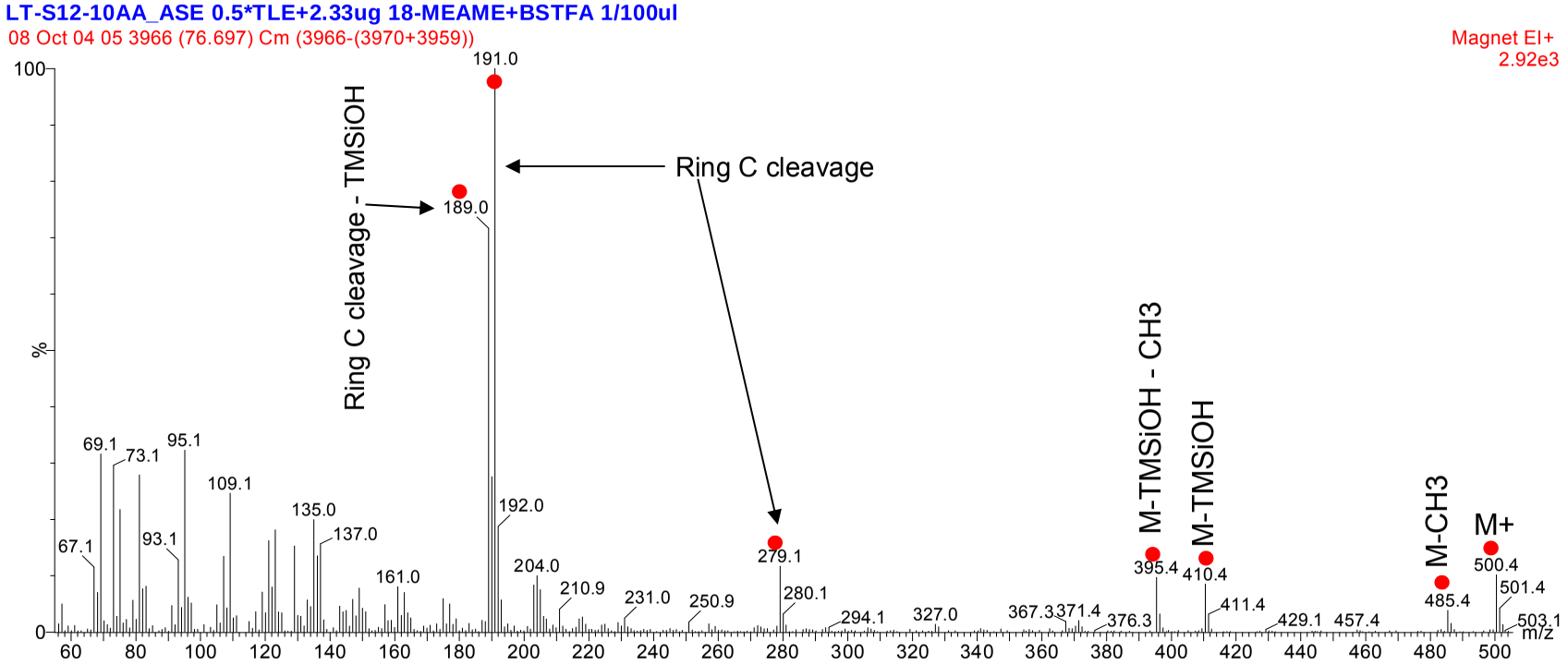

308

- Red dots indicate ions labeled in reference spectrum

Spectrum (along w dryocrassol, diplopterol, gammacer-2-ene, gammacer-3-one) in ten Haven *et al* (1989) *GCA* vol 53, pp 3073-3079; also contains structures and info on origins of MS fragments

Nicer spectrum: Venkatesan *et al* (1990) *Organic Geochemistry* vol 16, nos 4-6, pp 1015-1024

Sources of tetrahymanol (ciliate & bacterial) described in Harvey & McManus (1991) *GCA* vol 55, pp 3387-3390 & Harvey *et al* (1997) *Journal of Eukaryote Microbiology* vol 44, no 3, pp 189-193

61: Gammacer-3-one (gammacerone), samples & reference below

C30, 5 DBEs Sources: oxidation product of tetrahymanol in sediments

C30 Δ0 triterpenone

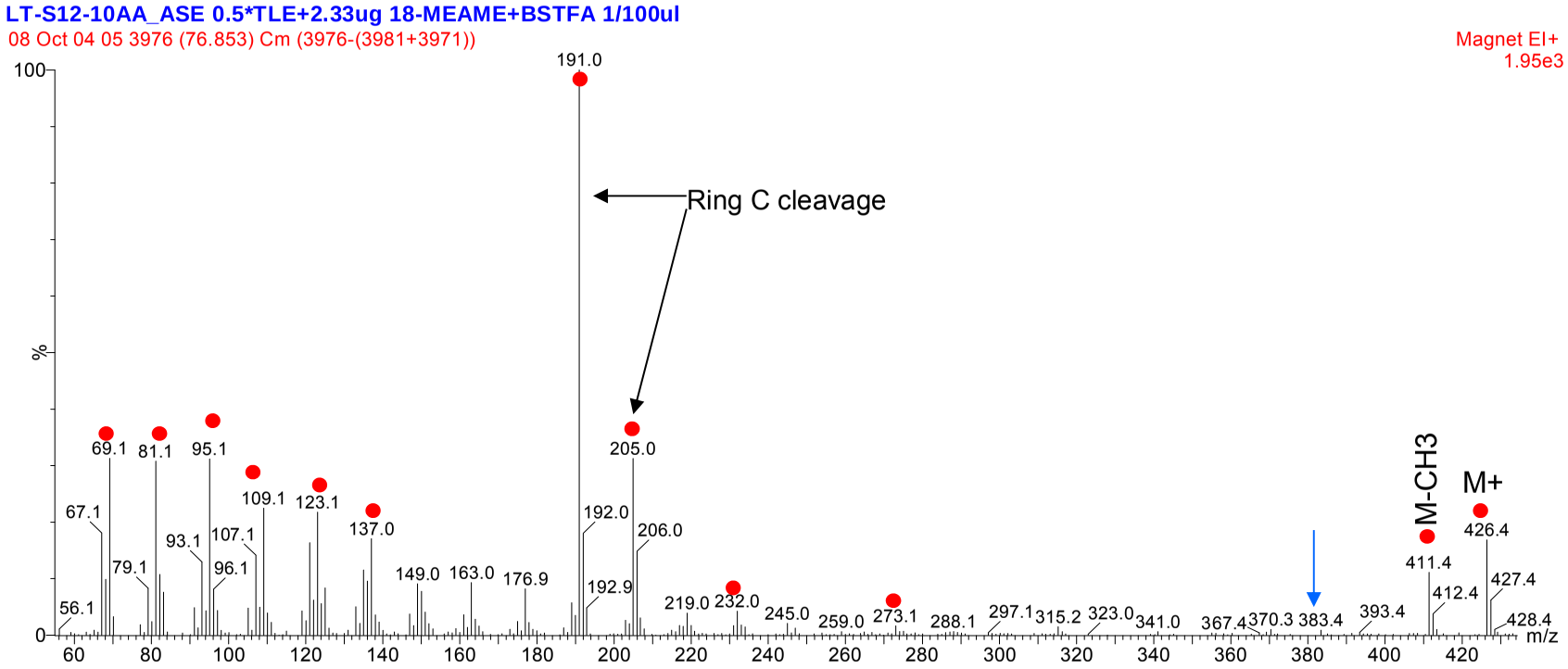

309

- Red dots indicate ions labeled in reference spectrum

Spectrum (along w dryocrassol, diplopterol, gammacer-2-ene, tetrahymanol) in ten Haven *et al* (1989) *GCA* vol 53, pp 3073-3079; also contains structures and info on origins of MS fragments

Also see Barakat & Yen (1990) *Organic Geochemistry* vol 15, no 3, pp 299-311: may be some hopan-3-one

Co-eluting w gammacerone, due to presence of m/z 383 (M-C3H7 fragment from loss of isopropyl on ring E)

62: Taraxer-14-en-3B-ol TMS (taraxerol), samples & reference below

C30, 6 DBEs Sources: dandelions/weeds, mangroves, etc.

C30 Δ14 triterpenol

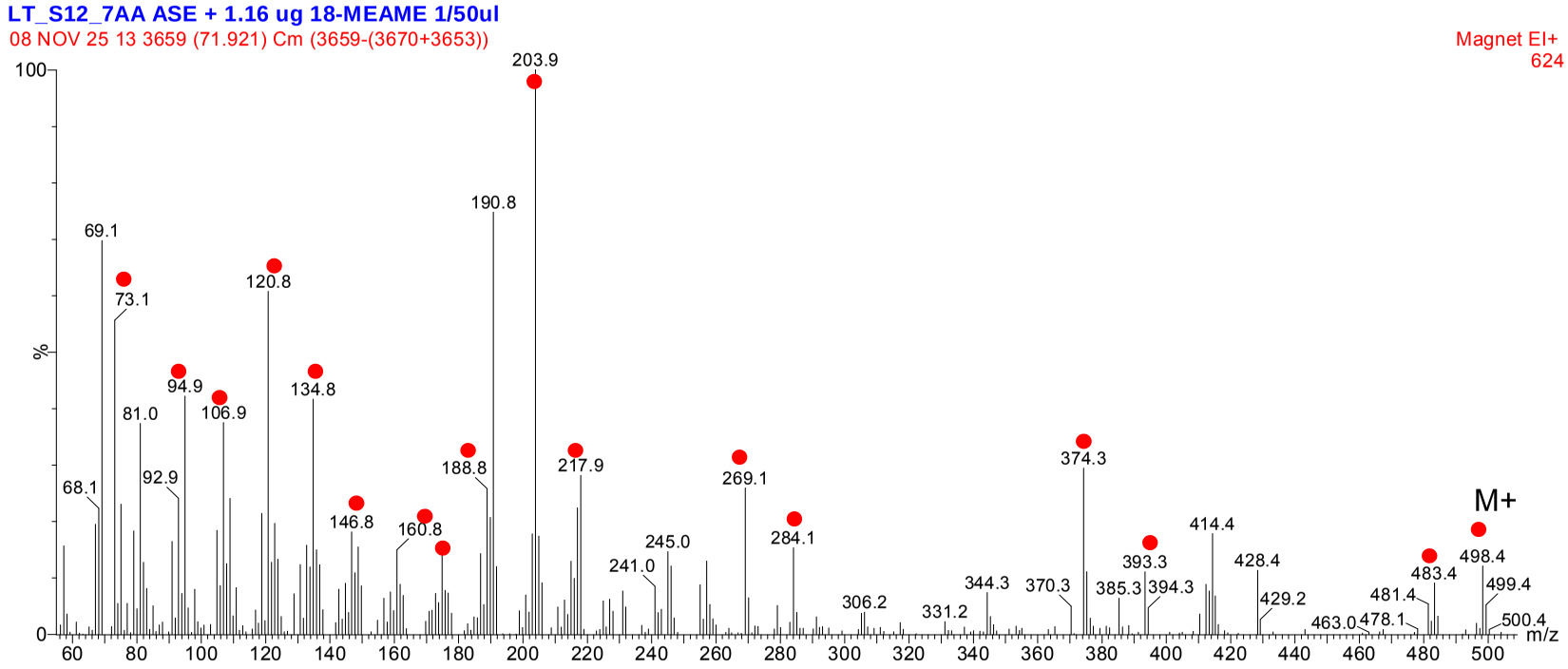

●Red dots indicate ions labeled in reference spectrum

Spectrum (along w d-amyrin, B-amyrin, germanicol, lupeol & triterpadienes & trienes) in Killops & Frewin (1994) *Organic Geochemistry* vol 21, no 12, pp 1193-1209; also contains some info on origins of MS fragments

63: Olean-18-en-3B-ol TMS (germanicol), samples & reference below

C30, 6 DBEs Sources: higher plants

C30 Δ18 triterpenol

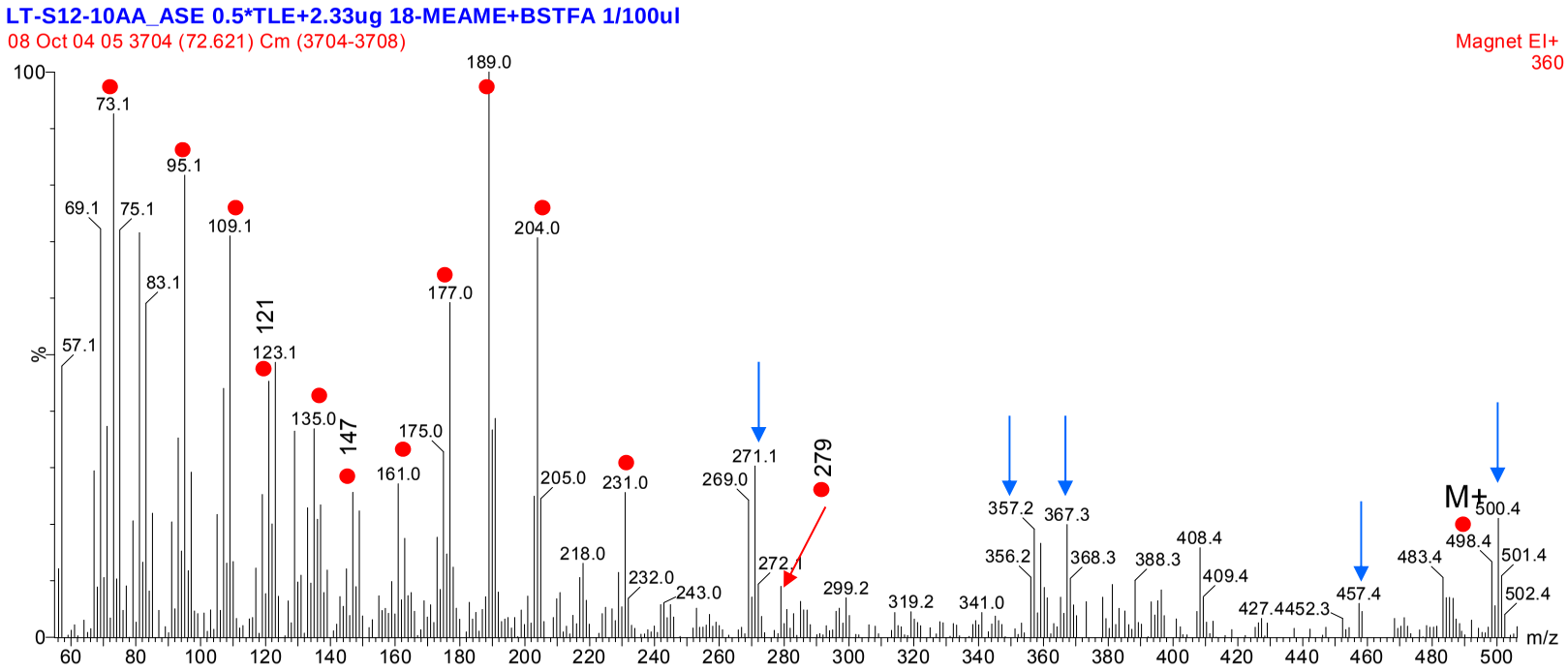

- Red dots indicate ions labeled in reference spectrum

NOTE: co-eluting w 4a-methyl-24-ethylcholest-22E-en-3B-ol (frags w arrows in blue)

Spectrum (along w d-amyrin, B-amyrin, germanicol, lupeol & triterpadienes & trienes) in Killops & Frewin (1994) *Organic Geochemistry* vol 21, no 12, pp 1193-1209; also contains some info on origins of MS fragments

64: Lup-20(29)-en-3B-ol TMS (lupeol), samples & reference below

C30, 6 DBEs Sources: higher plants

C30 Δ20(29) triterpenol

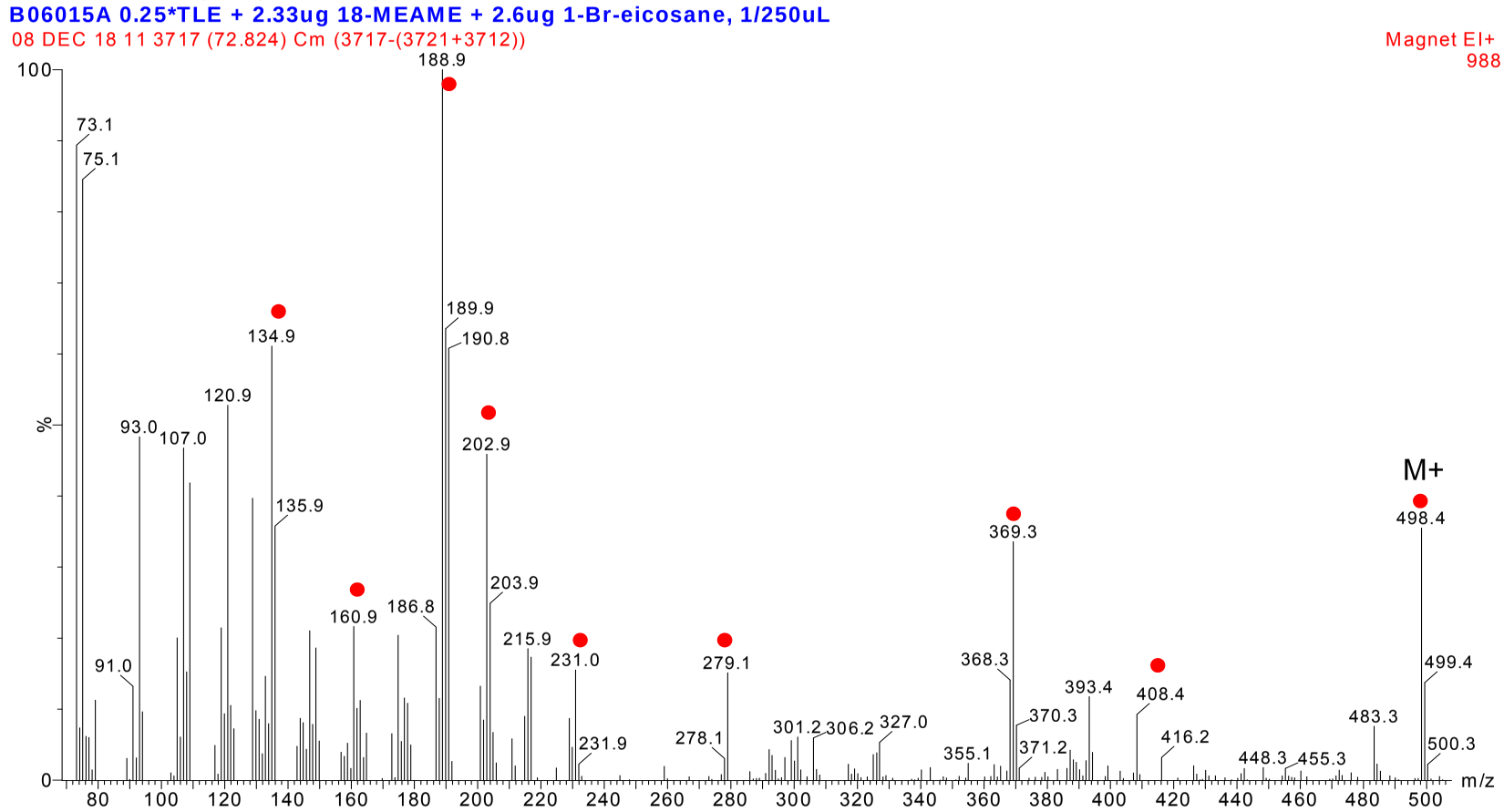

●Red dots indicate ions labeled in reference spectrum

Spectrum (along w d-amyrin, B-amyrin, germanicol, lupeol & triterpadienes & trienes) in Killops & Frewin (1994) *Organic Geochemistry* vol 21, no 12, pp 1193-1209; also contains some info on origins of MS fragments

Betulin TMS (NIST library)

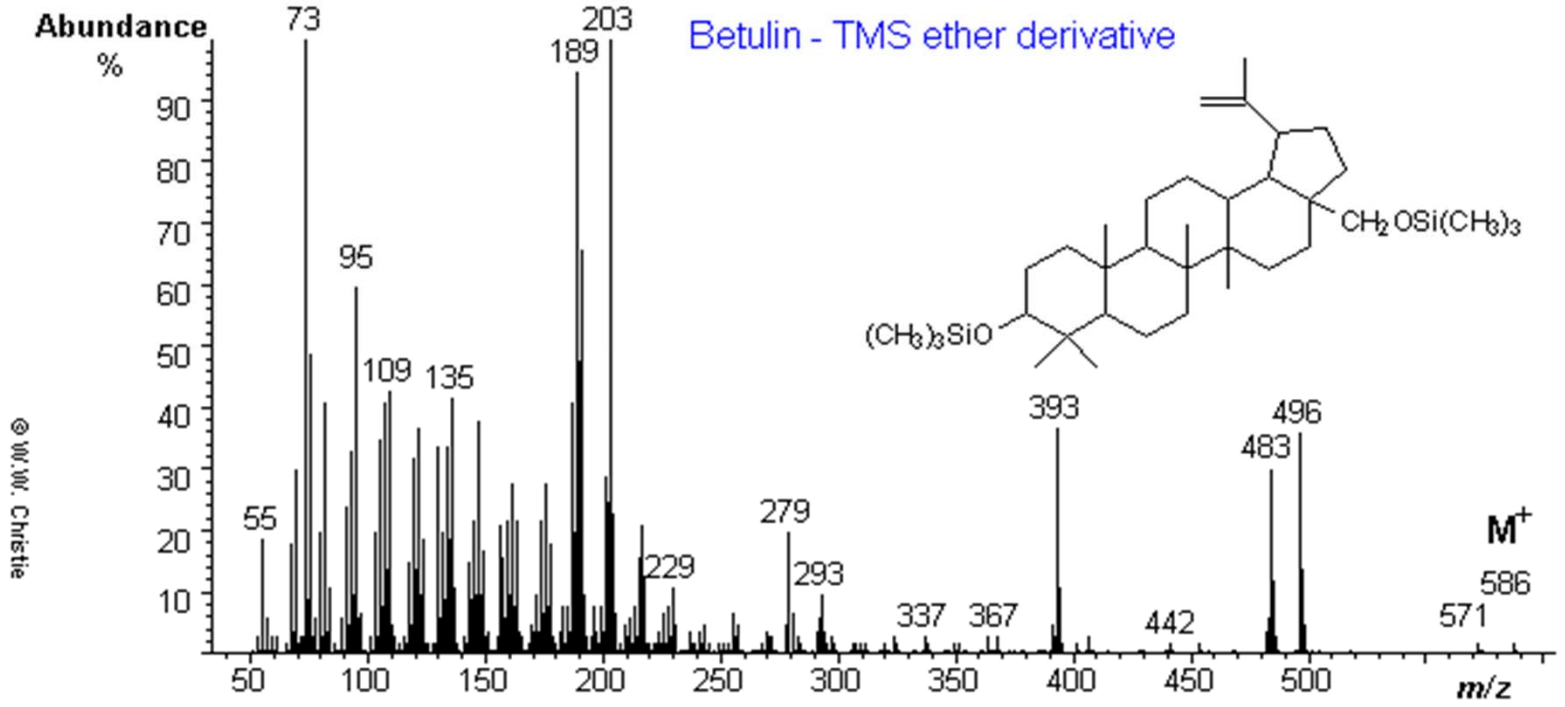

65: Friedelan-3-one (sample spectrum)

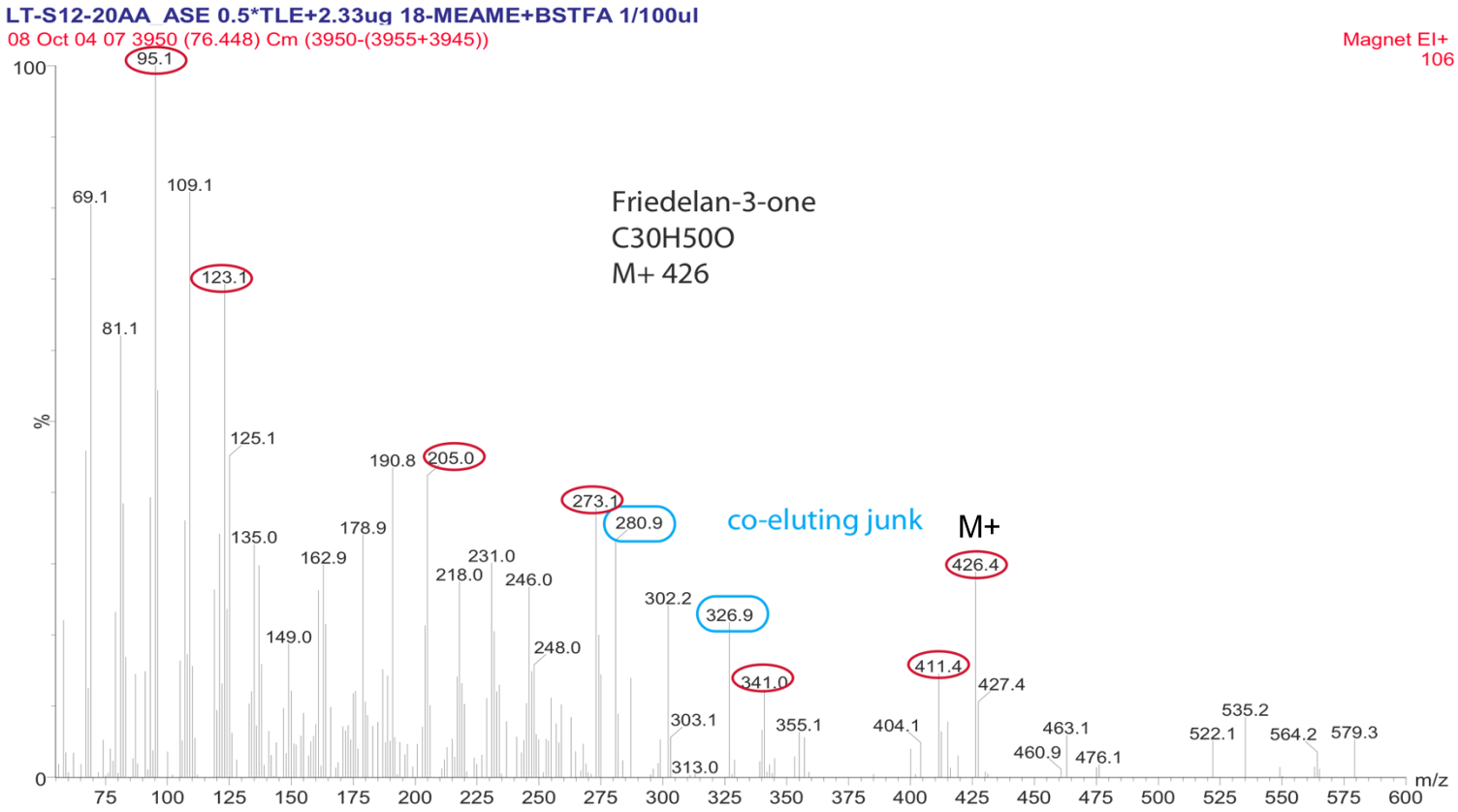

Red circles indicate ions labeled in reference spectrum, Y. Duan (2001) *Chinese Science Bulletin* v. 46 pp 1433-1436

Sources: oxidation of higher plant triterpenoids

Diols, keto-ols, enols

66: C_{20} terminal diol (α,ω)

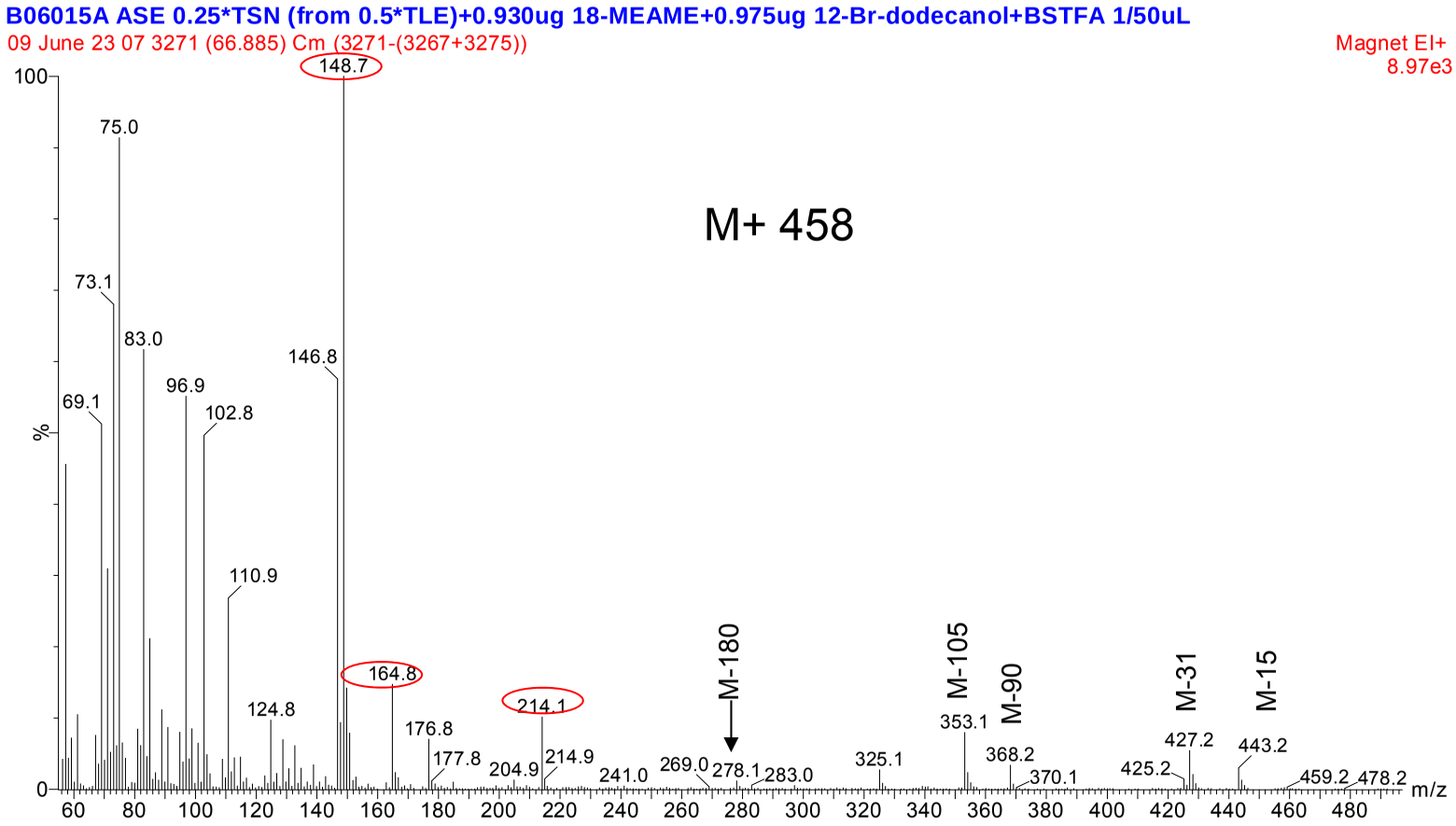

Red circles indicate ions labeled in reference spectrum (NIST 2.0 library)
Sources: unknown

67: C_{22} terminal diol (α,ω)

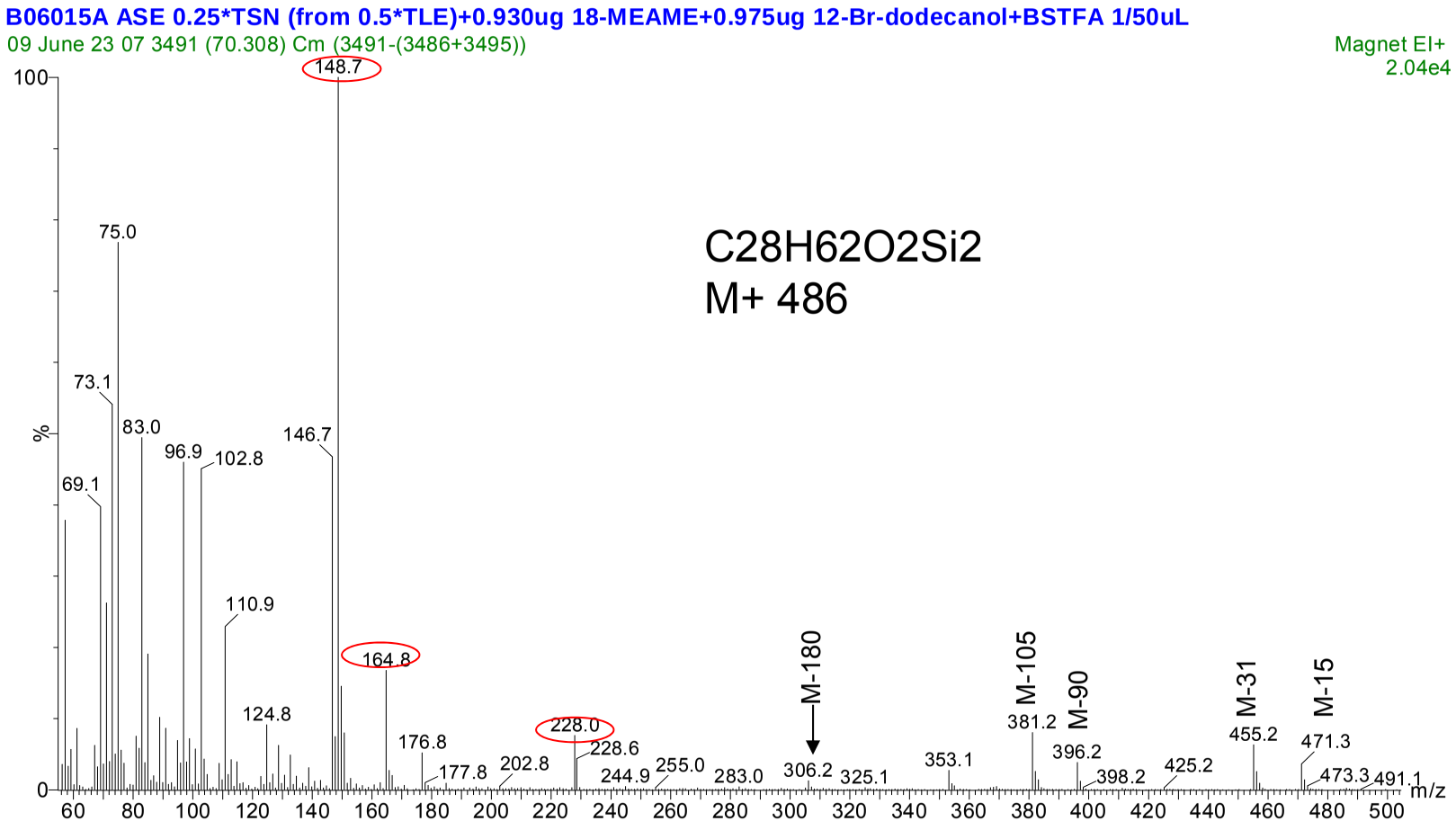

Red circles indicate ions labeled in reference spectrum (NIST 2.0 library)
Sources: unknown

67: C_{22} terminal diol (α,ω) (NIST library)

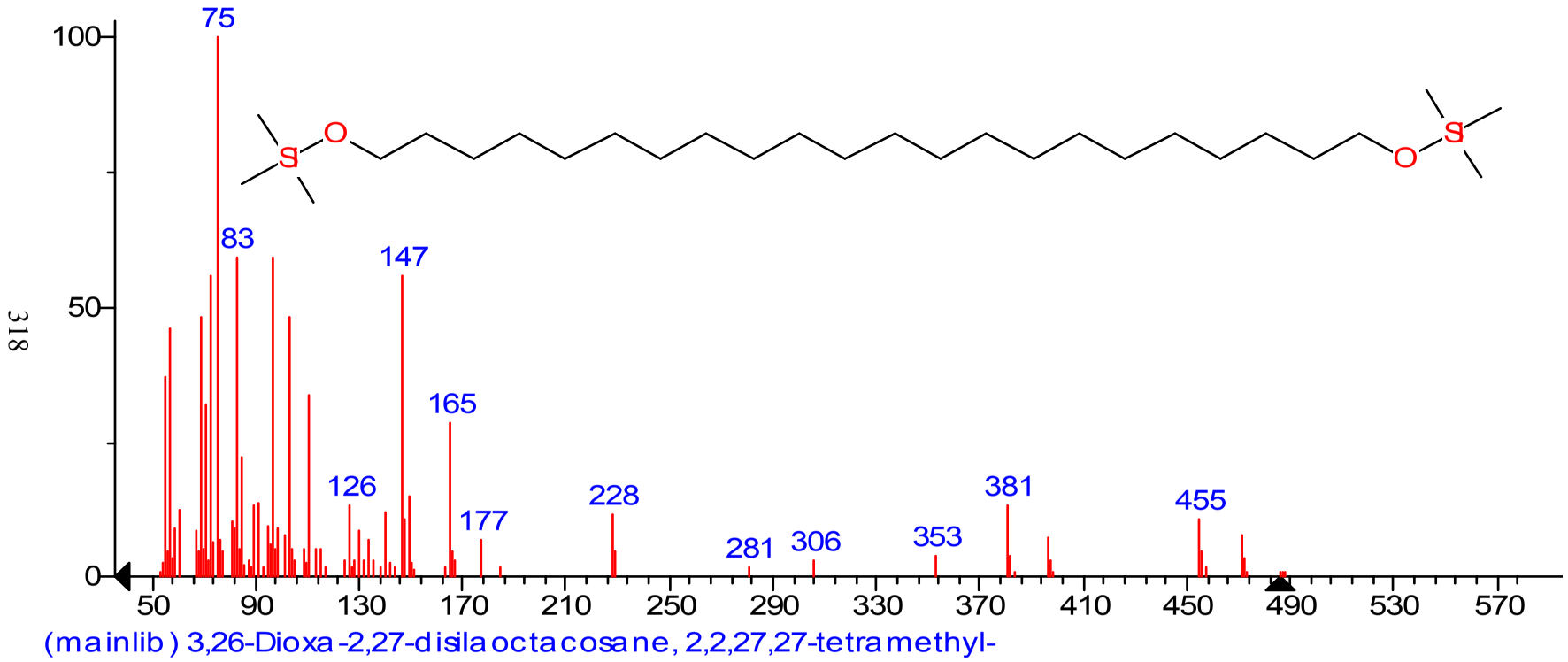

68: C_{24} terminal diol (α,ω)

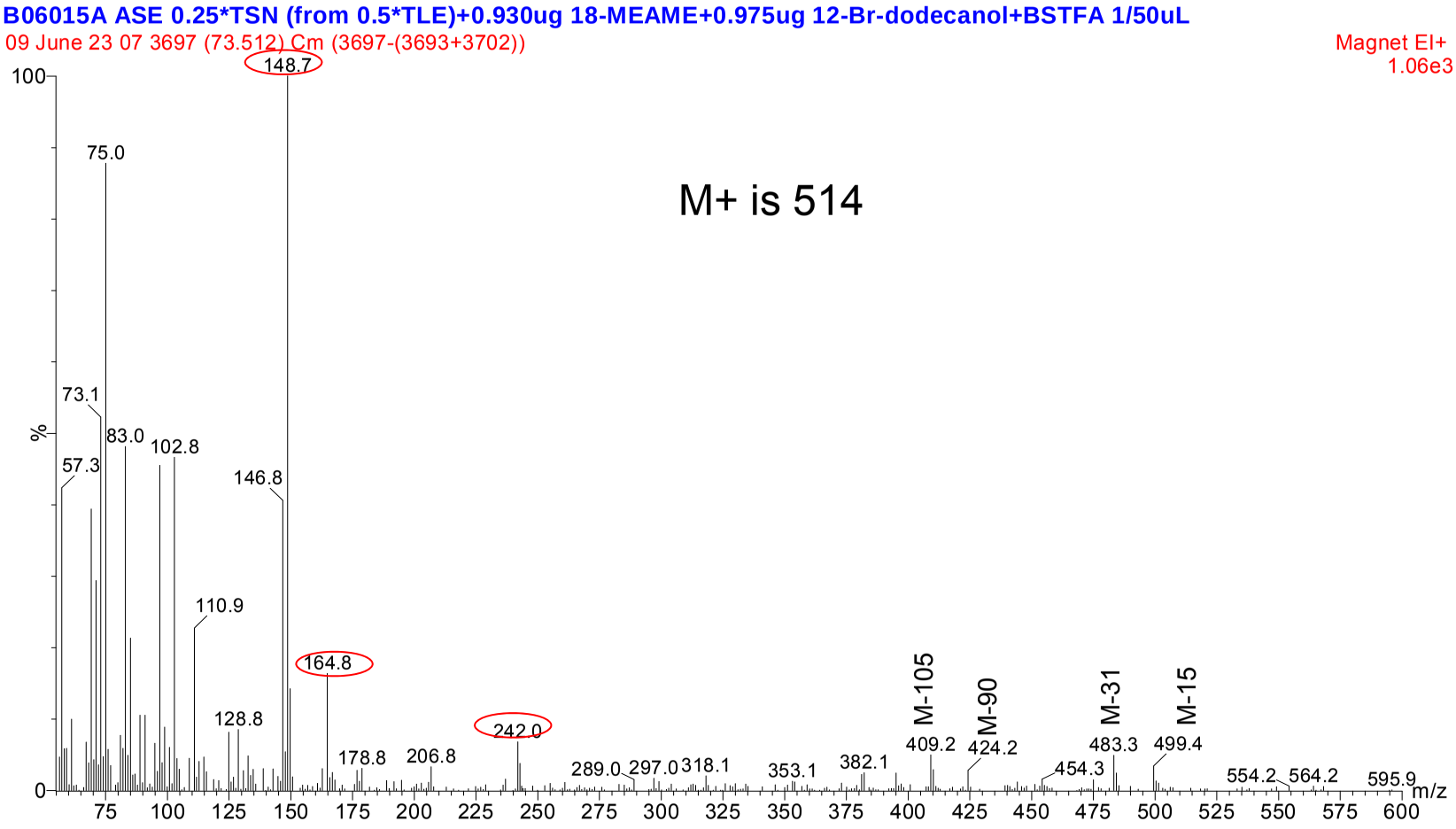

Red circles indicate ions labeled in reference spectrum (NIST 2.0 library)
Sources: unknown

69: C_{28} terminal diol (α,ω)

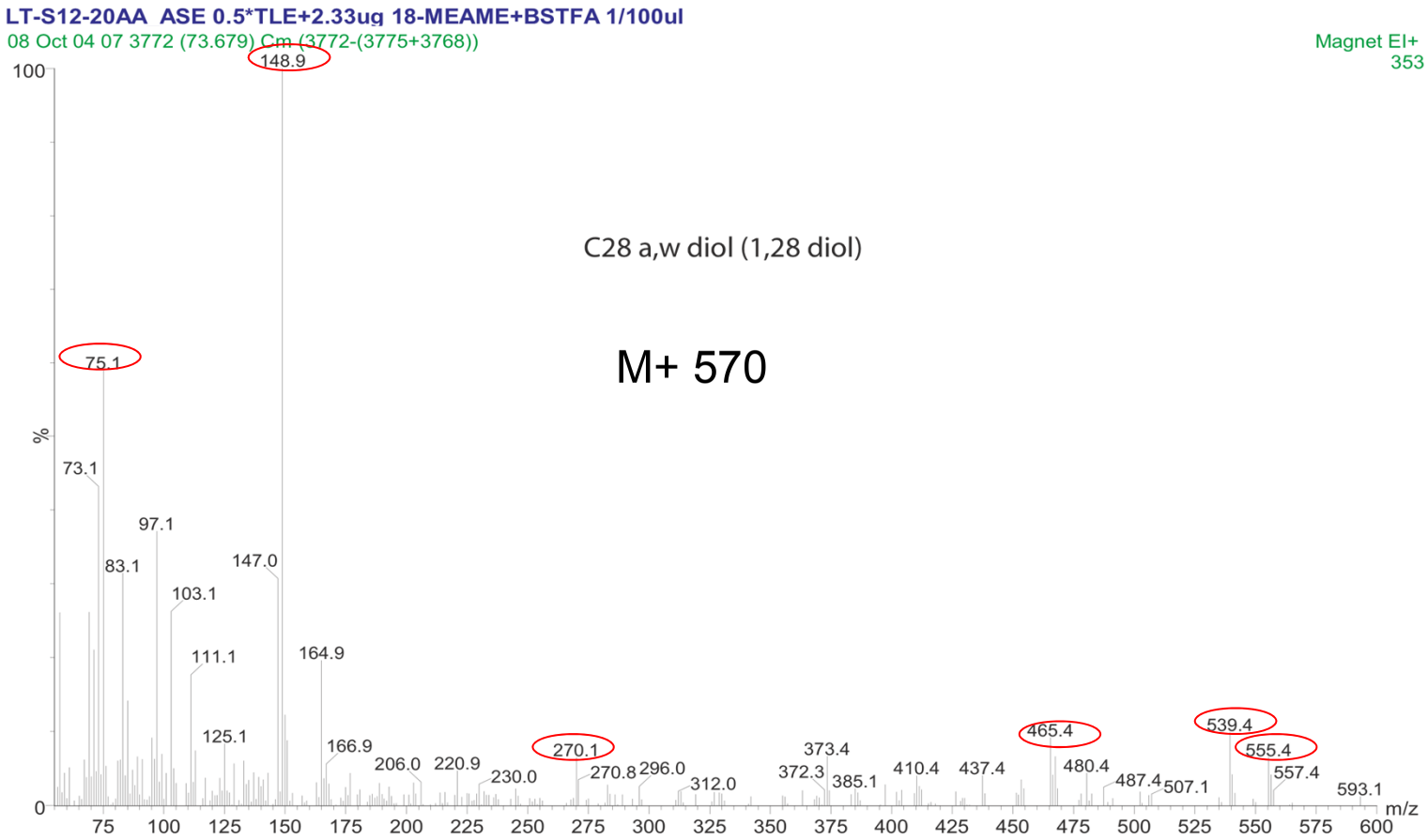

Red circles indicate ions labeled in reference spectrum, Mejanelle *et al* (2003) *Organic Geochemistry* Vol 34 pp 527 - 538

Sources: Precursor molecule for long chain diol and keto-ol synthesis in eustigmatophyte algae

70: C_{30} diols (positional isomers of dihydroxytriacontane)

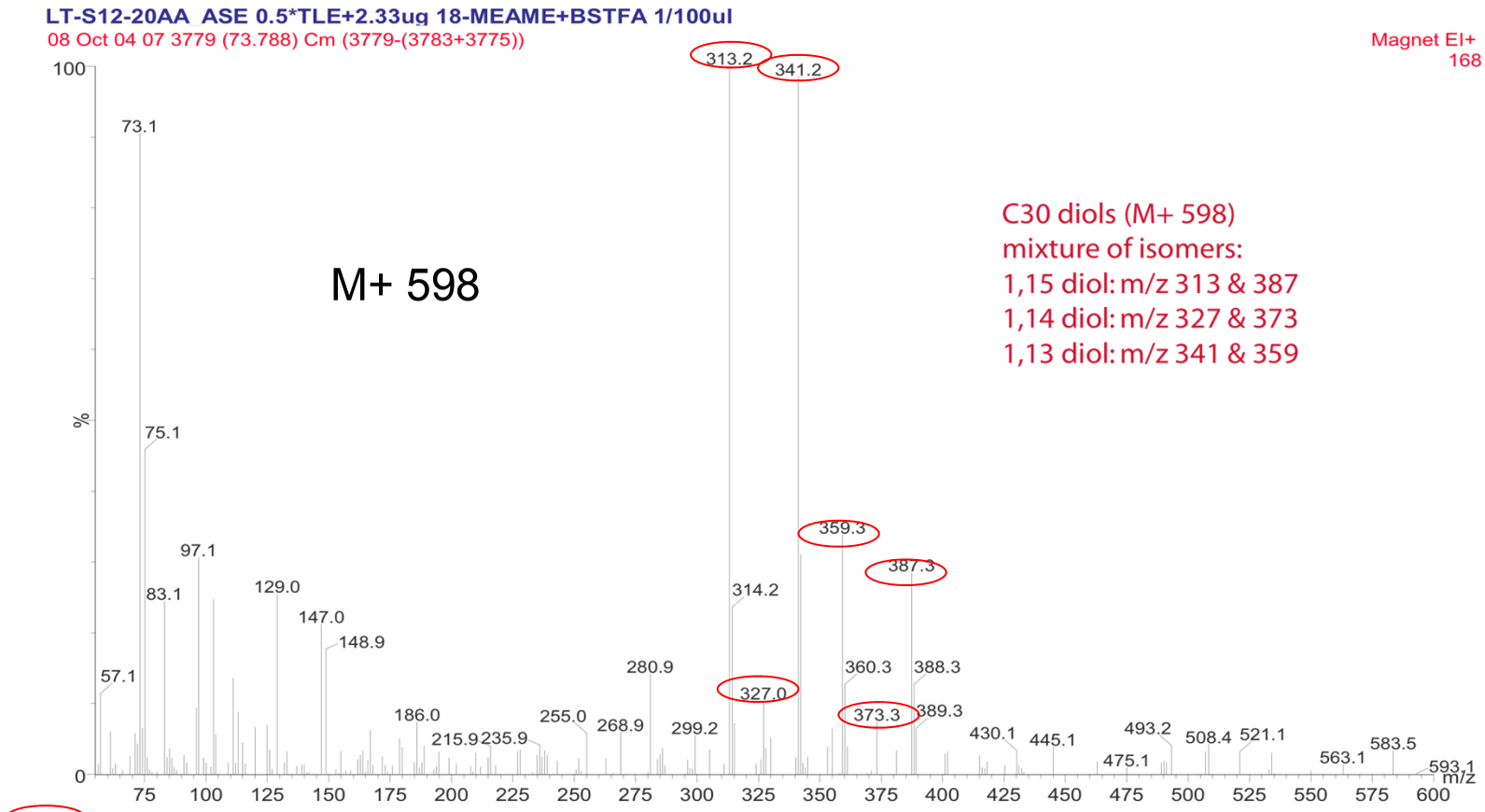

Red circles indicate ions labeled in reference spectrum, Mejanelle *et al* (2003) *Organic Geochemistry* Vol 34 pp 527 - 538

Sources: diatoms make mostly 1,14 isomer, other isomers from eustigmatophyte algae, esp *Nannochloropsis* sp. (marine)

71: C_{32} 1,15 diol (1,15 dihydroxydotriacontane)

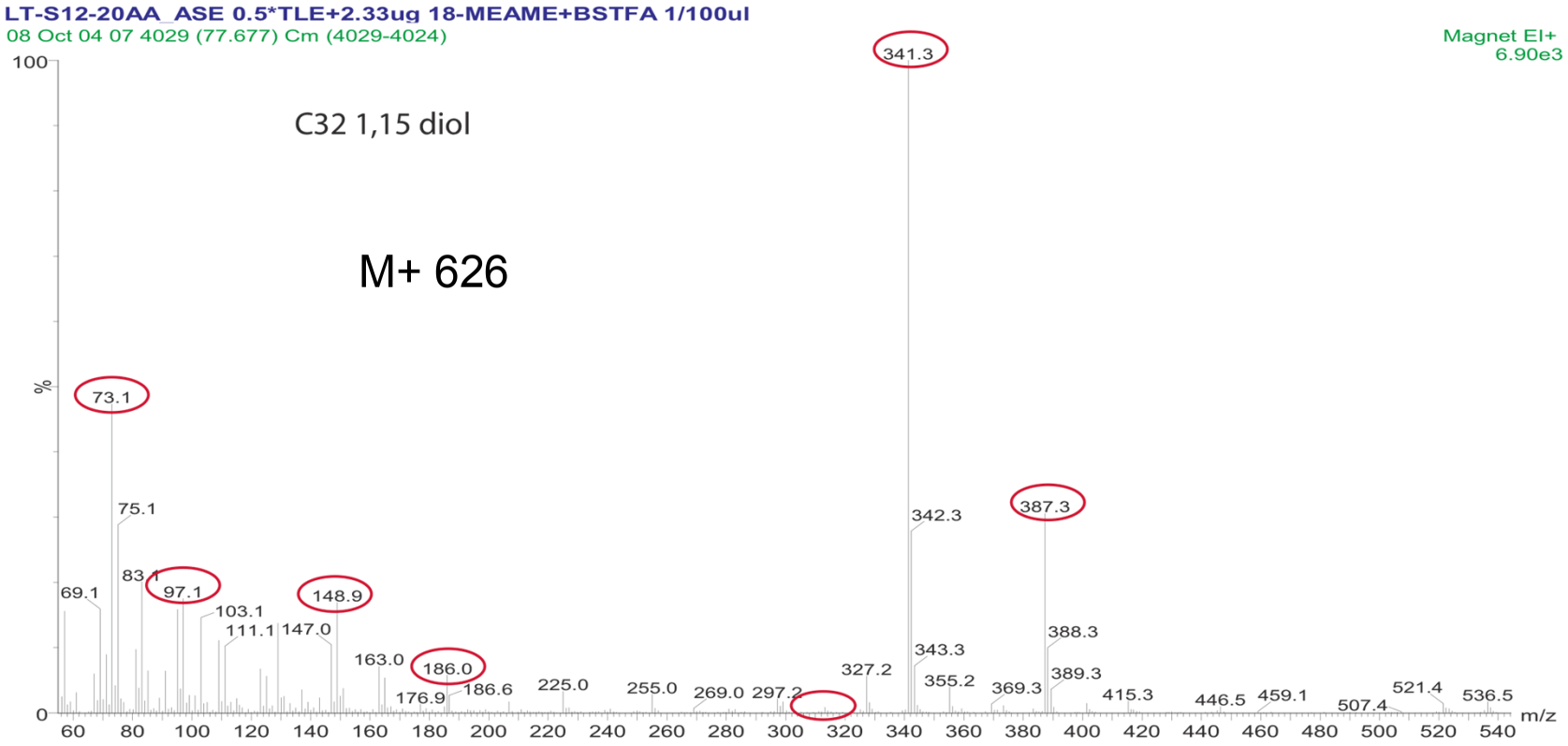

Red circles indicate ions labeled in reference spectrum, Volkman *et al* (1992) *Organic Geochemistry* Vol 18 pp 131 - 138

Sources: Eustigmatophyte algae, esp *Nannochloropsis* sp. (marine)

72: C_{30} 1,13 keto-ol (1-hydroxy, 13-keto-triacontane)

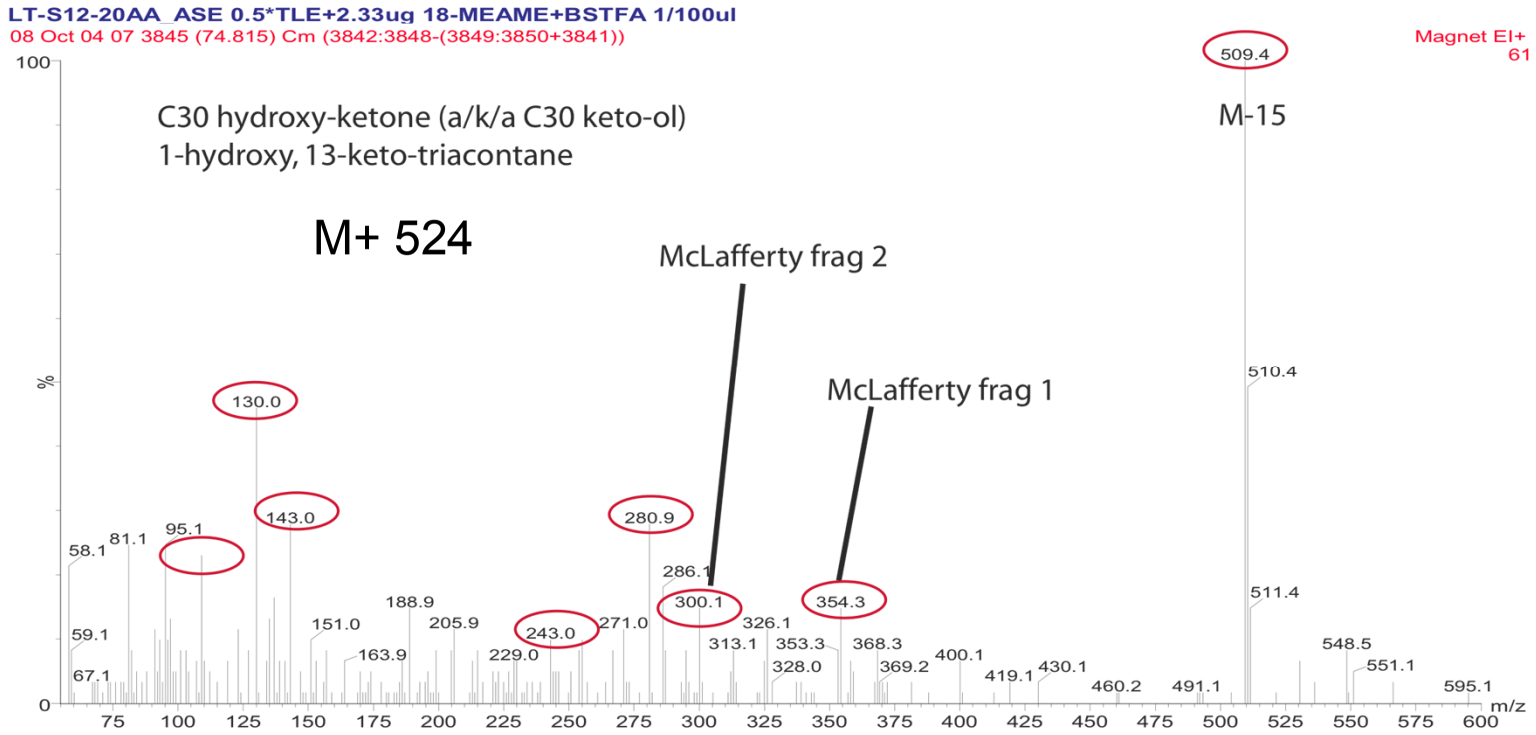

Red circles indicate ions labeled in reference spectrum, Mejanelle *et al* (2003) *Organic Geochemistry* Vol 34 pp 527 - 538

Sources: Eustigmatophyte algae esp *Nannochloropsis* sp. (marine)

73: C_{32} 1,15 keto-ol (1-hydroxy, 15-keto-dotriacontane)

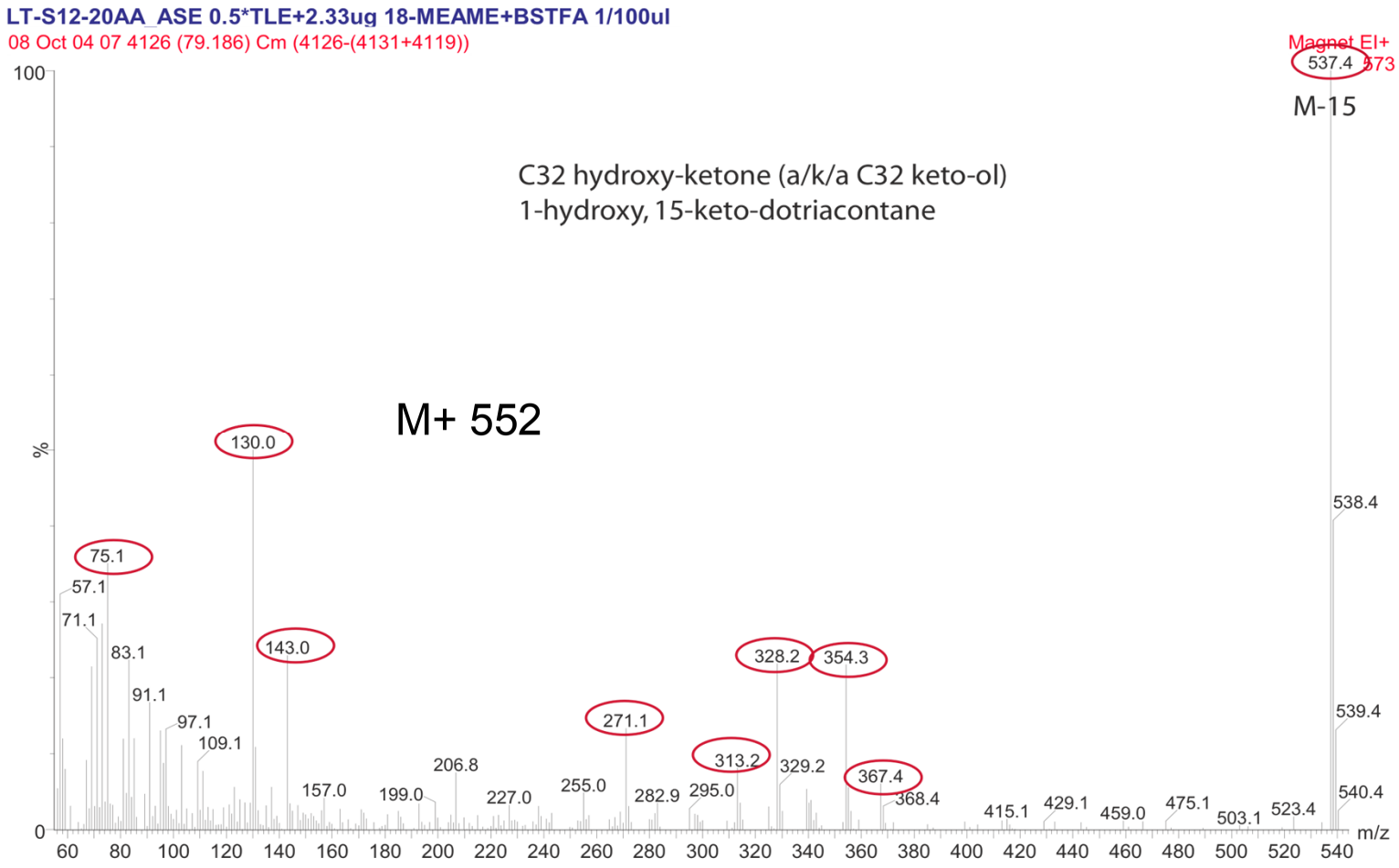

Red circles indicate ions labeled in reference spectrum, Mejanelle *et al* (2003) *Organic Geochemistry* Vol 34 pp 527 - 538

Sources: Eustigmatophyte algae esp *Nannochloropsis* sp. (marine)

74: C_{32} alkenol

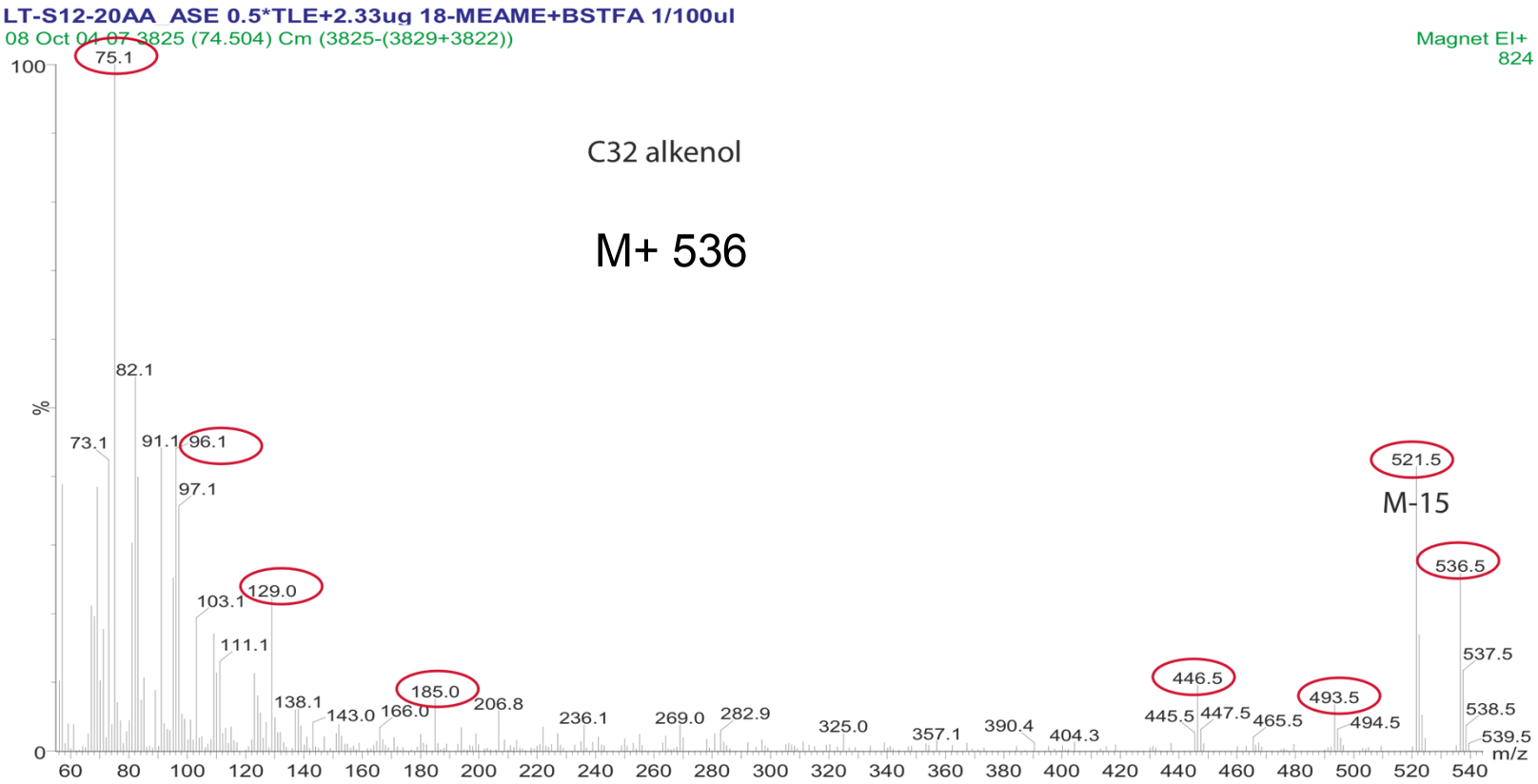

Red circles indicate ions labeled in reference spectrum, Mejanelle *et al* (2003) *Organic Geochemistry* Vol 34 pp 527 - 538

Sources: Precursor molecule for long chain diol and keto-ol synthesis in eustigmatophyte algae

Octadecenol (Δ9)

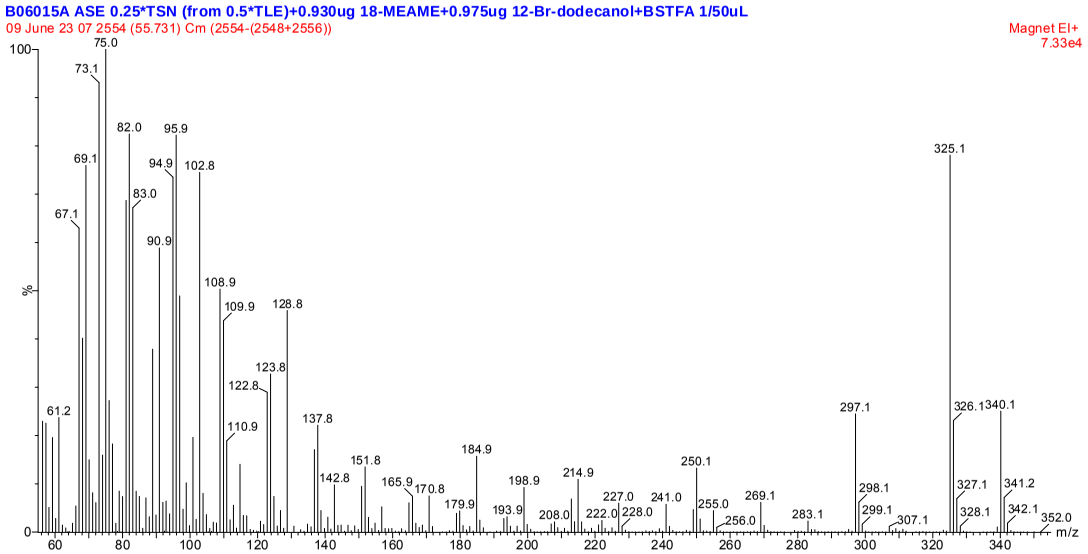

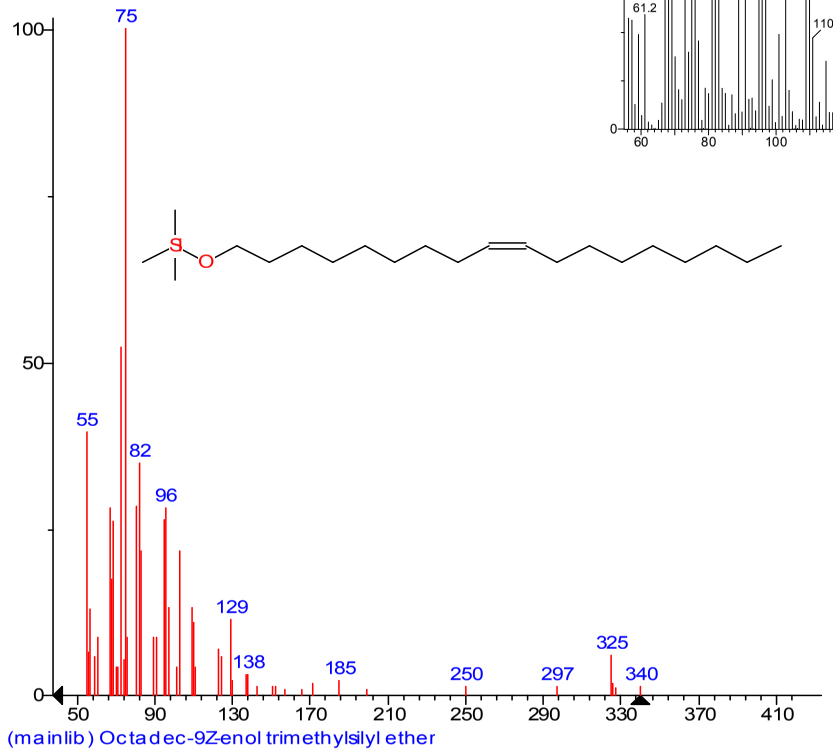

Alkenones (LCAs)
see binder for higher quality spectra

All alkenone spectra identified by personal communication with Emanuelle Grosjean, and confirmed with standard mixture containing LCAs

See also: Thiel *et al* (1997) *GCA* vol 61, pp 2053-2064

Source of LCAs is haptophyte microalgae; some combinations of LCAs can be used to reconstruct palaeo-temperatures and salinities

See also: Chu *et al* (2005) *GCA* vol 69, pp 4985-5003
Liu *et al* (2006) *Geophysical Research Letters* vol 33, pp L09707
Pearson *et al* (2008) *GCA* vol 72, pp 4035-4046

75: $C_{37:3}$ methyl (reference spectrum)

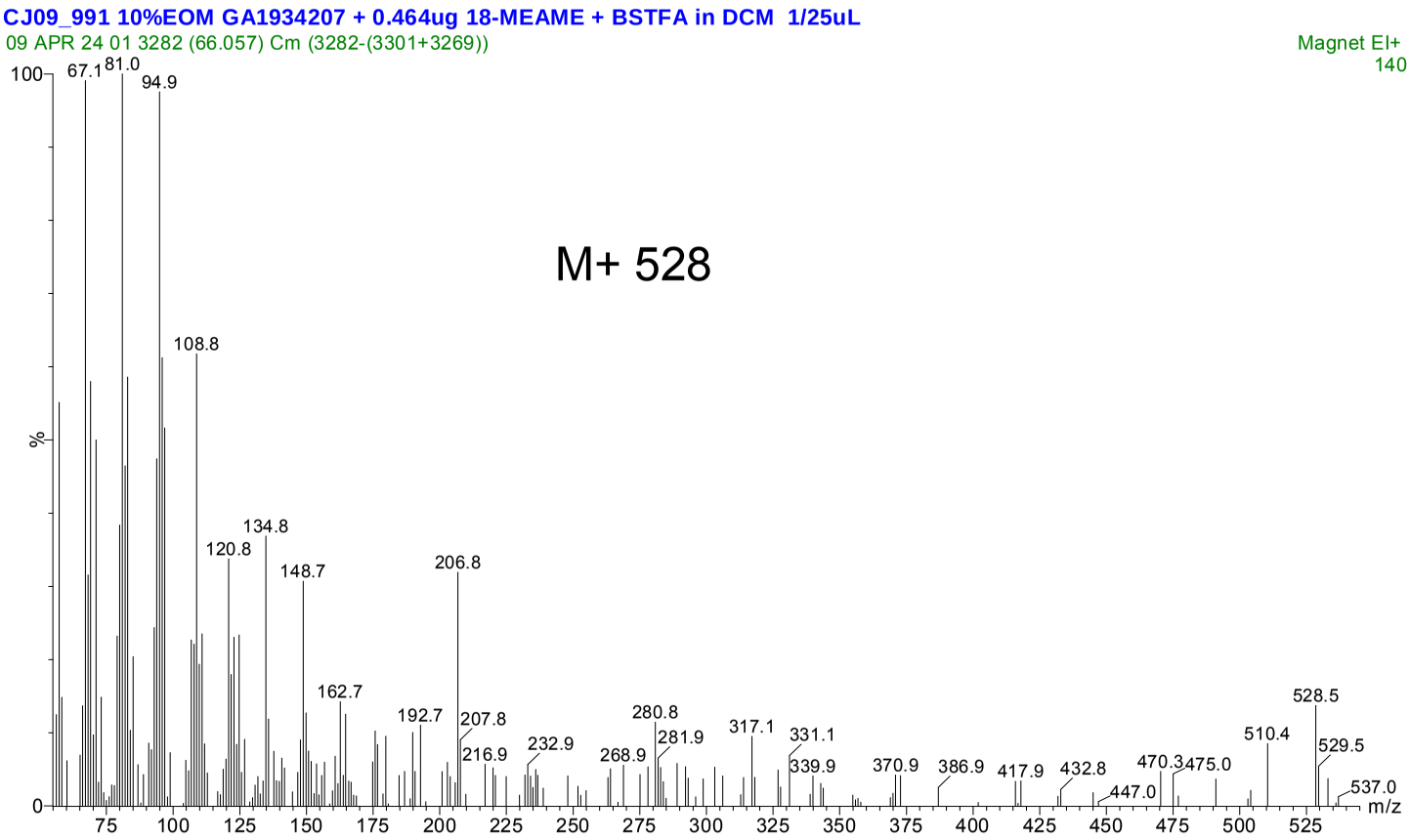

M+ 528

See section heading (LCAs) for source and spectra references

75: $C_{37:3}$ methyl (reference spectrum)

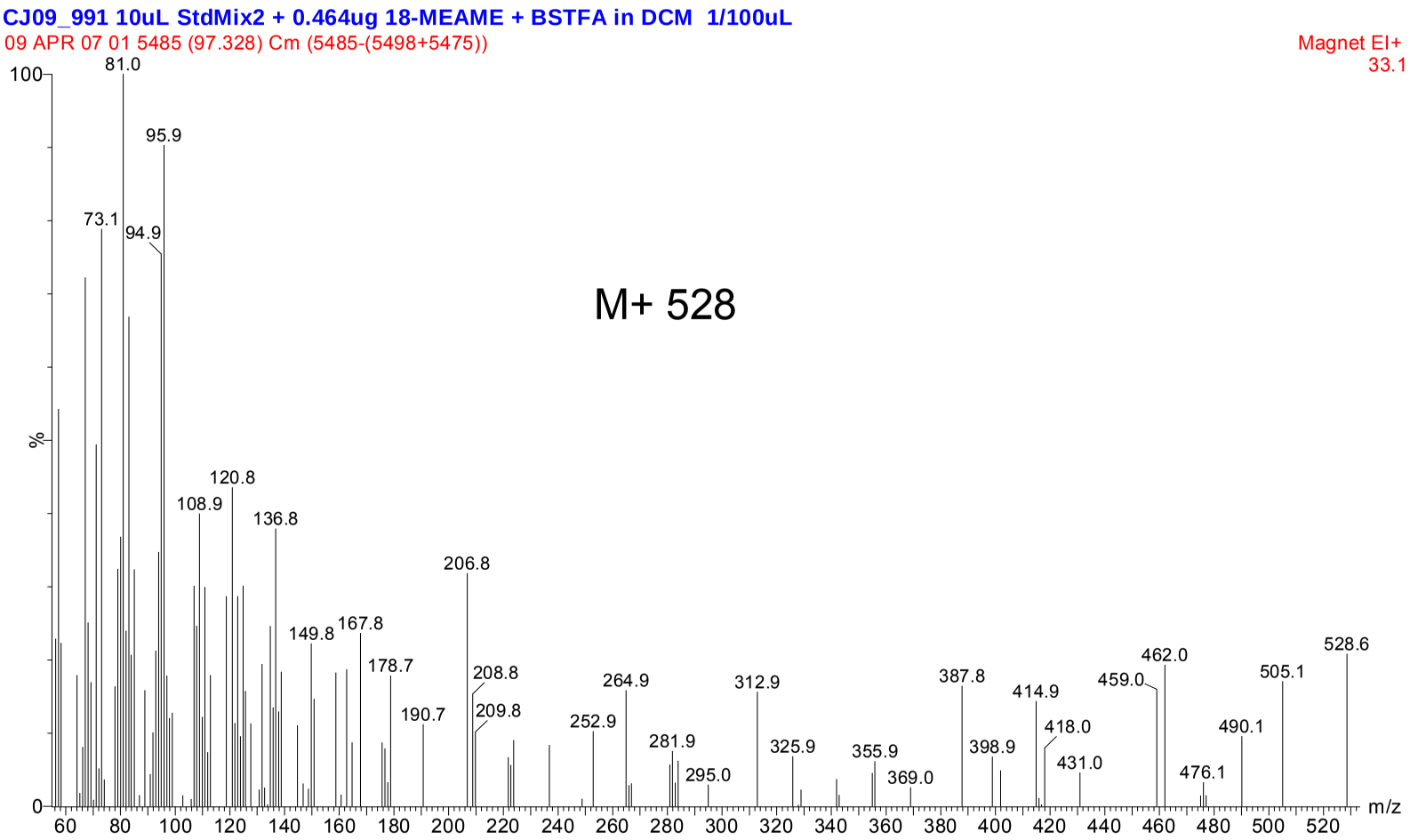

See section heading (LCAs) for source and spectra references

75: $C_{37:3}$ methyl (sample spectrum)

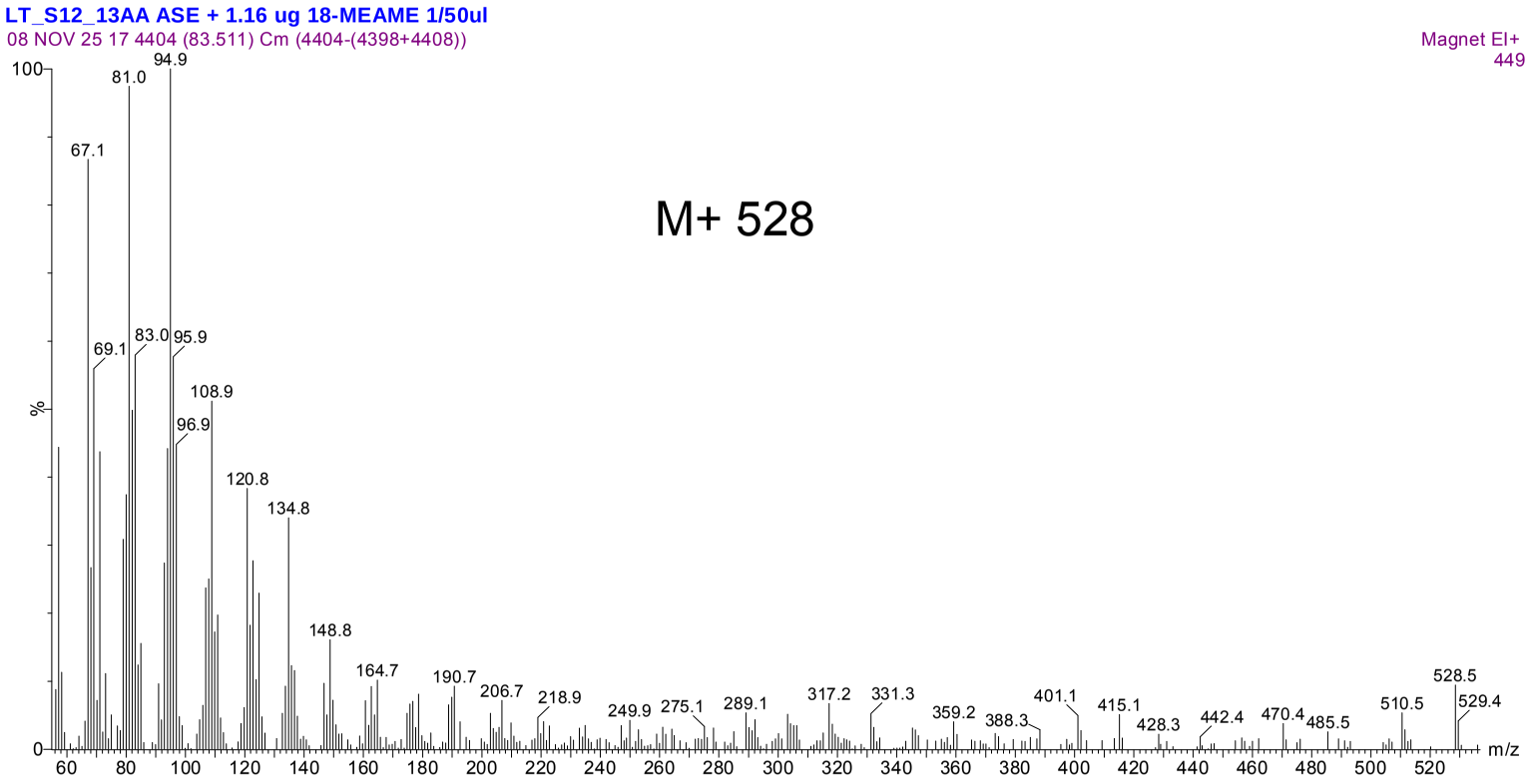

M+ 528

See section heading (LCAs) for source and spectra references

76: $C_{37:2}$ methyl (reference spectrum)

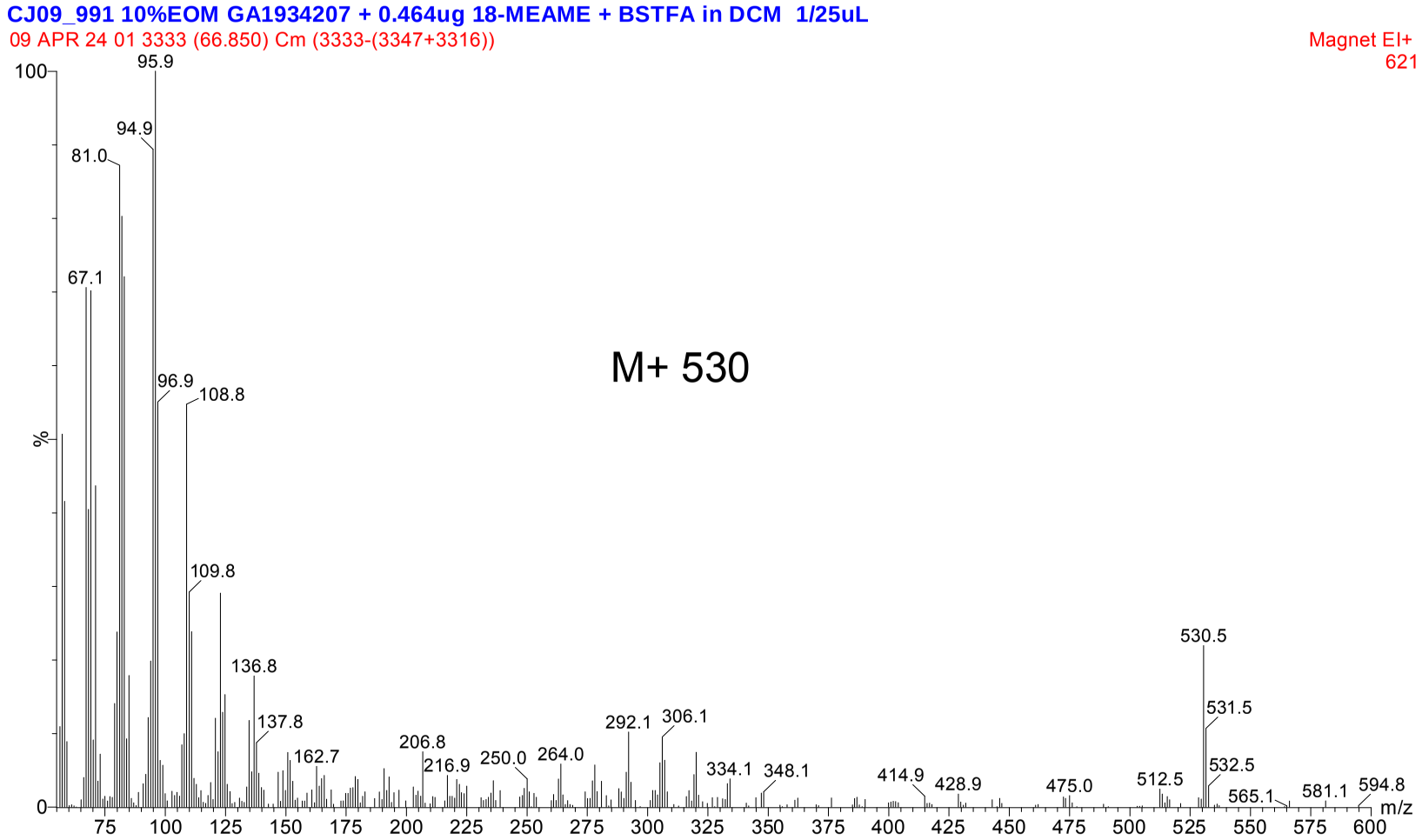

See section heading (LCAs) for source and spectra references

76: $C_{37:2}$ methyl (reference spectrum)

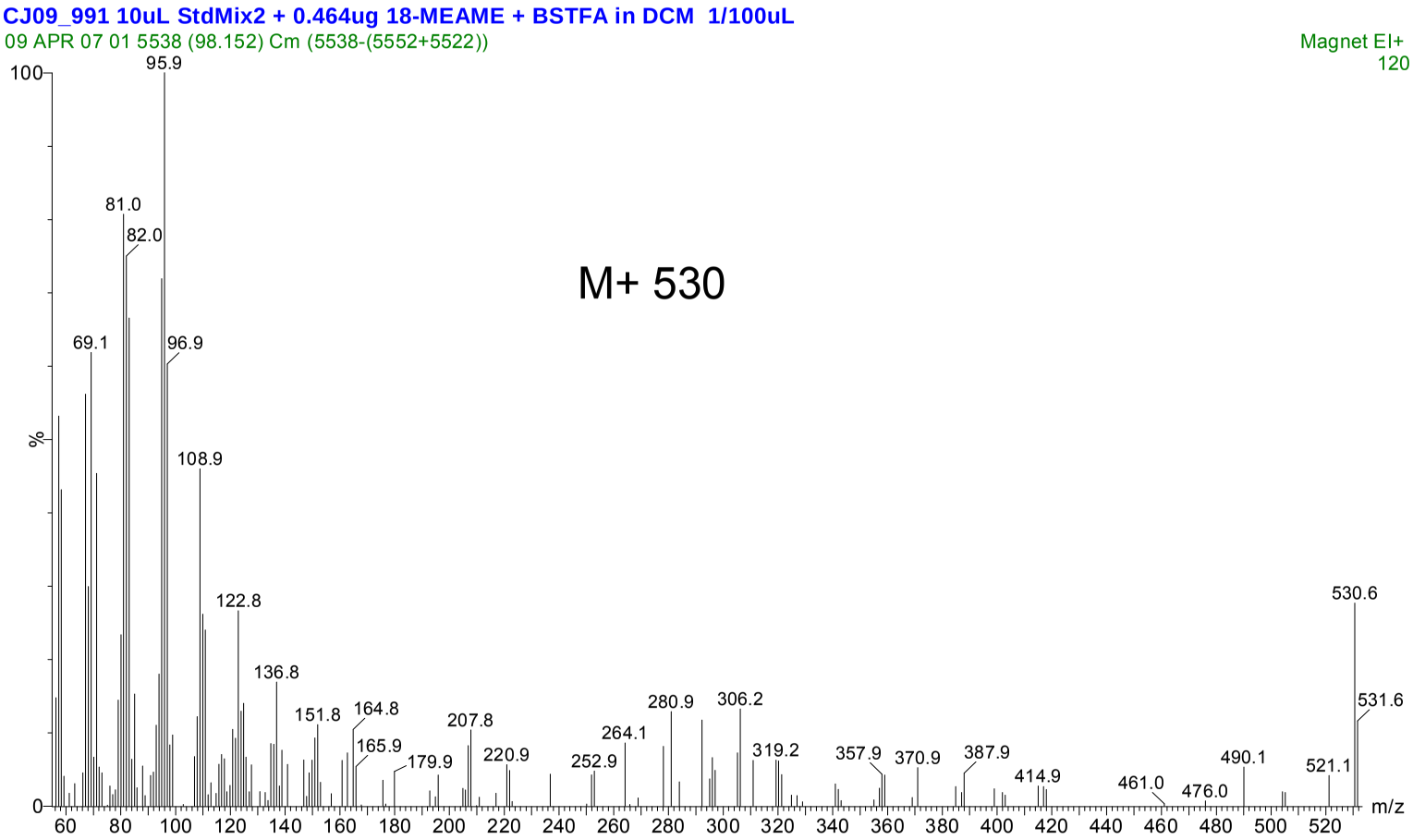

See section heading (LCAs) for source and spectra references

76: $C_{37:2}$ methyl (sample spectrum)

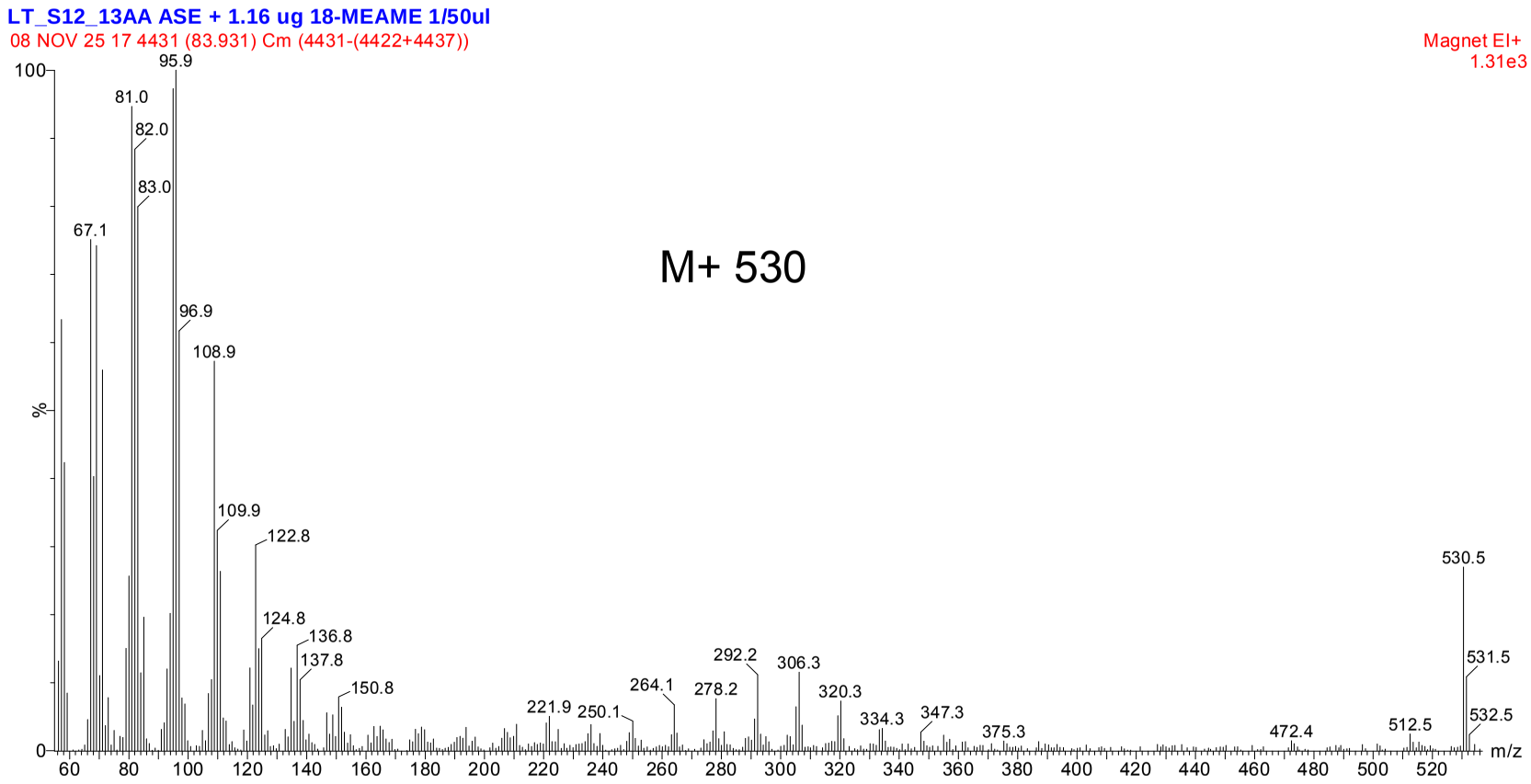

See section heading (LCAs) for source and spectra references

77: $C_{38:2}$ ethyl (reference spectrum)

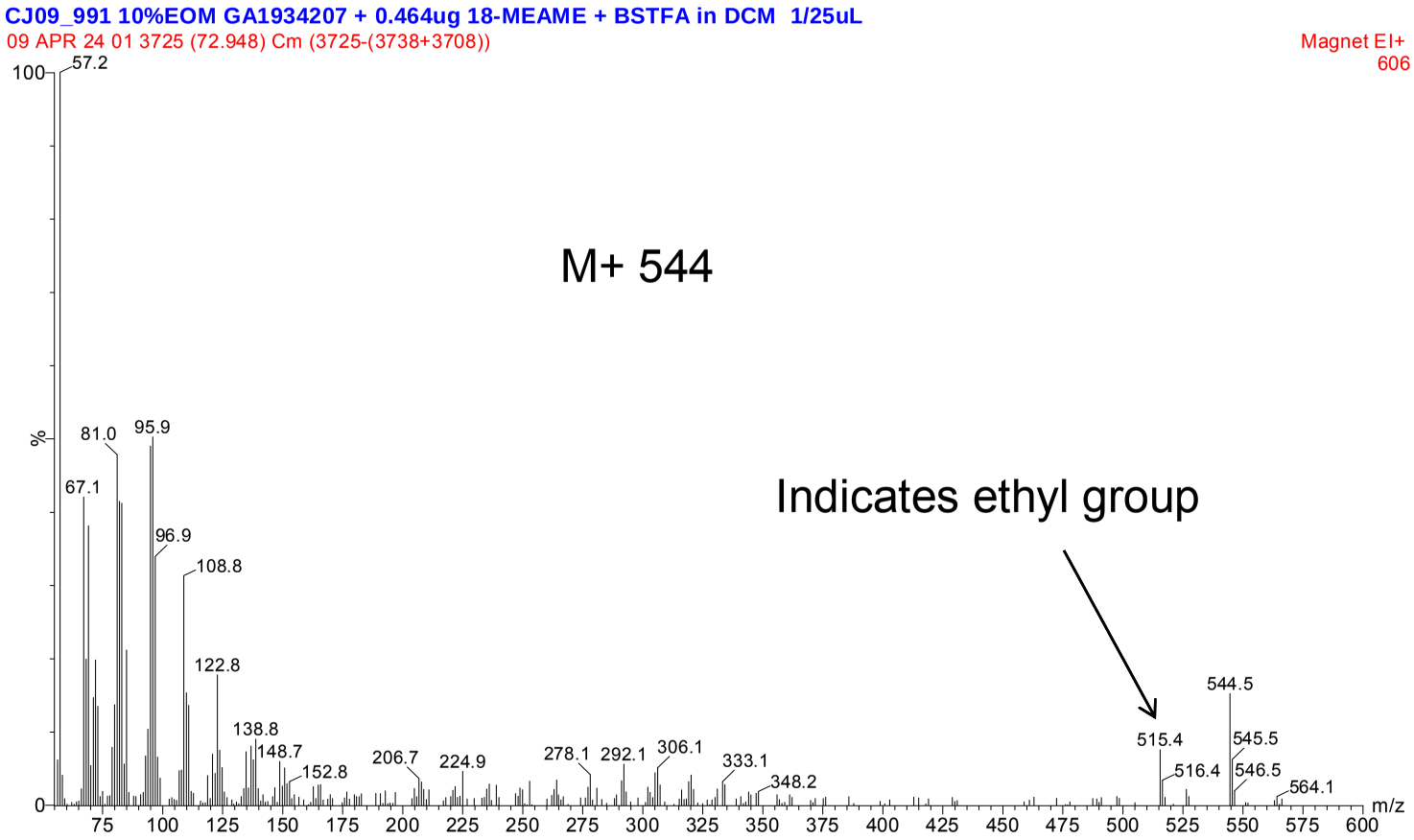

See section heading (LCAs) for source and spectra references

$C_{38:2}$ methyl (comes after ethyl, no 515 peak)

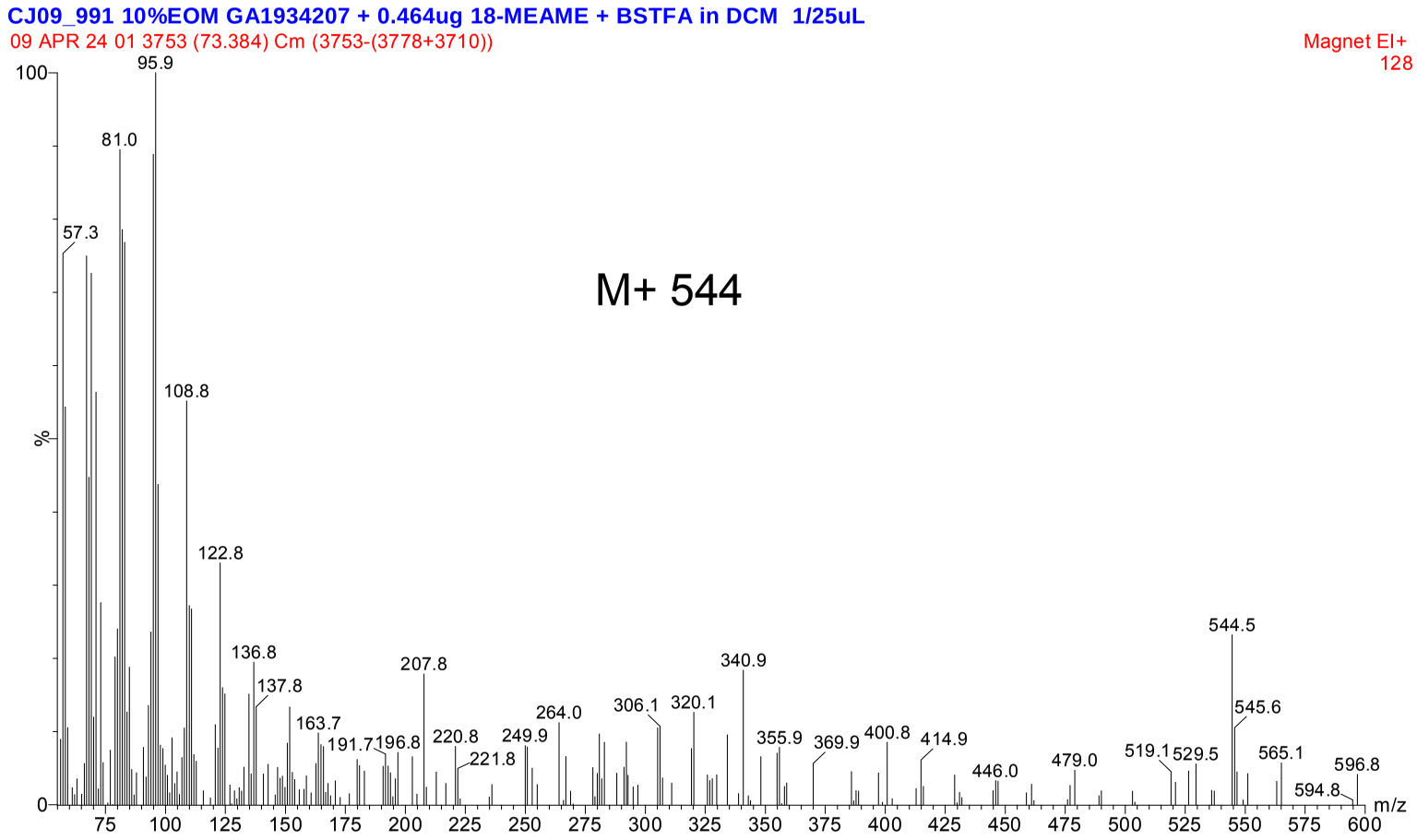

See section heading (LCAs) for source and spectra references

$C_{38:3}$ (ethyl?)

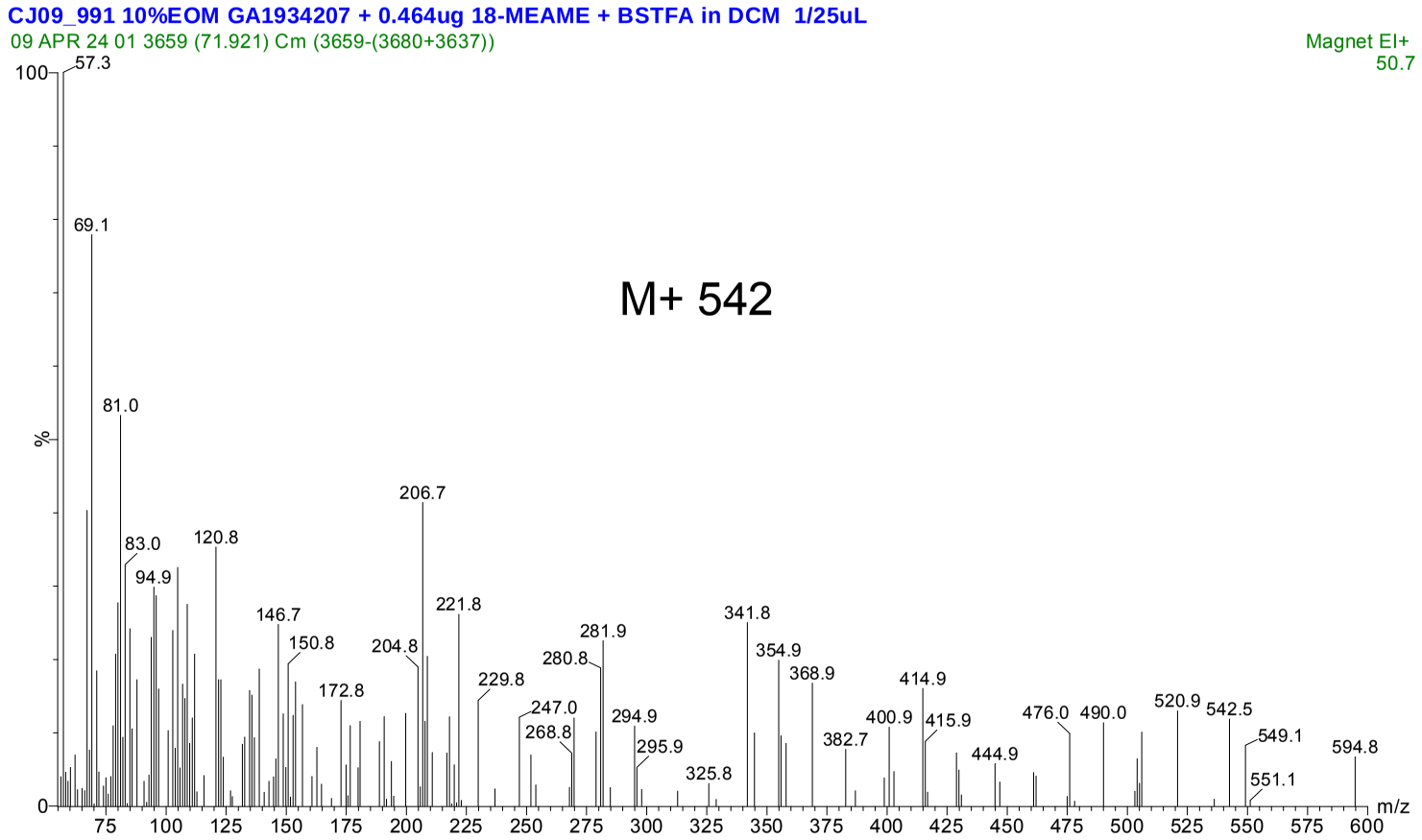

See section heading (LCAs) for source and spectra references

$C_{38:3}$ (methyl?)

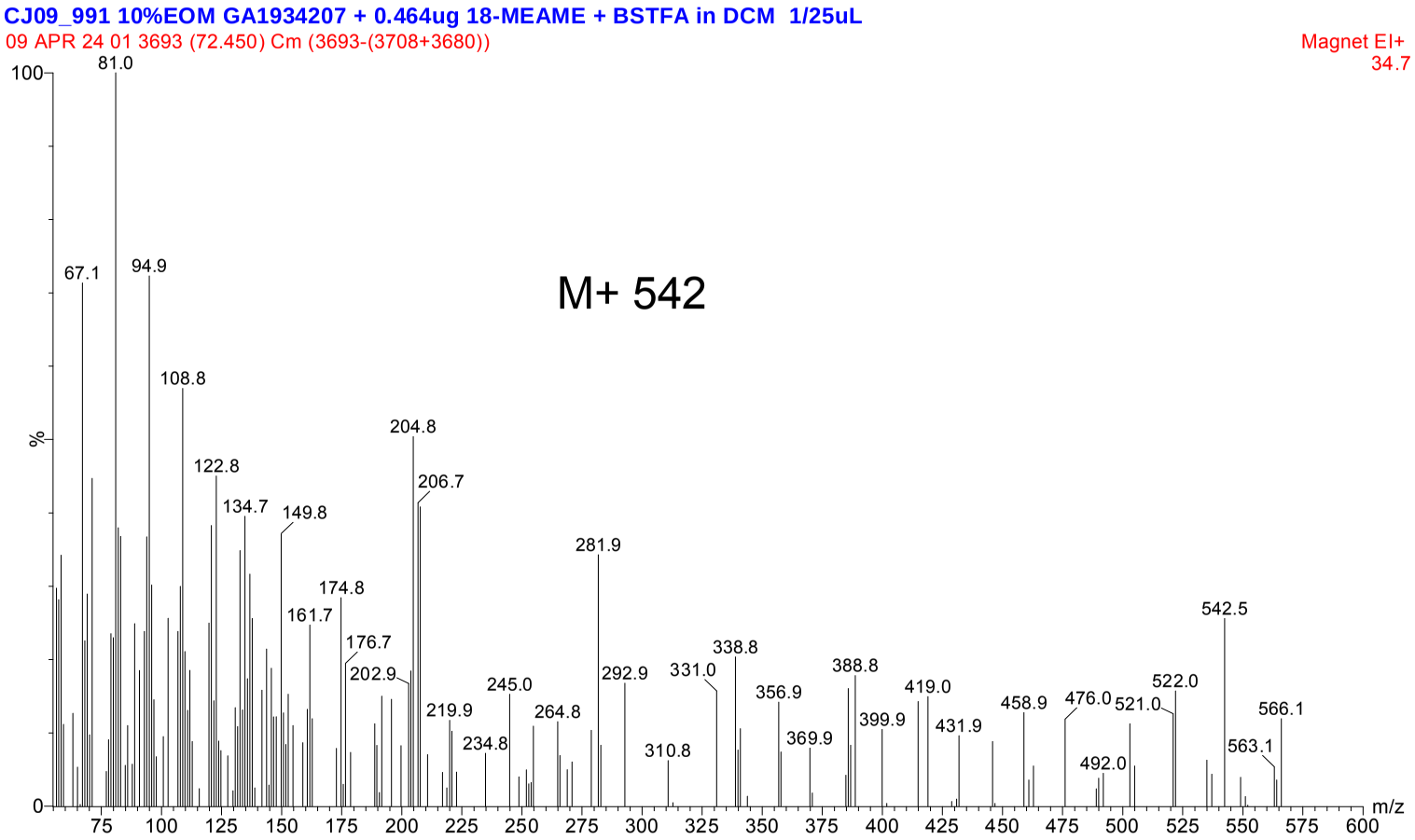

See section heading (LCAs) for source and spectra references

78: $C_{39:2}$ (reference spectrum)

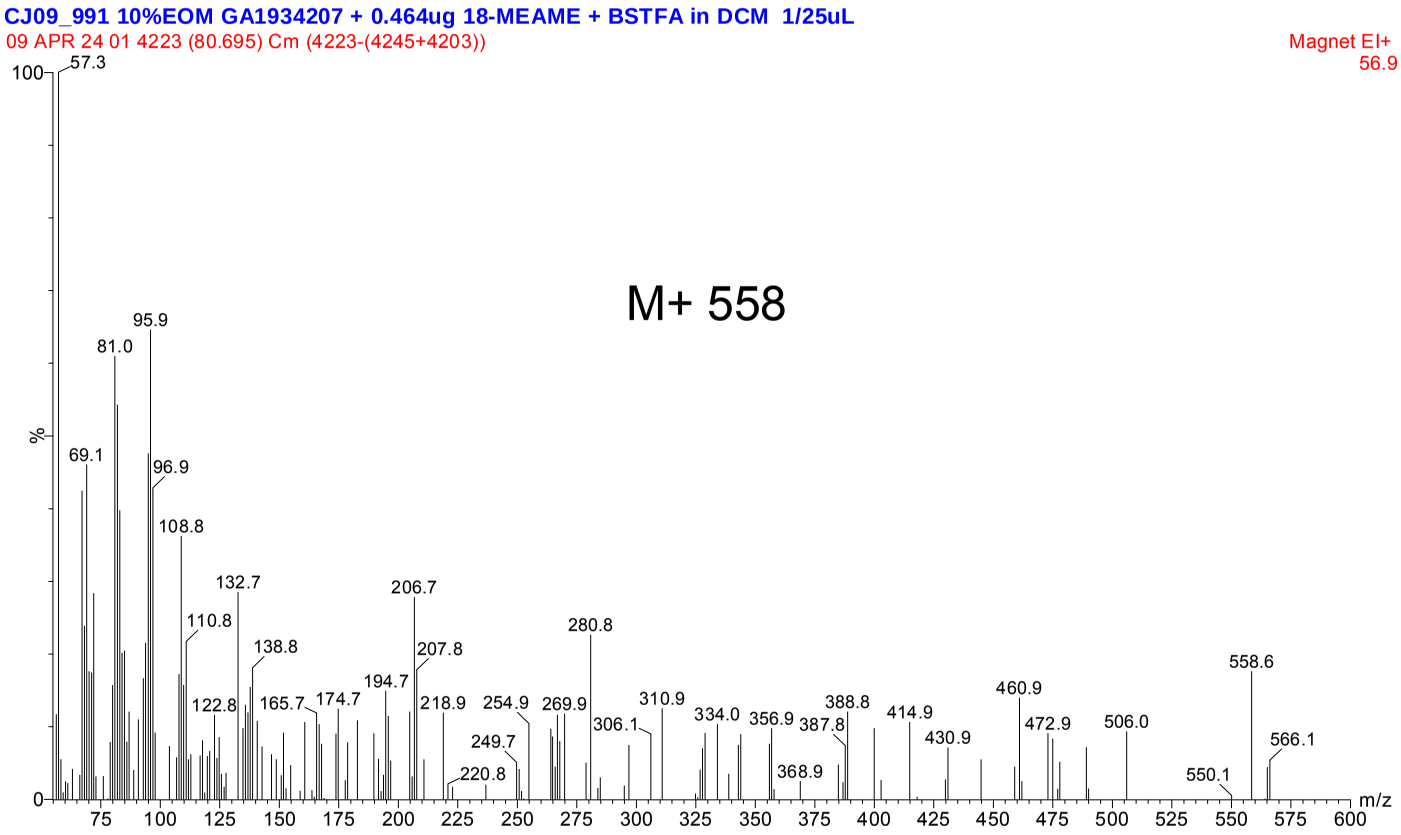

See section heading (LCAs) for source and spectra references

Mystery alkenone?

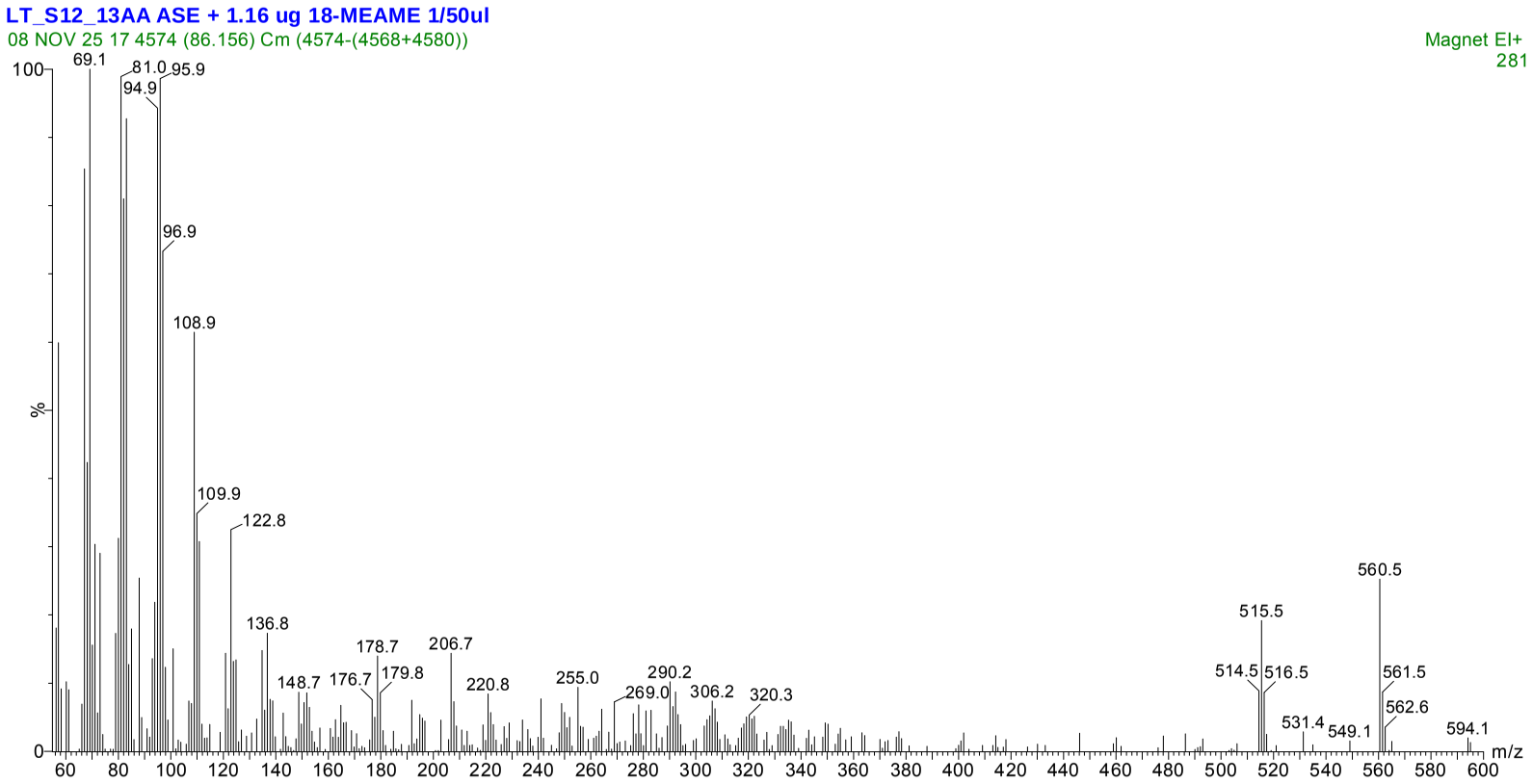

See section heading (LCAs) for source and spectra references

Miscellaneous & unidentified or tentatively identified lipids

79: Alpha-tocopherol (sample spectrum)

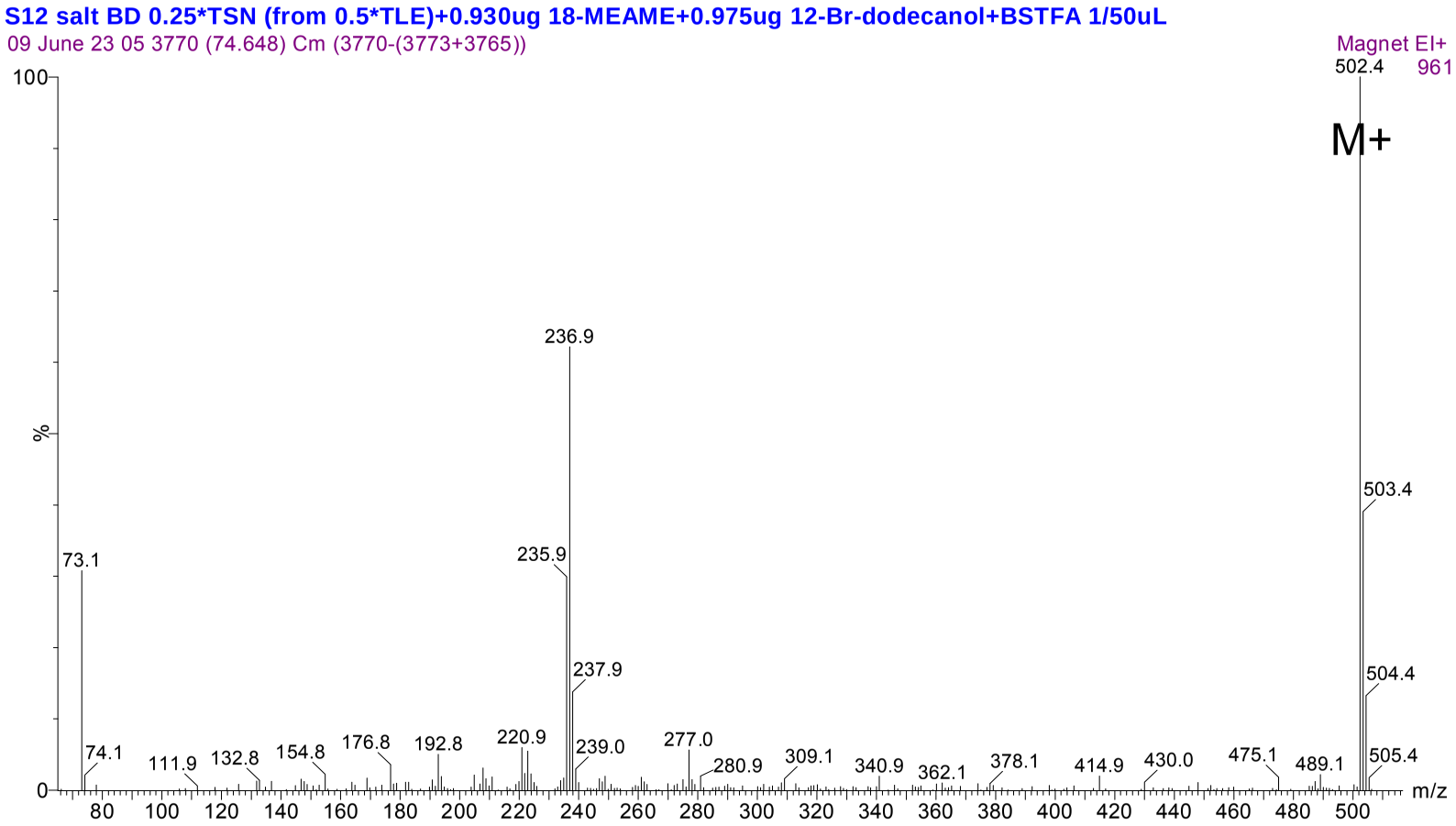

Source: chloroplasts of all photosynthetic organisms, including higher plants and cyanobacteria

Scherf & Rullkotter (2009), *Organic Geochemistry* vol 40 pp 1018

79: Alpha-tocopherol (NIST Library)

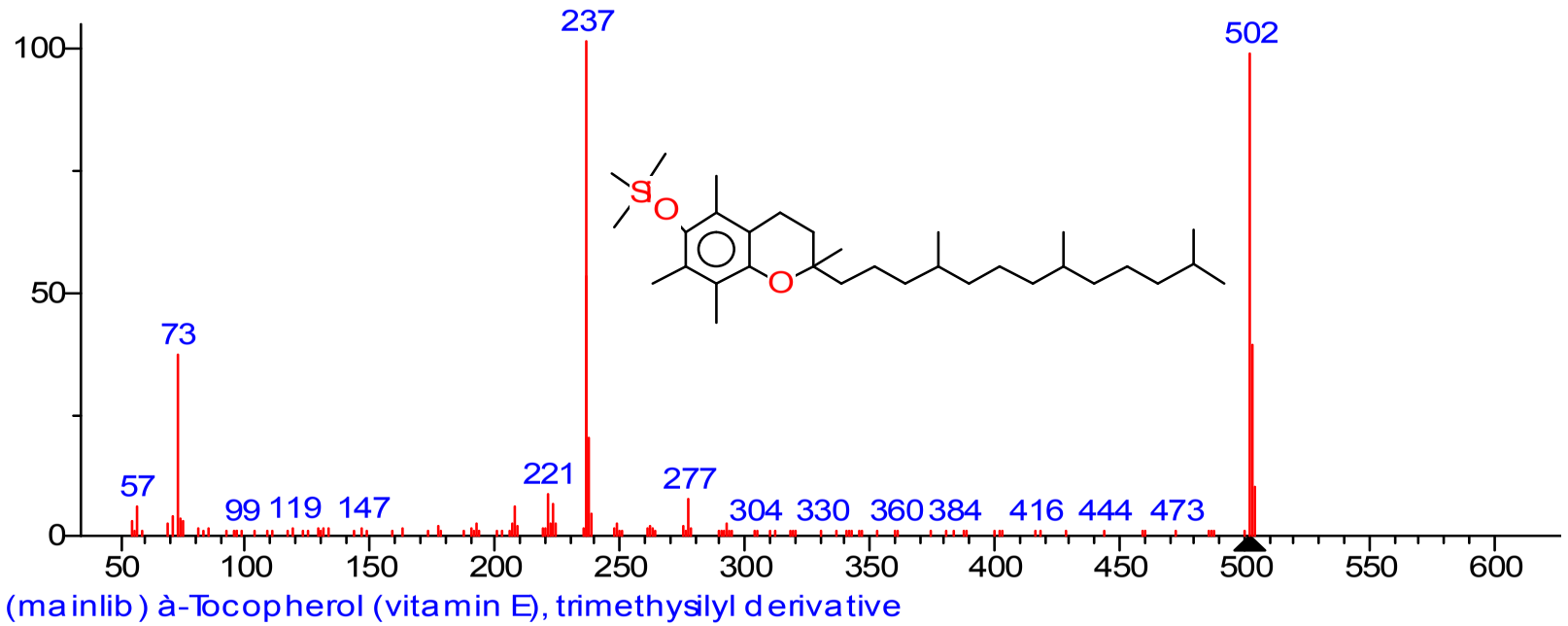

342

80: U1: C_{29} sterol, possibly 4,24-dimethylcholestenol

C29, 5 DBEs
C29 Δ5 or Δ7 Stenol

Sources: Dinoflagellates – known to produce 4,24 dimethyl sterols and stanols
Volkman *et al* (1998)
Organic Geochemistry vol 29,pp 1163-1179

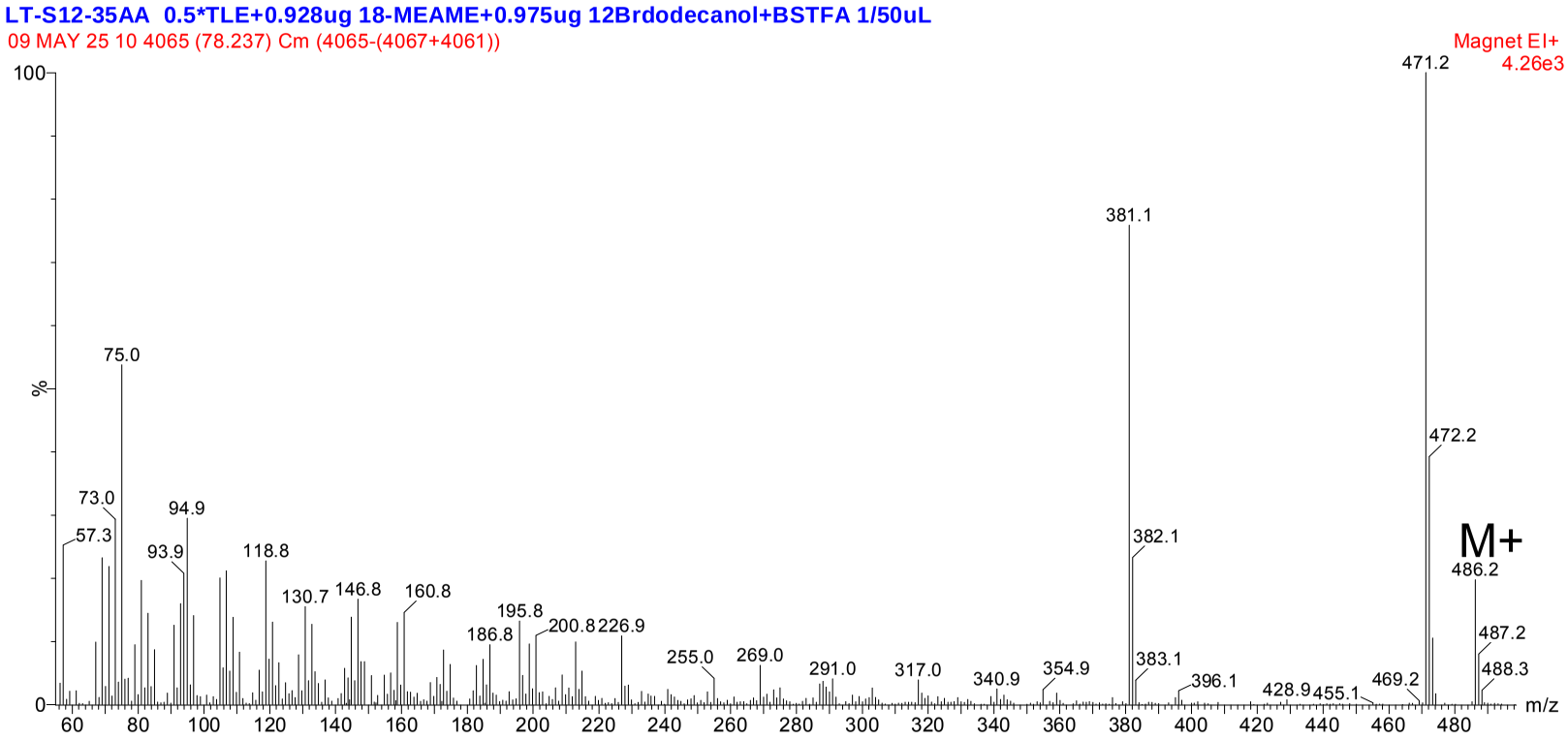

81: U2: C_{29} Δ5,22 sterol

C29, 6 DBEs

C29 Δ5,22 Stenol

Sources: algal sterol? Volkman *et al* (1998)

Organic Geochemistry vol 29,pp 1163-1179

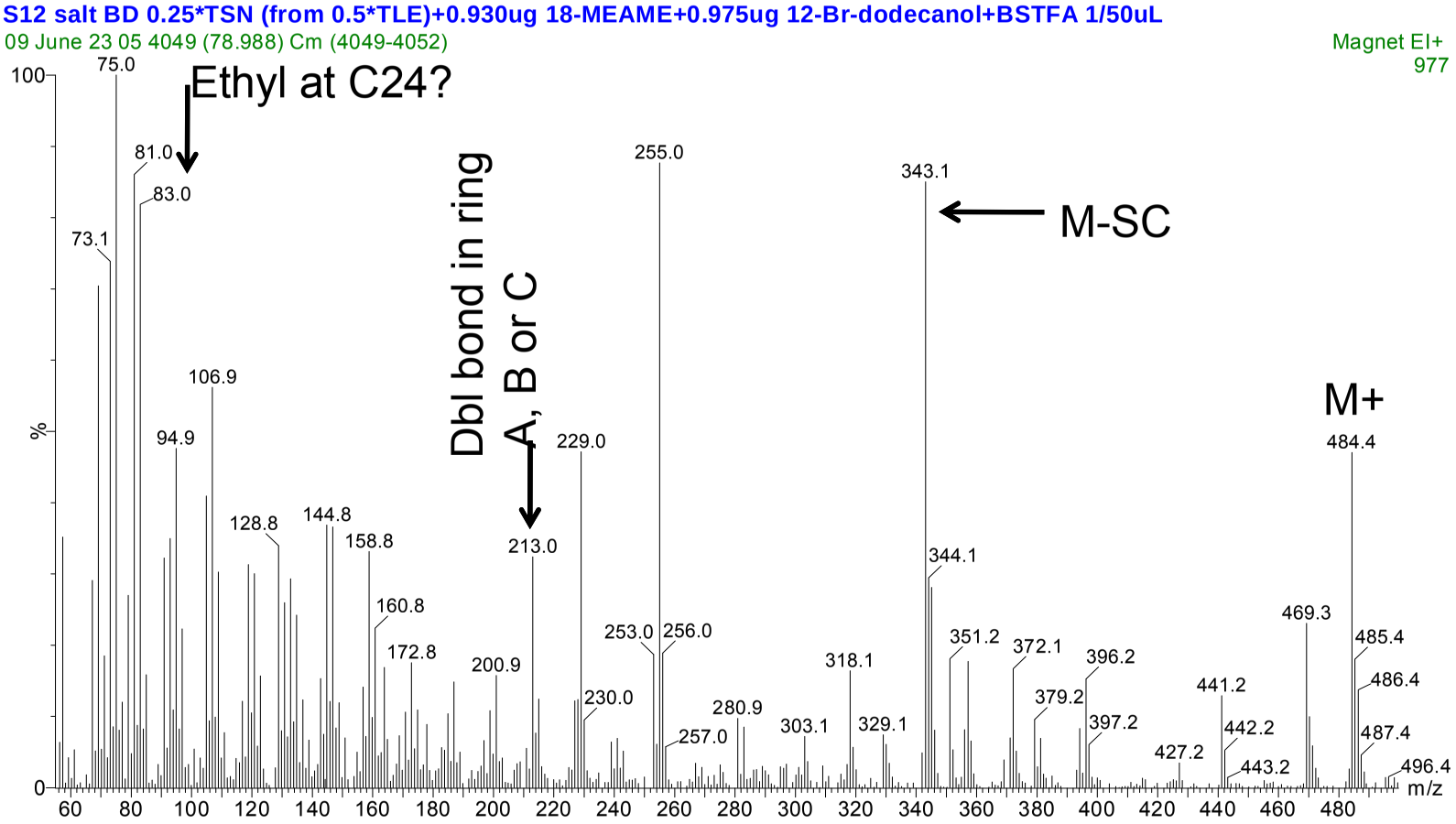

82: U3: C_{30} sterol

C30, 5 DBEs

C30 Δ? Stenol

Sources: microalgal sterol? Volkman *et al* (1998) *Organic Geochemistry* vol 29,pp 1163-1179

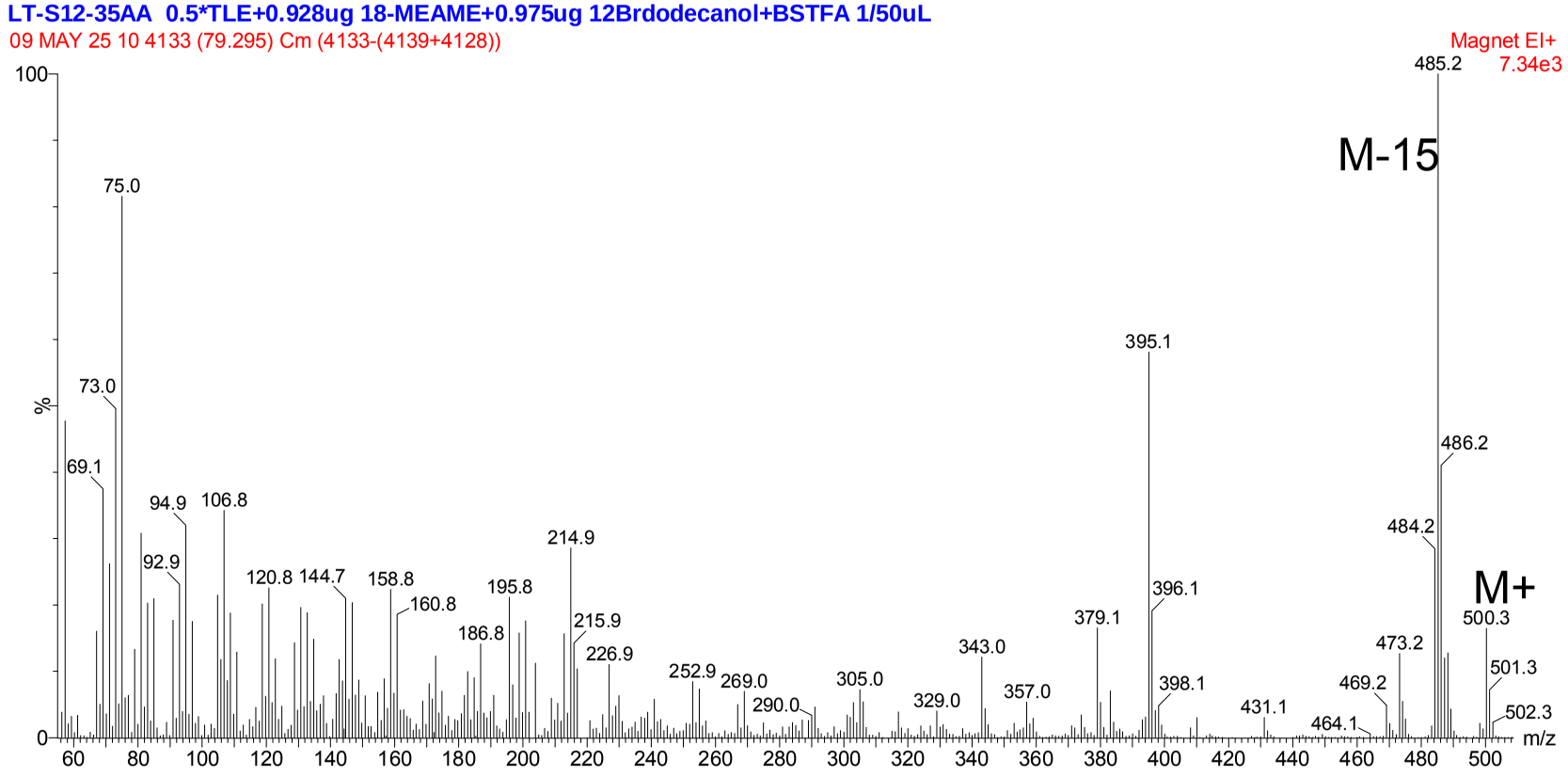

83: U4: Lupenone-like triterpenoid

C30, 6 DBEs
C30 Δ1 triterpenone

Sources: higher plants
see Heinzen *et al* (1996) *Phytochemical Analysis* vol 7, pp 237-244

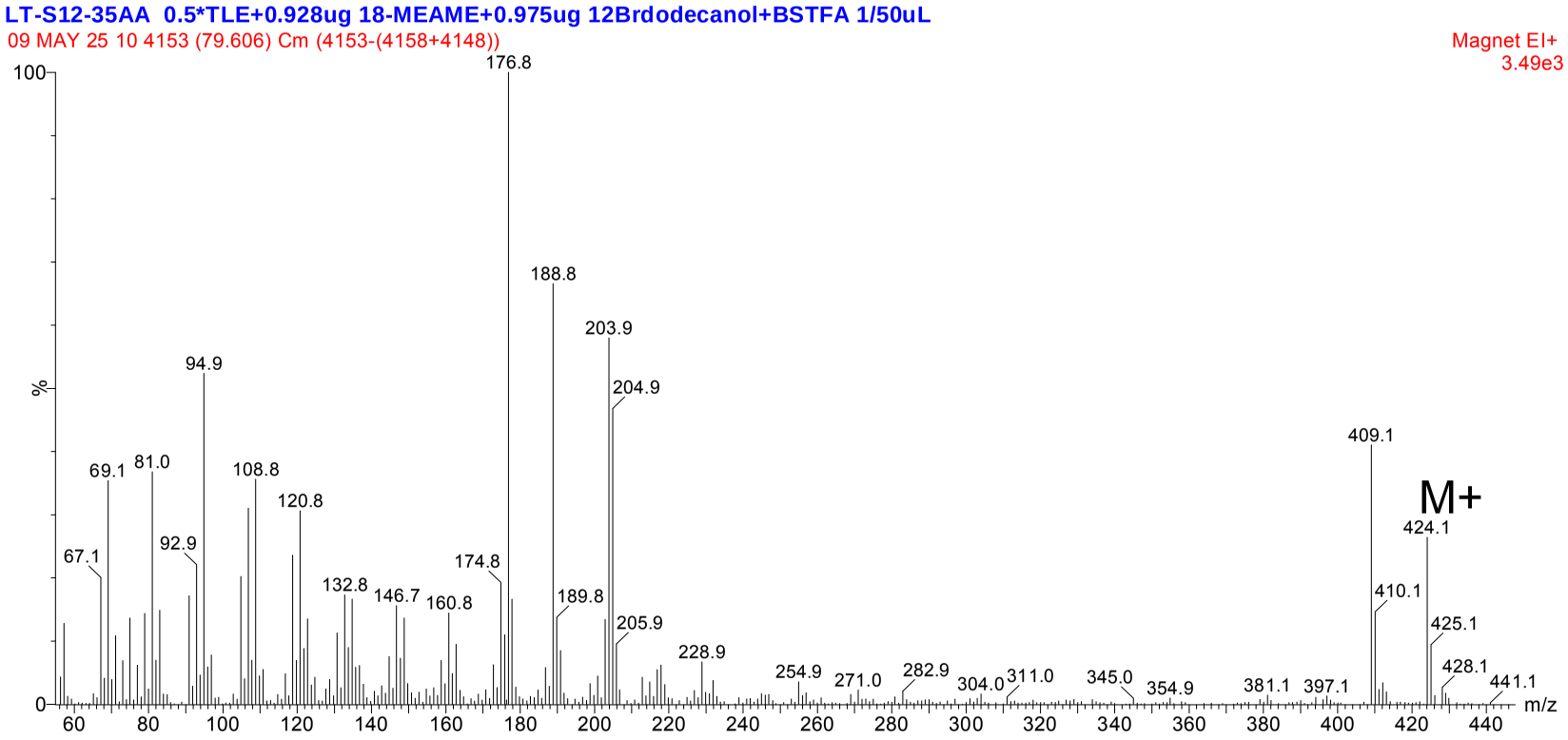

84: U5: unknown

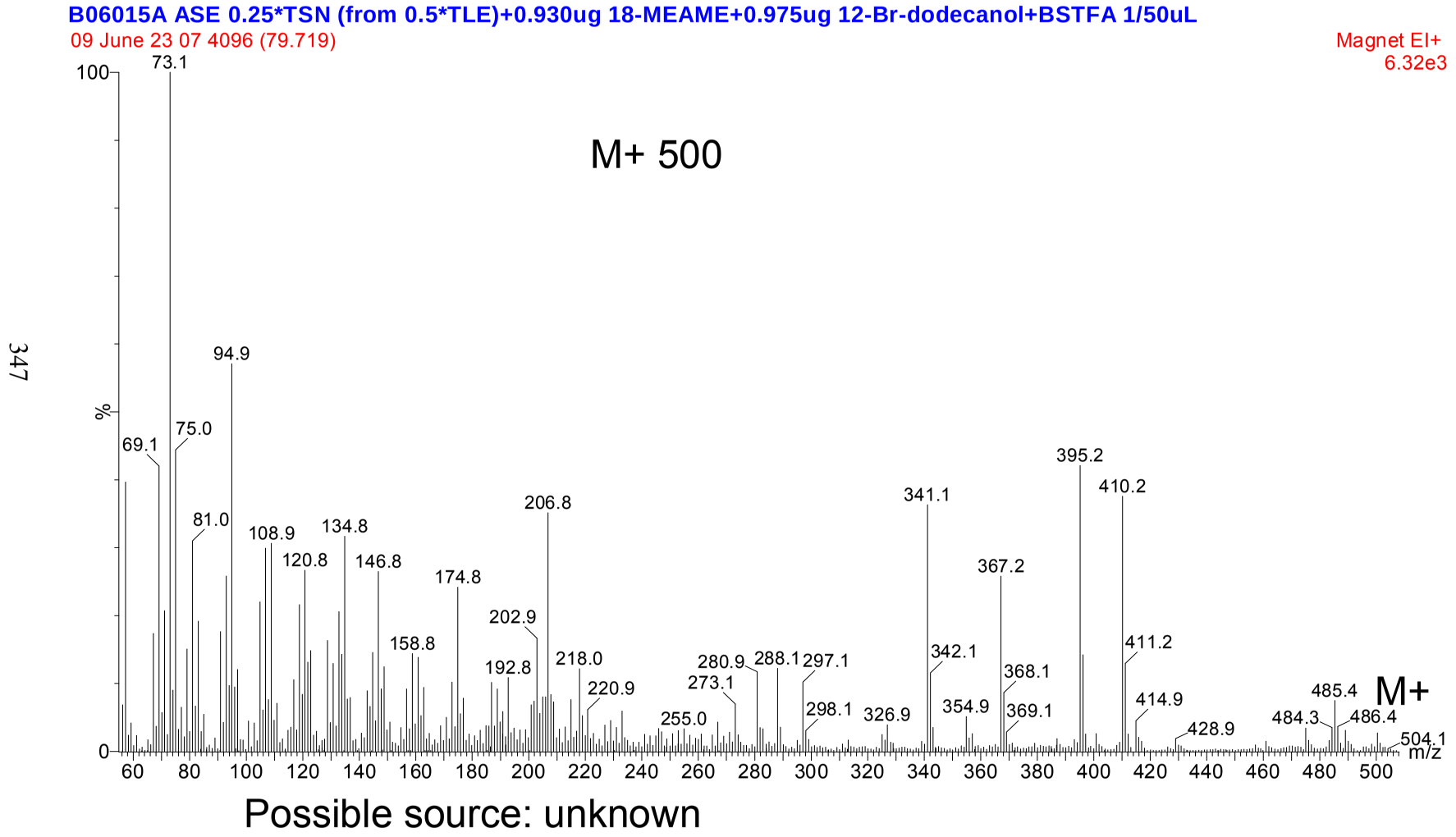

Possible source: unknown

85: U6: unknown

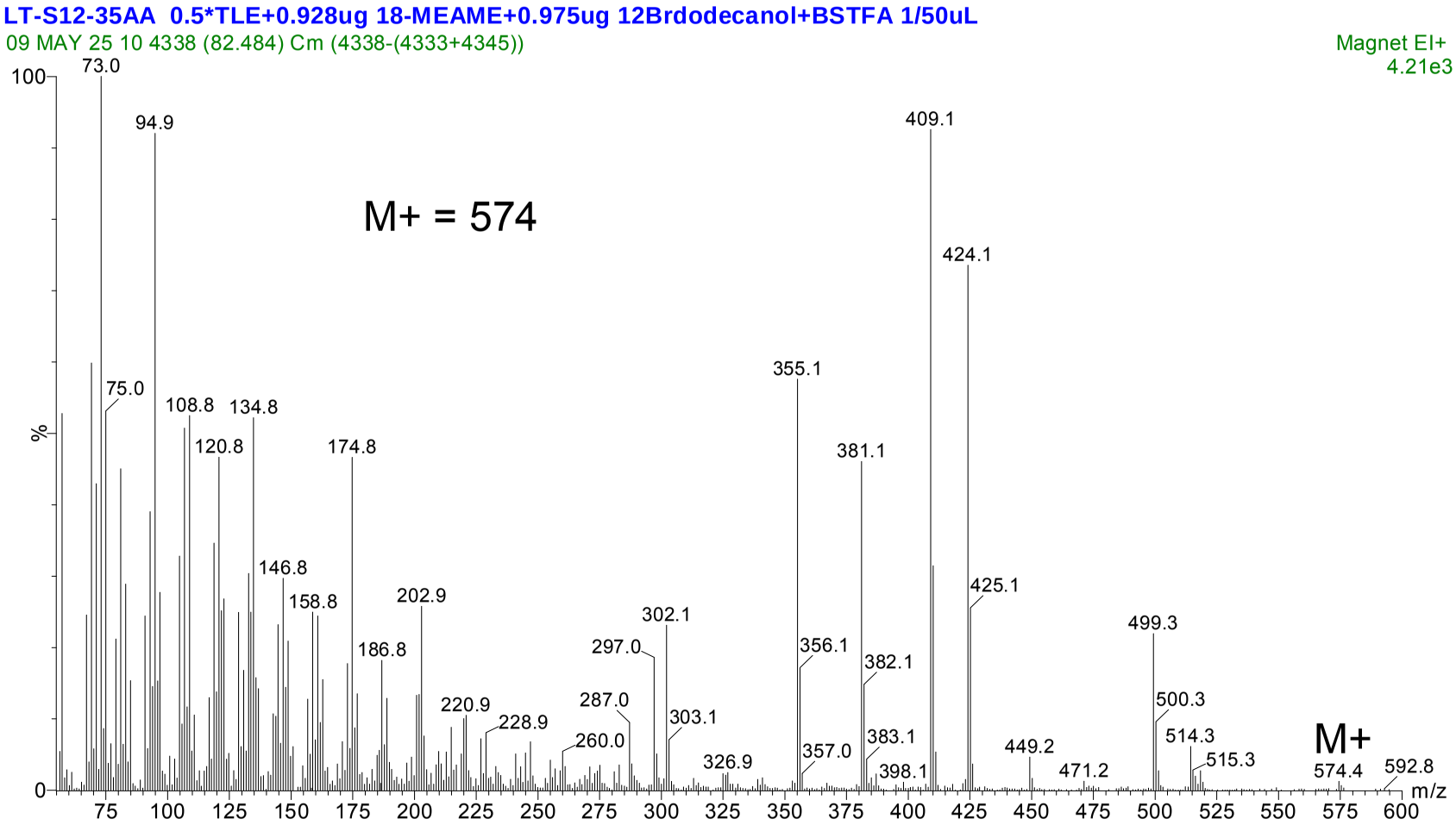

Possible source: unknown

86: U7: C_{29} sterol, possibly 24-ethylcholestenol (not Δ5 or Δ7, but some other double bond position)

C29, 5 DBEs

C29 Δ? Stenol

Sources: algal sterol? Volkman *et al* (1998) *Organic Geochemistry* vol 29,pp 1163-1179

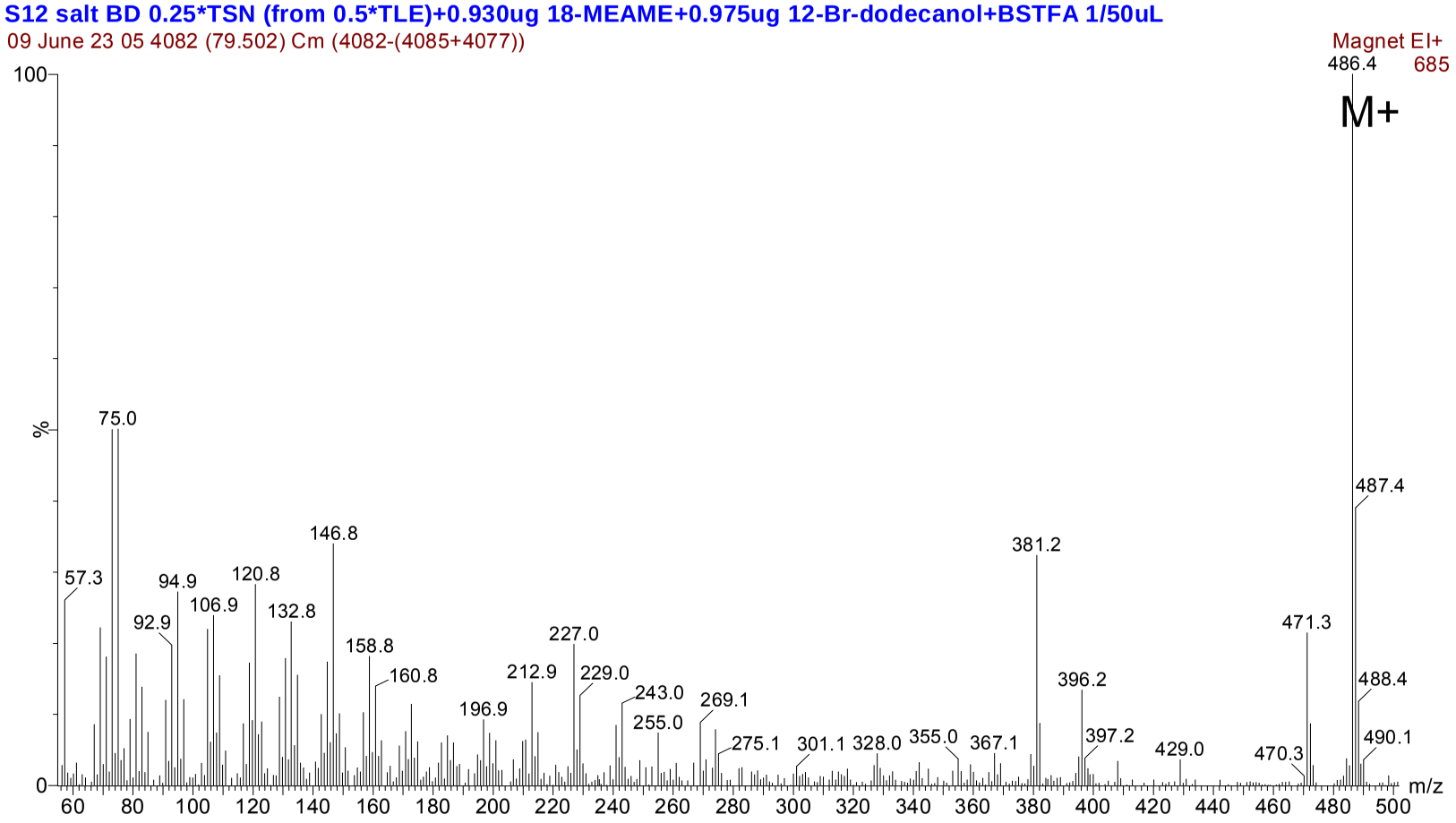

87: U8: 24-methylenecholestanol (stereochemistry unknown, likely 5α,3α based on elution position; but could be 5β,3α or 5α,3β)

C28, 5 DBEs
C28 Δ24(28) Stanol

Sources: Biohydrogenation of sterol produced by dinoflagellates or diatoms; or isomerization of 24-methyl-5β-cholestan-24(28)-en-3β-ol in sediments

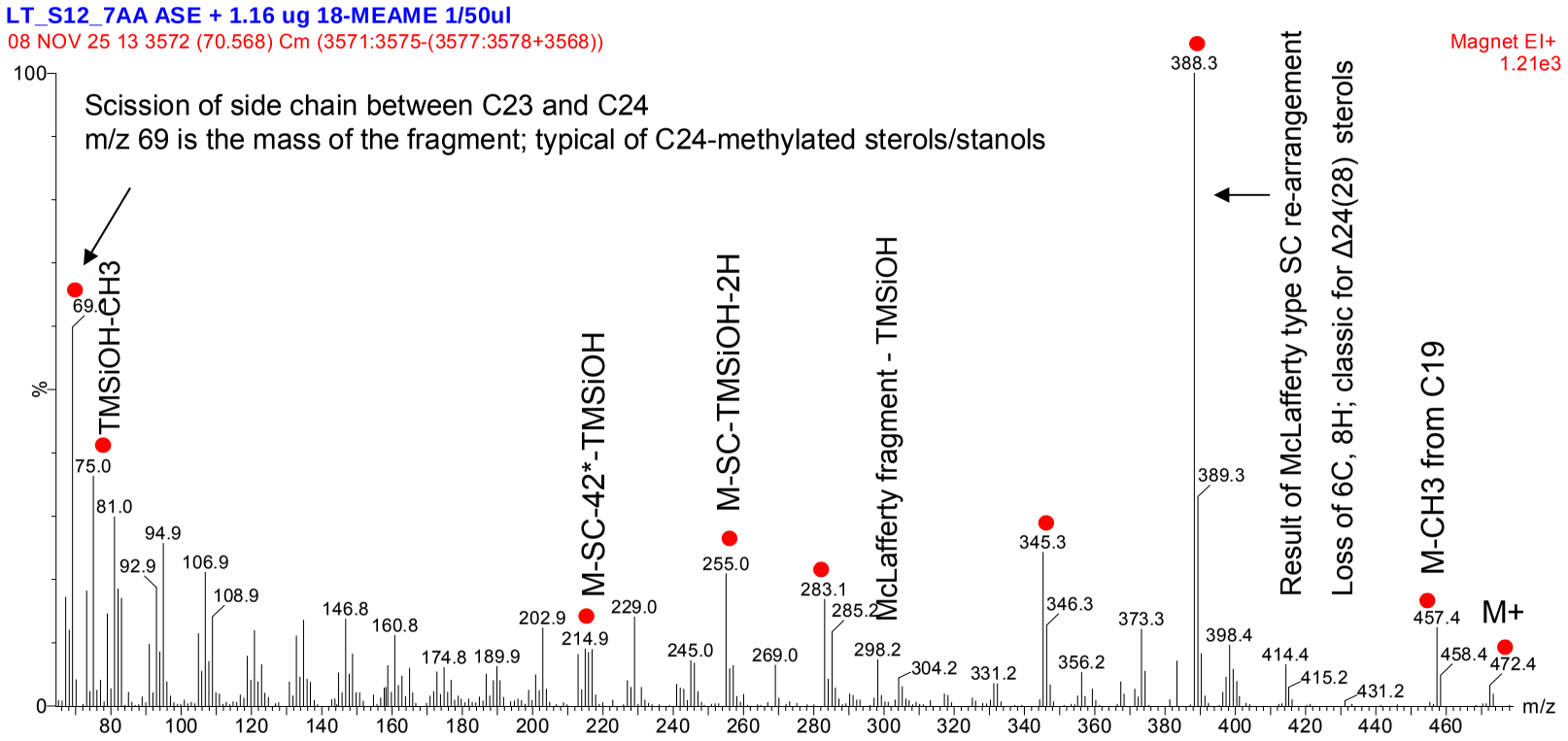

- Red dots indicate major ions
  MS id'd by comparison with 24-methyl-5B-cholestan-24(28)-en-3B-ol

*42 is C15, C16, C17, 6H

88: U9: C_{28} sterol, Me-group probably in sidechain, double bond position unknown

C28, 5 DBEs
C28 Δ? Stenol

Sources: unknown, though C_{28} sterols are produced by most microalgae - see Volkman *et al* (1998) *Organic Geochemistry* vol 29,pp 1163-1179

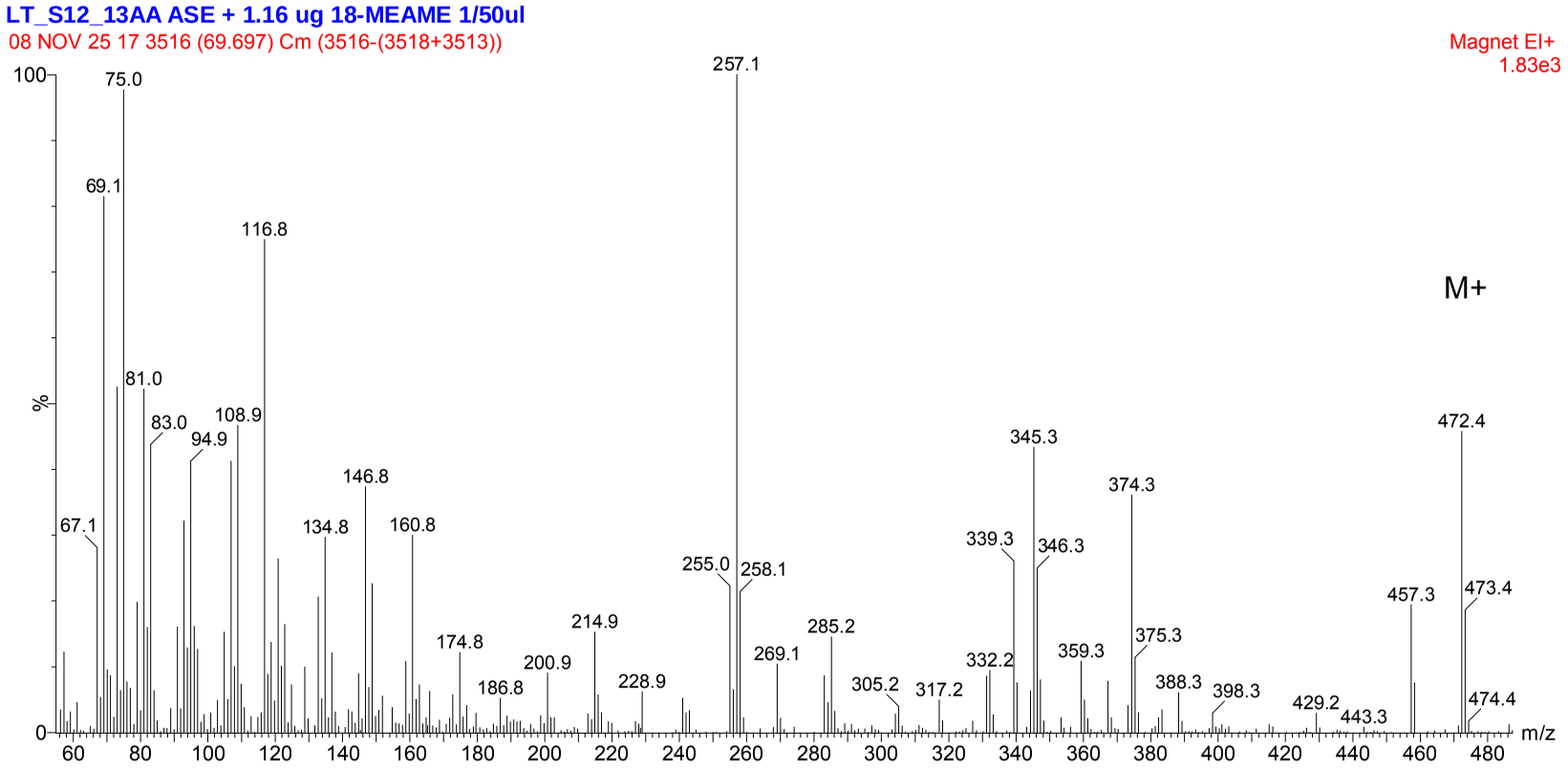

89: U10: C_{27} sterol with 8 DBEs (i.e. 4 double bonds); seems to have positional isomers or stereoisomers

C27, 8 DBEs Sources: probably produced by dehydration of cholesterol

C27 Δ?,?,?,? Stenol

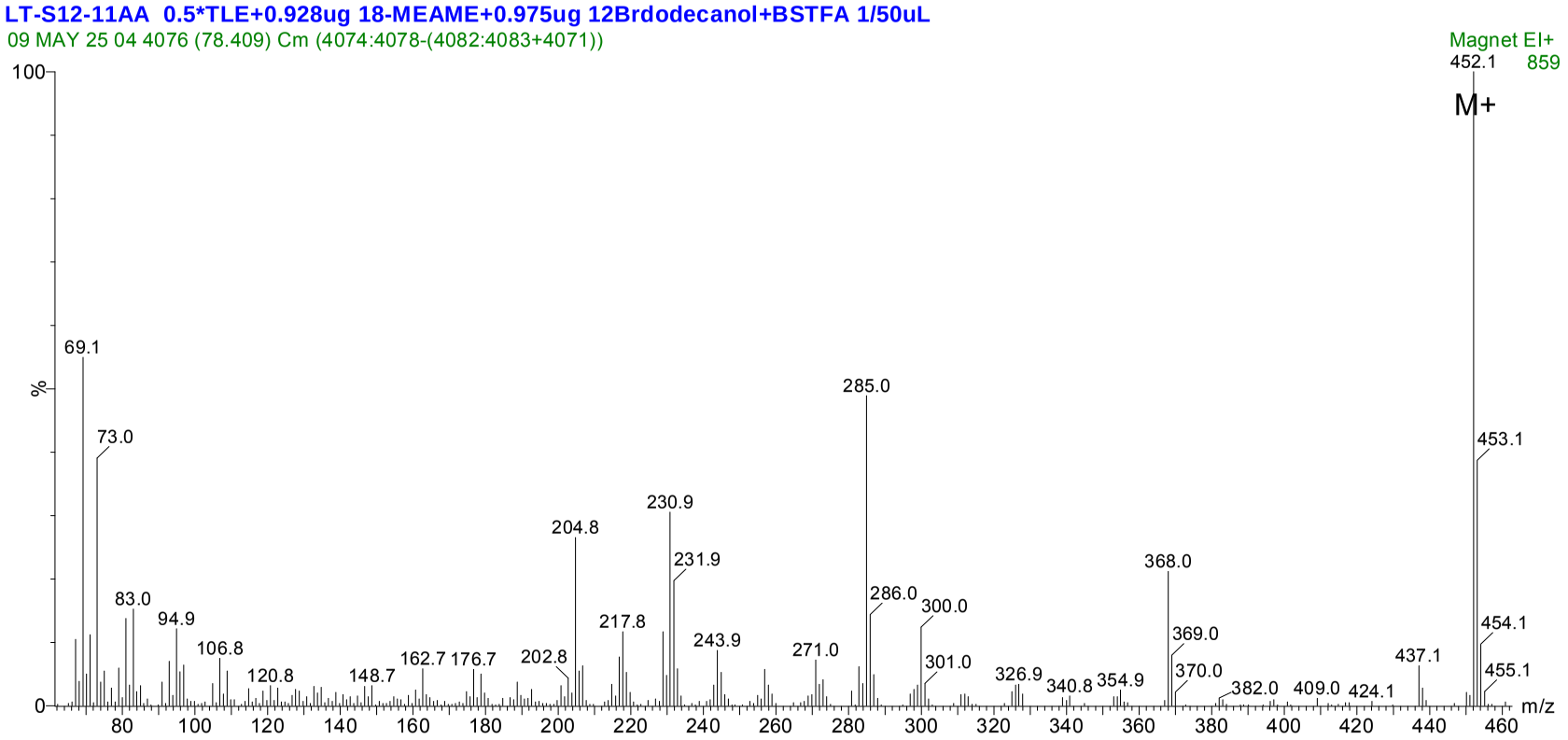

U10 stereo- or positional isomers?

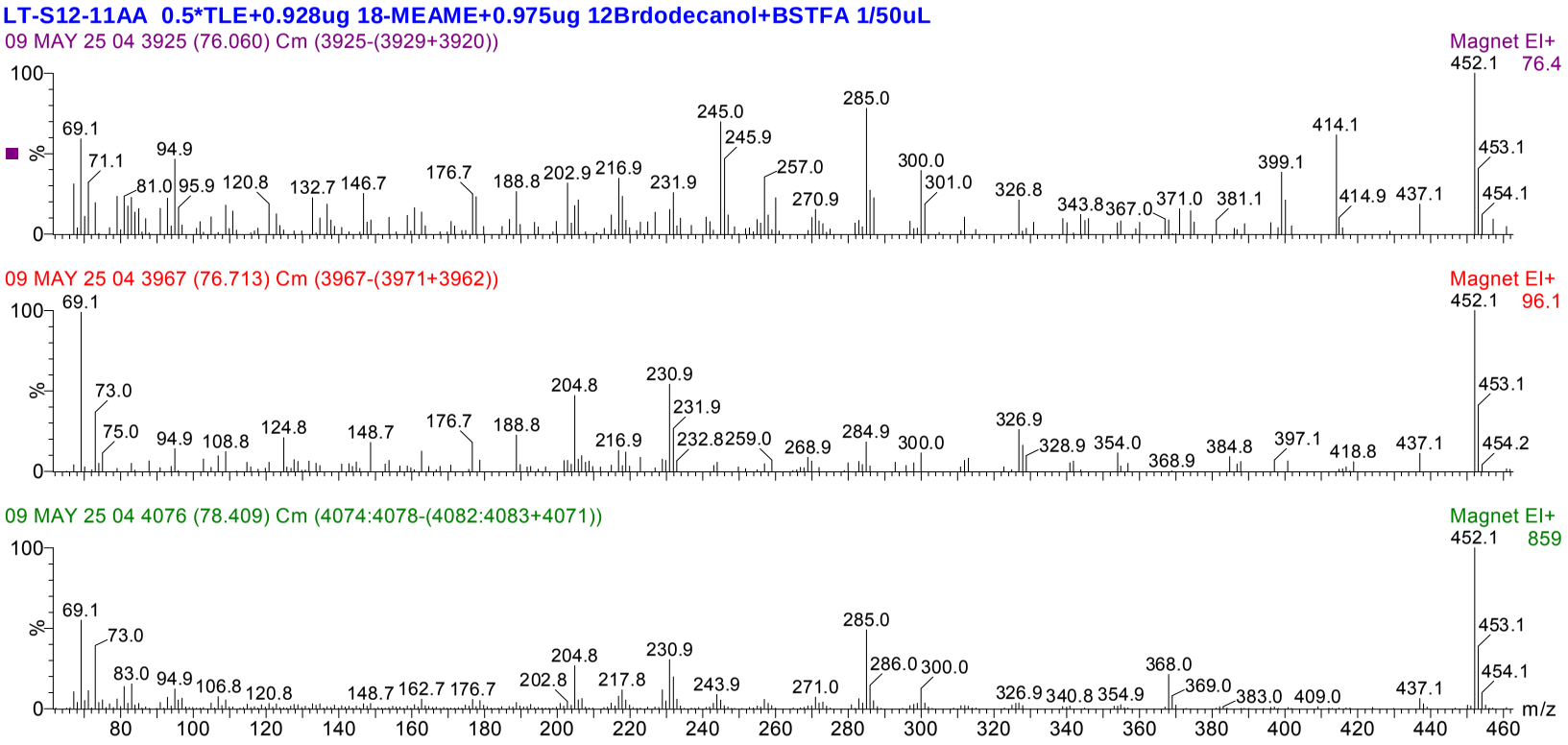

90: U11: C_{28} stanol, possibly methylated at C4 position

C28, 4 DBEs
C28 Δ0 Stanol

Sources: Microalgae* – dinoflagellates and haptophytes are known to produce 4-methyl sterols
Volkman *et al* (1998) *Organic Geochemistry* vol 29,pp 1163-1179

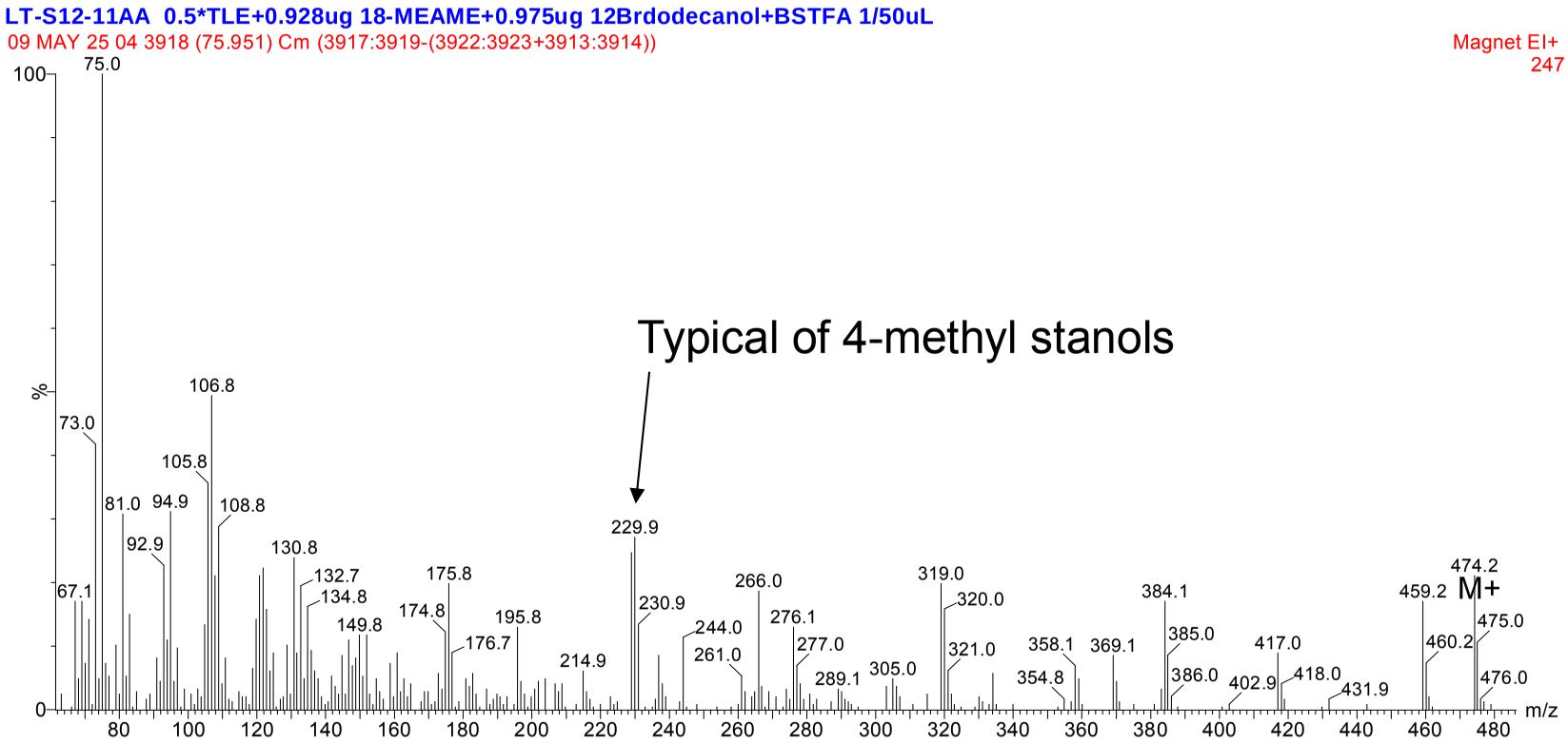

91: U12: C_{29} dimethyl stanol, 24Me Δ22; other methyl position unknown

C29, 4 DBEs
C29 Δ0 Stanol

Sources: Dinoflagellates are known to produce 4,24 dimethyl stanols; could be one of these

Volkman *et al* (1998) *Organic Geochemistry* vol 29,pp 1163-1179

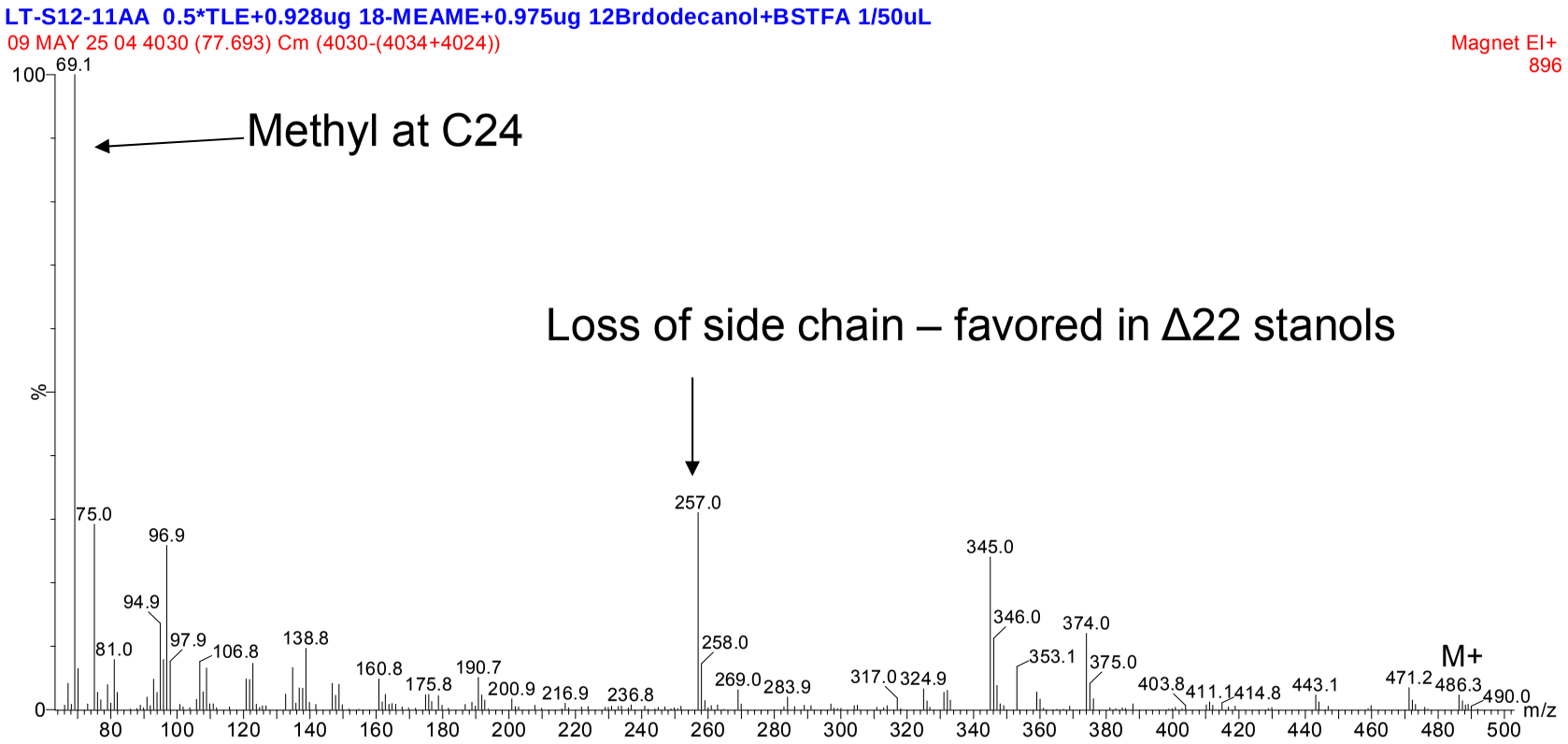

Possibly a stereo- or positional isomer of U12; only slightly separated on column, integrated together

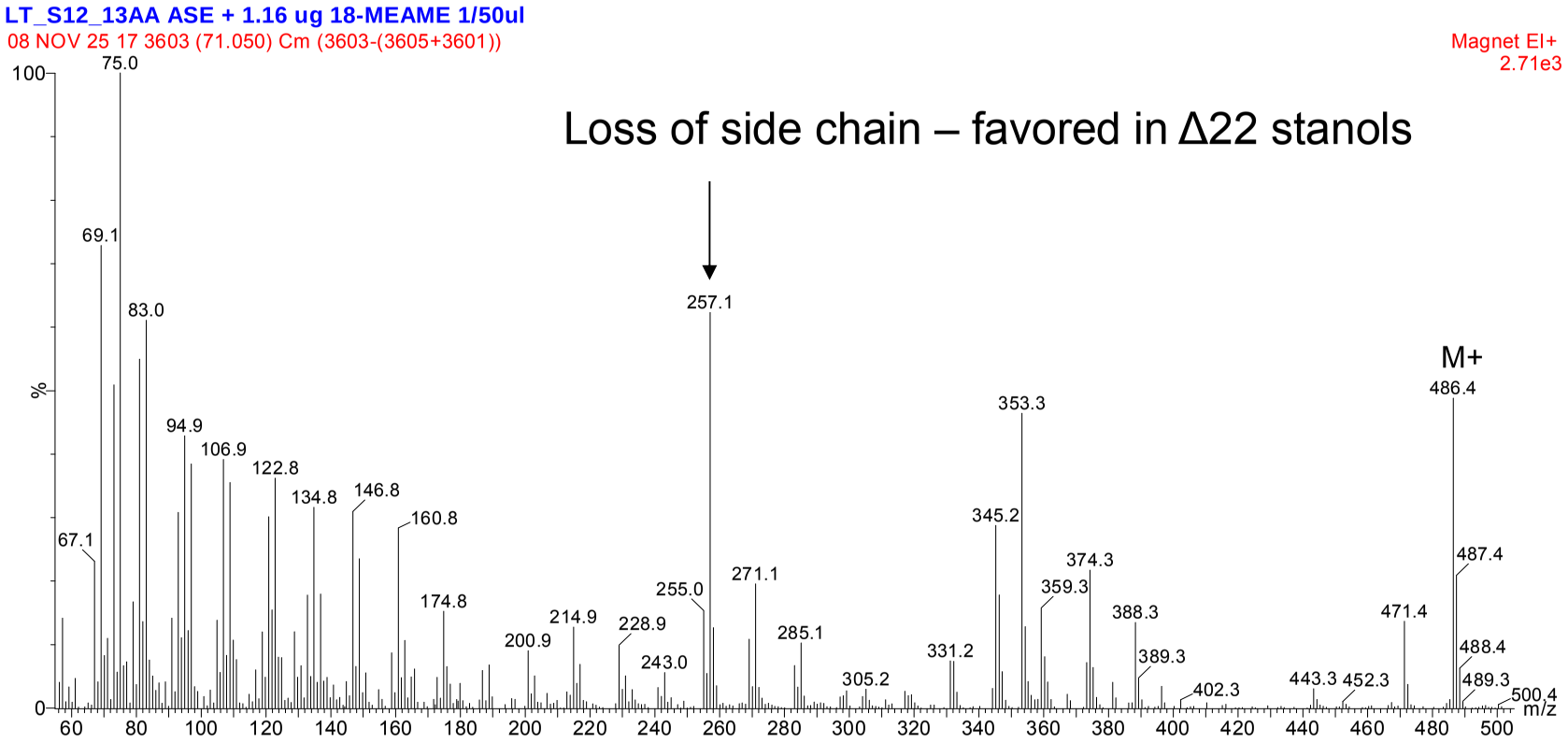

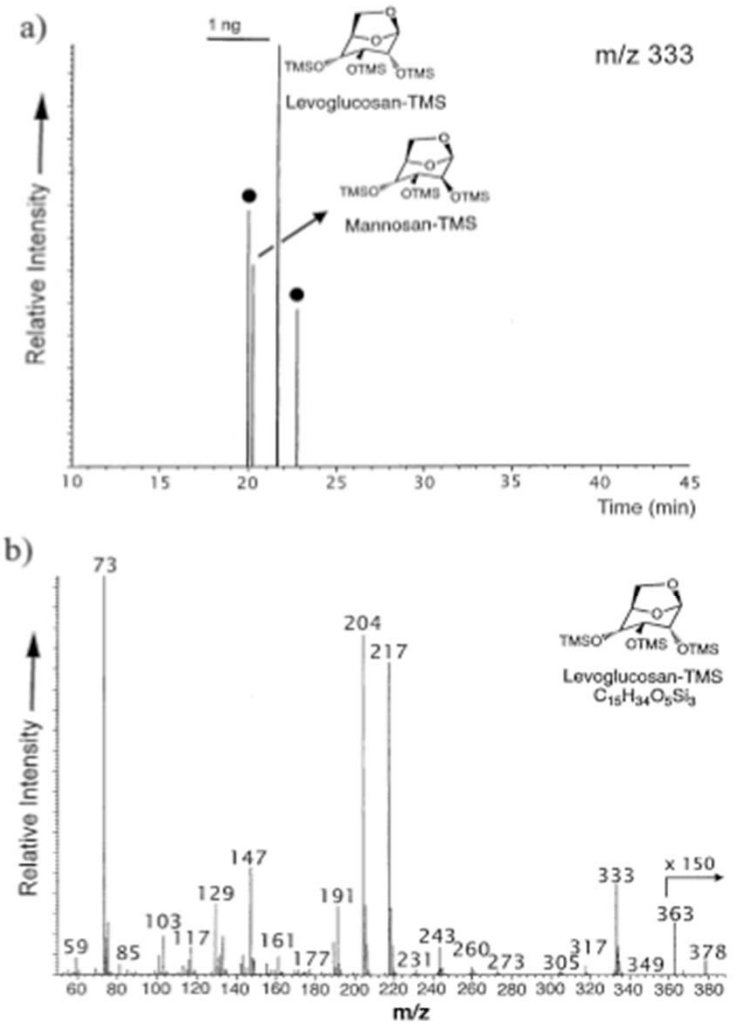

Fig. 2. Examples of (a) mass fragmentogram (m/z 333) key ion used for the characterization and quantification of levoglucosan-TMS (1,6-anhydro-β-D-glucopyranose-triTMS) and (b) mass spectrum of levoglucosan as the tritrimethylsilyl ether (dots over peaks in (a) are unknown monosaccharides).

Levoglucosan TMS

Source: biomass burning

Spectrum: Elias *et al* (2001) *Geochimica et Cosmochimica Acta*, Vol. 65, No. 2, pp 267–272

Elutes just before C12 alkanol on DB-5 MS column

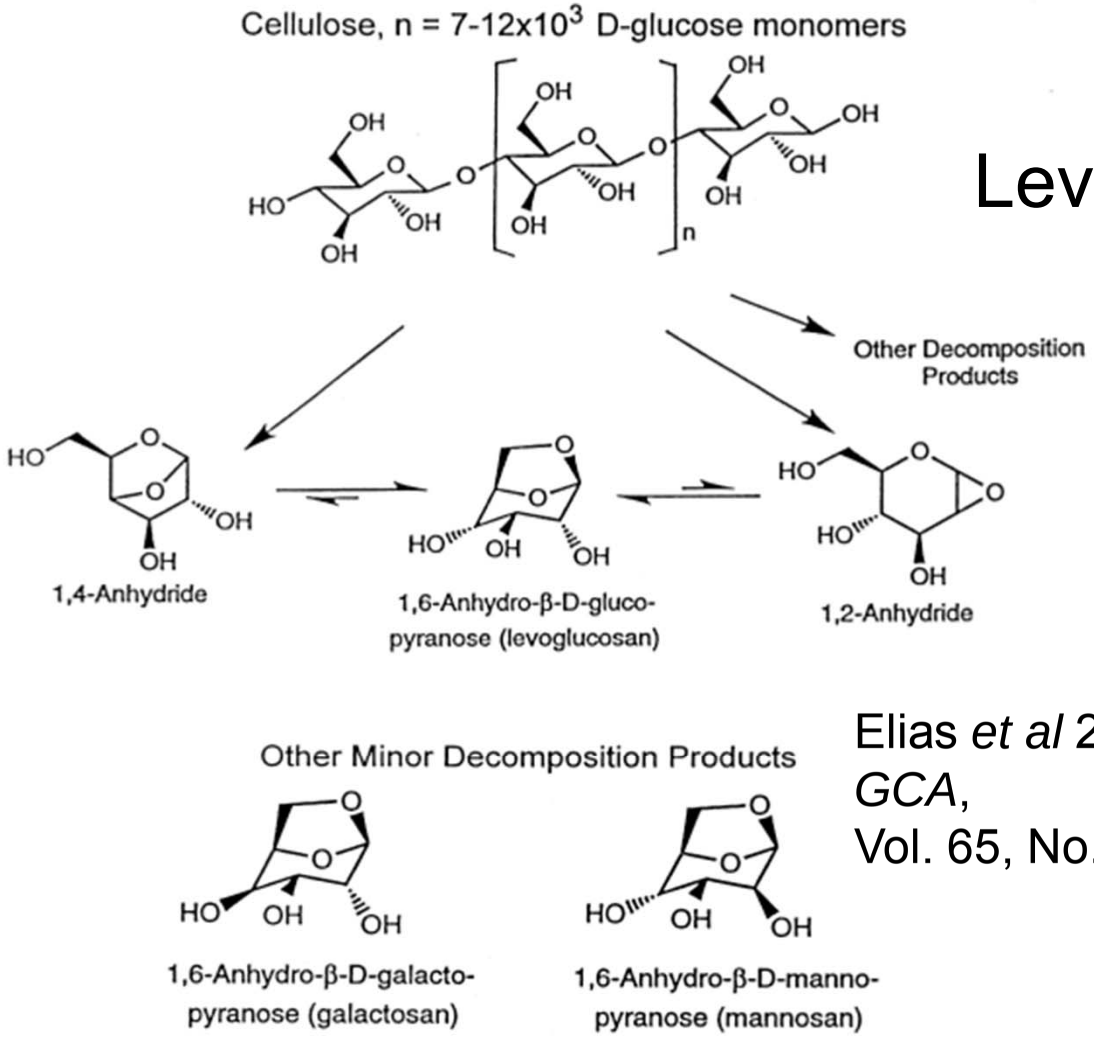

Fig. 1. Schematic showing the major decomposition products during the pyrolysis ($T > 300°C$) of cellulose and hemicellulose (adapted from Shafizadeh, 1984).

Levoglucosan source

Elias *et al* 2001
GCA,
Vol. 65, No. 2, pp. 267–272

E-15-heptadecanal (sample spectrum)

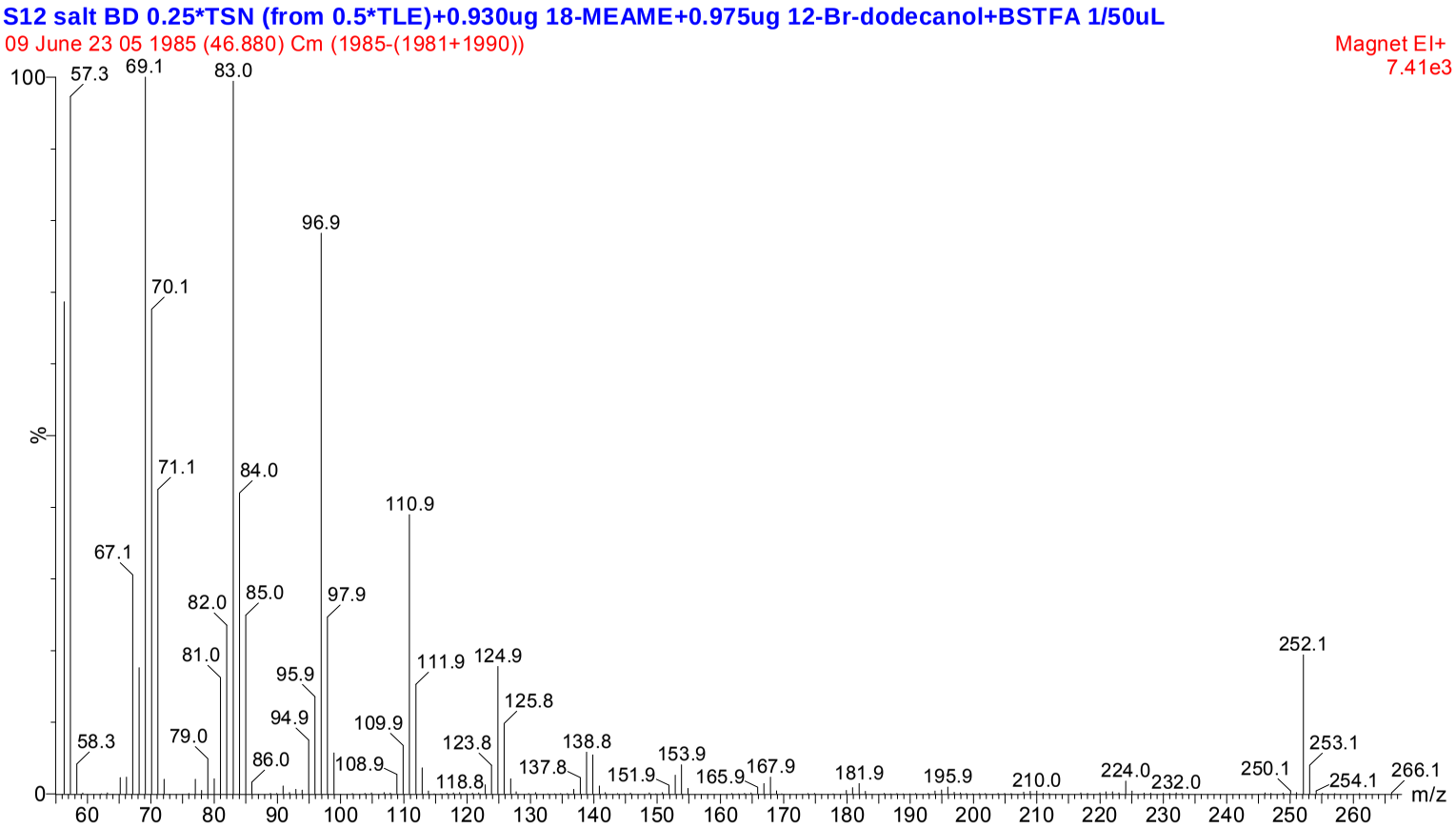

E-15-heptadecanal (NIST library)

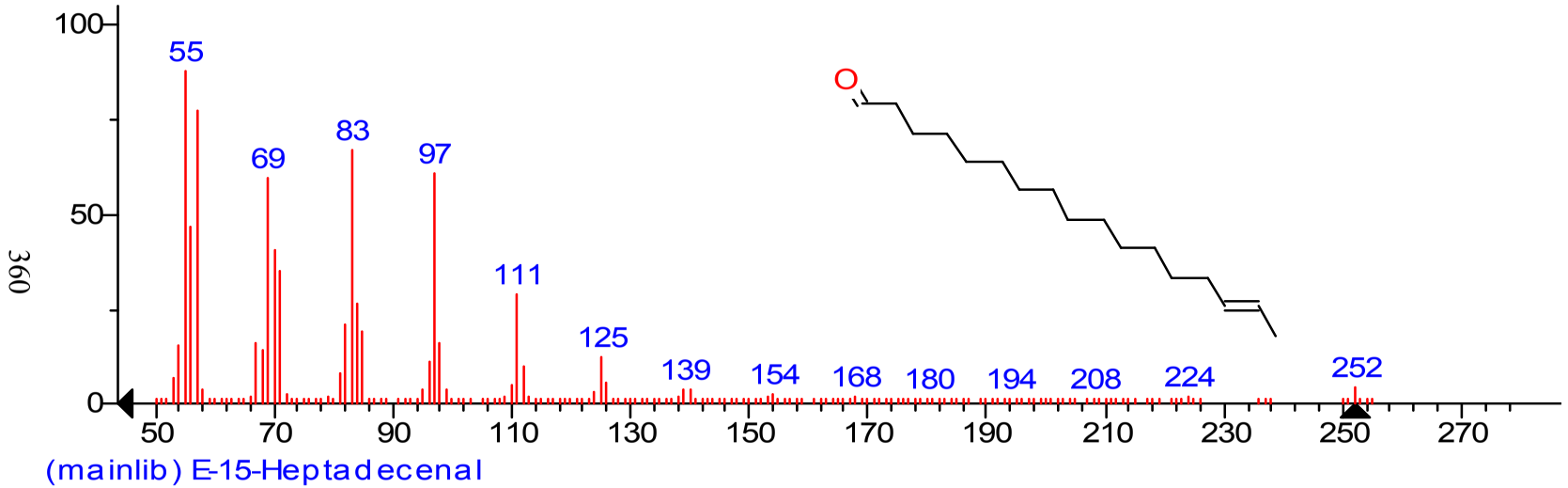

Name: E-15-Heptadecenal
Formula: C17H32O
MW: 252 CAS#: N/A NIST#: 130979
ID#: 5305 DB: mainlib